



Cruise Report

SIP-HOT II "Explorer"

(SIP-Hydrothermal deposit in Okinawa Trough)

CK16-01 (Exp. 908)



February 11 – March 17, 2016

This cruise report is a preliminary documentation as of the end of the cruise.

This report may not be corrected even if changes on contents (i.e. taxonomic classifications) may be found after its publication. This report may also be changed without notice. Data on this cruise report may be raw or unprocessed. If you are going to use or refer to the data written on this report, please ask the Co-Chief Scientists for latest information.

Users of data or results on this cruise report are requested to inform their results to the Planning and Coordination Unit, Project Team for Development of New-generation Research Protocol for Submarine Resources of JAMSTEC (sip-pc@jamstec.go.jp).

This report is to be cited as,

Kumagai, H., Nozaki, T., J.-i, Ishibashi, Maeda, L. and CK16-01 on-board member (2017) Cruise Report SIP-HOT II "Explorer" (SIP-Hydrothermal deposit in Okinawa Trough) CK16-01 (Exp. 908), JAMSTEC, pp. 443, Yokosuka, Japan,
(http://www.godac.jamstec.go.jp/catalog/data/doc_catalog/media/CK16-01-908_all.pdf).

CK16-01 Cruise Report Contents

1 Introduction

- 1.1 Scientific Backgrounds and Objectives (Kumagai /Nozaki/Ishibashi)
- 1.2 Geological settings and backgrounds (Kumagai /Nozaki/Ishibashi)
- 1.3 Site survey (Tsuji)
 - 1.3.1 Iheya-North Knoll
 - 1.3.2 Southern flank of the Iheya-Minor Ridge
- 1.4 Drilling strategy (Kumagai/Nozaki)
 - 1.4.1 Noho Site
 - 1.4.2 Iheya North Knoll

2 Logging while drilling (Saito/LWD Team)

- 2.1 Methods
 - 2.1.1 Tool descriptions
 - 2.1.2 Shipboard data flow and quality check
 - 2.1.3 Depth calibration for bit resistivity
- 2.2 Site C9017
 - 2.2.1 Logging data quality
 - 2.2.2 Log characterization
 - 2.2.3 Borehole images
 - 2.2.4 Temperature and pressure
- 2.3 Site C9018
 - 2.3.1 Logging data quality
 - 2.3.2 Log characterization
 - 2.3.3 Temperature and pressure
- 2.4 Site C9019
 - 2.4.1 Logging data quality
 - 2.4.2 Log characterization
 - 2.4.3 Temperature and pressure
- 2.5 Site C9020
 - 2.5.1 Logging data quality
 - 2.5.2 Log characterization
 - 2.5.3 Temperature and pressure
- 2.6 Site C9021
 - 2.6.1 Logging data quality

- 2.6.2 Log characterization
 - 2.6.3 Borehole image characterization
 - 2.6.4 Temperature and pressure
 - 2.7 Site C9022
 - 2.7.1 Logging data quality
 - 2.7.2 Log characterization
 - 2.7.3 Borehole images
 - 2.8 Site C9023
 - 2.8.1 Logging data quality
 - 2.8.2 Log characterization
 - 2.8.3 Borehole images
 - 2.8.4 Temperature and pressure
- 3 Downhole Measurements (Kitada/Wu)
 - 3.1 Temperature measurement in the borehole by TRDT
 - 3.1.1 Tool descriptions
 - 3.1.2 Experimental Site C9017C
 - 3.1.3 Experimental Site C9021B
 - 3.1.4 Experimental Site C9023E
 - 3.2 Geothermal Tool (PPS71)
 - 3.2.1 Tool descriptions
 - 3.2.2 Experimental Site C9017C
 - 3.2.3 Experimental Site C9021B
 - 3.2.4 Experimental Site C9023E
 - 3.3 Summary
- 4 ROV Operations (Masaki/Nozaki/Watanabe/Tanikawa/Hamada/Kinoshita/CDEX member)
 - 4.1 Summary of ROV operations
 - 4.2 Seabed survey by ROV video camera
 - 4.3 Deployment of the temporal flowmeter and Kuroko cultivation apparatus
 - 4.3.1 Temporal flowmeter
 - 4.3.2 Second generation Kuroko cultivation apparatus at the Hole C9024A
 - 4.3.3 Hybrid-type 2nd generation Kuroko cultivation apparatus at the Hole C9017B
 - 4.4 Data of temporal flowmeter
 - 4.5 Deployment of SAHF and POODLE
 - 4.5.1 Specification of SAHF

- 4.5.2 Specification of POODLE
 - 4.5.3 Operations of SAHF and POODLE deployment
 - 4.6 Independent hydraulic power unit and other hydraulic power tools
- 5 Core Studies
 - 5.1 Visual Core Description, XRD and SEM
 - (Yamasaki/Takaya/Nagase/Tindell/Yonezu/Totsuka/Mukae/Uno)
 - 5.1.1 Methods
 - 5.1.2 Site C9017
 - 5.1.3 Site C9019
 - 5.1.4 Site C9021
 - 5.1.5 Site C9023
 - 5.1.6 SEM observation (Nagase)
 - 5.2 X-ray computed tomography (XCT) data (Takaya/Yamasaki)
 - 5.2.1 Methods
 - 5.2.2 Hole C9017C
 - 5.2.3 Hole C9019B
 - 5.2.4 Hole C9019C
 - 5.2.5 Hole C9021B
 - 5.2.6 Hole C9023B
 - 5.2.7 Hole C9023D
 - 5.2.8 Hole C9023E
 - 5.3 Physical properties (Masaki/PP Team)
 - 5.3.1 Methods
 - 5.3.2 Site C9017
 - 5.3.3 Site C9019
 - 5.3.4 Site C9021
 - 5.3.5 Site C9023
 - 5.4 Interstitial water (Toki/IW Team)
 - 5.4.1 Interstitial water extraction
 - 5.4.2 Analytical method
 - 5.4.3 Analytical results
 - 5.5 Gas Geochemistry and Microbiology (Abe/Hirai/Kato/Nakagawa/Nunoura/Tasumi)
- 6 Operation (Kumagai/Maeda/Kido/Aoike)
 - 6.1 Summary of operations

6.2 Operation log of Leg. 1

- 6.2.1 Transit to Nago Bay
- 6.2.2 Operations in Iheya Small Ridge
- 6.2.3 Operations in Iheya North Knoll
- 6.2.4 Transit to Nago Bay

6.3 Operation log of Leg. 2

- 6.3.1 Exchange of members
- 6.3.2 Operation in Iheya Small Ridge
- 6.3.3 Operation in Iheya North Knoll
- 6.3.4 Sailing to Shimizu Port

Appendix

A-1 VCD Sheets

A-2 Log of thermo seals

Chapter 1: Introduction

1.1. Scientific Backgrounds and Objectives

H. Kumagai, T. Nozaki, and J.-i. Ishibashi

The earth system has developed throughout its history, and generally directed to enhancement of its heterogeneity, in other words the system differentiates as a result of the evolution. The hydrothermal activity is an essential phenomenon to drive geochemical differentiation on the Earth's surface within such a process. Not only has it acted as the very driver of such differentiation, some of the submarine resources are also the products of such a phenomenon. It means some anomalously concentrated elements or minerals are very valuable for resources for our civilization. There are several types of such resources even in submarine environment.

Here, volcanogenic massive sulfide (VMS) deposit is one of the major producers for Cu, Pb, Zn, Au and Ag resources, and occurs as in the worldwide geological strata formed from the Archean to Cenozoic eras (Slack, 1993; Sato and Kase, 1996; Mosier et al., 2009). There has been many Kuroko-type VMS deposits whose wallrocks are silicic volcanic rocks in the Japanese Island, especially in the Hokuroku Area, northeastern district of Japan (Sato, 1972; Ohmoto, 1996; Yamada and Yoshida, 2011). The modern analogue of such a Kuroko-type VMS deposit is considered to be a seafloor massive sulfide (SMS) deposit in an arc/back-arc setting (and/or rifting setting) (Halbach et al., 1989; Ishibashi et al., 2015; Nozaki et al., 2016). Since these SMS deposits in a back-arc setting are characterized by relatively shallower water depth and polymetallic mineralization, they have a high potential as new Cu, Pb, Zn, Au and Ag resources (Hannington et al., 2011). Three scientific drilling programs of ODP Leg 139, 158 and 169 targeting the metallogenic study on SMS at a mid-ocean ridge such as the Juan de Fuca and Mid-Atlantic Ridges have been conducted (Humphris et al., 1995; Zierenberg et al., 1998). Although three drilling cruises of the ODP Leg 193, IODP Exp. 331 and CK14-04 Cruise (Exp. 907) which target the seafloor hydrothermal deposits in an arc/back-arc setting were also performed in 2000, 2010 and 2014 (Binns et al., 2007; Takai et al., 2011), unraveling the subseafloor geological structures and comparative study with Kuroko-type VMS deposits on land are still hot topics because these studies are closely related with not only metallogenesis of VMS/SMS deposits but also developments of the effective exploration methods for subseafloor orebodies.

On the Iheya-North Knoll in the Okinawa Trough, an active hydrothermal vent complex was located in early 1990s. Since then, numbers of the expeditions to

investigate its activity. In late 2013 to early 2014, two new hydrothermal vent fields (Iheya-North Natsu and Aki Sites) were discovered through systematic exploration using a combination of acoustic equipment and chemical sensors (Kasaya et al., 2015; Nakamura et al., 2015). Moreover two drilling cruises of the IODP Exp. 331 and CK14-04 Cruise (Exp. 907) in 2010 and 2014 were conducted at the Iheya-North Knoll. A main research target of the IODP Exp. 331 was a subseafloor micro-biology, but a polymetallic massive sulfide ore was successively obtained from the flank of the NBC (North Big Chimney) mound (Takai et al., 2011). The main purpose of the CK14-04 Cruise (Exp. 907) was to investigate the distribution and connection of the subseafloor hydrothermal fluid reservoir covering the Iheya-North Original, Natsu and Aki Sites by using logging while drilling (LWD). Totally 211 m coring operation was also performed at the Holes C9015B, C9015C and C9016B as well as LWD. Comparative study between LWD data and core petrography/geochemistry implies that the subseafloor structure of the Iheya-North Knoll was composed by multi-layers of hemi-pelagic sediment, acidic and neutral hydrothermally altered clay and sulfide mineral-bearing cap rock (?) layers (Nozaki et al., 2015; Saito et al., 2015). Repeated occurrences of these layers detected by the CK14-04 Cruise and drilling operations during the IODP Exp. 331 and CK14-04 Cruise strongly suggest that subseafloor hydrothermal fluids flow laterally along with upper and bottom cap rocks, possibly leading the formation of several layers-ore bodies observed at the Matsumine deposit that is the largest Kuroko-type VMS deposit in the Japanese Island.

In this drilling expedition, eight holes for coring operations with/without LWD are proposed to comprehend the subseafloor geological structures and its related polymetallic mineralization. Our target areas are the Iheya-North Knoll and Noho Site that spreads on a southern flat basin from the Iheya-Minor Ridge. In the Iheya-North Knoll, we aim to sample systematically in order to provide a reliable set of physico-chemical property to utilize for SIP goals. It should include further investigation of distribution and connection of the subseafloor hydrothermal reservoir among three hydrothermal sites (Original, Natsu and Aki Sites) by additional LWD operations at the medium positions of these three sites in succession to the CK14-04 Cruise (Exp. 907). The Noho Site locates in a southern flat basin, vicinity of a sediment-covered rifting center at the Iheya-Minor Ridge. By four coring and three LWD operations along with the N-S transect starting from the active center of hydrothermalism, we aim to understand the alteration zonation and polymetallic subseafloor mineralization controlled by distances from the up-welling center of the hydrothermal site like as observed at a sediment-covered mid-ocean ridge (Bent Hill

deposit, Middle Valley). In this project, a typical T.D. for coring is planned down to 100 mbsf to investigate a large scale seafloor structures around the site and to obtain typical lithological samples such as unaltered and altered sediment, hydrothermal clay and massive sulfide layers. A planned T.D.s of precedent LWD operations is ca. 200 mbsf. Here, to obtain the physical property data on board, especially of massive sulfides, are given one of the highest priorities in this expedition for future collaboration with exploration geophysics. For example, an electromagnetic (EM) survey is prospective method to investigate sizes and distributions of the seafloor orebodies. As well as LWD, we plan to apply other geothermal logging tools (TRDT and PPS71) to measure seafloor temperature, pressure, flow rate of fluids and total gamma-ray intensity during/after the coring operations. Moreover, we are planning to install two long term monitoring systems both at the Iheya-North Koll and at the Noho Site. Secular changes of temperature, pressure and flow rate of hydrothermal fluids as well as a weight of sulfides precipitates within the volume during the flow paths will gives us insightful information toward the future Kuroko-ore cultivation project using artificial hydrothermal vents.

As the one of the prominent findings at IODP Exp. 331 “Deep-hot biosphere,” and its succession, SIP HOT I “Pathfinder” (CK14-04), a km-wide fluid reservoir may extend beneath Iheya-North Knoll (Takai et al., 2011; Kumagai et al., 2015). This implication was mainly derived from unexpected discharge of hydrothermal fluid. If such a reservoir extends beneath to the newly located two hydrothermal sites, their spatial scale exceeds a few kilometer in length, which corresponds to the scale of Kuroko-type VMS deposit on land. If it is the case, the spatial and textural discrepancy between land and submarine sulfide deposits may be resolved.

References:

- Binns, R. A., Barriga, F. J. A. S. and Miller, D. J. (2007) Leg 193 synthesis: anatomy of an active felsic-hosted hydrothermal system, eastern Manus Basin, Papua New Guinea. *Proc. ODP, Sci. Res.*, **193**, 1-17.
- Halbach, P., Nakamura, K. Wahsner, M., Lange, J., Sakai, H., Käselitz, L., Hansen, R.-D., Yamano, M., Post, J., Prause, B., Seifert, R., Michaelis, W., Teichmann, F., Kinoshita, M., Märten, A., Ishibashi, J., Czerwinski, S. and Blum, N. (1989) Probable modern analogue of Kuroko-type massive sulphide deposits in the Okinawa Trough back-arc basin. *Nature*, **338**, 496-499.
- Hannington, M., Jamieson, J., Monecke, T., Petersen, S. and Beaulieu, S. (2011) The

- abundance of seafloor massive sulfide deposits. *Geology*, **39**, 1155-1158.
- Humphris, S. E., Herzig, P. M., Miller, D. J., Alt, J. C., Becker, K., Brown, D., Burgmann, G., Chiba, H., Fouquet, Y., Gemmell, J. B., Guerin, G., Hannington, M. D., Holm, N. G., Honnorez, J. J., Iturrino, G. J., Knott, R., Ludwig, R., Nakamura, K., Petersen, S., Reysenbach, A.-L., Rona, P. A., Smith, S., Sturz, A. A., Tivey, M. K. and Zhao, X. (1995) The internal structure of an active sea-floor massive sulphide deposit. *Nature*, **377**, 713-716.
- Ishibashi, J.-I., Ikegami, F., Tsuji, T. and Urabe, T. (2015) Hydrothermal activity in the Okinawa Trough back-arc basin: Geological background and hydrothermal mineralization. *Subseafloor Biosphere Linked to Hydrothermal Systems*, 337-359.
- Kasaya, T., Machiyama, H., Kitada, K. and Nakamura, K. (2015) Trial exploration for hydrothermal activity using acoustic measurements at the North Iheya Knoll. *Geochem. J.*, **49**, 597-602.
- Kumagai, H., Takai, K., Kubo, Y., Saito, S., Nozaki, T., Yamamoto, H., Yamasaki, T., Suzuki, K. and CK14-04 Cruise members (2015) A kick-off drilling expedition at Iheya-North Knoll in Ore Genesis study of Ocean Resources in SIP. JpGU Abstract.
- Mosier, D. L., Berger, V. I. and Singer, D. A. (2009) Volcanogenic massive sulfide deposits of the world-database and grade and tonnage models. *USGS Open-File Rep.*, 2009-1034.
- Nakamura, K., Kawagucci, S., Kitada, K., Kumagai, H., Takai, K. and Okino, K. (2015) Water column imaging with multibeam echo-sounding in the mid-Okinawa Trough: Implications for distribution of deep-sea hydrothermal vent sites and the cause of acoustic water column anomaly. *Geochem. J.*, **49**, 579-596.
- Nozaki, T., Ishibashi, J.-I., Shimada, K., Nagase, T., Takaya, Y., Kato, Y., Kawagucci, S., Watsuji, T., Shibuya, T., Yamada, R., Saruhashi, T., Kyo, M. and Takai, K. (2016) Rapid growth of mineral deposits at artificial seafloor hydrothermal vents. *Sci. Rep.*, **6**, 22163, doi: 10.1038/srep22163.
- Nozaki, T., Takaya, Y., Yamasaki, T., Totsuka, S., Tsutsumi, S., Ishibashi, J.-I., Takai, K., Kumagai, H., Kawagucci, S., Miyazaki, J., Masaki, Y., Kubo, Y., Suzuki, K. and CK14-04 Cruise members (2015) Lithology, constituent mineral, geochemical composition of the drilled core obtained by CK14-04 Cruise, Okinawa Trough. JpGU Abstract.
- Ohmoto, H. (1996) Formation of volcanogenic massive sulfide deposits: The Kuroko perspective. *Ore. Geol. Rev.*, **10**, 135-177.
- Saito, S., Sanada, Y., Moe, K., Kido, Y., Hamada, Y., Kumagai, H., Nozaki, T., Takai, K. and Suzuki, K. (2015) Identification and characterization of the active hydrothermal

- deposits in Okinawa Trough, SW Japan: Estimates from logging-while-drilling. AGU Fall Meeting Abstract.
- Sato, K. and Kase, K. (1996) Pre-accretionary mineralization of Japan. *The Island Arc*, **5**, 216-228.
- Sato, T. (1972) Model for ore-forming solutions and ore-forming environments: Kuroko vs. veins in Miocene "Green Tuff" region of Japan. *Geol. Surv. Jap. Bull.*, **23**, 457-466.
- Slack, J. F. (1993) Descriptive and grade-tonnage models for Besshi-type massive sulphide deposits. *Geol. Assoc. Canada Spec. Pap.*, **40**, 343-371.
- Takai, K., Mottl, M. J., Nielsen, S. H. and The Expedition 331 Scientists (2011) Proceedings of Integrated Ocean Drilling Program 331, Tokyo (Integrated Ocean Drilling Program Management International, Inc.), doi: 10.2204/iodp.proc.331.2011.
- Yamada, R. and Yoshida, T. (2011) Relationships between Kuroko volcanogenic massive sulfide (VMS) deposits, felsic volcanism, and island arc development in the northeast Honshu arc, Japan. *Miner. Deposita*, **46**, 431-448.
- Zierenberg, R. A., Fouquet, Y., Miller, D. J., Bahr, J. M., Baker, P. A., Bjerkgård, T., Brunner, C. A., Duckworth, R. C., Gable, R., Gieskes, J., Goodfellow, W. D., Gröschel-Becker, H. M., Guèrin, G., Ishibashi, J., Iturrino, G., James, R. H., Lackschewitz, K. S., Marquez, L. L., Nehlig, P., Peter, J. M., Rigsby, C. A., Schultheiss, P., Shanks III, W. C., Simoneit, B. R. T., Summit, M., Teagle, D. A. H., Urbat, M. and Zuffa, G. G. (1998) The deep structure of a sea-floor hydrothermal deposit. *Nature*, **392**, 485-488.

1.2 Geological settings and backgrounds

H. Kumagai, T. Nozaki, and J.-i. Ishibashi

The Okinawa Trough is a seafloor depression extending southwestward from the Kyushu Island, southwest Japan, of which fore-arc is the Islands of Ryukyu (Fig.1-2-1). There has been suggested two models of its evolutionary history. One model argues that its rifting started at the southern part and propagated northeastward (e.g. Glasby and Notsu, 2003 and references there in). Another model argues that its rifting started its middle part and propagated both north and southward. These models are to be investigated by further geological and geochronological studies. In either model, the Okinawa Trough is regarded to be in an initial rifting stage prior to the normal/stable seafloor spreading as a main stage of back arc basin formation starting from 6 - 9 Ma according to the "collision -lateral back arc opening model" (Letouzey and Kimura, 1985). Further, Sibuet et al. (1998) argued that the Okinawa Trough is in the second stage of its rifting since 2 Ma. In a framework of arc-back arc volcanism, the present day's volcanic front is at the eastern edge of the Okinawa Trough although exact position is still under arguments especially in the southern extension from the Tokara Islands. Recently, new model has been proposed: the volcanic front in the Okinawa Trough passes upon the Izena-Hole (Yokose, 2015). This new model seems to be consistent with the recent discovery rush of active hydrothermal field lining on the NE-SW trending centered by the Izena-Hole (see. Press-releases by JOGMEC, JCG and AIST).

The Iheya-North Knoll is a volcanic complex built on a flat plain near the Eurasian continental slope in the middle part of the Okinawa Trough (Figs.1-2-1 and -2). It has two peak points; those altitudes are almost similar, shallower than 800 m water depth (WD) at 126°55.7'E, 27°46.3N, 126°56.1'E, 27°48.0'N, respectively. These peaks are on respective N-S or W-E trending ridge formed as small dome volcanic features (ca. ~100 m in diameters), sometimes associating with small craters on the top. Such morphological feature suggests that its magmatic activity is mainly felsic. In fact, siliceous pumices were widely observed and retrieved in the shallow lithological units on the top of the knoll (Oiwane et al., 2008). Some of the pumiceous layers showed graded bedding for upward in the piston-cored samples associating with relatively high heat flow in the pre-drilling survey by JAMSTEC (Masaki et al., 2011). Further, a relatively fresh banded pumice was sampled at the site of KY08-01 HFPC-23, which suggests that the recent volcanic activity of the Knoll (KY08-01 Leg.3 Cruise Report). The sedimentary fills were also widely found in local topographic lows even on the top of the knoll.

The Iheya-Minor Ridge where the Noho Site occurs is an elongated topographic

high within the Iheya-Depression, middle Okinawa Trough (Fig.1-2-3). According to its regional morphology, the Iheya Minor Ridge seems to be an edifice of mafic volcanism; however, the local morphology obtained AUV bathymetry indicates rather felsic volcanism (Kumagai et al., 2013). In addition, some andesitic lava fragments were obtained in the sampling conducted in 1980s by a manned submersible Shinkai 2000 (Naka et al., 1989). This suggests that the position and general trend of the ridge controlled by the regional tectonic condition mainly stress field of the region; however, its magmatism seems to be influenced somehow under the regional rifting conditions and arc-back arc system of which chemistry generally having felsic and mafic bi-modal compositions (Ishizuka et al., 1990).

References:

- Glasby, G. P. and Notsu, K. (2003) Submarine hydrothermal mineralization in the Okinawa Trough, SW of Japan: an overview. *Ore Geol. Rev.*, **23**, 299-339.
- Ishizuka, H., Kawanobe, Y. and Sakai, H. (1990) Petrology and geochemistry of volcanic rocks dredged from the Okinawa Trough, an active back-arc basin. *Geochem. J.*, **24**, 75-92.
- Kawagucci, S., Miyazaki, J., Nakajima, R., Nozaki, T., Takaya, Y., Kato, Y., Shibuya, T., Konno, U., Nakaguchi, Y., Hatada, K., Hirayama, H., Fujikura, K., Furushima, Y., Yamamoto, H., Watsuji, T., Ishibashi, J. and Takai, K. (2013) Post-drilling changes in fluid discharge, mineral deposition patterns and fluid chemistry for the seafloor hydrothermal activity in the Iheya-North hydrothermal field, Okinawa Trough. *Geochem. Geophys. Geosyst.*, **14**, 4774-4990.
- Kumagai, H., Machiyama, H., Nishio, Y., Nakamura, K., Kawagucci, S., Okamura, K., Tsuji, T., Kasaya, T., Asada, M., Masaki, Y. and Takai, K. (2013) Preliminary report on exploration of hydrothermalism near Iheya-Minor Ridge (YK12-16), Blue Earth 2013, Tokyo, March 2013 (w/ abstract in Japanese).
- Letouzey, J. and Kimura, M. (1985) Okinawa Trough genesis: structure and evolution of a backarc basin developed in a continent. *Mar. Petrol. Geol.*, **2**, 111-130.
- Masaki, Y., Kinoshita, M., Inagaki, F., Nakagawa, S. and Takai, K. (2011) Possible kilometer-scale hydrothermal circulation within the Iheya-North field, mid-Okinawa Trough, as inferred from heat flow data. *JAMSTEC Rep. Res. Develop.*, **12**, 1-12.
- Naka, J. (1989) Volcanic products of the Iheya Ridge, Central Okinawa Trough. *JAMSTEC Deep-Sea Res.*, **5**, 245-257.
- Oiwane, H., Kumagai, H., Masaki, Y., Tokuyama, H. and Kinoshita, M. (2008)

Characteristics of sediment in Iheya North Knoll and the acoustic blanking layer.
JpGU Abstract.

Sibuet, J.-C., Deffontaines, B., Hsu, S.-K., Thureau, N., Le Formal, J.-P., Liu, C.-S. and ACT party (1998) Okinawa trough backarc basin: Early tectonic and magmatic evolution. *J. Geophys. Res.*, **103**, 30245-30267.

Yokose, H. (2015) Quaternary submarine volcanism of northern Ryukyu island arc. In annual meeting of the Geological Society of Japan 2015 Abstract (in Japanese), The geological society of Japan, Nagano, September 2015.

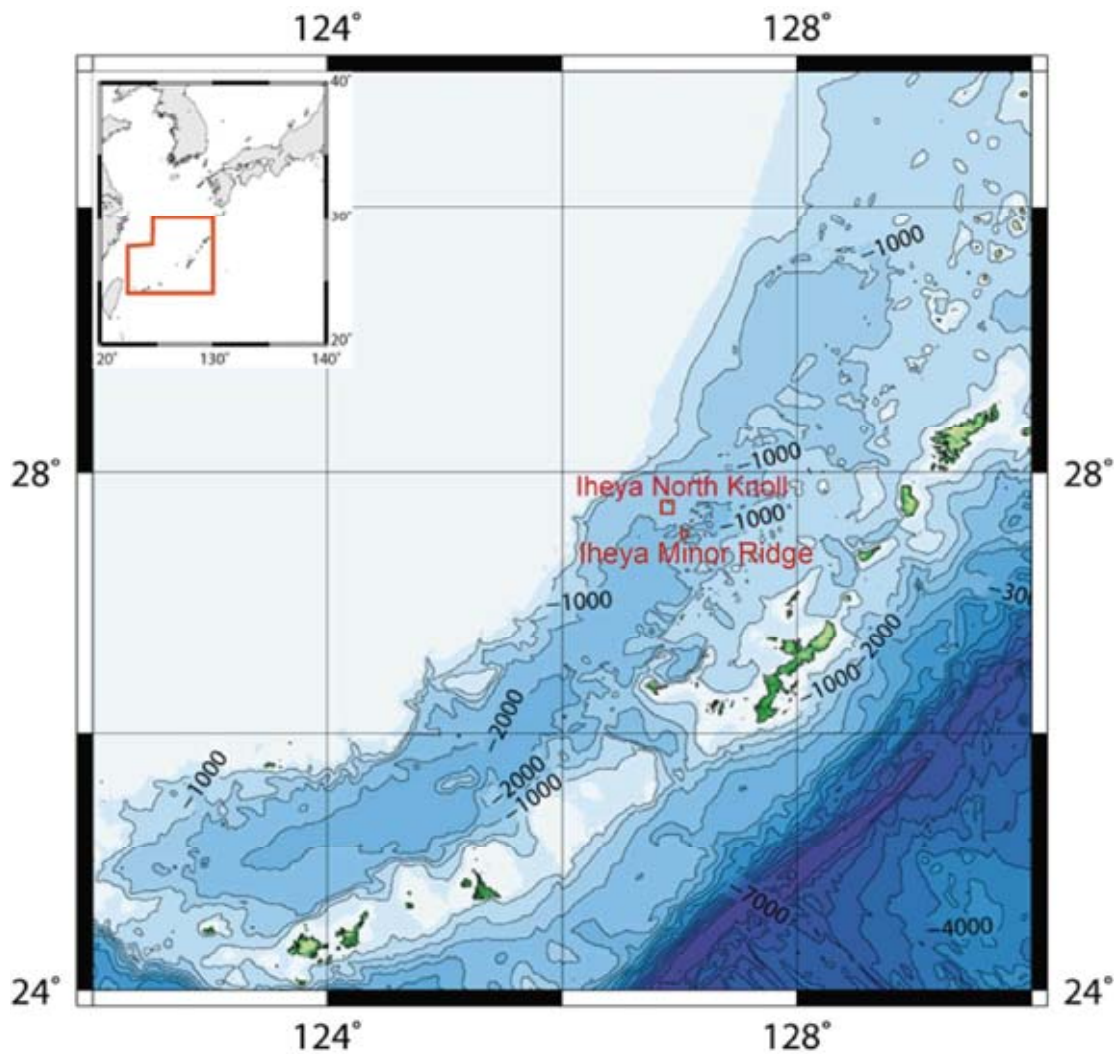


Figure 1-2-1: Topographic map of Okinawa Trough. Respective Iheya North Knoll and Iheya Minor Ridge is at an area indicated small red rectangular in the main panel, of which area is magnified in Figures 1-2-2 and 1-2-3.

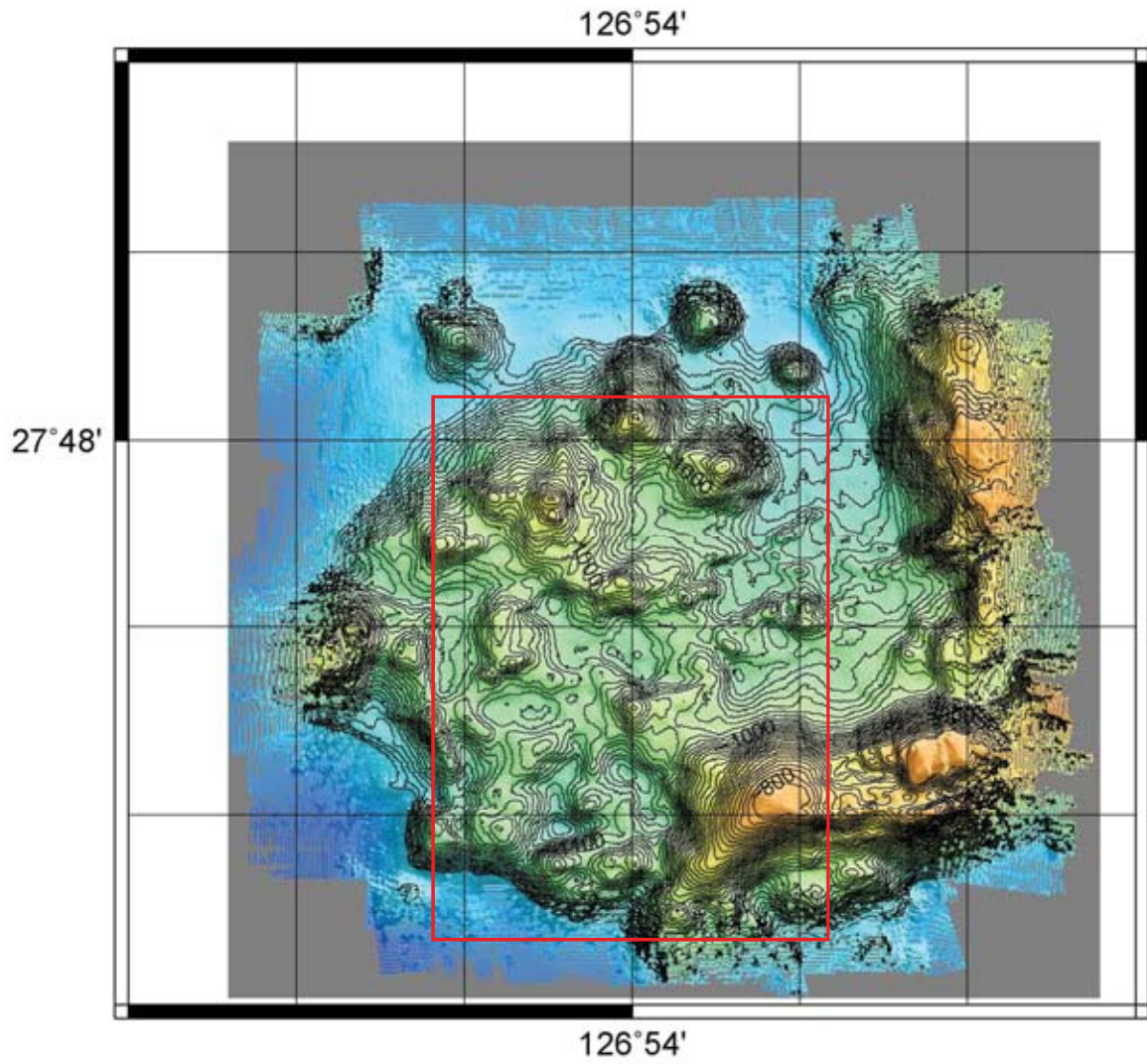


Figure 1-2-2: Bathymetric map of Iheya North Knoll. The area indicated as a red frame is magnified in Figure 1-3-1-1. Data were taken by R/V Natsushima at NT13-22 cruise. Here, the grid intervals are 1 nautical miles.

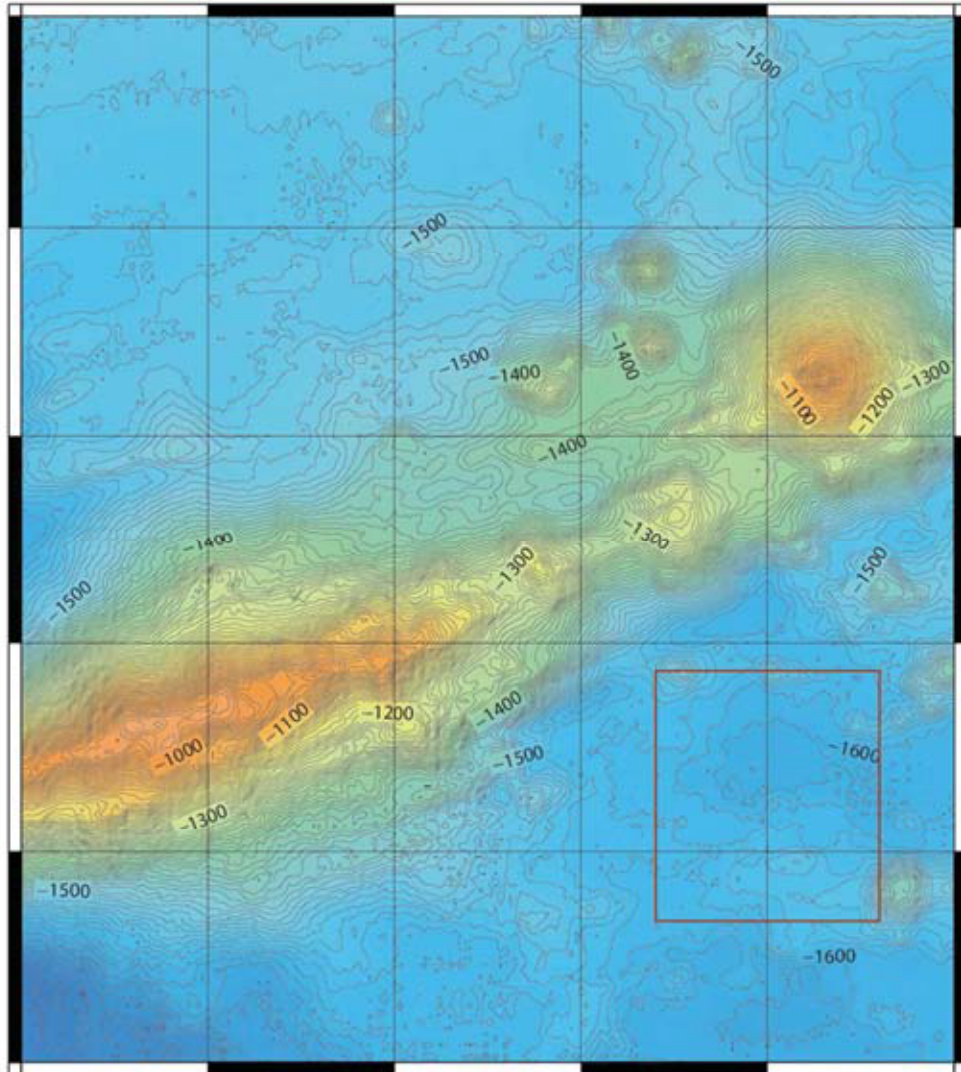


Figure 1-2-3: bathymetric map of southern flank of Iheya-Minor Ridge. The area indicated as a red frame is magnified in Figure 1-3-2-1. Data were taken by R/V Yokosuka at YK14-17 cruise.

1.3 Site Survey

T. Tsuji

1.3.1 Iheya-North Knoll

A grid of multichannel seismic (MCS) and single-channel seismic (SCS) profiles has been completed for the region of the Iheya North Knoll prior to the IODP Exp.331 (Fig.1-3-1-1; Takai et al., 2011; Tsuji et al., 2012).

We used multi-channel seismic data acquired during the YK07-03 cruise to characterize drilling sites at the Iheya North Knoll (Fig.1-3-1-2). A 48-channel, 1200-m-long streamer cable was used in this seismic survey. The source is GI airgun with ~5.8 L (355 cubic-inches). The seismic data were processed with a conventional processing sequence that included spherical divergence correction, deconvolution, common midpoint (CMP) sorting, normal moveout (NMO) correction, multiple suppression with a Radon filter, CMP stacking, migration, and bandpass filtering.

The seismic profiles shown in Figs.1-3-1-3, -4 and -5 were across LWD sites (Sites C9021, C9022 and C9023) for east-west direction. These seismic profiles show some characteristic reflection features at these sites. At the Hole C9021A, the shallower interval (< 70 m) is characterized as low reflectivity zone, which extends to the eastern low-amplitude mound. The deeper section is characterized as high amplitude reflectors dipping to east. At the Hole C9022A, the strong reflections are observed through the LWD interval. In the deeper interval (>100 mbsf), the east-dipping reflectors are observed. The Hole C9023A is located at the west edge of the low amplitude mound. High amplitude reflectors are continuously distributed from seafloor to 300 mbsf. Since this borehole is a little far from the seismic line (~400 m), we cannot compare with LWD results in detail.

The detailed bathymetry taken by the AUV Urashima mostly covers over the both studied areas of the Iheya North Knoll with much better than 1 m resolution: SeaBat7126 Multi-Beam Echo Sounder (MBES, Figs.1-3-1-3, -4 and -5). Using the AUV obtained ultra-high resolution bathymetries, detailed distribution of hydrothermal mounds and volcanic edifices are well mapped even in the newly recognized two hydrothermal fields: Iheya-North Natsu and Aki sites. Outside of the coverage of the Urashima MBES survey, bathymetric data taken by a ship-hulled MBES of R/Vs *Natsushima* or *Yokosuka* also covers. Also, numerous ROV or HOV dives have been conducted in the area. Such bottom observations are markedly helpful to choose the drilling sites. Details will be described in the section 1.4., Drilling Strategy.

Iheya North "Original" Site

The Iheya North Original Site was found in 1995 by a deep-tow survey (Momma et al., 1996). Its vents and mounds were located in elongated area trending NNW-SSE including approximately 10 active vents or mounds on the eastern flank of one of the peak of the knoll between 960 - 1000 m WD. Although the entire distribution is on the area, however, active and inactive vents align NNE-SSW locally (Fig.1-3-1-6). In the IODP Exp.331, five sites were drilled that align approximately on a track trending E-W. Within the 24 holes drilled, four became a kind of conduit of the discharging hydrothermal fluid, i.e. the artificial vents: the Holes C0013E, C0014G and C0016A and C0016B, which suggests an enormous fluid reservoir beneath the Iheya-North Original site. On those holes, secular variations of temperature, fluid chemistry, benthic megafauna and chimney formation were investigated (Kawagucci et al., 2013; Nakajima et al., 2015; Nozaki et al., 2016).

Iheya North Natsu Site

This site was newly found in January 2014 by a suite of MBES survey and ROV dives (Kasaya et al., 2015; Nakamura et al., 2015). Sea-floor surveys by ROV were still limited, however, an active chimney and several dead chimneys were located (Fig.1-3-1-7). This site is in a small depression at the almost the center of the knoll where sediment covers significantly.

Iheya North Aki Site

This site was also newly found in January 2014 by a suite of MBES survey and ROV dives (Kasaya et al., 2015; Nakamura et al., 2015). Sea-floor surveys by ROV were still limited; however, numerous active and dead chimneys, benthic colonies, bacterial mats, and crusts of native sulfur were well located (Fig.1-3-1-8). In comparison with the other two sites, this Aki-site is the largest hydrothermal field on the Iheya North Knoll. This site also develops in a small depression near the edge of the knoll where sediment covers significantly.

Further in the last expedition, the CK14-04 cruise of SIP, the enormous fluid reservoir should extend much widely connecting with all three hydrothermal sites beneath the Iheya-North Knoll (e.g., Kumagai et al., 2015). Because any full lines of evidences were not available for this interpretation, at least the connections between the Original-Natsu and Natsu-Aki sites should be investigated in this expedition.

1.3.2 Southern flank of the Iheya-Minor Ridge

Contrasting to the area of the Iheya-North Knoll, the seismic surveys in the area of the southern flank of the Iheya-Minor Ridge are quite limited (Figure 1-3-2-1; Ikegami et al., 2015). There is no grid survey of seismic reflection to date. Only one ridge perpendicular MCS track is available.

We used single-channel seismic data acquired during the YK12-16 cruise for characterization of drilling sites. The seismic profile shown in Figure 1-3-2-2 is in time-domain. The low quality of this seismic profile precludes us to interpret the detailed interpretation. The high amplitude reflectors of the seafloor at drilling sites indicate stiffer lithology and layered sequence.

Noho Site

The Noho-site is located on a flat plain extending from the southern flank of the Iheya-Minor Ridge (Figure 1-2-3). There are several trends of hydrothermal mounds formed by venting and collapse of hydrothermal chimney structures, mainly trending ridge parallel direction, ENE-WSW. Since its discovery, a few series of the ROV dive investigation were conducted (Miyazaki et al., 2015). Temperature of venting fluid in the area is mostly controlled by their water depth, which are higher than those of the Iheya-North Knoll.

References:

- Ikegami, F., Tsuji, T., Kumagai, H., Ishibashi, J.-i., and Takai, K. (2015) Active rifting structures in Iheya Graben and adjacent area of the Mid-Okinawa Trough observed through seismic reflection surveys. *Subseafloor Biosphere Linked to Hydrothermal Systems*, 361-368.
- Kasaya, T., Machiyama, H., Kitada, K. and Nakamura, K. (2015) Trial exploration for hydrothermal activity using acoustic measurements at the North Iheya Knoll. *Geochem. J.*, **49**, 597-602.
- Kawagucci, S., Miyazaki, J., Nakajima, R., Nozaki, T., Takaya, Y., Kato, Y., Shibuya, T., Konno, U., Nakaguchi, Y., Hatada, K., Hirayama, H., Fujikura, K., Furushima, Y., Yamamoto, H., Watsuji, T., Ishibashi, J. and Takai, K. (2013) Post-drilling changes in fluid discharge, mineral deposition patterns and fluid chemistry for the seafloor hydrothermal activity in the Iheya-North hydrothermal field, Okinawa Trough. *Geochem. Geophys. Geosyst.*, **14**, 4774-4990.
- Kumagai, H., Takai, K., Kubo, Y., Saito, S., Nozaki, T., Yamamoto, H., Yamasaki, T., Suzuki, K. and CK14-04 Cruise members (2015) A kick-off drilling expedition at

- Iheya-North Knoll in Ore Genesis study of Ocean Resources in SIP. JpGU Abstract.
- Miyazaki, J. and Shipboard Scientists of NT15-02, YK15-05 and NT15-13 (2015) An introduction of Noho-site, in InterRidge Japan Scientific Meeting (w/ abstract in Japanese), Kashiwa, December 2015.
- Momma, H., Iwase, R., Mitsuzawa, K., Kaiho, Y., Fujiwara, Y., Amitani, Y. and Aoki, M. (1996) Deep tow survey in Nanseisyoto Region (K95-07-NSS). *JAMSTEC J. Deep Sea Res.*, **12**, 196-210.
- Nakajima, R., Yamamoto, H., Kawagucci, S., Takaya, Y., Nozaki, T., Chen, C., Fujikura, K., Miwa, T. and Takai, K. (2015) Post-drilling changes in seabed landscape and megabenthos in a deep-sea hydrothermal system, the Iheya North field, Okinawa Trough. *PLoS ONE*, **10**, e0123095, doi:10.1371/journal.pone.012.
- Nakamura, K., Kawagucci, S., Kitada, K., Kumagai, H., Takai, K. and Okino, K. (2015) Water column imaging with multibeam echo-sounding in the mid-Okinawa Trough: Implications for distribution of deep-sea hydrothermal vent sites and the cause of acoustic water column anomaly. *Geochem. J.*, **49**, 579-596.
- Nozaki, T., Ishibashi, J.-I., Shimada, K., Nagase, T., Takaya, Y., Kato, Y., Kawagucci, S., Watsuji, T., Shibuya, T., Yamada, R., Saruhashi, T., Kyo, M. and Takai, K. (2016) Rapid growth of mineral deposits at artificial seafloor hydrothermal vents. *Sci. Rep.*, **6**, 22163, doi: 10.1038/srep22163.
- Takai, K., Mottl, M. J., Nielsen, S. H. and The Expedition 331 Scientists (2011) Proceedings of Integrated Ocean Drilling Program 331, Tokyo (Integrated Ocean Drilling Program Management International, Inc.), doi: 10.2204/iodp.proc.331.2011.
- Tsuji, T., Takai, K., Oiwane, H., Nakamura, Y., Masaki, Y., Kumagai, H., Kinoshita, M., Yamamoto, F., Okano, T. and Kuramoto, S. (2012) Hydrothermal fluid flow system around the Iheya North Knoll in the mid-Okinawa trough based on seismic reflection data. *J. Volcanol. Geotherm. Res.*, **213-214**, 41-50.

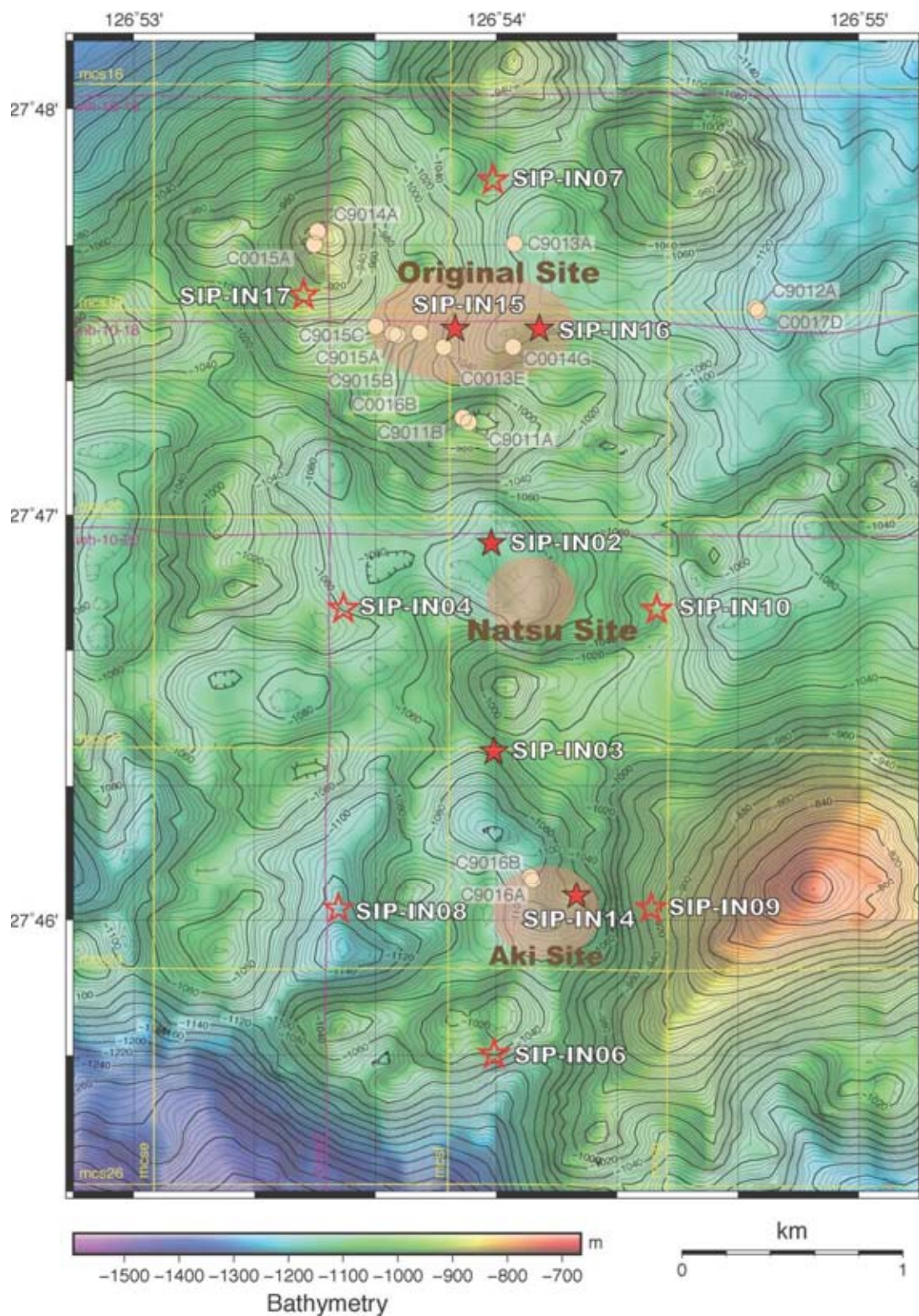


Figure 1-3-1-1 : Site-survey grid on Iheya-North Knoll conducted prior to IODP Exp. 331 and proposed sites in SIP HOT II expedition (CK16-01) with the positions of the legacy holes by IODP and SIP HOT I (filled yellow circles).

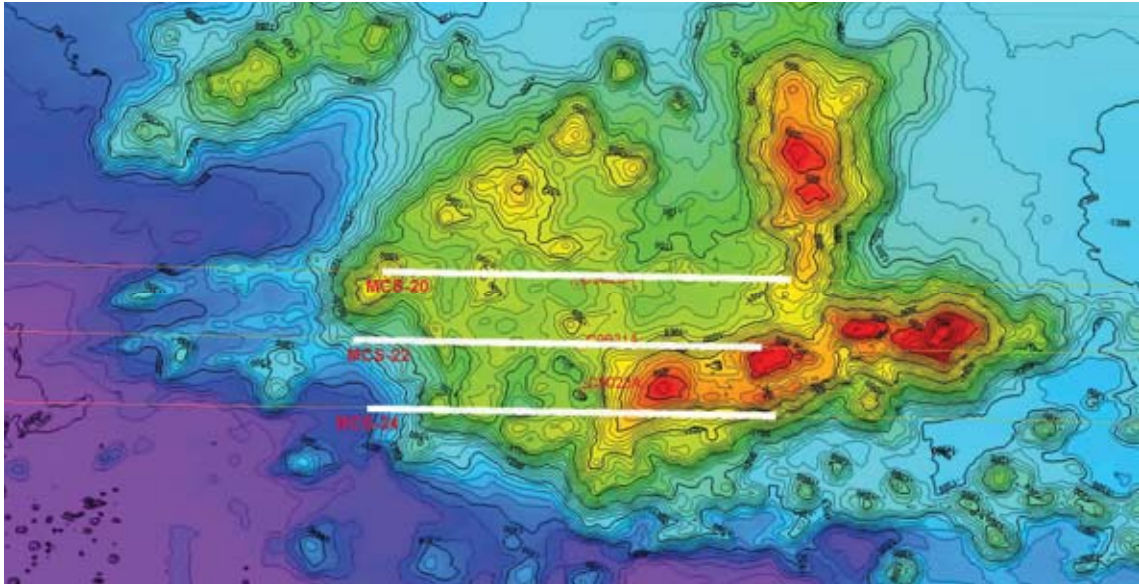


Figure 1-3-1-2: Bathymetric map of the Iheya North Knoll area showing seismic survey lines and well locations.

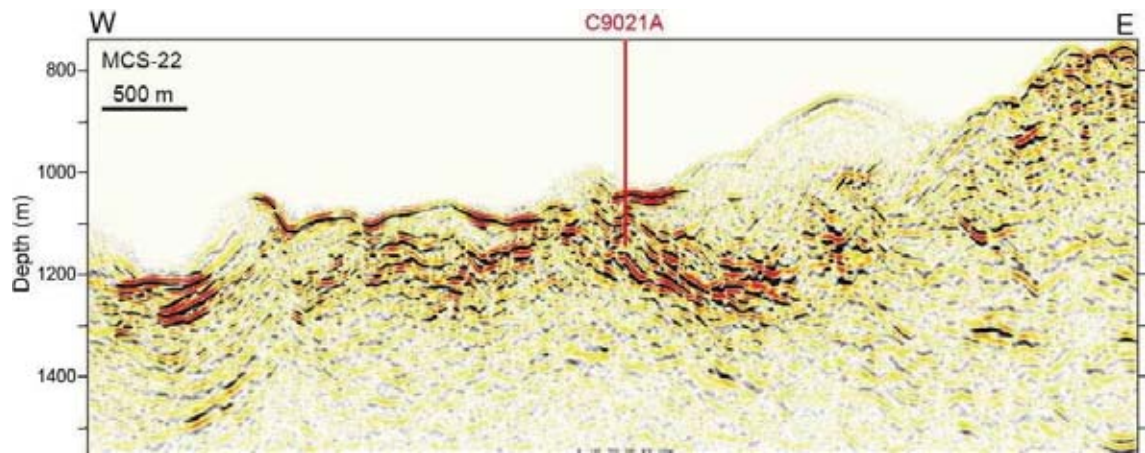


Figure 1-3-1-3: Depth-domain seismic reflection profile (KY07-03, MCS-22) across Hole C9021A. Location of this profile is in Figure 1-3-1-2.

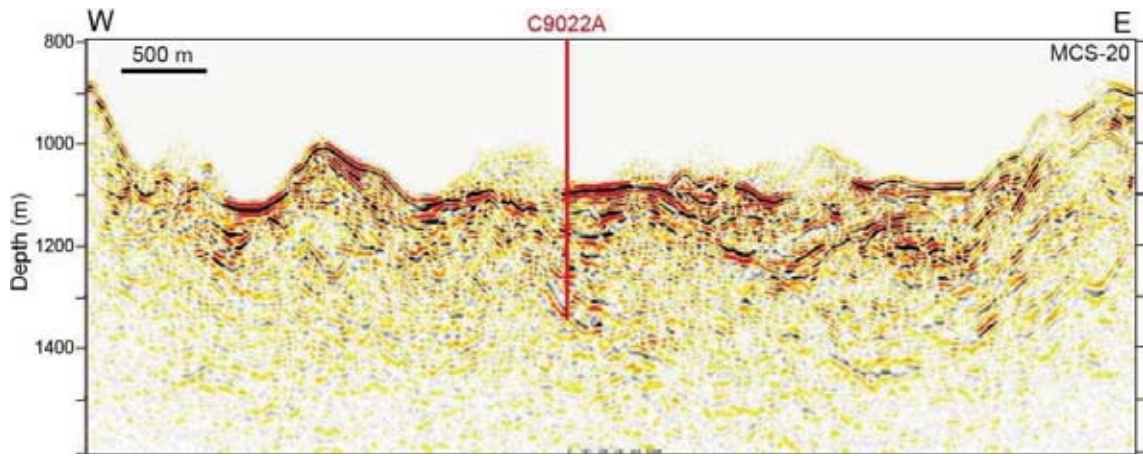


Figure 1-3-1-4: Depth-domain seismic reflection profile (KY07-03, MCS-20) across Hole C9022A. Location of this profile is in Figure 1-3-1-2.

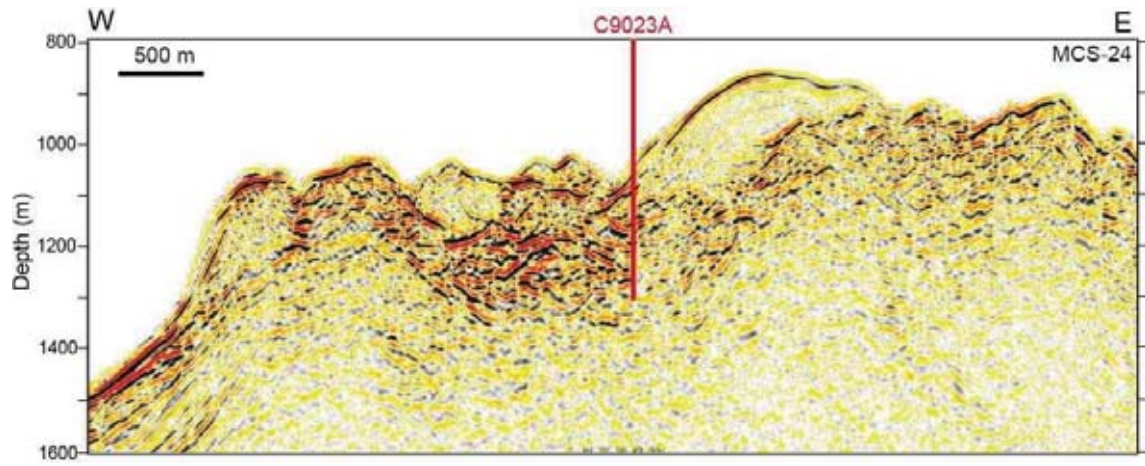


Figure 1-3-1-5: Depth-domain seismic reflection profile (KY07-03, MCS-24) across Hole C9023A. Location of this profile is in Figure 1-3-1-2.

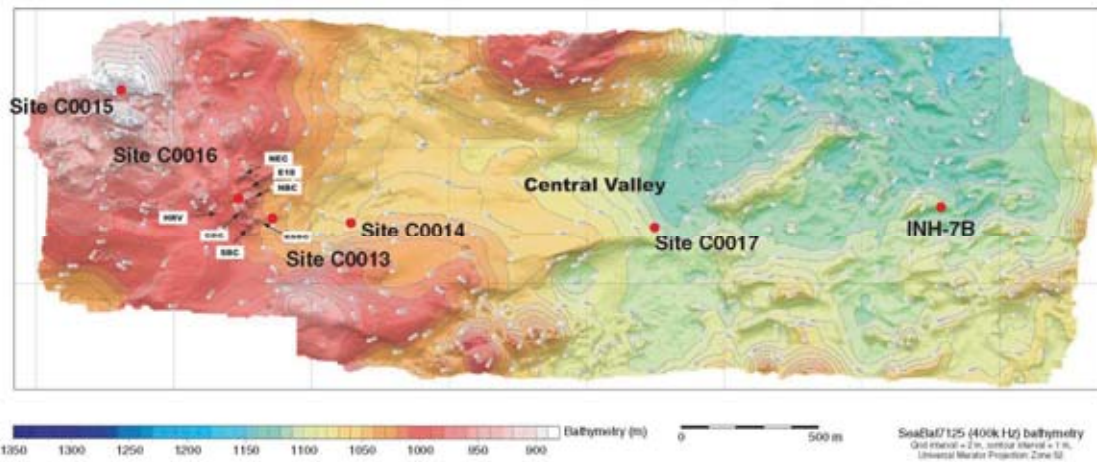


Figure 1-3-1-6: Detailed bathymetric map of Iheya-North Original Site. Data were taken by AUV Urashima, YK07-07.

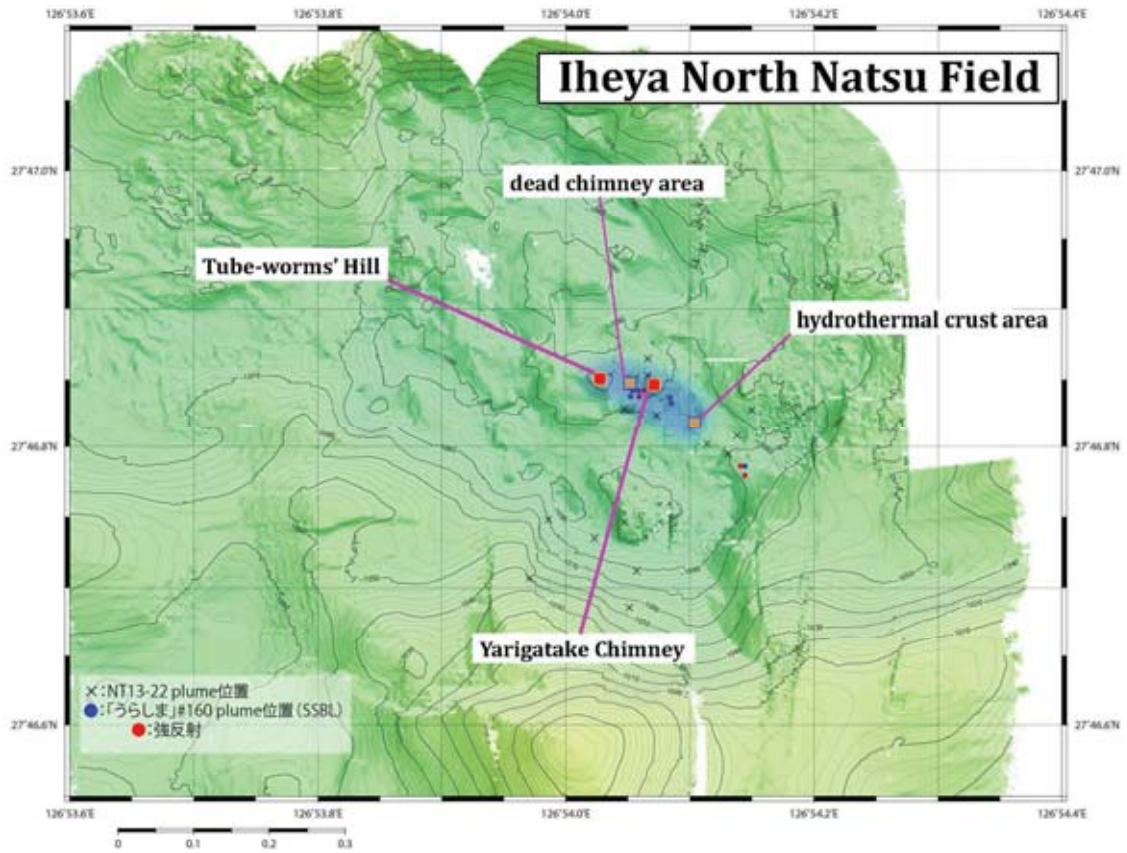


Figure 1-3-1-7: Detailed bathymetric map of Iheya-North Natsu-site. Data were taken by AUV Urashima, YK13-14.

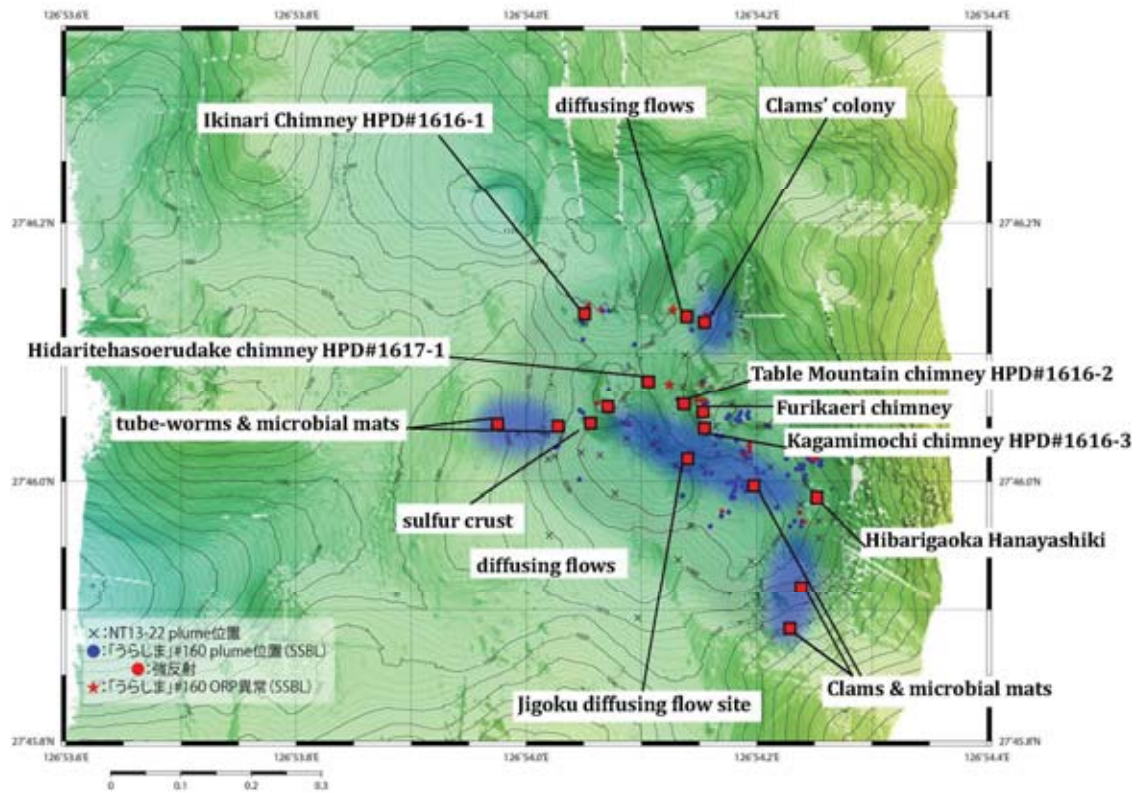


Figure 1-3-1-8: Detailed bathymetric of Iheya-North Aki-site. Data were taken by AUV Urashima, YK13-14.

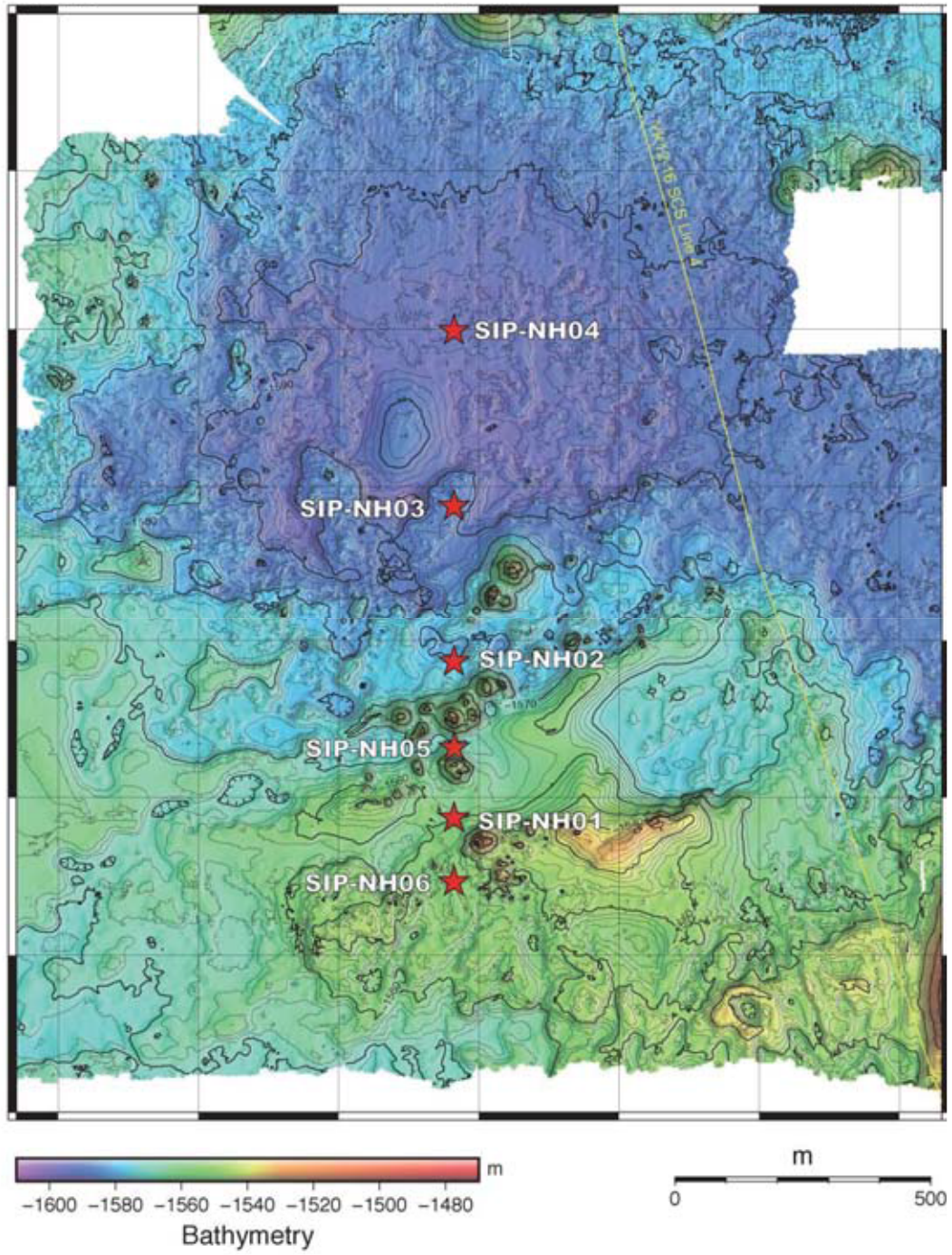


Figure 1-3-2-1: Site survey track on Noho-Site, southern flank of Iheya Minor Ridge. The proposed sites are shown as red stars.

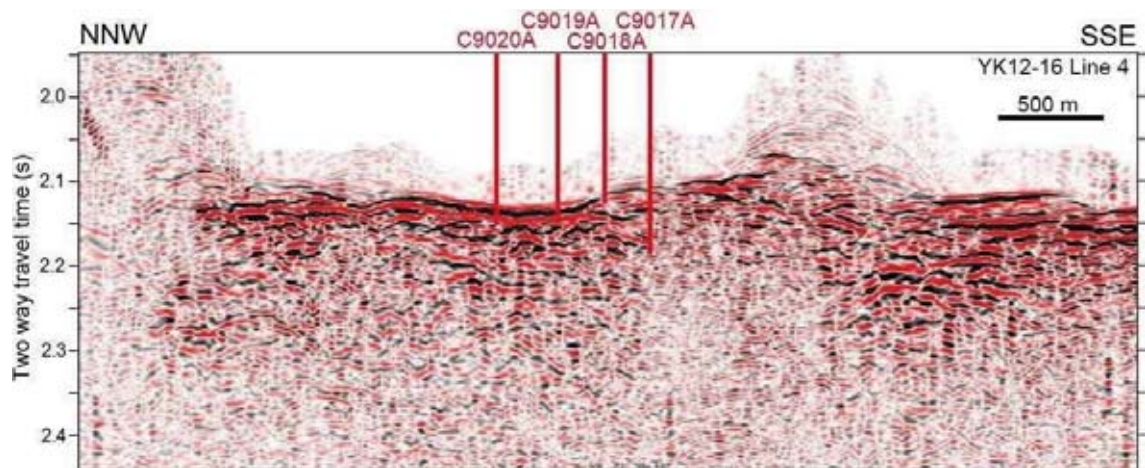


Figure 1-3-2-2: Time-domain seismic profile (YK12-16) across Holes C9017A, C9018A, C9019A and C9020A. Location of this profile is in Figure 1-3-2-1.

1.4 Drilling Strategy

H. Kumagai and T. Nozaki

We drilled seven sites for logging, two sites for installation of monitoring apparatus and four sites for coring during the CK16-01 cruise as following localities: four were in the Noho site (Sites C9017 - 9020; Figs.1-4-1 to 1-4-5); the other four were in the Iheya-North Knoll (Sites C9021 - 9024; Figs.1-4-6 to 1-4-10). The aims of the drilling were,

- 1) to investigate the universality and connectivity of vast hydrothermal reservoirs beneath the seafloor that potentially the place for ore-genesis, by applying LWD with resistivity image tools,
- 2) to obtain massive sulfide ore specimen to measure intact physical properties that will be provided to the development of remote sensing for future exploration instruments and techniques,
- 3) to install a "Kuroko-cultivation" apparatus for long term monitoring by forming additional artificial vents

Throughout these investigations, further characterization of ore-genesis environment and to evaluate the areas of hydrothermal fluid reservoir beneath both the areas of the Iheya-North Knoll and Noho Site will be executed. According to the results of the CK14-04 cruise, coring strategy with guiding LWD information becomes very efficient especially in case of very poor core recovery. Thus we firstly tried to conduct two series of LWD drilling both in the Noho Site and Iheya-North Knoll.

1.4.1 Noho Site

The Site C9017 was firstly chosen as a center of the area of active hydrothermal discharge mounds indicated as SIP-NH01 in the drilling plan (Fig.1-4-1). According to the seafloor observation by ROV, the site was re-chosen at the northern flank of the active mound. Instead, two observation apparatus (SAHF and POODLE) were set on seabed (See, ROV chapter). Finally, the spud point was determined on relatively flat terrace 20 m southwestward from the planned position (Fig.1-4-2).

Following the Sites 9018, 9019 and 9020 were firstly planned to make regular interval from the proposed SIP-NH01 to northward anticipated thermal gradient within the sediment cover. Here, the Site C9018 was planned as SIP-NH02. During the site survey of JAMSTEC-ROV, the vicinity of the site was mostly flat and covered hemi-pelagic

sediments (Fig.1-4-3). Even any pre-site survey was not available in the vicinity of the SIP-NH03, the proposed site was chosen as a mid-point within a flat plain; however, there was a rather big volcanic boulder stone in the vicinity. Thus, we tried to find much appropriate position for northeastward. Away from the original proposed position, the Hole C9019A was drilled 50 m away from the proposal position (Fig.1-4-4). The proposed SIP-NH04 was a LWD contingency site in the original plan. Unfortunately, precedent two sites had very hard layers just beneath the seafloor, which inhibited to the LWD tool penetration for observation. Thus we tried the most distant site from SIP-NH01 where the water depth was deepest in the Noho area. The planned position was the just foot of the mound, then, we circumvented the mound northeastward (Fig.1-4-5).

1.4.2 Iheya North Knoll

The Sites C9021 and C9022 were chosen to investigate connectivity of the hydrothermal reservoir beneath the Iheya-North Knoll. To approach this goal, both the sites were set between the active two sites: the Site C9021 is between the Aki and Natsu sites, the Site C9022 is the Natsu and Original sites (Figs.1-4-6,-7 and -8). Here the Site C9022 is set in a local depression that seems to be a volcanic crater. The Site C9023 was set to further comparison between LWD and core samples. Thus in this goal, the site was chosen near the top of the active mound having a very active chimney, "Hidarite ha soerudake (HSK)-chimney" only less than 10-m away from the chimney (Fig.1-4-9). The Site C9024 was selected on the hydrothermally altered plain where numerous cracks and discharging have been observed since the IODP Exp. 331 drilling. The site (C9024) is ca. 15 m south from the Hole C0014G (Fig.1-4-10).

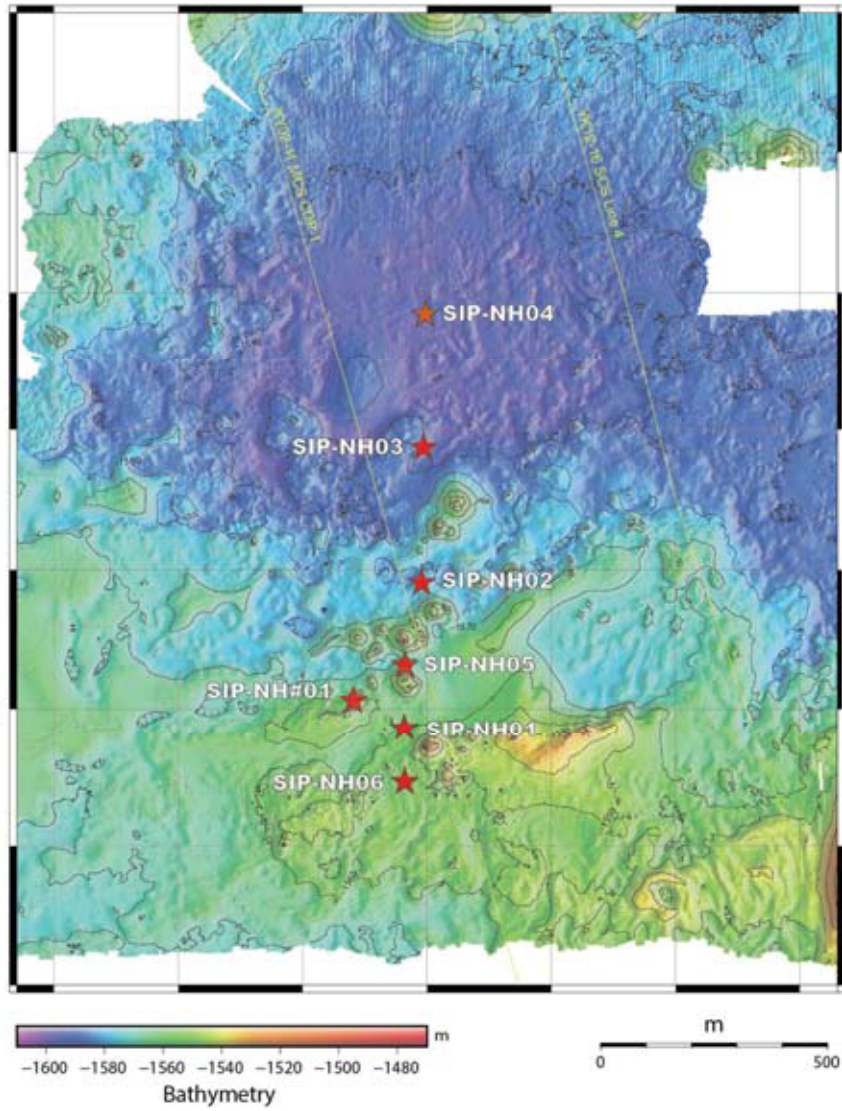


Figure 1-4-1: Proposed drill localities in southern flank of Iheya-Minor Ridge,

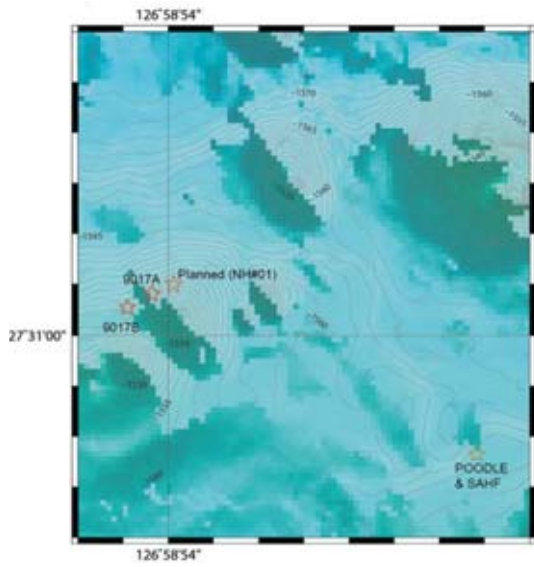


Figure 1-4-2: The 1st site drilled as site C9017.

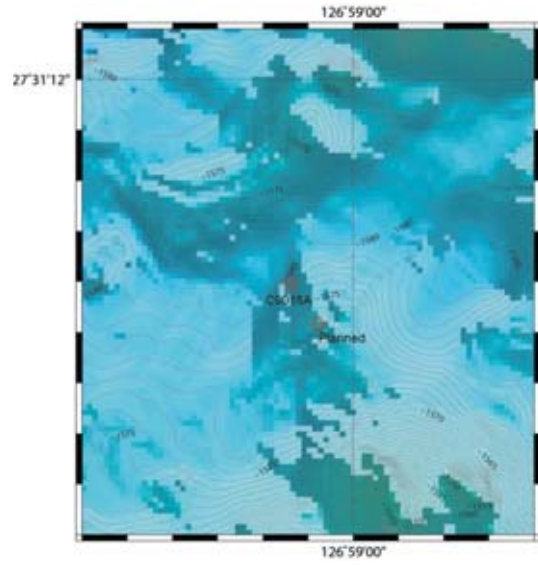


Figure 1-4-3: The 2nd site drilled as site C9018.

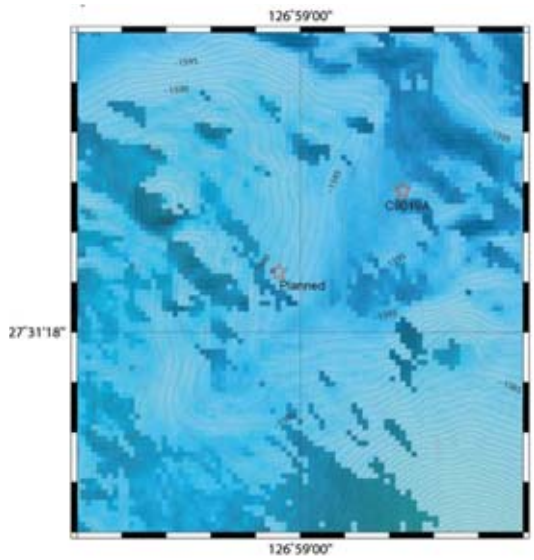


Figure 1-4-4: The 3rd site drilled as Site C9019.

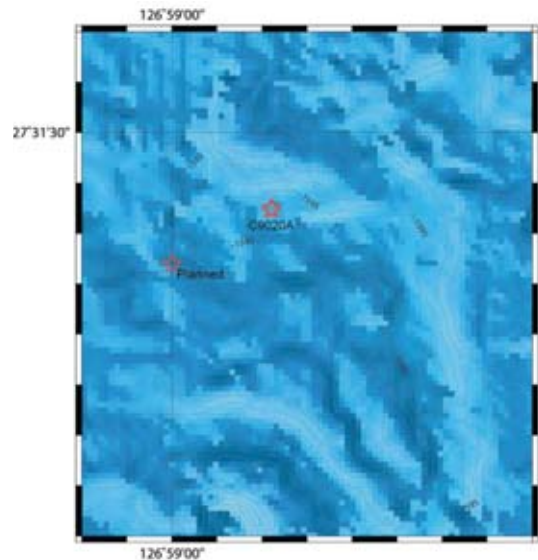


Figure 1-4-5: The 4th site drilled as Site C9020.

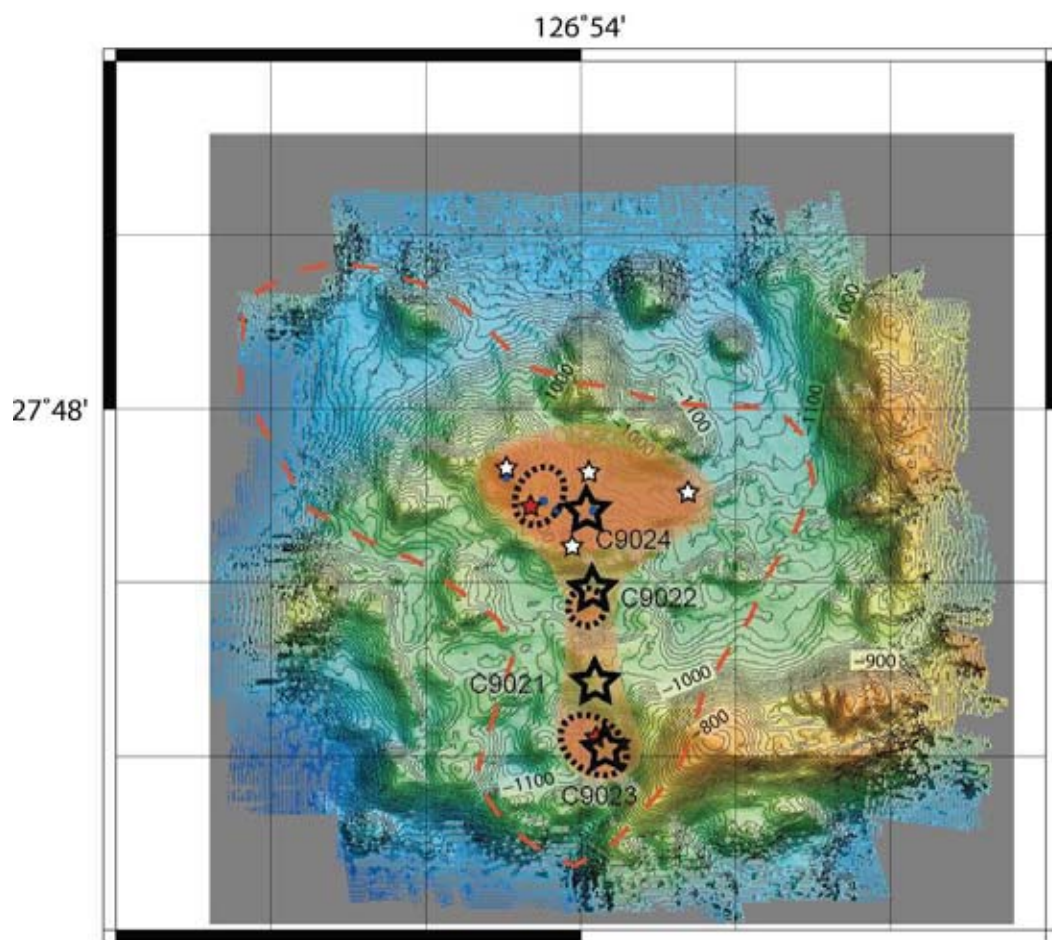


Figure 1-4-6: Position of newly drilled sites in CK16-01: open large stars. Small stars: sites drilled in CK14-04, blue dots: sites drilled in IODP Exp.331.

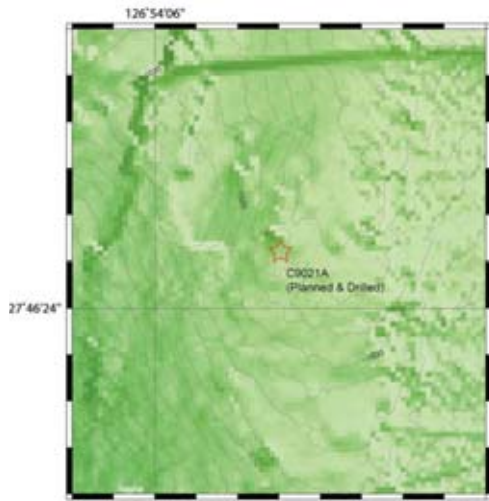


Figure 1-4-7: C9021A planned as SIP-NH03.

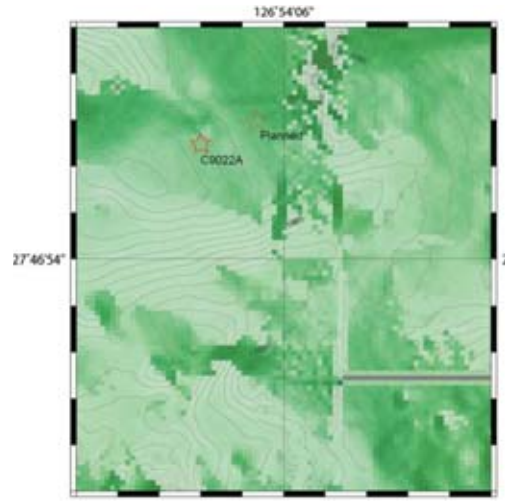


Figure 1-4-8: C9022A planned as SIP-NH02.

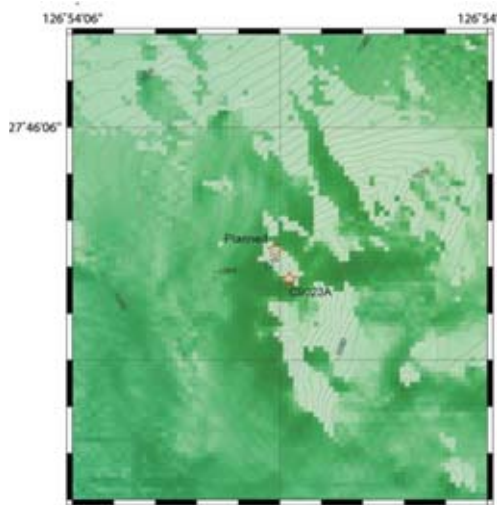


Figure 1-4-9: C9023A planned as SIP-NH14.

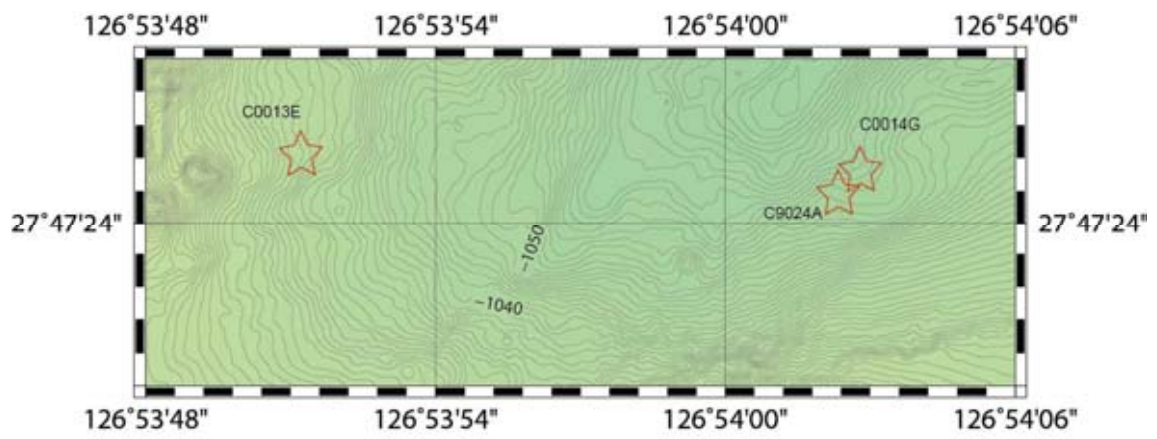


Figure 1-4-10: C9024A planned as SIP-NH16.

Chapter 2: Logging while drilling

S. Saito and LWD Team

2.1 Methods

2.1.1 Tool descriptions

Logging-while-drilling (LWD) tools are supplemented by a measurement-while-drilling (MWD) tool that is located above of the LWD tools in the bottom-hole assembly (BHA) and measures downhole drilling parameters and well bore direction. The MWD tool transmits the drilling parameters and a selected LWD data set by mud-pulse telemetry to the surface for real-time monitoring. Complete LWD data are recorded to downhole memory and retrieved when the tools are brought to the surface. LWD tools are usually powered by batteries or a drilling fluid turbine in MWD. However, we did not use lithium batteries for safety reason in this cruise, because high borehole temperature is expected due to hydrothermal fluids. The tools take measurements at regular time intervals and are synchronized with an acquisition system on the drilling rig that matches time with drilling depth. Drilling depth is determined using a drawworks encoder that measures the vertical motion of the top drive. After drilling, the LWD tools are retrieved and their data downloaded. The Schlumberger Maxwell logging system merges time and depth data (from the surface system) and the downhole time-measurement data (from the tools) into depth-measurement data files. Data files are then transferred to onboard log data processing and analysis team led by the logging staff scientists (LSS) for further processing using the Schlumberger's TechLog software and then passed to the hands of logging scientists for further interpretation. Expedition logging scientists tied these logs to core measurements and seismic data to help define lithofacies, structure, and physical properties (Kinoshita et al., 2009; Strasser et al., 2014). LWD and MWD data acquisition was conducted under contract by Schlumberger Drilling and Measurements Services.

The LWD and MWD tools used in this expedition were Schlumberger's arcVISION 675 (Resistivity) with Annular Pressure While Drilling (APWD) (annular borehole temperature and pressure), geoVISION (Resistivity, resistivity image and NGR [natural gamma ray]) and the MWD TeleScope 675 (drilling mechanics data and real-time telemetry) with APWD. All of these tools had a 6.75 inch (17.1 cm) diameter

and were located above an 8.5 inch (21.6 cm) drill bit. BHA had stabilizers to centralize the collars and keep measurement sensors near the borehole wall. **Fig. 2-1-1-1** and **Table 2-1-1-1** show the configuration of the LWD BHA and locations of the measurement sensors relative to the bit. The principal measurements recorded by each tool are listed in **Table 2-1-1-2**.

The measurement principles of these LWD tools are described below. LWD and MWD data were obtained to provide a wide range of in situ measurements and drilling parameters, including natural gamma ray, resistivity, borehole resistivity image, annular pressure and temperature. The advantage of LWD/MWD over wireline logging is that measurements are taken immediately after the borehole is drilled, thus minimizing the effects of disturbance and invasion of drilling mud into the formation. As target of this expedition is hydrothermal formations, LWD-MWD is only measurement can do while drilling under continuous circulation using non-stop driller (NSD) system. TeleScope and arcVISION were modified for 175 degC temperature proof from 150 degC standard. Key measurement, temperature from APWD is taken by two sensors from arcVISION and TeleScope from different positions. Combining these measurements with surface drilling parameters allows for improved real-time monitoring of drilling progress and assessment of data quality.

arcVISION tool

The arcVISION tool measures propagation resistivities. Electromagnetic waves are attenuated and phase-shifted when they propagate in an electrically conductive medium, and the degree of attenuation and phase-shift depends on the resistivity of the formation (Bonner et al., 1995, 1996). Phase-shift resistivity has relatively high vertical resolution and a shallow depth of investigation, whereas attenuation resistivity has lower vertical resolution and a greater depth of investigation. The dual-frequency (2 MHz and 400 kHz) array of coils in the arcVISION makes ten phase-shift and ten attenuation measurements at five transmitter-receiver separations of 16, 22, 28, 34, and 40 inches (40.6, 55.9, 71.1, 86.4, and 101.6 cm), which correspond to several depths of investigation. The measurement accuracy, range, depth of investigation and vertical resolution are shown in **Tables 2-1-1-3, -4, and -5**, respectively.

APWD

APWD can be mounted in TeleScope and arcVISION. APWD measures temperature and pressure of the borehole fluid in the annulus (the space between the drill string and the borehole wall). Annular pressure data were used to calculate the equivalent circulating density (ECD), which is the density of the drilling fluid during pumping. Changes in downhole pressure can reveal flow from or into the formation. Such pressure changes and flows are related to formation pressure and permeability and may indicate the presence of fractures. Measurement specifications of APWD are shown in **Table 2-1-1-6**.

geoVISION tool

The geoVISION tool provides laterolog-type resistivity measurements of the formation and high-resolution electrical resistivity images of the borehole wall. The tool contains two transmitter coils and three button electrodes for measurements of five depths of investigation. Bit resistivity has most deepest investigation depth. The lower transmitter coil generates a current that flows through the bit and into the formation, returning to the drill collar far up the tool string. By measuring the axial current through the bit for a given voltage, resistivity around the bit is determined based on Ohm's law. In the Bit resistivity measurement, tools, strings and bit connected below the geoVISION is used as an electrode. Ring resistivity shows both of moderate depth of investigation (7 in) and high vertical resolution (2–3 in). The upper and lower transmitter coils produce currents in the collar that flow out of the tool at the ring electrode. A 1.5-inch (3.8-cm) electrode located 129 cm from the bottom of the tool provides a focused lateral resistivity measurement. The same current-focusing system of the Ring resistivity is applied in the Button resistivity measurement. Three button electrodes are longitudinally located along the tool. The button electrodes provide three depths of resistivity investigation such as ~1 inches (shallow), 3 inches (middle), and 5 inches (deep) with resistivity image corresponding to the each investigation depth. **Tables 2-1-1-7 and -8** show specifications of the measurement accuracy, range, depth of investigation and vertical resolution of the geoVISION resistivity, respectively.

The geoVISION tool also contains a scintillation detector that provides an azimuthal total natural gamma ray measurement. The gamma ray sensor has a range of operability of 0–250 gAPI and an accuracy of $\pm 7\%$ corresponding to a statistical

resolution of ± 3 gAPI at 100 gAPI and ROP of 100 ft/h. Its depth of investigation is between 5 and 15 inches (**Table 2-1-1-9**).

TeleScope tool

The TeleScope MWD tool transmits data uphole through the fluid in the drill pipe in a process known as “mud-pulse telemetry.” A modulator in the tool generates a continuous 12 Hz pressure wave within the drilling fluid and changes the phase of this signal to transmit bit words encoding various measurements made by the MWD tool or by other LWD tools in the BHA. Three pressure transducers attached to the standpipe. The first one is at the active standpipe, the second is at the manifold next to the junction box, and the third is at NSD to acquire the pressure signal that is then decoded by the Schlumberger surface software. (2 sensors are standard when without NSD). The MWD real-time data transmission rate is adjustable, depending primarily on water depth and drilling fluid density, and was 6 bits/s during Expedition CK16-01.

In addition to transmitting uphole, selected measurements from the other LWD tools, the TeleScope acquires operational and drilling mechanics data, including collar rotation per minute, drilling fluid turbine rotation per minute, stick and slip, and axial and torsional vibration. The TeleScope also contains a turbine that powers the entire LWD string when drilling fluid is circulated at a sufficient flow rate (300–600 gal/min).

2.1.2 Shipboard data flow and quality check

For each LWD/MWD operation, two types of data were collected: (1) real-time data that include all MWD data and selected LWD data and (2) LWD data recorded downhole and stored in the tool’s memory. Data are originally recorded downhole at a preset sampling interval, and no depth information is recorded in the tool. The depth-referenced version is obtained after merging the time (downhole) with the time-depth relationship recorded on the surface by the Maxwell system. All the depth-converted data for LWD/MWD are provided in digital log information standard (DLIS) format by the field engineers.

After determining the depth of the mudline based on the gamma ray and resistivity logs, the depth reference for all logging data was shifted from the rig floor to

the seafloor (LWD depth below seafloor [mLSF]). The depth-shifted versions of the LWD/MWD data are available in DLIS format, and the main scalar logs were extracted and converted into log ASCII standard (LAS) files. All files were distributed to the shipboard scientists through the shipboard data servers. The geoVISION resistivity image data were processed on board the *Chikyu* using Schlumberger's TechLog software. Logging staff scientists used drilling control logs to identify the sequence of drilling events and assess any possible impact on data quality. Drilling control logs include drilling surface parameters (e.g., ROP, surface weight on bit [SWOB], hook load [HKLD], and standpipe pressure [SPPA]) and downhole drilling parameters (e.g., collar [bit] rotation [CRPM], hole deviation [HDEVI], radial shock rate [SKR_R], tangential shock rate [SKR_T], shock peak [SHKPK], and stick-slip indicator [SLIP]). Elapsed time of the main geophysical measurements after bit penetration, including annular pressure and temperature logs, were also assessed to identify any anomalous zones. Tool rotation was also checked; it must be higher than 35 rpm to allow good quality azimuthal measurements and associated images. In zones of high stick-slip, even if CRPM is set to a typical value of 100 rpm, it can greatly vary locally (and exceed 250 rpm), resulting in lower quality images.

2.1.3 Depth calibration for bit resistivity

In the first LWD measurement at C9017A, depth difference was observed between bit resistivity and other resistivity data acquired by geoVISION. This difference was caused by the long distance between the bit and the geoVISION. In order to compare those resistivity data acquired in Expedition CK16-01 properly, we applied a depth calibration to the bit resistivity with 6 meters' upward shift based on distance between drill bit and sensor for the bit resistivity.

For the standard LWD deployment, geoVISION is equipped just above the drill bit (**Fig. 2-1-3-1a**). An advantage of the bit resistivity measurement is that the resistivity response can be detected in advance to the other resistivity measurements for optimal and safe drilling. During Expedition CK16-01 another LWD tool, arcVISION was equipped between the drill bit and geoVISION in order to measure temperature and pressure earlier than other properties. Therefore, the distance between the source (drill bit) and sensor (tool bottom), about 12 meters, is longer than the standard configuration (**Fig. 2-1-3-1b**). An appropriate depth calibration is required for the meaningful comparison of all

resistivity data.

Based on the assumption that the data projection point is located at the middle point between the bottom of the bit and the bit resistivity sensor, two possible shift values were tested for the bit resistivity depth calibration (**Figs. 2-1-3-1a and b**). From this comparison, the appropriate depth shift is approximately 6 meters upward, if a sharp resistivity change at the seafloor is used as an indicator for the calibration. This result means that '*usual*' depth calibration between bit resistivity and ring resistivity was applied, but '*additional*' depth calibration should be applied for the specific tool configuration deployed during Expedition CK16-01. By comparing with ring resistivity smoothed by moving average with different window length (**Fig. 2-1-3-2**), the long-wavelength variation of the bit resistivity variation is similar to the long-wavelength trend of ring resistivity, while absolute values are different. These characteristics reflect the difference of spatial resolution and horizontal penetration depth by using the long distance resistivity measurement.

Preliminary investigation for the depth calibration of the bit resistivity in the nonstandard configuration has done. Further evaluation on the difference in absolute values between the bit resistivity and other resistivity data should be continued for effective use of the information.

References:

- Bonner, S., Fredette, M., Lovell, J., Montaron, B., Rosthal, R., Tabanou, J., Wu, P., Clark, B., Mills, R., and Williams, R., 1996. Resistivity while drilling - images from the string. Schlumberger, Oilfield Review 8, no1, p.p. 4-19.
- Bonner, S., Tabanou, J., Wu, P., Seydoux, J., Moriarty, K., Seal, B., Kwok, E., and Kuchenbecker, M., 1995. New 2-MHz multiarray borehole-compensated resistivity tool developed for MWD in slim holes. Proc. SPE Annu. Tech. Conf., Pap. SPE 30547.
- Kinoshita, M., Tobin, H., Ashi, J., Kimura, G., Lallemand, S., Sreaton, E.J., Curewitz, D., Masago, H., Moe, K.T., and the Expedition 314/315/316 Scientists, 2009. Proc. IODP, 314/315/316: Washington, DC (Integrated Ocean Drilling Program Management International, Inc.). doi:10.2204/iodp.proc.314315316.2009.
- Strasser, M., Dugan, B., Kanagawa, K., Moore, G.F., Toczko, S., Maeda, L., and the Expedition 338 Scientists, 2014. Proc. IODP, 338: Yokohama (Integrated Ocean Drilling Program). doi:10.2204/iodp.proc.338.2014.

Captions:

- Table 2-1-1-1: Sensor offsets from drill bit.
- Table 2-1-1-2: MWD-LWD tool acronyms, descriptions, and units.
- Table 2-1-1-3: arcVISION resistivity accuracy and range.
- Table 2-1-1-4: arcVISION resistivity depth of investigation.
- Table 2-1-1-5: arcVISION resistivity vertical resolution.
- Table 2-1-1-6: APWD sensor resolution and accuracy.
- Table 2-1-1-7: geoVISION resistivity accuracy and range.
- Table 2-1-1-8: geoVISION resistivity depth of investigation and vertical resolution.
- Table 2-1-1-9: geoVISION gamma ray range, resolution and accuracy.
- Fig. 2-1-1-1: Configuration of the LWD-BHA for Expedition CK16-01.
- Fig. 2-1-3-1: Schematics of resistivity measurements by geoVISION tool. (a) Standard LWD configuration. (b) Special LWD configuration for Expedition CK16-01.
- Fig. 2-1-3-2: Comparison between ring resistivity and bit resistivity at C9017A (a) with 7.3 m depth shift and (b) with 6.0 m depth shift. (c) Comparison between averaged ring resistivity and depth shifted bit resistivity.

Table 2-1-1-1: Sensor offsets from drill bit.

Sensor	Offset [m]	
	C9017A C9018A C9019A	C9020A C9021A C9022A C9023A
APWD	7.52	7.70
ARC Resistivity	8.24	8.41
GVR Gamma Ray	12.92	13.01
Ring Resistivity	13.28	13.37
BD Resistivity	13.45	13.54
BM Resistivity	13.45	13.54
BS Resistivity	13.45	13.54
MWD APWD	19.28	19.44
D+I	19.28	19.44

Table 2-1-1-2: MWD-LWD tool acronyms, descriptions, and units.

Tool	Output	Description	Unit
Surface		Drilling parameter	
	BD	Bit Depth	m
	TD	Total Depth	m
	TVD	True Vertical Depth	m
	HKLD	Hookload	kkgf
	SPPA	Standpipe Pressure	kkgf
	ROP*5	5 feet average of Rate of Penetration	m/h
	SWOB	Surface weight on bit	kkgf
MWD (TeleScope+APWD)		Measurements while drilling	
	CRPM	Average MWD collar RPM	rpm
	SHKR	Shock Rate	
	SHKRSK	Shock Risk	1/s
	STICK	Stick Slip Indicator	c/min
	DHAP	Downhole Annular Pressure	kPa
	DHAT	Downhole Annular Temperature	°C
	RGX	Rotating Axial Accelerometer	rpm
	RHX	Rotating Axial Magnetometer	rpm
arcVISION+APWD memory		Array resistivity tool	
	AXXH, AXXL	Attenuation resistivity at source-receiver spacing XX, where XX=16, 22, 28, 34, and 40 inches. H: high frequency (2MHz). L: Low frequency (400kHz).	ohm-m
	PXXH, PXXL	Phase-shift resistivity at source-receiver spacing XX, where XX= 16, 22, 28, 34, and 40 inches. H: high frequency (2MHz). L: Low frequency (400kHz).	ohm-m
	SHKL	Tool Shock Level	
	SHKR	Shock Rate	1/s
	DHAP	Downhole Annular Pressure	kPa
	DHAT	Downhole Annular Temperature	°C
	ECD	Equivalent Circulating Density	g/cc
	TAB_RES	Resistivity Time After Bit	h

Table 2-1-1-3: arcVISION resistivity accuracy and range.

Measurement	Accuracy	Range
2 MHz phase-shift resistivity	+2%	0.2-60 ohm.m
	+/- 0.3 mS/m	60-3000 ohm.m
400 kHz phase-shift resistivity	+2%	0.1-10 ohm.m
	+/- 2 mS/m	10-100 ohm.m
2MHz attenuation resistivity	+3%	0.2-25 ohm.m
	+/- 1.5 mS/m	25-50 ohm.m
400kHz attenuation resistivity	+3%	0.1-3 ohm.m
	+/- 10 mS/m	3-10 ohm.m

Table 2-1-1-4: arcVISION resistivity depth of investigation.

Measurement	Spacing [in]				
	16	22	28	34	40
R = 1.0 ohm.m (depth of investigation in dadii and in)					
2 MHz phase-shift resistivity	13	14	15	17	18
400 kHz phase-shift resistivity	17	19	22	25	27
2 MHz attenuation resistivity	19	22	24	26	29
400 kHz attenuation resistivity	27	30	33	36	38
R = 10 ohm.m (depth of investigation in dadii and in)					
2 MHz phase-shift resistivity	18	22	25	28	30
2 MHz attenuation resistivity	31	34	36	38	40

Table 2-1-1-5: arcVISION resistivity vertical resolution.

Measurement	Spacing [in]				
	16	22	28	34	40
R = 1.0 ohm.m (vertical resolution values in ft)					
2 MHz phase-shift resistivity	0.7	0.7	0.7	0.7	0.7
400 kHz phase-shift resistivity	1.0	1.0	1.0	1.0	1.0
2 MHz attenuation resistivity	1.8	1.8	1.8	1.8	1.8
400 kHz attenuation resistivity	3.0	3.0	3.0	3.0	3.0
R = 10 ohm.m (vertical resolution values in ft)					
2 MHz phase-shift resistivity	1.0	1.0	1.0	1.0	1.0
2 MHz attenuation resistivity	4.0	5.0	6.0	6.0	6.0

Table 2-1-1-6: APWD sensor resolution and accuracy.

Resolution	1 psi
Accuracy	0 to 0.1% of fullscale
Available ranges	0 to 20,000 psi
Annular temperature resolution	1 degC
Annular temperature accuracy	1 degC

Table 2-1-1-7: geoVISION resistivity accuracy and range.

Measurement	Accuracy below 2000 ohm-m	Accuracy above 2000 ohm-m	Range
Bit resistivity	+5%	+20%	0.2-20000 ohm.m
Ring resistivity	+5%	+20%	0.2-20000 ohm.m
Azimuthal button electrode resistivity	+5%	+20%	0.2-1000 ohm-m

Table 2-1-1-8: geoVISION resistivity depth of investigation and vertical resolution.

Measurement	Depth of investigation [in]	Vertical response [in]
Bit resistivity	>12	>12-24
Ring resistivity	7	2-3
Button Deep resistivity	5	2-3
Button Medium resistivity	3	2-3
Button Shallow resistivity	1	2-3

† Sensor offset from bit is set as longer than that of the recommended assembly

Table 2-1-1-9: geoVISION gamma ray range, resolution and accuracy.

Range	Statistical resolution	Vertical resolution	Accuracy
0-250 gAPI	+3 gAPI at 100 gAPI and 100ft/h	1.5 in	+7%

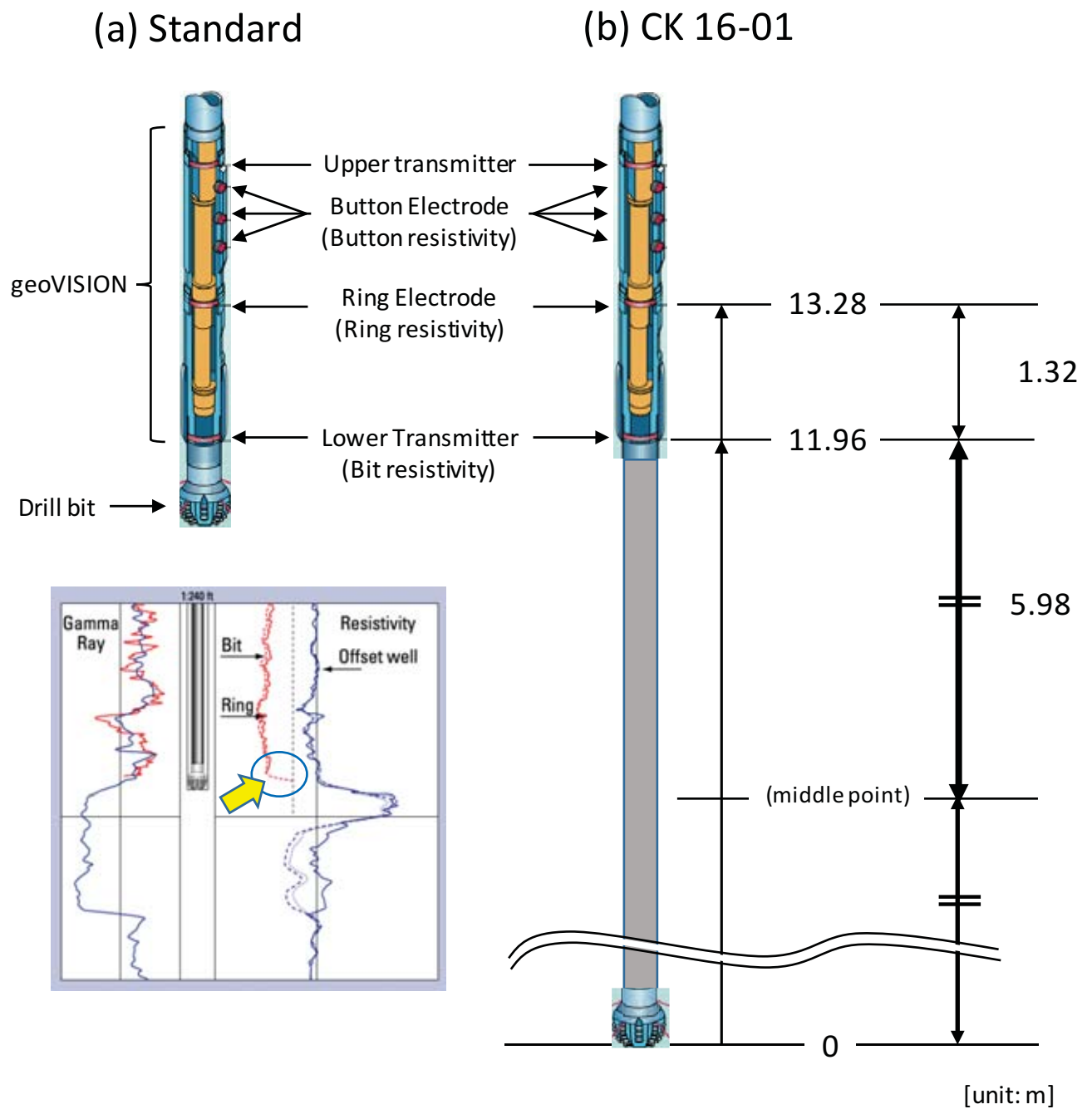


Figure 2-1-3-1: Schematics of resistivity measurements by geoVISION tool. (a) Standard LWD configuration. (b) Special LWD configuration for Expedition CK16-01.

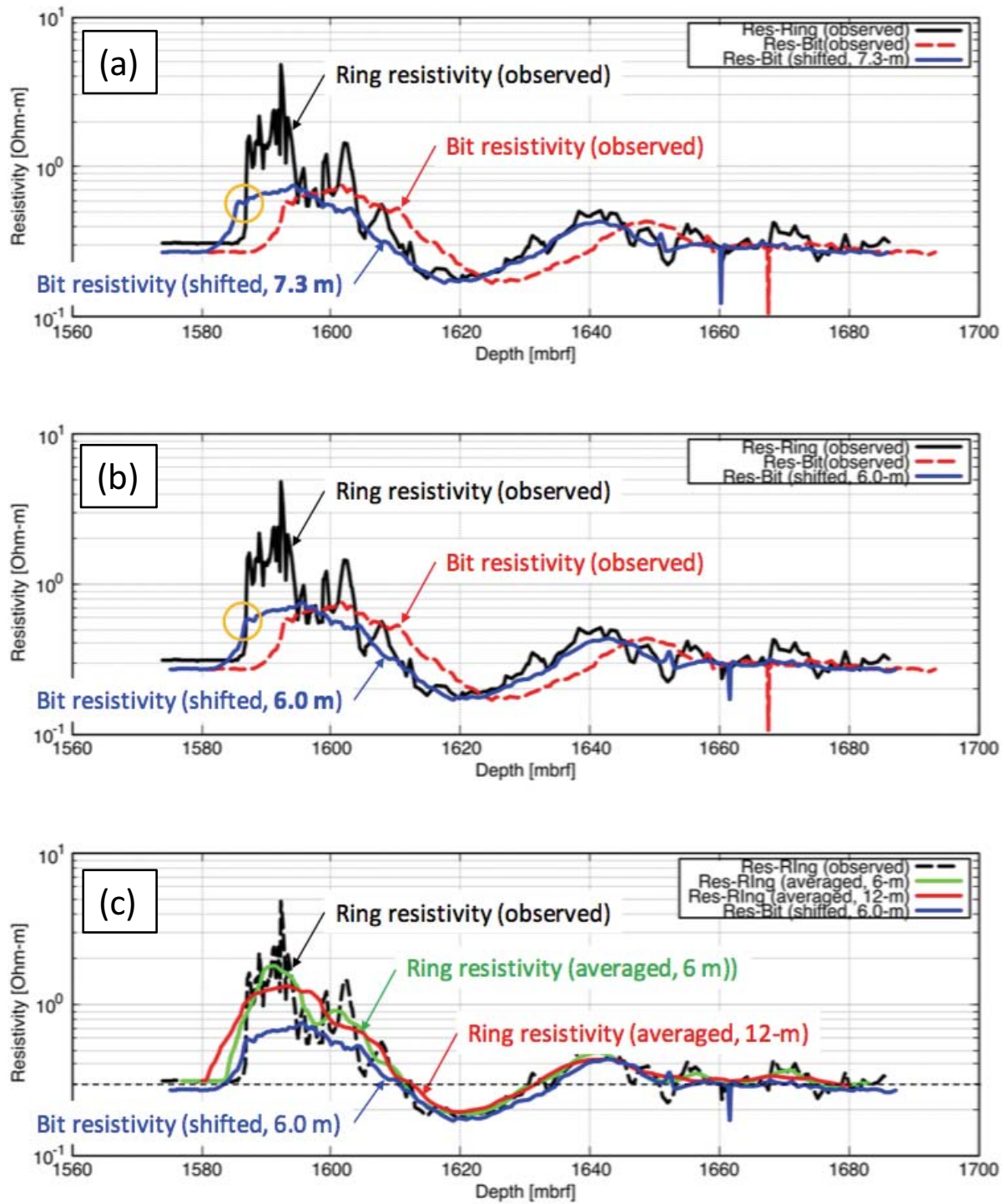


Figure 2-1-3-2: Comparison between ring resistivity and bit resistivity at C9017A (a) with 7.3 m depth shift and (b) with 6.0 m depth shift. (c) Comparison between averaged ring resistivity and depth shifted bit resistivity.

2.2 Site C9017 (SIP-NH01)

2.2.1 Logging data quality

Data quality control was performed by monitoring real time data during data acquisition and onboard data processing. The LSS and logging scientists assessed real time drilling mechanical parameters and data from the LWD tools in terms of realistic values for the expected lithology in the drilled interval in Hole C9017A.

LWD data quality logs are shown in **Fig. 2-2-1-1** (in depth) and **Fig. 2-2-1-2** (in time), and a composite LWD log is shown in **Fig. 2-2-1-3**. The mudline was confirmed at 1613.5 mBRT by the arcVISION resistivity curves. The total drilled depth is 1700.0 mBRT (113 mbsf). Though strong stick-and-slip and unstable ROP status caused by hard formation were observed during the overall drilling period, logging data quality is good. The pressure values gradually increased with depth but no specific anomalies were detected. Temperature values measured by the TeleScope was almost constant, but the temperature profile measured by the arcVISION was slightly fluctuated. As a result of large ROP below 43 mbsf, original borehole images contain substantial amount of missing data. After data processing by Schlumberger's engineers, the image data quality was improved (**Fig. 2-2-1-4**).

2.2.2 Log characterization

LWD logs acquired in Hole C9017A are summarized in **Fig. 2-2-1-3**. Combined visual inspections of the natural gamma ray and resistivity logs allow the definition of a single logging unit with four distinct zones.

Logging Unit 1 (0–101 mbsf) was defined for the entire logged section in the hole. The gamma ray values increase across the mudline, show a positive excursion (~160 gAPI) at ~1.5 mbsf, and drifts between 20 and 50 gAPI in the interval down to 24 mbsf. The log then shows a constant baseline below 20 gAPI in the interval of 24–56 mbsf. In the lower part of the section the gamma ray values exhibit a fluctuated trend with a series of positive peaks up to 150 gAPI at 57.5, 64, 72.5, 75, 81, 84, 93, and 99 mbsf. All resistivity logs except for the bit resistivity log (showing averaged trend) displays a similar trend throughout the entire section. The resistivity values sharply increase at the mudline, range between 0.8 and 6 ohm-m in the interval down to 8 mbsf, and then gradually decrease with depth. The resistivity logs show extremely low values around 0.2–0.3 ohm-m in the interval 24–42 mbsf, followed by gradual increasing trend from 0.3 to 0.5 ohm-m down to 58 mbsf. In the lowermost part of the section, the

resistivity logs exhibit a constant baseline around 0.3 ohm-m with minor fluctuations. A distinct negative peak identified at 65 mbsf shows the lowest resistivity value (~0.1 ohm-m) in the logged section.

The logging unit is subdivided into four zones based on the log characteristics described above; upper resistive zone (~0–24 mbsf), upper conductive zone (~24–42 mbsf), transitional resistive zone (~42–58 mbsf), and lower conductive zone (~58–101 mbsf).

2.2.3 Borehole images

Borehole images acquired in borehole C9017 are displayed in **Fig. 2-2-1-3**. The static and dynamic borehole images are successfully acquired through the borehole (0-101.0 mbsf).

The borehole images in the upper resistive zone (0–24 mbsf) show massive and heterogeneous structure. Low angle bed boundaries and irregular-shaped subvertical conductive features are locally identified in this zone. The borehole images in the upper conductive zone (24–42 mbsf) show also massive and heterogeneous structure with several weak bed boundaries. Both subhorizontal and subvertical conductive features are observed. Conductive spots (<10 cm in diameter) are scattered throughout this zone. The borehole images in the transitional resistive zone (42–58 mbsf) show massive and heterogeneous structure with only few bed boundaries and no notable features except for scattered conductive spots. In the lower conductive zone (58–101 mbsf), the borehole images exhibit layered formation with a number of low to medium angle bed boundaries. Slightly dipping discontinuous conductive layers are commonly observed. The most conductive layer (~0.1 ohm-m, ~50 cm in diameter) is imaged at ~65 mbsf (**Fig. 2-2-3-1**). The borehole images in the lowermost part of the zone (~85–100 mbsf) shows layered intervals with heterogeneous texture and irregular-shape resistive fragments.

2.2.4 Temperature and pressure

Temperature and pressure logs acquired in Hole C9017A are displayed in **Figs. 2-2-1-1** and **-3**. Temperature measured by arcVISION is 3–4°C at seafloor. The value increases with depth and reaches 8°C at 21.5 mbsf. The profile shows fluctuations between 21.5 mbsf and TD (6–13°C). Telescope annular temperature has lower values than that of arcVISION. The baseline increases with depth from 4°C (mudline) to 8°C with less fluctuation. A baseline of the annular pressure obtained by arcVISION increases with depth from 15.8 MPa (mudline) to 17.0 MPa (TD). No significant

anomaly is observed in the pressure log.

Figure captions

Fig. 2-2-1-1: LWD temperature, pressure, drilling parameters, and data quality logs in depth, Hole C9017A. TEMP: annular temperature by arcVISION, DHAT_2: annular temperature by TeleScope, APRS_ARC: annular pressure by arcVISION, DHAP_2: annular pressure by TeleScope, ECD_ARC: equivalent circular density by arcVISION, ROP5: rate of penetration averaged over the last 5 ft, RPM: rotational speed, CRPM_RT: real time collar rotational speed, STICK_RT, real time stick slip indicator, SWOB: surface weight on bit, TORQ: torque, TAB_RAB_BS: shallow button resistivity time after bit, TAB_RAB_BM: medium button resistivity time after bit, TAB_RAB_BD: deep resistivity time after bit, TAB_RAB_RING: ring resistivity time after bit, TAB_RAB_BIT: bit resistivity time after bit, TAB_GR: gamma ray time after bit.

Fig. 2-2-1-2: LWD temperature, pressure, drilling parameters, and data quality logs in time, Hole C9017A. ECD_TIME: equivalent circulation density, DHAP: annular pressure, DHAT: annular temperature, SPPA: standpipe pressure, SWOB: surface weight on bit, HKLA: hook load, STICK: stick slip indicator, CRPM: collar rotation speed, RPM: rotation speed, ROP5: Rate of penetration averaged over the last 5 ft, TVD: true vertical depth.

Fig. 2-2-1-3: Composite LWD log, Hole C9017A. ROP5: rate of penetration averaged over the last 5 ft, GR_RAB: natural gamma radiation, RES_RING: ring resistivity, RES_BIT: bit resistivity, RES_BIT -6m: depth shifted bit resistivity, RES_BD: deep button resistivity, RES_BM: medium button resistivity, RES_BS: shallow button resistivity, APRS_ARC: annular pressure measured by arcVISION, ATMP: annular temperature measured by arcVISION.

Fig. 2-2-1-4: Quality improvement of borehole images by data processing, Hole C9017A.

Fig. 2-2-3-1: A representative borehole image showing weakly layered formation with discontinuous conductive layers at 65 mbsf.

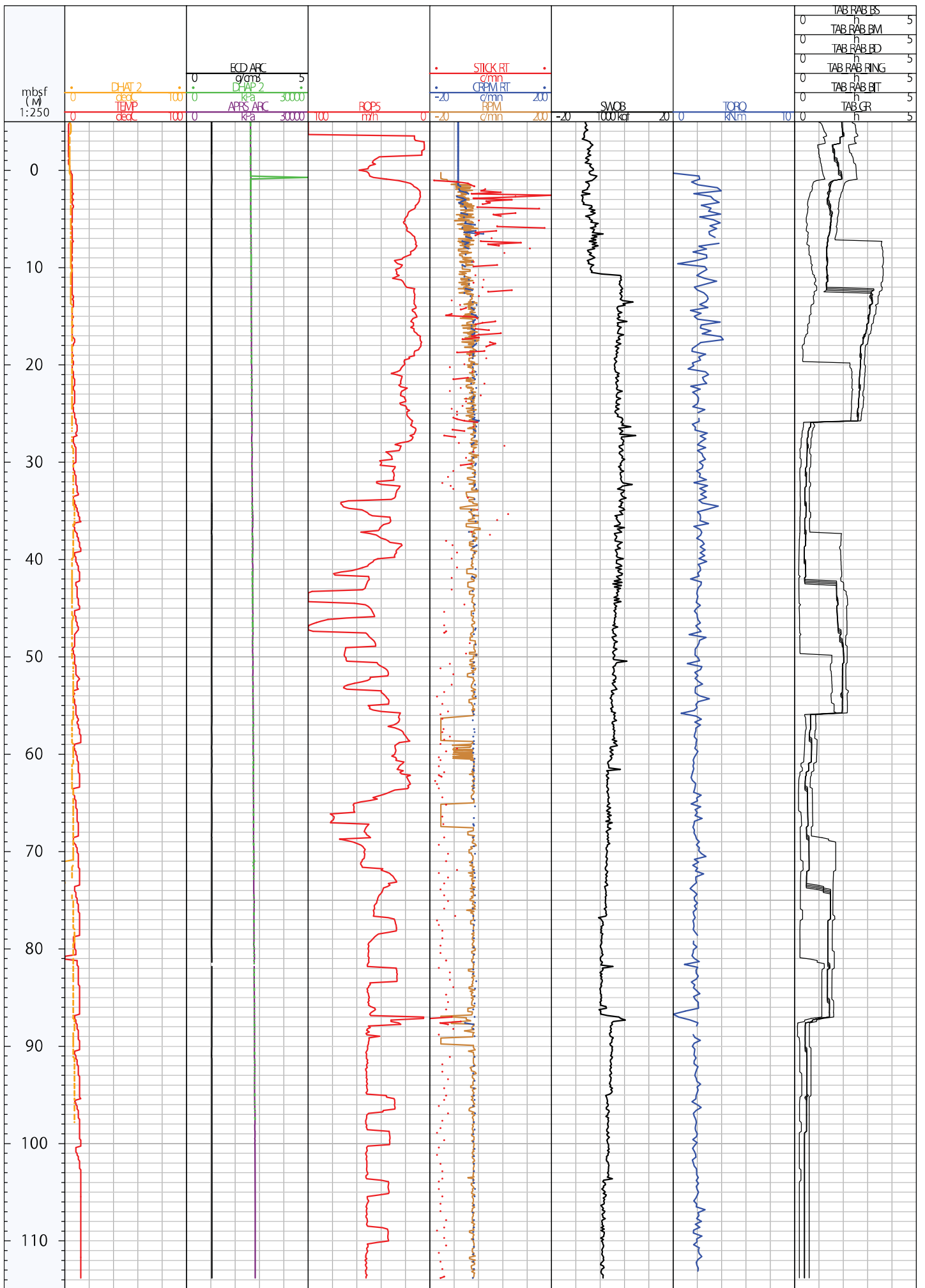


Figure 2-2-1-1: LWD temperature, pressure, drilling parameters, and data quality logs in depth, Hole C9017A.

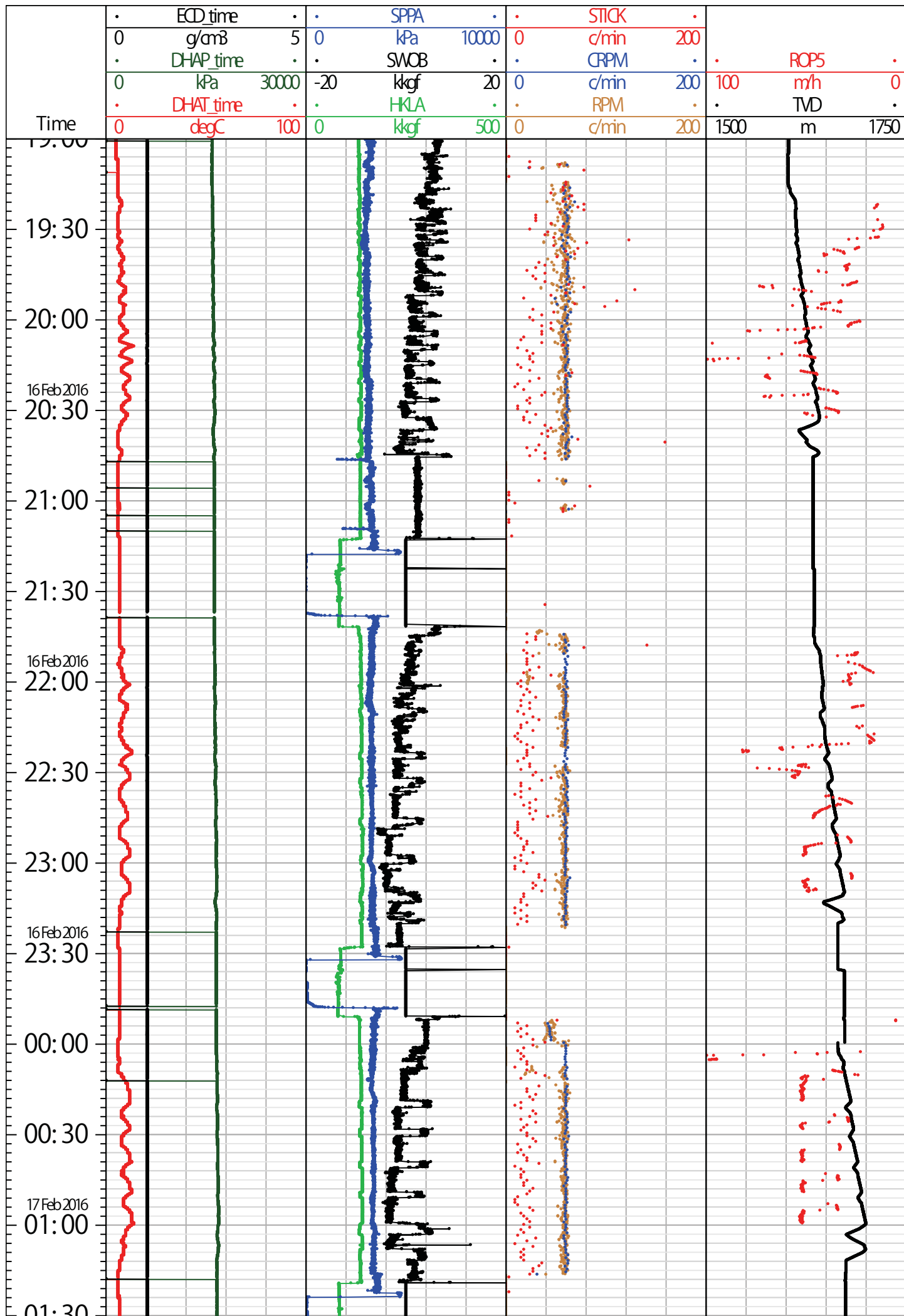


Figure 2-2-1-2: LWD temperature, pressure, drilling parameters, and data quality logs in time, Hole C9017A.

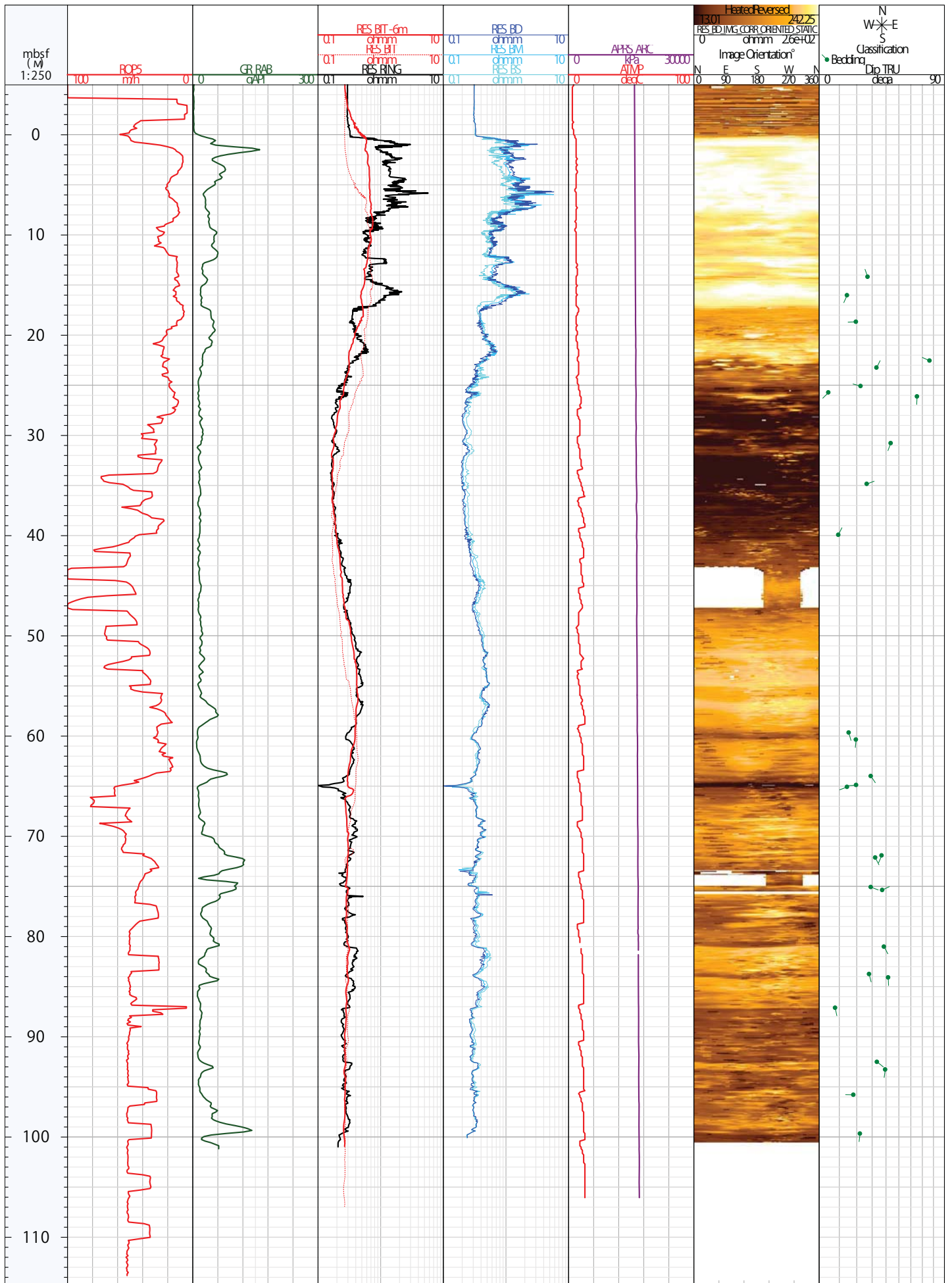


Figure 2-2-1-3: Composite LWD log, Hole C9017A.

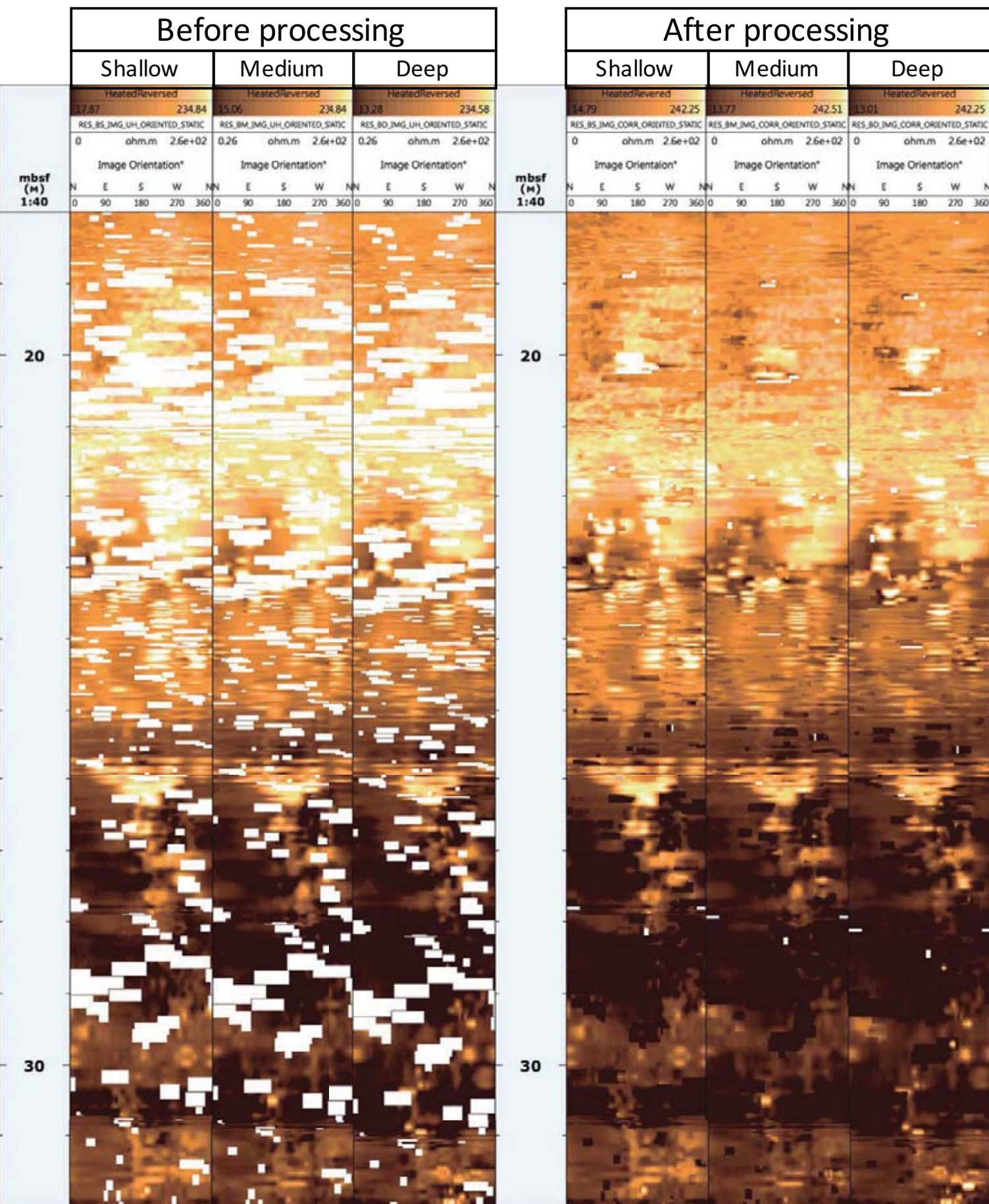


Figure 2-2-1-4: Quality improvement of borehole images by data processing, Hole C9017A.

2.3 Site C9018 (SIP-NH02)

2.3.1 Logging data quality

Data quality control was performed by monitoring real time data during data acquisition and onboard data processing. The LSS and logging scientists assessed real time drilling mechanical parameters and data from the LWD tools in terms of realistic values for the expected lithology in the drilled interval in Hole C9018A.

LWD data quality logs are shown in **Fig. 2-3-1-1**, and a composite LWD log is shown in **Fig. 2-3-1-2**. The mudline was confirmed at 1613.5 mBRT by the arcVISION resistivity curves. The drilling was terminated at 1623.0 mBRT (9.5 mbsf) because of low ROP (ratio of penetration) and strong stick-and-slip due to a hard formation encountered just below the seafloor. The APWD and resistivity sensors of arcVISION reached to 2.0 mbsf and 1.3 mbsf, respectively. The geoVISION gamma ray, resistivity, and borehole image data could not be obtained because the tool did not reach the seafloor.

2.3.2 Log characterization

Drilling operation was terminated at 9.5 mbsf due to very low penetration rate below 3.5 mbsf. No gamma ray and resistivity data were acquired above the mudline. The LWD logs acquired in Hole C9018A are summarized in **Fig. 2-3-1-2**.

2.3.3 Temperature and pressure (C9018)

Temperature and pressure logs acquired in Hole C9018A are displayed in **Figs. 2-3-1-1** and **-2**. Annular temperature and pressure were measured by arcVISION. The temperature log was obtained only at an interval between mudline to 1.0 mbsf (TD). Temperature shows nearly constant value of 6 °C in the interval. Annular pressure data recorded in the interval of mudline to TD show a constant trend (16.1 MPa).

Figure captions:

Fig. 2-3-1-1: LWD temperature, pressure, drilling parameters, and data quality logs, Hole C9018A. TEMP: annular temperature by arcVISION, DHAT_2: annular temperature by TeleScope, APRS_ARC: annular pressure by arcVISION, DHAP_2: annular pressure by TeleScope, ECD_ARC: equivalent circular density by arcVISION, ROP5: rate of penetration averaged over the last 5 ft, RPM: rotational speed, CRPM_RT: real time collar rotational speed, STICK_RT, real time stick slip indicator, SWOB: surface weight on bit, TORQ: torque, TAB_RAB_BS: shallow button resistivity time after bit, TAB_RAB_BM: medium button resistivity time after bit, TAB_RAB_BD: deep resistivity time after bit, TAB_RAB_RING: ring resistivity time after bit, TAB_RAB_BIT: bit resistivity time after bit, TAB_GR: gamma ray time after bit.

Fig. 2-3-1-2: Composite LWD log, Hole C9018A. ROP5: rate of penetration averaged over the last 5 ft, GR_RAB: natural gamma radiation, RES_RING: ring resistivity, RES_BIT: bit resistivity, RES_BIT -6m: depth shifted bit resistivity, RES_BD: deep button resistivity, RES_BM: medium button resistivity, RES_BS: shallow button resistivity, APRS_ARC: annular pressure measured by arcVISION, ATMP: annular temperature measured by arcVISION.

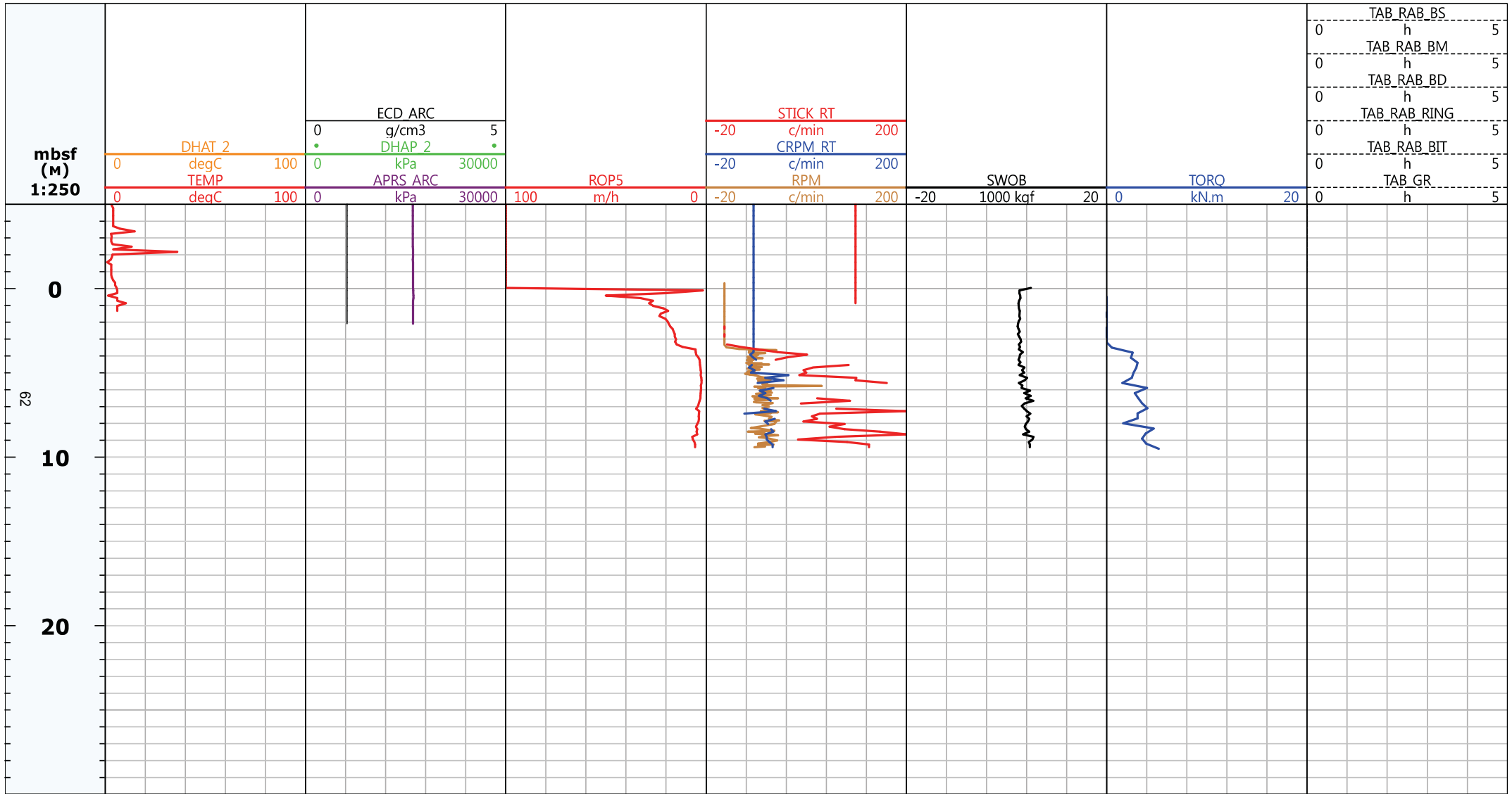


Figure 2-3-1-1: LWD temperature, pressure, drilling parameters, and data quality logs, Hole C9018A.

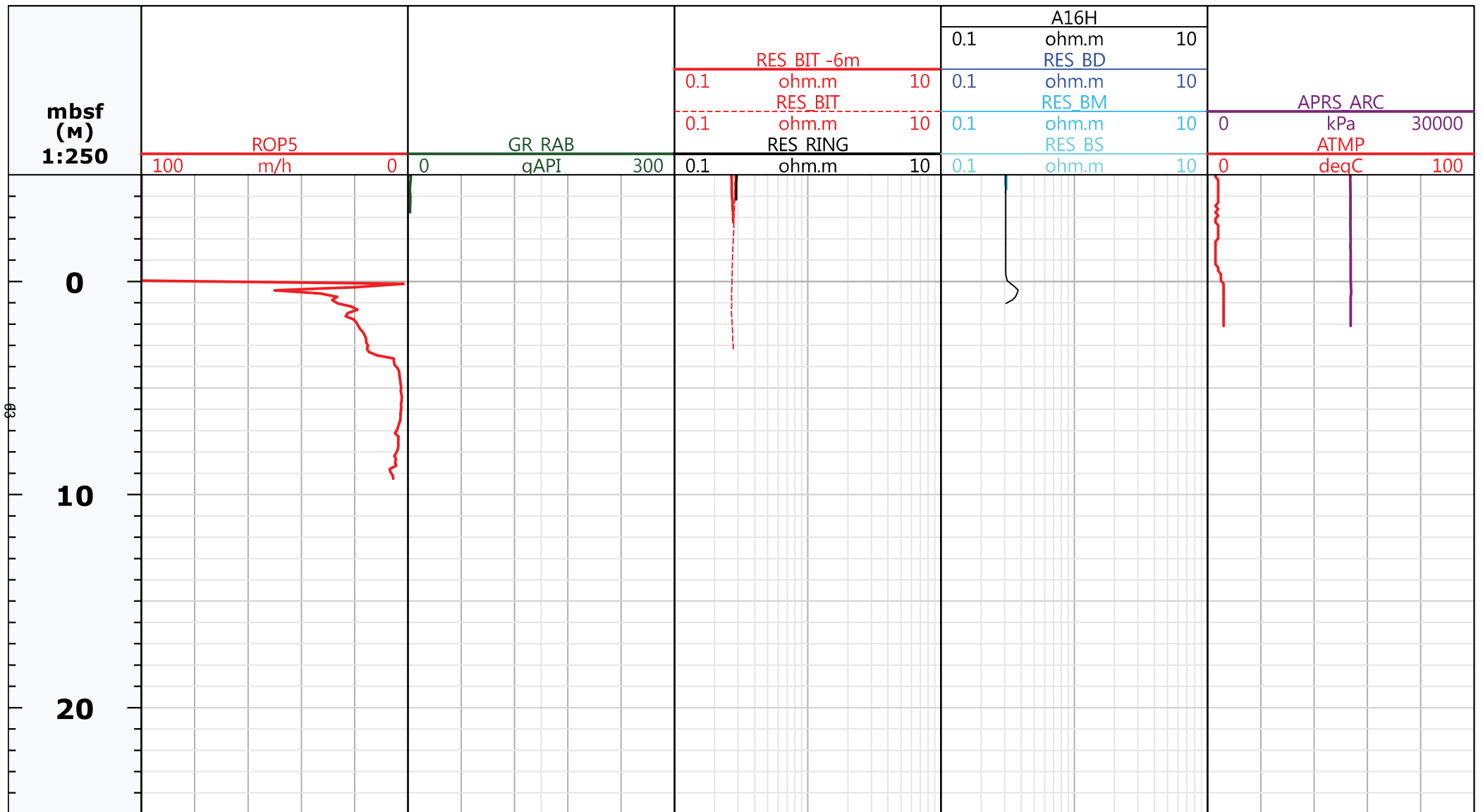


Figure 2-3-1-2: Composite LWD log, Hole C9018A.

2.4 Site C9019 (SIP-NH03)

2.4.1 Logging data quality

Data quality control was performed by monitoring real time data during data acquisition and onboard data processing. The LSS and logging scientists assessed real time drilling mechanical parameters and data from the LWD tools in terms of realistic values for the expected lithology in the drilled interval in Hole C9019A.

LWD data quality logs are shown in **Fig. 2-4-1-1**, and a composite LWD log is shown in **Fig. 2-4-1-2**. The mudline was confirmed at 1630.5 mBRT by the arcVISION gamma ray curve. The drilling was terminated at 1645.5 mBRT (15.0 mbsf) because the signal from arcVISION was lost and the stand pipe pressure was dropped. The APWD sensor of arcVISION and geoVISION reached to 8.0 mbsf and 2.0 mbsf, respectively. Although the arcVISION reached below the seafloor, resistivity data were missed due to a communication error. Resistivity borehole image data were not generated.

2.4.2 Log characterization

One logging unit was defined based on limited available logs. Logging Unit 1 (0–2 mbsf) exhibits a sharp increasing trend of gamma ray from the mudline to 2 mbsf up to 165 gAPI. The resistivity log shows a tiny increasing trend from 0.3 to 0.4 ohm-m. The LWD logs acquired in Hole C9019A are summarized in **Fig. 2-4-1-2**.

2.4.3 Temperature and Pressure (C9019)

Temperature and pressure logs acquired in Hole C9019A are displayed in **Figs. 2-4-1-1** and **-2**. ArcVISION annular temperature and pressure data were collected between mudline and 4.4 mbsf (TD). In this interval, the temperature shows nearly constant values of 5-6 °C. The pressure slightly increases with depth from 16.2 MPa (mudline) to 16.3 MPa (TD).

Figure captions:

Fig. 2-4-1-1: LWD temperature, pressure, drilling parameters, and data quality logs, Hole C9019A. TEMP: annular temperature by arcVISION, DHAT_2: annular temperature by TeleScope, APRS_ARC: annular pressure by arcVISION, DHAP_2: annular pressure by TeleScope, ECD_ARC: equivalent circular density by arcVISION, ROP5: rate of penetration averaged over the last 5 ft, RPM: rotational speed, CRPM_RT: real time collar rotational speed, STICK_RT, real time stick slip indicator, SWOB: surface weight on bit, TORQ: torque, TAB_RAB_BS: shallow button resistivity time after bit, TAB_RAB_BM: medium button resistivity time after bit, TAB_RAB_BD: deep resistivity time after bit, TAB_RAB_RING: ring resistivity time after bit, TAB_RAB_BIT: bit resistivity time after bit, TAB_GR: gamma ray time after bit.

Fig. 2-4-1-2: Composite LWD log, Hole C9019A. ROP5: rate of penetration averaged over the last 5 ft, GR_RAB: natural gamma radiation, RES_RING: ring resistivity, RES_BIT: bit resistivity, RES_BIT -6m: depth shifted bit resistivity, RES_BD: deep button resistivity, RES_BM: medium button resistivity, RES_BS: shallow button resistivity, APRS_ARC: annular pressure measured by arcVISION, ATMP: annular temperature measured by arcVISION.

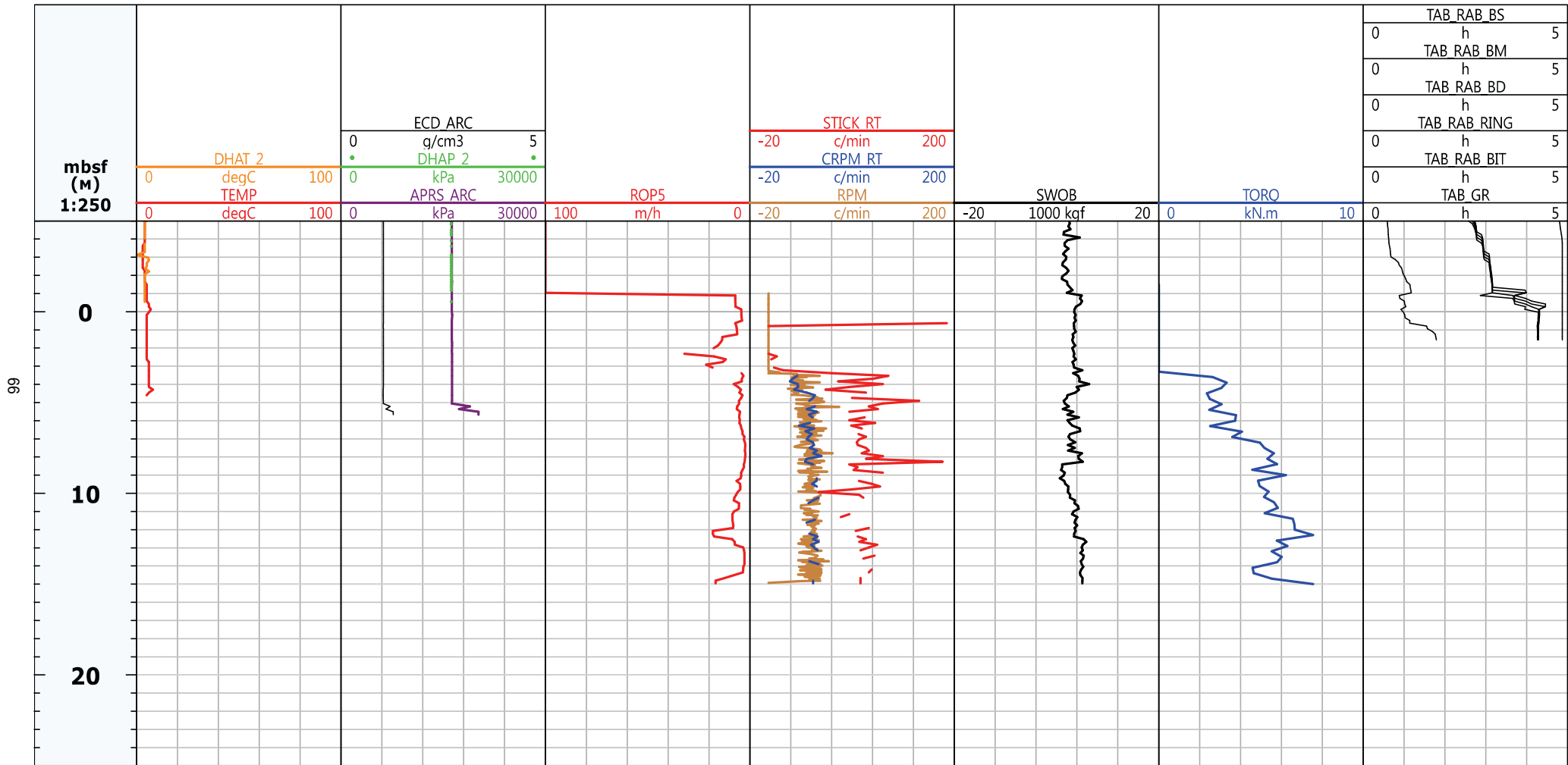


Figure 2-4-1-1: LWD temperature, pressure, drilling parameters, and data quality logs, Hole C9019A.-

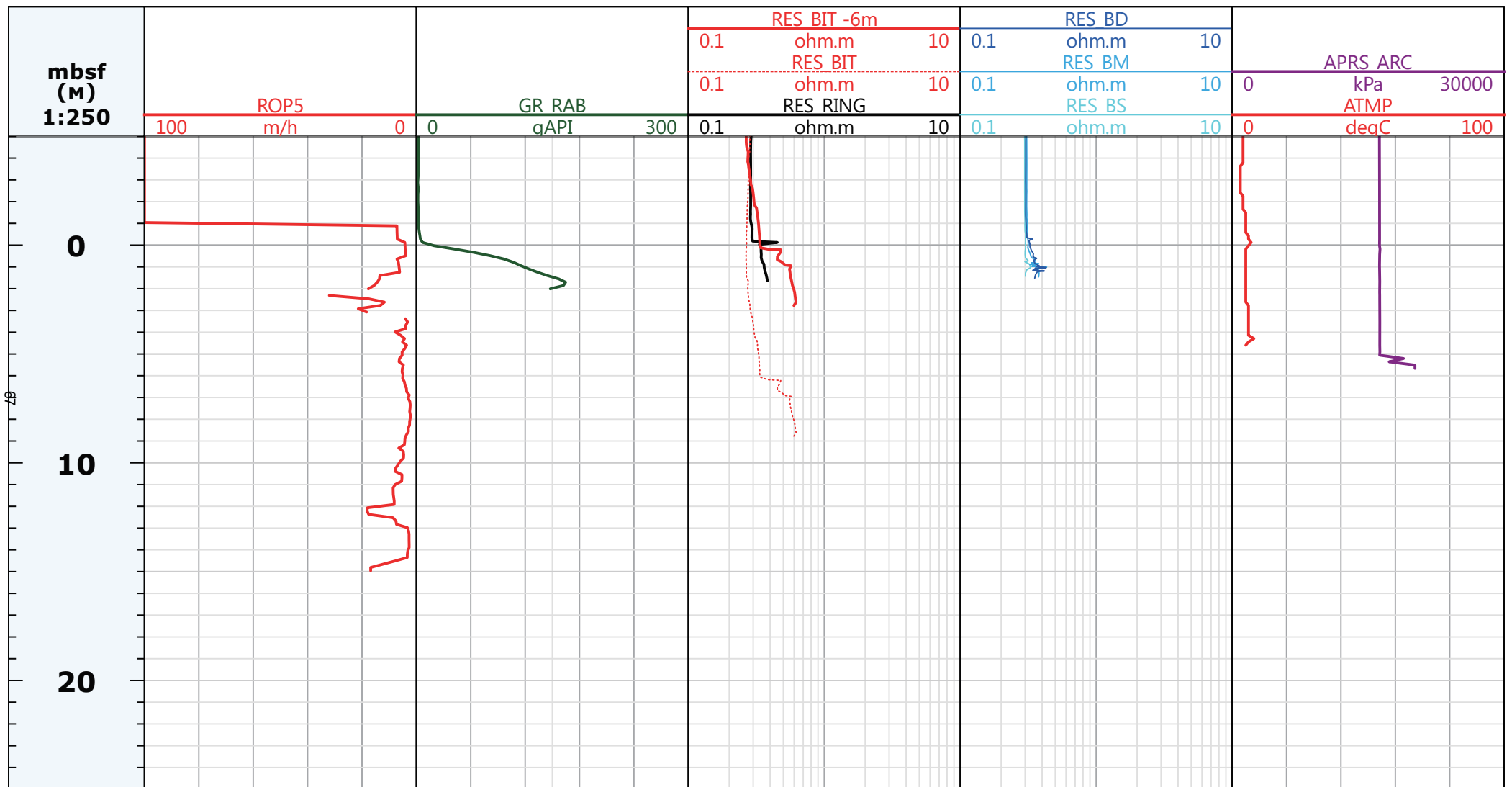


Figure 2-4-1-2: Composite LWD log, Hole C9019A.

2.5 Site C9020 (SIP-NH04)

2.5.1 Logging data quality

Data quality control was performed by monitoring real time data during data acquisition and onboard data processing. The LSS and logging scientists assessed real time drilling mechanical parameters and data from the LWD tools in terms of realistic values for the expected lithology in the drilled interval in Hole C9020A.

LWD data quality logs are shown in **Fig. 2-5-1-1**, and a composite LWD log is shown in **Fig. 2-5-1-2**. The mudline was confirmed at 1628.0 mBRT by the arcVISION resistivity curves. The drilling was terminated at 1637.0 mBRT (9.0 mbsf) because of low ROP (ratio of penetration) and strong stick-and-slip due to a hard formation encountered just below the seafloor. The APWD and resistivity sensors of arcVISION reached to 1.3 mbsf and 0.6 mbsf, respectively. The geoVISION gamma ray, resistivity, and borehole image data could not be obtained because the tool did not reach the seafloor.

2.5.2 Log characterization

One logging unit was defined based on limited available logs. Logging Unit 1 (0–1 mbsf) exhibits an increasing trend of resistivity (0.3–0.6 ohm-m) in this interval. No gamma ray data were acquired above the mudline. The LWD logs acquired in Hole C9020A are summarized in **Fig. 2-5-1-2**.

2.5.3 Temperature and Pressure

Annular temperature and pressure were measured by arcVISION in the interval between the mudline and 0.7 mbsf. In this short interval, the temperature and pressure shows constant values of 7°C and 16.2 MPa, respectively (**Figs. 2-5-1-1 and -2**).

Figure captions:

Fig. 2-5-1-1: LWD temperature, pressure, drilling parameters, and data quality logs, Hole C9020A. TEMP: annular temperature by arcVISION, DHAT_2: annular temperature by TeleScope, APRS_ARC: annular pressure by arcVISION, DHAP_2: annular pressure by TeleScope, ECD_ARC: equivalent circular density by arcVISION, ROP5: rate of penetration averaged over the last 5 ft, RPM: rotational speed, CRPM_RT: real time collar rotational speed, STICK_RT, real time stick slip indicator, SWOB: surface weight on bit, TORQ: torque, TAB_RAB_BS: shallow button resistivity time after bit, TAB_RAB_BM: medium button resistivity time after bit, TAB_RAB_BD: deep resistivity time after bit, TAB_RAB_RING: ring resistivity time after bit, TAB_RAB_BIT: bit resistivity time after bit, TAB_GR: gamma ray time after bit.

Fig. 2-5-1-2: Composite LWD log, Hole C9020A. ROP5: rate of penetration averaged over the last 5 ft, GR_RAB: natural gamma radiation, RES_RING: ring resistivity, RES_BIT: bit resistivity, RES_BIT -6m: depth shifted bit resistivity, RES_BD: deep button resistivity, RES_BM: medium button resistivity, RES_BS: shallow button resistivity, APRS_ARC: annular pressure measured by arcVISION, ATMP: annular temperature measured by arcVISION.

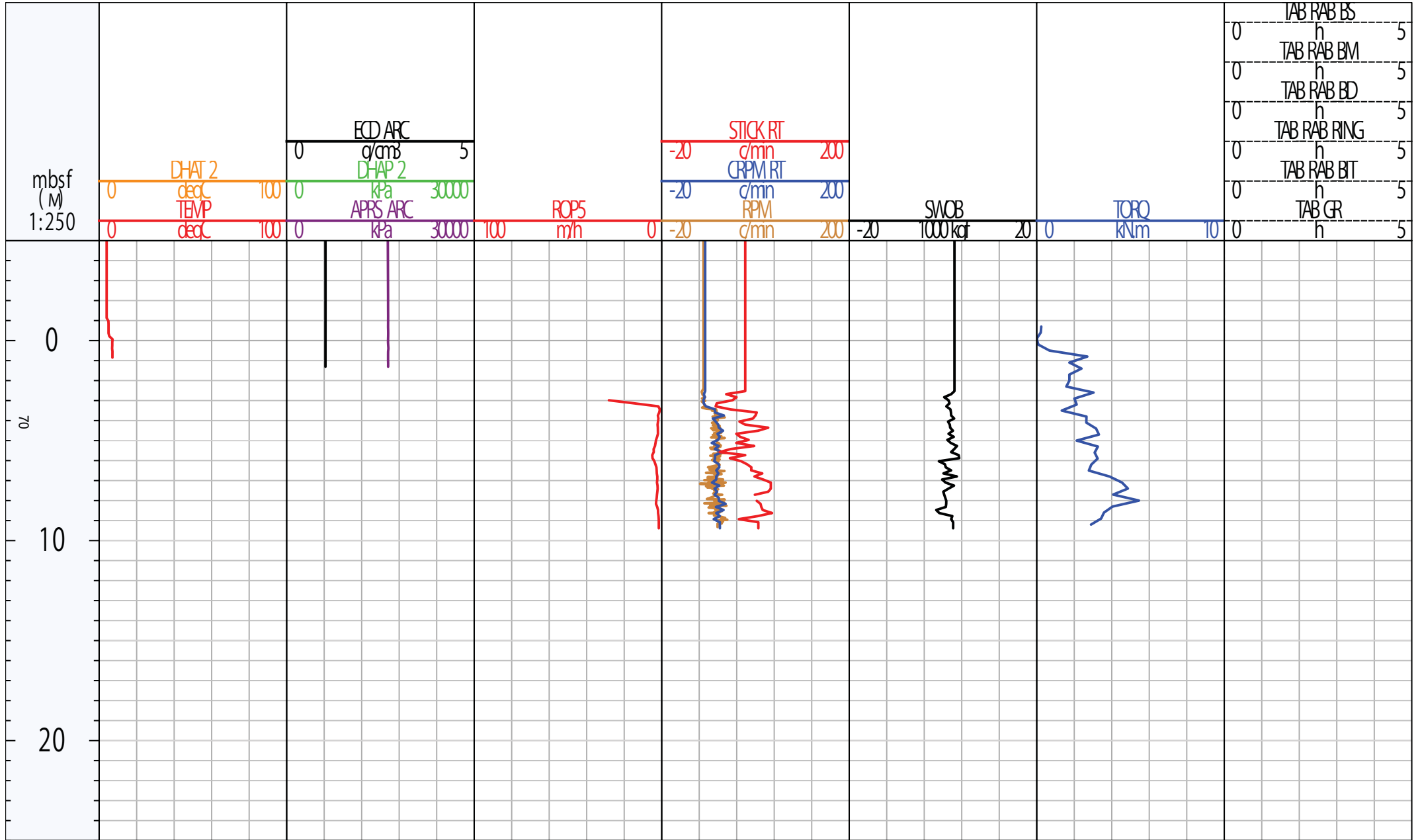


Figure 2-5-1-1: LWD temperature, pressure, drilling parameters, and data quality logs, Hole C9020A.

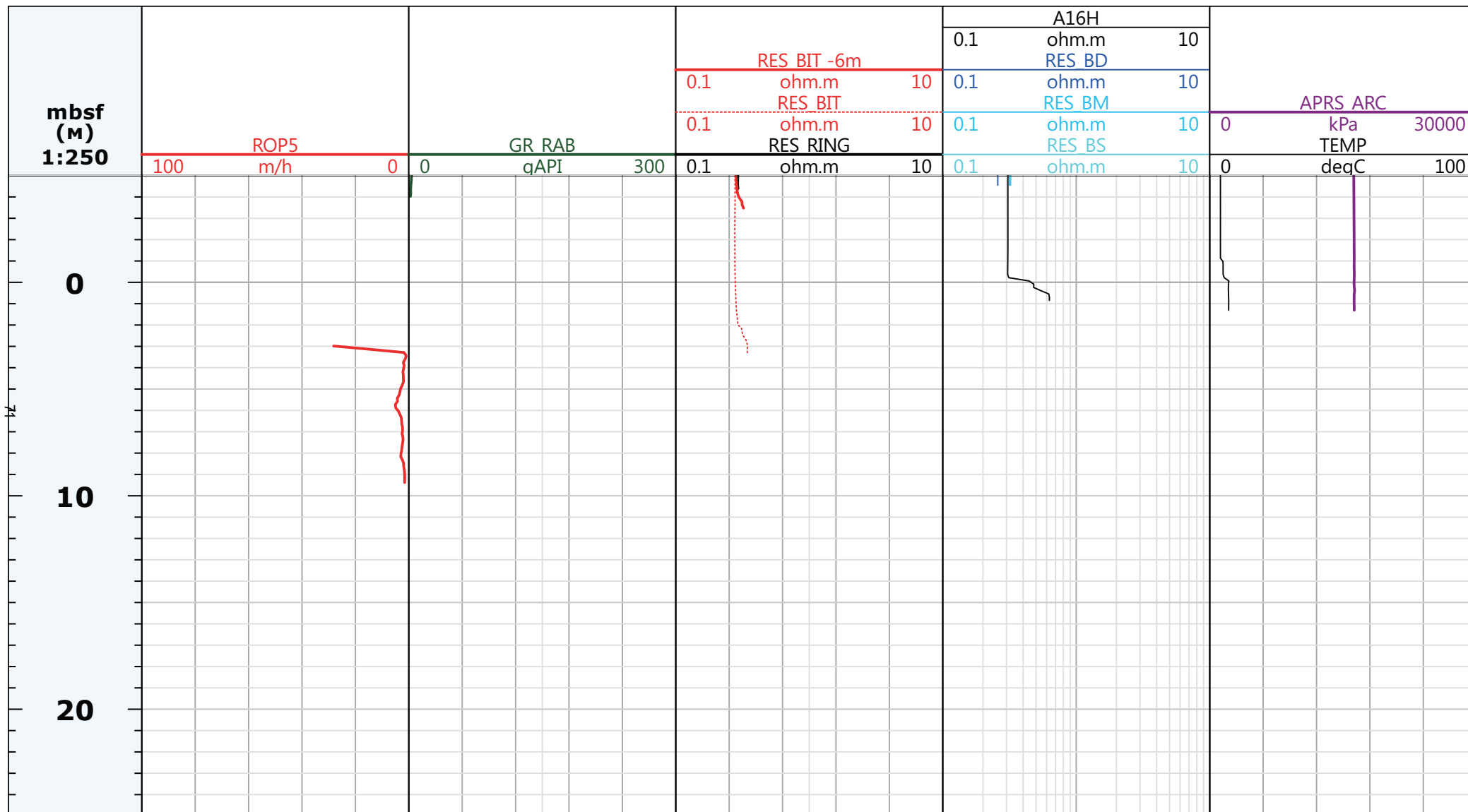


Figure 2-5-1-2: Composite LWD log, Hole C9020A.

2.6 Site C9021 (SIP-IN03)

2.6.1 Logging data quality

Data quality control was performed by monitoring real time data during data acquisition and onboard data processing. The LSS and logging scientists assessed real time drilling mechanical parameters and data from the LWD tools in terms of realistic values for the expected lithology in the drilled interval in Hole C9021A.

LWD data quality logs are shown in **Fig. 2-6-1-1** (in depth) and **Fig. 2-6-1-2** (in time), and a composite LWD log is shown in **Fig. 2-6-1-3**. The mudline was confirmed at 1049.0 mBRT by the gamma ray curve and resistivity curves of geoVISION. The total drilled depth is 1150.5 mBRT (101.5 mbsf). The overall quality of the logging data is good. Temperature anomalies were observed around 80 mbsf and 90 mbsf up to about 20°C by the arcVISION. Small pressure anomalies corresponding to the temperature anomalies were also observed. ROP data was lost in the uppermost interval down to 15 mbsf due to data communication errors. The gamma ray and resistivity curves seemed in good response to the formations. Although unstable stick-and-slip was observed below 68 mbsf, the borehole images quality was good.

2.6.2 Log characterization

LWD logs acquired in Hole C9021A are summarized in **Fig. 2-6-1-3**. Combined visual inspections of the natural gamma ray and resistivity logs allow the definition of two logging units.

Logging Unit 1 (0–65.5 mbsf) exhibits an initial increase in gamma ray up to 28 gAPI from the mudline to 0.2 mbsf. Then the values maintain a constant baseline around 30 gAPI with minor fluctuations. Resistivity values show an increasing trend from the mudline (0.3 ohm-m) to 19 mbsf (0.9 ohm-m) and a decreasing trend down to the bottom of the unit (0.4 ohm-m). No significant peaks of resistivity values are observed throughout the unit.

Logging Unit 2 (65.5 mbsf to TD) is characterized by higher gamma ray and resistivity values with larger fluctuation than Unit 1. The gamma ray log shows a gradual increasing trend from the top of the unit (~20 gAPI) to 70 mbsf (~90 gAPI), and maintain the higher values fluctuating between 60 and 90 gAPI down to the bottom of the unit. The resistivity values increase from the top of the unit (~0.4 ohm-m) to 72 mbsf (~2.5 ohm-m), show fluctuated values between 1 and 2 ohm-m in the interval of 72 to 82 mbsf, then a gradual increasing trend up to ~3 ohm-m down to the bottom of

the unit.

2.6.3 Borehole Image Characterization

Borehole images acquired in Hole C9021A are well correlated to the downhole variation of resistivity by unit scale (**Fig. 2-6-1-3**).

The borehole images in Logging Unit 1 (0-65.5 mbsf) are not clear to extract geological features such as bedding planes or fractures on fine scale images. The borehole images shows azimuthally biased from west (resistive) to east (conductive) as vertical zonal features. These asymmetric images observed throughout the unit may be produced due to LWD measurements in contact with one side of the borehole.

Borehole images acquired in Logging Unit 2 (66.5 mbsf to TD) exhibit a number of resistive intervals composed of resistive spots (up to ~20 cm in diameter) with conductive matrix. The shape of the resistive spot is variable between rounded to angular. At least three major packages of resistive spot are identified in the unit at ~69–73, ~75–80 and ~83–88 mbsf. Several shallow-dipping planes can be identified between or within the packages at 73.5 mbsf, 76.5 mbsf and 85.0 mbsf.

2.6.4 Temperature and Pressure

Temperature and pressure logs acquired in Hole C9021A are displayed in **Figs. 2-6-1-1** and **-3**. Baselines of the annular temperature measured by arcVISION and Telescope are approximately constant value (9–10°C) in the entire drilled interval. The arcVISION annular temperature shows clear peaks at 79.8 and 91.0 mbsf, and a weak anomaly between the peaks (86.6 mbsf). Temperature of the peaks and the small anomaly reaches 22, 23 and 12°C, corresponding to increase of 12, 14 and 3°C from the baseline, respectively. Several minor anomalies up to 3–4°C higher than the baseline were observed at 54.4, 70.1, 81.0 mbsf by Telescope. Annular pressure logs measured by both arcVISION and Telescope have a baseline which increases with depth from 10.4 MPa (mudline) to 11.3 MPa (TD). Five significant positive peaks were observed in arcVISION pressure log at 78.2, 79.6, 81.6, 86.6, and 90.6 mbsf. The shallower three peaks can be considered as one broad pressure anomaly, which indicates 0.5 MPa increase from the baseline. The deeper two positive peaks show pressure gain of 0.8 and 0.9 MPa, respectively. The depths of the pressure peaks clearly correspond to the depths of peaks in the arcVISION temperature log. The Telescope pressure values show two significant peaks at 72.6 mbsf (11.6 MPa) and 78.7 mbsf (11.6 MPa). Because the pressure sensor of the Telescope locates 8.4 m above that of the arcVISION (see “Method” section, this chapter), these peaks in the Telescope pressure also can

correspond to the temperature peaks of 79.8 and 86.6 mbsf.

Figure captions:

Fig. 2-6-1-1: LWD temperature, pressure, drilling parameters, and data quality logs in depth, Hole C9021A. TEMP: annular temperature by arcVISION, DHAT_2: annular temperature by TeleScope, APRS_ARC: annular pressure by arcVISION, DHAP_2: annular pressure by TeleScope, ECD_ARC: equivalent circular density by arcVISION, ROP5: rate of penetration averaged over the last 5 ft, RPM: rotational speed, CRPM_RT: real time collar rotational speed, STICK_RT, real time stick slip indicator, SWOB: surface weight on bit, TORQ: torque, TAB_RAB_BS: shallow button resistivity time after bit, TAB_RAB_BM: medium button resistivity time after bit, TAB_RAB_BD: deep resistivity time after bit, TAB_RAB_RING: ring resistivity time after bit, TAB_RAB_BIT: bit resistivity time after bit, TAB_GR: gamma ray time after bit.

Fig. 2-6-1-2: LWD temperature, pressure, drilling parameters, and data quality logs in time, Hole C9021A. ECD_TIME: equivalent circulation density, DHAP: annular pressure, DHAT: annular temperature, SPPA: standpipe pressure, SWOB: surface weight on bit, HKLA: hook load, STICK: stick slip indicator, CRPM: collar rotation speed, RPM: rotation speed, ROP5: Rate of penetration averaged over the last 5 ft, TVD: true vertical depth.

Fig. 2-6-1-3: Composite LWD log, Hole C9021A. ROP5: rate of penetration averaged over the last 5 ft, GR_RAB: natural gamma radiation, RES_RING: ring resistivity, RES_BIT: bit resistivity, RES_BIT -6m: depth shifted bit resistivity, RES_BD: deep button resistivity, RES_BM: medium button resistivity, RES_BS: shallow button resistivity, APRS_ARC: annular pressure measured by arcVISION, ATMP: annular temperature measured by arcVISION.

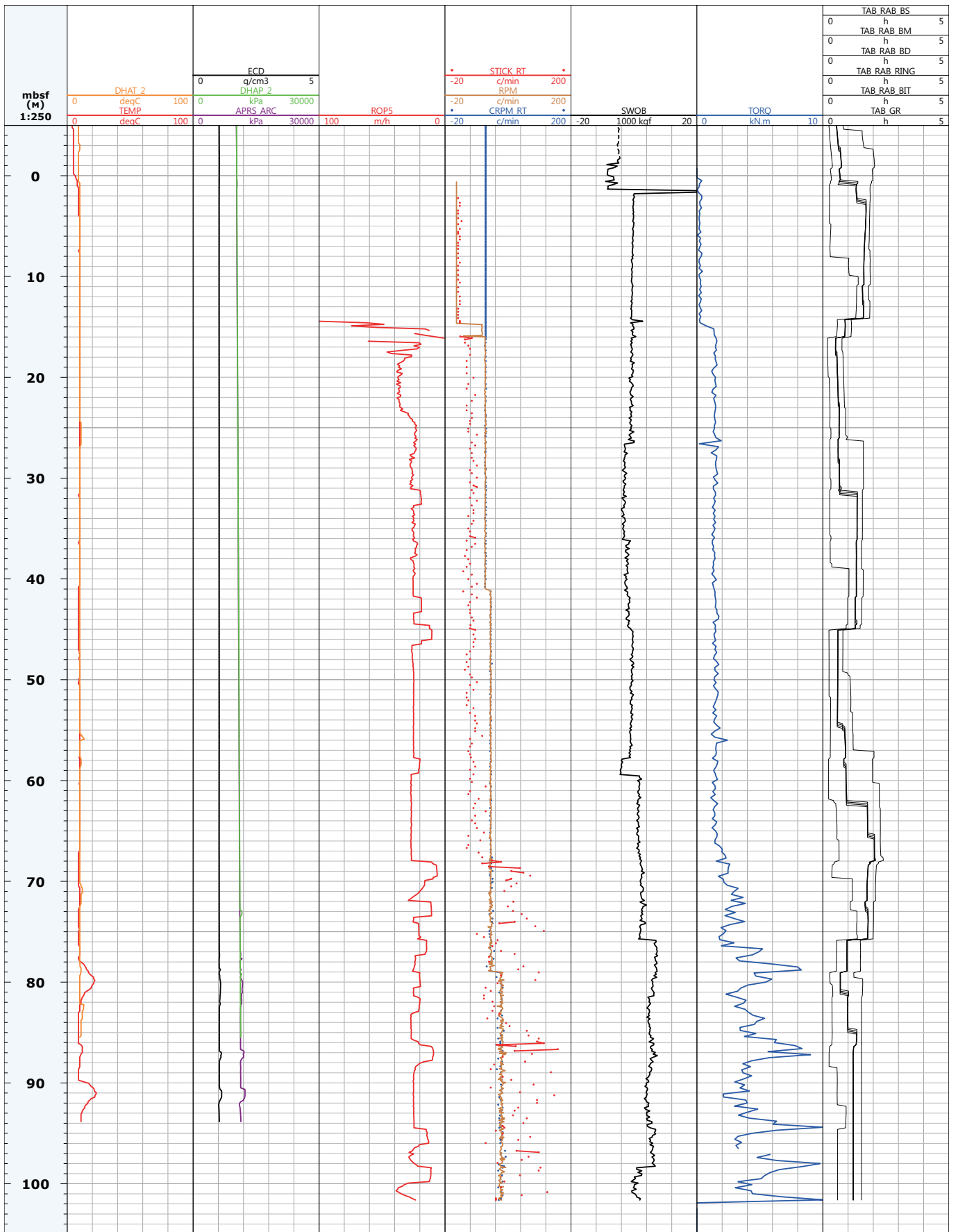


Figure 2-6-1-1: LWD temperature, pressure, drilling parameters, and data quality logs in depth, Hole C9021A.

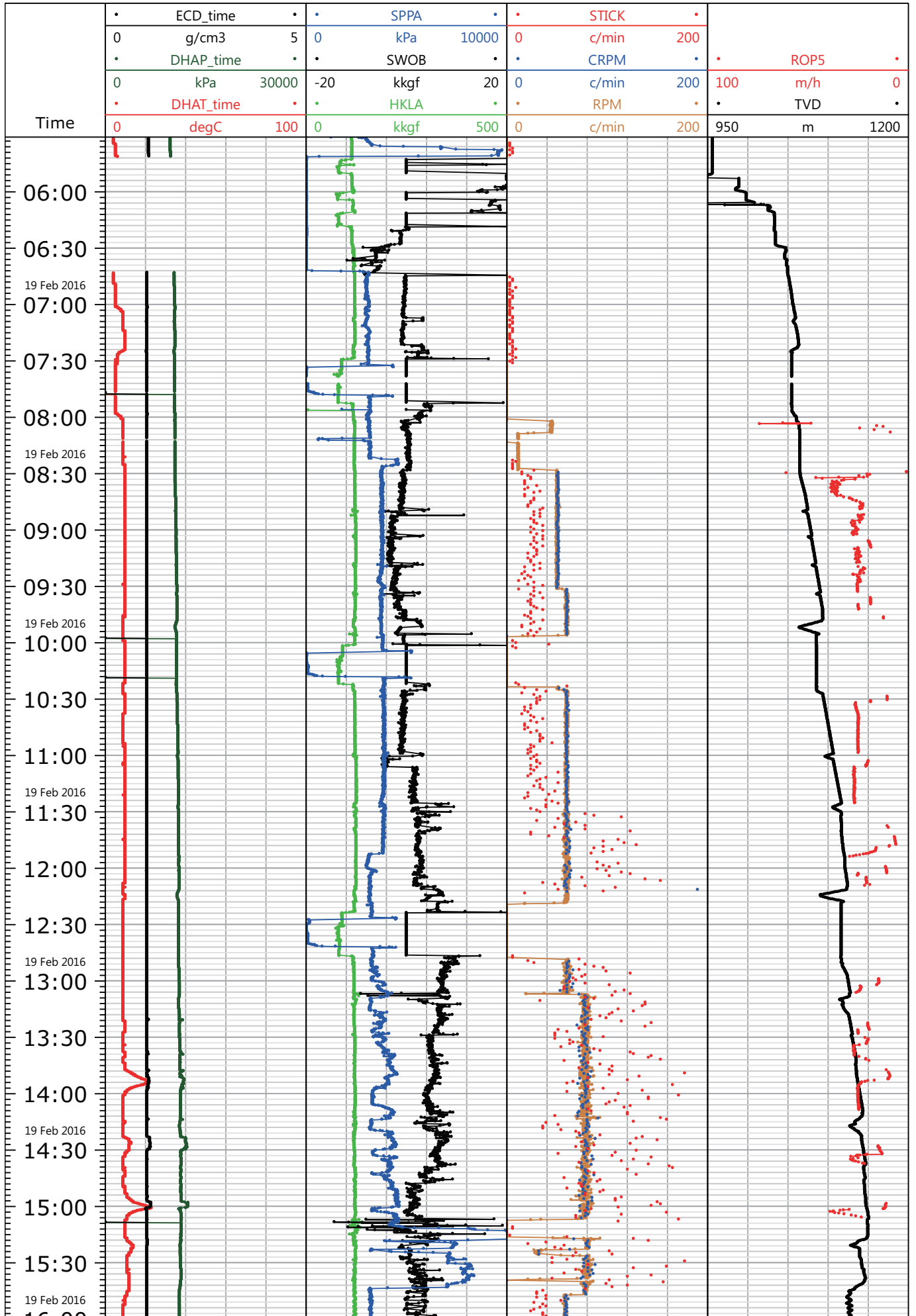


Figure 2-6-1-2: LWD temperature, pressure, drilling parameters, and data quality logs in time, Hole C9021A.

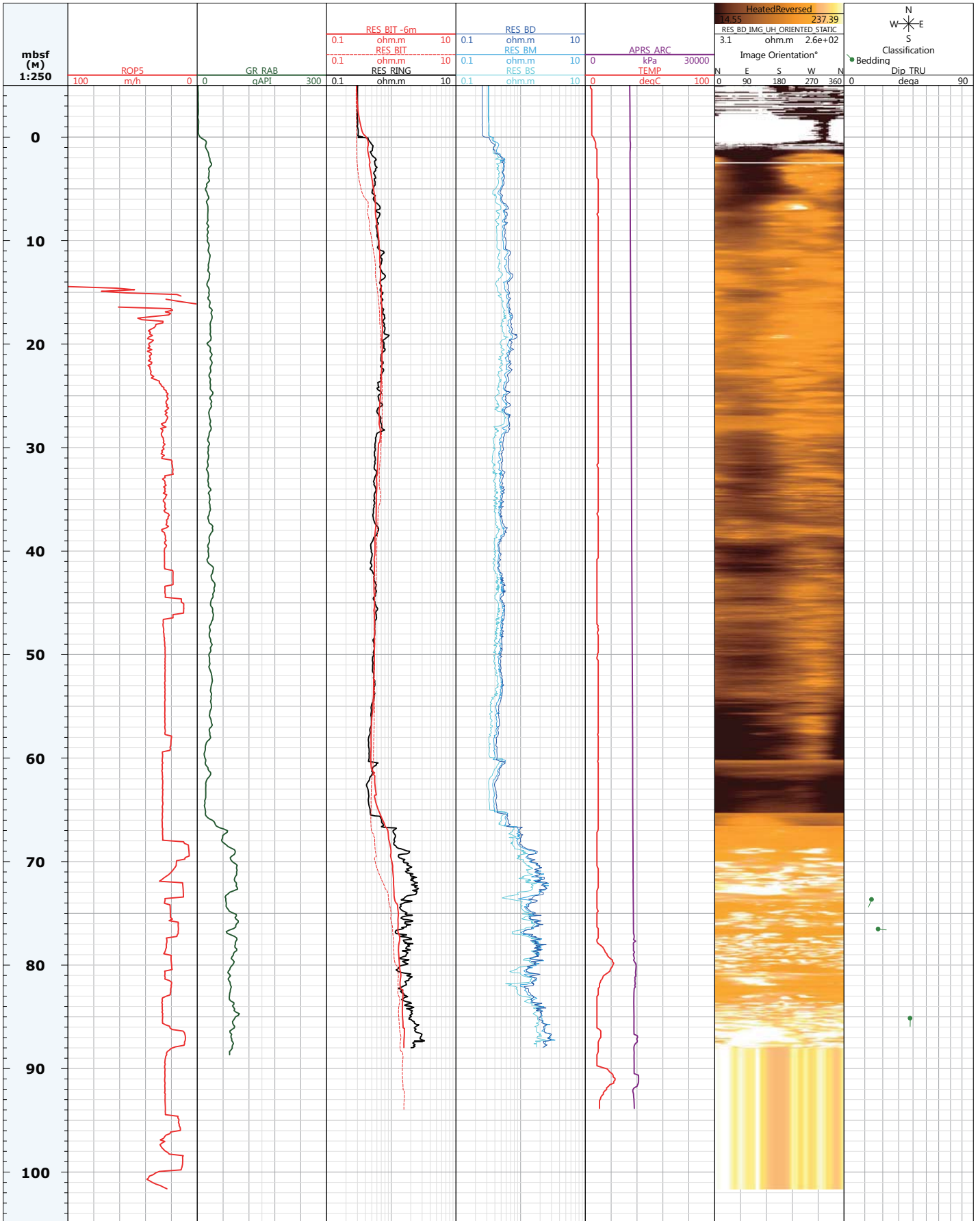


Figure 2-6-1-3: Composite LWD log, Hole C9021A.

2.7 Site C9022 (SIP-NH02)

2.7.1 Logging data quality

Data quality control was performed by monitoring real time data during data acquisition and onboard data processing. The LSS and logging scientists assessed real time drilling mechanical parameters and data from the LWD tools in terms of realistic values for the expected lithology in the drilled interval in Hole C9022A.

LWD data quality logs are shown in **Figs. 2-7-1-1** (in depth) and **Fig. 2-7-1-2** (in time), and a composite LWD log is shown in **Fig. 2-7-1-3**. The mudline was confirmed at 1116.5 mBRT by the gamma ray curve and resistivity curves of geoVISION. The total drilled depth is 1354.5 mBRT (238.0 mbsf). The overall quality of the processed logging data was good. WOB (weight on bit) signals were lost from 108 mbsf to 208 mbsf due to data communication error. Other drilling parameters were mostly stable. The pressure values gradually increased with depth but no specific anomalies were detected. Temperature values were almost constant, but slight fluctuations were observed by the arcVISION. Data quality of the borehole images is good except for the interval from 101 to 105.5 mbsf where the data are missing due to higher ROP (rate of penetration) beyond the recommended value (35–40 m/hr).

2.7.2 Log characterization

LWD logs acquired in Hole C9022A are summarized in **Fig. 2-7-1-3**. The natural gamma ray and resistivity logs are successfully acquired through the borehole (0–230 mbsf). Based on these log trends we divided into three logging units based mainly on the resistivity logs. All resistivity logs show the similar trend though the entire section. We defined a relatively conductive formation in the upper interval as Logging Unit 1 (0–105.0 mbsf), an interval of high frequency change in resistivity as Logging Unit 2 (105.0 to 162.7 mbsf), and the lowermost interval with cyclic trend of the resistivity as Logging Unit 3 (160 to 220 mbsf). The detailed characterization of each logging unit is described below.

Logging Unit 1 (0–105.0 mbsf) was defined as an interval of general increasing trend of gamma ray and decreasing trend of resistivity. The resistivity values just beneath the seafloor increase up to 1 ohm.m at ~1 mbsf, decrease from 1 ohm.m (~6 mbsf) to ~0.4 ohm.m (~10 mbsf), and then gradually increase with depth up to 0.8 ohm-m at ~33 mbsf. In the lower part of the unit, the resistivity logs show a sharp decrease (~0.8 to 0.3 ohm.m) at 34–35 mbsf, and show variable values between 0.2 and 0.5 ohm.m. There are two resistive peaks at 42 mbsf (0.8 ohm.m) and 44 mbsf (~3

ohm.m). The gamma ray values range from 20 to 70 gAPI in the interval of 0–54 mbsf. The range of gamma ray value shifts to 60-90 gAPI at ~54 mbsf. In the lower part of the unit (54-105 mbsf), two positive gamma ray peaks (~140 gAPI) are identified at 96 mbsf and 99 mbsf.

Logging Unit 2 (105.0–162.7 mbsf) exhibits a sharp increase of resistivity (~1 ohm.m) at the top. The resistivity logs show a gradual increasing trend (~4–7 ohm.m) from the top to 121 mbsf and a sequence of high frequency response (ranging from 0.3 to 1.5 ohm.m) in the lower part. The gamma ray log shows a constant baseline of ~60 gAPI with a number of positive excursions and fluctuations. Positive excursions of gamma ray (~120-150 gAPI) occur in the lower part of this unit (147 to 159 mbsf), which shows negative correlations with the resistivity response (~0.4 ohm.m).

Logging Unit 3 (162.7–225.4 mbsf) is defined for the interval characterized by cyclic changes in resistivity value with minor fluctuations. The cycles are composed of three resistive intervals of 163–172, 194–202, and 219–224 mbsf (<3 ohm.m) and two conductive intervals of 172–194 and 202–219 mbsf (>0.3–0.4 ohm.m). The gamma ray curve in the upper half of the unit (163–190 mbsf) shows the similar feature to the lower part of Logging Unit 2, whereas the curve in the lower part of the unit (190–216 mbsf) shows decreasing trend from 120 to 30 gAPI.

2.7.3 Borehole Images

Borehole images acquired in Hole C9022 are well correlated to the downhole variation of resistivity in both unit scale and meter scale. A total of 47 features were picked as dipping bed boundaries or fractures (**Fig. 2-7-3-1**).

General characteristics of the borehole images in Logging Unit 1 (0–105.0 mbsf) are marked by poorly layered formations in 0–34 mbsf and layered formations in 34–105 mbsf. The images in 0–34 mbsf show no obvious dipping planes due to both poor quality of the images and massive feature of the formation. Irregular-shaped resistive boulders are identified in 0–8 mbsf (**Fig. 2-7-3-1**). A number of bedding planes (0–50 degrees of dipping angle with variable azimuth) are identified in 34–60 mbsf.

Borehole images in Logging Unit 2 (105.0–162.7 mbsf) are characterized by irregularly layered structures with steep dipping geometry. A number of thin conductive and resistive layers with irregular planes are commonly developed throughout the unit. The dipping angle of these layers ranges between ~25 and 75 degrees. Some of the high angle resistive plane clearly cut the low angle formation, indicating fracture filled with resistive material (e.g., ~106, 128, 133, 145, and 155 mbsf; **Fig. 2-7-3-2**). Images in ~113–121 mbsf shows breccia-like feature composed of a number of irregular-shaped

resistive blocks with conductive matrix.

Borehole images in Logging Unit 3 (162.7–225.4 mbsf) exhibit a sequence of heterogeneous formation with irregular structures and local conductive and resistive layers. The dipping angle of these layers ranges between ~7 and 30 degrees. Images in ~214–219 mbsf shows breccia-like feature composed of a number of rounded-shaped conductive blocks with resistive matrix.

Figure captions:

Fig. 2-7-1-1: LWD temperature, pressure, drilling parameters, and data quality logs in depth, Hole C9022A. TEMP: annular temperature by arcVISION, DHAT_2: annular temperature by TeleScope, APRS_ARC: annular pressure by arcVISION, DHAP_2: annular pressure by TeleScope, ECD_ARC: equivalent circular density by arcVISION, ROP5: rate of penetration averaged over the last 5 ft, RPM: rotational speed, CRPM_RT: real time collar rotational speed, STICK_RT, real time stick slip indicator, SWOB: surface weight on bit, TORQ: torque, TAB_RAB_BS: shallow button resistivity time after bit, TAB_RAB_BM: medium button resistivity time after bit, TAB_RAB_BD: deep resistivity time after bit, TAB_RAB_RING: ring resistivity time after bit, TAB_RAB_BIT: bit resistivity time after bit, TAB_GR: gamma ray time after bit.

Fig. 2-7-1-2: LWD temperature, pressure, drilling parameters, and data quality logs in time, Hole C9022A. ECD_TIME: equivalent circulation density, DHAP: annular pressure, DHAT: annular temperature, SPPA: standpipe pressure, SWOB: surface weight on bit, HKLA: hook load, STICK: stick slip indicator, CRPM: collar rotation speed, RPM: rotation speed, ROP5: Rate of penetration averaged over the last 5 ft, TVD: true vertical depth.

Fig. 2-7-1-3: Composite LWD log, Hole C9022A. ROP5: rate of penetration averaged over the last 5 ft, GR_RAB: natural gamma radiation, RES_RING: ring resistivity, RES_BIT: bit resistivity, RES_BIT -6m: depth shifted bit resistivity, RES_BD: deep button resistivity, RES_BM: medium button resistivity, RES_BS: shallow button resistivity, APRS_ARC: annular pressure measured by arcVISION, ATMP: annular temperature measured by arcVISION.

Fig. 2-7-3-1: A representative borehole images showing irregular-shaped resistive boulders in poorly layered formations.

Fig. 2-7-3-2: A representative borehole images both with the high and low angle resistive plane clearly in the layered formation.

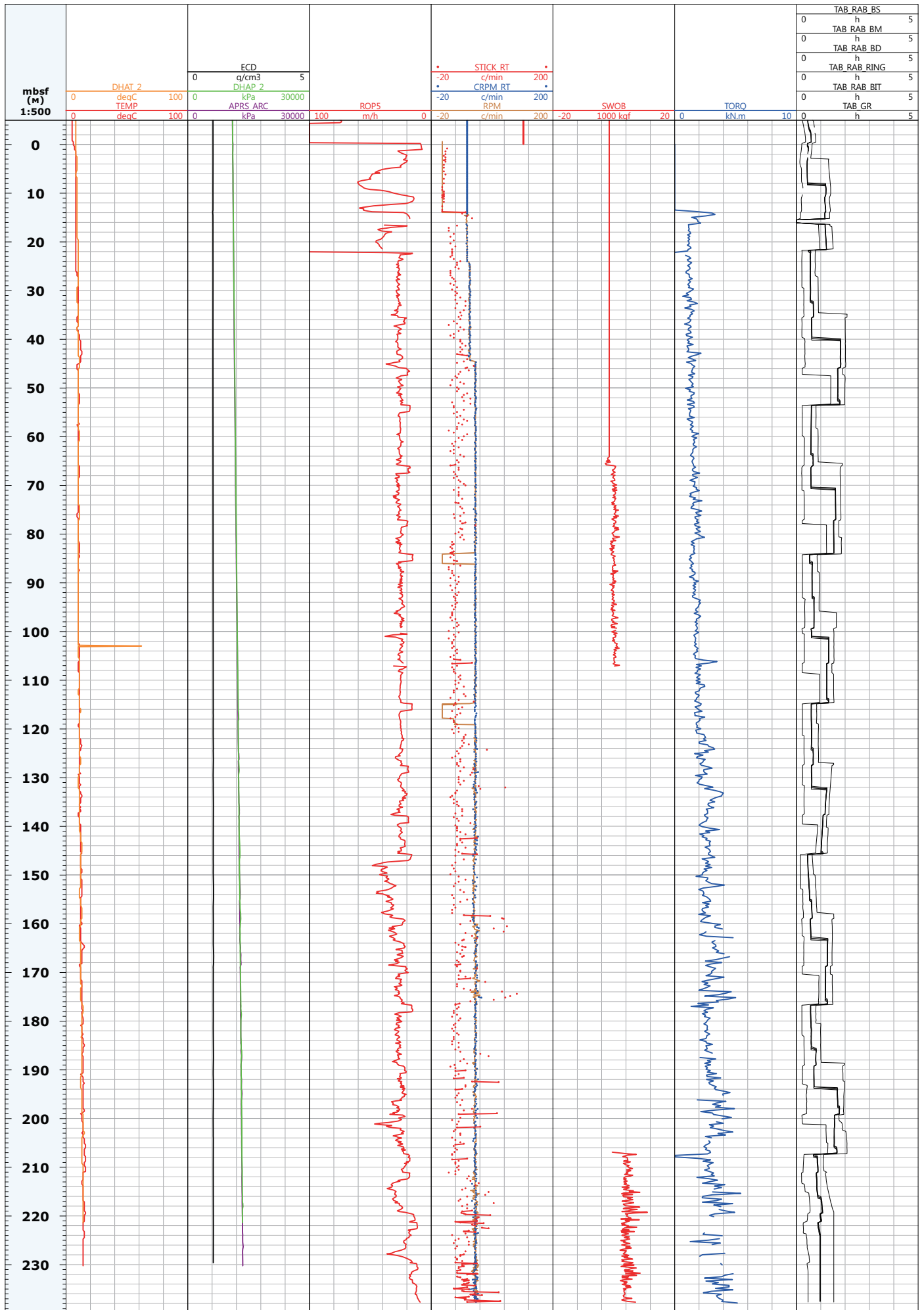


Figure 2-7-1-1: LWD temperature, pressure, drilling parameters, and data quality logs in depth, Hole C9022A.

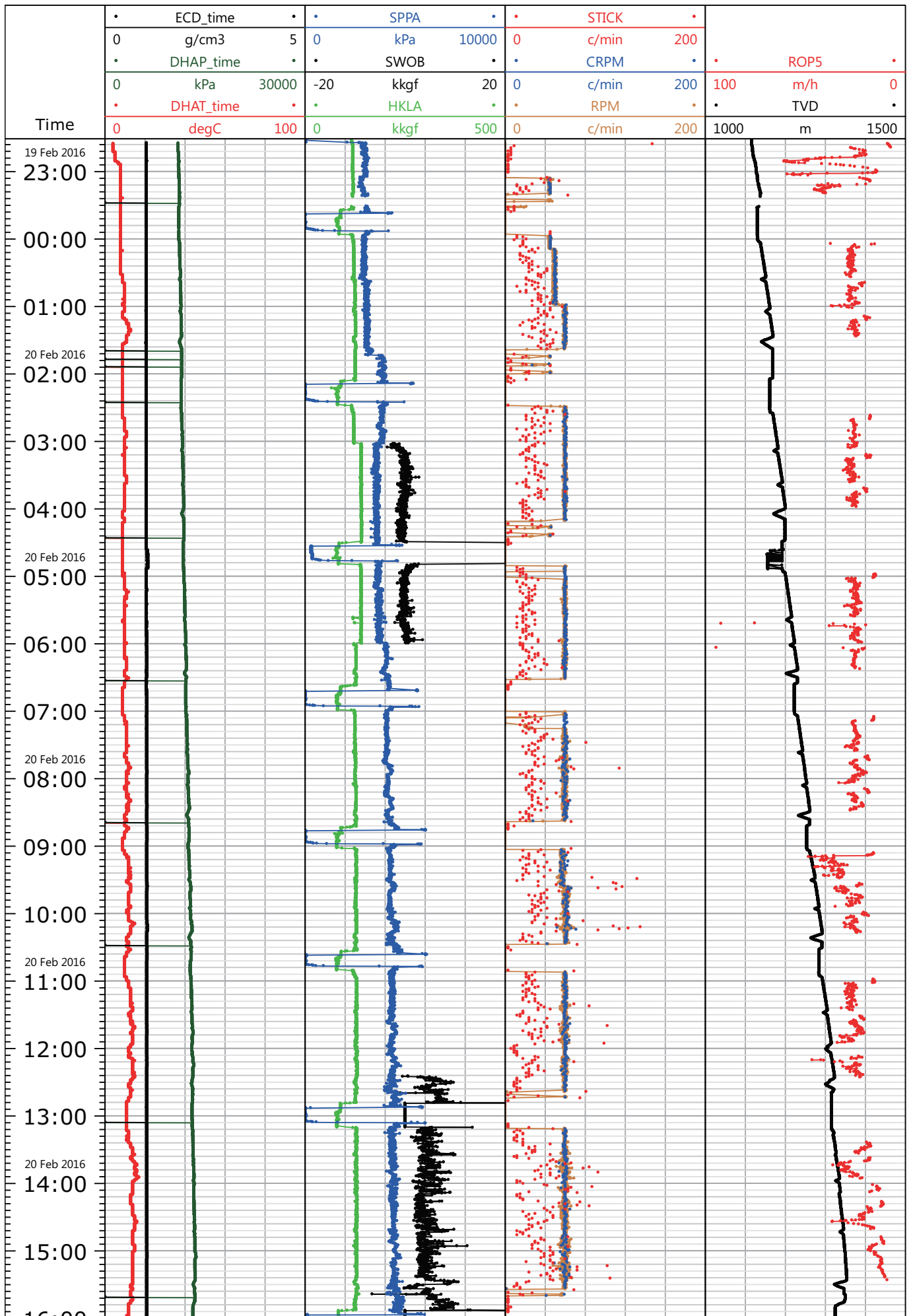


Figure 2-7-1-2: LWD temperature, pressure, drilling parameters, and data quality logs in time, Hole C9022A.

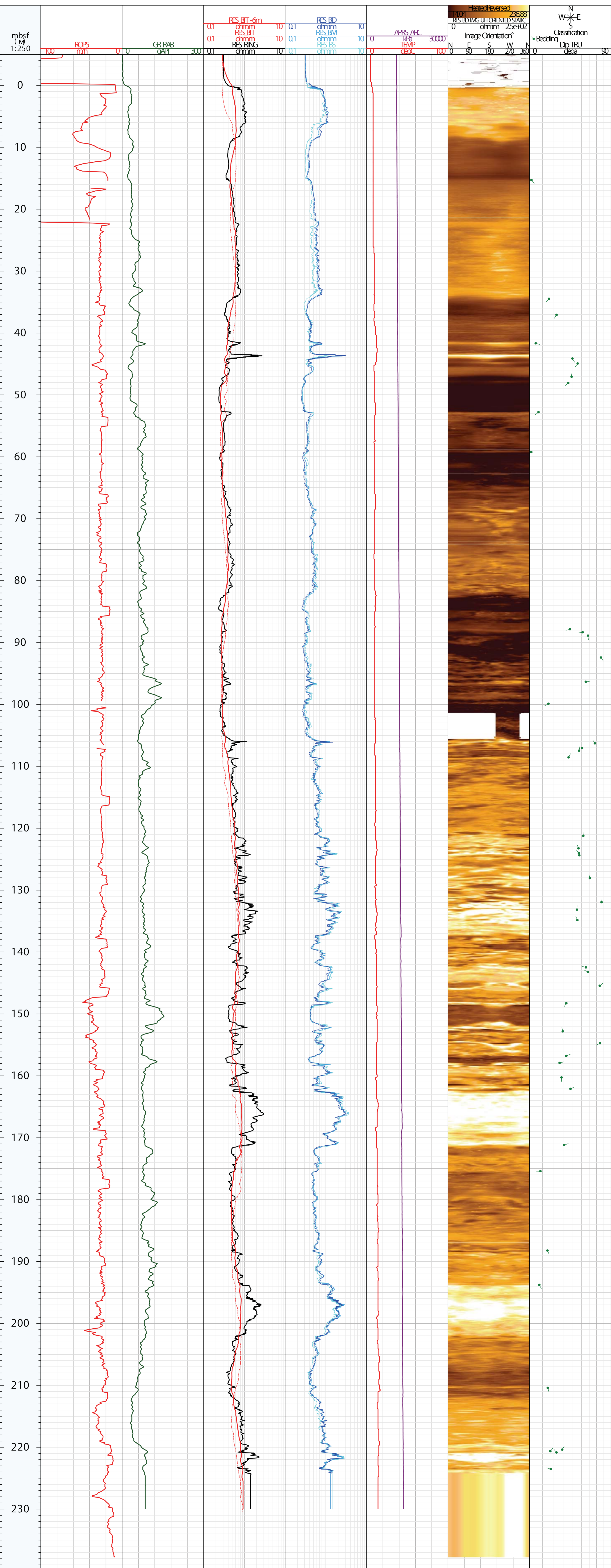


Figure 2-7-1-3: Composite LWD log, Hole C9022A.

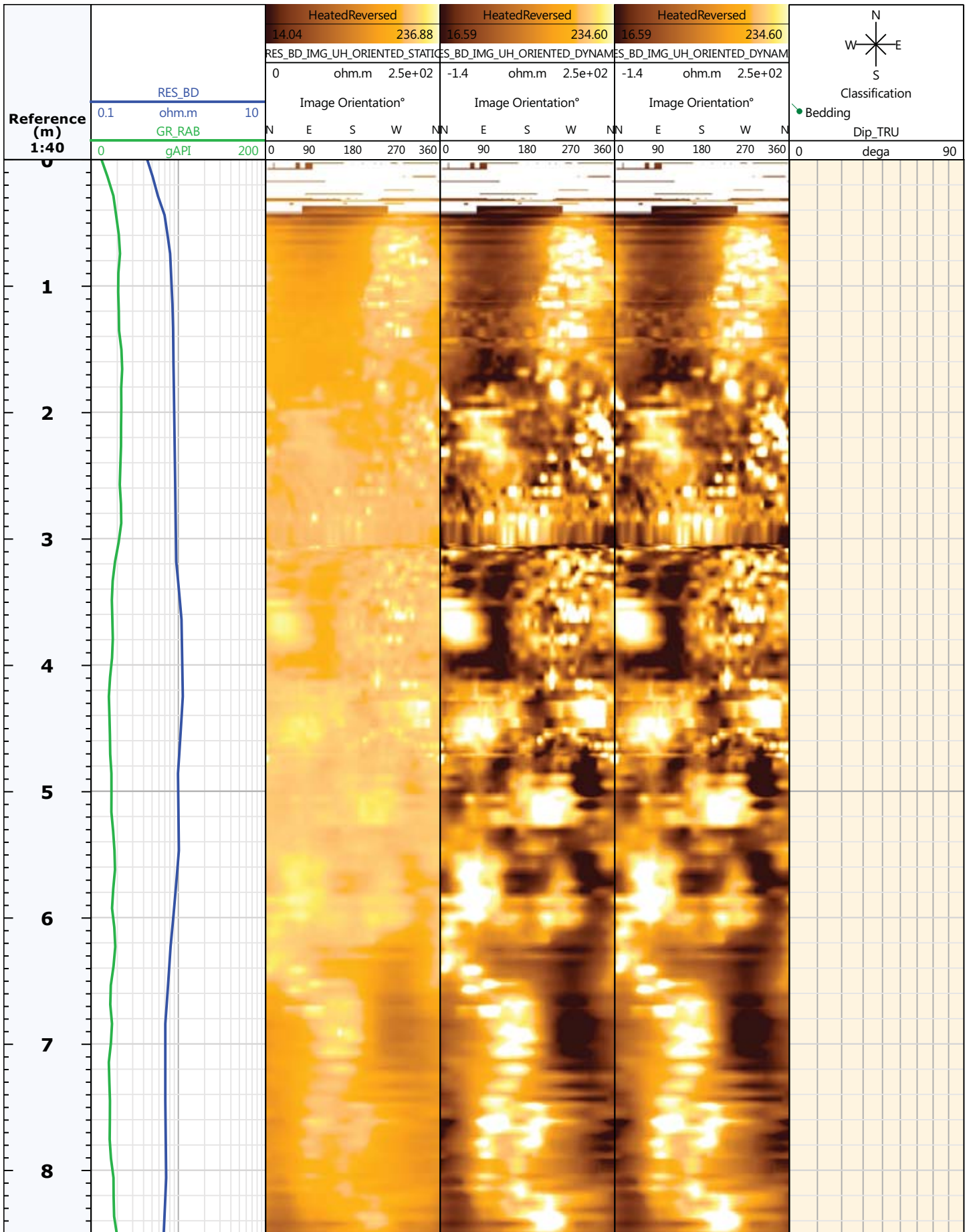


Figure 2-7-3-1: A representative borehole images showing irregular-shaped resistive boulders in poorly layered formations.

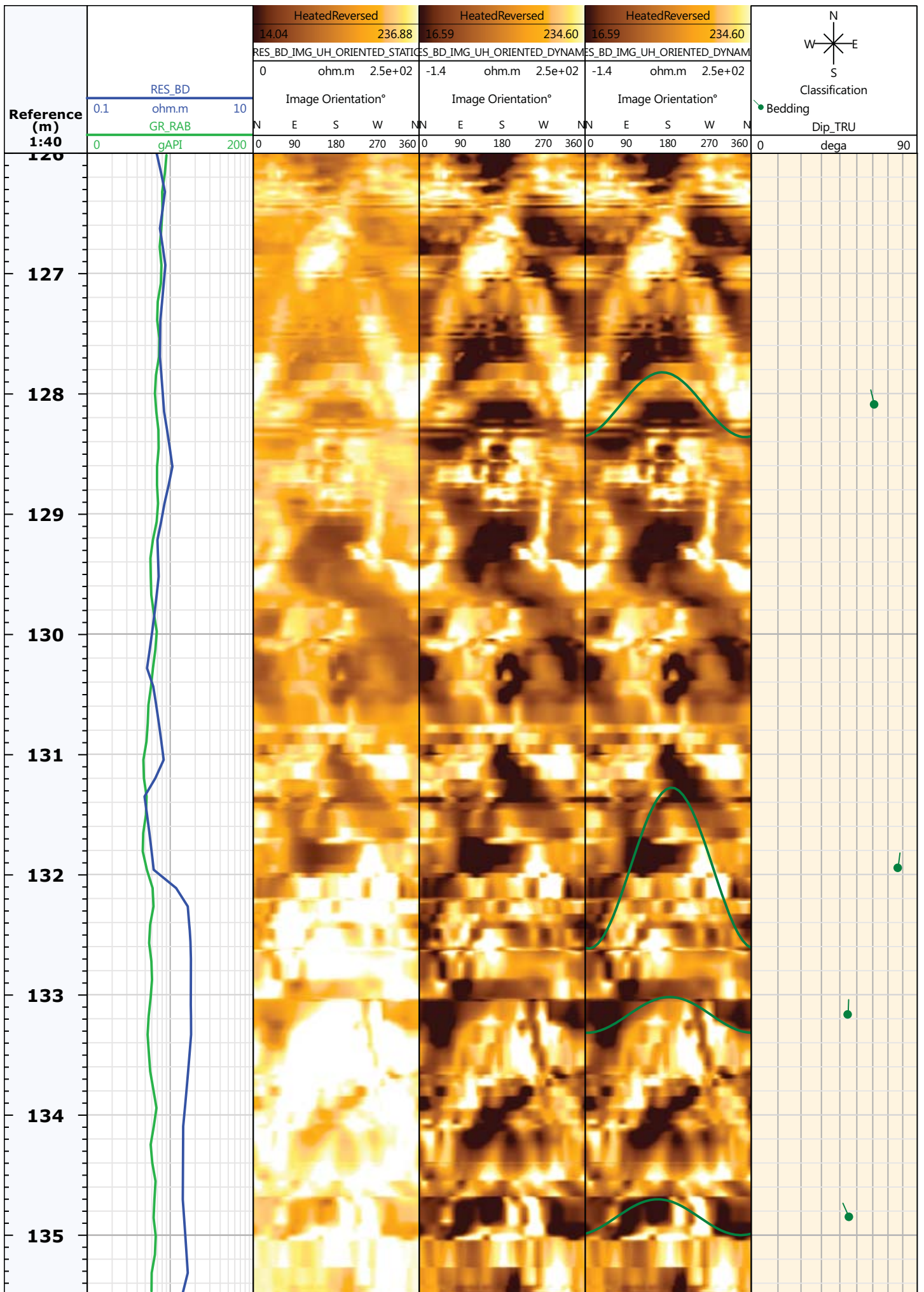


Figure 2-7-3-2: A representative borehole images both with the high and low angle resistive plane clearly in the layered formation.

2.8 Site C9023 (NH14)

2.8.1 Logging data quality

Data quality control was performed by monitoring real time data during data acquisition and onboard data processing. The LSS and logging scientists assessed real time drilling mechanical parameters and data from the LWD tools in terms of realistic values for the expected lithology in the drilled interval in Hole C9023A.

LWD data quality logs are shown in **Fig. 2-8-1-1** (in depth) and **Fig. 2-8-1-2** (in time), and a composite LWD log is shown in **Fig. 2-8-1-3**. The mudline was confirmed at 1100.0 mBRT by the gamma ray curve and resistivity curves of geoVISION. The total drilled depth is 1300.0 mBRT (200 mbsf). The annular pressure profile shows a gradual increasing trend from the seafloor, followed by suddenly decrease at 179 mbsf. The temperature profile is almost flat, but high temperature anomalies were observed more than 30°C below 171 mbsf by TeleScope and more than 40–60°C below 179 mbsf by arcVISION. High gamma ray anomalies more than 800 gAPI (2 mbsf) and more than 300 gAPI (143 mbsf) were observed. Data quality of resistivity borehole image was also good, but shallow button resistivity image below about 176 mbsf was affected by the hole condition (**Fig. 2-8-1-4**).

Another logging data set was acquired while reaming up the LWD tools from 1300 mbsf to 1278 mbsf. The LWD data quality logs are shown in **Fig. 2-8-1-5** and a composite LWD log is shown in **Fig. 2-8-1-6**. Good repeatability is confirmed by the comparison between gamma ray and resistivity curves. Difference of the resistivity profiles between two measurements could be caused by the change of the hole condition. The temperature profile while reaming-up was also different from that measured while drilling (**Fig. 2-8-1-7**).

2.8.2 Log characterization

LWD logs in Hole C9023A are summarized in **Fig. 2-8-1-3**. We successfully acquired natural gamma ray and electric resistivity logs through the entire section (0-186.7 mbsf). All resistivity logs except for the bit resistivity log (showing averaged trend) displays a similar trend throughout the section. Overall, the relationship between resistivity and gamma ray has negative correlation. However, we observed a few positive correlations between resistivity and gamma ray (e.g., at 93-95 mbsf and 117-125 mbsf). Based on the natural gamma ray and resistivity logs, we defined four logging units. We characterized Units 1 and 3 as conductive zones, and Units 2 and 4 as resistive zones. The resistivity value gradually increases through Unit 1 to Unit 2.

Significant decrease in resistivity was then observed at the boundary between Unit 2 and Unit 3. The resistivity value increases again through Unit 3 to Unit 4. Therefore, two large trends in resistivity value (from low to high resistivity) can be observed through the whole logged interval. The detailed description of each logging unit is described below.

Logging Unit 1 is defined for the interval 0–78.0 mbsf. This logging unit is characterized as high gamma ray values (60–858 gAPI), and low resistivity value (~0.2–1.1 ohm.m). The gamma ray is largely fluctuated. The gamma ray log shows the highest value up to 858 gAPI just beneath the seafloor (~1.8 mbsf). This high gamma ray interval is further characterized as the lowest resistivity zone (~0.15 ohm.m). Through the Logging Unit 1, the gamma ray gradually decreases with depth. In contrast, the resistivity value slightly increases with depth.

Logging Unit 2 is defined for the interval 78.0–138.1 mbsf. This unit is characterized as low gamma ray (~60 gAPI), and high resistivity values (~0.4–10 ohm.m). The gamma ray is constantly low through this unit. The resistivity value is fluctuated and gradually increases with depth.

Logging Unit 3 is defined for the interval 138.1–167.0 mbsf. The natural gamma ray values of this unit are high (~60–200 gAPI) and gradually decreases with depth. The highest gamma ray value in this unit (~331 gAPI) is observed at 143.2 mbsf. The gamma ray values sharply decrease at the bottom of this logging unit (i.e., boundary between Units 3 and 4). The resistivity is very low and not varied through this unit (0.3–0.6 ohm.m).

Logging Unit 4 is defined for the interval 167.0–186.7 mbsf. The gamma ray is very low (~40 gAPI) and is not varied through this logging unit. In contrast, the resistivity is largely varied (~0.3–1.1 ohm.m). The resistivity value has sharp contrast at 176 mbsf, where two distinct sequences are bounded.

Ream-up Logging

In the Hole C9023A, ream-up logging was conducted from the bottom of the hole to 178.2 mbsf (bit depth). The geoVISION gamma ray and button resistivity (resistivity image) data were acquired in the interval between 187.2–165.2 mbsf and 186.7–164.7 mbsf, respectively (**Fig. 2-8-1-6**). The most part of the logged interval is equivalent to the Logging Unit 4, which defined in the drill-down section. The gamma ray log shows constant baseline (~40 gAPI) from the TD to 167.5 mbsf. In this interval, resistivity log shows fluctuations in both large and fine scales. The resistivity values decrease from ~3.0 to 0.4 ohm-m (TD–178.5 mbsf), increase up to ~4.0 ohm-m (178.5–

173.7 mbsf), and drop down to 0.4 ohm-m (178.5–167.5 mbsf). Both of the gamma ray and resistivity profiles show a significant baseline shift at 167.0 mbsf, which corresponds to the depth of the unit boundary between the Logging Unit 3 and 4 (see above). The gamma ray baseline varies up to ~120 gAPI and resistivity logs show stable values (0.3 ohm-m) above that depth. These gamma ray and resistivity profiles obtained by ream up logging shows much similarity with those obtained by drill-down logging. The comparison of the dill down log and ream up log is shown in **Fig. 2-8-1-7**. The gamma ray values measured while ream-up logging are slightly lower than those measured while drill-down logging, especially in the interval 165.2–178.5 mbsf. The resistivity data measured while ream-up logging also show smaller values comparing to the drill-down resistivity, showing a remarkable curve separation of the shallow button resistivity. Some resistive peaks disappear in the ream up log (e.g. 167.1 mbsf).

2.8.3 Borehole images

Borehole images acquired in Hole C9023A are displayed in **Fig. 2-8-1-3**. Continuous borehole images were acquired throughout the logged interval (0-187 mbsf). The images are well correlated to the downhole variation of resistivity and natural gamma ray curves. Logging Unit 1 (0-78.0 mbsf) and Unit 3 (138.1-167.0 mbsf) are recognized as resistive zones (darker color in resistivity image), and Logging Unit 2 (78.0-138.1 mbsf) and Unit 4 (167.0-186.7 mbsf) are conductive zones (brighter color). We extracted geometry of bedding planes, conductive and resistive fractures from sinusoidal curves on the dynamic and static images (**Fig. 2-8-1-3**). We identified an enormous number of conductive fractures in the resistive sections (i.e., Units 2 and 4). The characterization of each unit is described below.

Logging Unit 1 (0–78.0 mbsf) is identified as conductive zone. Only a small number of beddings and conductive fractures are identified in this unit, partially due to low quality of the image data and/or massive and heterogeneous nature of the formation. Low angle conductive fractures dipping to southeast are concentrated at the interval from 39 to 42 mbsf.

Various types of fractures are intensively developed in the borehole images acquired in Logging Unit 2 (78.0–138.1 mbsf). The overall texture is characterized by a fracture network system composed of various thickness (few cm to ~10 cm scale) and geometry of fractures or cracks filled with relatively conductive material (but still as resistive as ~1 ohm.m) than the host rock (~2–10 ohm.m). Both low and high angle conductive fractures are co-developed (conjugated) and cut each other. Combination of the low and high angle fractures forms “blocky texture” in few meters scale. Thin minor

(secondary) conductive fractures are also developed within the blocks and form micro-blocks with grid-like or random network structures in few cm scale. Most of features show that low angle fracture is formed primary and high angle fracture is secondary. The borehole images in the conductive intervals (e.g., 89–90 and 92–98 mbsf) between the resistive intervals exhibit massive and heterogeneous features with conductive spots. No clear textures are extracted below 125 mbsf due to low quality of the images.

Logging Unit 3 (138.1-167.0 mbsf) is a conductive zone. In the static images, two clear conductive zones can be identified at 143~146 mbsf and 150-152 mbsf. At the top of the shallower conductive zone (~143 mbsf), one resistive fracture can be identified. In this conductive logging unit, we cannot identify clear structures.

Logging Unit 4 (167.0-186.7 mbsf) is characterized as resistive zone, but the resistivity decreases at ~175 mbsf. The resistivity increases again at the bottom of the borehole. Several fractures are observed at the bottom of this unit (184–187 mbsf). The dips of these fractures are relatively steep, ranging from 40 to 85 degrees (**Fig. 2-8-1-3**). Because temperature increases at these fractures, they could work as hydrothermal fluid pathway.

Ream-up logging

The borehole images were also obtained by the ream-up logging in the interval between 186.7–164.7 mbsf (**Fig. 2-8-1-6**). The images show good correlations with the resistivity and gamma ray log profiles. Higher gamma ray and low resistivity interval in the Logging Unit 4 (180.5–176.8 mbsf) and low gamma ray and low resistivity part, corresponding to the Logging Unit 3 (167.0–164.7 mbsf) are clearly shown as darker zone in the image log as well as that acquired by drill-down log. Although the ream-up images are unclear comparing to drill-down log images, fracture geometry is extracted by fitting sinusoidal curves with image contrast on the static and dynamic ones (**Fig. 2-8-1-6**). Two conductive fractures are identified in the images at 174.2 and 184.6 mbsf. The dips and directions of the fractures are 55 degrees to the north and 74 degrees to the north-east, respectively. These attitudes of the conductive fractures are consistent with the fractures identified in the drill-down log images (**Fig. 2-8-1-3**).

2.8.4 Temperature and Pressure (C9023)

Annular temperature and pressure measured by both arcVISION and Telescope in Hole C9023A are displayed in **Figs. 2-8-1-1** and **-3**. Baselines of temperature slightly increase with depth from 12°C (mudline) to 20°C (178.3 mbsf) for arcVISION and from

11°C (mudline) to 18°C (170.1 mbsf) for Telescope. Below 178.3 mbsf, the baselines of arcVISION temperatures significantly increase to 40°C and keep the value to 181.5 mbsf. The temperature increases with depth from 40°C (181.5 mbsf) to 60°C (186.5 mbsf), accompanying two positive peaks up to 52°C (183.2 mbsf) and 65°C (185.1 mbsf). Then the baseline shows a decreasing trend to 56°C (TD). The Telescope temperature also shows an anomalous increase with depth from 170.1 mbsf. The temperature value reaches 36°C at 178.0 mbsf, then the value is constant to TD. Baselines of the annular pressure obtained by arcVISION and Telescope increase with depth from 10.9 MPa (mudline) to 12.8 MPa (179.1 mbsf). The Telescope pressure keeps the trend to TD, whereas the arcVISION pressure shows a local decrease of 0.3 MPa at 179.7 mbsf. The baseline of the arcVISION pressure is maintained as approximately-constant value from that depth to TD with some fluctuation (12.2-12.5 MPa).

Figure Captions:

Fig. 2-8-1-1: LWD temperature, pressure, drilling parameters, and data quality logs in depth, Hole C9023A. TEMP: annular temperature by arcVISION, DHAT_2: annular temperature by TeleScope, APRS_ARC: annular pressure by arcVISION, DHAP_2: annular pressure by TeleScope, ECD_ARC: equivalent circular density by arcVISION, ROP5: rate of penetration averaged over the last 5 ft, RPM: rotational speed, CRPM_RT: real time collar rotational speed, STICK_RT, real time stick slip indicator, SWOB: surface weight on bit, TORQ: torque, TAB_RAB_BS: shallow button resistivity time after bit, TAB_RAB_BM: medium button resistivity time after bit, TAB_RAB_BD: deep resistivity time after bit, TAB_RAB_RING: ring resistivity time after bit, TAB_RAB_BIT: bit resistivity time after bit, TAB_GR: gamma ray time after bit.

Fig. 2-8-1-2: LWD temperature, pressure, drilling parameters, and data quality logs in time, Hole C9023A. ECD_TIME: equivalent circulation density, DHAP: annular pressure, DHAT: annular temperature, SPPA: standpipe pressure, SWOB: surface weight on bit, HKLA: hook load, STICK: stick slip indicator, CRPM: collar rotation speed, RPM: rotation speed, ROP5: Rate of penetration averaged over the last 5 ft, TVD: true vertical depth.

Fig. 2-8-1-3: Composite LWD log while drilling down, Hole C9023A. ROP5: rate of penetration averaged over the last 5 ft, GR_RAB: natural gamma radiation, RES_RING: ring resistivity, RES_BIT: bit resistivity, RES_BIT -6m: depth shifted bit resistivity, RES_BD: deep button resistivity, RES_BM: medium button resistivity, RES_BS: shallow button resistivity, APRS_ARC: annular pressure measured by arcVISION, ATMP: annular temperature measured by arcVISION.

Fig. 2-8-1-4: Comparison of borehole images generated by shallow button resistivity. The image acquired while reaming-up is affected by borehole condition, Hole C9023A.

Fig. 2-8-1-5: LWD temperature, pressure, drilling parameters, and data quality logs acquired while reaming-up, Hole C9023A. TEMP: annular temperature by arcVISION, DHAT_2: annular temperature by TeleScope, APRS_ARC: annular pressure by arcVISION, DHAP_2: annular pressure by TeleScope, ECD_ARC: equivalent circular density by arcVISION, ROP5: rate of penetration averaged over the last 5 ft, RPM:

rotational speed, CRPM_RT: real time collar rotational speed, STICK_RT, real time stick slip indicator, SWOB: surface weight on bit, TORQ: torque, TAB_RAB_BS: shallow button resistivity time after bit, TAB_RAB_BM: medium button resistivity time after bit, TAB_RAB_BD: deep resistivity time after bit, TAB_RAB_RING: ring resistivity time after bit, TAB_RAB_BIT: bit resistivity time after bit, TAB_GR: gamma ray time after bit.

Fig. 2-8-1-6: Composite LWD log while reaming-up, Hole C9023A. ROP5: rate of penetration averaged over the last 5 ft, GR_RAB: natural gamma radiation, RES_RING: ring resistivity, RES_BIT: bit resistivity, RES_BIT -6m: depth shifted bit resistivity, RES_BD: deep button resistivity, RES_BM: medium button resistivity, RES_BS: shallow button resistivity, APRS_ARC: annular pressure measured by arcVISION, ATMP: annular temperature measured by arcVISION.

Fig. 2-8-1-7: C9023A Comparison of LWD logs between while drilling down and while reaming-up. GR_RAB: gamma ray, RES_BS: shallow button resistivity, RES_BM: medium button resistivity, RES_BD: deep button resistivity, TEMP: annular temperature by arcVISION, APRS_ARC: annular pressure by arcVISION.

Fig. 2-8-1-8: A representative borehole images showing blocky fracture network in Logging Unit 2, Hole C9023A (CONFIDENTIAL).

Fig. 2-8-1-9: Borehole images acquired from the lowermost part of the section, Hole 9023A (CONFIDENTIAL).

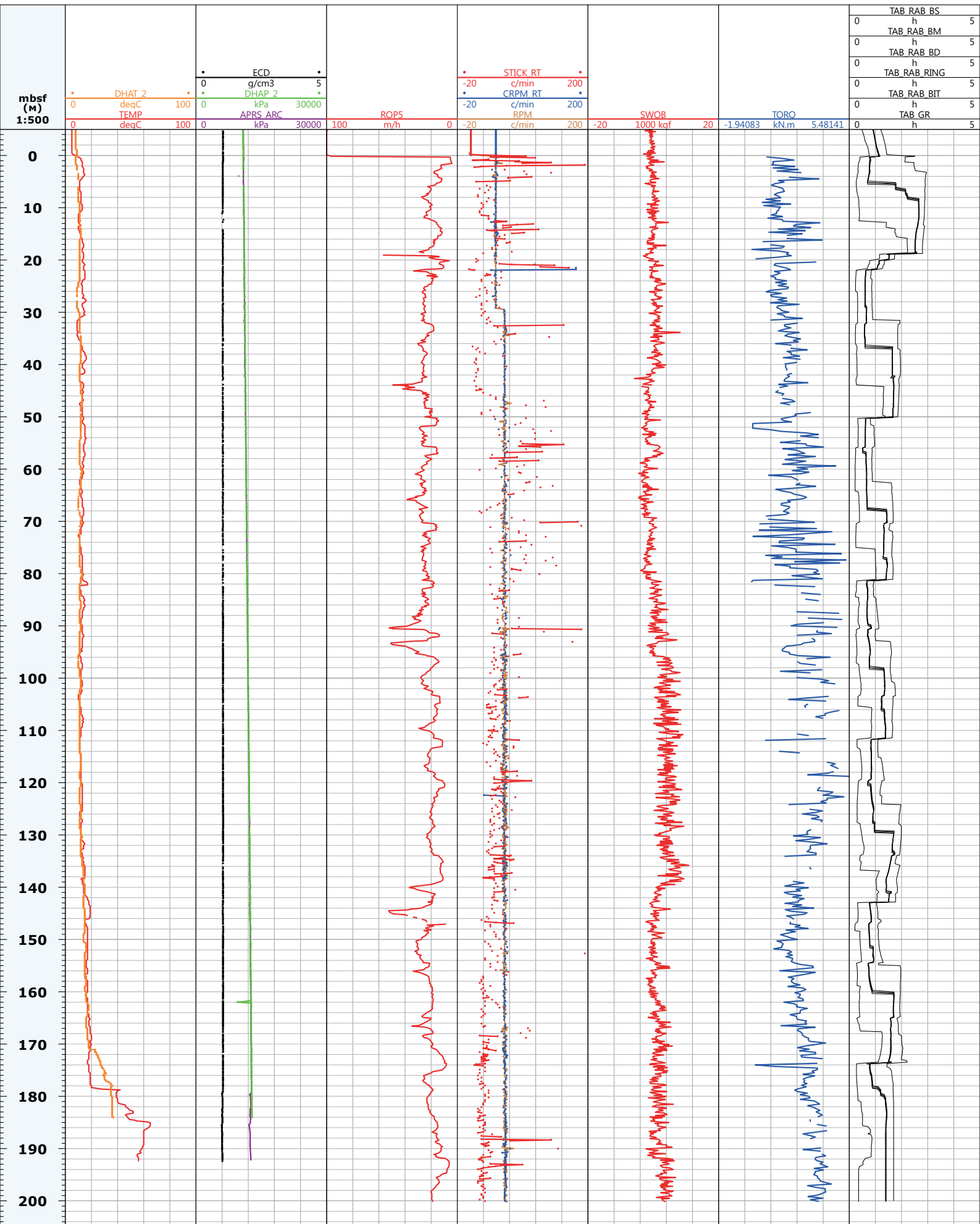


Figure 2-8-1-1: LWD temperature, pressure, drilling parameters, and data quality logs in depth, Hole C9023A.

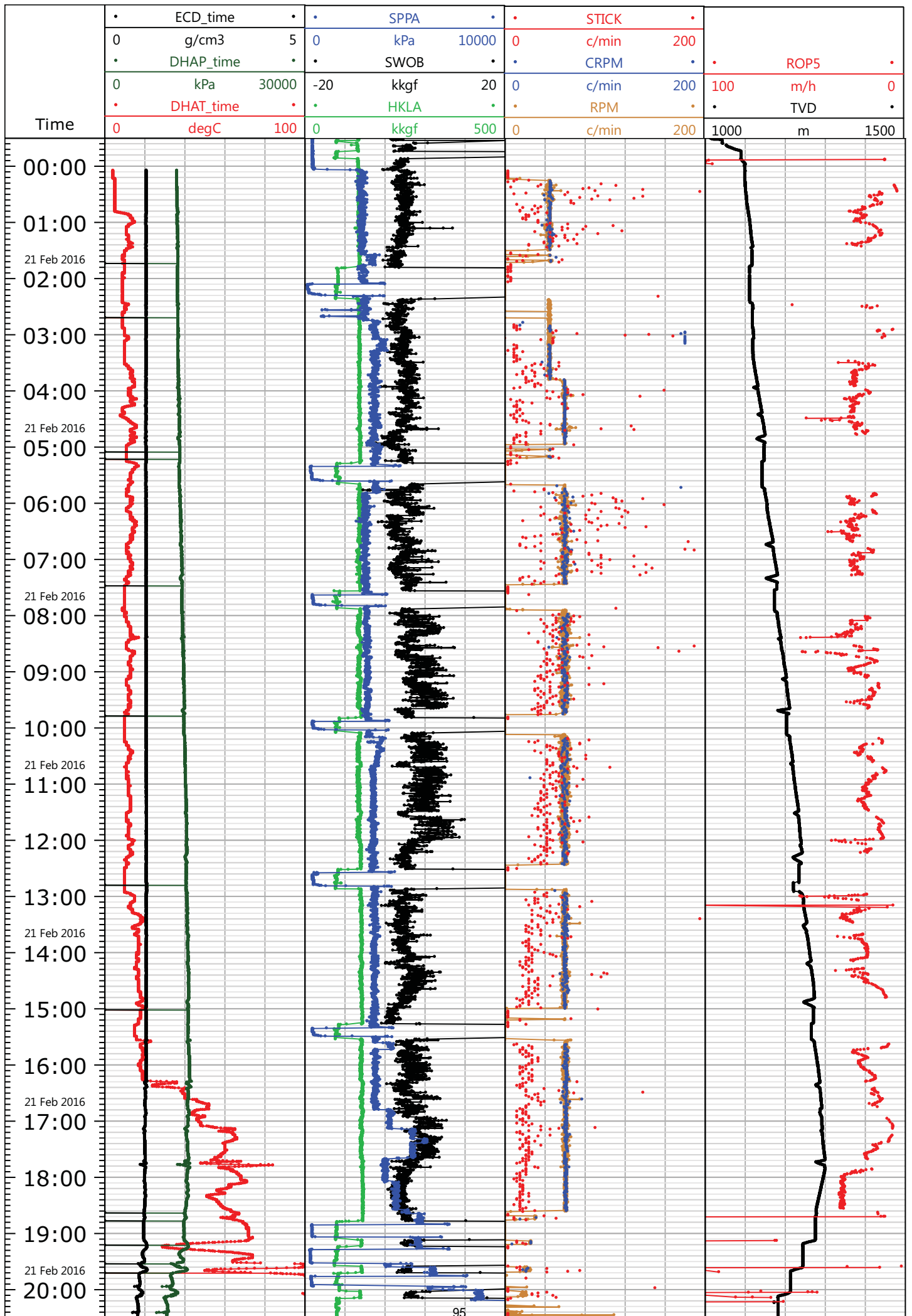


Figure 2-8-1-2: LWD temperature, pressure, drilling parameters, and data quality logs in time, Hole C9023A.

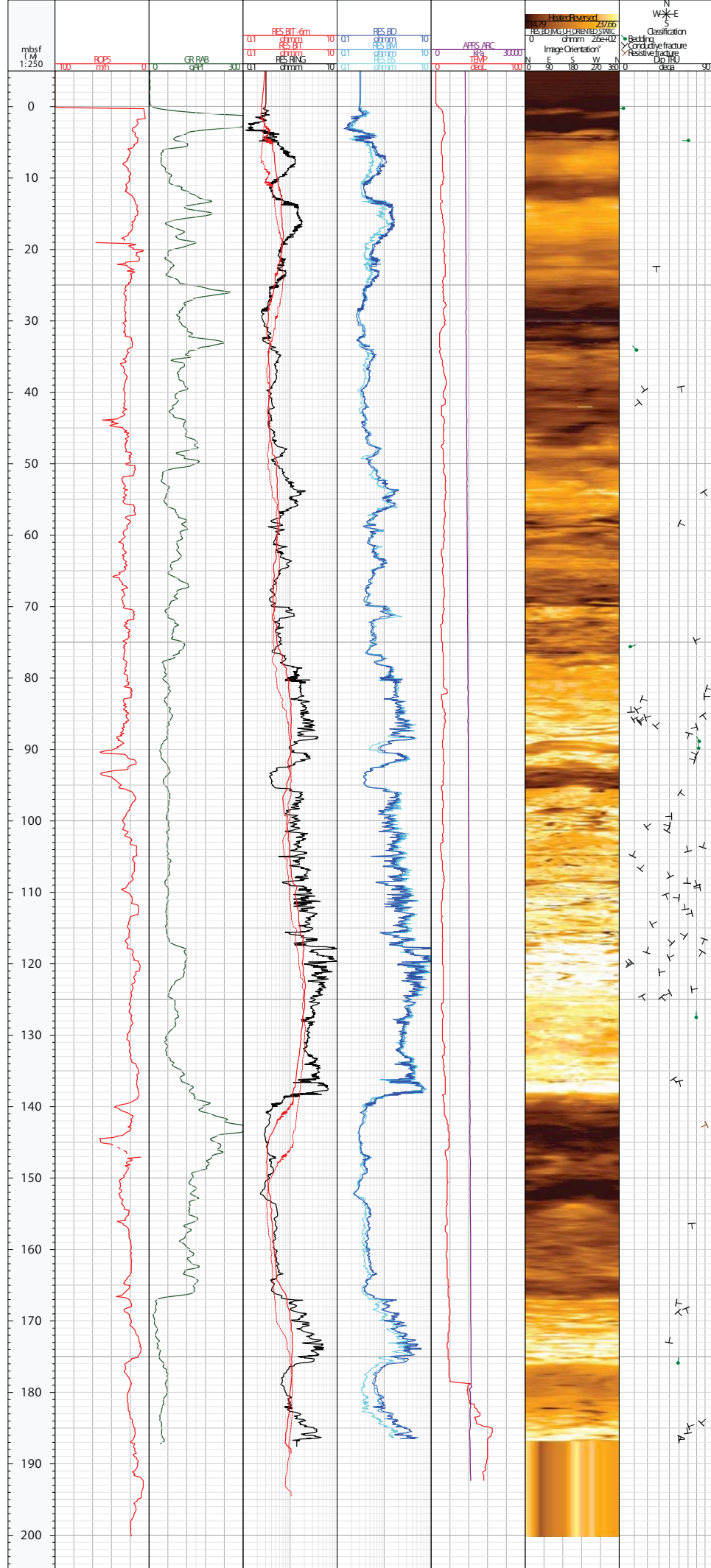


Figure 2-8-1-3: Composite LWD log⁹⁶ while drilling down, Hole C9023A.

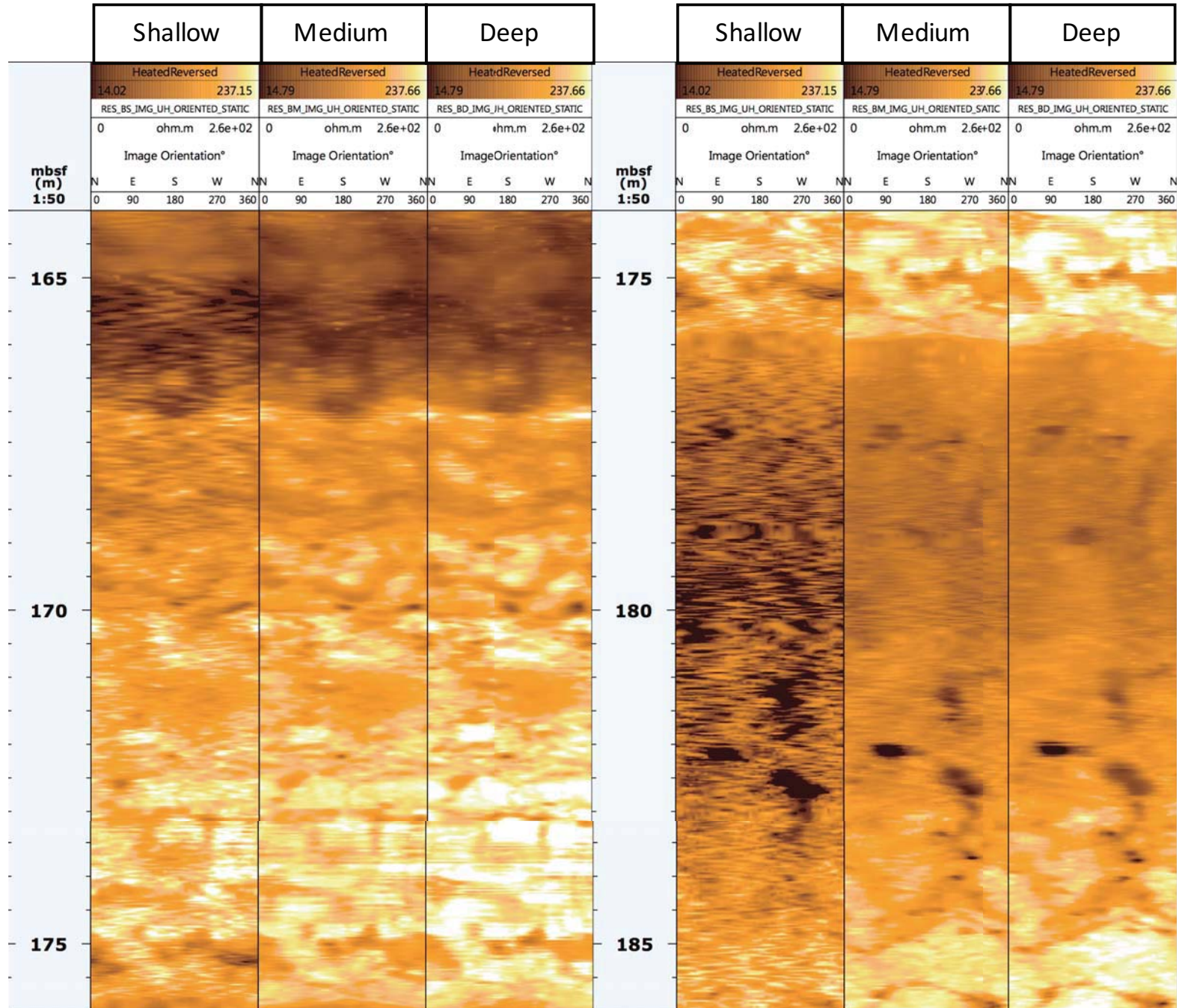


Figure 2-8-1-4: Comparison of borehole images generated by shallow button resistivity. The image acquired while reaming-up is affected by borehole condition, Hole C9023A

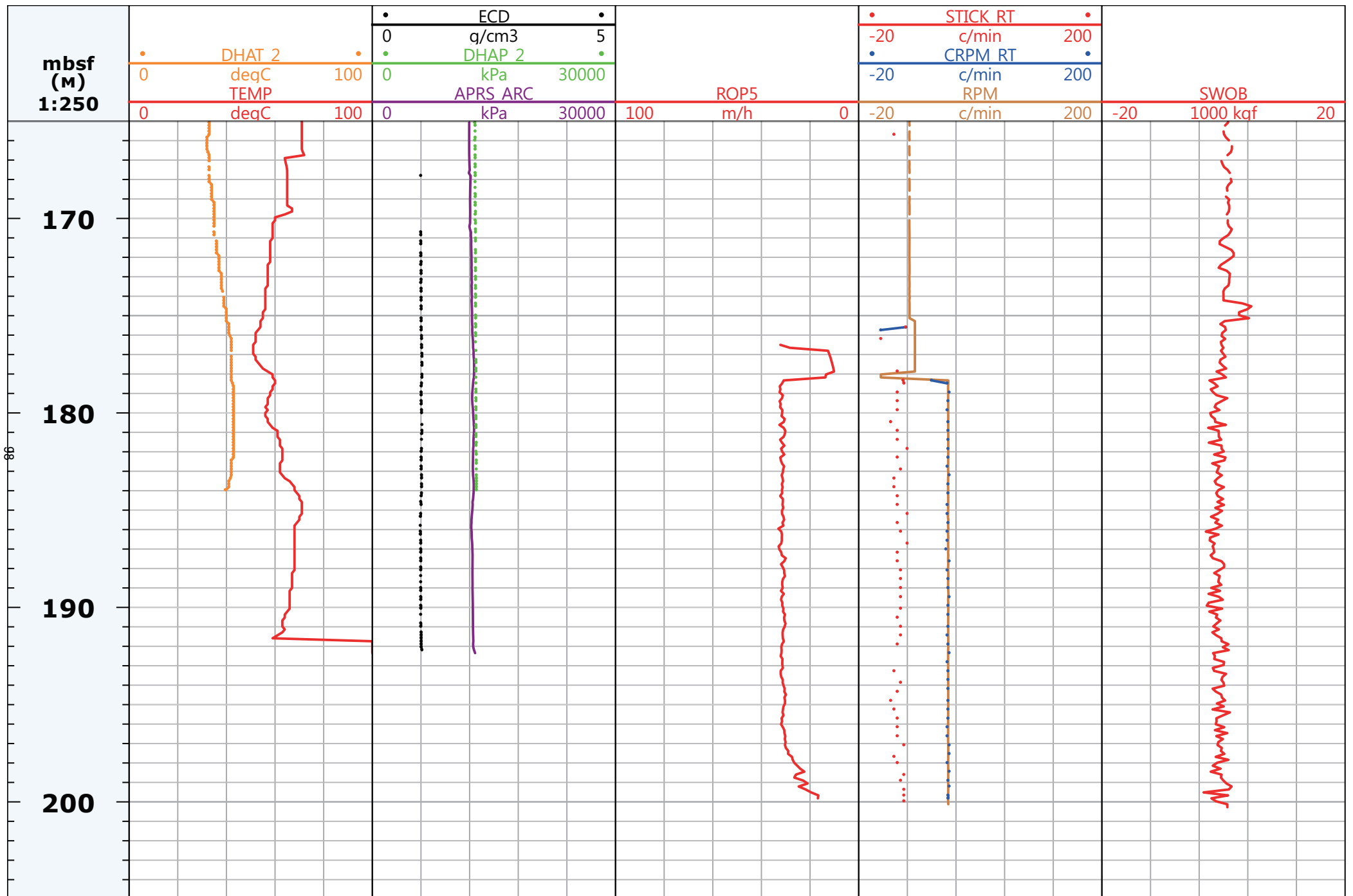


Figure 2-8-1-5: LWD temperature, pressure, drilling parameters, and data quality logs acquired while reaming-up, Hole C9023A.

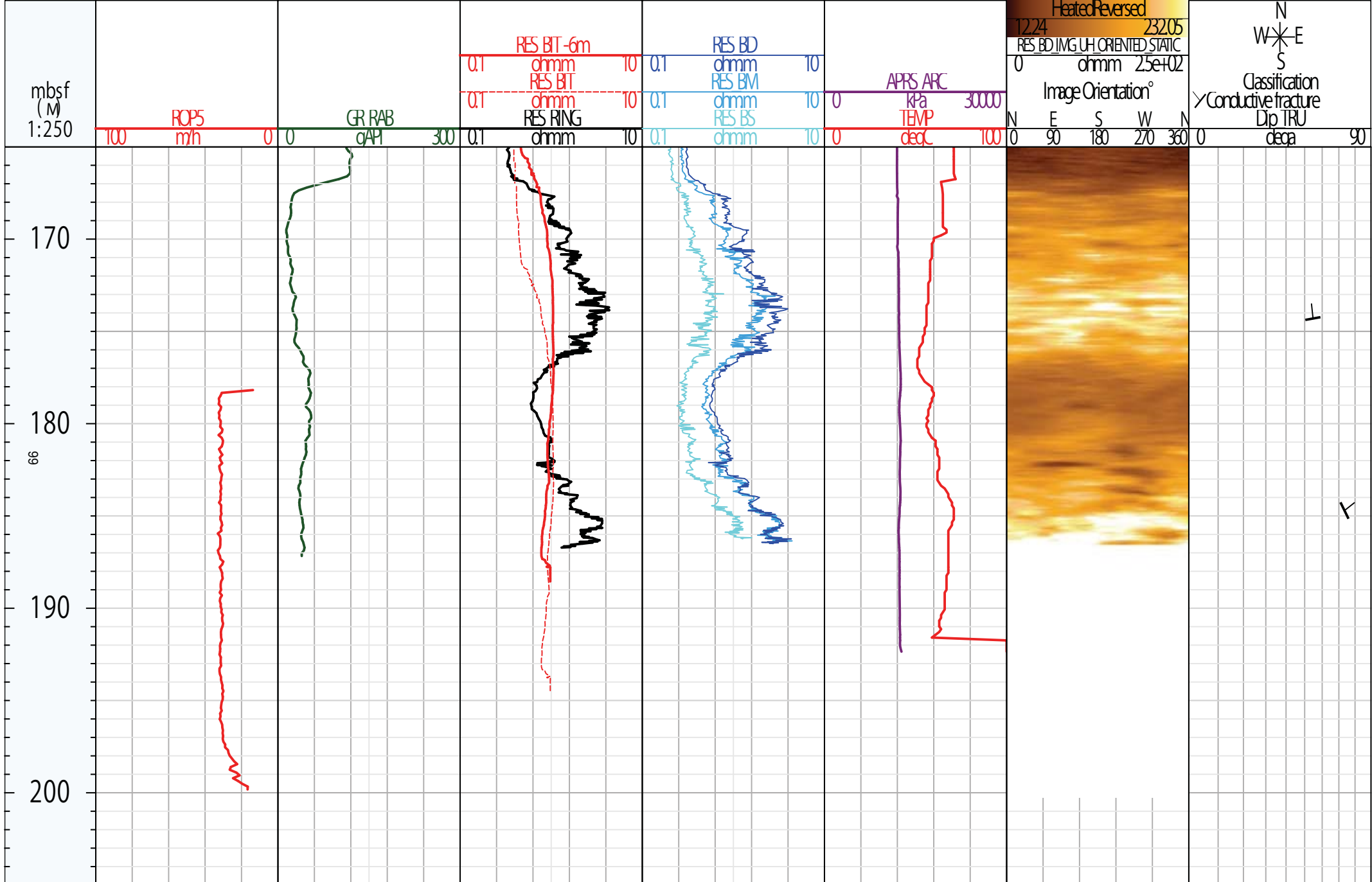


Figure 2-8-1-6: Composite LWD log while reaming-up, Hole C9023A.

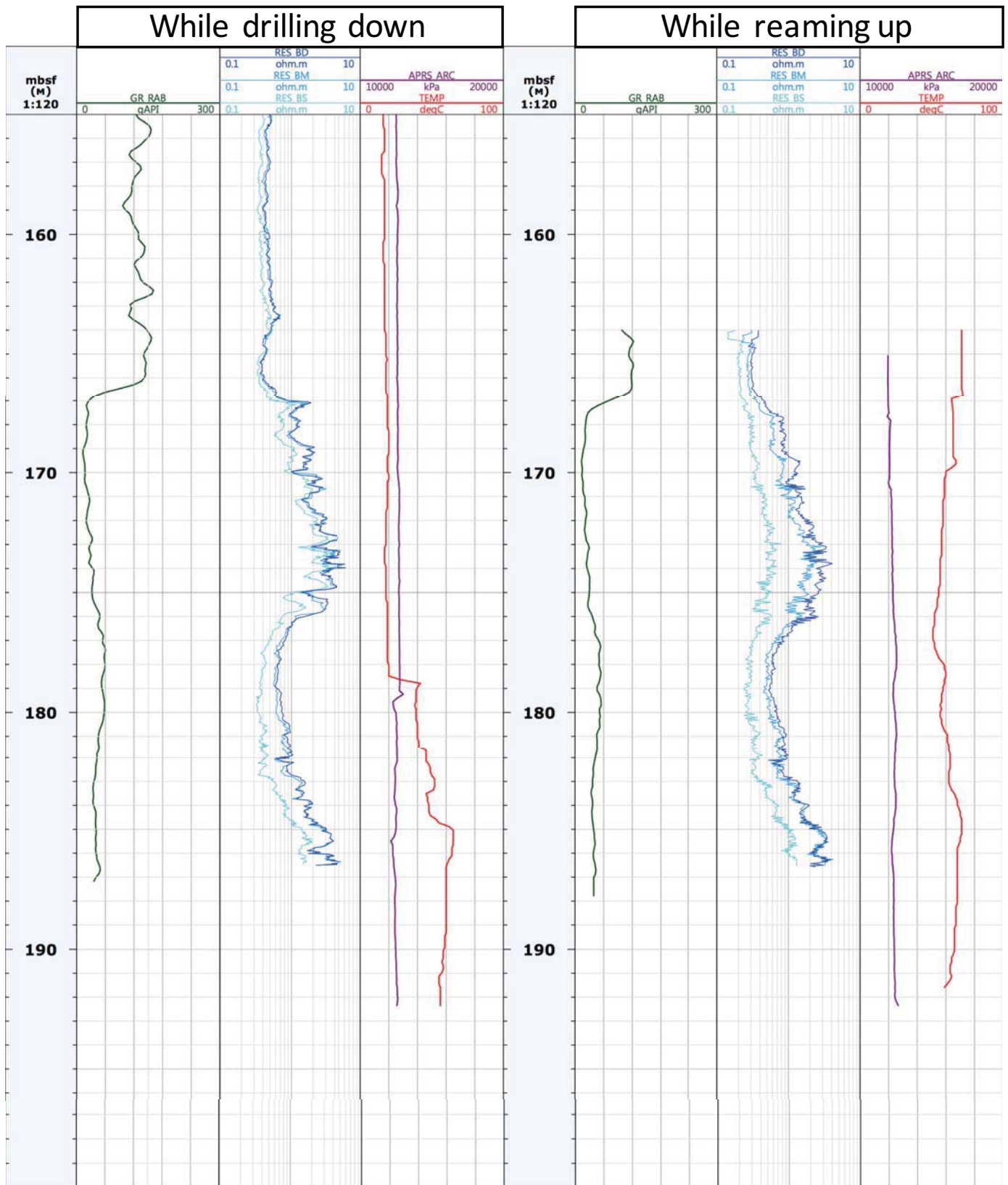


Figure 2-8-1-7: C9023A Comparison of LWD logs between while drilling down and while reaming-up.

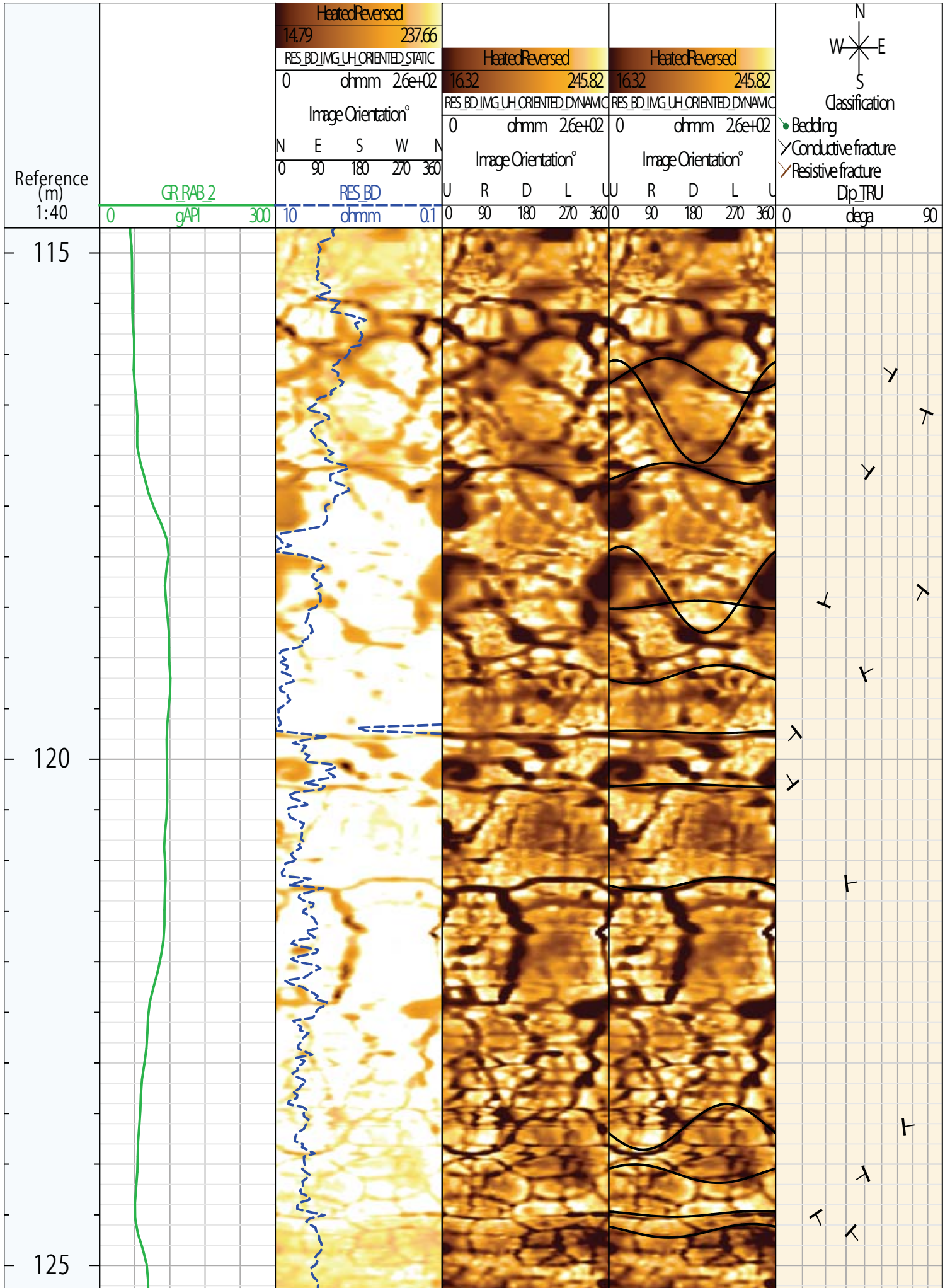


Figure 2-8-1-8: A representative borehole images showing blocky fracture network in Logging Unit 2, Hole C9023A (CONFIDENTIAL).

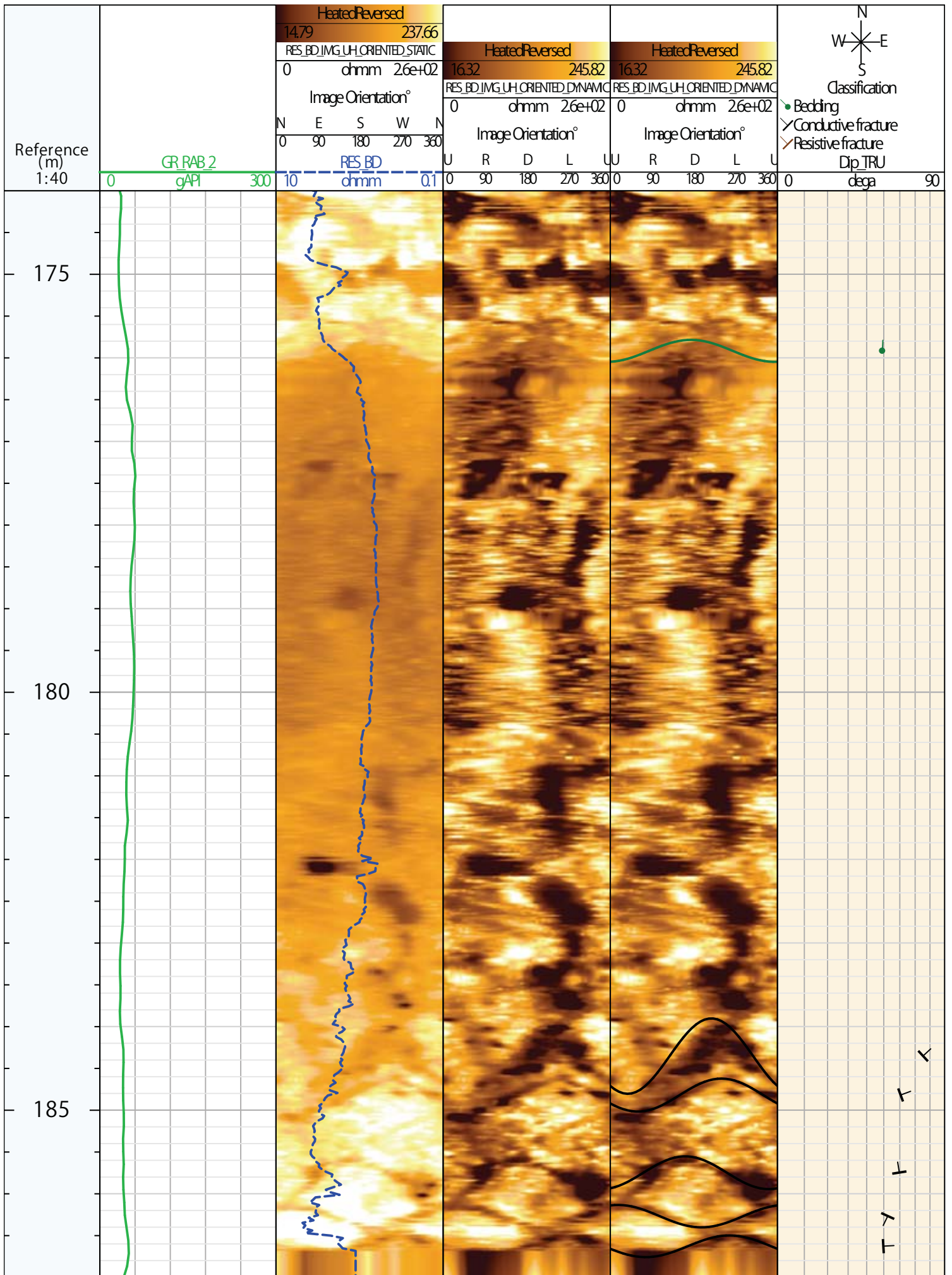


Figure 2-8-1-9: Borehole images acquired from the lowermost part of the section, Hole 9023A (CONFIDENTIAL).

Chapter 3: Downhole Measurements

K. Kitada and H. Y. Wu

To understand the hydrothermal activity and how it drives with the submarine resource in earth processes are the main targets of this expedition. For this reason, the logging while drilling and in-situ temperature measurements are applied to obtain the realistic geothermal data in each Iheya North Knoll and Noho sites. This down-hole measurements pursuit the geothermal profile along the borehole and undisturbed temperature in deep-hot zones. These data would provide the information of subseafloor hydrothermal reservoir in the mid Okinawa Trough.

3.1. Temperature measurement in the borehole by TRDT

3.1.1 Tool descriptions

TRDT (Thermo-Resistant Downhole Thermometer, Fig.3-1-1-1) was designed by JAMSTEC as a memory downhole tool to measure in-situ borehole temperature under the extreme high temperature environment, such as hydrothermal field in the oceanic crust. TRDT consists of Pt100 class-S temperature sensor, pressure housing, Dewar flask, heat insulator, heat sink, and electric board. Electrical controller in TRDT was protected from rapid temperature increasing by Dewar flask. The pressure rating is 50MPa. First trial was conducted in the CK14-04 cruise by free-fall, but no temperature data was recorded due to the strong vibration during the operation. After the cruise, TRDT was re-modified to improve the function against vibration and passed the high temperature, vibration and shock tests to ensure the safety of borehole logging. The temperature test demonstrated that TRDT operational time at 350°C is about 4.5 hour which is estimated by the temperature profile on the internal electric board due to the temperature rating of 125°C.

Before the operation, TRDT clock was synchronized to the Information Management System (IMS) time server onboard D/V Chikyū and the sampling rate was set to 1 Hz for all TRDT operation. During the operation in this cruise, TRDT was set inside the temperature measurement device (TMD) and TMD was attached to the bottom of the inner core barrel at the drill floor. The inner core barrel is capable of deploying free-fall

or wire lines and landing at the bit depth as surveyed depth. In wire-line system, TRDT was run into the drilling pipe until 10 meters above the bit depth, and then the shear off (free fall) was applied by high wire speed to release TRDT. The bottom of TMD was about 180cm below the drill bit (Fig.3-1-1-1), allowing to measure the in-situ open borehole temperature. After reached at the bottom, temperature measurement was conducted for 10-15min without seawater gel or mud circulating. A sinker bar assembly was deployed through the drill pipe to pick up the inner core barrel with TRDT. The temperature memory data until we recovered the tool was downloaded through the PC at laboratory.

3.1.2 Experimental Site C9017C (NH01)

Operation:

TRDT operation (Run#1) was begun at 12:00 after the coring operation on Mar. 4th, 2016. TRDT was dropped to the surveyed depth (1704 mBRT) by free-fall and took a survey from 13:01 to 13:44. After the measurement at the bottom, TRDT was retrieved by wireline and on the drilling deck at 14:25. Data was downloaded and checked at laboratory. However, we found the data logger was shut down and the backup memory records stopped on the time of free fall

After the PPS71 operation at Site C9017C, we applied the second TRDT operation (TRDT Run#2) at 20:00. TRDT was dropped to the surveyed depth (1600 mBRT) by free-fall to confirm the tool toughness and the operational procedure. After reached to the bottom, TRDT was retrieved by wireline without measurement time at the bottom and on the drilling deck at 20:58. The data was downloaded and checked at laboratory.

Data Quality:

At the both Run#1 and Run#2, visual inspection revealed no damage on the tool surface and also the internal parts including the electric board. The battery was also not damaged and TRDT was operated without any problem after TRDT was restarted. However, the recorded data shows that the data recording was stopped around the beginning of the free-fall into the borehole (12:48 at Run#1 and 19:58 at Run#2).

Shock monitoring was done by CDEX engineer during all the TRDT operations. Acceleration data was measured at 1 kHz by the shock logger attached at just above TRDT. Acceleration data was successfully recovered during all the operation. Collected data showed the amplitude of the vertical shocks along the drill pipe were ~300 – 650 G at dropping the TRDT tool and ~500 – 650 G at reaching to the bottom. We assumed that one possibility of stop recording stop could be caused by the strong shocks at the release timing. Although the shock absorber sheet (β -GEL) from TAICA Co., Ltd. was wrapped around the TRDT pressure housing in three portions after the Run#1, no significant difference was observed.

Interpretation:

The recovered data indicated the data logger was stopped around releasing the tool at the drill floor. It is failed to get the survey data.

3.1.3 Experimental Site C9021B (IN03)

Operation:

TRDT operation (Run#3) was begun at 22:00 after the coring operation on Mar. 6th, 2016. TRDT was lower down to the surveyed depth (1115 mBRT) by wireline to avoid damage from the strong vibration during the deployment and took a survey from 23:21 on Mar. 6th to 00:40 on Mar. 7th. The shear off like PPS71 was also applied on TRDT to release the wire. To stabilize the borehole conduction, drillers pumped Guar Gum mud continuously (60spm X 0.5Mpa). After the measurement at the bottom, TRDT was retrieved by wireline and on the drilling deck at 01:07.

Data Quality:

No damage was observed on the tool surface and the internal parts including the electric board is still in good condition. The temperature logging data are recovered successfully at laboratory. We confirmed that there is no influence on the measuring instrument in the shock, which approved in safe operation by using wireline during the TRDT installation and recovery.

Interpretation:

TRDT measured 9.3 – 11.3 °C at the survey depth. Fig.3-1-3-1 shows time series plot of the temperature change. After started the measurement at the bottom, the temperature still changes with time. During lowering the sinker bar assembly to pick up TRDT, the TRDT position was kept at the bottom. The temperature became more stable and close to the constant, but still gradually increase from 10.1 to 10.6 °C during this period, showing that it took more than 1 hour to keep the temperature be stable in this borehole. The temperature also have a small variation with the amplitude of 0.1-0.2 °C. This can be caused by the ships heave movement.

3.1.4 Experimental Site C9023E (IN14)

Operation:

C9023E borehole in the Aki-site, the Iheya North Noll, is expected to extremely high temperature environments. The thermo labels (NiGK Corporation) for the backup temperature indicator were attached on the outside wall of the pressure housing. TRDT operation (Run#4) was begun at 21:30 after the coring operation on Mar. 12th, 2016. TRDT was lower down to the surveyed depth (1288 mBRT) by wireline to avoid damage from the strong vibration during the deployment and took a survey from 22:17 to 23:02. After the measurement at the bottom, TRDT was retrieved by wireline and on the drilling deck at 23:25. The thermo labels were recovered at laboratory (Fig.3-1-4-1).

Data Quality:

No damage was observed on the tool surface and the internal electric board. After opened the pressure housing, the internal parts, especially heat sinks were still warm. The estimated temperature by the IR camera was 44.1 °C at maximum. The temperature logging data were recovered successfully at laboratory. We confirmed that there is no influence on the measuring instrument in the shock. Only the O-rings at both end caps were partly damaged by high temperature. Thermo labels show the estimated temperature is more than 300°C. After the operation, TRDT clock was 2 second ahead compared to the IMS time server onboard D/V Chikyu.

Interpretation:

TRDT measured 205.3 – 244.6 °C at the survey depth from 22:17 to 23:02. Fig.3-1-4-2

shows time series plot of the temperature change. After started the measurement at the bottom hole, the temperature increased linearly. The temperature still continued to increase linearly even the driller lowered down the sinker bar assembly to pick up TRDT. Seawater was also pumped into drill strings when wire-line system connected to TRDT. At that time the temperature kept increasing to the maximum 244.6 °C at 22:53. This increasing temperature curve suggested that the temperature above the depth of the drill bit is higher than the surveyed depth.

From the beginning of the measurement at the bottom hole, the temperature continued to increase linearly. This suggests that the inside borehole was cooled down by pumping seawater through drill pipe during the coring and lowering down the TMD assembly to the bottom hole. To recover the in-situ temperature data more precisely, the measurement time should kept as long as possible by considering the temperature rating of the TRDT. The operational procedure is also important to succeed in temperature logging. At TRDT Run#3 and Run#4, TRDT was deployed by wireline to avoid damage from the strong vibration during the deployment. In order to get in-situ temperature data, the key factors are: (1) keeping the borehole for recovering the temperature after the coring; (2) TRDT sensor deployment without pumping seawater.

Figure Captions:

Fig.3-1-1-1

Temperature gauge position of the TRDT landed at the drill bit.

Fig.3-1-3-1

Time series plot of the temperature change during the TRDT Run#3 at Site C9021B.

The light green shaded area shows temperature measurement at the survey depth (1115mBRT) from 23:21 on Mar. 6th to 00:40 on Mar. 7th.

Fig.3-1-4-1

Thermo labels attached on the outside wall of the pressure housing during the TRDT Run#4 at Site C9023E. Thermo labels show the estimated temperature is more than 300°C.

Fig.3-1-4-2

Time series plot of the temperature change during the TRDT Run#4 at Site C9023E.

The light green shaded area shows temperature measurement at the survey depth (1288mBRT) from 22:17 to 23:02 on Mar. 12th. The grey shaded areas show the periods during lowering down and pulling up the TRDT sensor assembly.

Fig.3-1-1-1 Temperature gauge position of the TRDT landed at the drill bit

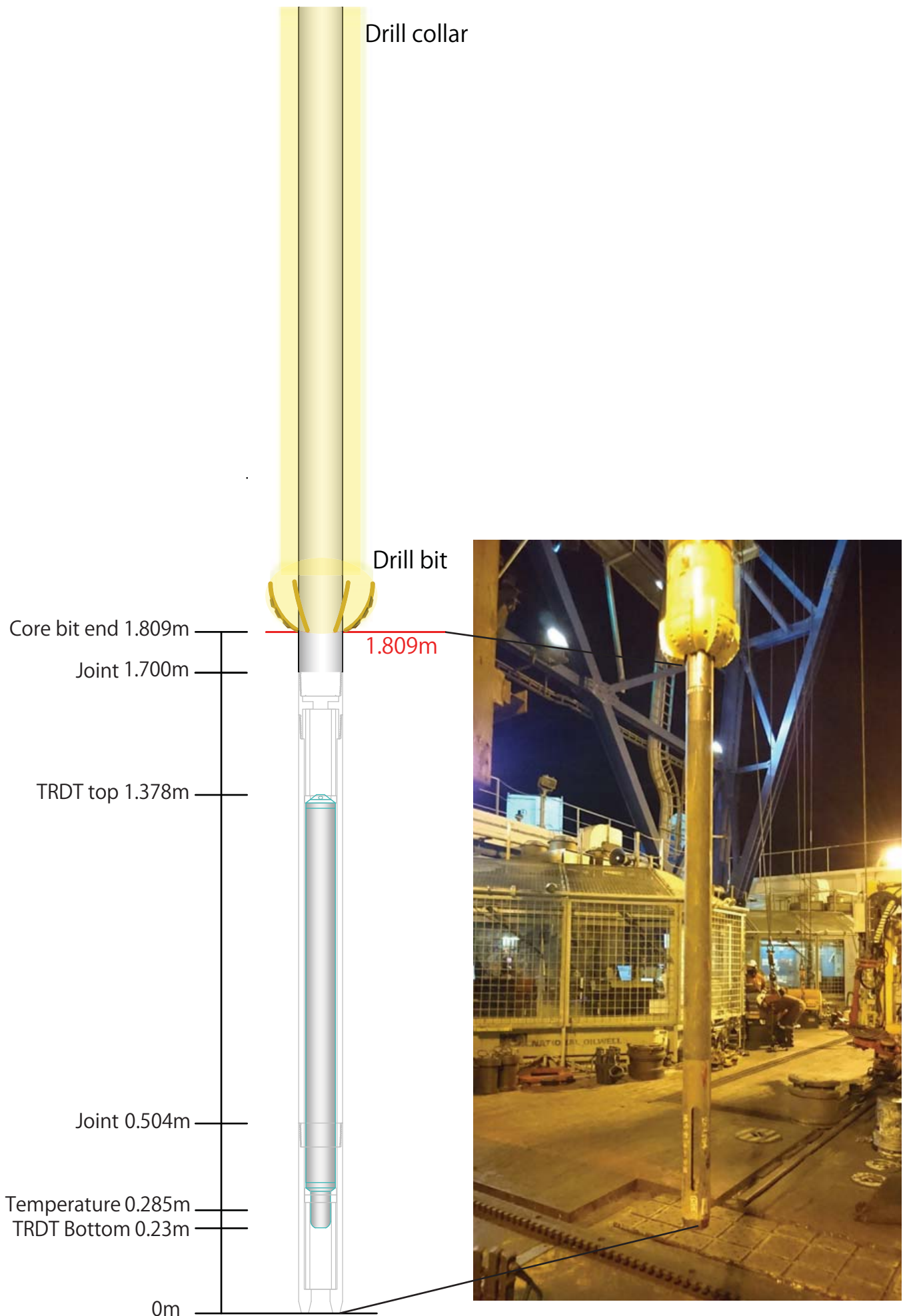


Fig.3-1-3-1 Time series plot of the temperature change during the TRDT Run#3 at Site C9021B

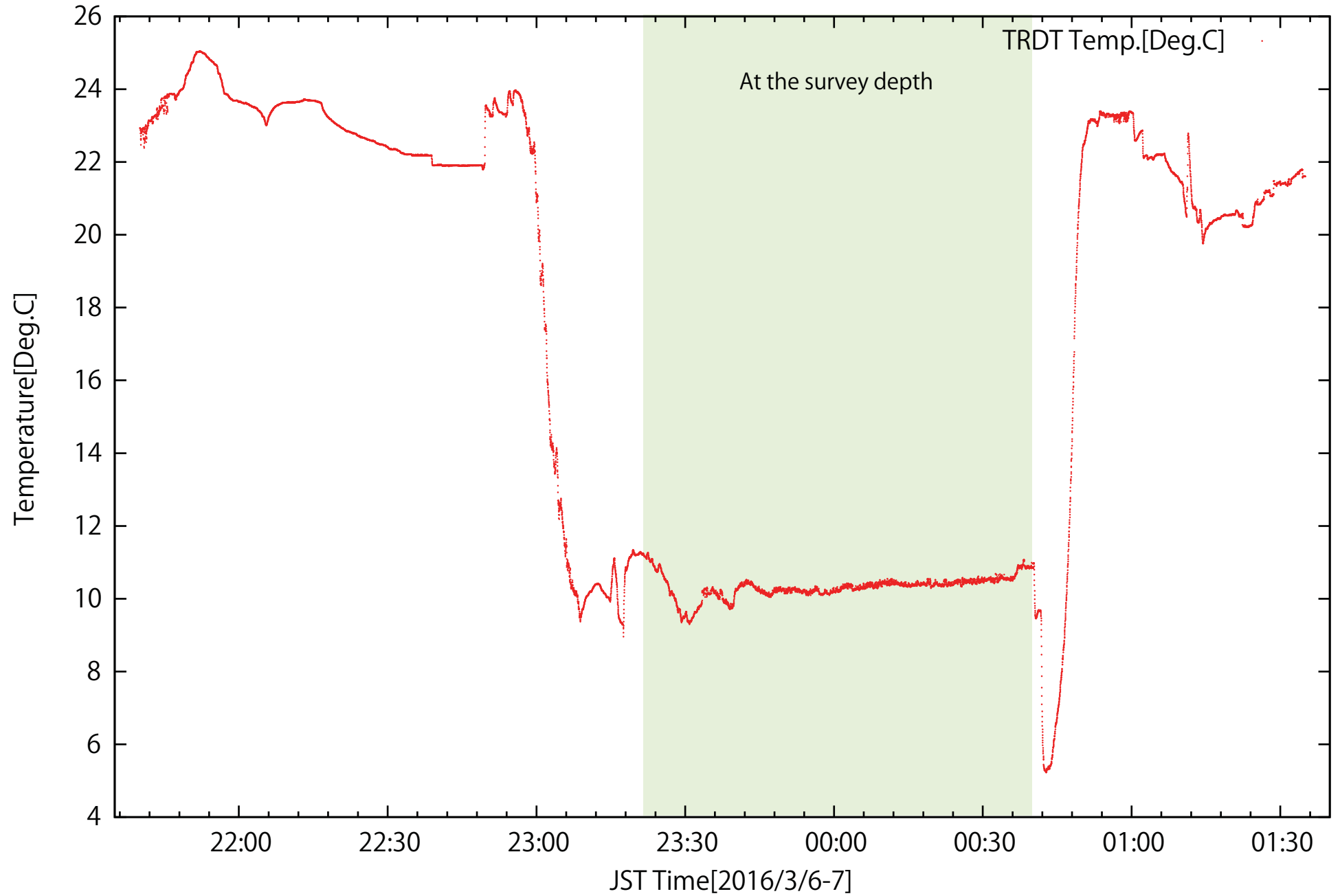








Fig.3-1-4-1 Thermo labels attached on the outside wall of the pressure housing during the TRDT Run#4 at Site C9023E

CHIKYU Operation

Last Update 19/Feb/2016

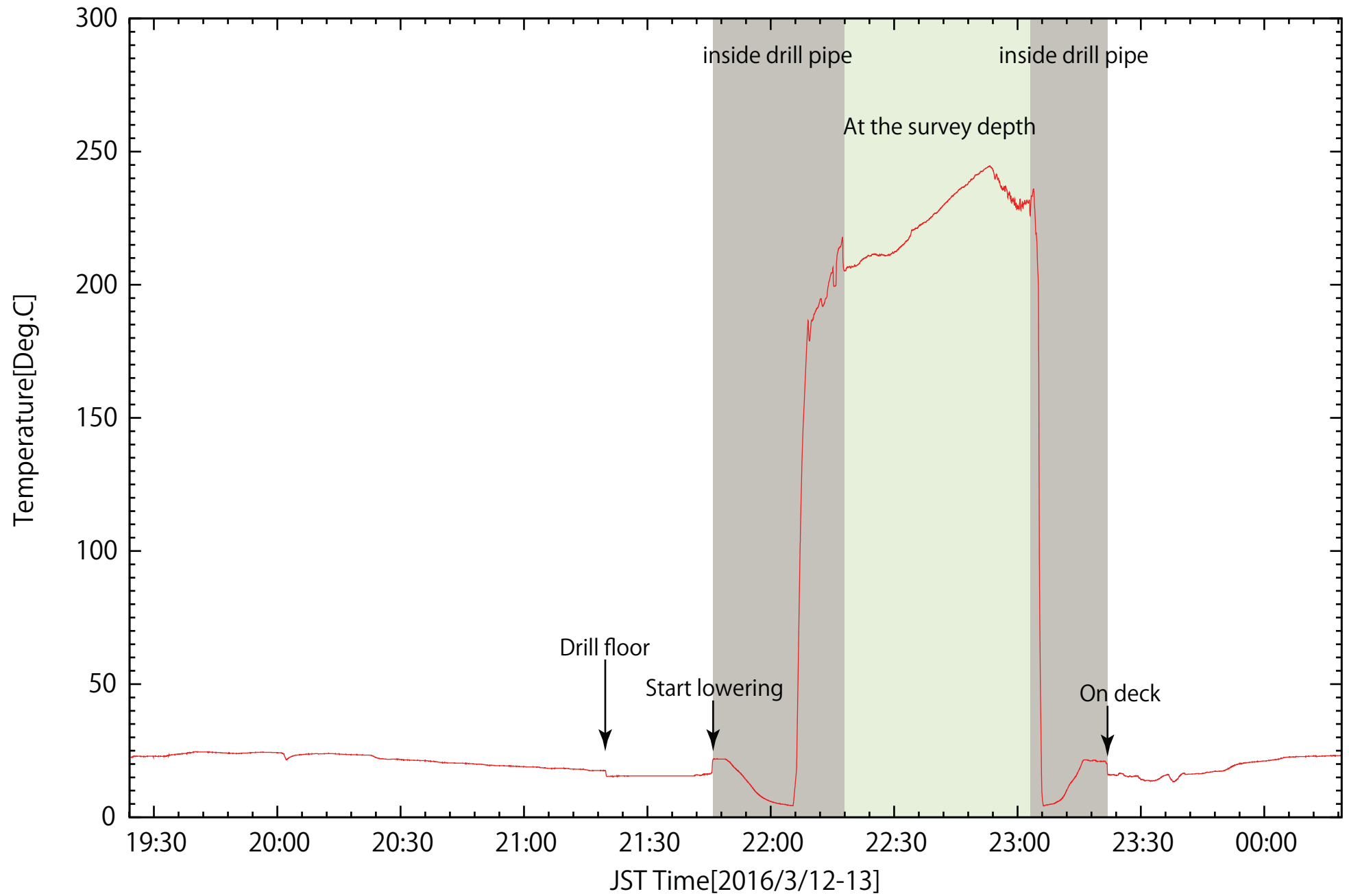
Thermo labels Log Sheet

Date&time of core recovery (Y/M/D, time) : 2016/3/12 ,				Comment: TRDT (Ca. 1288 mBRT) 188 mbsf = almost same depth of core betw of 7X.			
Exp: 908	Site: C9023	Hole: E	Core: 17) Type: (X)				

5E-50	5E-75	5E-100	5E-125	5E-170	5E-210	G-1	G-2
High	High	High	High	High	High	High	High
							
Low	Low	Low	Low	Low	Low	Low	Low

111

Fig.3-1-4-2 Time series plot of the temperature change during the TRDT Run#4 at Site C9023E



3.2. Geothermal Tool (PPS71)

3.2.1 Tool descriptions

PPS71 is the geothermal tool provided by Pioneer Petrotech Services (PPS). In this expedition, GSC (Geophysical Surveying Co., Ltd.) was ordered to operate this tool by CDEX, JAMSTEC. PPS71 Geothermal Tools are designed for extreme, high temperature downhole conditions. The robust electronics combined with vacuum flask technology allow these products to perform at 350 °C (662 °F) continuously, for four hours.

The tool is designed to measure pressure, temperature, casing collar location, flow meter (Spinner) and gamma ray, when configured as either a memory tool or surface read out tool. We set PPS71 as a memory tool in this expedition by considering the borehole circulation and drilling strings should keep rotating to prevent the stock in the bottom of borehole.

By combining the downhole measurements with a depth recorder, such as IMS data in Chikyū drilling system, we have the capability to create synchronized profile logs. By synchronized time-series data, we compare to the Drilling Control Information System (DCIS) to change the reference to depth base. Additionally the temperature and pressure profiles can be integrated with Logging While Drilling (LWD) data.

The components of PPS71 (Fig.3-2-1-1) from top to bottom included casing collar locator, gamma ray detector, Resistance Temperature Detector (RTD) sensor, pressure sensor and flow-meter (Spinner). The sensitivity of Gamma measurement is 10 CPS/API. In temperature measurement, PPS71 equipped Pt1000, 4 wires RTD sensor. The module temperature rating is 350 °C with flask housing. Silicon-Sapphire type of pressure sensor with the pressure range of 10k psi was used for the PPS71. The flow reed-switch by magnetic was installed as flow-meter; flow rate range can be recorded from 5 to 7000 rpm in the data logger. In the memory mode, the battery can keep recording 4 hours in 350 °C environment.

3.2.2 Experimental Site C9017C (NH01)

Operation:

After the coring reach the target depth (121 mbsf) on Mar. 4th, 2016, PPS71 was run down to the bottom of the borehole and took a survey from 14:30 to 18:45 with POOH until 5 meter below the seafloor (1591.5 mBRT). The excessive over pull (20-30kN) occurred at depth 1675-1670 mBRT, the drilling pipes passed through this area by 10 rpm pipes rotation.

Data Quality:

PPS71 was recovered around 20:00, Mar. 4th on the drilling deck. The outlook of PPS71 was in good shape, no damage observed on the tool surface. GSC engineers disconnected the battery and downloaded the data in the Core Tech workshop. However, the recorded data were divided in seven one. The electricity was cut off about 834m (WD=1558 mbsl) in the end, since then it didn't record measurement. The existed files show the continuous recording indicated the PPS71 worked in fine conditions. After checking the logging chamber, the battery connector was broken (Fig.3-2-2-1). Due to the high vibrations and shocking (refer to TRDT operations, shock monitoring), the battery locking sleeve come into the inside with stopped motion, and loose connection in several times. The movement of the battery made the power circuit down and the black down also stopped the logger for recording. Although the checking by eyes, the tool body and each sensor were showed the good status by lab operation test.

From the available data and time stamps from GSC, the timing, which the shock generated to PPS71, is consistent with the time when data broke off. A spacer shocked to a battery head with a down force. This spacer was equipped with the short spring for holding connection of a battery into a flask housing. Originally a spacer is installed for preventing the loose connection of the battery by a shock. However the spring compressed in the vibration and the spacer moved freely in this interspace and hammered the end of battery. This kind of shock cased the damage of battery connector eventually.

Interpretation:

The recovered data indicated the data logger was stopped before the tool run into the borehole (around 800 meters core line depth). It is failed to get the survey data.

3.2.3 Experimental Site C9021B (IN03)

Operation:

After the coring reach the target depth (121 mbsf) on Mar. 7th, 2016, PPS71 was run down to the bottom of the borehole and took a survey from 01:15 to 04:45 with POOH until 5 meter below the sea floor (1054 mBRT). To stabilize the borehole condition, drillers pumped Guar Gum mud into the borehole continuously (60spm X 0.5Mpa).

Data Quality:

PPS71 was recovered around 05:00, Mar. 7th on the drilling deck. The outlook of PPS71 is in good shape, no damage observed on the tool surface. GSC engineers disconnected the battery and downloaded the data in the Core Tech workshop. The logging data including temperature, pressure, and gamma ray are recovered successfully. GSC engineers confirmed that there is no influence on the measuring instrument in the shock, which arose in this measurement.

Before the PPS71 measurements in this borehole, the Gamma ray dummy test was applied on the Core Tech workshop in the drilling rig with drilling pipe. The gamma ray tester for physical properties measurements was used as a source. We tested 5 locations with Gamma ray tester, including lab, workshop, drill bit, stabilizer and drill collar. The high percentage of block rate can be detected in the drilling pipes (Fig.3-2-3-1). It explained that the low values of Gamma ray in PPS71 measurement.

Also the water-tank temperature test applied in the core-processing lab, all of temperature measurement tools (2 PPS71, 1TRDT) were put in the water tank and continuous recorded the temperature until disconnected the logging on the sampling table. The collected data shows the decay curves in three tools and about one degree C differed between PPS71 and TRDT tools.

Interpretation:

We processed the data and converted to depth base in Techlog (Fig.3-2-3-2) and noticed that the gamma ray value displayed between 0 to 267.7 gAPI; the total average is 4.0. In

the LWD logging, the gamma ray sensor showed the average value of 45.4 gAPI. The gamma ray value was rapid increasing below 68 mbsf in LWD gamma ray logging; it is inconsistent with PPS71 gamma ray measurement in the bottom. The gammy test explained the high block rate in the drilling pipes and indicated that the PPS71 read the background values inside the drilling pipes, which did not represent any formation signals. In the temperature data, PPS71 measured 12.8 – 14 °C while the POOH of drilling pipes. The temperature dropped at the bottom of the borehole (68 mbsf), which is corresponded with LWD temperature log. The same decreasing trend of these temperature records implied the borehole temperature would be influenced by local pressure change. The pressure gauge recorded the hydrostatic pore pressure in the borehole. The pressure variation in the depth 20 and 55 mbsf are corresponded to the PPS71 temperature change, these variations are related to the drill pipes disconnection in these depths. Flow-meter did not record the data during the measurement due to the high viscosity drilling fluid.

3.2.4 Experimental Site C9023E (IN14)

Operation:

After the coring reach the target depth (121 mbsf) on Mar. 7th, 2016, PPS71 was run down to the bottom of the borehole and took a survey from 00:00 to 04:45 with POOH until 5 meter below the seafloor (1005 mBRT). To avoid the shock in the pipe strings, drillers designed the low logging speed (0.1m/sec). Excessive overpull 30kN was found at 1191 mBRT and 30-40kN at 1115 mBRT. GSC engineers took the outlook check on the drilling rig. They found the sleeve of CCL and Gamma ray sensors was detached. Also the battery connector was buckled when they were going to download the data. We could not get the logging data due to the failure of connection to the logger. The logger of PPS71 may be broken during the measuring.

Data Quality:

Unable download survey data from PPS71, quality check of survey data was tried after unloading. After this cruise, GSC engineers dumped the data directly from PPS71 memory. However, the data records stopped on 01:29AM, Mar. 13th. Comparing to the drilling report, this timing is consistent with the time driller shearing the wire to release

PPS71. We assumed that the huge impact with PPS71 and drilling pipe would be the reason made tool damaged.

Interpretation:

Unable analyze the survey data from PPS71, data analysis of PPS71 data was tried after unloading. After the data recovering on-land, we observed the temperature decreasing above the target depth inside the pipe ($\sim 4^{\circ}\text{C}$, compare to the thermal gradient around 24°C) in Fig.3-2-4-1. After passing through the low temperature zone, the temperature was increasing rapidly, the maximum temperature recorded in the tool is 209.09°C . The temperature dropped to 160°C when the tool was out of the pipe. The last data recorded 150°C when tool broken. This curve implied the hot-zone in Site C9023E located right above the target depth. Gamma-ray also showed the low number counts inside the drilling pipe. The two extreme high peaks may be caused by the impact.

Figure Captions:

Fig.3-2-1-1

Components of PPS71 include battery, casing collar locator, Gamma ray sensor, temperature sensor, pressure sensor and spinner for flow rate measurement.

Fig.3-2-2-1

The battery connector broken by spacer impact during the first run at Site C9017C.

Fig.3-2-3-1

Onboard tests for Gamma ray measurements. The values of Gamma ray reading is significant dropped in the pipes.

Fig.3-2-3-2

The PPS71 and TRDT measurements with LWD images and loggings. PPS71 measured the higher temperature than LWD temperature logging. Gamma ray reading is smaller than LWD logging due to the Gamma ray sensor of PPS71 in the drilling strings. All the measurement detected the temperature decreasing around ~68 mbsf in C9021B (IN03) borehole. Pressure curve shows the hydrostatic pore pressure in the borehole. No available spinner data recorded in this borehole.

Fig.3-2-4-1

The PPS71 temperature measured with time at Site C9023E. The tools stopped recording the data due to the damage when the driller dropped down the sinker bar.

Fig.3-2-1-1 Components of PPS71

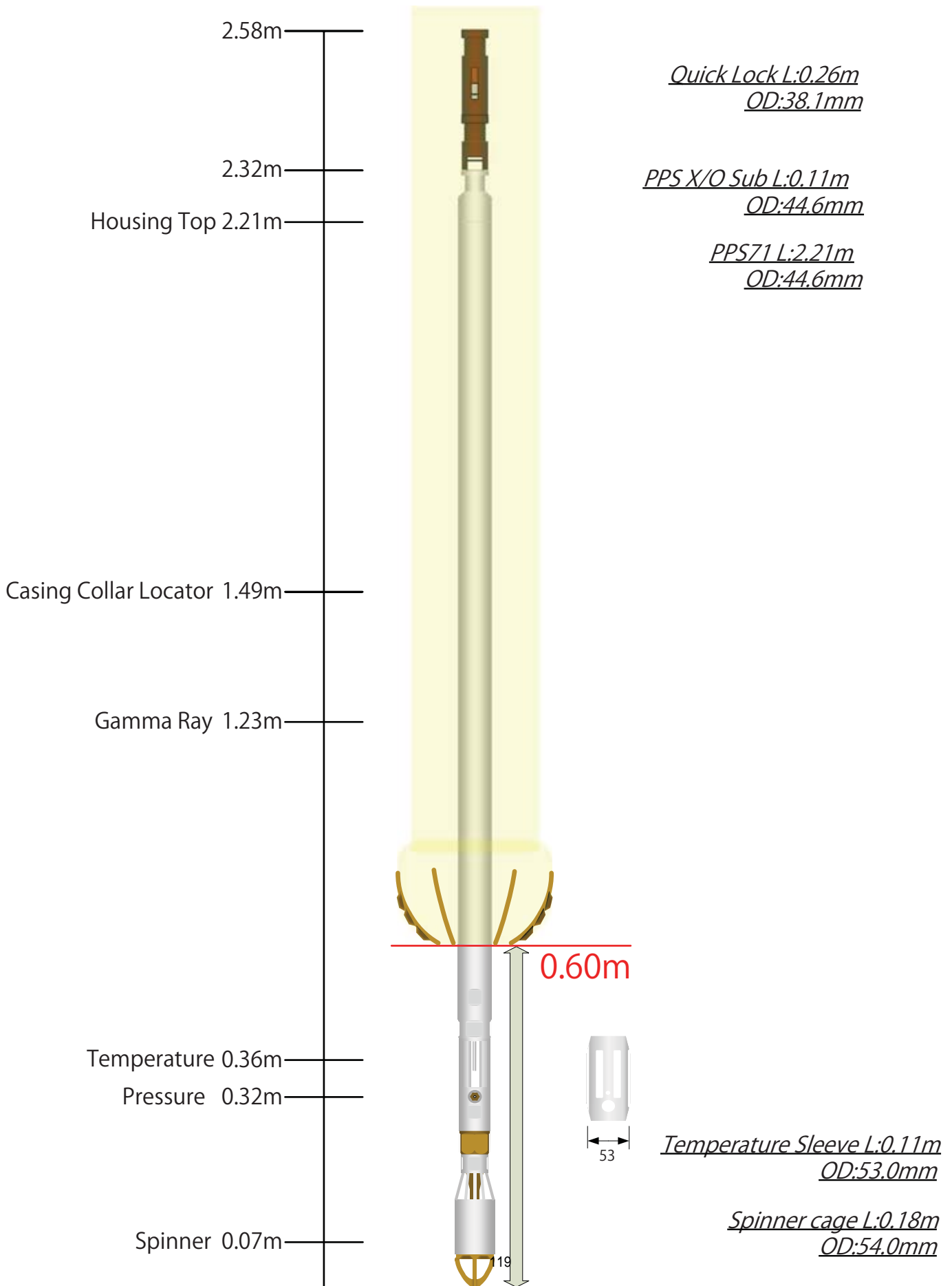


Fig.3-2-2-1 The battery connector broken by spacer impact during the first run

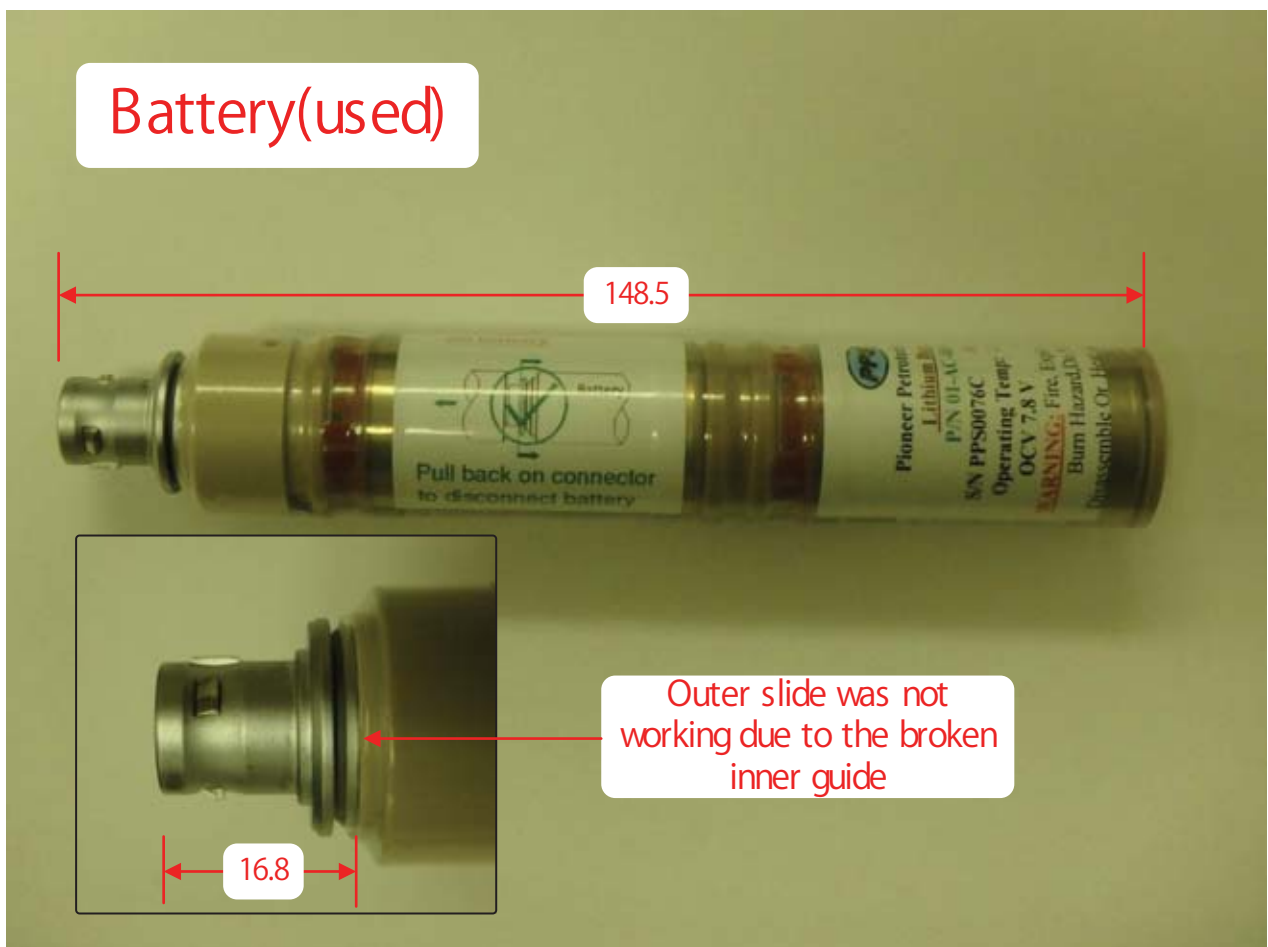


Fig.3-2-3-1 Onboard tests for Gamma ray measurements

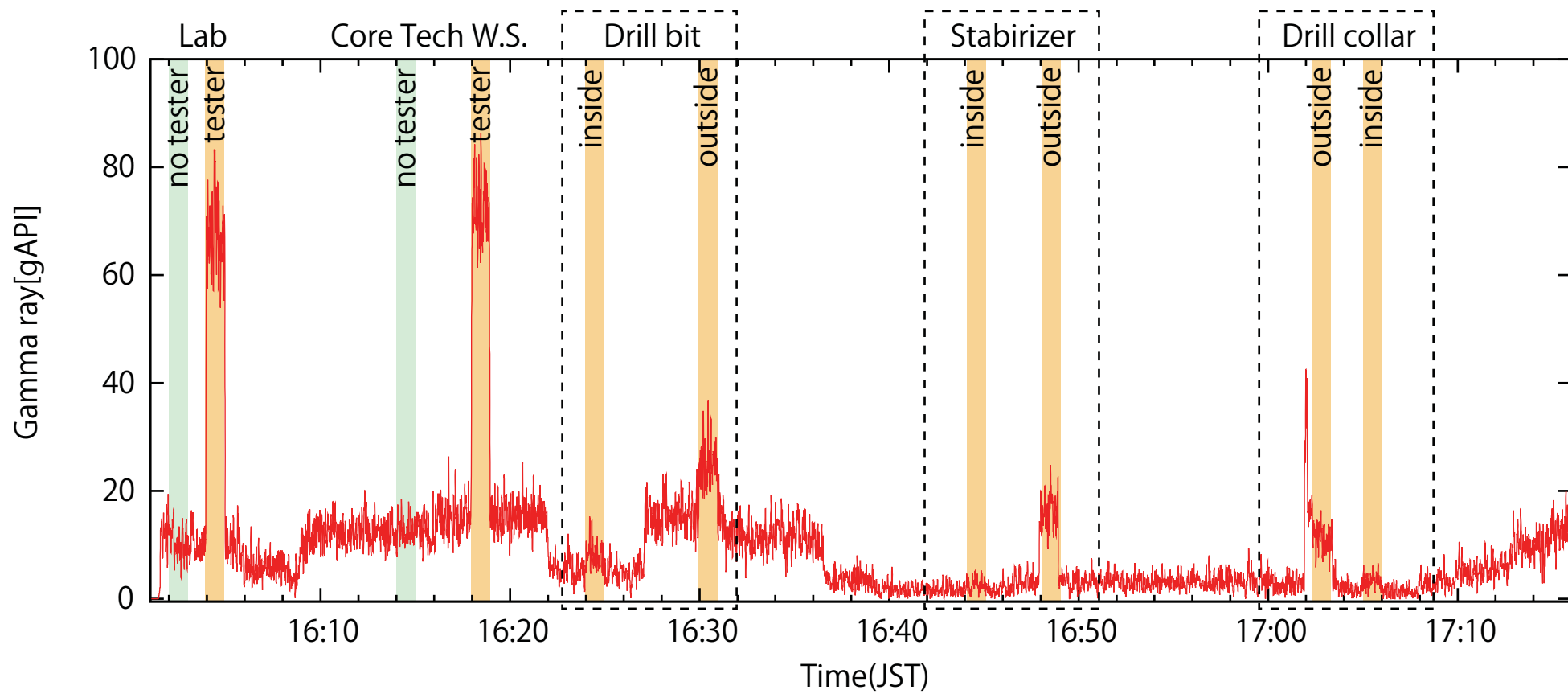


Fig.3-2-3-2 The PPS71 and TRDT measurements with LWD images and loggings

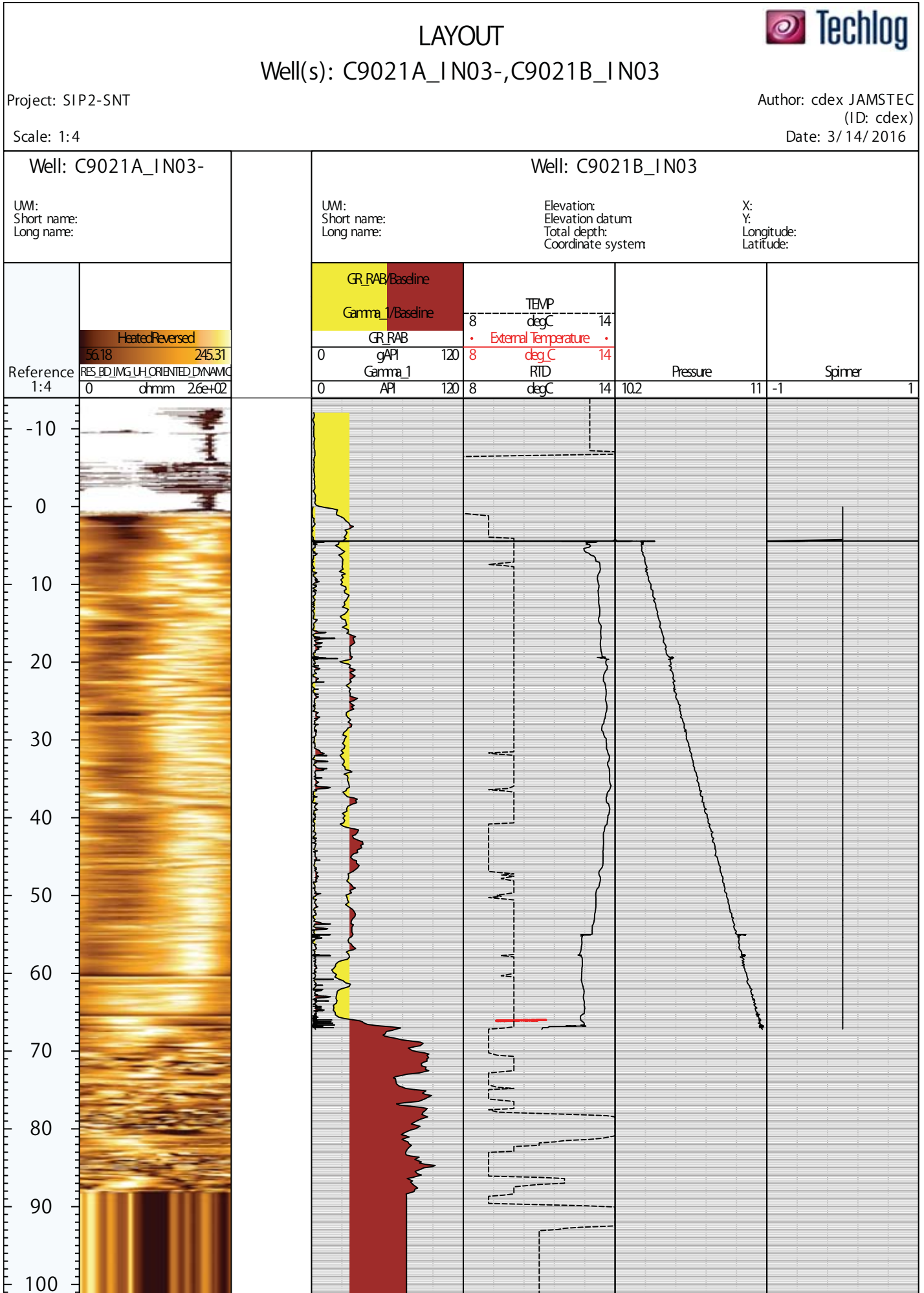
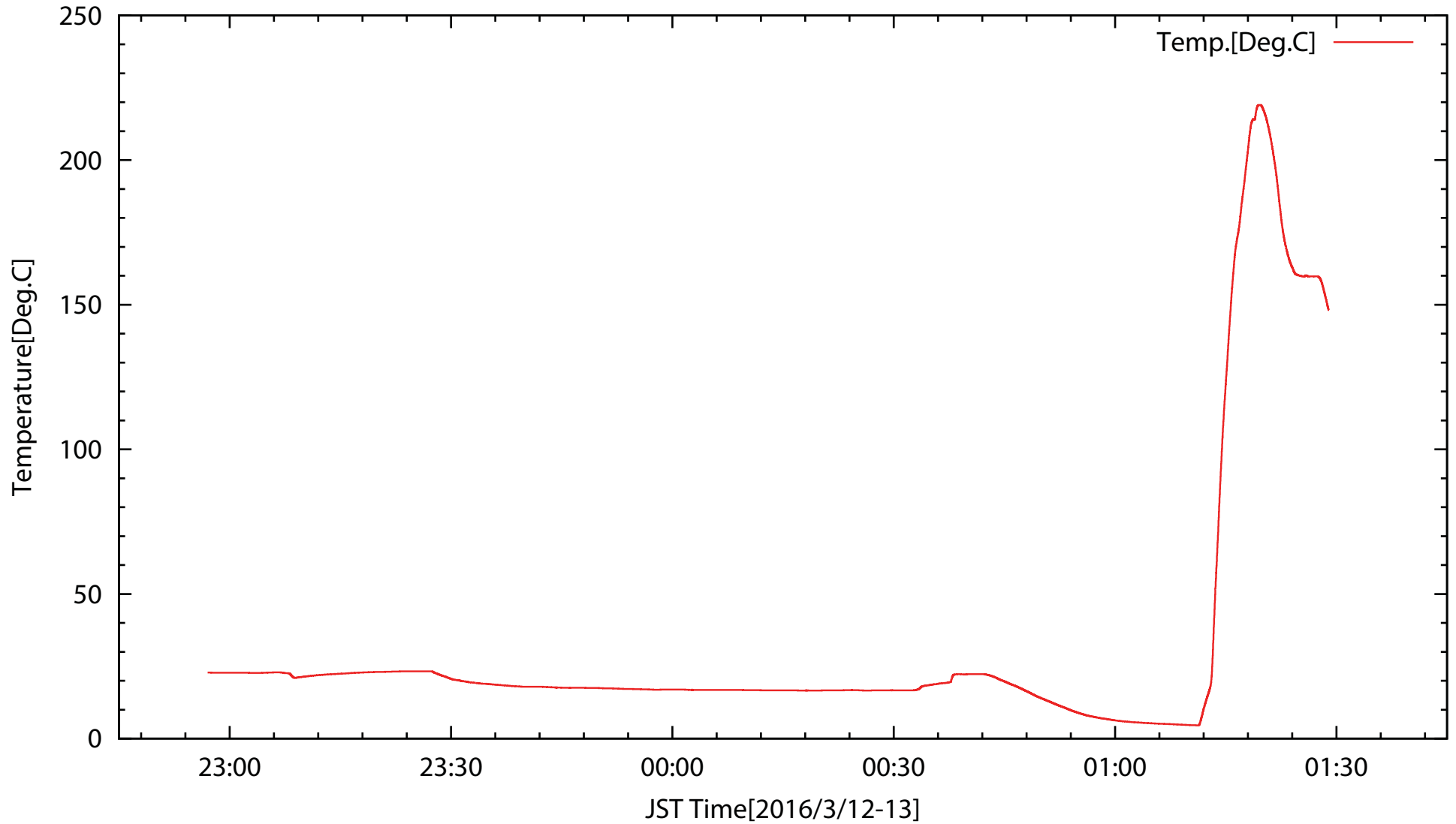


Fig.3-2-4-1 The PPS71 temperature measured with time at Site C9023E



3.3 Summary:

In first two runs of TRDT measurements, we realized the strong vibrations of free fall is the reason making the data-logger stop. The tool was improved in the third run by wrapped β -GEL outside the tool and installed inside the chamber as a damper. This successful measurement operated by wire-line proved the re-modified works did reduce the vibrations and impact effectively. The high temperature was obtained in the fourth run and showed its capability running the measurements in the geothermal borehole.

The 2 of 3 runs of PPS71 were failed in operations during this expedition. The main reason of measurement failure may be related to the high impacts and vibrations in the borehole. The enduring of PPS71 applied in ocean drillings was questionable. The battery connector is weak to take the impact from spacer. Also there is no shock absorbing installed inside the chamber. Although we recovered the temperature data from tool's memory on land. We strongly suggest improving PPS71 capabilities and sensors protection for the future oceanic borehole logging.

Chapter 4: ROV Operations

Y. Masaki, T. Nozaki, M. Watanabe, W. Tanikawa, Y. Hamada, M. Kinoshita, and
CDEX member

4.1 Summary of ROV operations

"HYDRA MAGNUM" is a remotely operate vehicle (ROV) loading on *D/V Chikyu* during the CK16-01 Cruise, which was operated by Oceaneering International Inc. to support the drilling operation and conduct various ROV operations such as the deployment of the Kuroko cultivation apparatus. In the drilling operation, it is difficult to obtain the subsurface data and subsurface samples without any sample disturbances, which can be complemented by ROV operations. During the CK16-01 Cruise (Exp. 908), we have tried many brand-new operations by using a ROV.

ROV operations associated with *D/V Chikyu* at the middle Okinawa Trough was started during the IODP Exp. 331 in 2010, and semi-annual post-drilling ROV dive surveys have observed artificial hydrothermal vents formed on the Holes C0013E, C0014G, C0016A and C0016B. During the CK14-04 Cruise (Exp. 907), careful site survey was carried out before and after the drilling operation so as to avoid hard drilling conditions and confirm the newly hydrothermal fluid effluent by drilling operations. Heat flow data using SAHF and subsurface sediment core samples using a M-BARI corer were obtained by ROV operations.

ROV operations during the CK16-01 Cruise were carried out before and after drilling operations to observe seabed. In addition to geological seabed surveys, we tried to deploy the monitoring instruments of SAHF (Stand Alone Heat Flow) and POODLE (Pressure and "Ondo" On Deep-seafloor for Long-term monitoring Equipment, where Ondo means temperature in Japanese) to measure subsurface heat flow and pressure/temperature of interstitial water. At the Holes C9024A and C9017B of the Original Site, Iheya-North Knoll and Noho Site, southern flank of the Iheya Minor Ridge, two Kuroko cultivation apparatuses were installed by drilling tools and ROV hydraulic tools including IHPU, hydraulic drill and so on. Moreover, sulfide scale of the artificial vent of the Holes C0013E and C0014G was tried to be removed and then, after rejuvenation of hydrothermal effluent, a temporal flowmeter was installed to conduct "Monitoring While Drilling (MWD)" during the coring operations. In this chapter, outlines of ROV operations, results of seabed survey, the temporal flowmeter and functions of specific ROV hydraulic tools are introduced. Table 4-1-1 shows the summary of the ROV dive log during the CK16-01 Cruise.

Caption:

Table 4-1-1 Summary of the ROV dive logs.

Table 4-1-1 Summary of the ROV dive logs.

Date	Observation time	Location	Hole	Latitude	Longitude	Seabed video survey	Remarks
16-Feb-16	6:37			27-30.9909N	126-58.9792E	POODLE & SAHF deployment	
17-Feb-16	4:14	SIP NH-01	C9017A	27-31.0085N	126-58.8963E	Post-drilling	Slight hydrothermal plume?
17-Feb-16	7:02	SIP NH-02	C9018A	27-31.1597N	126-58.9860E	Pre-drilling	
17-Feb-16	12:16	SIP-NH-02	C9018A	27-31.1597N	126-58.9860E	Post-drilling	
17-Feb-16	13:35	SIP NH-03	C9019A	27-31.3286N	126-59.0230E	Pre-drilling	
17-Feb-16	19:00	SIP-NH-03	C9019A	27-31.3286N	126-59.0230E	Post-drilling	
18-Feb-16	2:52	SIP NH-01	C9017A	27-31.0085N	126-58.8963E	Post-drilling	Plume become vigorous and black smoker
18-Feb-16	6:00	SIP NH-04	C9020A	27-31.4847N	126-59.0221E	Pre-drilling	
18-Feb-16	19:20	SIP NH-04	C9020A	27-31.4847N	126-59.0221E	Post-drilling	Rock sampling
19-Feb-16	2:40	SIP IN-03	C9021A	27-46.4119N	126-54.1304E	Pre-drilling	
19-Feb-16	17:20	SIP IN-03	C9021A	27-46.4119N	126-54.1304E	Post-drilling	Rock sampling
19-Feb-16	21:50	SIP IN-02	C9022A	27-46.9246N	126-54.0810E	Pre-drilling	
20-Feb-16	18:45	SIP IN-02	C9022A	27-46.9246N	126-54.0810E	Post-drilling	
20-Feb-16	22:30	SIP IN-14	C9023A	27-46.0694N	126-54.1559E	Pre-drilling	
21-Feb-16	22:07	SIP IN-14	C9023A	27-46.0694N	126-54.1559E	Post-drilling	
22-Feb-16	2:03		C0014G	27-47.4165N	126-54.0463E	Short hydraulic drill	
22-Feb-16	5:02		C0014G	27-47.4165N	126-54.0463E	Long hydraulic drill	
22-Feb-16	8:06		C0014G	27-47.4165N	126-54.0463E	Temporal flowmeter deployment	
22-Feb-16	10:15		C0013E	27-47.4157N	126-53.8546E	Long hydraulic drill	
22-Feb-16	14:24		C0013E	27-47.4157N	126-53.8546E	Long hydraulic drill again	
22-Feb-16	18:40		C0014G	27-47.4165N	126-54.0463E	Recheck the temporal flow meter	
25-Feb-16	10:36	SIP IN-16	C9024A	27-47.4094N	126-54.0397E	2nd gen. monitoring system deployment	
28-Feb-16	3:11	SIP NH-01	C9017B	27-31.0059N	126-58.8904E	Hybrid-type monitoring system deployment	
5-Mar-16	0:27	SIP NH-01	C9017B	27-31.0059N	126-58.8904E	Temporal flowmeter recovery from the hybrid monitoring system	
13-Mar-16	8:17		C0014G	27-47.4165N	126-54.0463E	Temporal flowmeter recovery	
13-Mar-16	8:17	SIP IN-16	C9024A	27-47.4094N	126-54.0397E	Temporal flowmeter recovery from the 2nd gen. monitoring system, but failed	

4.2 Seabed survey by ROV video camera

Seabed survey by ROV video camera is an essential process to determine the exact position of drilling site before starting a drilling operation. After the pull out of hole (POOH), ROV seabed survey was also performed to observe the circumstances of drilled hole and whether newly hydrothermal fluid started to be discharged. Such observation is necessary to determine the exact location of the candidate site for deployment of the Kuroko cultivation apparatus.

Noho Site

Just after POOH, quite limited visibility condition was observed in the vicinity of the Hole C9017A of Noho Site, mainly due to suspended substances possibly derived from hydrothermal plume. This hydrothermal plume became much more active one day later from POOH and the color of hydrothermal discharge has also changed from gray to black. Fig. 4-2-1 shows the hydrothermal discharge of the Hole C9017A after one day from POOH and Table 4-2-1 shows the dive log after POOH at the Hole C9017A on 18th February. We have decided to install one Kuroko cultivation apparatus at the Hole C9017A. The new hydrothermal effluent was not observed at the Holes C9018A, C9019A and C9020A of the Noho Site after drilling operations (Figs. 4-2-2, -3, and -4) because these three holes where seafloor surface consisted of altered sediment located northern area from the active sulfide mound of the Hole C9017A.

Iheya-North Knoll

At the Holes C9021A and C9022A locating at between the Natsu and Aki Sites, Original and Natsu Sites of the Iheya-North Knoll, seabed surface mainly consisted of unaltered pumice with hemi-pelagic soft sediment. After POOH, any hydrothermal discharges were not observed at the Holes C9021A and C9022A (Figs. 4-2-5 and -6) like as the Holes C9018A, C9019A and C9020A. On the contrary, at the Hole C9023A located at the center part of the active mound of the Aki Site, Iheya-North Knoll, vigorous hydrothermal discharge in black color was observed just after POOH (Fig. 4-2-7).

After the LWD operations, the Hole C9024A at the Original Site of the Iheya-North Knoll, dozen meters southwest from the Hole C0014G, was drilled for deployment of the Kuroko cultivation apparatus. We could observe transparent color hydrothermal fluid at the Hole C9024A after POOH (Fig. 4-2-8).

Captions:

Table 4-2-1 ROV dive log the Hole C9017A of the Noho Site on 18th Feb. 2016.

Fig. 4-2-1 ROV dive photo of the Hole C9017A one day later from POOH.

Fig. 4-2-2 ROV dive photo of the Hole C9018A after POOH.

Fig. 4-2-3 ROV dive photo of the Hole C9019A after POOH.

Fig. 4-2-4 ROV dive photo of the Hole C9020A after POOH.

Fig. 4-2-5 ROV dive photo of the Hole C9021A after POOH.

Fig. 4-2-6 ROV dive photo of the Hole C9022A after POOH.

Fig. 4-2-7 ROV dive photo of the Hole C9023A after POOH.

Fig. 4-2-8 ROV dive photo of the Hole C9024A after POOH.

Table 4-2-1 ROV dive log the Hole C9017A of the Noho Site on 18th Feb. 2016.

18-Feb-16 Post drilling at Hole C9017A	
Time (JST)	Notes
3:09	MAGNUM went out from the cage
3:10	saw seafloor (head 218 degree 2 m)
3:14	saw fragments or dead chimneys
3:18	started to find the hole
3:26	arrived at the hole of C9017A
3:36	saw " <i>goemon koshiori ebi</i> "
3:48	went back to the cage
3:50	(head 122 degrees 30 m)
3:51	gravel, looks rough surface
3:55	(head 205 degrees 15 m)
4:00	arrived at the " <i>yubikuwae chimney</i> "
4:37	done the survey

18-Feb-16 Pre drilling at Hole C9020A	
Time (JST)	Notes
6:02	MAGNUM went out from the cage
6:04	arrived at the seafloor (depth 1599 m)
6:05	trid to finr the marker
6:10	(head 240 degrees 15 m)
6:13	head to north 30 m
6:16	head to north 20 m
6:17	head 90 degrees 30 m
6:19	(depth 1598 m)
6:20	(head 240 degrees 15 m)
6:22	stopped
6:24	stacked the cables
6:34	done survey, back to cage

18-Feb-16 Post drilling at Hole C9020A	
Time (JST)	Notes
19:29	MAGNUM landed in front of the target sample (depth 1599 m)
19:32	sampled rock, but lost
19:38	sampled finally



Figure 4-2-1

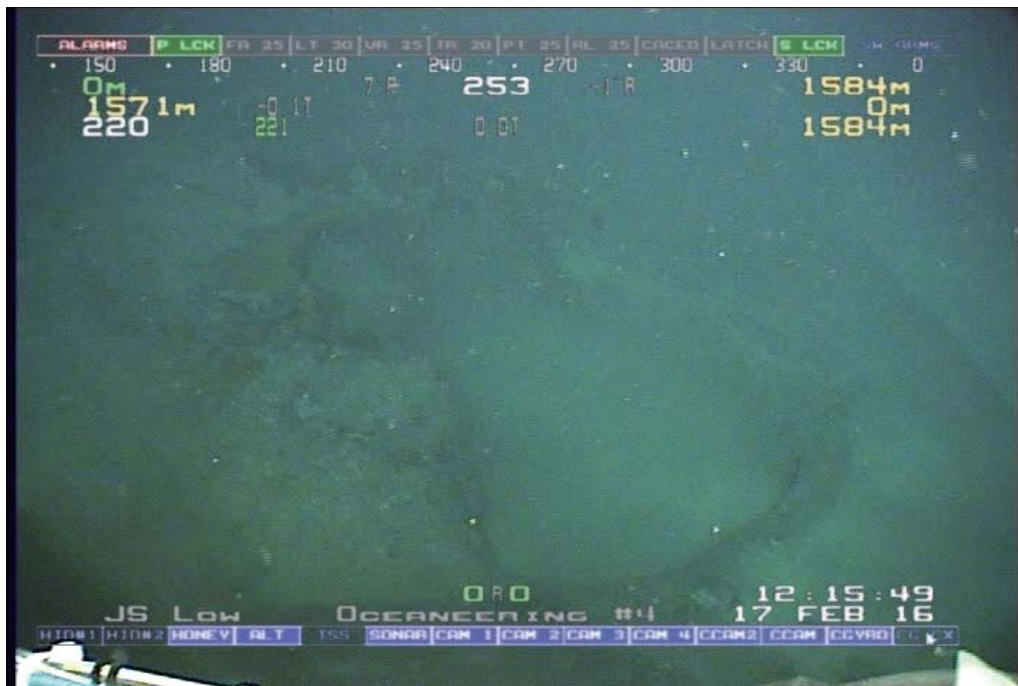


Figure 4-2-2

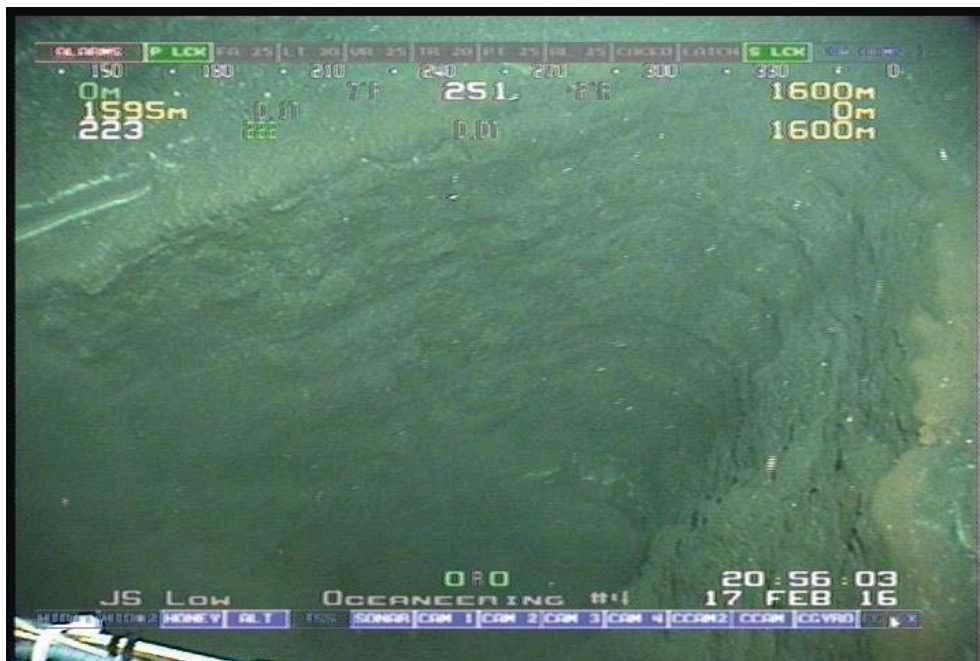


Figure 4-2-3

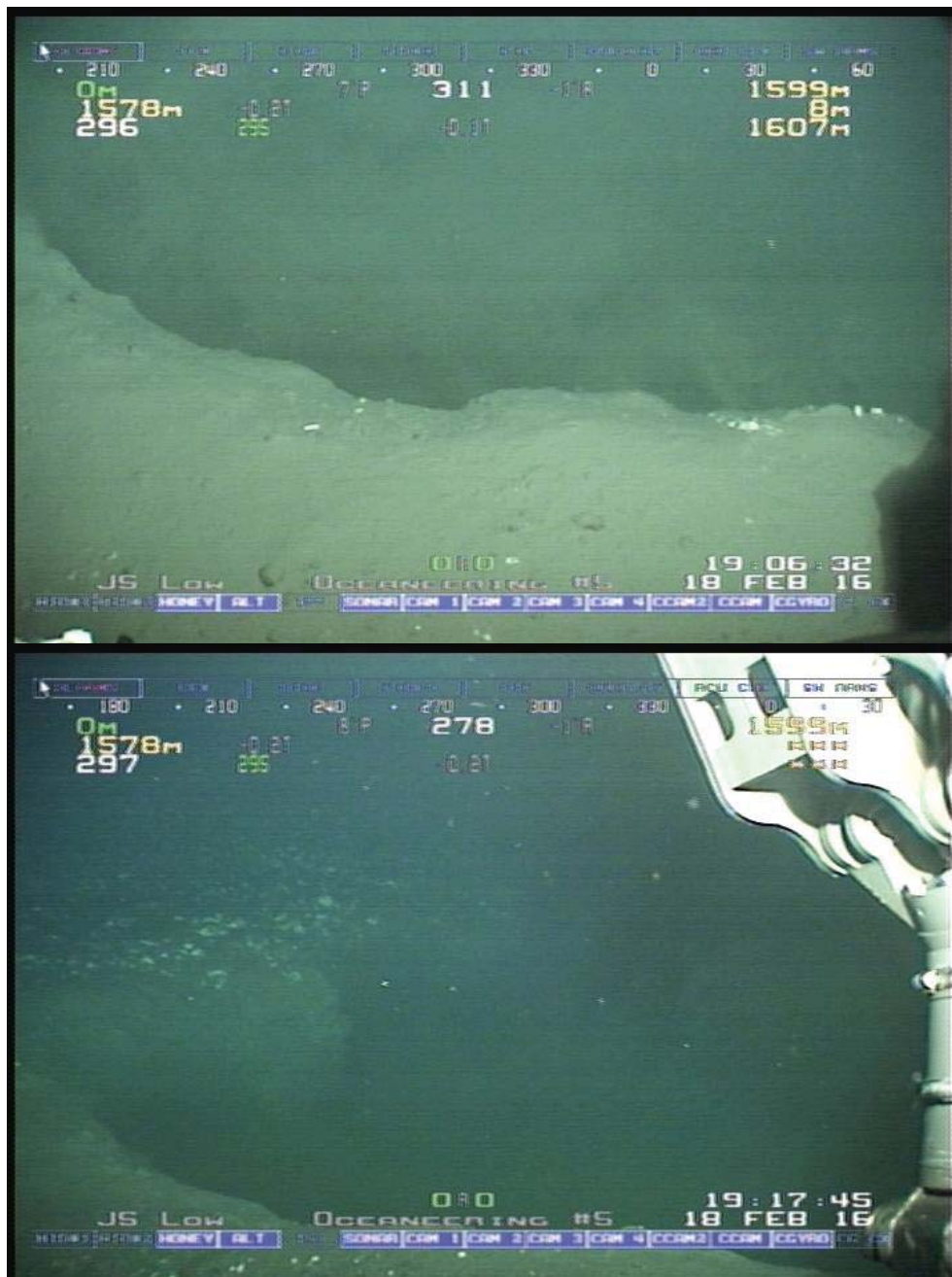


Figure 4-2-4

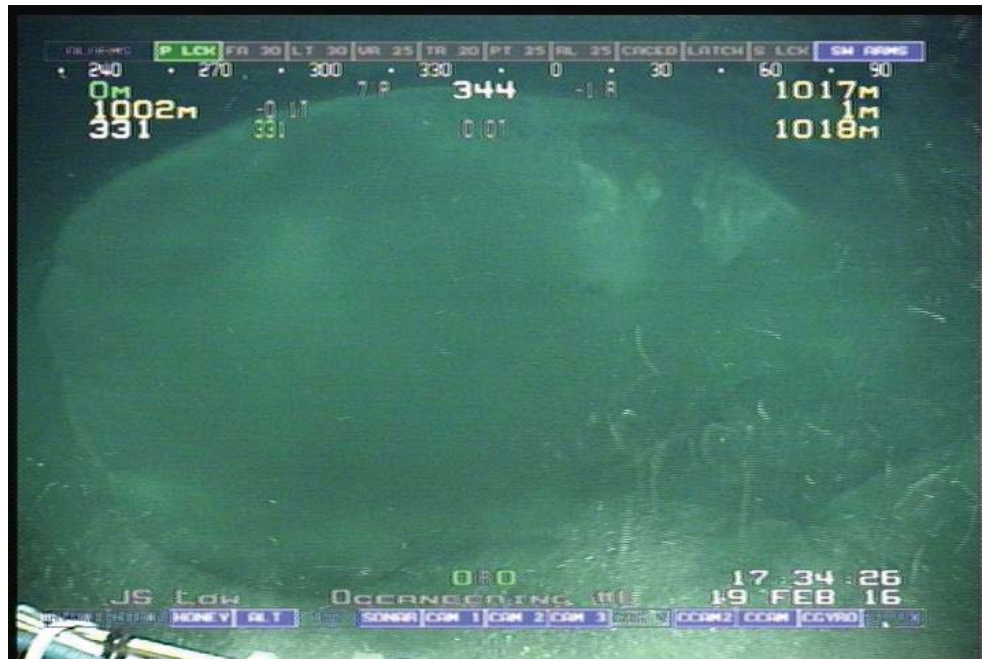


Figure 4-2-5



Figure 4-2-6

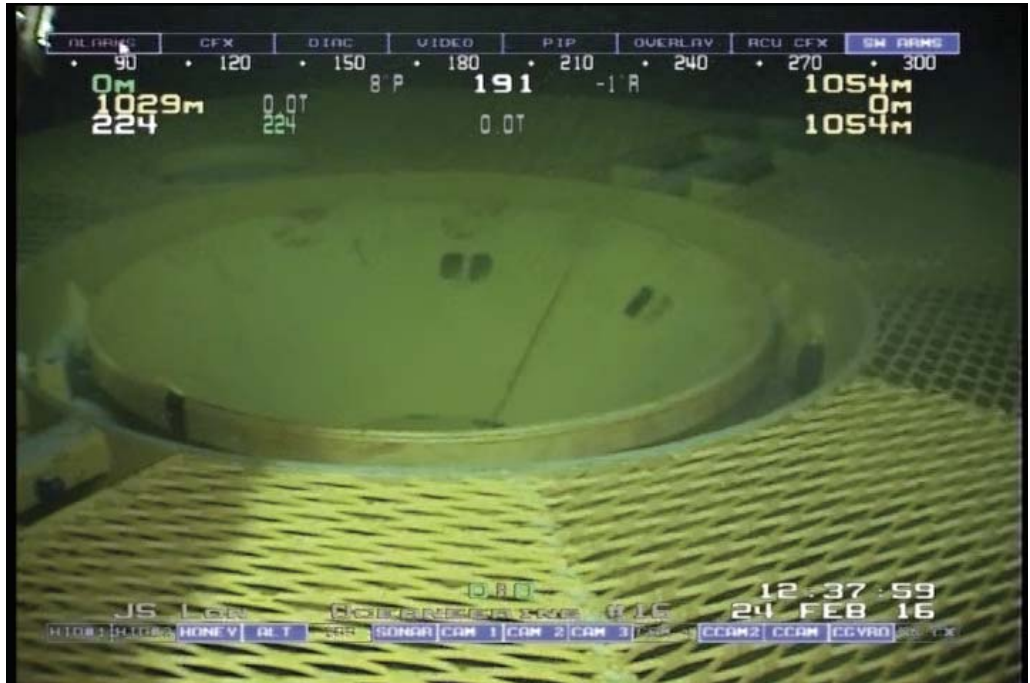


Figure 4-2-8

4.3 Deployment of the temporal flowmeter and Kuroko cultivation apparatus

4.3.1 Temporal flowmeter

Temporal flowmeter for the MWD operation has three analogue meters of pressure, temperature and flow rate as well as digital pressure and temperature sensors together with their loggers (Figs. 4-3-1-1 and -2). The orange colored valve at the upper part of the temporal flowmeter is the ball valve to regulate the flow rate of hydrothermal fluid. The white colored part surrounded a yellow protect frame below the ball valve is an analogue flowmeter (Fig. 4-3-1-1). If hydrothermal fluid discharges through the temporal flowmeter, the indicator line within the analogue flowmeter gauge will drift upward.

After LWD operations, we have tried to remove a sulfide scale within the steel pipe of the corrosion cap on the artificial hydrothermal vents of the Holes C0014G and C0013E which were both formed by IODP Exp. 331 in 2010. At first, at the Hole C0014G, we used a short-type ROV hydraulic drill with a stroke length of 5 inch. Although the short-type hydraulic drill was not able to penetrate the sulfide scale, 3 cm long sulfide core sample was obtained. Then, a long-type hydraulic drill with a 16-inch stroke length was used. The long drill successfully penetrated the sulfide scale and 20 cm long sulfide core sample was obtained. Since vigorous hydrothermal discharge was observed after penetration of the sulfide scale, we deployed the temporal flowmeter on the Hole C0014G (Fig. 4-3-1-3). Analogue pressure, temperature and flowmeter gauges exhibited values of ca. 23 psi, 320°C and 200 L/min, respectively. Finally, the ball valve was closed by using a manual torque tool to detect the weak fluctuations in pressure and temperature of hydrothermal fluid during the coring operations. The sulfide scale within the steel pipe of corrosion cap at the Hole C0013E was also tried to be removed by long-type hydraulic drill and deploy another temporal flowmeter, but the long-type hydraulic drill was not able to penetrate the sulfide scale.

At the Hole C9024A of the Original Site, Iheya-North Knoll and Hole C9017B of the Noho Site, temporal flowmeters were deployed on the manifold unit of the Kuroko cultivation apparatus (Figs. 4-3-1-4 and 4-3-1-5). After deployment, the ball valve was closed by using a manual torque tool. Detailed specifications of the flowmeter, P/T sensor and their loggers were shown in Table 4-3-1-1.

4.3.2 Second generation Kuroko cultivation apparatus at the Hole C9024A

Kuroko cultivation apparatus is a long-term monitoring system for hydrothermal fluid at the artificial hydrothermal vent. This apparatus is largely divided into two units; (1) manifold unit and (2) cultivation cell unit (Fig. 4-3-2-1). The manifold unit induces hydrothermal fluid from the underlying casing pipe and has three vent pipes, allowing us

deploying various instruments. The cultivation cell unit is equipped with a P/T sensor, flowmeter, load cell and their sensor loggers to monitor pressure, temperature and flow rate of hydrothermal fluid and weight of hydrothermal precipitate within the cell (Fig. 4-3-2-2). Flowmeter and load cell are attached in the basal part of the cell unit, whereas P/T sensors are mounted on the top center part as well as the basal part (Fig. 4-3-2-2). This Kuroko cultivation apparatus were deployed on the funnel-shaped ROV platform (Fig. 4-3-2-1) which enables us the easy access and landing by ROVs.

During the CK16-01 Cruise, one manifold unit with the 2nd generation-type cultivation cell unit (monitoring system) and 150 m-long casing pipe was deployed at the Hole C9024A of the Original Site, Iheya-North Knoll, on 25th Feb. 2016. Tables 4-3-2-1, -2 and -3 shows detailed specifications of P/T sensor, flowmeter, load cell and their loggers, and Fig. 4-3-2-3 illustrated the path diagram of hydrothermal fluid through the 2nd generation-type cultivation cell and manifold units. There are three vents for hydrothermal fluid on the manifold unit and flow direction can be controlled by three valves equipped at the basal part of the manifold unit (PIV1, PIV2 and PIV3; Fig. 4-3-2-4). Opening and closing of these valves was conducted by using a ROV manual torque tool.

After the deployment of the manifold unit together with the temporal flowmeter and cultivation cell unit on 25th Feb., at first hydrothermal fluid was discharged only from the temporal flowmeter to do monitoring while drilling (MWD) during the coring operations. After observing hydrothermal effluent from the temporal flowmeter, its ball valve was closed on 25th Feb. After the coring operations on 13th Mar., PIVs of the temporal flowmeter were closed, followed by openings of PIVs of the cultivation cell unit. Then, we could observe vigorous hydrothermal effluent from the cultivation cell part (Fig. 4-3-2-5) and analogue temperature gauge indicated 290°C. This cultivation cell part will be recovered by the KR16-17 Cruise by *R/V Kairei* with *ROV Kaiko Mk-IV*.

4.3.3 Hybrid-type 2nd generation Kuroko cultivation apparatus at the Hole C9017B

“Hybrid-type” means that the manifold unit of the Kuroko cultivation apparatus was deployed on a tripod which compensate angulation of the seabed (Fig. 4-3-3-1). We have broadened the LWD hole of the Hole C9017A by re-drilling and tried to deploy the hybrid-type Kuroko cultivation apparatus on this hole on 26th Feb. However, a lock system between tripod and manifold unit including the funnel-shaped ROV platform did not function well, and thus we decided to abandon this hole. Another hole of C9017B was drilled until 50 mbsf, where we could observe clear hydrothermal shimmering just after POOH (Fig. 4-3-3-2). After POOH, the Kuroko cultivation apparatus with a 19 m-long

casing pipe was deployed on the Hole C9017B on 28th Feb. Since the lock system between the tripod and manifold unit including the funnel-shaped ROV platform did not function well, the manifold unit of the Kuroko cultivation apparatus was directly settled down on the seabed of the Hole C9017B (Fig. 4-3-3-3). Owing to existence of the annulus space between drilling hole wall and casing pipe, some fractions of hydrothermal fluid was leaked from the basal part of the manifold unit (Fig. 4-3-3-3), but clear hydrothermal discharge could be observed from the temporal flowmeter vent pipe. The analogue temperature gauge of the temporal flowmeter indicated ca. 80°C. After the coring operation, the temporal flowmeter was successfully recovered on 5th Mar. and then hydrothermal discharge was observed from the vent pipe of the cultivation cell unit after the valve operations (Fig. 4-3-3-4). This cultivation cell part will be recovered by the KR16-17 Cruise by *R/V Kairei* with *ROV Kaiko Mk-IV*.

Detailed specifications of P/T sensor, flowmeter, load cell and their loggers are tabulated in Tables 4-3-2-1, -2 and -3, and the path diagram of hydrothermal fluid through the hybrid-type 2nd generation-type cultivation cell and manifold units is given in Fig. 4-3-3-5.

Captions:

Table 4-3-1-1 Detailed specifications of the flowmeter, sensor and their loggers.

Table 4-3-2-1 Detailed specifications of a P/T sensor.

Table 4-3-2-2 Detailed specifications of a flowmeter.

Table 4-3-2-3 Detailed specifications of a load cell.

Fig. 4-3-1-1 Exterior appearance of the temporal flowmeter.

Fig. 4-3-1-2 Alignment of the digital pressure and temperature sensors in the temporal flowmeter.

Fig. 4-3-1-3 Deployed temporal flowmeter on the Hole C0014G.

Fig. 4-3-1-4 Temporal flowmeter equipped on the manifold unit of the Kuroko cultivation apparatus on the Hole C9024A.

Fig. 4-3-1-5 Temporal flowmeter equipped on the manifold unit of the Kuroko cultivation apparatus on the Hole C9017B.

Fig. 4-3-2-1 Kuroko cultivation apparatus composed of manifold and cultivation cell units.

Fig. 4-3-2-2 Alignments of sensors and their loggers on the cultivation cell part.

Fig. 4-3-2-3 Path diagram of hydrothermal fluid through the 2nd generation-type cultivation cell unit.

Fig. 4-3-2-4 Valve positions regulating the flow direction of hydrothermal fluid through the manifold unit.

Fig. 4-3-2-5 Vigorous hydrothermal discharge from the vent pipe of the cultivation cell part just after opening PIVs.

Fig. 4-3-3-1 Photo image of the hybrid-type 2nd generation Kuroko cultivation apparatus.

Fig. 4-3-3-2 Hydrothermal shimmering from the Hole C9017B just after POOH.

Fig. 4-3-3-3 Hybrid-type 2nd generation Kuroko cultivation apparatus without tripod and funnel-shaped ROV platform was directly settled down on the Hole C9017B.

Fig. 4-3-3-4 Hydrothermal discharge from the vent pipe of the cultivation cell part just after valve operations.

Fig. 4-3-3-5 Path diagram of hydrothermal fluid through the hybrid-type 2nd generation-type cultivation cell unit.

Table 4-3-1-1 Assignments and sampling rate of the flowmeter, sensor and their loggers of the temporal flowmeter and Kuroko cultivation apparatus.

Location	Hole	Cell #/flowmeter/PT/LC	Sensor	Logger	Cabel	Sampling rate	Starting time	Remarks
	C0014G	Temporal flowmeter	290371	O-0021	30"	1 min	22/2/2016 6:15AM	
SIP IN-16	C9024A	Cell #3 LC	1420293	SLL-0016	30"	2 min	24/2/2016 08:05PM	
SIP IN-16	C9024A	Cell #3 WFS	151503	159699	30"	1 min	24/2/2016 08:18PM	Listening period 10second
SIP IN-16	C9024A	Cell #3 short probe	297452	O-0010	30"	2 min	24/2/2016 08:30PM	
SIP IN-16	C9024A	Cell #3 long probe	297446	O-0012	60"	2 min	24/2/2016 08:35PM	
SIP IN-16	C9024A	Temporal flow meter	290373	O-0022	30"	1 min	24/2/2016 09:25PM	
SIP NH-01	C9017B	Cell #4 LC	1420292	SLL-0017	30"	2 min	26/2/2016 11:59PM	
SIP NH-01	C9017B	Cell #4 WFS	1595697	151504	30"	1min	26/2/2016 11:52PM	Listening period 15second
SIP NH-01	C9017B	Cell #4 short probe	297448	O-0009	30"	2 min	27/2/2016 12:25AM	
SIP NH-01	C9017B	Cell #4 long probe	297443	O-0015	60"	2 min	27/2/2016 12:30AM	
SIP NH-01	C9017B	1st generation long	290375	O-0007	90"	2 min	26/2/2016 06:45PM	
SIP NH-01	C9017B	1st generation short	290377	O-0008	30"	2 min	26/2/2016 06:15PM	
SIP NH-01	C9017B	Temporal flow meter	290374	O-0004	30"	1 min	26/2/2016 05:50PM	

Table 4-3-2-1 Detailed specifications of a P/T sensor.

<i>P/T sensor</i>	<i>Specifications</i>
Company	Paine electronics
Pressure range	0 - 5000 psi
Proof pressure	7500 psi
Burst pressure	10000 psi
Excitation	1 to 20 VDC (10 VDC normal)
Input resistance	1500 ± 300 Ω
Output resistance	1500 ± 150 Ω
Output at zero pressure over the calibrated temperature range	0 ± 2.5 mV/V
Full scale sensitivity over the calibrated temperature range	2.60 mV/V. normal
Operating temperature range, sensing element	-40 °F to 600 °F
Operating temperature range connector element	-30 °F to +200 °F
Calibrated temperature range	+75 to 500 °F
Total error (non-linearity, hysteresis, and thermal effects) bounds shall be	0.20%
Weight	16.0 oz maximum
Electrical connections	
	Pin Function
	1 + Excitation
	2 + Signal
	3 - Signal
	4 - Excitation
	5 R. T. D
	6 R. T. D
Installation information	59 °flare metal to metal seal. Mates with autoclave engineers SFCX562CS20 female fitting. Recommended torque value: 180-220 in-lbs (20-25Nm)
Insulation resistance	All conductors together to case: 10000 MΩ minimum at 50 VDC and +77°F
Platinum resistance temperature detector (RTD)	Platinum resistance temperature detector (RTD): 0°C, 1000 Ω ± 0.06% Ω TO IEC751, ClassA
External case pressure	2000 psia maximum (4500 feet maximum, sea water)

Table 4-3-2-2 Detailed specifications of a flowmeter.

<i>Flowmeter</i>	<i>Specifications</i>
Company	Hoffer flow controls, inc
Pressure rating	6000 psi
Maximum operating depth	4000 meters
Teledyne XSE-4-BCR (4-PIN) connector	
Standard calibration	243 GPM (gallon/minutes)
Uncertainty	± 0.25 %

Table 4-3-2-3 Detailed specifications of a load cell.

<i>Load cell</i>	<i>Specifications</i>
Company	SIT stellar technology
Capacity	± 500 kg
Output	3 MV/V nominal
Polarity	+ Compression
Excitation	2.5V
Accuracy	0.25 % FSO BFSL
Linearity	0.20 % FSO NOM
Hysteresis	0.20 % FSO NOM
Compensated temp range	20 °C to 90 °C
Operating temp range	-5 °C to 90 °C
Temperature effect on zero	0.01% FSO/ °F
Temperature effect on span	0.01% READING/ °F
Zero balance	1% FSO
Overload without damage	750 kg
Bridge resistance	5000 ohms nominal
Insulation resistance	>5000 ohms
Construction	All welded stainless steel
Case pressure	4500 psi

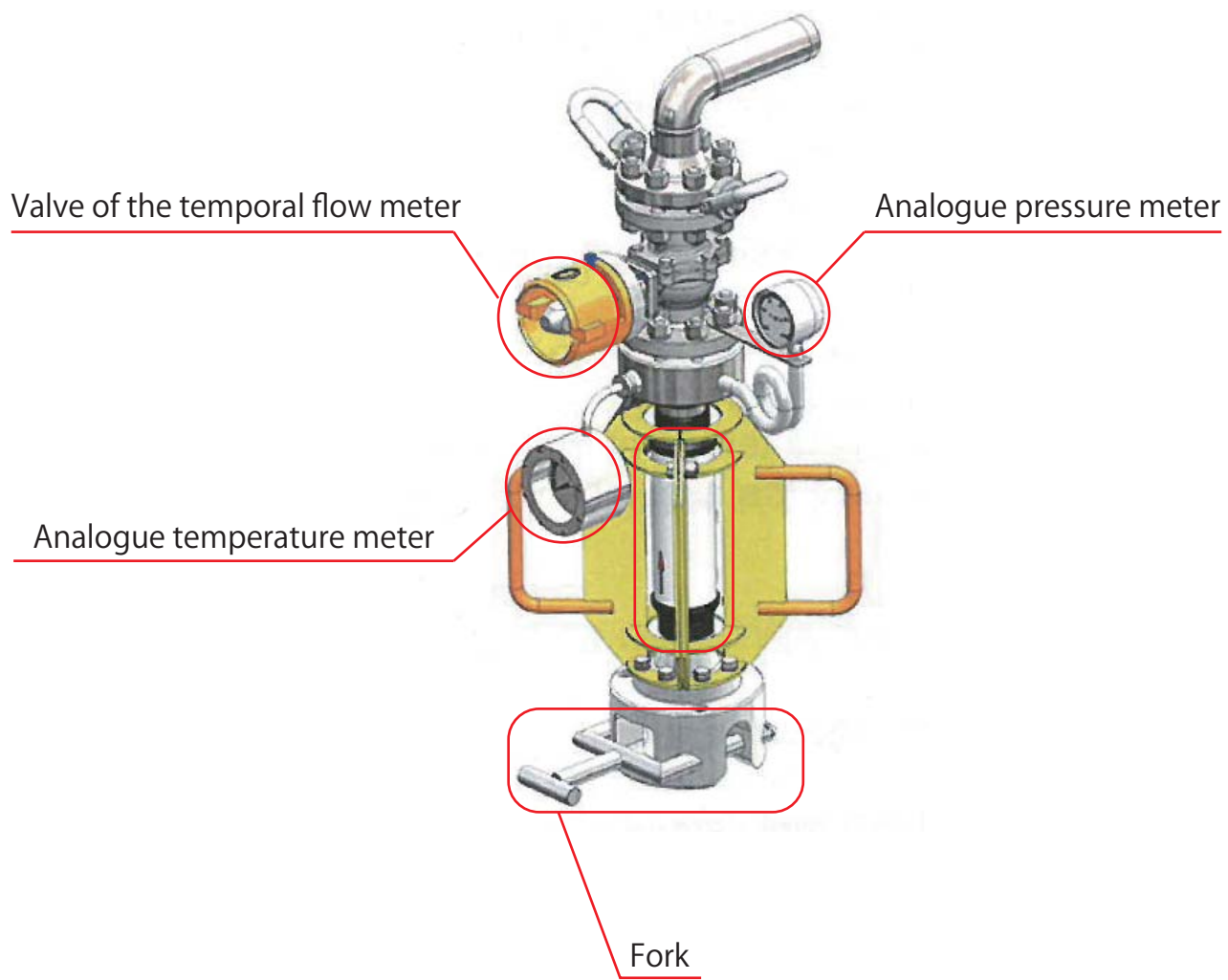


Figure 4-3-1-1

Front

Back

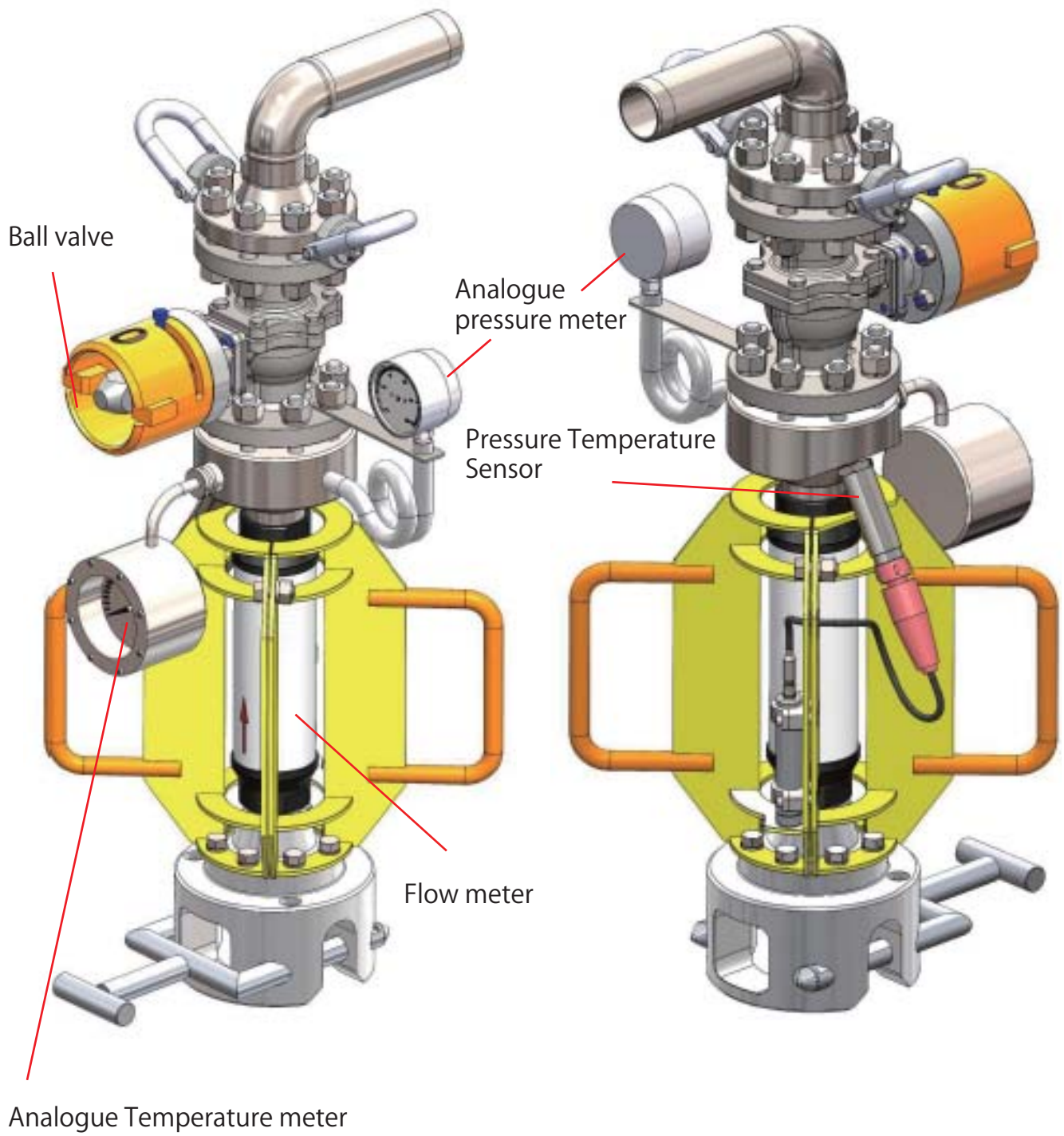


Figure 4-3-1-2

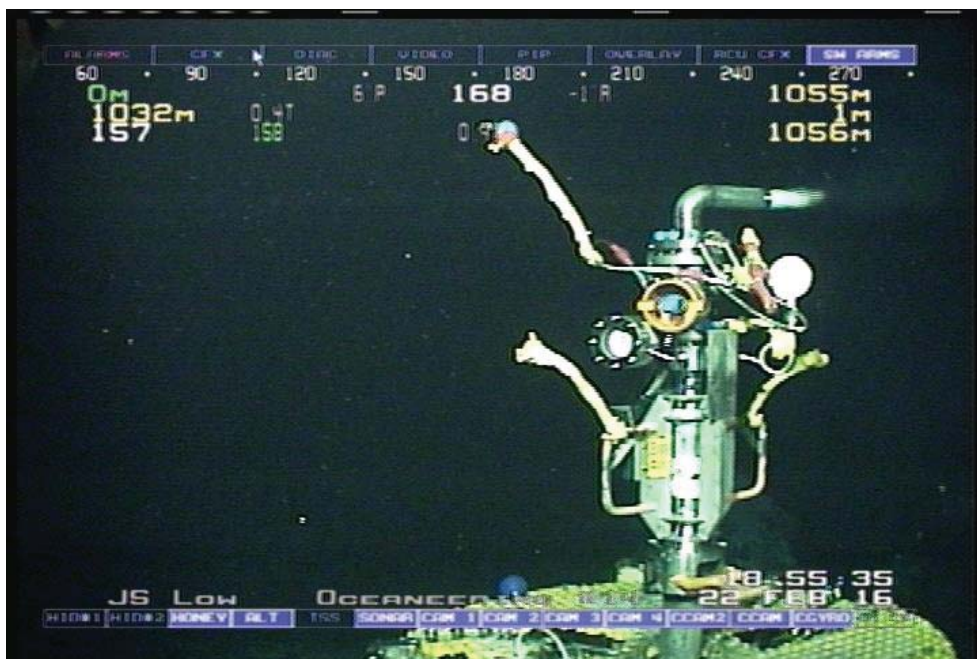


Figure 4-3-1-3



Figure 4-3-1-4



Figure 4-3-2-1

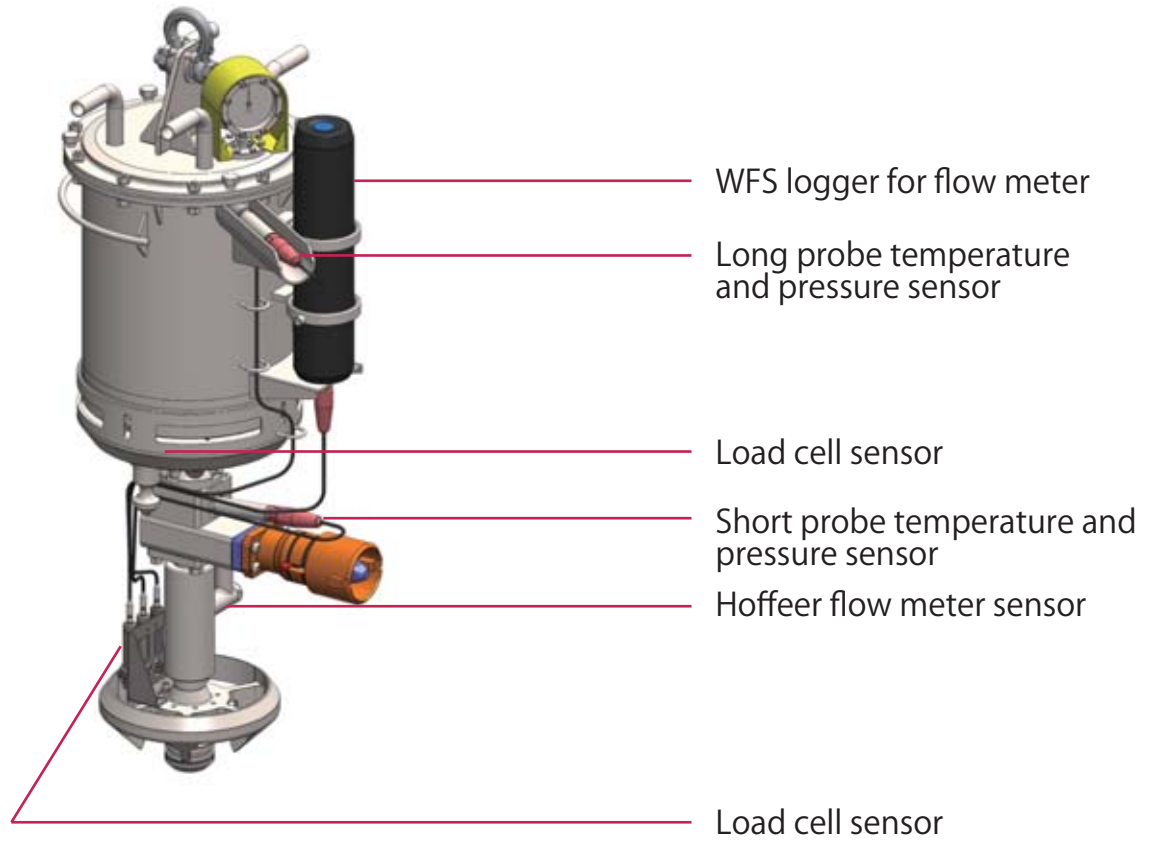


Figure 4-3-2-2

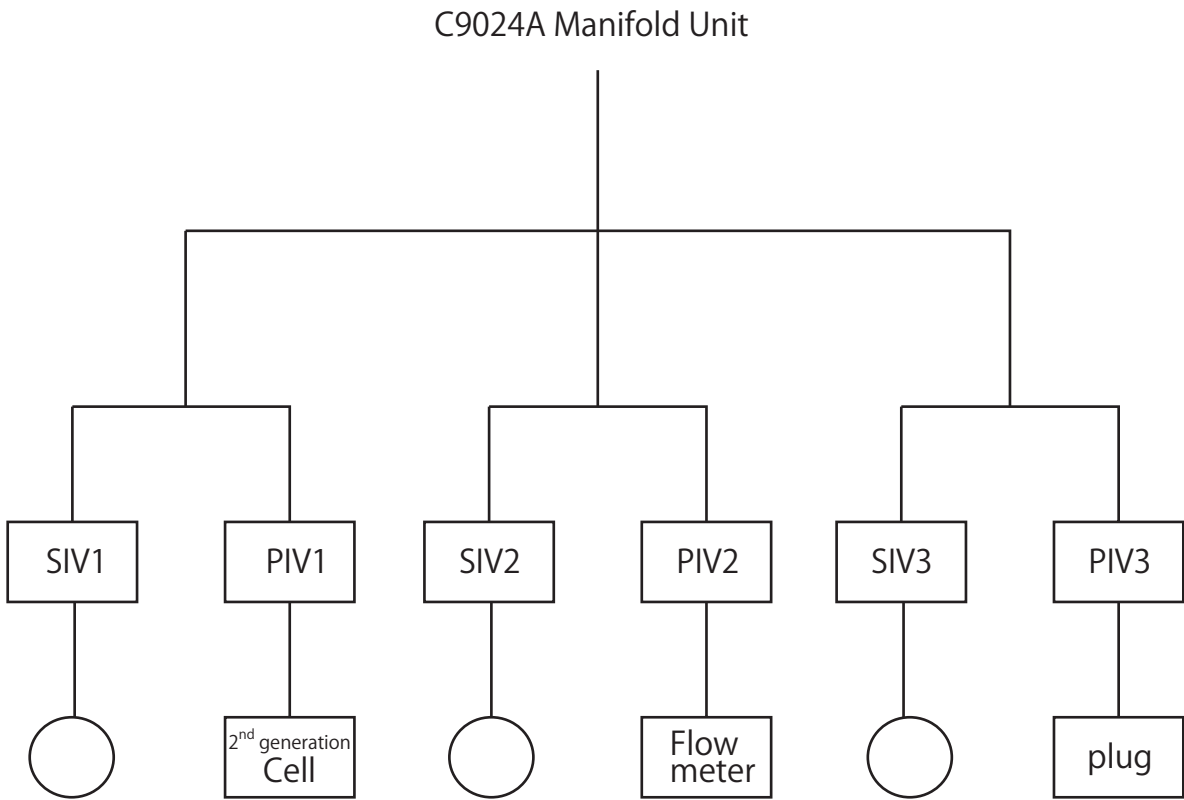


Figure 4-3-2-3

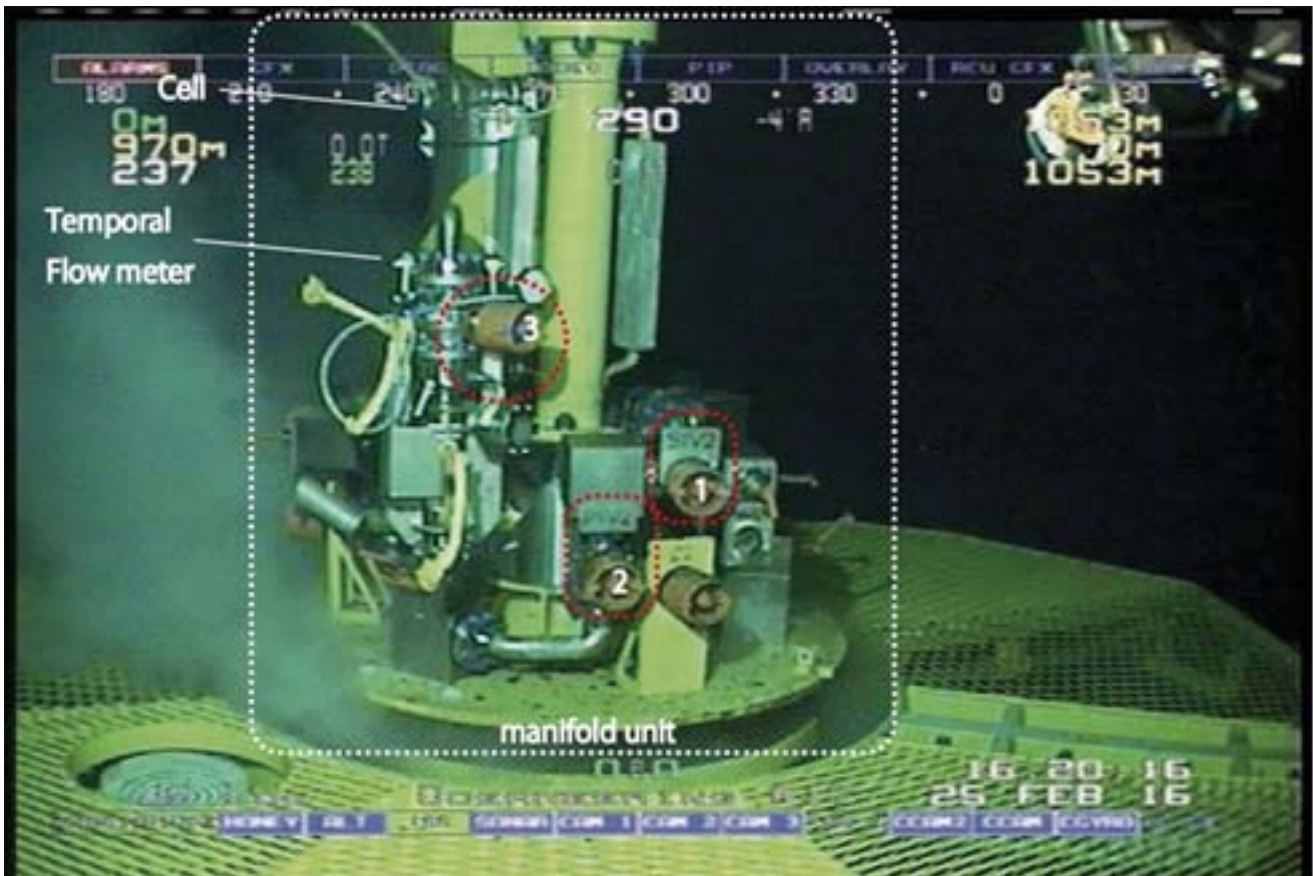


Figure 4-3-2-4



Figure 4-3-2-5

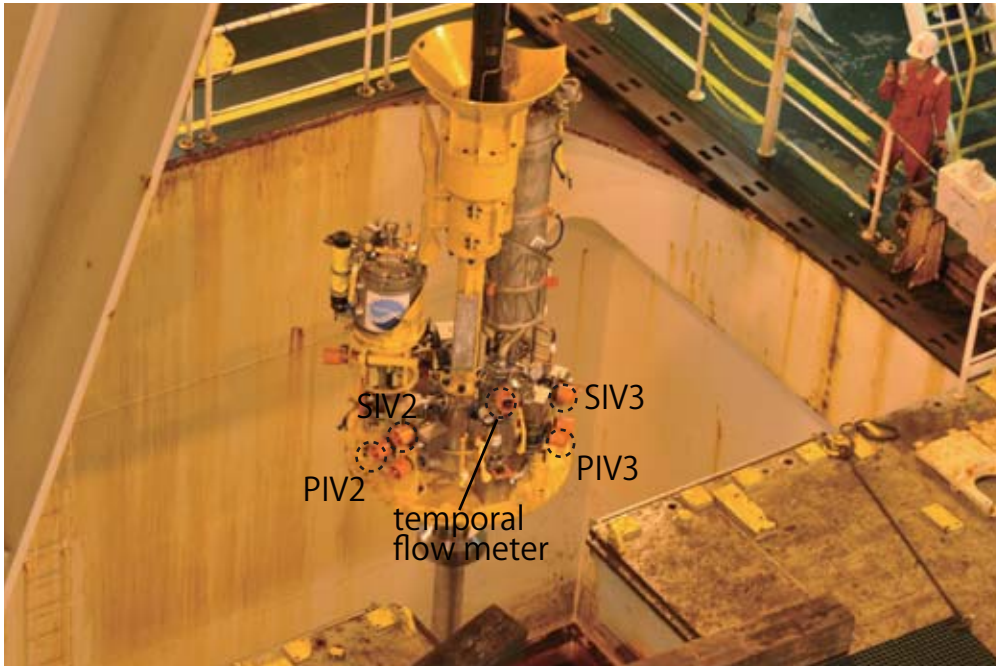


Figure 4-3-3-1



Figure 4-3-3-2

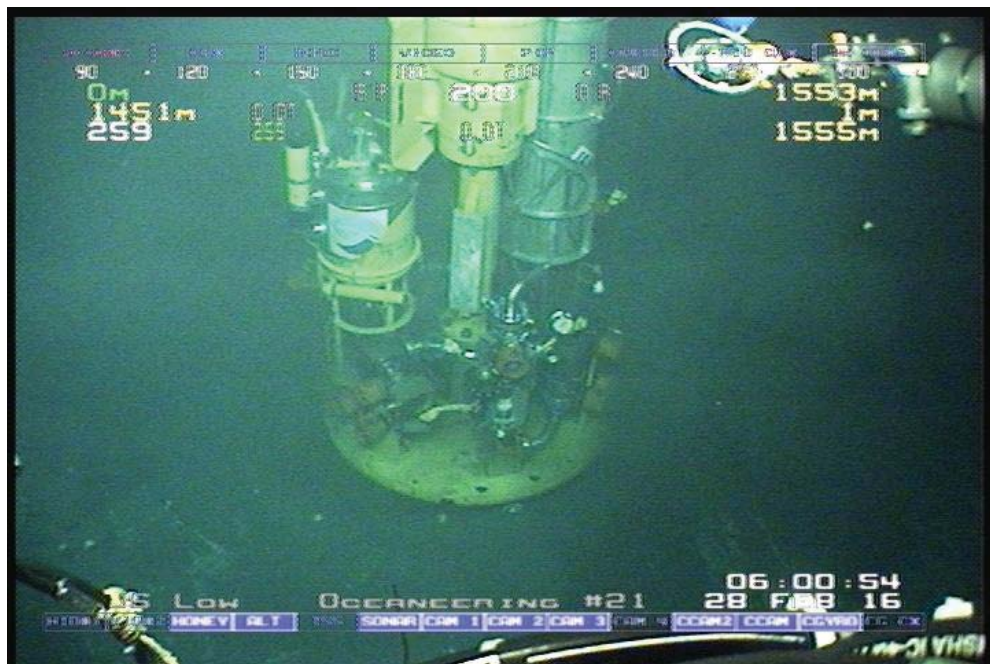


Figure 4-3-3-3



Figure 4-3-3-4

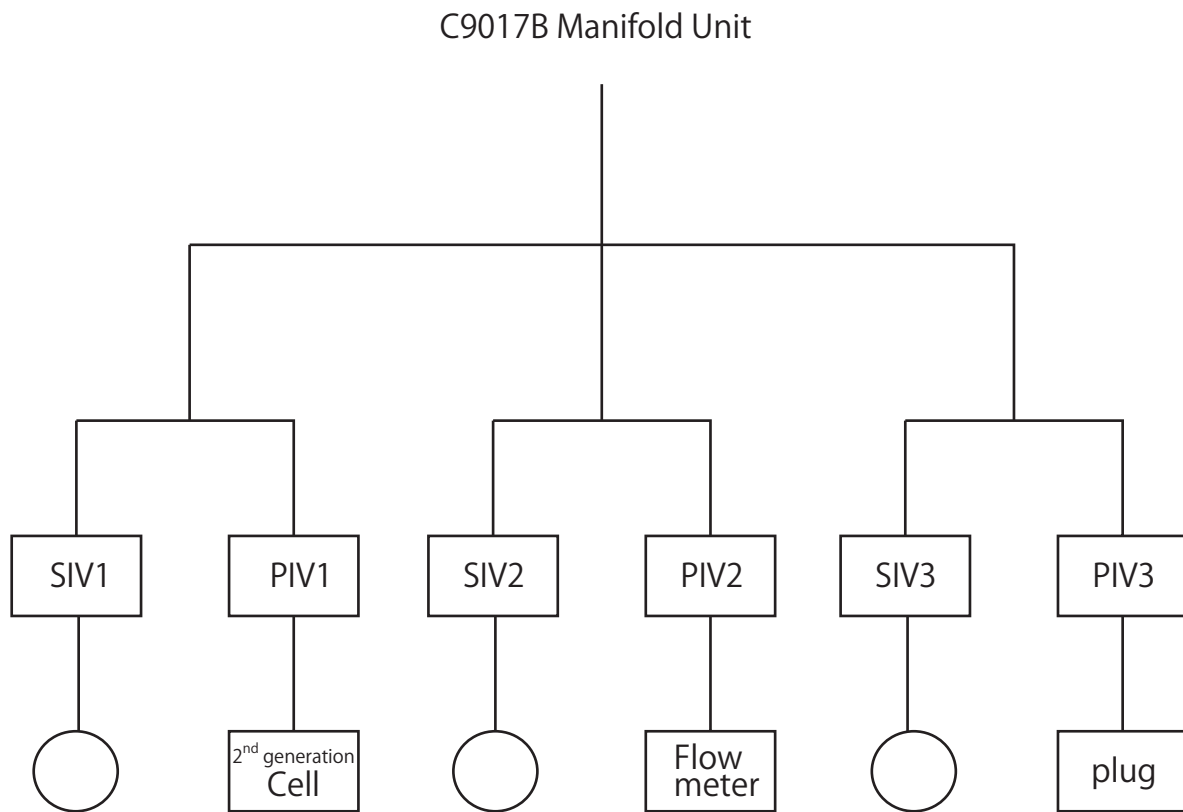


Figure 4-3-3-5

4.4 Data of temporal flowmeter

After finishing the coring operations at the Noho Site, the temporal flowmeter deployed on the manifold unit of the Hole C9017B was recovered by ROV manipulator on 5th Mar. Sensor measurement period was 6 days from 28th Feb. to 5th Mar. in 2016 and secular change of the P/T sensor data were shown in Fig. 4-4-1. Temperature of the analogue gauge was ca. 80°C, however the maximum temperature of the digital P/T sensor was up to 12°C. Detailed analysis of these data will be conducted in the near future.

The two temporal flowmeters on the Holes C9024A and C0014G at the Original Site of the Iheya-North Knoll were also tried to be recovered. Due to the scale of hydrothermal precipitate, these flowmeters were strongly fixed with a vent pipe. We tried lifted temporal flowmeters many times by using a ROV manipulator, the temporal flowmeter of the Hole C0014G was managed to be recovered, however another temporal flowmeter of the Hole C9024A was not able to be recovered. Thus, this flowmeter will be tried to be recovered during the KR16-17 Cruise. The sensor measurement period on the Hole C0014G was 20 days from 22th Feb. to 13th Mar. in 2016 and P/T sensor data were shown in Fig. 4-4-2. Timings of two positive anomalies of temperature up to ca. 40°C on 22th Feb. were concurrent with opening of the ball valve. Although the maximum value of the digital temperature sensors (ca. 40°C) was largely deviated from the analogue one (320°C), detailed analysis of these data will be conducted in the near future.

Captions:

Fig. 4-4-1 Secular change of P/T sensor data of the Hole C9017B.

Fig. 4-4-2 Secular change of P/T sensor data of the Hole C0014G.

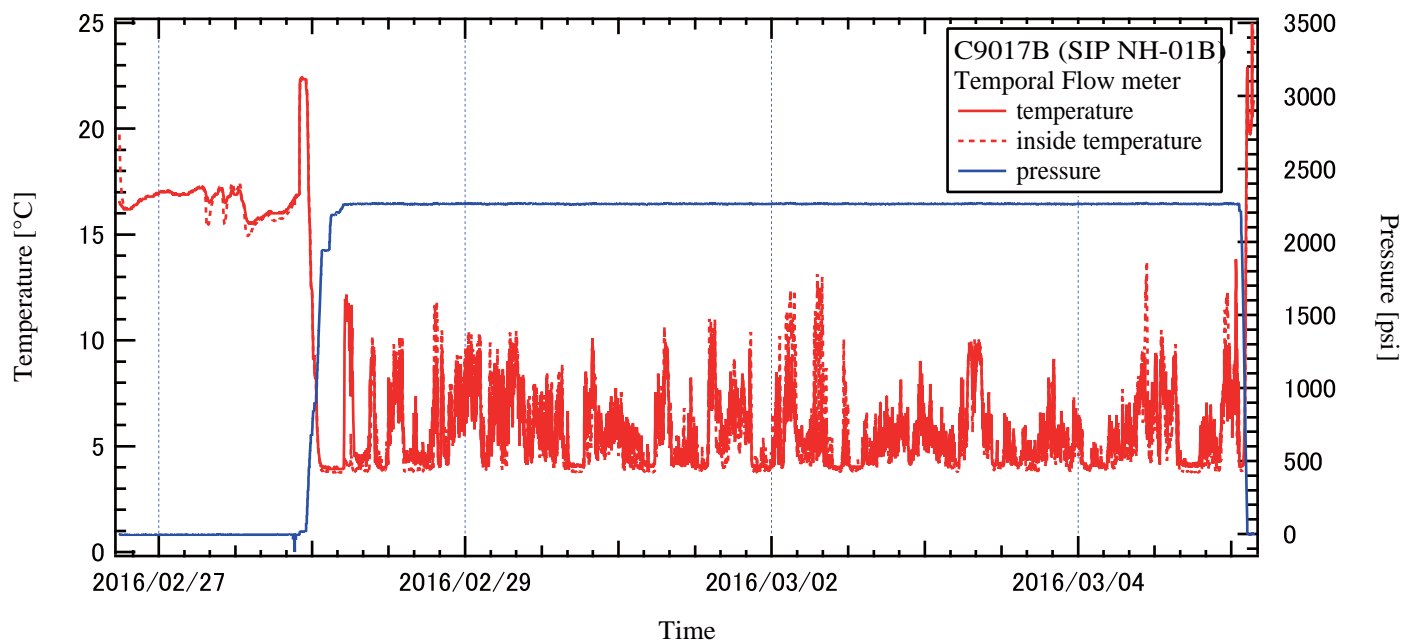


Figure 4-4-1

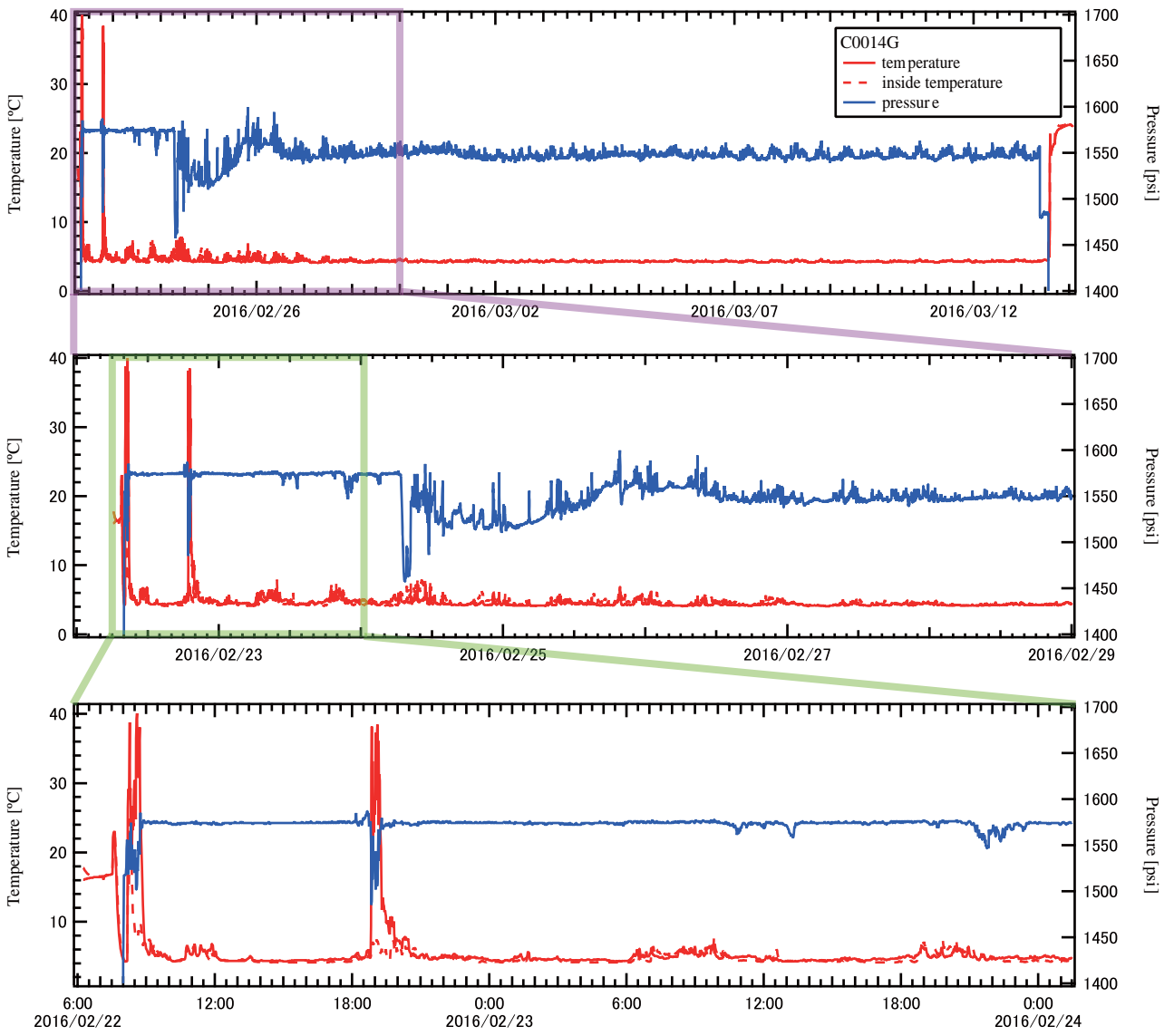


Figure 4-4-2

4.5 Deployment of SAHF and POODLE

During the CK16-01 Cruise, subsurface heat flow and pressure measurements were carried out using a SAHF (Stand Alone Heat Flow; Kinoshita et al., 2006) and POODLE (Pressure and Temperature Ondo On Deep-seafloor for Long-term monitoring Equipment, where Ondo is temperature in Japanese). These apparatuses can observe temporal variations of heat flow and pressure near the seafloor surface before, during and after drilling operations. The main purpose of installing these apparatuses is to observe hydrological change induced by drilling operation based on temperature and pressure changes of subsurface interstitial water. We have deployed SAHF and POODLE at the Noho Site in 7 hours before starting the LWD operation at the Hole C9017A on 16th Feb. These apparatuses are planned to be recovered during another cruise within one year. The water depth of the installation location was 1,566 mbsl and detailed specifications of SAHF and POODLE are given in this section.

4.5.1 Specification of SAHF

Stand-Alone Heat Flow meter (SAHF) is designed to measure subsurface heat flow by using HOVs or ROVs. Fig. 4-5-1-1 shows a schematic diagram and photo image of SAHF, respectively. The geothermal gradient can be determined by 5 thermistors data attached along with the probe. The specification of SAHF is as follows:

Material: Titanium alloy

Weight: 3.1 kg in air

Probe length: 600 mm

Number of thermistors: 5

External Interface: RS232C (9600BAUD, 8bit, Non-Parity, 2 Stop Bit)

Measurement interval: 1 min

4.5.2 Specification of POODLE

Fig. 4-5-2-1 shows schematic diagrams of POODLE system. This system is composed of two pressure and temperature sensors with one ROV homer. POODLE system has four legs which can insert seafloor sediment and fix the same position during measurement. The ROV homer flashes a signal to show the location of the POODLE system on a deep-seafloor, which enables us easier recovery operation. Pressure and temperature sensors are attached along with legs and uppermost sensors located on 3 cm below from the top part of legs. The measurement intervals of pressure and temperature sensors were set to be 1 and 10 sec, respectively.

4.5.3 Operations of SAHF and POODLE deployment

Before starting the LWD operation at the Hole C9017A of the Noho Site, SAHF #7 and POODLE were deployed on a seafloor within 100 m from a planned LWD hole position on 16 Feb. 2016. Table 4-5-3-1 shows a ROV dive event log during the SAHF and POODLE deployment operations. SAHF was loaded on the ROV cage and POODLE was taken by the ROV manipulators because a sample basket was not attached with ROV. While the ROV was descending ca. 30 m above from a seafloor, POODLE was dropped from the manipulators. Then, ROV immediately went out from the cage to search the dropped POODLE. POODLE was found on a seafloor, however it has flipped upside down and one of the four legs has been deformed by impact at landing. Despite of such trouble, the POODLE system was managed to deployed on a seafloor (Fig. 4-5-3-1a). After deploying POODLE, ROV went back to the cage so as to pick up the SAHF and descended to a seafloor again. SAHF was deployed next to the POODLE position (Fig. 4-5-3-1b) and vertical penetration length of the SAHF probe was 60 cm. The deployment location of SAHF and POODLE was about 100 m WNW away from the Hole C9017A. Fig. 4-5-3-2 shows the ROV dive track as well as deployment positions of SAHF and POODLE.

Captions

Table 4-5-3-1 ROV dive log during SAHF and POODLE deployment operations.

Fig. 4-5-1-1 Schematic diagram (a) and Photo image (b) of SAHF.

Fig. 4-5-2-1 Schematic diagrams of POODLE.

Fig. 4-5-3-1 Dive photo images of (a) POODLE and (b) SAHF deployments.

Fig. 4-5-3-2 ROV dive track for SAHF and POODLE deployment near the Site C9017.

Reference

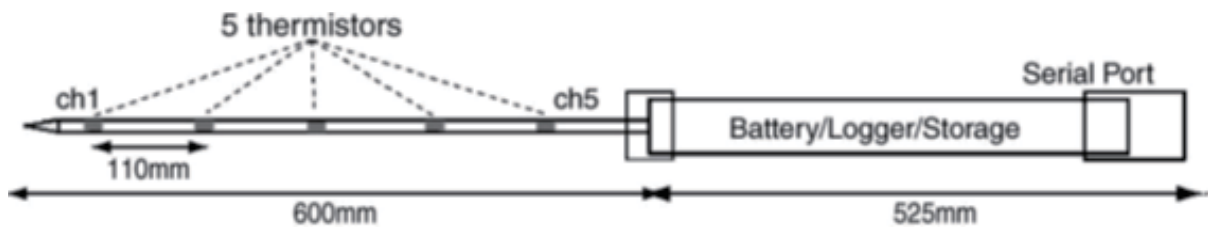
Kinoshita, M., Kawada, Y., Tanaka, A. and Urabe, T. (2006) Recharge/discharge interface in the Suiyo Seamount hydrothermal system detected by submersible-operated heat flow measurements. *Earth Planet. Sci. Lett.*, **245**, 498-508.

Table 4-5-3-1 ROV dive log during SAHF and POODLE deployment operations.

16th Feb 2016 POODLE & SAHF deployment

<i>Dive Log</i>	
Time (JST)	Notes
6:41	Time into the seawater
7:26	MAGNUM stopped at the depth of 1520 m (head 213 degree)
7:27	POODLE dropped from the manipulator
7:29	MAGNUM went out from the cage
7:31	MAGNUM landed
7:38	POODLE found at the back side of monitor
7:41	found POODLE and penetrated the seafloor
7:50	back to cage to pick up SAHF
7:58	picked up the SAHF
8:02	SAHF calibration
8:07	penetrated the SAHF

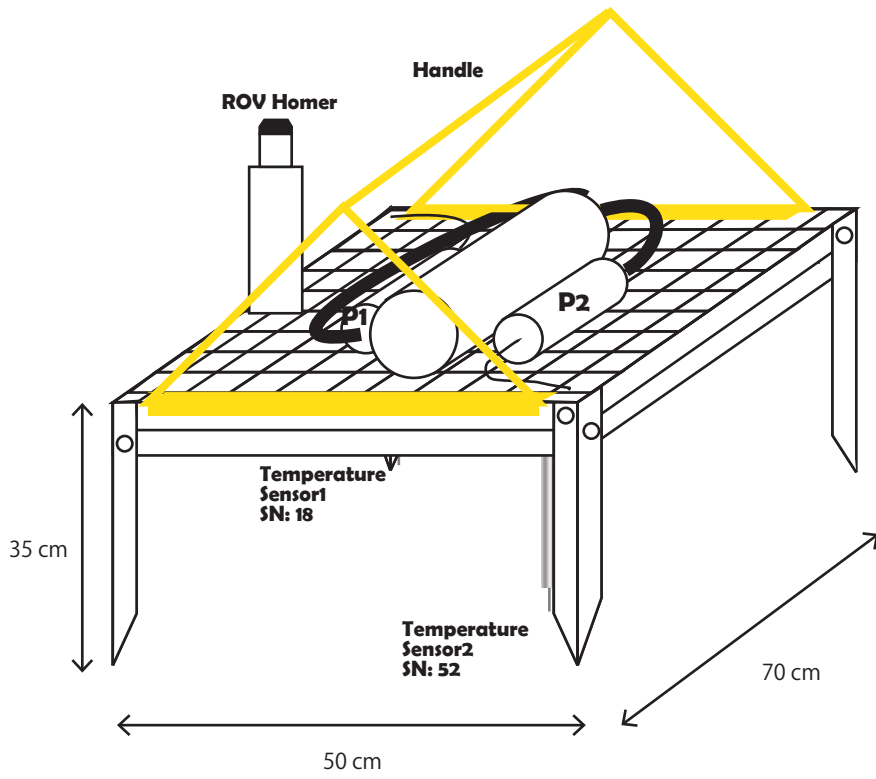
(a)



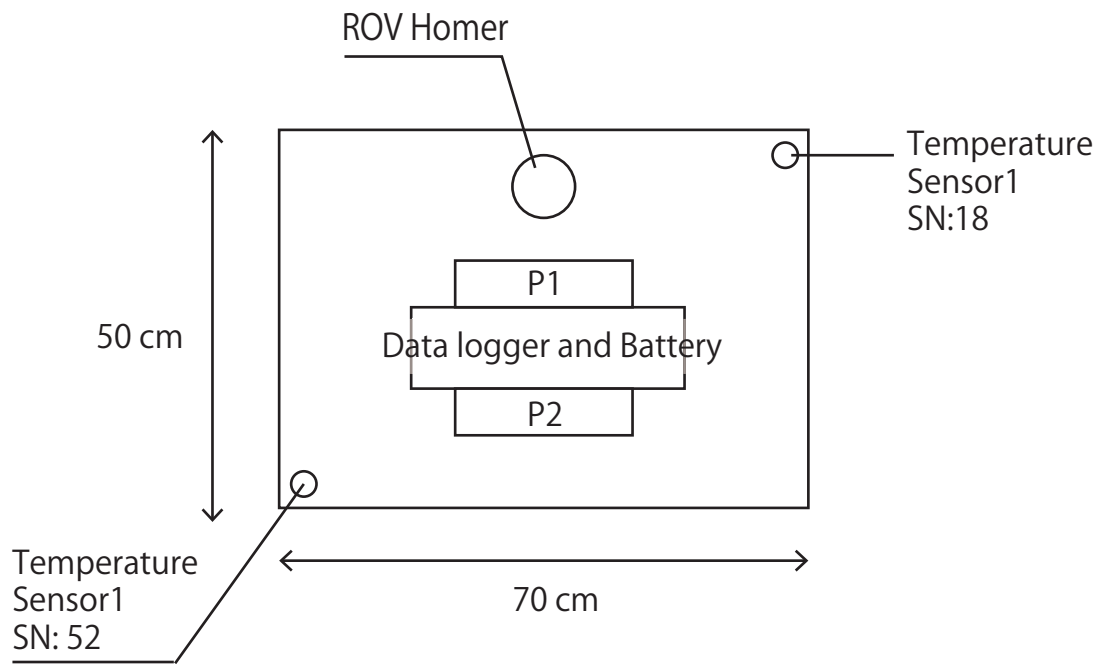
(b)



Figure 4-5-1-1



(a)



(b)

Figure 4-5-2-1



Figure 4-5-3-1

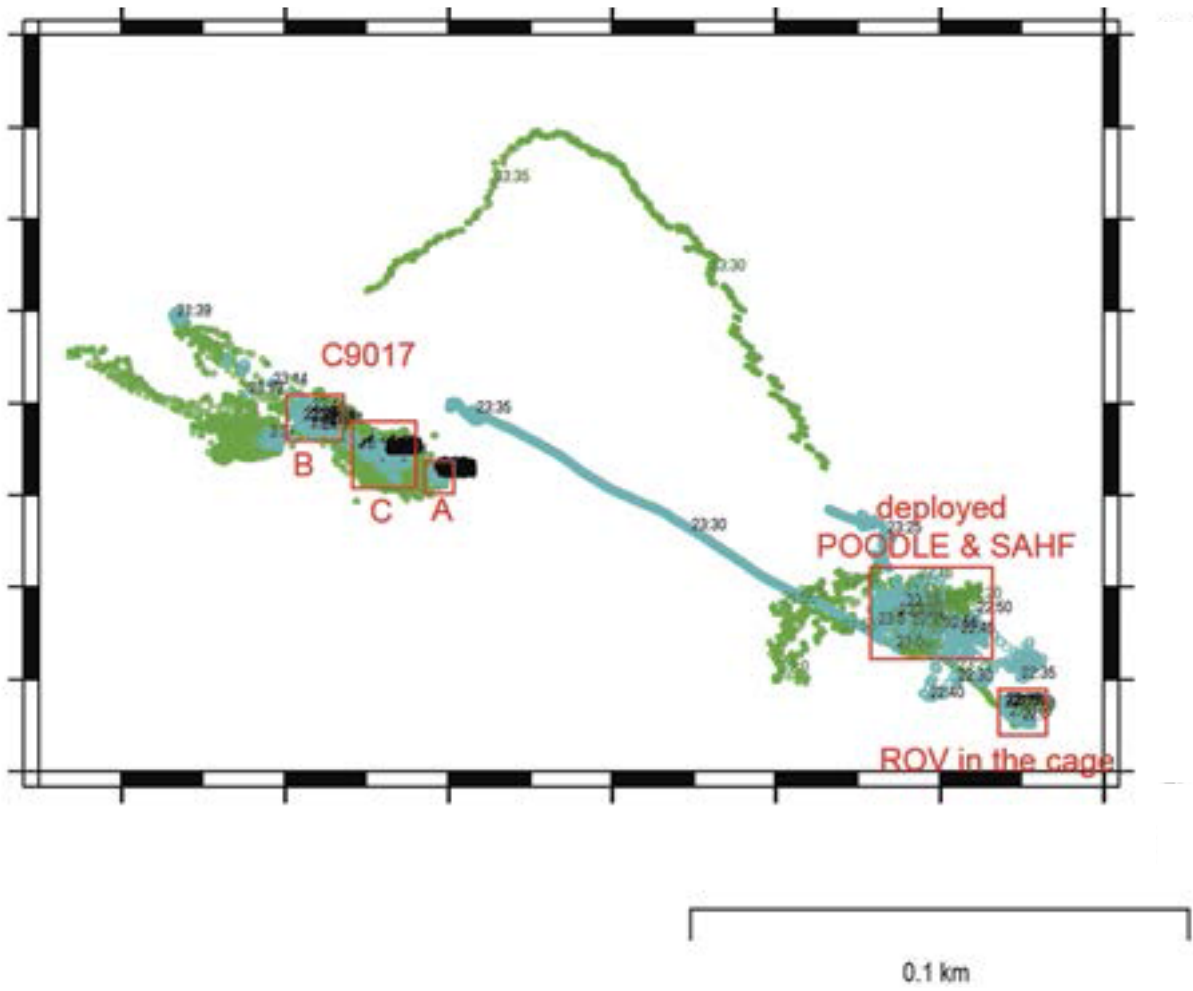


Figure 4-5-3-2

4.6 IHPU and other hydraulic tools

In the CK16-01 Cruise, we have developed various hydraulic tools and power supply unit in order to accomplish deployment temporal flowmeters and Kuroko cultivation apparatuses on the artificial hydrothermal vent. In this section, specifications of each hydraulic tool are depicted.

Independent hydraulic power unit (IHPU)

IHPU is a power supply unit of hydraulic pressure to various tools equipped with a ROV (Fig. 4-6-1). The IHPU is independent with the hydraulic power system of the ROV. So, if the IHPU was damaged and seawater invaded into this tool, the hydraulic power system of the ROV will be protected. Detailed specifications are as follows:

Size: 700 mm (L) x 494 mm (W) x 400 mm (H)

Weight: 110 kg (in air), 87 kg (in water)

Operation temperature range: 0 - 60 °C

Hydraulic inlet pressure: 207 bar

Hydraulic demand flow: 30 LPM

Hydraulic fluid type: Shell Tellus 32

IHPU Hydraulics

Working pressure: 207 bar

Maximum flow rate: 20 LPM

Fluid type: Shell Tellus 32

Hydraulic connections: 3/4" JIC male (pressure/return/case drain)

Electrical connections

RS232 at pressure canister: Subconn MBH8M male

RS485 at five function manifold: IE55-1508-FCR

Hydraulic power drill

Hydraulic power drill (Figs. 4-6-2a and b) was developed to remove scale within the steel pipe of the corrosion cap. The hydraulic power of this drill is supplied from the IHPU and its stroke lengths are 5 and 16 inch, respectively. This drill is fixed on the steel pipe by anchor clasp during the operation. Detailed specifications are as follows:

Short stroke type

Weight: 65 kg (in air), 54 kg (in water)

Size: 521 mm (L) x 449 mm (W) x 861 mm (H)

Hydraulic fluid: Shell Tellus 32

Hydraulic motor (Parker F11-19)

Drill motor maximum hydraulic flow: 30 LPM

Drill motor minimum hydraulic flow: 20 LPM

Drill motor hydraulic pressure: 420 bar

Drill motor nominal hydraulic pressure: 210 bar

Drill motor maximum torque: 60 Nm

Hydraulic cylinder

Drill cylinder hydraulic flow: 1 LPM

Drill cylinder maximum hydraulic pressure: 124 bar

Long stroke type

Weight: 120 kg (in air), 100 kg (in water)

Size: 550 mm (L) x 488 mm (W) x 1,350 mm (H)

Hydraulic fluid: Shell Tellus 32

Hydraulic motor (Parker F11-19)

Drill motor maximum hydraulic flow: 30 LPM

Drill motor minimum hydraulic flow: 20 LPM

Drill motor hydraulic pressure: 420 bar

Drill motor nominal hydraulic pressure: 210 bar

Drill motor maximum torque: 60 Nm

Hydraulic cylinder

Drill cylinder hydraulic flow: 1 LPM

Drill cylinder maximum hydraulic pressure: 69 bar

Manual and hydraulic power torque tools

Manual and hydraulic power torque tools (Figs. 4-6-3a and b) were developed to rotate various valves of the temporal flowmeter and Kuroko cultivation apparatus to regulate flow rate of hydrothermal fluid. The hydraulic power of the torque tool except for manual one is supplied from the IHPU. Detailed specifications are as follows:

Manual torque tool

Weight: 6 kg (in air), 5 kg (in water)

Size: 350 (L) x 130 (W) x 130 (H)

Hydraulic power torque tool

Weight: 40 kg (in air), 32 kg (in water)
Normal torque tool range: 50 - 2,711 Nm
Maximum torque: 3,500 Nm
Maximum RPM: 10 RPM at 22 LPM
System pressure: 207 bar
Hydraulic flow: 22 LPM
Hydraulic fluid: Shell Tellus 32

Captions

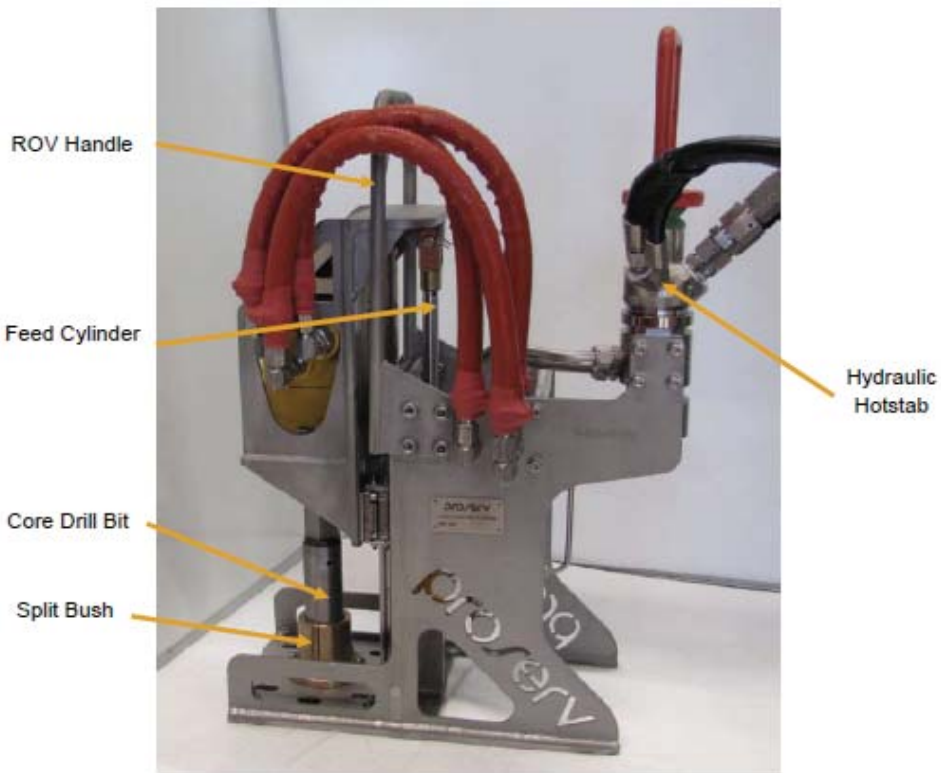
Fig. 4-6-1 Independent Hydraulic Power Unit (IHPU).

Fig. 4-6-2 (a) Short-type and (b) long-type hydraulic power drills.

Fig. 4-6-3 (a) Manual and (b) hydraulic power torque tools.



Figure 4-6-1



(a)



(b)

Figure 4-6-2



(a)



(b)

Figure 4-6-3

Chapter 5: Core Studies

5.1 Visual Core Description, XRD and SEM

T. Yamasaki, Y. Takaya, T. Nagase, T. Tindell, K. Yonezu, S. Totsuka, N. Mukae, and Y. Uno

5.1.1 Methods

Visual Core Description

Method for visual core description (VCD) essentially follows that of Expedition 331 Scientist (2011). We describe archive halves of recovered cores to document lithological information together with descriptions of hydrothermal alteration and mineralization (Mazzullo and Graham, 1988). Lithological features were observed visually and recorded in section-scale templates using the shipboard database software J-CORES. Some graphic patterns for lithologies were newly added during Expedition 908/CK16-01, although generally follows that of Expedition 331 Scientist (2011). The graphic patterns encountered during Expedition 908/CK16-01 are summarized in Fig.5-1-1-1. Symbols for sedimentary structures, soft-sediment deformation structures, severity of core disturbance, and features were after Expedition 331 Scientist (2011).

The classification scheme for clastic lithology basically follows Mazzullo and Graham (1988) and Expedition 331 Scientist (2011), but strict identification between sand and silt (0.625 mm), and silt and clay (0.0039 mm) could not be realized due to absence of a sedimentologist in the shipboard VCD team. We did not use separate patterns for more heavily indurated examples of the same lithologies (e.g., silty clay versus silty claystone) because the distinction is somewhat arbitrary. Color descriptive adjectives essentially follow Revised Standard Soil Color Charts (Oyama and Takeda, 1967).

Many of the sediments and rocks recovered during Expedition 908/CK16-01 have undergone hydrothermal alteration and/or sulfide mineralization. During Expedition 908/CK16-01, all rocks logged were graded according to whether they are fresh (<2% by volume alteration products) or have slight (2% to <10%), moderate (10% to <40%), high (40% to <80%), very high (80% to <95%), or complete (95%–100%) alteration. Additionally, through incorporation of VCDs with the results of XRD mineralogical analysis, the style of alteration for each altered interval was determined. Alteration intensity and style were summarized in Microsoft Excel sheet by core, section, and interval for all holes drilled and included on the section scale VCDs.

Seafloor and sub-seafloor sulfide mineralization can occur as massive sulfides; semi-massive sulfides; sulfide minerals in stockwork, stringers, or veins; sulfide filling voids in rocks; sulfide-filled breccia; disseminated sulfides; and metalliferous (sulfide and oxide) sediments (Table5-1-1-1). Sulfide mineralization styles and sulfide and sulfate mineral species were observed visually and summarized in Microsoft Excel sheet. Sulfide and sulfate mineral distribution were also recorded in Microsoft Excel sheet.

X-ray diffraction

In total, 111 samples were prepared for XRD analyses. The samples were selected essentially from representative portions of lithological units. The amount of each sample was *ca.* 5cc. Samples were dried by vacuum dryer (LABCONCO, FREEZE DRY SYSTEM/FREEZE ONE4.5) for more than 24 hours, prior to milling. Milling was carried out using a multi-beads shocker (YASUI KIKAI Co., PV1103[s]). The instrument settings were; 3000 rpm, 40 seconds, 3 cycles, and continuous operation (no off time). In cases where samples were bigger than 2 cm³, they were broken into <5 mm³ with a WC mortar.

Powder X-ray diffraction (XRD) analyses was carried out using a PANalytical CubiX PRO (PW3800) diffractometer. Samples were collected at irregular intervals where needed to represent the range of lithology encountered during drilling and provide a more quantitative context for visual core description. The aim was to identify the minerals in the bulk of recovery during Expedition 908. Data processing was carried out using X'Pert HighScore Version 2.1 (2.10), which is produced by PANalytical B.V. (Almelo, Netherlands). X'Pert HighScore matched diffraction peaks from the measured sample to JCPDS card and crystal structures from the Inorganic Crystal Structure Database, which contains thousands of powder XRD patterns from synthetic material and minerals. The majority of these reference patterns were similar to single crystal analyses, which does not allow for the effects of preferred orientation or stacking disorders. These effects can be particularly significant for clay minerals and phyllosilicates. The program therefore provided a guide to potential phases, which were then interpreted by the operator. XRD results for constituent minerals was tabulated, in approximate order of abundance for each sample analyzed, and included in the site reports. Peak heights may be strongly influenced by factors other than abundance, so no quantitative measurement is implied. In particular, abundances of clay and phyllosilicate minerals are not quantitatively estimated and are likely to be underestimated.

Instrument settings were as follows:

Generator = 45 kV and 40 mA.

Irradiation type = Cu $K\alpha$

Wavelengths = 1.54060 Å ($K\alpha_1$) and 1.54443 Å ($K\alpha_2$).

Step spacing = $0.01^\circ 2\theta$.

Scan step time = 3.000 s.

Divergent slit = automatic.

Irradiated length = 10 mm.

Scanning range = 2° to $60^\circ 2\theta$.

Spinning = yes

Scanning electron microscopy

In order to confirm mineral morphologies and occurrences, such as very fine-grained aggregation, observation using scanning electron microscopy was carried out on selected samples. Observed samples were fixed on sample holders by a double-faced carbon-tape. After platinum coating, using a JEOL JFC-1800 nano fine coater, all samples were observed on a JEOL 5770 SEM equipped with both backscattering and X-ray spectroscopic (energy-dispersive spectrometry [EDS]) detectors operating at accelerating voltages of 5–15 kV. For some samples, optical stereo-microphotographs were taken by using stereo optical microscopy (Zeiss SteREO Discovery V12).

5.1.2 Site C9017

Overview

Hole C9017C was cored at Site 9017. In total 16 cores were recovered from Hole C9017C, with total penetration at 121.0 mbsf. Intervals of Core 1X to 3X (0.0–24.0 mbsf) and 12X to 16X (73.5–121.0 mbsd) were cored by an Extended Shoe Coring System (ESCS), and interval of Core 4H to 11H (24.0–73.5 mbsf) were cored by Hydraulic Piston Corer System (HPCS). Differences in the coring method result in a drastic difference in recovery rates.

Hole C9017C was subdivided to 24 lithological units (Fig.5-1-2-1). In summary, Unit 1 to Unit 2 (0.0–23.31 mbsf) consist of vesicular aphyric basalt. Units 3 to 7 (from 24.0–40.055 mbsf) are made up of hydrothermal clay to gravel containing volcanic clasts. Some intervals are very loose and consist of soupy clay matrix. Units 8

to 10 (48.8–68.395 mbsf) are composed of gray-greenish gray mottled hydrothermal clay to grit. This interval characteristically contained spherical aggregates of wairakite. Grain size of matrix particles increased in the deeper portion of this interval. Units 11 to 12 (69.7–73.5 mbsf) were dark greenish gray hydrothermal gravel to grit including some sulfidic layers. From Unit 13 to Unit 24 (73.5–112.42 mbsf), alternation of altered volcanic rock layer and hydrothermal clay-grit were observed, although precise observation of lithological variation were difficult due to the poor recovery rate.

Unit description

Unit 1 (0.0–10.27 mbsf) consists of relatively fresh, black vesicular aphyric basalt (Fig.5-1-2-2). Vesicles were filled with sulfides and white materials (gypsum?). Unit 2 (19.0–23.31 mbsf) is composed of altered vesicular aphyric basalt associated with sulfide- and sulfate bearing sand-mud layers (possibly be hydrothermal sand-mud). Constituents of this unit were more altered compared to that of Unit 1.

Unit 3 (24.0–27.68 mbsf) consists of dark olive gray hydrothermal clay with volcanoclastic gravel (scoria-like pebbles). Matrix of clay in this unit was generally very soft with a substantial portion of the matrix flowed out. XRD analyses confirmed the presence of pyrite in the matrix. The matrix became more consolidated at 27.68 mbsf therefore it was assigned as the Unit 4 (27.68–28.5 mbsf) interval. Unit 4 is dark gray matrix supported hydrothermal gravel. Although the above Unit 3 does not show an anhydrite peak in the XRD results, this unit shows a strong signature of anhydrite in the matrix. Small (4–5 mm in diameter) spherical aggregates of wairakite are present in this interval. Minor quantities of hydrothermal clay, matrix-supported, and zeolite spherules are present in this unit.

Units 5 to 7 (28.5–40.055 mbsf) is made up of similar materials with Units 3 and 4. Unit 5 (28.5–29.52 mbsf) shows alternation of mottled hydrothermal gravel, matrix-supported and loose (soupy) hydrothermal clay with volcanic clasts/pebbles. Unit 6 (29.52–29.98 mbsf) consists of hydrothermal clay showing patchy alteration and Unit 7 (29.98–40.055 mbsf) is composed of hydrothermal gravel, matrix-supported. Cores from Unit 3 to Unit 7 showed patchy mottled alteration patterns (Fig.5-1-2-3). Patchy darker portions were rich in sulfide minerals and showed remnant volcanic rock texture in some cases.

Unit 8 (48.8–53.87 mbsf) is characterized by abundant spherical aggregates of wairakite (Fig.5-1-2-4). Patchy darker portions were observed also in this unit. Most patchy portions showed vesicular volcanic texture, in which the outer shape of the clasts was obscured (Fig.5-1-2-5). The matrix becomes coarsened towards Unit 9 (53.87–66.814 mbsf), although this unit is composed of similar materials with that of the Unit 8. Spherical aggregate of wairakite were larger (~5 mm) than that of other units (Fig.5-1-2-6). Some fluid pathways with alteration of rims suggest fluid percolation was present in several intervals (Fig.5-1-2-7). Unit 10 (66.814–68.395 mbsf) is composed of essentially similar materials of Unit 9, loose soupy clay matrix.

Notable, sulfide mineral-rich intervals were located in Unit 11 (69.7–70.78 mbsf). This unit consists of gray-light gray/dark greenish gray to greenish gray hydrothermal grit with a sulfide-rich layer (69.7–70.12 mbsf; Fig.5-1-2-8). Pyrite and pyrrhotite were confirmed by VCD and XRD. Unit 12 (70.78–73.5 mbsf) was dark greenish gray gradation from hydrothermal grit, matrix supported to hydrothermal grit, clast-supported.

From Unit 13 to Unit 24 (73.5–112.42 mbsf), recovered cores show roughly an alternation of altered volcanic rock layer and hydrothermal clay-grit. Thickness of each unit was unclear due to poor recovery. Order of lithological appearance toward the bottom hole was as follows;

Unit 13 (73.5–73.64 mbsf): Gray to dark greenish gray, very angular slightly altered volcanic rock fragments.

Unit 14 (73.64–73.82 mbsf): Gray to greenish gray hydrothermal sand/silt intercalated formation.

Unit 15 (73.82–83.09 mbsf): Black, angular, relatively fresh vesicular basaltic fragments.

Unit 16 (92.5–93.355 mbsf): Mixture of bluish gray - light gray hydrothermal clay/sand and highly to strongly- altered volcanic fragments.

Unit 17 (93.355–93.395 mbsf): Black-dark gray, vesicular basaltic fragments and/or volcanoclastic hydrothermal sand.

Unit 18 (93.395–102.0 mbsf): Mixture of bluish gray - light gray hydrothermal clay/sand and highly to strongly- altered volcanic fragments.

Unit 19 (102.0–102.17 mbsf): Bluish gray subangular volcanic fragments with disseminated sulfide mineralization.

Unit 20 (102.17–102.565 mbsf): Greenish gray hydrothermal clay with highly altered

volcanic rock fragments. Disseminated sulfide mineralization in the matrix and fragments.

Unit 21 (102.565–102.885 mbsf): Bluish gray, hydrothermal sand/clay with variously altered volcanic fragments. Subangular (0.5–1.5 cm in size) dark gray vesicular volcanic rocks exhibiting mottled texture.

Unit 22 (111.5–111.81 mbsf): Greenish gray, vesicular altered volcanic rocks.

Unit 23 (111.81–111.88 mbsf): Subangular subrounded fragments of greenish gray altered volcanic rocks.

Unit 24 (111.88–112.42 mbsf): Dark gray hydrothermal sand with disseminated sulfide mineralization.

Summary of relations Unit 13 through 24 were summarized in Fig. 5-1-2-9. Volcanic rock fragments in Unit 13 and Unit 15 were relatively fresh. The rocks from Unit 15 were vesicular basaltic rocks similar to top of the hole. Volcanics in Unit 19 and 22 are somewhat altered. Intercalated hydrothermal clay/sand and volcanic rock fragments were generally highly altered, and showed greenish color.

5.1.3 Site C9019

Overview

Two holes, Holes C9019B and C were cored at this site. Hole C9019B was cored by the Hydraulic Piston Corer System (HPCS) and recovered 4.6 m of core samples (rate of recovery = 95.9%) from a total penetration of 4.6 mbsf. Hole C9019C was cored by Extended Shoe Coring System (ESCS) and recovered 0.59 m core samples from total penetration of 9.5 mbsf (recovery = 6.2 %).

Unit description

Hole C9019B

Hole C9019B was composed of sediment layers from top to 4.6 mbsf, and fragments of volcanic rocks recovered by core catcher. Totally 13 lithological units were identified in Hole C9019B;

Unit 1 (0.0–0.44 mbsf): Fine-grained brownish black mud with fine-grained pyrite.

Unit 2 (0.44–0.74 mbsf): Gradation from gray pumiceous grit to sandy clay.

Unit 3 (0.74–0.91 mbsf): Gradation from dark gray pumiceous gravel to pumiceous grit.

Unit 4 (0.91–1.05 mbsf): Dark greenish gray volcanoclastic mud.

Unit 5 (1.05–1.12 mbsf): Dark olive gray volcanoclastic sand with volcanic fragments.

- Unit 6 (1.12–2.06 mbsf): Dark-light gray hydrothermal gravel-grit with white mottled gypsum and/or native sulfur crystals.
- Unit 7 (2.06–2.17 mbsf): Black hydrothermal grit (scoria-like volcanic fragments).
- Unit 8 (2.17–2.28 mbsf): Brownish black soupy hydrothermal sand with aggregates of fine-grained gypsum and hematite.
- Unit 9 (2.28–3.32 mbsf): Dark gray hydrothermal silt with aggregates of fine-grained gypsum.
- Unit 10 (3.32–3.39 mbsf): Brownish black soupy hydrothermal clay with aggregates of fibrous gypsum.
- Unit 11 (3.39–3.45 mbsf): Dark gray hydrothermal clay.
- Unit 12 (3.45–3.90 mbsf): Dark gray to black hydrothermal gravel.
- Unit 13 (3.90–4.51 mbsf): Olive black hydrothermal clay.

All units were identified within cores, and samples in the core catcher were not assigned unit number in this hole. The core catcher was filled with dark gray volcanic rock fragments. Lithological summary of Hole C9019B is shown in Fig.5-1-3-1.

Units in the Hole C9019B are comprised roughly of five normal-grading units (GU). That is; GU I interval 0–0.91 mbsf (Unit 1–3), GU II interval 0.91–2.28 mbsf (Unit 4–8), GU III interval 2.28–3.39 mbsf (Unit 9–10), GU IV interval 3.39–3.90 mbsf (Unit 11–12) and GU V >3.90 mbsf (Unit 13 to core catcher).

Sediments from Unit 2 to Unit 6 characteristically contained white mottled gypsum and native sulfur crystals (Fig.5-1-3-2), and tiny particles of pyrite and hematite. The boundary between Unit 5 and Unit 6 showed apparent dip of 40°. Although grit and gravel of Hole C9019B were expediently described as “pumiceous”, identification or confirmation of volcanoclastic fragments or pebbles could not be achieved, due to the muddy matrix. Those pebbles seem to be vesicular volcanoclastic fragments and likely to be scoria, based on information on rocks from the core catcher and Site C9017.

Hole C9019C

Hole C9019C was composed of sediment layers from the top to 0.495 mbsf, with fragments of volcanic rocks recovered by core catcher. In total, 1 lithological unit was identified in Hole C9019C;

Unit 1 (0.0–0.495 mbsf): Reddish black hydrothermal grit, matrix supported.

Samples in the core catcher were not assigned unit number. The core catcher was filled with dark gray volcanic rock fragments. Lithological summary of Hole C9019B is shown in Fig.5-1-3-3.

Matrix of hydrothermal grit in Unit 1 consists of soupy silt (Fig.5-1-3-4). Apparent (?) normal grading from top to the bottom was observed. Reddish black iron oxide, aggregates of gypsum and pyrite crystals were observed throughout the unit. Existence of sphalerite, pyrrhotite, chalcopyrite and pyrite were confirmed by XRD analyses at 0.32 mbsf. Black, angular drilling breccia of vesicular aphyric basalts were recovered by core catcher (Fig.5-1-3-5).

5.1.4 Site C9021

Overview

Hole C9021B was cored at this site. In total 12 cores were recovered, with a total penetration of 107.5 mbsf. Intervals of Core 1H to 8H (0.0–75.0 mbsf) were cored by Hydraulic Piston Corer System (HPCS) and interval of Core 9X to 12X (75.0–107.5 mbsf) were cored by Extended Shoe Coring System (ESCS). Differences in the coring method result in drastic differences in recovery rates.

Hole C9021B is made up of two essentially different types of lithologies, namely a series of pumiceous gravels (Units 1–10, 0.0–67.39 mbsf) and altered volcanic rocks (Units 11–15, 67.39–98.445 m). Summary of units and lithological variations in Hole C9021B were shown in Fig.5-1-4-1. The upper pumiceous gravels were sub-grouped as Unit 1 (0.0–26.935 mbsf), Units 2–3 (28.62–38.62 mbsf), Units 4–5 (38.62–42.505 mbsf), Unit 6 (42.505–53.395 mbsf) and Units 7–10 (53.395–67.39 mbsf). Color changes in representative core samples were shown in Fig.5-1-4-2. Unit 1 consists of pumiceous gravel, clast-supported. Units 2 is comprised of weakly altered mottled pumiceous gravel, clast-supported. This unit is characterized by yellowish or ochreous weak alteration. This alteration color changed to greenish gray in Unit 3. Unit 4 consists of greenish gray pumiceous gravel. Unit 5 is 47 cm thick greenish gray, clayey hydrothermal sand. Below this interval, dark gray volcanoclastic (pumiceous) gravels are distributed as Unit 6. Unit 7 to 10 are composed of dark greenish gray volcanoclastic (pumiceous) gravels. Altered volcanic rocks are present at 67.4 mbsf (Unit 11). Alteration intensity of the volcanic rocks or volcanoclastic fragments increased with

depth.

Unit description

Unit 1 consists of light gray, unaltered pumiceous gravel, clast-supported. Since the matrix is unconsolidated, soupy and fine matrix could have flowed out, during coring and/or core processing. The remaining matrix material seems to be fine-grained pumiceous sand. Size of pebbles in pumice gravels range from <1.0 cm to ~5.0 cm. Most of the pumice fragments show fibrous foam, and are so-called woody pumices. Some fragments of obsidian-like dense glass with dark gray color were also observed throughout the unit. Existence of glasses was confirmed by XRD analyses. Reverse grading was observed in some intervals (Fig.5-1-4-3). A thin layer (1.5 cm thick) of highly altered dark-gray to greenish gray hydrothermal (tuffaceous) clay was observed at 23.95 mbsf. Celadonite/glaucanite was confirmed at this interval (Fig.5-1-4-4). Color of overall sections changed gradually toward bottom of the hole, and clear changing was confirmed at 28.62 mbsf.

Unit 2 is comprised of weakly altered mottled pumiceous gravel. Overall brownish or yellowish color and mottled patterns exhibited by cm- to tens of cm-scale, patchy brownish stain with diffused outline and brownish fragments (Figs.5-1-4-5 and -6). Constituent materials were essentially the same with that of the Unit 1 and only difference seemed to be degree of alteration. Based on XRD results, glass was also preserved in this unit, irrespective of overall brownish or yellowish alteration. At the base of Unit 2, a 30 cm thick hydrothermal sand layer was observed at 36.7 mbsf (C9021B_04H-09 to 04H-CC). This sand seemed to be essentially the same as the matrix of the overlying pumiceous gravel, thus we did not assign individual unit number for this interval. Unit 3 is a transitional unit from Unit 2 to Unit 4. The color of the core changes from brownish of yellowish to greenish, and constituents were basically the same as that of Unit 2.

Unit 4 (38.62–41.74 mbsf) is characterized by appearance of greenish color in the matrix portion. This unit consists of greenish gray volcanoclastic gravel. Although constituent fragments were of pumice-origin, these fragments seemed to be denser than that of the above units and thus were not exactly the same as the pumice fragments in the overlying Units 1 and 2. Therefore, we assigned lithological name of “volcanoclastic gravel/conglomerate/breccia” for this interval. Based on XRD analyses, greenish color was derived from Celadonite/Glaucanite. Unit 5 (41.74–42.505) is light greenish gray,

clayey hydrothermal sand with some pumice fragments. This unit also exhibited greenish color as with overlying Unit 4 (Fig.5-1-4-7).

Unit 6 (42.505–53.395 mbsf) is characterized by disappearance of greenish color in the matrix portion. Constituents of both units were similar, but different in alteration degree. These two units show very dark color. Although constituent pumiceous fragments did not resemble pumices in Units 1 and 2 in terms of their color (Fig.5-1-4-2), existence of glass in Unit 6 were confirmed by XRD analyses. Thus, pumiceous fragments are still fresh in Unit 6. In addition, celadonite/glaucanite were not be detected by XRD analyses in this unit. Unit 6 consists of gray to dark gray volcanoclastic gravel, clast-supported. Brownish mottled texture similar to Unit 2 was observed in some intervals. Large (>5.0 cm) fractured single pumice fragments were commonly observed in this unit (Fig.5-1-4-8).

Unit 7 (53.395–60.265 mbsf) shows a weakly greenish color matrix. Mottled and disseminated light greenish clay were observed in the matrix. The greenish color in matrix becomes deeper with increasing depth, in a large sense (Fig.5-1-4-2). Unit 8 (60.265–62.63 mbsf) consists of similar materials to Unit 7. Greenish alteration intensities seemed to be more strong than Unit 7. Unit 10 (62.85–67.39) is essentially the same lithology as with Unit 8. Thin (22 cm thick) gray to light gray volcanoclastic (tuffaceous) mud of Unit 9, are intercalated with Unit 8 and Unit 7. The boundary of the mud layer of Unit 9 shows a greenish gray alteration rim (1–2 cm thick) and the lower side of the mud layer was probably pathway of fluids (Fig.5-1-4-9). Celadonite/glaucanite and chlorite were identified from Unit 8 and 9, by XRD analyses.

From Unit 11 (67.39-67.68 mbsf; core 8H, section 2), several pieces of dense volcanoclastic rock pebbles were recovered from each core (cores 9X, 10X, 11X and 12X). There is the possibility that some of pieces derived from upper intervals as drilling waste. As a result of detailed evaluation, the following features have become clear; 1) most of pieces within a core resemble each other, and (2) color, alteration style and alteration intensity gradually changed with increasing depth (Fig.5-1-4-10). Therefore, it is regarded that basically all recovered pieces exhibit lithology of drilling intervals.

Unit 11 consists of dark gray altered volcanic rocks or volcanoclastic fragments. Texturally it resembled silicification and original igneous texture was unclear. Unit 12

(75.0–75.23 mbsf) consists of dark gray to pale greenish gray variously altered volcanoclastic fragments. Color changed from dark gray to light gray. Unit 13 (84.5–84.7 mbsf) is composed of light greenish gray to greenish gray variously altered volcanoclastic fragments. Unit 14 contains two types of volcanoclastic fragments; dark greenish gray, relatively massive altered volcanoclastic fragments, and another one was yellowish white, banded (or laminated) altered volcanic rock fragments. The banded texture is mm-scale. Unit 15 (98.0–98.445 mbsf) consists of a mixture of variously altered volcanoclastic rock fragments. Massive, dark gray fragments, banded fragments, yellowish, banded dark gray fragments, and banded, yellowish-brown fragments were observed.

5.1.5 Hole C9023

Overview

Three holes, Holes C9023B, D and E were cored in this site. The penetration depth and the total recovery length of each hole were 9.5 m and 0.345m (recovery rate: 3.63 %) for Hole C9023B, 127.0 m and 12.28 m (9.67 %) for Hole C9023D, and 208.5 m and 3.555 m (1.71 %) for Hole C9023E. At the Hole C9023E, coring was started under 125.0 mbsf in order to complement the continuation of Hole 9023D due to abandonment of drilling because of technical problems.

Unit description

Hole C9023B

Only one section (C9023B 1X-CC) was recovered from Hole C9023B. This core was divided into three lithological units as follows;

Unit 1 (0.0–0.15 mbsf): massive sulfide rocks

Unit 2 (0.15–0.20 mbsf): sulfate-sulfide gravel, clast-supported

Unit 3 (0.20–0.345 mbsf): hydrothermal clay

Lithological summary of Hole C9023B are shown in Fig.5-1-5-1.

Unit 1 consists of some highly mineralized sulfide ore fragments. In this unit, two types of ore, black colored and yellow colored ore (corresponds to Kuroko and Oko in kuroko type deposit) were observed. The black ore is composed of sphalerite, galena, chalcopyrite and minor amount of pyrite, and the yellow ore is composed of quartz, chalcopyrite, pyrite and minor amount of sphalerite. XRD analysis of yellow ore fragment

also shows sulfide mineral assemblage of pyrite, chalcopyrite, sphalerite and galena. Although actual thickness of these layers was unclear due to drilling disturbance, order of sequence was well preserved; black ore is sequentially above yellow ore.

Sulfate-sulfide ore fragments in Unit 2 are composed of anhydrite, pyrite, chalcopyrite and minor amount of galena and sphalerite. These ores were dark gray to black in color and were broken into gravel (~1 cm), probably due to drilling. Unit 3 was white to light gray hydrothermal clay containing abundant pyrite grains. In addition to these minerals, some black and yellow ore fragments (~8 mm) were observed between 0.27–0.30 mbsf. XRD analysis shows that hydrothermal clay sample between 0.30–0.31 mbsf is composed of anhydrite, clinocllore, pyrite and sphalerite.

Hole C9023D

Hole 9023D was cored with Hydraulic Piston Corer System (HPCS) (core 2H, 4H and 5H) and Extended Shoe Coring System (ESCS) (core 1X, 3X and 6–16X). Cores recovered from Hole C9023D were divided into 23 lithological units as follows;

Unit 1 (0.0–0.265 mbsf): sulfate-sulfide gravel, clast-supported (0.0-0.10 mbsf) and sulfate-sulfide gravel, matrix-supported (0.10-0.265 mbsf)

Unit 2 (0.265–0.29 mbsf): sulfate-sulfide gravel, matrix-supported

Unit 3 (9.50–11.935 mbsf): gradation from hydrothermal gravel, clast-supported, to sulfidic hydrothermal grit (9.50–9.735 mbsf), gradation from sulfate-sulfide gravel, clast-supported, to sulfidic hydrothermal grit (9.725–10.435 mbsf), sulfate-sulfide gravel, matrix-supported/clast-supported (10.435–11.475 mbsf, 11.635–12.935 mbsf), and sulfidic sand (11.475-11.635 mbsf)

Unit 4 (13.0–1.325 mbsf): hydrothermal gravel, matrix-supported (13.0–13.28 mbsf) and hydrothermal mud (13.28–13.325 mbsf)

Unit 5 (22.5–22.85 mbsf): sulfate-sulfide gravel, clast-supported

Unit 6 (22.85–23.035 mbsf): hydrothermal gravel, matrix-supported

Unit 7 (31.0–33.225 mbsf): gradation from sulfate-sulfide gravel, clast-supported, to sulfidic hydrothermal grit (31.0–32.01 mbsf) and sulfate-sulfide gravel, clast-supported (32.01–33.225 mbsf)

Unit 8 (33.5–33.55 mbsf): silicified volcanic/volcaniclastic rocks

Unit 9 (43.0–43.175 mbsf): volcaniclastic gravel/conglomerate/breccia

Unit 10 (43.175–43.4 mbsf): hydrothermal clay

Unit 11 (52.5–52.59 mbsf): volcaniclastic gravel/conglomerate/breccia

Unit 12 (52.59-52.87 mbsf): hydrothermal clay

- Unit 13 (52.87–53.01 mbsf): silicified volcanic rocks (52.87–52.93 mbsf) and volcanoclastic gravel/conglomerate/breccia (52.93–53.01 mbsf)
- Unit 14 (60.5–61.155 mbsf): hydrothermal clay
- Unit 15 (61.115–61.2 mbsf): hydrothermal clay with silicified rock fragment
- Unit 16 (70.0–71.1 mbsf): hydrothermal clay
- Unit 17 (79.5–79.795 mbsf): hydrothermal clay
- Unit 18 (79.795–79.81 mbsf): silicified volcanic/volcanoclastic rocks
- Unit 19 (86.5–86.825 mbsf): silicified volcanic/volcanoclastic rocks
- Unit 20 (93.0–93.36 mbsf): silicified volcanic/volcanoclastic rocks
- Unit 21 (102.0–102.535 mbsf): silicified volcanic/volcanoclastic rocks
- Unit 22 (109.0–109.395 mbsf): silicified volcanic/volcanoclastic rocks
- Unit 23 (118.5–119.04 mbsf) silicified volcanic/volcanoclastic rocks

Lithological summary of Hole C9023D is shown in Fig.5-1-5-2. From Core 6X to 16X, the recovery rate was very low. This means significant loss of materials during coring operation. Therefore, in this interval, we carefully sectioned units for the purpose of reconstruction of lithological distribution by further on-land detailed examination. In addition, it is noted that we provisionally described fine-grained greenish gray volcanogenic rock fragment as ‘tuffaceous’ based on similarity to so-called ‘green tuff’. However it is unclear that those kinds of materials were truly tuff or volcanic rocks (intrusives or lavas) due to detailed thin section observation. Confirmation of this problem presently remains.

Upper part of Unit 1 (0.0–0.10 mbsf) consists of gray colored low-grade sulfate-sulfide ore fragments. These ore fragments are composed of anhydrite, sphalerite, chalcopyrite and galena. Lower part of Unit 1 (0.10–0.265 mbsf) was gray to dark gray colored sulfate-sulfide sand/gravel. Sulfide minerals are mainly composed of sphalerite and chalcopyrite. The sequence of this unit was similar to Unit 2–Unit 3 of Hole C9023B.

Unit 2 consists mainly of whitish gray sulfate-sulfide sand to gravel. Anhydrite and minor amounts of pyrite and sphalerite are also distributed in this Unit. Some crystalline anhydrite grains (~ 5mm) are observed.

Unit 3 consists of sulfate-sulfide sand/gravel. Consolidated clay or lithic fragments were also observed as gravels. Anhydrite, chlorite, sphalerite, pyrite, galena and chalcopyrite were confirmed by XRD analysis of sandy sample from 9.66 mbsf to

9.67 mbsf. Constituent materials of overall units were essentially similar, although lithological notation varies depends on the grain size distribution, the proportion of each constituent mineral and the presence or absence of grading texture. The uppermost part of this unit (2H sec. 1; 9.50–9.735 mbsf) consists of consolidated clayey sand with fine euhedral pyrite (~ 0.1 mm in diameter) and sphalerite grains. Below 9.735 mbsf, sulfate, sulfide and silicified volcanoclastics (and/or consolidated clay fragment) gravel/sand was dominantly distributed. The matrix is composed of hydrothermal sand/clay, euhedral pyrite and sphalerite. Minor amount of transparent anhydrite crystals and aggregation of sphalerite grains were sparsely observed. In addition, weak peaks of chlorite and chalcopyrite are also detected by XRD in the whole unit. Interval between 11.475–11.635 mbsf was identified as highly mineralized sulfidic sand. This interval is composed of anhydrite, lithic fragment, pyrite and sphalerite aggregate (Fig.5-1-5-3). Although normal grading textures were observed in several intervals (9.50–9.725 mbsf, 9.735–10.435 mbsf, 10.96–11.475 mbsf, 12.055–12.285 mbsf and 12.285–12.505 mbsf), those textures were possibly artifacts of drilling disturbance.

Except for the lowest interval (13.28–13.325 mbsf), Unit 4 consists of white anhydrite gravel and light grayish clayey matrix. The matrix is composed of clay, very fine pyrite and sphalerite/pyrite aggregate. Clots of sphalerite and pyrite aggregates were also sparsely observed. Chlorite and talc are detected by XRD analysis. Lowest interval of the unit consists of intercalation of anhydritic clay and sulfidic clay. This clay seems to be a drilling artifact. Sulfide minerals are notably concentrated in the lowest part of this unit (13.30–13.325 mbsf).

Sulfate-sulfide gravel in Unit 5 is composed of sphalerite/pyrite aggregations, white rounded anhydrite grains and lithic fragments (and is possibly drilling waste). The percentages of sulfide minerals was approximately 80% in this unit.

Unit 6 was white anhydrite gravel, matrix supported, containing tiny (~1.0 mm) black spots of sphalerite/pyrite aggregate. The matrix is composed of light greenish gray clay.

Unit 7 consists of sulfidic sand and sulfate-sulfide gravel. The uppermost part of this section was homogeneous sulfidic sand. Lithic fragments containing anhydrite and sulfide were sparsely distributed. Native sulfur was observed at 31.425 mbsf (Fig.5-1-5-4) and 32.19 mbsf. Apparent horizontal grading texture observed in the whole unit was

caused by the core splitting procedure (vibration and cooling water).

In the Core 6X (unit 8), only a 5 cm core sample, composed of mixed pebbles of bluish altered (silicified) volcanic or volcanoclastic, tuffaceous rock and anhydrite + sulfide lithic fragments, was recovered. A thin (~1.0 mm) sulfide vein was observed in altered volcanogenic rock.

Unit 9 consists of light greenish gray altered volcanic or volcanoclastic, tuffaceous rock, altered volcanogenic clasts (composed of anhydrite and fine sulfide minerals). This unit is characterized by the presence of relatively large and hard rock fragments compared to Unit 10 below. XRD analysis of this greenish rock fragments shows that the mineral assemblages are (1) quartz, chlorite, vermiculite and illite/muscovite, and (2) anhydrite and chlorite.

Unit 10 consists of gray hydrothermal clay (possibly highly altered volcanogenic, tuffaceous rock) containing whitish fragments of altered volcanogenic clast and chalcopyrite/pyrite veins was dominantly distributed. This unit is characterized by the existence of whitish fragments/clay, and this material does not be observed within the relatively large and hard rock fragments in Unit 9.

Unit 11 consists of gray altered volcanic clast. These clasts are composed of anhydrite and fine sulfide minerals. Unit 12 consists of light gray (upper half) to light greenish gray (lower half) hydrothermal clay containing gray to greenish gray altered volcanogenic, tuffaceous fragments (~3 cm), anhydrite (~5 mm) and fine pyrite grains. XRD analysis shows that the amount of chlorite increases compared to the above units. Unit 13 consists of dark gray silicified volcanic clasts with anhydrite veinlets and fine-grained pyrite. Below 53.44 mbsf (the lower part of unit 13), the fragments were crushed and compacted by drilling disturbance.

Unit 14 and Unit 15 were light gray to gray hydrothermal clay with fine pyrite grains similar to Unit 13. Some light greenish gray large clasts (~4 cm), whitish clots of anhydrite and fracture filling whitish anhydrite were observed in Unit 14. Unit 15 contains black silicified rock clast (~3 cm). Unit 15 does not contain fracture filling whitish anhydrite. Unit 16 and Unit 17 exhibit similar lithology to Unit 14. We assigned individual unit numbers due to very low recovery rates.

Unit 18 corresponds to the lowest part of section 11X-CC. This section was also hydrothermal clay similar to Unit 14, 16 and 17, but the color changes to light greenish gray. Some light gray to light greenish gray silicified volcanoclastic fragments (~1.0 cm) containing sulfide grains were observed in this unit.

Unit 19 consists of light gray to greenish gray silicified volcanoclastic rocks, in which clots of sulfide aggregates and minor whitish anhydrite is contained, with drilling derived clay (possibly grinded silicified volcanoclastic rocks by drilling). Some sulfide stringer can be observed. Unit 20–22 have a similar lithology to Unit 19. But in Unit 21, clots of anhydrite-sulfide aggregate and sulfide stringers were observed more frequently than Unit 19 and 20. In Unit 22, occurrence of clots becomes more frequent and the sulfide proportion in these clots increases, i.e. increasing mineralization degree with depth from Unit 19 to Unit 22. Unit 23 is also similar to Unit 19–22, but mineralization degree is much lower than that of Unit 21 and 22.

Hole C9023E

Hole C9023E was cored with Extended Shoe Coring System (ESCS). The coring was conducted below 125.0 mbsf in order to complement the underlying portion of Hole 9023D. Cores recovered from Hole 9023E were divided into 13 lithological units as follows;

Unit 1 (125.0–125.135 mbsf): silicified volcanoclastic rocks

Unit 2 (135.0–135.18 mbsf): silicified volcanoclastic rocks

Unit 3 (135.18–135.335 mbsf): silicified volcanoclastic rocks

Unit 4 (144.0–144.41 mbsf): silicified volcanoclastic rocks

Unit 5 (153.50–153.935 mbsf): silicified volcanoclastic rocks

Unit 6 (163.0–163.26 mbsf): silicified volcanic breccia

Unit 7 (163.26–163.545 mbsf): silicified volcanoclastic rocks

Unit 8 (172.50–172.74 mbsf): silicified volcanoclastic rocks

Unit 9 (172.74–172.77 mbsf): silicified volcanoclastic rocks

Unit 10 (172.77–172.86 mbsf): hydrothermal clay

Unit 11 (189.50–189.595 mbsf): silicified volcanoclastic rocks

Unit 12 (199.0–199.94 mbsf): silicified volcanoclastic rocks

Unit 13 (199.94–200.24 mbsf): silicified volcanoclastic rocks

Lithological summary of Hole C9023E are shown in Fig.5-1-5-5. Generally, core

samples recovered from Hole C9023E were greenish silicified volcanic rocks (including crushed/grinded silicified rock samples, by drilling). These rocks could also be 'tuffaceous', but confirmation remains for further on-land detailed examination. Recovery rate of Hole C9023E was very low due to combination of bedrock condition and coring method (ESCS). Therefore, in a similar manner to the Hole C9023D, we carefully sectioned units. Almost all samples were recovered from Core Catcher (CC) (except for 5X-01, 9X-01) and were strongly disturbed (compacted) by drilling, especially at the lower part of each section.

Unit 1 consists of pale green to light greenish gray silicified volcanoclastic rocks. Thin lamination (or gneissose) texture was characteristically observed in this section. Lenticular and/or granule quartz, thin (~1 mm) sulfide vein, and small greenish spots (aggregate of sulfide and greenish mineral) were also observed. XRD analysis shows that the main constituent minerals are quartz, K-feldspar, illite/muscovite and chlorite. Unit 2 shows similar lithology to Unit 1.

Unit 3 is described as drilling disturbed mixture of compacted fragments containing sulfide minerals. In particular interval from 135.21 mbsf to 135.25 mbsf exhibits greenish gray color and has many black clots (~3 mm) of sulfides (sphalerite and chalcopyrite) aggregate. Peaks of sphalerite, chlorite, pyrite and chalcopyrite were confirmed by XRD analysis of the sulfide-rich portion (black colored portion). The rock fragments (altered volcanogenic rocks) show no lamination texture. In addition, massive and highly altered whitish green to light green volcanoclastic rocks were observed in this unit.

Unit 4 is greenish gray silicified volcanoclastic breccia with fine-grained pyrite. Silicification is weaker than Unit 2. From 144.23 mbsf to 144.26 mbsf, whitish spherical aggregate of anhydrite (~6 mm) were observed (Fig.5-1-5-6). This interval roughly corresponds to a temperature anomaly below the high resistivity zone observed by LWD.

Unit 5 consists of light greenish volcanoclastic rocks with fine-grained pyrite (~1.0 mm) and clots of anhydrite (~1.0 cm). Fracture filling anhydrite and vein-style sulfide mineralization was observed.

Unit 6 was light greenish gray volcanoclastic fragments with anhydrite/sulfide network/stockwork veins (Fig.5-1-5-7). Anhydrite, chlorite, illite/muscovite and pyrite

are detected in XRD analysis. Lithology of Unit 7 is similar to that of Unit 6. However, the amount of fracture filling anhydrite decreases significantly, and the silicification degree of the rock fragments in the lower part of this unit is higher than that of the Unit 6.

Unit 8 consists of light gray to light greenish gray silicified volcanoclastic rocks with thin (~1.0 mm) quartz/sulfide veins, clots of quartz and pyrite, and the aggregation of quartz, sulfide and greenish material filling vesicles of the rock fragments. In XRD analysis, chlorite and illite/muscovite were detected. The lithology of Unit 9 was essentially similar to that of Unit 8, but the color changes to greenish gray.

Unit 10 consists of hydrothermal clay (possibly drilling derived clay) containing small (~5 mm) light greenish gray rock fragments.

Unit 11 was light gray to gray highly silicified volcanoclastic breccia. Thin (~1.0 mm) sulfide veins and whitish quartz-rich irregular shaped veins were observed. This interval roughly corresponds to the high resistivity zone at ~185 mbsf observed by LWD. XRD analysis of the rock fragment shows that the constituent minerals are quartz, K-feldspar and pyrite.

The lithology of Unit 12 was light greenish gray silicified volcanoclastic rocks with whitish quartz/muscovite veins (~3.0 mm). Gray quartz and pyrite veins (~1.0 mm) were also observed. The silicification degree of this unit is weaker than that of Unit 11. Quartz, illite/muscovite and chlorite were detected in XRD analysis.

The deepest lithological unit (Unit 13) was a pale greenish light gray drilling disturbed mixture of compacted clayey fragments with greenish silicified fragments. Drilling derived laminated texture was observed in the lowest part of this unit.

5.1.6 SEM observation

T. Nagase

Hole C9017C

Sample ID : C9017C-1X-1-1.5-1.6

Aggregate of pyrite spherules occurred from silicified volcanoclastic rock. The surface of the spherule exhibits framboidal-like texture consisting of small pyrite crystals with 50-150 μm in size (Fig.5-1-6-1). Pyrrhotite, which shows a tabular hexagon form, covers on the pyrite crystals (Fig.5-1-6-2). The size of pyrrhotite crystal is 10-20 μm .

Sample ID: C9017C-9H-3-97-98

Surface texture of wairakeite spherule occurred from hydrothermal sand. The spherules consist of aggregate of wairakeite crystals with 100 μm -1mm in size (Fig.5-1-6-3). The surface of wairakeite is covered by muscovite (sericite) and other minerals, and some crystals show hopper habit. Muscovite exhibits an euhedral crystal form of hexagonal platy with 1-2 μm in width (Fig.5-1-6-4).

Sample ID: C9017C-10H-01-21-22

Surface texture of wairakeite spherule occurred from gray-light gray/dark greenish gray to greenish gray colored hydrothermal grit. The surface was covered by clay minerals with an irregular form (Fig.5-1-6-5). At local, anorthite crystals cover on the surface (Fig.5-1-6-6).

Hole C9019B

Sample ID: C9019B-1H-CC-10-10.5

Anhydrite crystal occurred from dark gray altered volcanic clast (Fig.5-1-6-7). The crystal shows an euhedral form.

Hole C9021B

Sample ID: C9021B-6H-08-102-102.5

Pyrite spherule (framboidal pyrite) from gray-colored volcanoclastic (pumiceous) gravel (Fig.5-1-6-8). The spherules were found out in void space of pumice. The size is 10-50 μm in diameter, and fine crystals within the spherule are several μm in width. The crystal form shows irregular octahedral forms.

Hole C9023D

Sample ID: C9023D-1X-2-8-9

Sulfide and sulfate aggregate occurred from gray colored sulfidic sand with pumiceous fragment. The aggregate consists of sphalerite, chalcopyrite, galena, pyrite and anhydrite. Sphalerite shows a euhedral form with 0.5-1mm in size (Fig.5-1-6-9).

Sample ID: C9023D-5H-02-40-41

Sulfide and sulfate aggregate occurred from sulfidic sand and sulfate-sulfide gravel. The aggregate consists of sphalerite, chalcopyrite, galena, pyrite and anhydrite. Coarse grains of pyrite show cubic form with 1mm in width. Wurtzite and sphalerite show various form hexagon pyramidal stacking of plate, tetragon and irregular octahedron (Figs.5-1-6-10 and -11). All crystals show euhedral form.

References:

- Expedition 331 Scientists, 2011. Expedition 331 methods. In Takai, K., Mottl, M.J., Nielsen, S.H., and the Expedition 331 Scientists, Proc. IODP, 331: Tokyo (Integrated Ocean Drilling Program Management International, Inc.). doi:10.2204/iodp.proc.331.102.2011
- Mazzullo, J., and Graham, A.G. (Eds.), 1988. Handbook for shipboard sedimentologists. ODP Tech. Note, 8. doi:10.2973/odp.tn.8.1988
- Oyama, M. and Takehara, H. (Eds.), 1967. *Revised Standard Soil Color Charts*. Fijihira Industry Co.,LTD., 20p.

Captions:

Table 5-1-1-1: Styles of sulfide mineralization.

Fig. 5-1-1-1: Graphic patterns used on visual core descriptions.

Fig. 5-1-2-1: Downhole lithological variation and unit division of Hole C9017C. The second blue-gray column exhibits total penetration (blue + gray) and recovered interval (blue) throughout the Hole. Depth scale is meter below seafloor (mbsf).

Fig. 5-1-2-2: Close-up photograph of sample from Hole C9019C, Unit 1 (C9019C_01X-CC_25.5–34.5 cm). Representative lithology of Unit 1.

Fig. 5-1-2-3: Close-up photograph of sample from Hole C9019C, Unit 7 (C9019C_05H-03_32.0–50.0 cm). Representative portion of patchy alteration.

Fig. 5-1-2-4: Close-up photograph of sample from Hole C9019C, Unit 8 (C9019C_07H-08_10.0–28.0 cm). Representative occurrence of spherical aggregates of wairakite.

Fig. 5-1-2-5: Close-up photograph of sample from Hole C9019C, Unit 8 (C9019C_07H-05_1.0–16.0 cm). Patchy portions show vesicular volcanic texture and outer shape of the clasts are obscured.

Fig. 5-1-2-6: Close-up photograph of sample from Hole C9019C, Unit 9 (C9019C_09H-02_49.0–63.0 cm). Boundary between loose matrix and consolidated matrix portions in Unit 9. Large spherical aggregates of wairakite were observed.

Fig. 5-1-2-7: Close-up photograph of sample from Hole C9019C, Unit 9 (C9019C_09H-07_23.0–45.0 cm). The alteration rim suggests fluid percolation, indicative of the pathway of fluids in Unit 9.

Fig. 5-1-2-8: Close-up photograph of sample from Hole C9019C, Unit 11 (C9019C_10H-02_0.0–13.0 cm). Sulfide-rich portion. Pyrite and pyrrhotite were confirmed by VCD and XRD.

Fig. 5-1-2-9: Order of lithological appearance from Unit 13 to Unit 24. Relatively hard, altered volcanic rocks and soft, altered hydrothermal clay/sand were recovered alternately.

Fig. 5-1-3-1: Downhole lithological variation and unit division of Hole C9019B. CC and mbsf denote core catcher and meters below seafloor. The second blue-gray column exhibits total penetration (blue + gray) and recovered interval (blue) throughout the Hole.

Fig. 5-1-3-2: Close-up photograph of a sample from Hole C9019B, Unit 6 (C9019B_01H-02_11.0–26.0cm). Relatively large yellowish fragments of native sulfur/gypsum in 13.0-15.0 cm and tiny white grains throughout the pictured interval.

Fig. 5-1-3-3: X-CT image, MSCL image and downhole lithological variation and unit division of Hole C9019C.

Fig. 5-1-3-4: Close-up photograph of sample from Hole C9019C, Unit 1 (C9019C_01X-01_10.0–26.0 cm). Tiny reddish brown particles throughout the pictured interval are observed.

Fig. 5-1-3-5: Close-up photograph of a representative sample from Hole C9019C, core catcher (C9019C_01X-CC_19.0–22.5 cm). Fresh, vesicular basaltic rock.

Fig. 5-1-4-1: Downhole lithological variation and unit division of Hole C9021B. The second blue-gray column exhibits total penetration (blue + gray) and recovered interval (blue) throughout the Hole. Depth scale is meter below seafloor (mbsf).

Fig. 5-1-4-2: Comparison of tonal variation of Units in the upper pumiceous gravel sequences, Hole C9021B.

Fig. 5-1-4-3: Typical occurrences of reverse grading in Hole C9021B, Unit 1 (C9021B_02H-05). Three grading units could be identified in this section.

Fig. 5-1-4-4: Close-up photograph of sample from Hole C9021B, Unit 1 (C9021B_03H-05_84.0-100.0 cm). Thin layer of highly altered hydrothermal clay.

Fig. 5-1-4-5: Close-up photograph of sample from Hole C9021B, Unit 2 (C9021B_04H-01_91.0–101.0 cm). Occurrence of patchy brownish stain with diffused outline (showing white dashed lines).

Fig. 5-1-4-6: Close-up photograph of a sample from Hole C9021B, Unit 2 (C9021B_04H-03_18.0–42.0 cm). Brownish, angular pumice fragments coated/stained by Fe-oxide.

Fig. 5-1-4-7: Close-up photograph showing unit boundary between Unit 4 and Unit 5, Hole C9021B (C9021B_05H-04_52.0–100.5 cm).

Fig. 5-1-4-8: Occurrence of fractured large single pumice fragments in Unit 6 (C9021B_06H-03).

Fig. 5-1-4-9: Occurrence of gray to light gray volcanoclastic (tuffaceous) mud, Unit 9 (C9021B_07H-07_0–55.5 cm). Upper and lower borders of the mud layer show greenish rims.

Fig. 5-1-4-10: Comparison of volcanoclastic fragments from Unit 11 to Unit 15. Color of the fragments is roughly similar within each core, and gradually change from shallower to deeper cores.

Fig. 5-1-5-1: Downhole lithological variation and unit division of Hole C9023B. CC and mbsf denote core catcher and m below seafloor. The second blue-gray column exhibits total penetration (blue + gray) and recovered interval (blue) throughout the Hole.

Fig. 5-1-5-2: Downhole lithological variation and unit division of Hole C9023D. CC and mbsf denote core catcher and m below seafloor. The second blue-gray column exhibits total penetration (blue + gray) and recovered interval (blue) throughout the Hole.

Fig. 5-1-5-3: Close-up photograph of a sample from Hole C9023D, Unit 3 (C9023D_02H-03_69.0-94.0 cm). Highly mineralized sulfidic sand observed in the interval 11.475-11.635 mbsf.

Fig. 5-1-5-4: Close-up photograph of sample from Hole C9023D, Unit 7 (C9023D_05H-01_39.0-50.0 cm). Small spherical native sulfur in homogeneous sulfidic sand observed at 31.425 mbsf.

Fig. 5-1-5-5: Downhole lithological variation and unit division of Hole C9023E. CC and mbsf denote core catcher and m below seafloor. The second blue-gray column exhibits total penetration (blue + gray) and recovered interval (blue) throughout the Hole.

Fig. 5-1-5-6: Close-up photograph of sample from Hole C9023E, Unit 4 (C9023E_03X-CC_21.0-28.0 cm). Whitish spherical aggregate of anhydrite (-6 mm) observed in the interval 144.23-144.26 mbsf.

Fig. 5-1-5-7: Close-up photograph of sample from Hole C9023E, Unit 6 (C9023E_05X-01_7.0-13.0 cm). Anhydrite/sulfide network/stockwork veins in light greenish silicified volcanoclastic rocks observed in this unit.

Fig. 5-1-6-1: SEM image of pyrite spherules (C9017C-1X-1-1.5-1.6).

Fig. 5-1-6-2: SEM image of pyrrhotite crystals on pyrite spherule (C9017C-1X-1-1.5-1.6).

Fig. 5-1-6-3: SEM image of surface texture of wairakeite spherule (C9017C-9H-3-97-98).

Fig. 5-1-6-4: SEM image of muscovite crystals on wairakeite crystal surface (C9017C-9H-3-97-98).

Fig. 5-1-6-5: SEM image of wairakeite crystal surface (C9017C-10H-01-21-22).

Fig. 5-1-6-6: SEM image of anorthite crystals cover on wairakeite spherule (C9017C-10H-01-21-22).

Fig. 5-1-6-7: SEM image of anhydrite crystal (C9019B-1H-CC-10-10.5).

Fig. 5-1-6-8: SEM image of syrite spherule (framboidal pyrite) in pumice (C9021B-6H-08-102-102.5).

Fig. 5-1-6-9: SEM image of spharelite in sulfide-sulfate sand (C9021B-6H-08-102-102.5).

Fig. 5-1-6-10: SEM image of wurtzite in sulfide-sulfate sand (C9023D-5H-02-40-41).

Fig. 5-1-6-11: SEM image of sphalerite in sulfide-sulfate sand (C9023D-5H-02-40-41).

Table 5-1-1-1 Styles of sulfide mineralization

Style of alteration	Diagnostic features
Massive sulfide	Rocks containing >75% sulfide minerals.
Semimassive sulfide	Rocks containing >25%–75% sulfide minerals, which form aggregates or intergrowths.
Disseminated sulfide	Rocks containing 5%–25% disseminated sulfides.
Void fill	Minerals partially or totally filling a void (vesicle, etc.).
Vein/Stringer sulfide	Rocks containing sulfide in fractures.
Detrital sulfide	Clastic sulfide fragments in sediment.

*After Expedition 331 Scientists (2011).

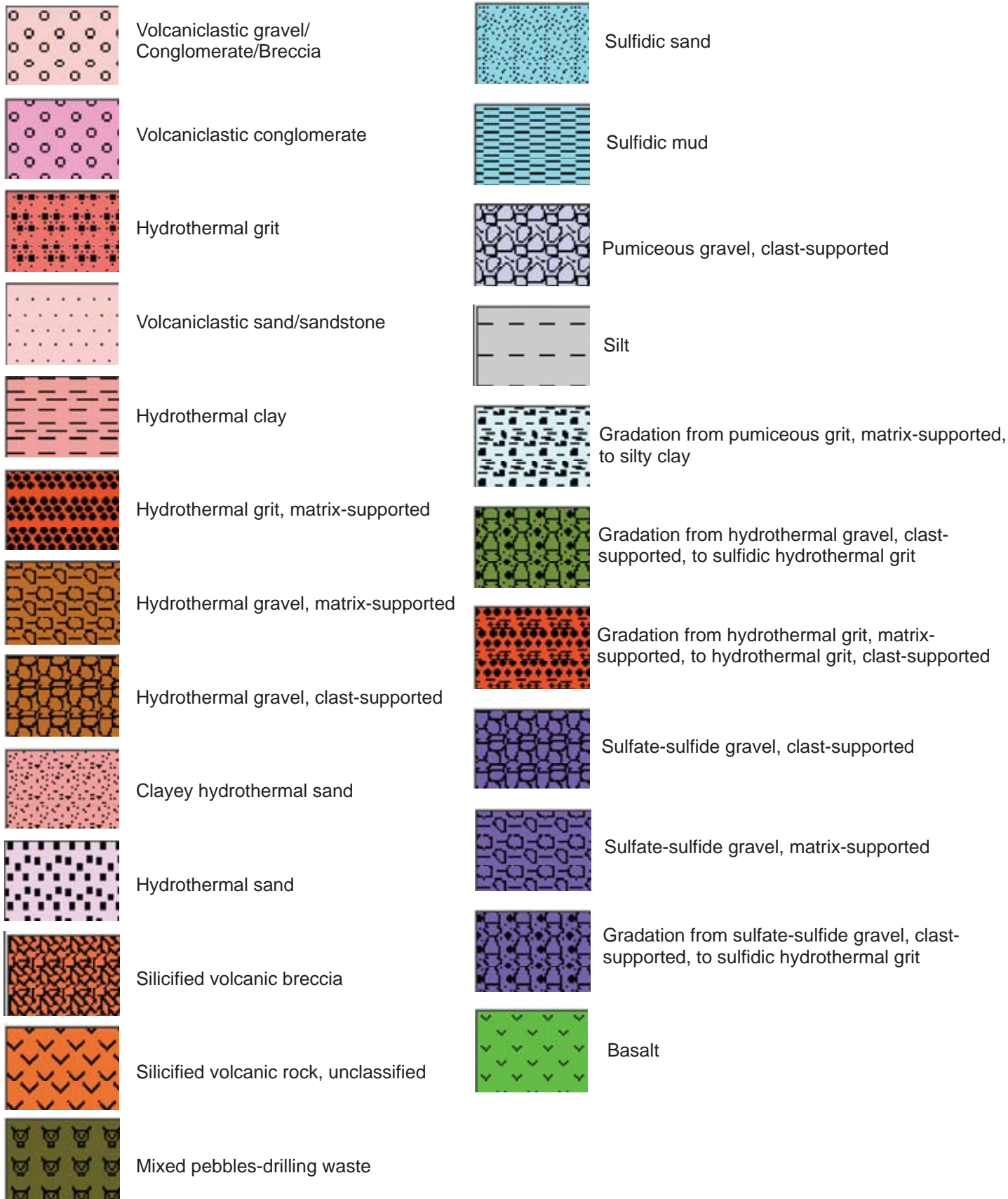


Figure 5-1-1-1

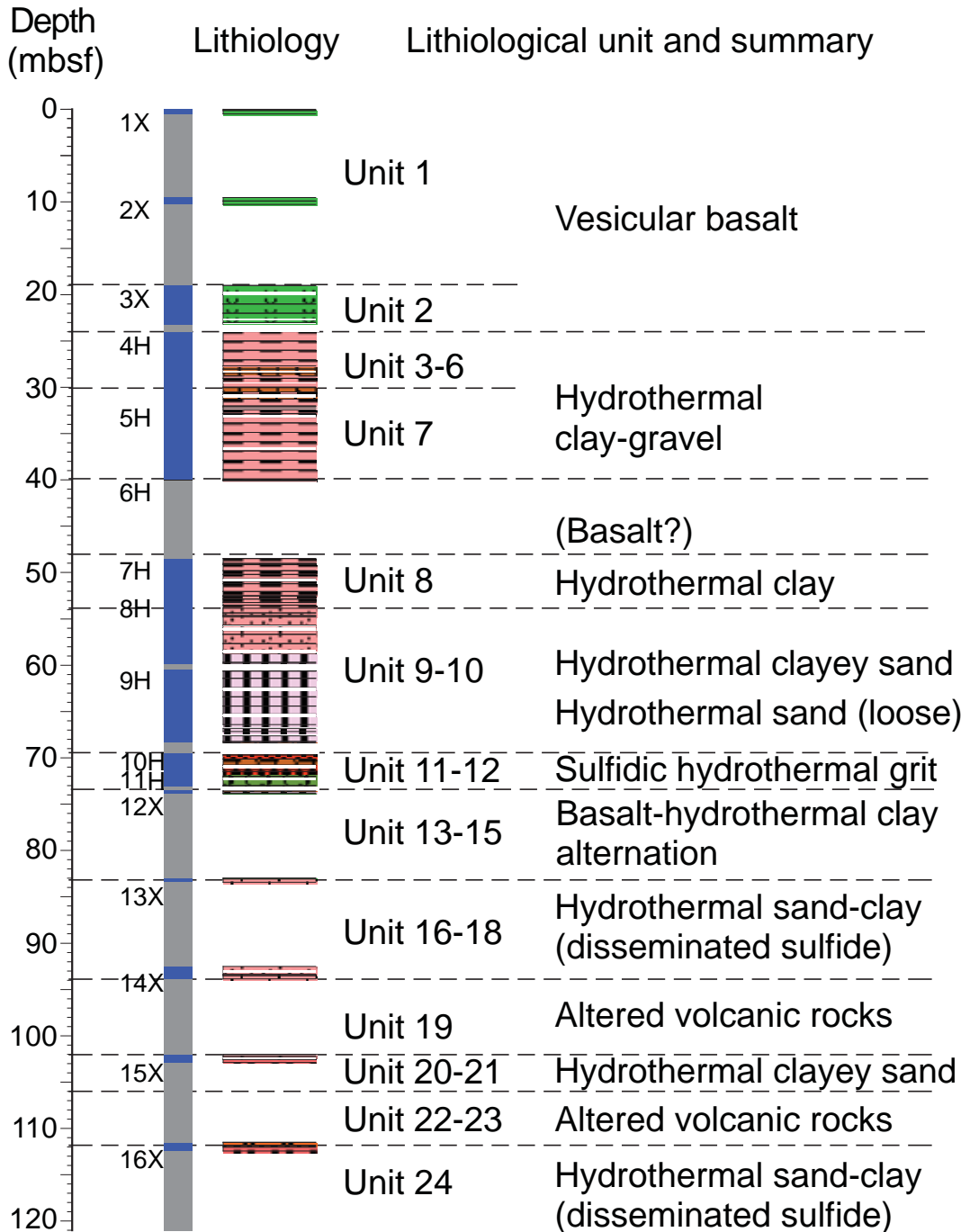


Figure 5-1-2-1



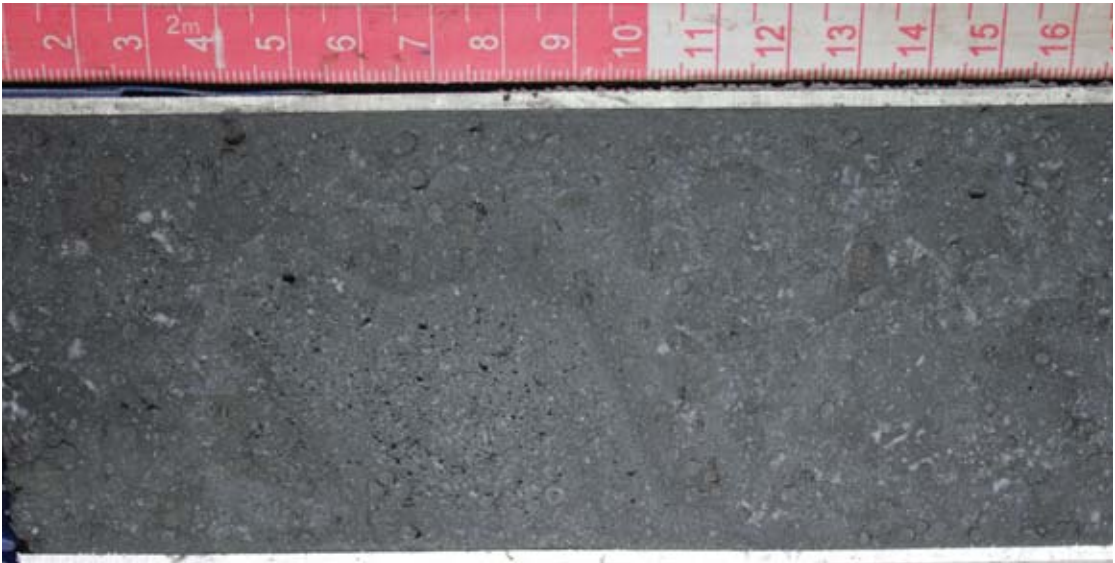
Figure 5-1-2-2_C9017C_01X-CC_26.0-37.0cm



208 Figure 5-1-2-3_5H3_32-60 cm



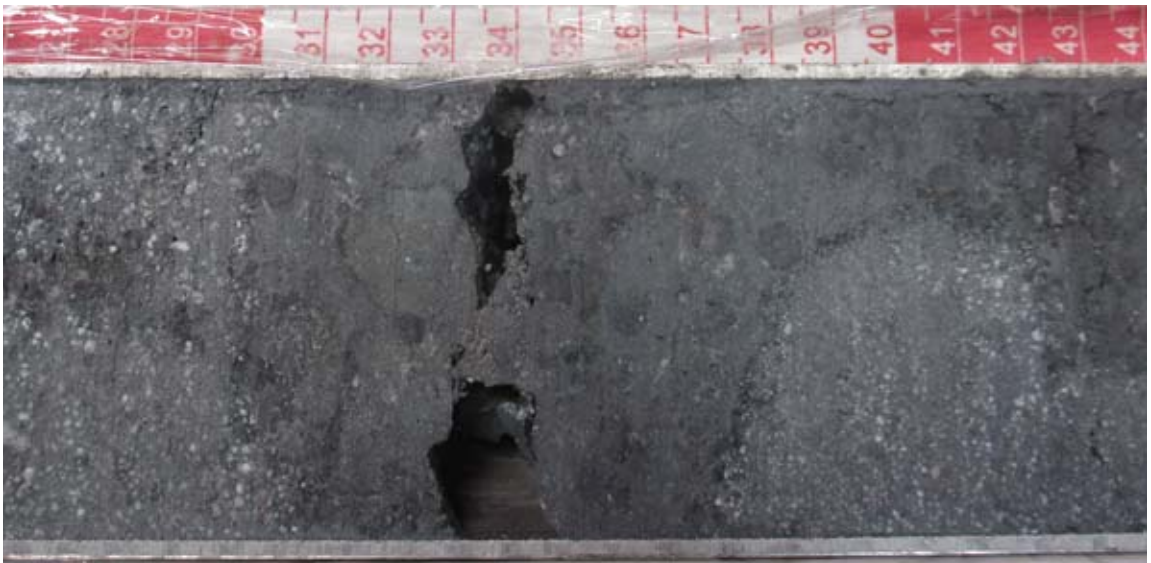
Figure 5-1-2-4_07H08_10-28



210 Figure 5-1-2-5_7H5_1.0-16.0cm



211 Figure 5-1-2-6_9H2_46-65



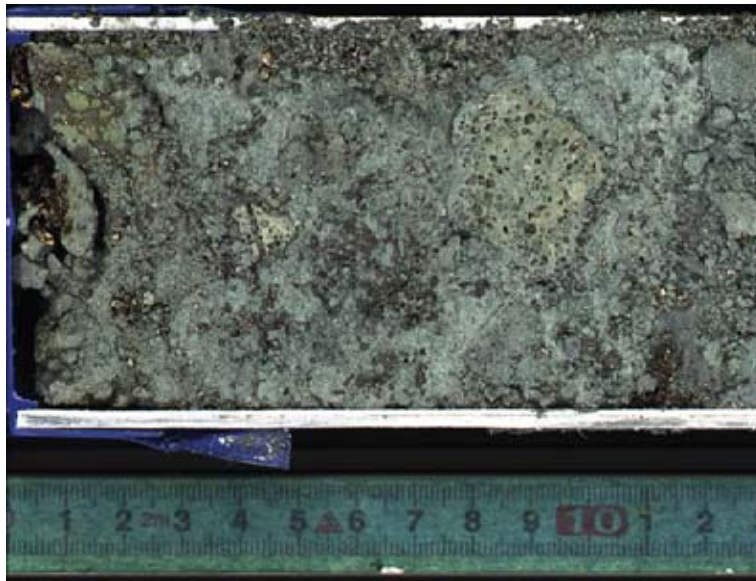


Figure 5-1-2-8-10H-2

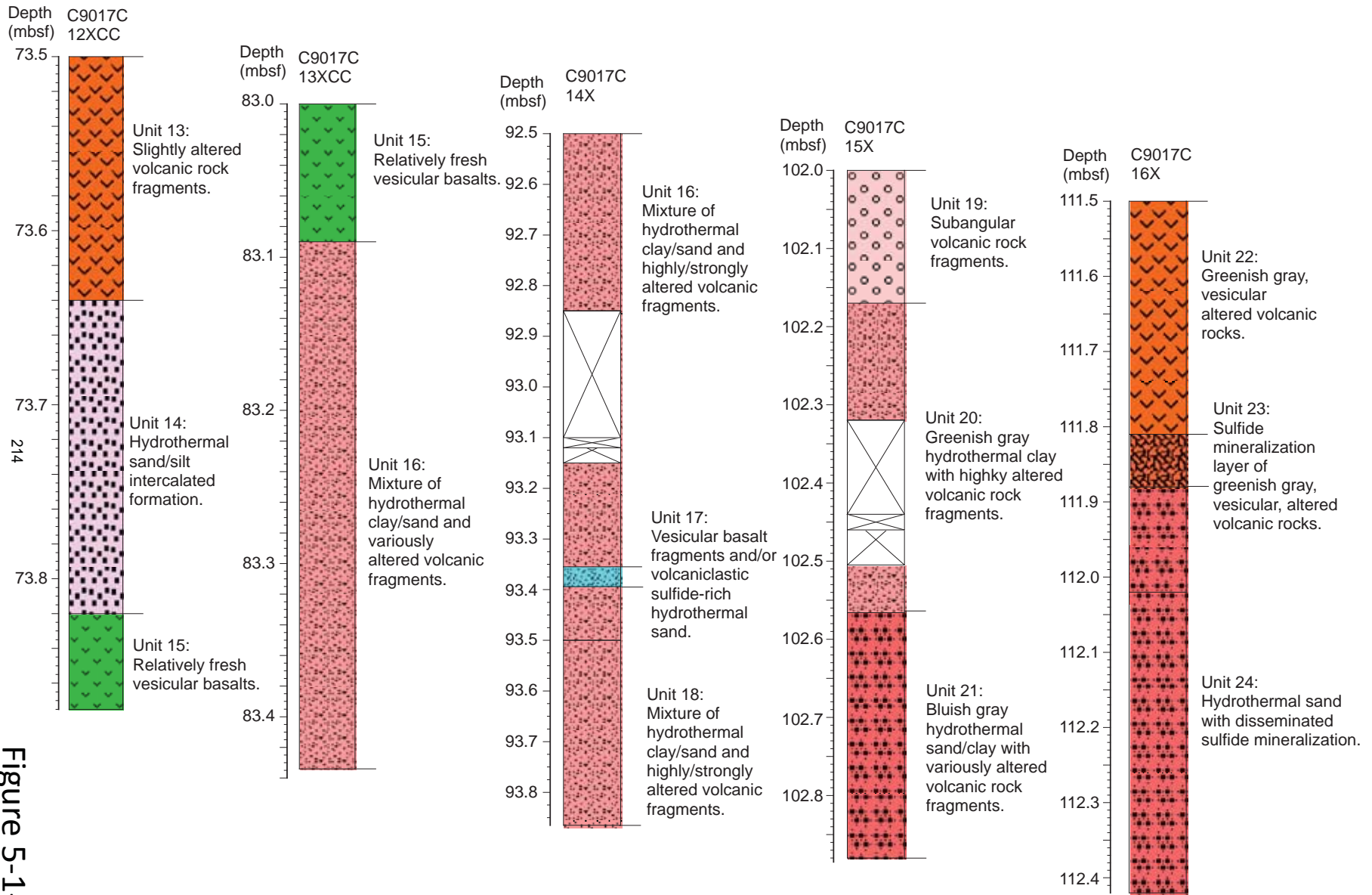


Figure 5-1-2-9

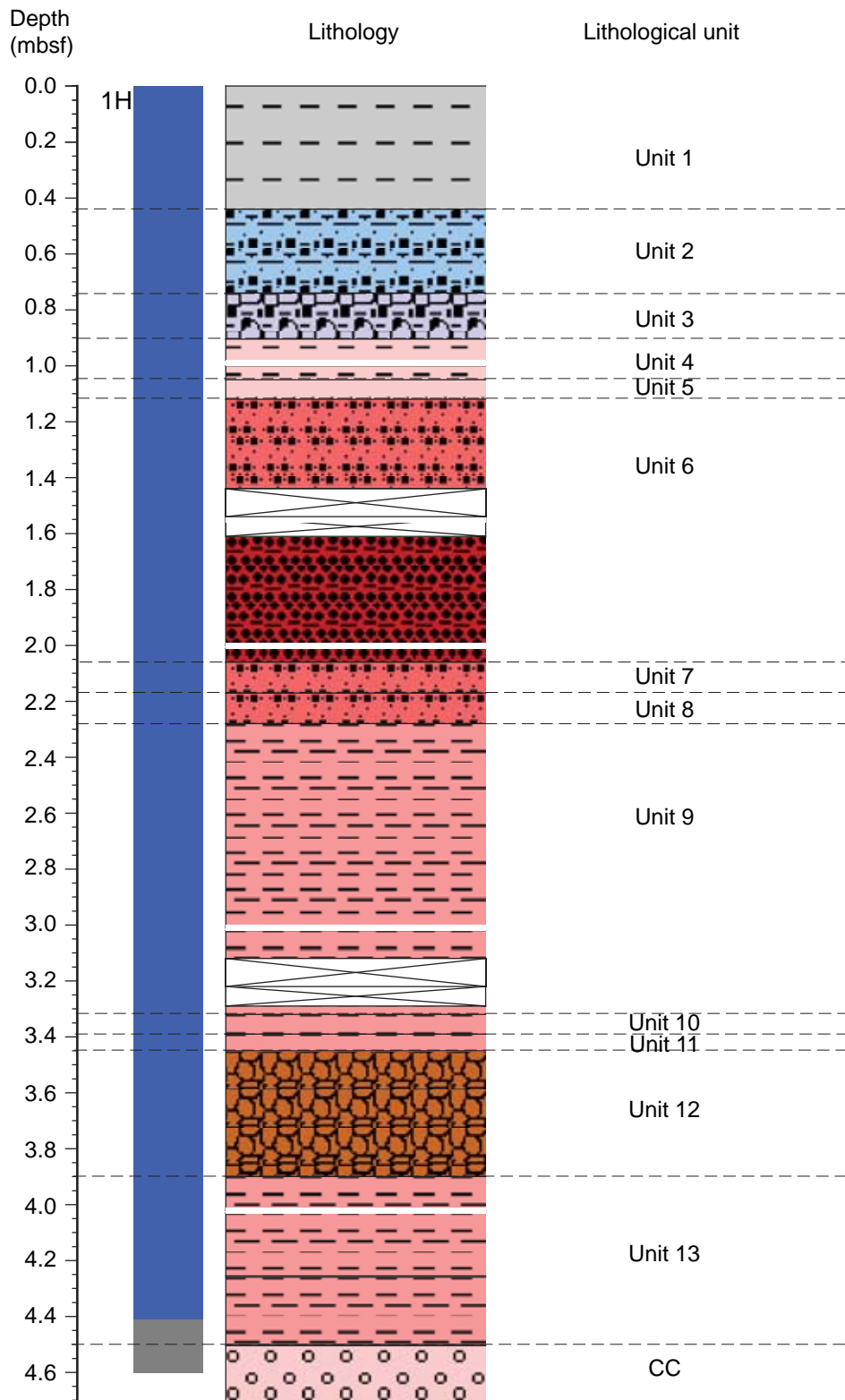




Figure 5-1-3-2_C9019B_01H-02_11.0-26.0cm

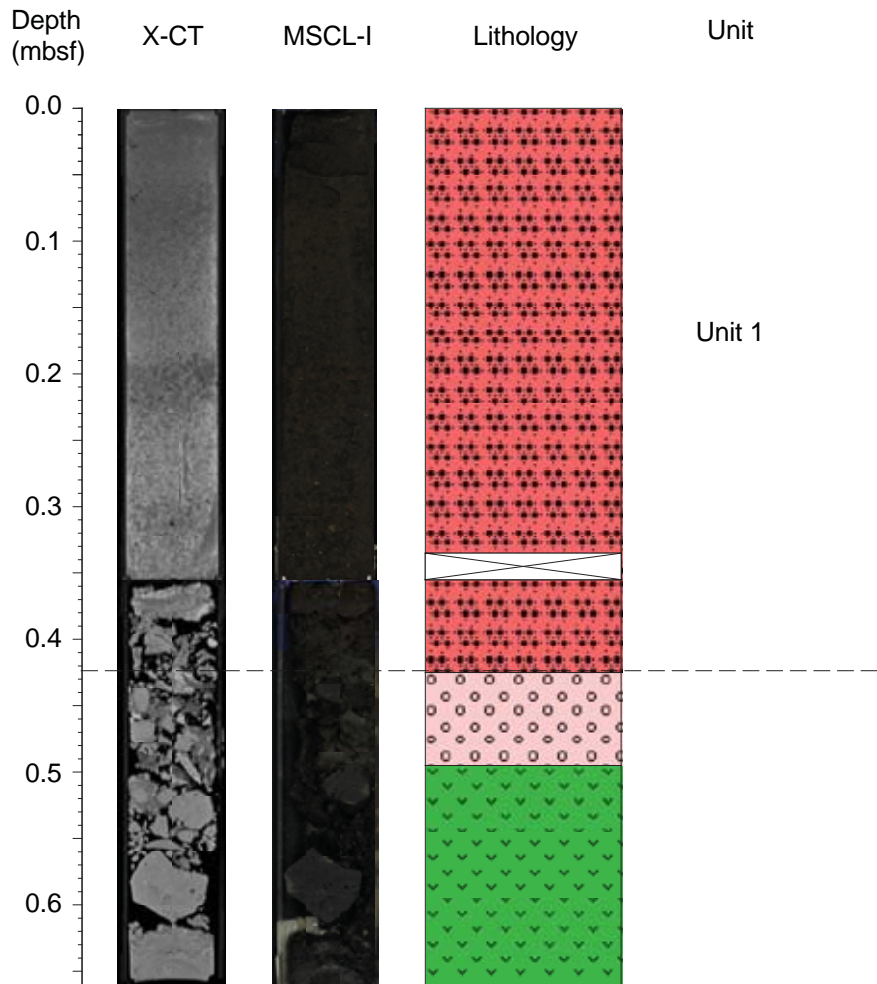




Figure 5-1-3-4_C9019C_01X-01_11.0-26.0cm



Figure 5-1-3-5_C9019C-1X-CC_A_19.0-25.5 cm

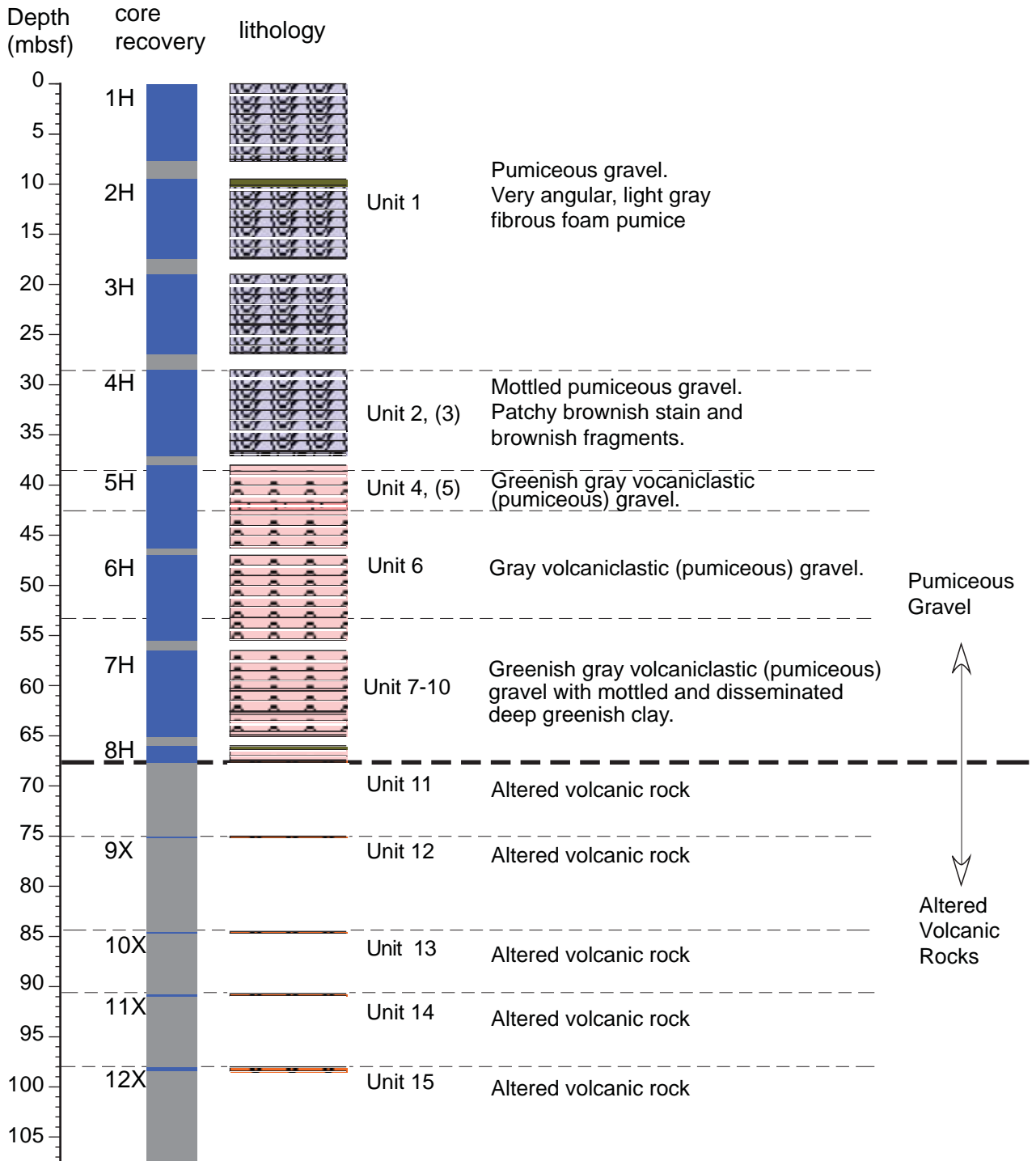


Figure 5-1-4-1

Unit 1 (2H6)



Unit 2 (4H3)



Unit 4 (5H3)



Unit 6 (5H8)



Unit 7 (7H3)



Unit 10 (7H8)



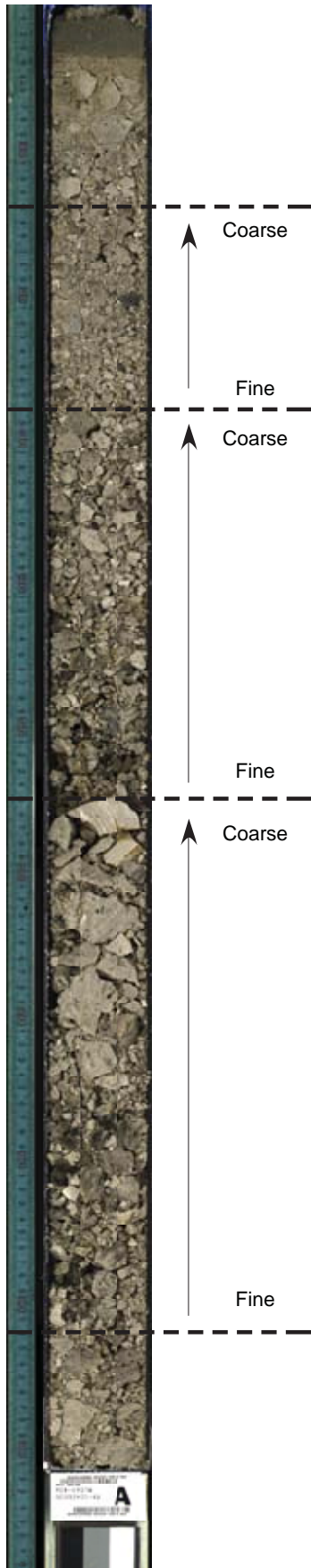




Figure 5-1-4-4_C9021B-3H-5

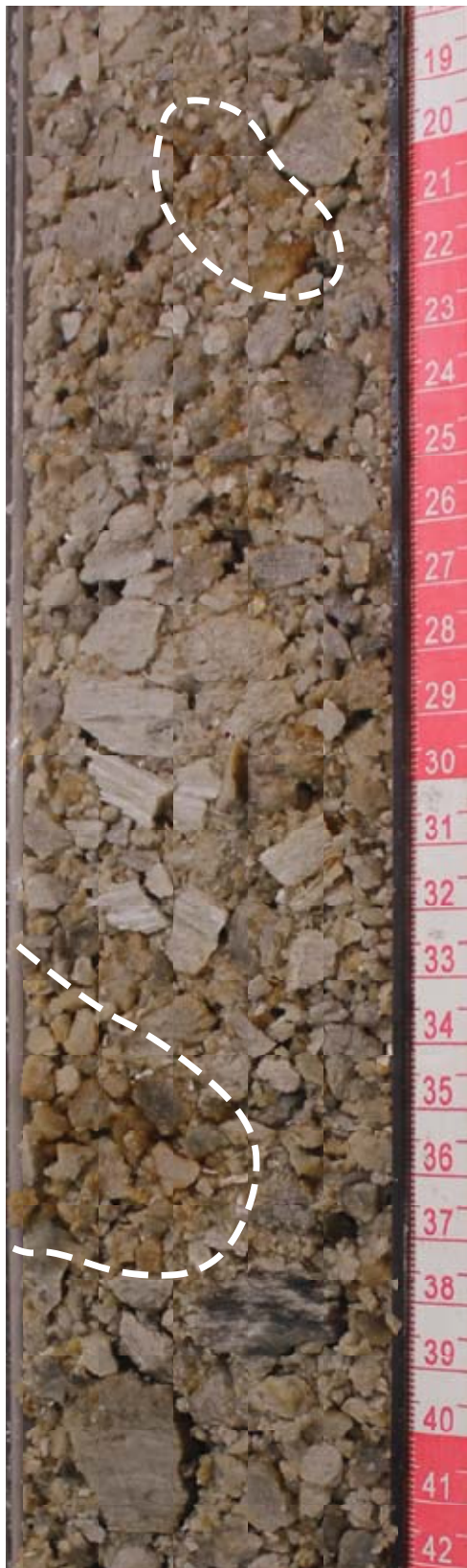


Figure 5-1-4-5

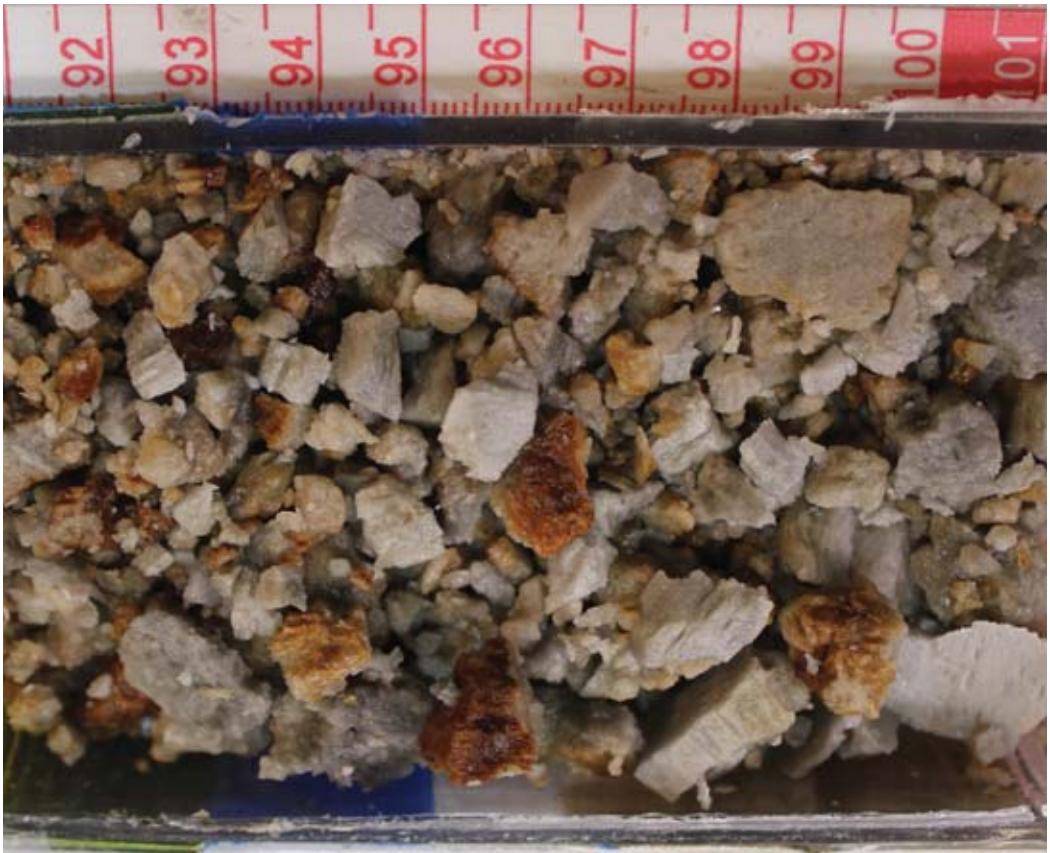
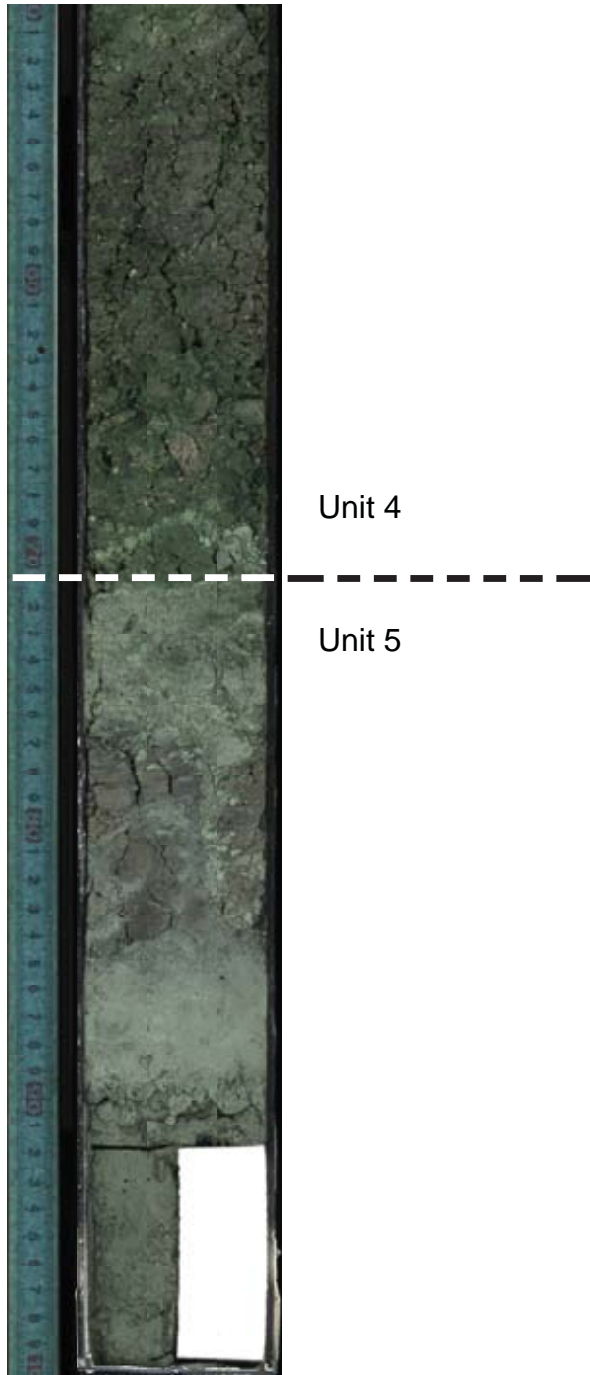


Figure 5-1-4-6_C9021B_04H-01_91.0-101.0



Unit 4

Unit 5

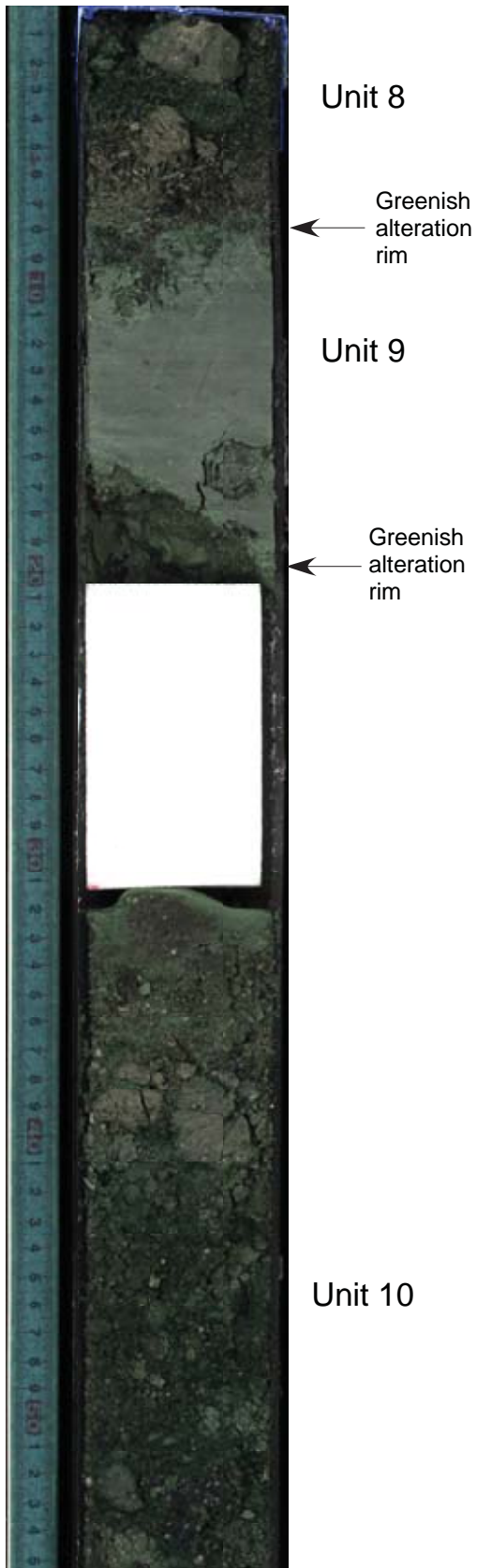


Fractured
single
pumice
fragment(s)

Fractured
single
pumice
fragment

Fractured
single
pumice
fragment

Figure 5-1-4-8_C9021B-6H-3



Unit 8

Greenish alteration rim

Unit 9

Greenish alteration rim

Unit 10

Volcaniclastic fragments

Dark gray



Light gray



Dark khaki gray

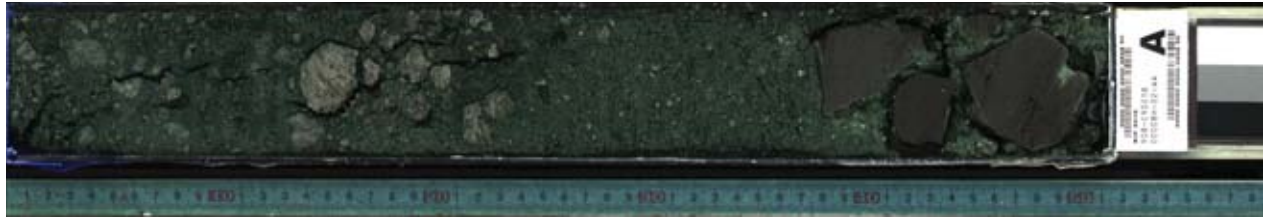


Khaki gray

Unit 10

Unit 11

8H2



9XCC



Unit 12

10XCC



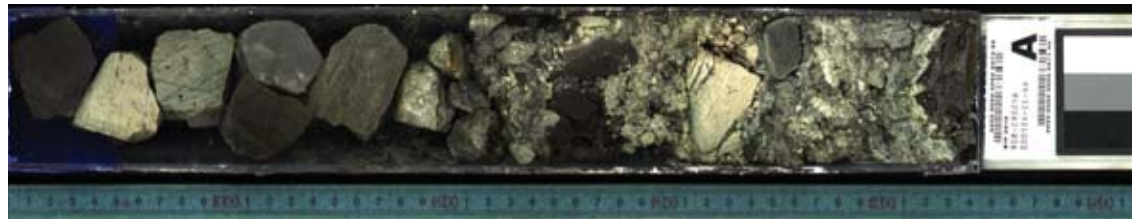
Unit 13

11XCC

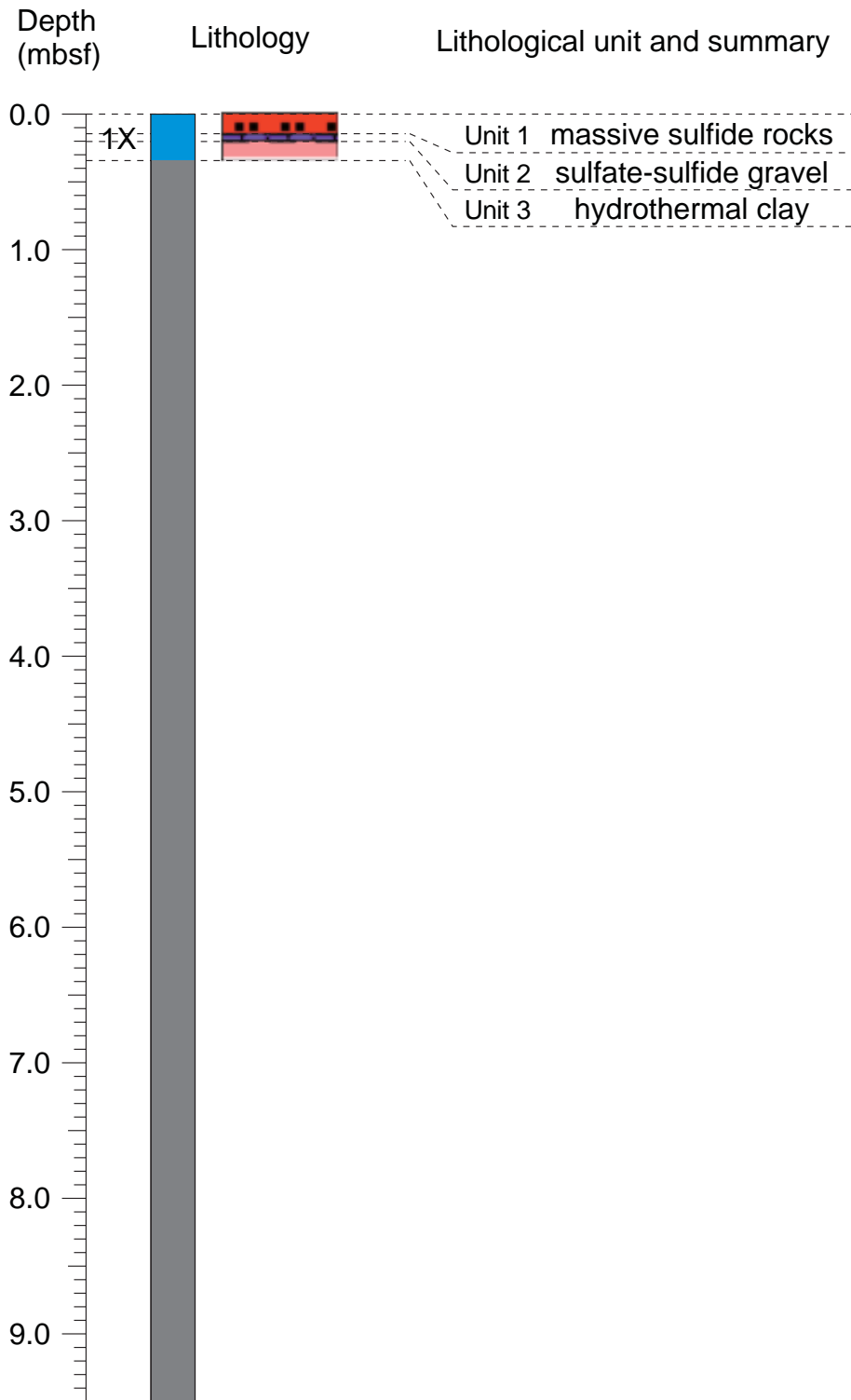


Unit 14

12XCC



Unit 15



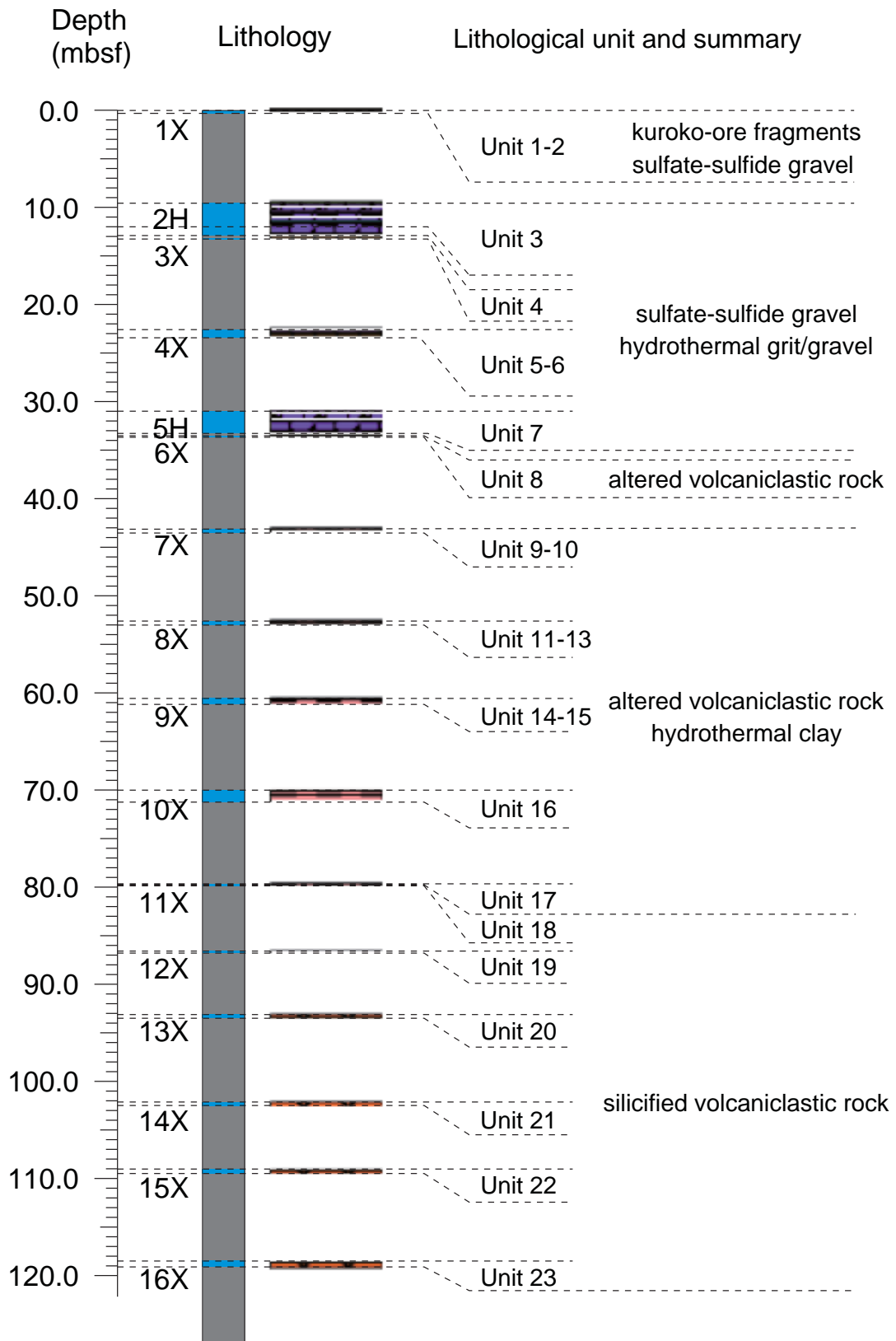




Figure 5-1-5-3_C9023D_2H-03_69-94cm



Figure 5-1-5-4_C9023D_5H-01_39-50cm

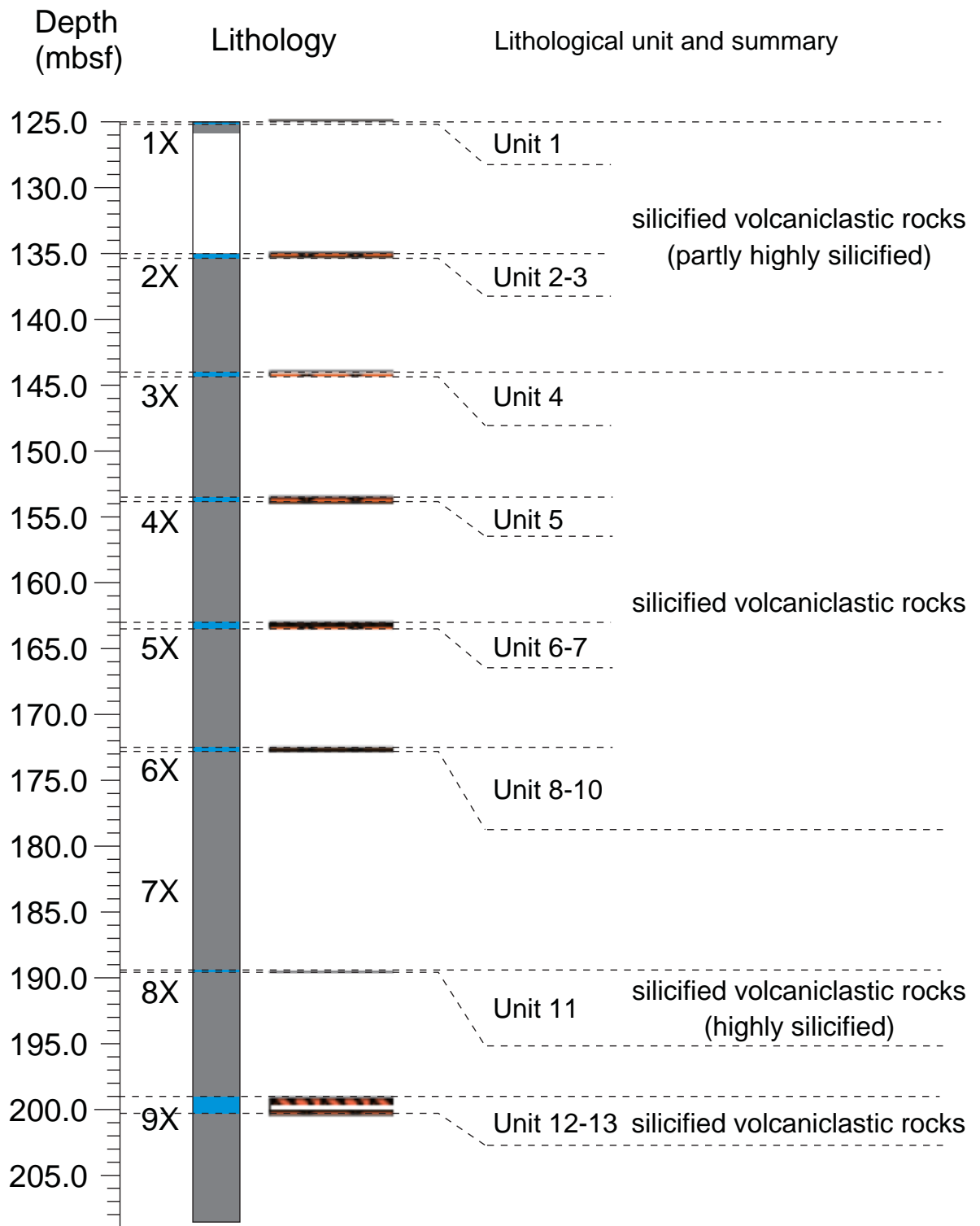


Figure 5-1-5-5



Figure 5-1-5-6_C9023E_3X-CC_21-28cm



Figure 5-1-5-7_C9023E_5X-01_7-13cm

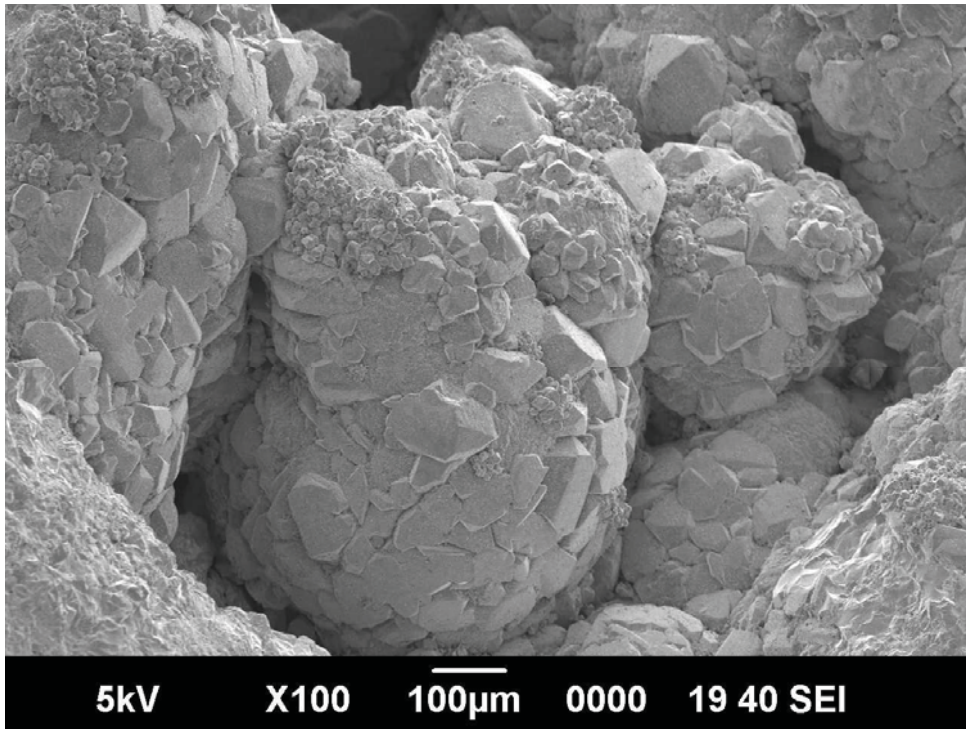


Figure 5-1-6-1

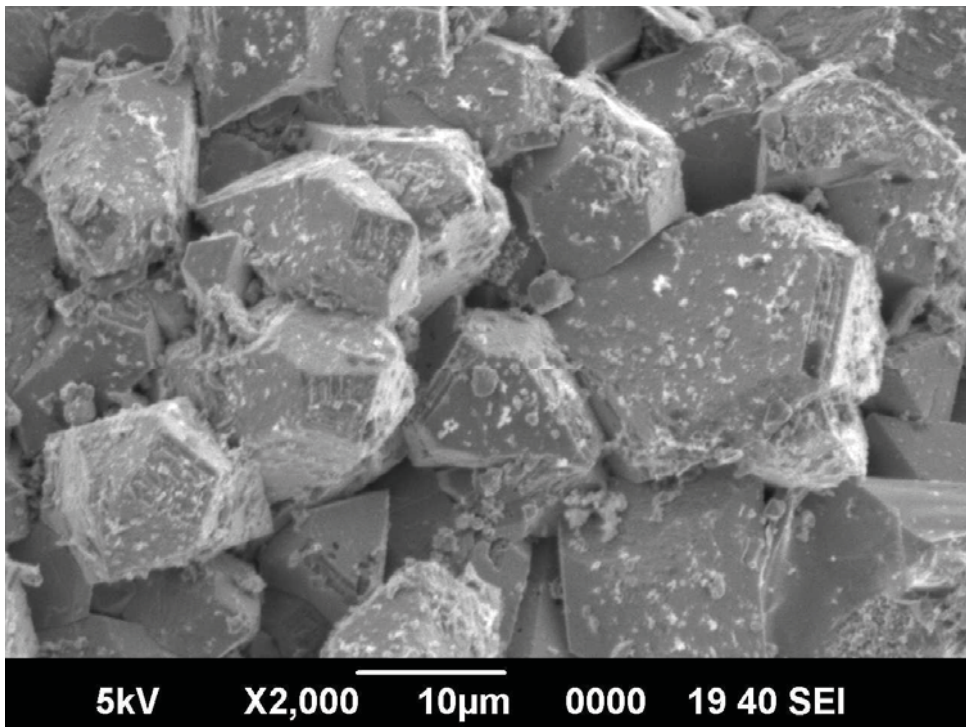


Figure 5-1-6-2

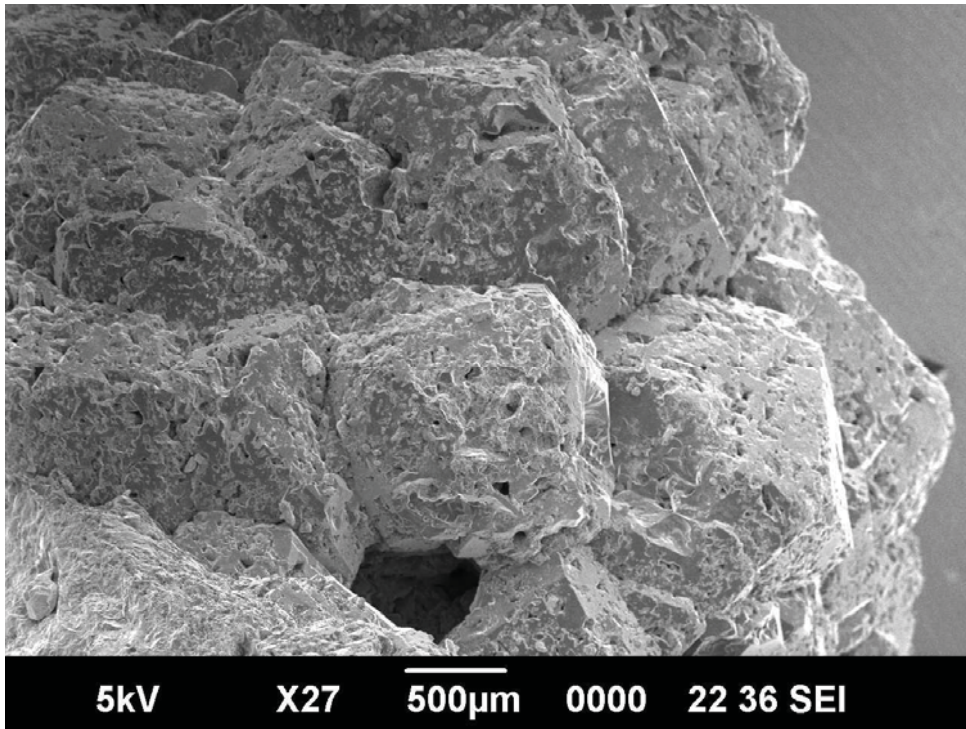


Figure 5-1-6-3

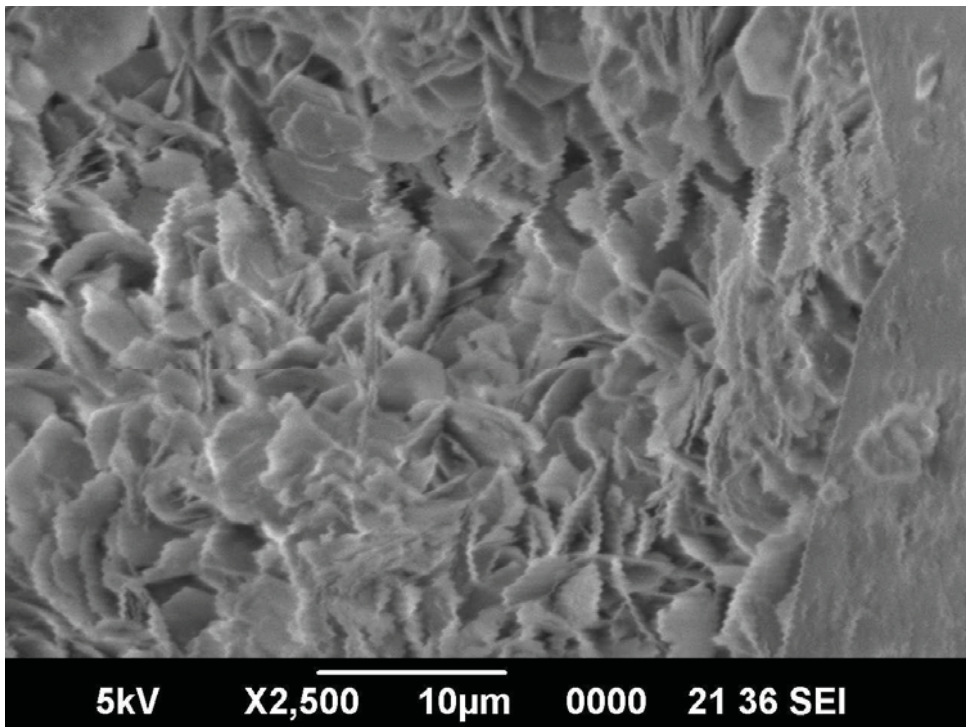


Figure 5-1-6-4

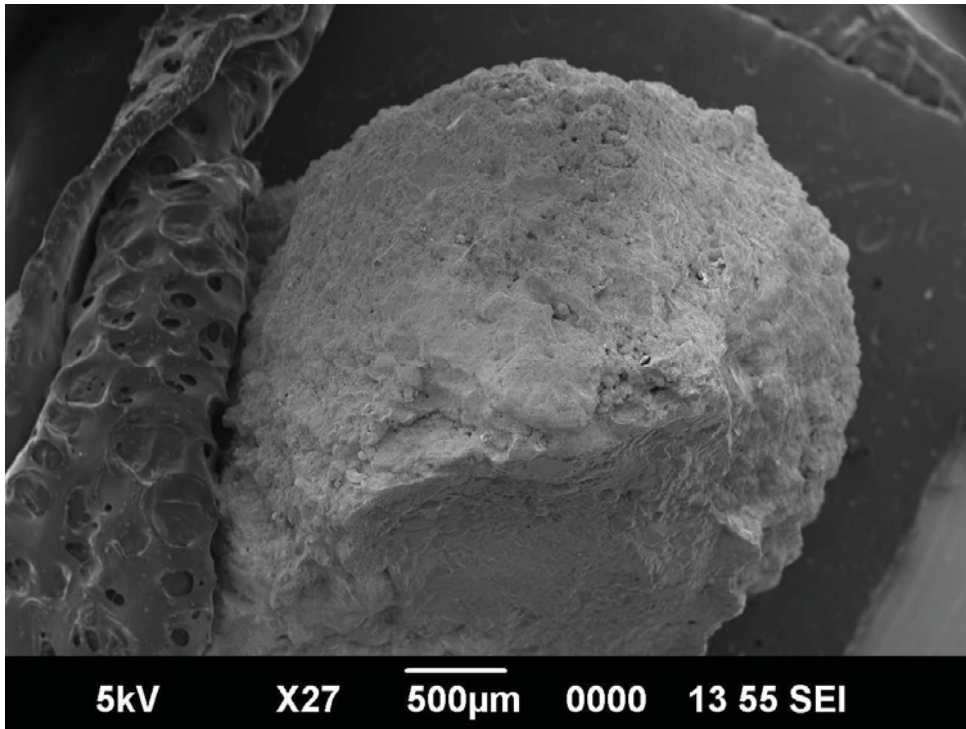


Figure 5-1-6-5

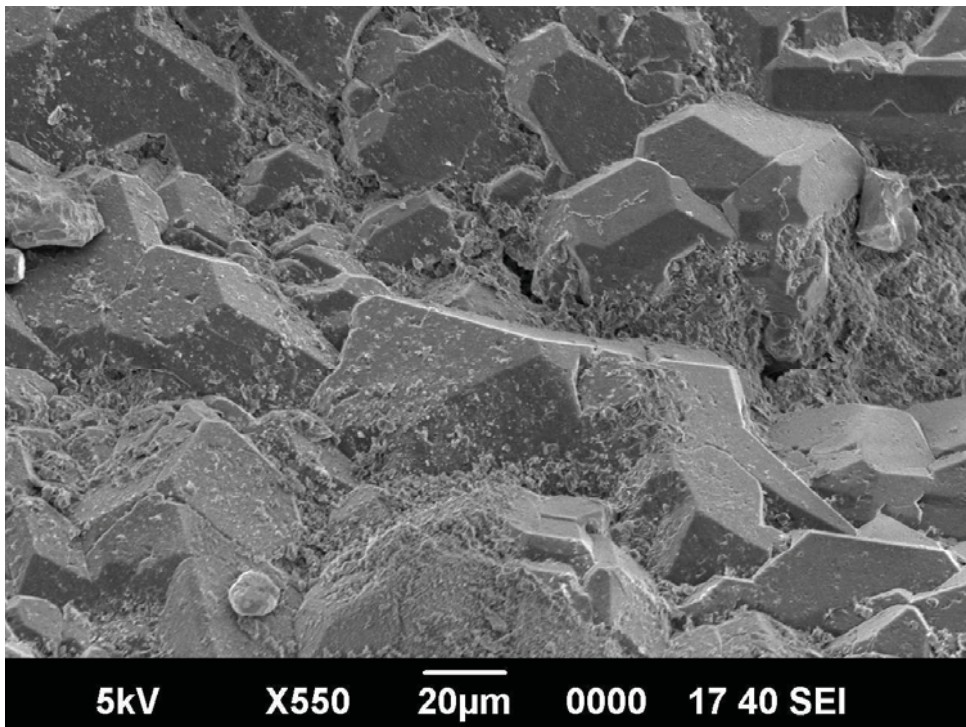


Figure 5-1-6-6

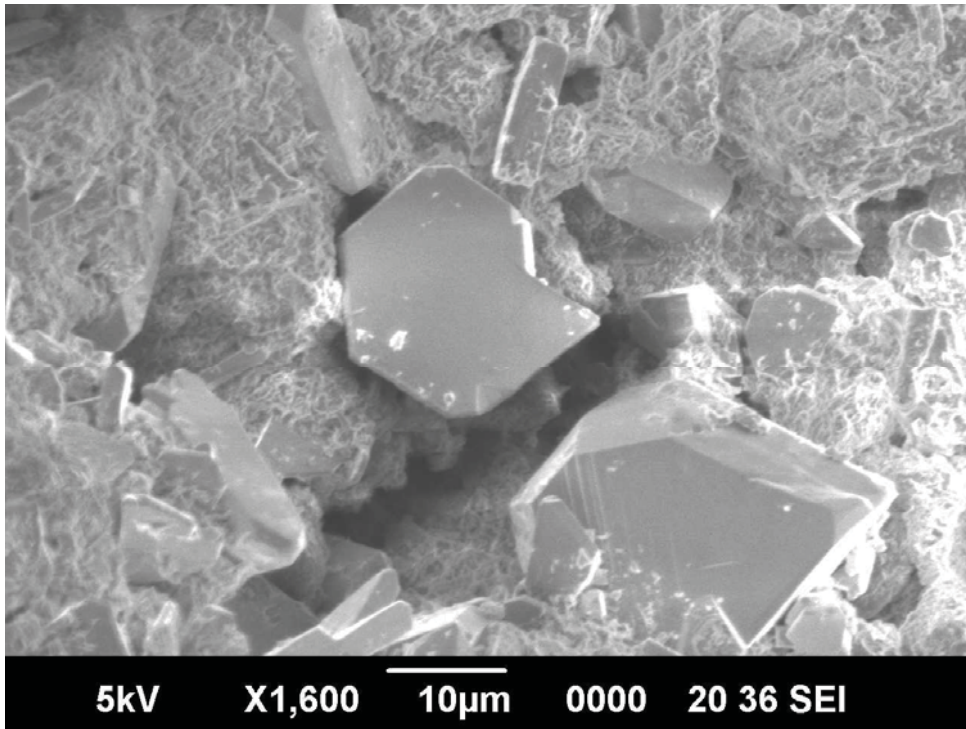


Figure 5-1-6-7

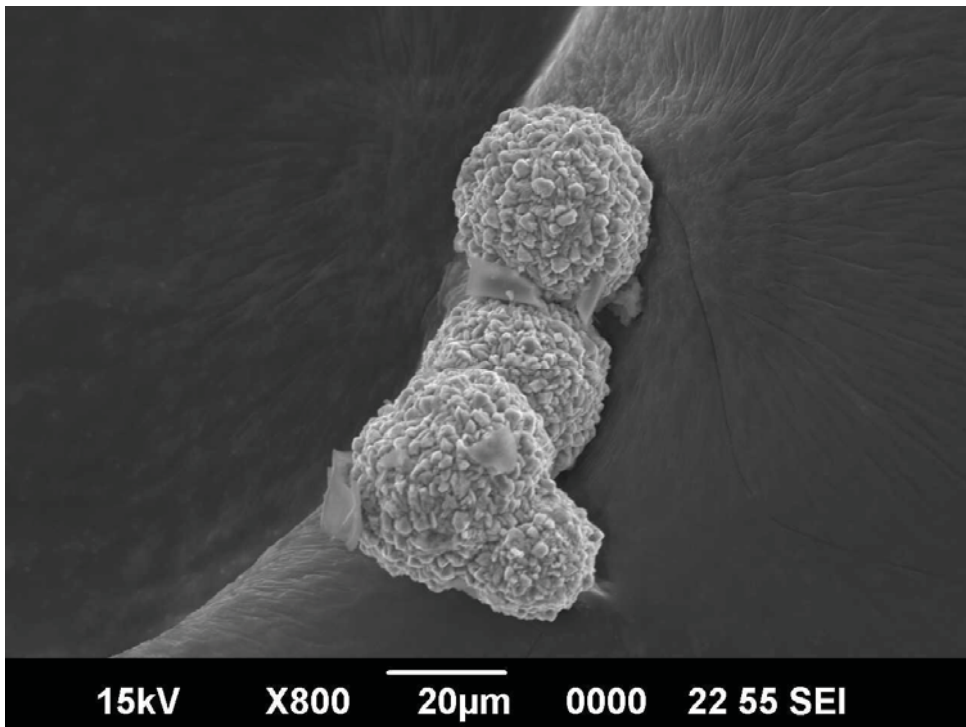


Figure 5-1-6-8

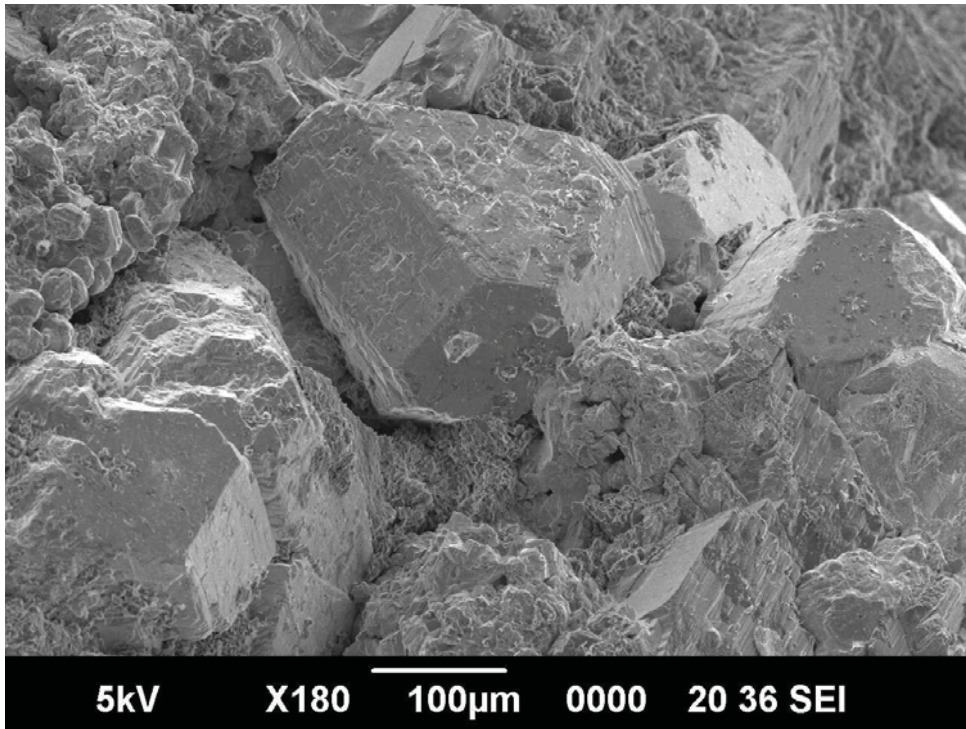


Figure 5-1-6-9

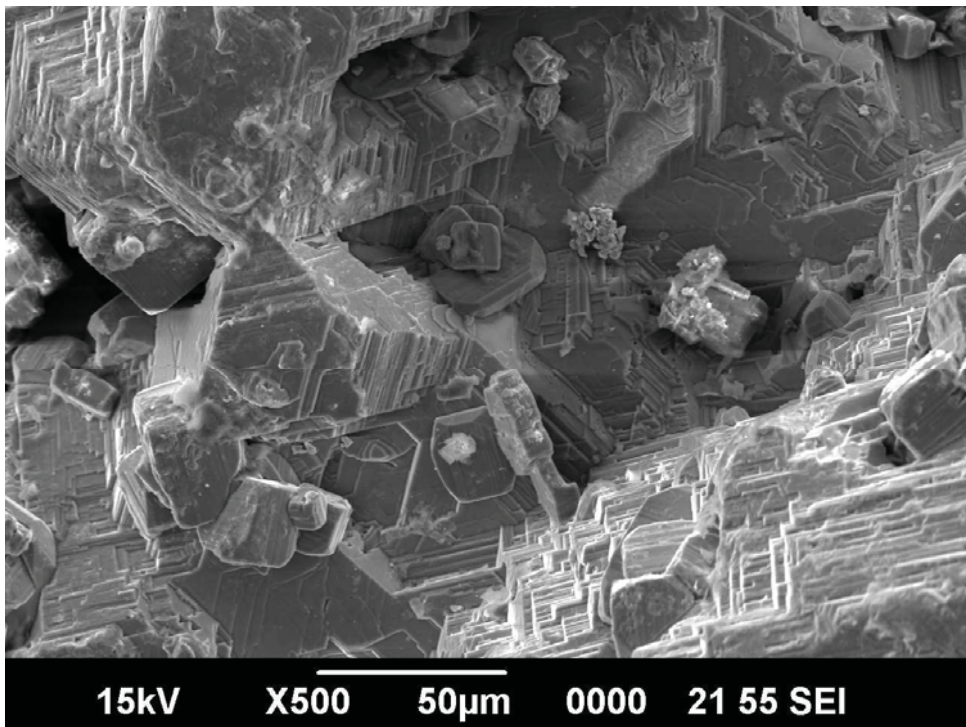


Figure 5-1-6-10

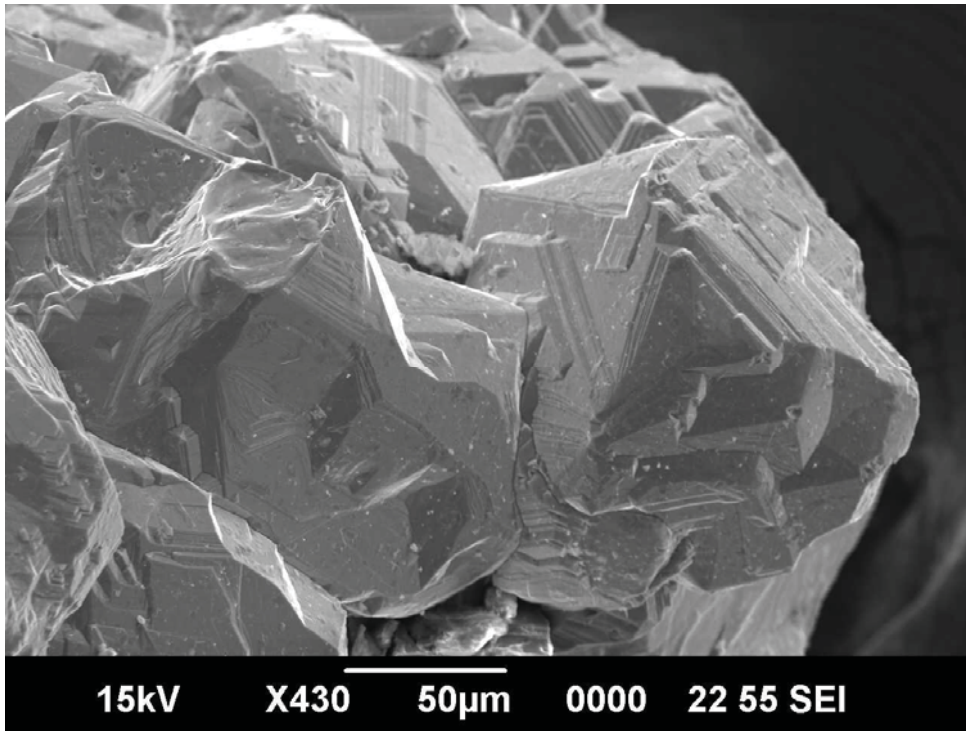


Figure 5-1-6-11

5.2 X-ray computed tomography (XCT) data

Y. Takaya and T. Yamasaki

5.2.1 Method

X-ray computed tomography (XCT) images were used to assist in deciding locations for obtaining whole-round samples and also to provide a guide to core description of which lithologies had been removed by whole-round sampling. We followed the shipboard operation manual prepared by CDEX/Japan Agency for Marine Earth Science and Technology (JAMSTEC), as well as methods used during previous expeditions (e.g., IODP Expeditions 319 and 331, and SIP Expedition 907/CK14-04; Expedition 331 Scientists, 2011). The X-ray CT instrument on the *Chikyu* is a GE Healthcare Discovery CT750HD. Data generated for each core consist of core-axis-normal planes of X-ray attenuation values with dimensions of 512×512 pixels, and generates 0.625 mm thick slice images every 0.5 s (about 1,600 images for 1 m length section). These data was stored as the Digital Imaging and Communication in Medicine (DICOM) formatted files. The brightness of CT images reflects CT number that is a normalized value of the calculated X-ray absorption coefficient of a pixel in a computed program. Thus the images provide information on structure/texture and density (associate with consolidation degree and permeability) of the target material in a qualitative manner. In the Expedition 908/CK16-01, all core sections (190 sections: C9017C; 71 sections, C9019B; 7sections, C9019C; 2 sections, C9021B; 72 sections, C9023B; 1 section, C9023D; 27 sections, C9023E; 10 sections) were scanned by XCT. In this chapter, characteristic features of XCT units were described. In general, uppermost portion of each cores were filled with drilling waste (mixture of fallen rock fragments from above intervals of a hole and in-situ materials), thus those lithologies were not considered in unit classification.

References:

Expedition 331 Scientists, 2011. Expedition 331 methods. In Takai, K., Mottl, M.J., Nielsen, S.H., and the Expedition 331 Scientists, Proc. IODP, 331: Tokyo (Integrated Ocean Drilling Program Management International, Inc.). doi:10.2204/iodp.proc.331.102.2011

5.2.2 Hole C9017C

The lithology of Hole C9017C was divided into 24 units by VCD. In XCT

observation, core samples from C9017C are divided to 6 characteristic XCT units.

The first unit (1X-01–3X-CC; 0.0–24.0 mbsf) is composed of fresh vesicular basalts (porous gray fragments in XCT images) and of crushed/grinded materials of those fragments (homogeneous gray portion in XCT images). The size of the rock fragment decreases with depth. Some light gray layers and/or veins are composed of clay minerals (anhydrite?). The second unit (4X-01–6H-CC; 24.0–48.5 mbsf) consists of hydrothermal clay and some remaining basaltic rock fragments. Light color portions are composed of anhydrite and fine-grained sulfide minerals. In some section, many whitish patches or spots of anhydrite aggregate were characteristically observed (Fig.5-2-2-1). The third unit (7H-01–9H-CC; 48.5–69.5 mbsf) is also composed of hydrothermal clay. In this unit, many spherical aggregates of wairakite were confirmed by VCD/XRD. In XCT image, wairakite aggregates were observed as spherules with slightly lighter color than the surrounding hydrothermal clay (Fig.5-2-2-2). Small white dots were sulfide minerals (mainly pyrite). The fourth unit (10H-01–10H-CC; 69.5–71.0 mbsf) was hydrothermal gravel/grit/clay. This unit shows relatively loose texture. Many black void spaces and many sulfide minerals showed by light colors were also observed in this unit. The color variation of XCT image of the fifth unit (11H-01–11H-CC; 71.0–73.05 mbsf) is similar to the previous unit, but this unit clearly shows several grading textures (Fig.5-2-2-3). The sixth unit (12X-CC–16X-CC; 73.05–121.0 mbsf) is composed of altered volcanogenic rock fragments with gray color, and light gray to whitish portions of crushed/grinded/compacted materials of those fragments with disseminated sulfide minerals (Fig.5-2-2-4).

5.2.3 Hole C9019B

Only one core sample (1H-01–1H-CC) was recovered from Hole C9019B and the lithology was divided into 13 units by VCD. In XCT observation, the core samples are divided to 7 XCT units.

The first unit (1H-01 0.0–44.0 cm; 0.0–0.44 mbsf) shows gray–light gray–whitish lamination texture (Fig.5-2-3-1). The lamination texture was defined as difference of the amount of fine-grained pyrite grains. The second unit (1H-01 44.0–74.0 cm; 0.44–0.74 mbsf) is gray to light gray heterogeneous portion. This unit corresponds to pumiceous grits of VCD unit 2. In this unit, subrounded volcanoclastic (?) clots (< 1.0 cm) were observed by VCD. Such clots are probably major cause of the heterogeneous texture in this interval. The third unit (1H-01 74.0–91.0 cm; 0.74–0.91 mbsf) is essentially similar to the first unit. The fourth unit (1H-01 91.0–1H-03 5.0 cm;

0.91–2.06 mbsf) is homogeneous gray color and is composed mainly of hydrothermal clay. Some whitish spots and irregular-shaped patches were native sulfur, gypsum crystals and small volcanic clasts. The lower part of this unit showed loose texture. Some void spaces (shown as black portion in XCT images) and soupy portions (light gray) were observed. Fifth unit (1H-03 5.0–16.0 cm; 2.06–2.17 mbsf) and sixth unit (1H-03 16.0–1H-05 22.5 cm; 2.17–4.255 mbsf) are essentially similar to the first unit and fourth unit, respectively. The seventh unit (1H-06 0.0–1H-CC 20.0 cm; 4.255–4.60 mbsf) is composed of gray matrix with light gray fragments and whitish dots. The light gray and whitish portions were volcanic rock fragments and gypsum/anhydrite aggregates, respectively.

5.2.4 Hole C9019C

As with Hole C9019B, only one core sample was recovered from Hole C9019C. The lithology of C9019C was divided into 2 units in VCD. In XCT observation, samples are also divided into 2 XCT units.

The first unit (1X-01 0.0–1X-CC 7.0 cm; 0.0–0.425 mbsf) is composed of soupy silt matrix and hydrothermal grit with iron oxide, aggregates of sulfide minerals and aggregates of gypsum/anhydrite. This unit showed normal grading in terms of VCD. The grading was observed as gradual color change from light gray whitish gray in XCT image. Light gray colored rock fragments and some gray homogeneous clay were observed in the second unit (1X-CC 7.0–30.5 cm; 0.425–0.66 mbsf).

5.2.5 Hole C9021B

Based on VCDs, 13 lithological units were divided in core samples recovered from Hole C9021B. In XCT observation, the core samples are divided to 9 XCT units. Upper seven units are composed mainly of pumiceous fragments and the lower two units are composed mainly of altered volcanogenic rock fragments.

From top to 67.4 mbsf (7H-07 32.0 cm), relatively homogeneous gray color in XCT images were observed (Fig.5-2-5-1). Shape of individual pumice fragments was observed as weak tone variations. Although color, alteration degrees, and containing clay minerals were quite different between the upper and lower part in terms of VCDs, it was very difficult to distinguish these differences within XCT images. There are some distinct layers/intervals in 36.58–38.0 mbsf (4H-09 0.0–4H-CC, 20.0 cm; second unit), 41.74–42.08 mbsf (5H-04 71.0–100.5 cm; fourth unit), and 62.63–62.85 mbsf (7H-07

10.0–32.0 cm; sixth unit) in pumiceous formation. The rest of intervals are divided as the first unit (0.0–36.58 mbsf), third unit (38.0–41.74 mbsf), and fifth unit (42.08–63.53 mbsf), respectively. The second unit is composed of light gray matrix and gray rock fragments with small amount of whitish patches (Fig.5-2-5-2). The matrix part is composed mainly of pumiceous sand. Alteration degree of some pumiceous fragments is significantly higher than that of the surrounding portion, and clay minerals are observed as whitish patches. In the fourth and sixth units, homogeneous light gray layer (light greenish gray clay in VCD) with some grayish fragments (altered pumice) were observed (Fig.5-2-5-3).

In seventh unit (7H-07 32.0–8H-02 38.0 cm; 62.85–67.39 mbsf), light gray rock fragments (altered/silicified volcanic rocks) with laminated texture and with surrounding gray material (altered pumiceous sand/grit) were observed. Eighth unit is composed of homogeneous light gray rock fragments (altered/silicified volcanic rocks) and small amount of gray–light gray material. Some rock fragments showed laminated texture also (Fig.5-2-5-4).

5.2.6 Hole C9023B

Only one section sample was recovered from Hole C9023B (1X-CC). This section was divided into 3 lithological units by VCD and 2 XCT units were realized in XCT observation.

There were many bright (high density) fragments/gravels in the first unit (1X-CC 0.0–15.0 cm; 0.0–0.15 mbsf) (Fig.5-2-6-1). These fragments were sulfide ores and sulfate-sulfide gravels. On the other hand, the second unit (1X-CC 15.0–34.5 cm; 0.15–0.345 mbsf) is composed of hydrothermal clay containing abundant pyrite crystals. The XCT image shows light gray to whitish laminated texture with some whitish gravels.

5.2.7 Hole C9023D

Cores recovered from Hole C9023D were divided into 23 lithological units by VCD. In XCT observation, 8 XCT units are identified.

The first unit (1X-01–CC; 0.0-9.5 mbsf) contained light gray–whitish gray fragments within matrix. Rock fragments were observed in the upper portion of this unit. Because the most part of this unit showed very bright color in XCT images, it was difficult to identify those structure/texture. This unit is composed of sulfate-sulfide

gravels/sands and some clay minerals, the brightness (color contrast) in XCT image reflected abundance of these minerals. The second unit (2H-01-CC; 9.5–13.0 mbsf) was gray–light gray–white colored gravels/sands. Several intervals with grading textures were observed (Fig.5-2-7-1). These gravels/sands are composed of aggregates of anhydrite, sulfids (pyrite, sphalerite) and lithic fragments. The amount of bright (high density) fragments increased in the lower portion of each grading unit. The third unit (3X-CC–4H-CC; 9.5–31.0 mbsf) consists of many light gray–white anhydrite gravels and gray matrix (hydrothermal clay) (Fig.5-2-7-2). The upper portion of 4H-01 is similar to unit 2, which is composed mainly of sulfate/sulfide gravels, and is considered to be drilling waste. Thus, this portion was eliminated from unit 3. The fourth unit (5H-01-CC; 31.0–33.5 mbsf) is similar to unit 2, but the amount of bright (dense) fragments is much larger than that of unit 2. Weak normal grading texture was observed in the top of the 5H-01 to the bottom of 5X-CC. The fifth unit (6H-CC 0.0–7X-CC 17.5 cm; 33.5–43.175 mbsf) is composed of gray rock fragments and light gray–white gravels, which corresponded to altered tuffaceous rocks and anhydrite with fine grained sulfide mineral, respectively. The sixth unit (7X-CC 17.5–40.0 cm; 43.175–43.4 mbsf) consists of gray–light gray matrix of hydrothermal clay. Thick whitish veins (anhydrite/gypsum and sulfide minerals) were also observed. Sulfide portion was slightly brighter than sulfate portion. The seventh unit generally shows grayish color and is composed mainly of hydrothermal clay and silicified volcanic rocks. Some light gray–white colored veins and fragments were sparsely observed. These bright portions corresponded to anhydrite and pyrite. The eighth unit is composed of gray–light gray rock fragments with whitish veins and black/white spots (Fig.5-2-7-3). Black and bright spots correspond to pore space in silicified rocks and sulfide minerals, respectively.

5.2.8 Hole C9023E

Based on VCD, 13 lithological units were identified in Hole C9023E. In XCT observation, 3 XCT units were recognized.

The first unit (1X-CC–4X-CC; 125.0-163.0 mbsf) consists of gray rock fragments/matrix with some whitish patches and thin veins (Fig.5-2-8-1). These rock fragments and matrix were silicified volcanic rocks and clayey grinded materials (due to drilling) of these fragments. Whitish parts correspond to sulfide minerals (pyrite, chalcopyrite and sphalerite). Some aggregates of anhydrite were also observed in VCD and were recognized as light gray patches in XCT image. Although lamination or gneissose texture was observed in some volcanic rock fragments by VCD, such texture

was not observed by XCT images (the upper part of Fig.5-2-8-1). The second unit is composed of gray–light gray rock fragments with thick network/stockwork veining matrix (Fig.5-2-8-2). Rock fragments consisted of silicified volcanic breccia and the veining matrix was anhydrite with some sulfide minerals. The third unit is similar to the first unit. However, rock fragments in section 8X-CC show slightly brighter color than the other part of this unit. These fragments were highly silicified and were observed as whitish color.

Captions:

Fig. 5-2-2-1 Cross section X-CT and scanned color images of C9017C 4H-05. Whitish patches in CT image correspond to aggregates of anhydrite.

Fig. 5-2-2-2 Cross section X-CT and scanned color images of C9017C 9H-04. Whitish patches in CT image correspond to aggregates of wairakite.

Fig. 5-2-2-3 Cross section X-CT and scanned color images of C9017C 11H-02. Two normal grading textures are recognized in this section.

Fig. 5-2-2-4 Cross section X-CT and scanned color images of C9017C 16X-CC. Sulfide minerals is concentrated in light gray – whitish portion in CT image.

Fig. 5-2-3-1 Cross section X-CT and scanned color images of C9019B 1H-01. The first to fourth units are recognized in this section.

Fig. 5-2-5-1 Cross section X-CT and scanned color images of C9021B 1H-06 (typical pumiceous formation).

Fig. 5-2-5-2 Cross section X-CT and scanned color images of C9021B 4H-09. Pumiceous sand is recognized as slight light color in CT image.

Fig. 5-2-5-3 Cross section X-CT and scanned color images of C9021B 5H-04. The light gray portion in the lower part of this section corresponds to the fourth unit.

Fig. 5-2-5-4 Cross section X-CT and scanned color images of C9021B 10X-CC.

Fig. 5-2-6-1 Cross section X-CT and scanned color images of C9023B 1X-CC. The rock fragments in the upper part of this section (first unit) are mainly composed of sulfide minerals which correspond to “Kuroko” and “Okō” in Kuroko-type deposit.

Fig. 5-2-7-1 Cross section X-CT and scanned color images of C9023D 2H-03. Normal grading textures are recognized below 22.5 cm.

Fig. 5-2-7-2 Cross section X-CT and scanned color images of C9023D 3X-CC. Whitish gravels correspond to the anhydrite aggregates.

Fig. 5-2-7-3 Cross section X-CT and scanned color images of C9023D 15X-CC. Whitish dots and veins (mainly sulfide minerals) are observed in CT image.

Fig. 5-2-8-1 Cross section X-CT and scanned color images of C9023E 2X-CC.

Fig. 5-2-8-2 Cross section X-CT and scanned color images of C9023E 5X-01. Whitish network/stockwork veining matrix is composed of anhydrite with fine-grained sulfide minerals.

CT image Scanned color image

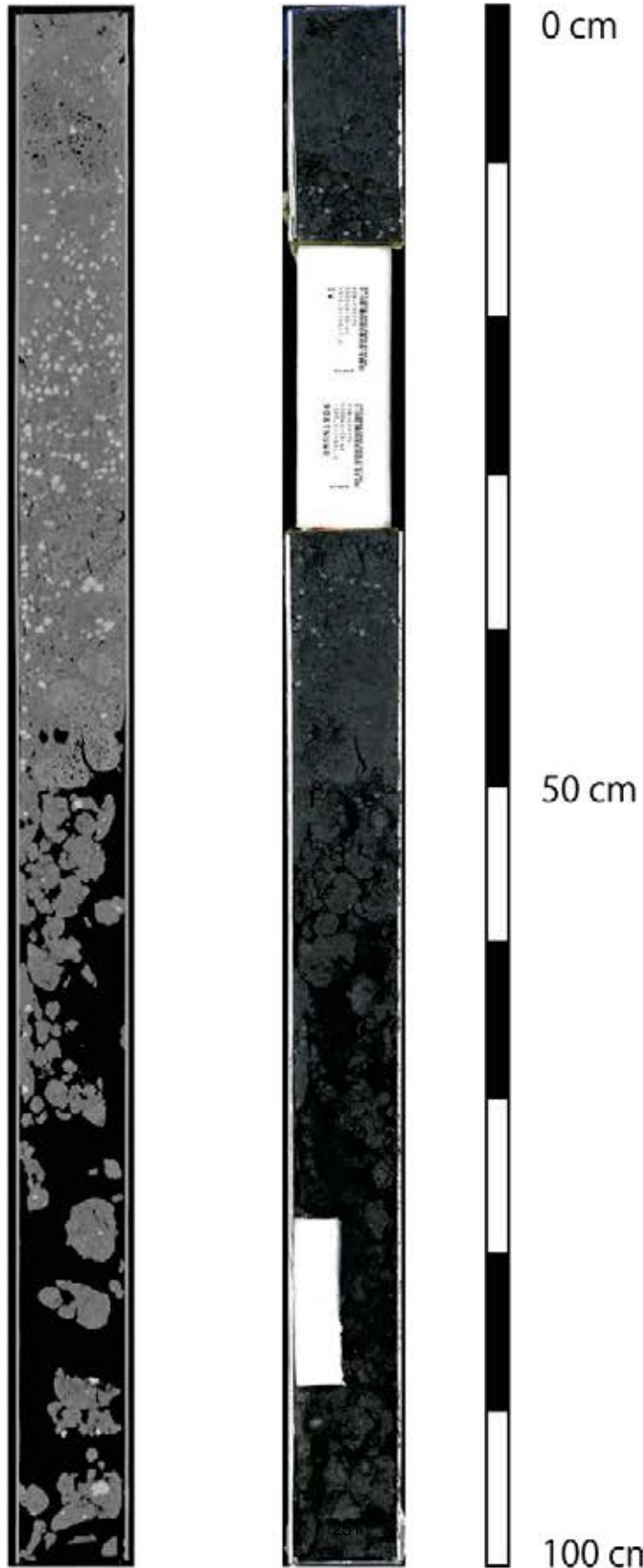


Figure 5-2-2-1

CT image Scanned color image

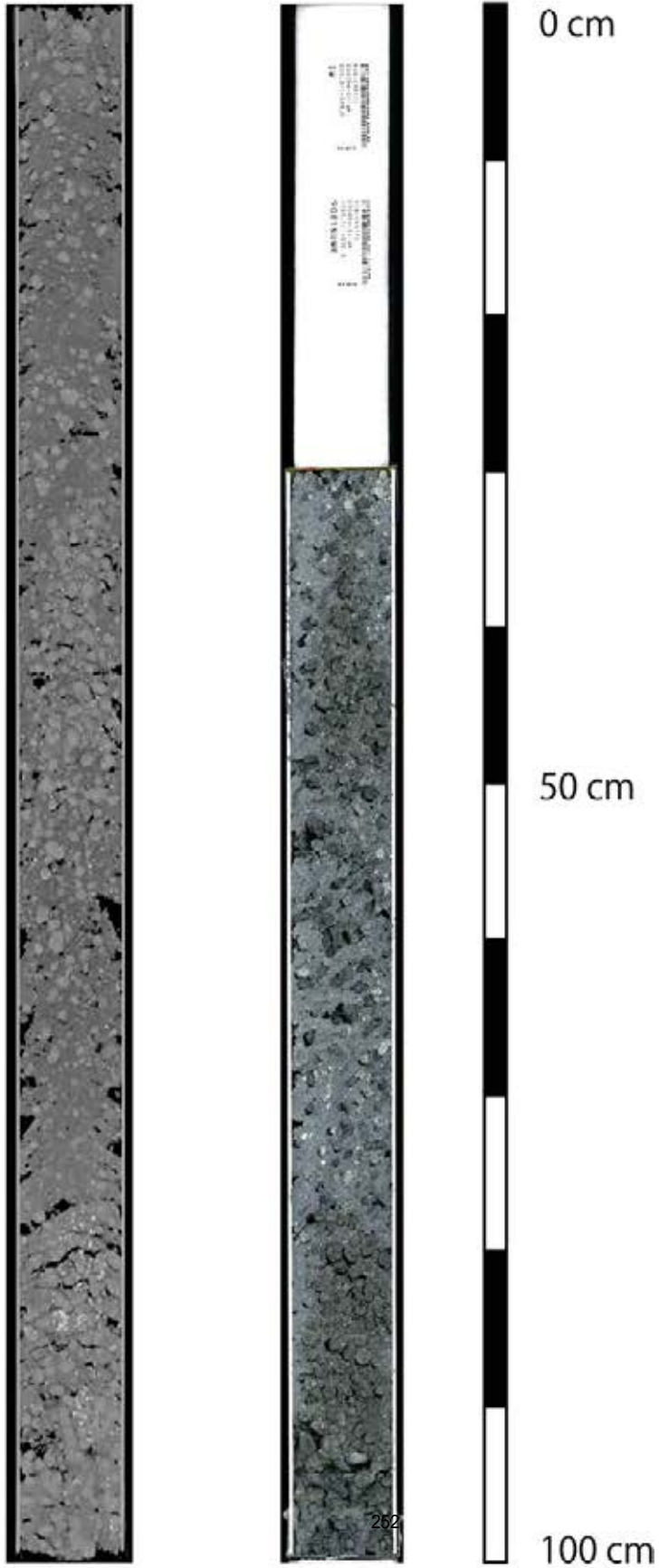
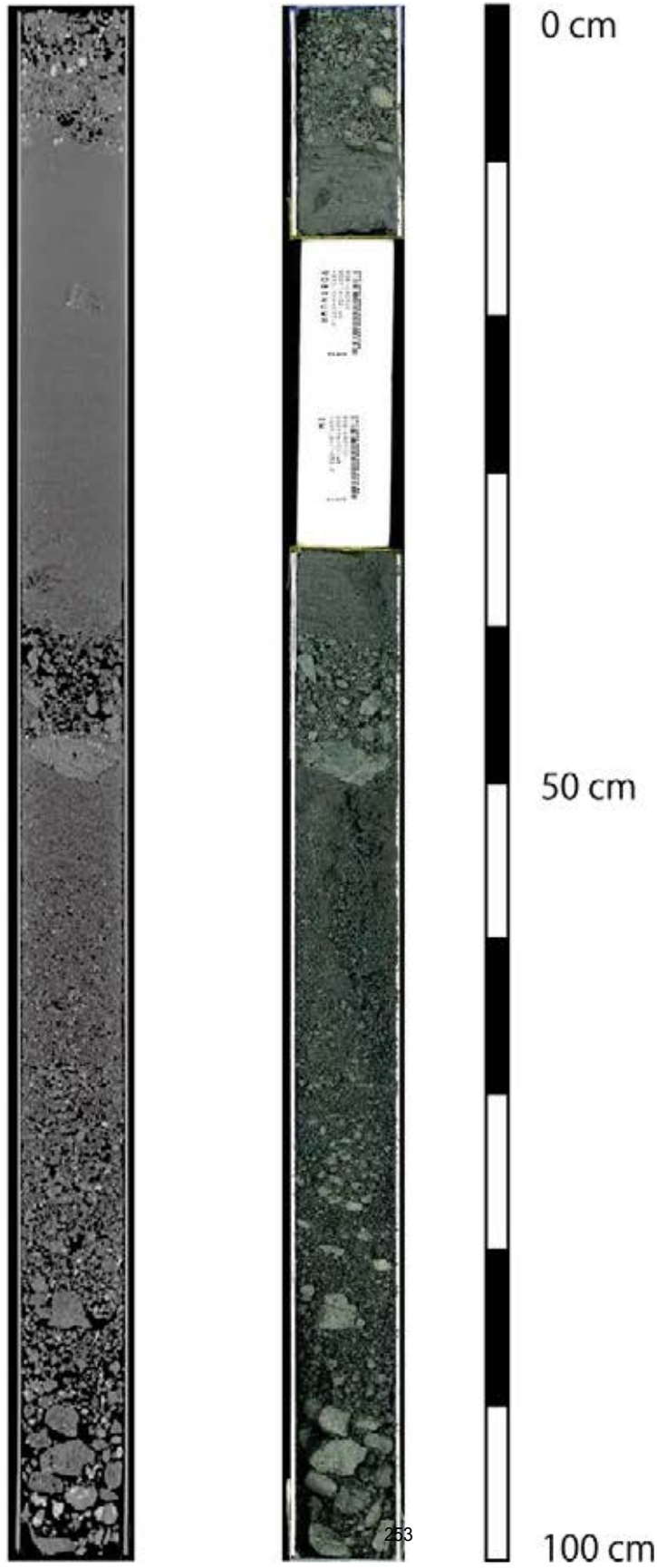


Figure 5-2-2-2

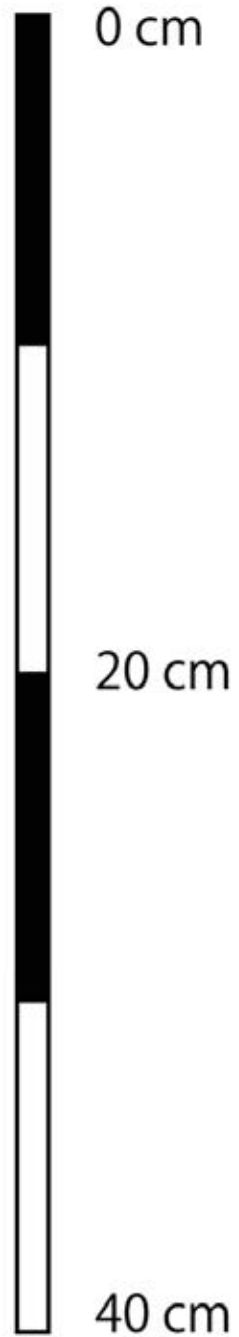
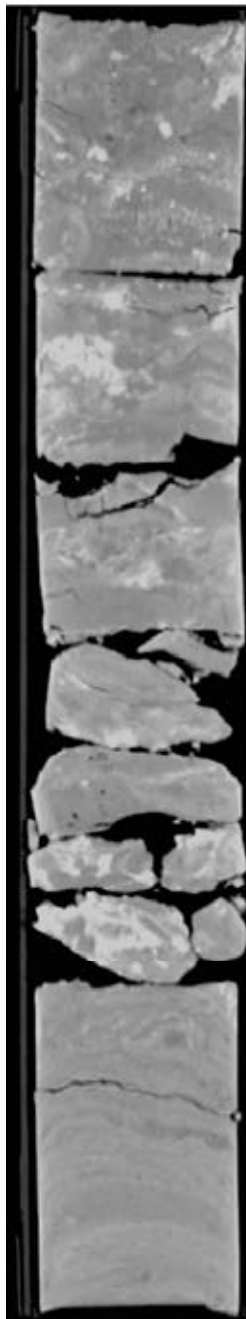
CT image Scanned color image



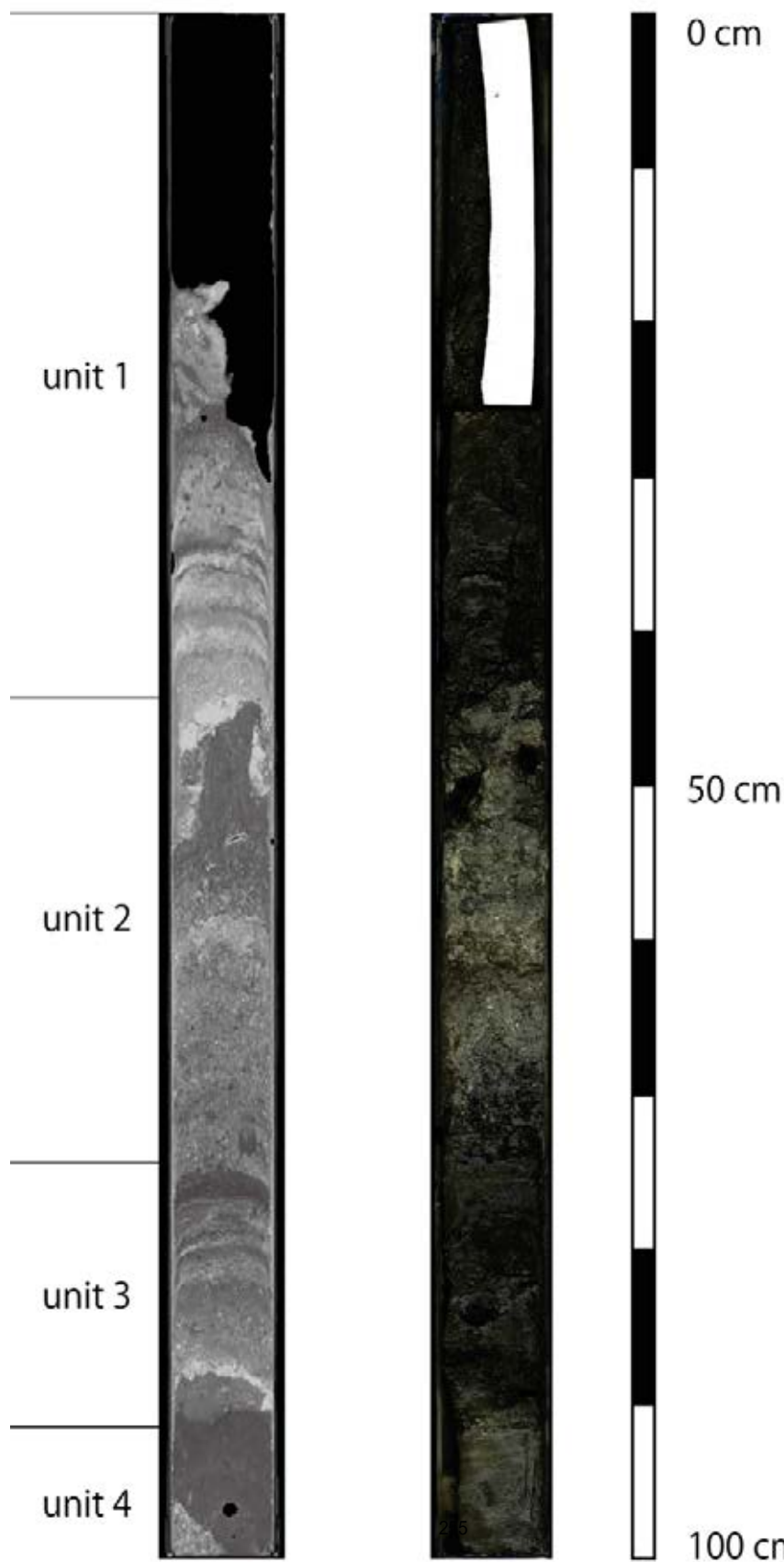
233

Figure 5-2-2-3

CT image Scanned color image

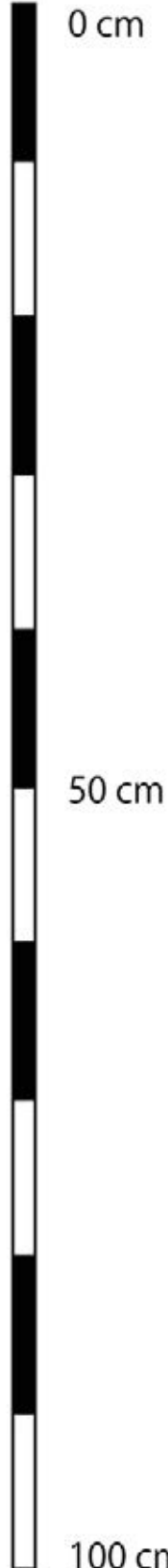


CT image Scanned color image



100 cm Figure 5-2-3-1

CT image Scanned color image

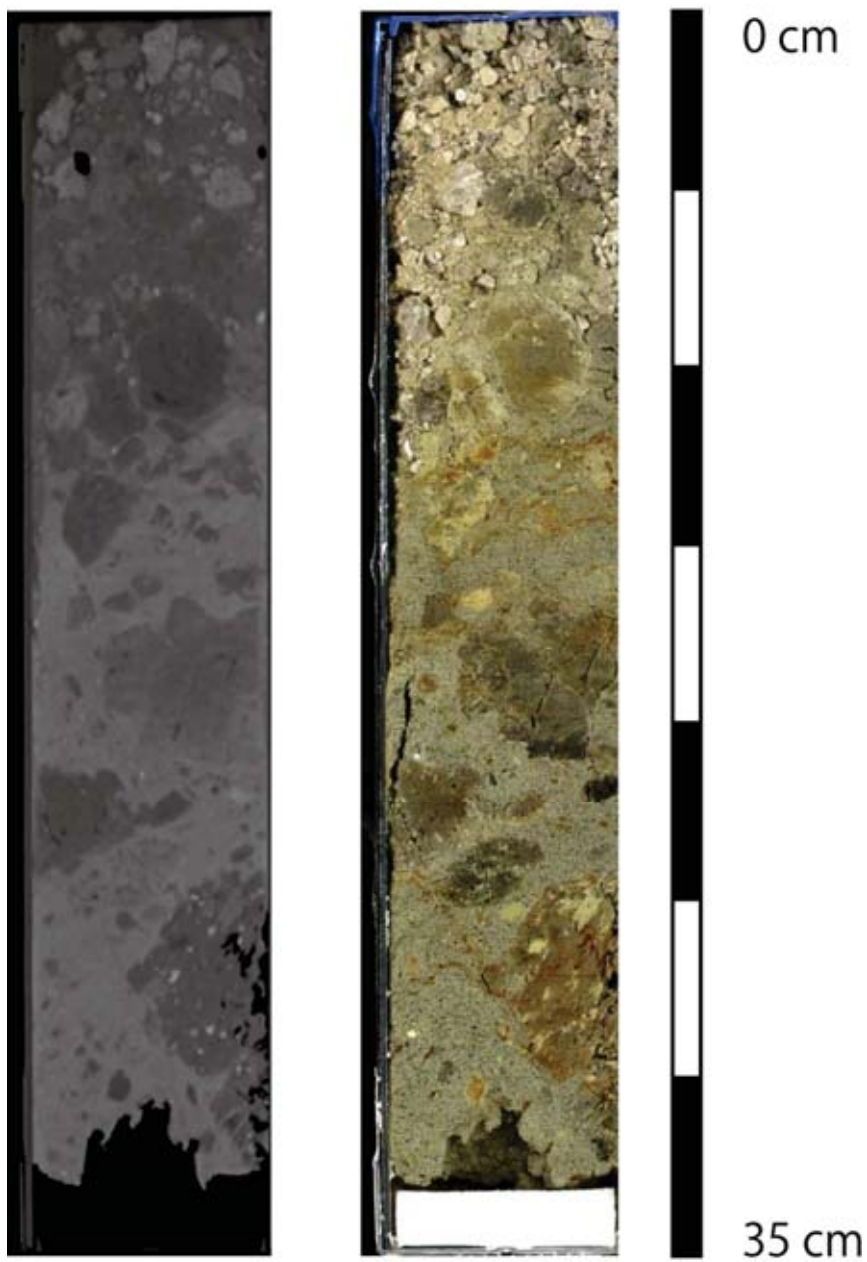


0 cm

50 cm

100 cm Figure 5-2-5-1

CT image Scanned color image



CT image Scanned color image

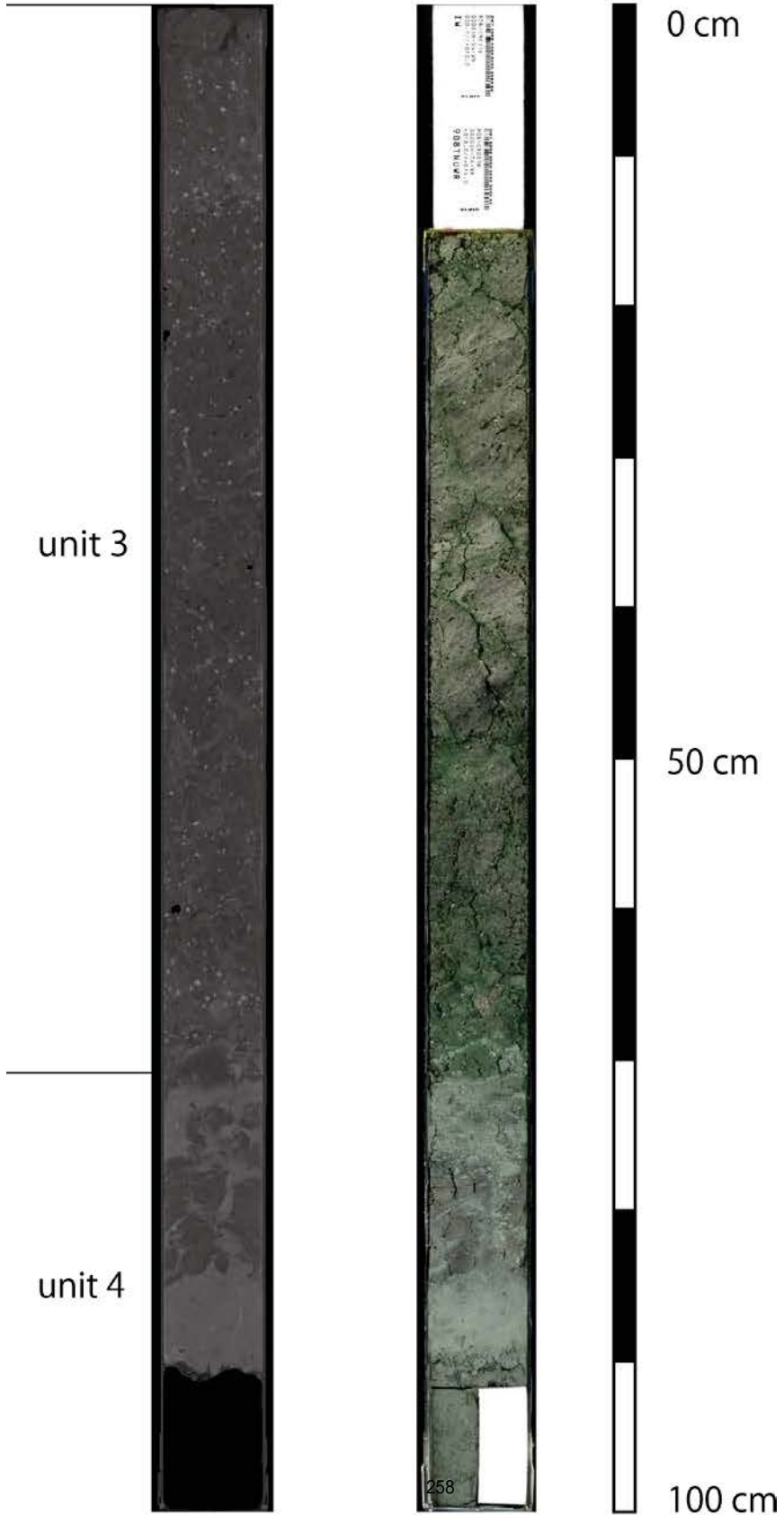
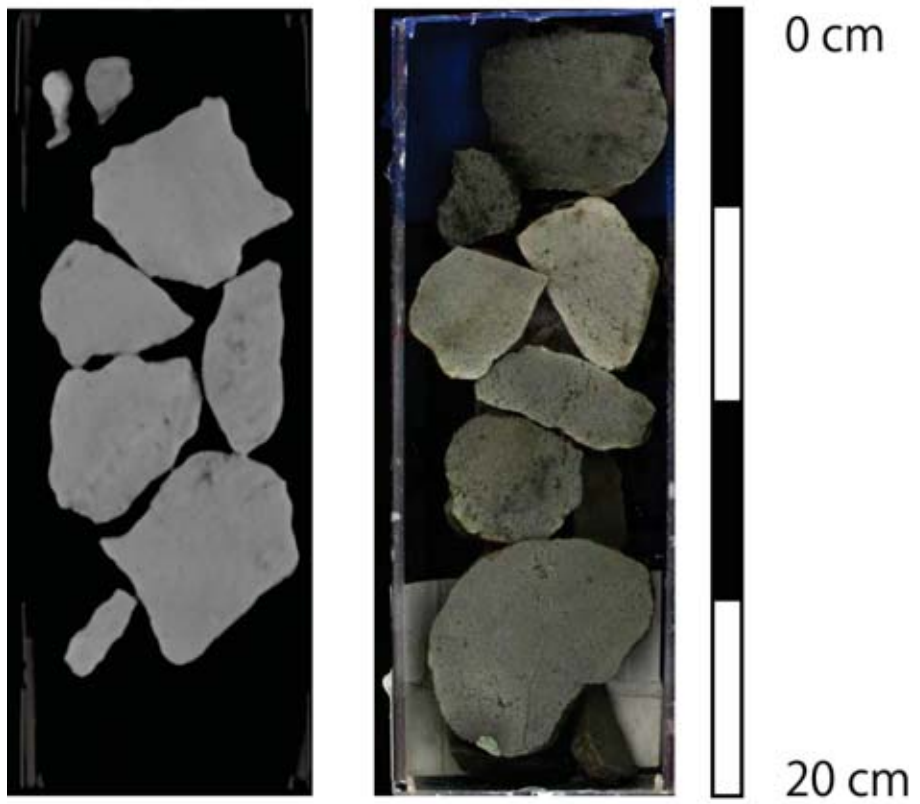
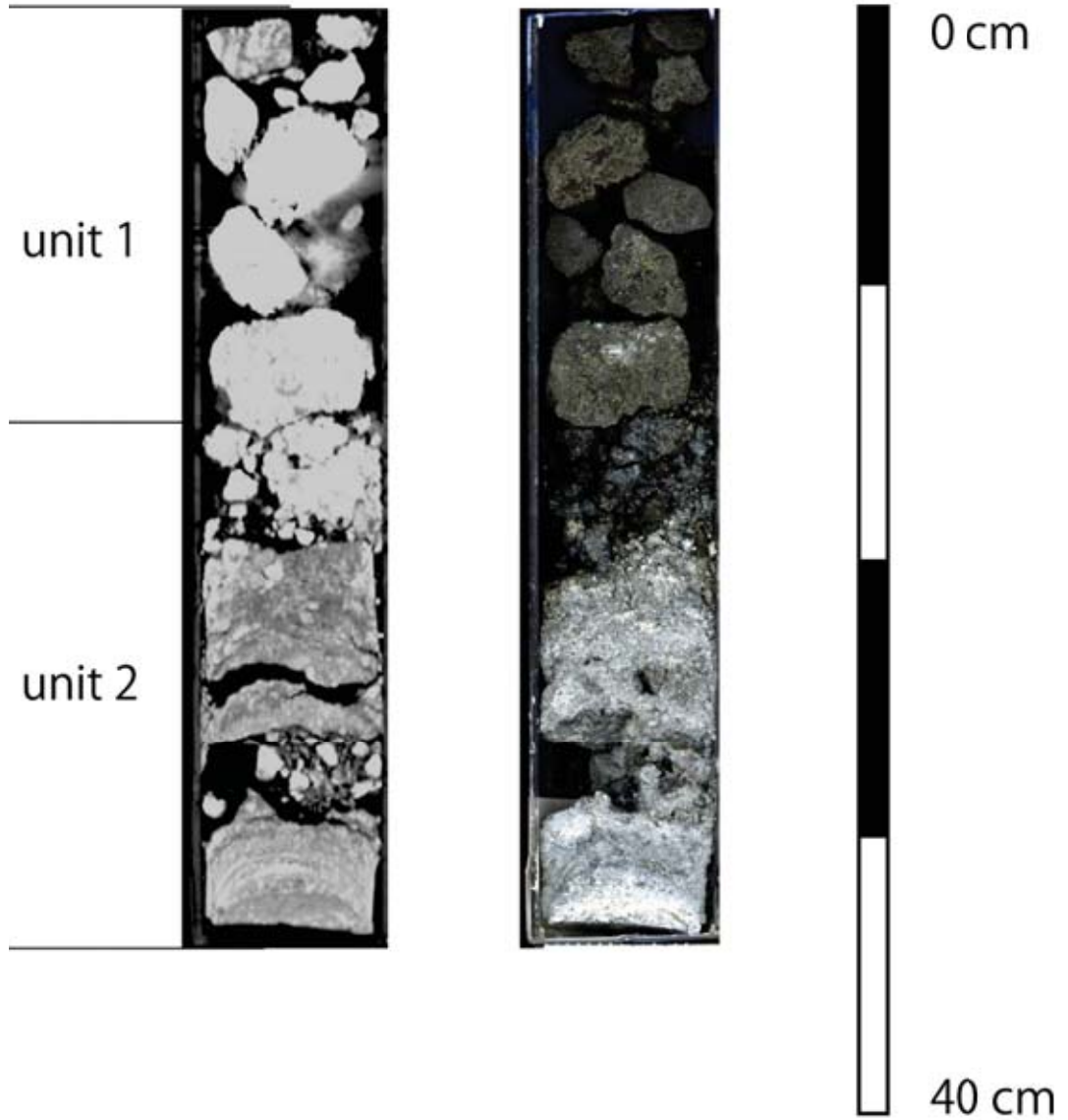


Figure 5-2-5-3

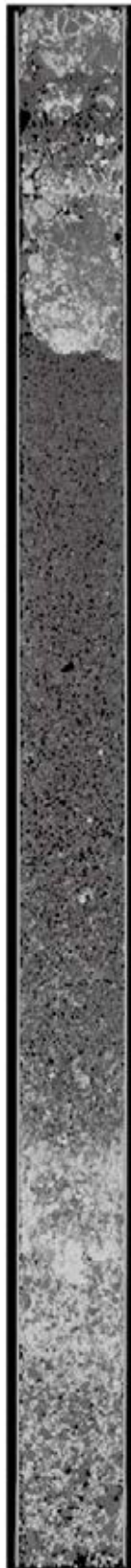
CT image Scanned color image



CT image Scanned color image



CT image Scanned color image



0 cm

50 cm

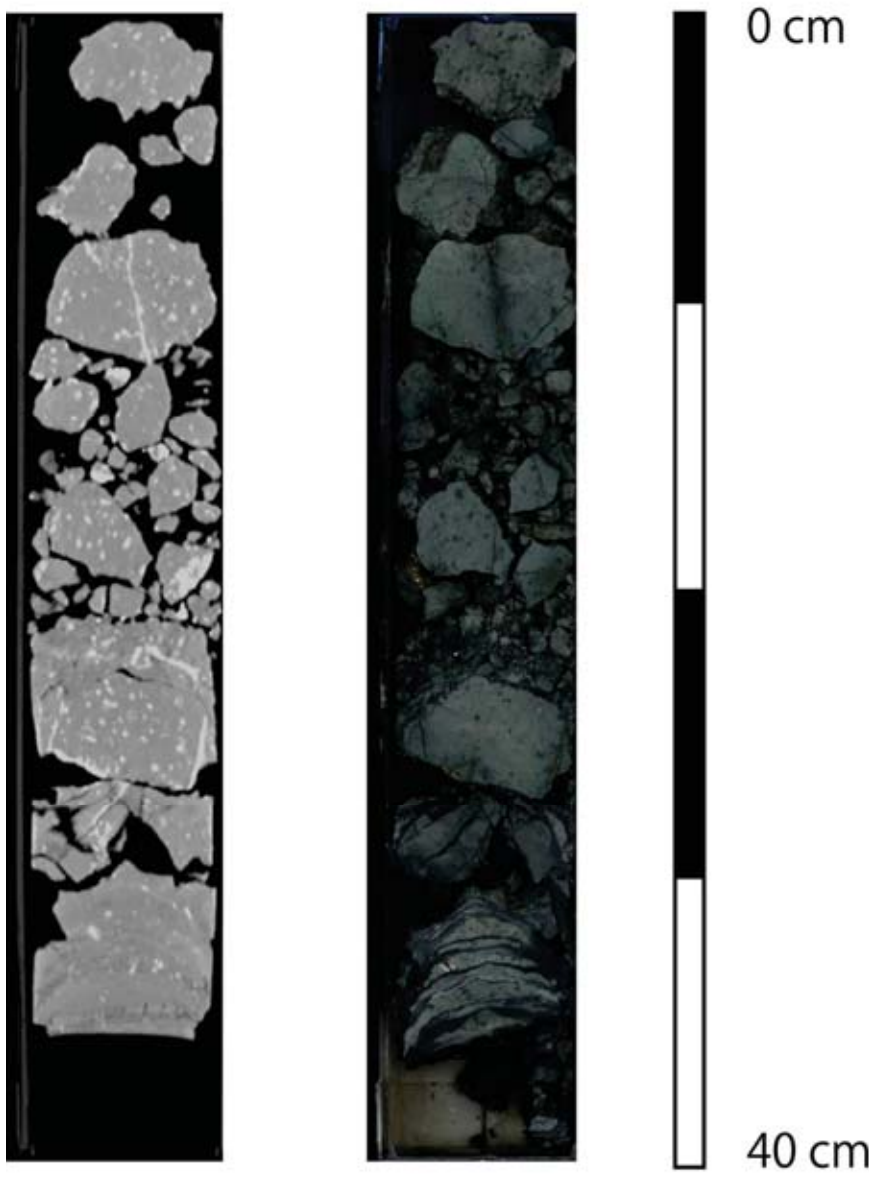
100 cm

Figure 5-2-7-1

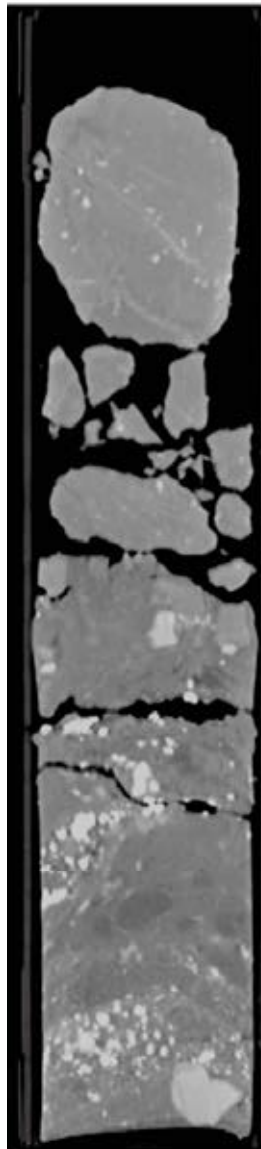
CT image Scanned color image



CT image Scanned color image

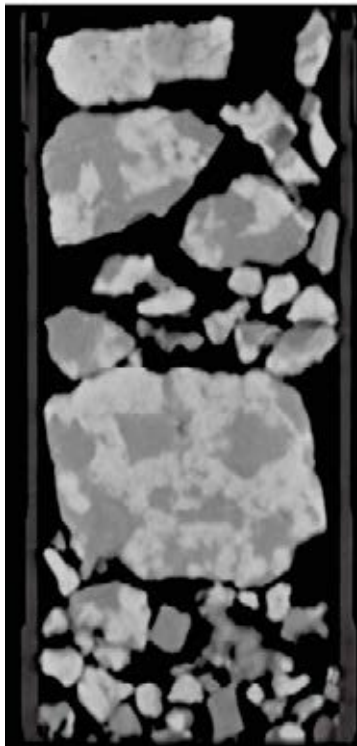


CT image Scanned color image



CT image

Scanned color image



5.3 Physical properties

Y. Masaki and PP Team

5.3.1 Methods

Physical properties (PP) measurements provide basic information to assess rock and sediment properties, to characterize lithologic units and states of consolidation, deformation, and chemical diagenesis, and to correlate core, downhole measurement and logging data (Blum, 1997). Most of the methods and systems described here are the same as for previous IODP Chikyu Expeditions. In addition to these are three third-party tools that have not previously been used in IODP Chikyu Expeditions, namely a portable XRF system, a spectroscopic personal radiation detector, and an advanced impedance analyzer. For the cored intervals, X-ray CT images are first taken of core sections. Then, gamma ray attenuation (GRA) density, magnetic susceptibility, natural gamma radiation and *P*-wave velocity are measured for whole-round core sections (MSCL-W) using the multisensor core logger (MSCL) system (Geotek Ltd., London, United Kingdom) when the deviation of core sample temperature (i.e. the temperature of the core liner) from room temperature is within ± 3 K. After MSCL-W measurements, thermal conductivity measurements are carried out using a full-space needle probe before cores are split into archive and working halves. If the core sample is too hard to insert the needle probe, thermal conductivity measurements are carried out on the working half of split cores using the half-space method. Moisture and density (MAD) are measured on discrete samples collected from core working halves. Resistivity is measured on the working half of split cores or on 20 mm cubic samples if the core sample is hard. *P*-wave velocity is measured in three orthogonal directions on 20 mm cubic samples. Penetration strength and dosimetry are measured on the working half of split cores. Portable-XRF analyses are performed on the archive half of split cores. **Table 5-3-1-1** shows the sampling frequency for physical property measurements. When aluminium liner is used instead of plastic liner, the methodology for some of the physical property measurements is modified. Details about each measurement are given in the following sections.

Whole-round Multi-Sensor Core Logger (MSCL-W)

During MSCL-W measurements, gamma ray attenuation (GRA) density and magnetic susceptibility data for core samples are obtained at 4 cm intervals, and natural gamma radiation (NGR) measurements are conducted at 16 cm intervals. However, when the sample length is less than 40 cm the NGR measurements are conducted at 8 cm intervals, and at 4 cm intervals when the sample length is less than 10 cm. We do not perform MSCL-W measurements on core catcher samples because the physical properties

of core catcher samples are probably influenced by artificial disturbance during core processing. However, when only core catcher samples are available for physical property measurements due to low core recovery rate, MSCL-W measurements are performed on core catchers. Magnetic susceptibility measurement is skipped when aluminum liner is used.

Gamma ray attenuation density

Bulk density can be used to evaluate pore volume in sediment and rock, which provides information on the consolidation state of the sediment. GRA density is based on the detection of a gamma ray beam produced by a cesium source. The beam, produced by a ^{137}Cs gamma ray source at a radiation level of 370 MBq within a lead shield with a 5 mm collimator, is directed through whole-round cores. The gamma ray detector includes a scintillator and an integral photomultiplier tube to record the gamma rays that pass through the whole-round core. GRA bulk density (ρ_b) is calculated as:

$$\rho_b = (1/\eta d) \times \ln(I_0/I)$$

where

- I_0 = gamma ray source intensity,
- I = measured intensity of gamma rays passing through the sample,
- η = Compton attenuation coefficient, and
- d = sample diameter.

The Compton attenuation coefficient (μ) and source intensity (I_0) are treated as constants, so ρ_b can be calculated from I . The gamma ray detector is calibrated with a sealed calibration core (a standard core liner filled with pure water [Elix] and aluminum cylinders of various diameters). To establish the calibration curves, gamma ray counts are measured through each aluminum cylinder for 60 s. Each aluminum cylinder has a density of 2.71 g/cm^3 , and d is 1, 2, 3, 4, 5, or 6 cm. The relationship between I and ηd is

$$\ln(I) = A(\eta d) + B$$

where A and B are coefficients determined from the calibration experiment. The spatial resolution is 5 mm.

Porosity (ϕ) estimated from MSCL density (GRA porosity) is calculated using the following equation as;

$$\phi = (\rho_s - \rho_b)/(\rho_s - \rho_f)$$

where

ρ_s = grain density,

ρ_f = density of pore fluid.

Here, we simply assume that ρ_s and ρ_f are constant for all data, as 2.648 g/cm³ (density of quartz) and 1.024 g/cm³ (density of sea water) respectively. Therefore, if the actual grain density is higher than the density of quartz, we might underestimate porosity.

Magnetic susceptibility

Magnetic susceptibility is the degree to which a material can be magnetized by an external magnetic field. Therefore, magnetic susceptibility provides information on sediment composition. A Bartington loop sensor with an 8 cm loop diameter is used to measure magnetic susceptibility. An oscillator circuit in the sensor produces a low-intensity (~80 A/m RMS), non-saturating, alternating magnetic field (0.565 kHz). Any material near the sensor that has a magnetic susceptibility causes a change in the oscillator frequency. This pulse frequency is then converted into a magnetic susceptibility value. The spatial resolution of the loop sensor is 23–27 mm, and it is accurate to within 5%. Magnetic susceptibility data are obtained at 4 cm intervals with an acquisition time of 1 s.

Natural gamma radiation

Natural gamma radiation measurements provide insights into sediment composition and thus can be used to identify lithology. Whole-round cores are monitored for natural gamma ray (NGR) emissions to obtain spatial variability in radioactivity and to establish gamma ray logs of cores for correlation with the down-hole gamma ray logs. A lead-shielded counter, optically coupled to a photomultiplier tube and connected to a bias base that supplies high-voltage power and a signal preamplifier, is used. Two horizontal and two vertical sensors are mounted in a lead, cube-shaped housing. The NGR system records radioactive decay of ⁴⁰K, ²³²Th, and ²³⁸U. The NGR has a resolution of 120–170 mm, and measurements are conducted at 16 cm intervals with a count time of 30 s. Background radiation noise is determined by taking measurements on a water-filled calibration core. Two radioactive isotope standards (¹³³Ba and ⁶⁰Co) are used for the energy calibration and adjustment of the spectral detection windows.

Moisture and density

Moisture and density (MAD) measurements

Approximately 5 to 10 cm³ of material is taken from the working half of the core for each MAD measurement. We collect MAD samples near the location of the resistivity measurement. The wet sample mass (M_t) is measured, after which the samples are placed in a convection oven for >24 h at 105° ± 5°C. Dried samples are then cooled in a

desiccator for at least 1 h before the dry mass (M_{dry}) and dry volume (V_{dry}) are measured. Wet and dry masses are determined using a paired electronic balance system, which is designed to compensate for the ship's heave. The sample mass is counterbalanced with a precisely known mass (40 g) that is suitable for sample mass measurements in the range 30 – 50 g. The sample mass is determined to a precision of ± 0.01 g. The balance system is calibrated every 12 hours. Dry volume is measured using a helium-displacement Quantachrome penta-pycnometer (Quantachrome Instruments, Boynton Beach, FL, USA), which includes 5 cells with a nominal precision of ± 0.04 cm³. Each reported value consists of an average of five measurements. A reference volume (calibrated sphere) is run with each set of four samples, and the sphere is rotated among the cells to check for any systematic error.

For calculation of bulk density, dry density, grain density, porosity, and void ratio, IODP Method C (Blum, 1997) is used. Water content, porosity, and void ratio are defined by the mass or volume of extracted water before and after removal of all water present in the sample through the drying process. This includes interstitial water (inside the pores) and water bound in hydrous minerals. Standard seawater density ($\rho_w = 1.024$ g/cm³) is assumed for the density of pore water.

Water content

Pore water mass (M_w), salt mass (M_s), pore water volume (V_{pw}), and salt volume (V_s) can be calculated by

$$M_w = (M_t - M_{dry}) / (1 - s),$$

$$M_s = M_w - (M_t - M_{dry}) = (M_t - M_{dry})s / (1 - s),$$

$$V_{pw} = M_w / \rho_w = (M_t - M_{dry}) / [(1 - s)\rho_w], \text{ and}$$

$$V_s = M_s / \rho_{salt} = [(M_t - M_{dry})s / (1 - s)] / \rho_{salt},$$

where

M_t = total mass of the saturated sample,

M_{dry} = mass of the dried sample,

s = salinity (35‰),

ρ_w = density of pore fluid, and

ρ_{salt} = density of salt (2.22 g/cm³).

Water content (W_c) is determined following the methods of the American Society for Testing and Materials (ASTM) designation D2216 (ASTM International, 1990). Corrections are required for salt when measuring the water content of marine samples. In addition to the recommended water content calculation in ASTM D2216 (i.e., the ratio of pore fluid mass to dry sediment mass [percent dry weight]), we also calculate the ratio of

pore fluid mass to total sample mass (percent wet weight). The equations for water content are

$$W_c (\% \text{ dry weight}) = (M_t - M_{dry}) / (M_{dry} - sM_t) \text{ and}$$

$$W_c (\% \text{ wet weight}) = (M_t - M_{dry}) \times (1 - s) / M_t.$$

Bulk density

Bulk density (ρ_b) is the density of the saturated samples, defined as $\rho_b = M_t / V_t$, where total wet mass (M_t) is measured using the balance, and total volume (V_t) is determined from the pycnometer measurements of dry volume (V_d) and the calculated volumes of the pore fluid and salt ($V_t = V_{pw} + V_d - V_s$).

Porosity and void ratio

Porosity (ϕ) and void ratio (e) are calculated using the following equations:

$$\phi = V_{pw} / V_t$$

$$e = \phi / (1 - \phi)$$

Grain density

Grain density (ρ_g) is determined from measurements of dry mass and dry volume made in the balance and in the pycnometer, respectively. Mass and volume are corrected for as:

$$\rho_g = (M_{dry} - M_s) / (V_d - V_s).$$

Alternative method for loose sediment

Several core sections are composed by loose and soft material and disaggregated by drilling disturbance so that water stored within the sediment particles can probably squeeze out easily during sampling. In these cases, the saturated water content could be underestimated if we apply the procedure described above. Therefore, a syringe tube is used for MAD sampling to measure total volume (V_t) of loose sediment samples. Bulk density and porosity is then calculated using the dry mass (M_{dry}) and dry volume (V_d) measured by the balance and pycnometer.

Thermal Conductivity

Thermal conductivity is an important physical property indicator, since how much heat flows through a material depends on its composition, porosity and lithology structure. Thermal conductivity is measured on unconsolidated sediment and rock samples by two TeKa TK04 thermal conductivity meter units (Blum, 1997), on whole-round core samples (Von Herzen and Maxwell, 1959; Vacquier, 1985) using a needle probe method (VLQ probe) and/or on split cores

using a half-space method (mini HLQ probe), respectively.

The TK04 thermal conductivity measurements are based on a transient heat flow method. A heating wire and a temperature sensor are incorporated in a needle probe. When the wire is heated, the surface temperature of the probe is calculated from the recorded temperature versus time measurement curve based on the simple calculation of the thermal conductivity coefficient, since:

$$T(t) = (q/4\pi k) \ln(t) + C,$$

where

$T(t)$ = temperature as a function of time,

q = constant linear heat input per unit length,

k = thermal conductivity,

t = time after the start of heating, and

C = constant.

The value of k can be determined through a least-squares fitting of temperature vs. time. A special approximation method (SAM) in the TK04 software automatically detects disturbances and determines the optimal time interval of the heating curve for evaluation. Heating power is adjusted manually as necessary for each sample.

In this Expedition, thermal conductivity measurements are made two or three times per core (ca. >9.5 m). For the whole-round cores, a 2 mm diameter temperature probe (VLQ) is inserted into the working half of the core. At the beginning of each measurement, temperature in the samples is monitored automatically without applying a heater current until the background thermal drift is determined to be <0.2 mKh⁻¹. The heater circuit then closes automatically and the temperature increase in the probe is recorded.

During each 24 h period, the TK04 is calibrated with standard blocks; the blocks have nominal conductivities of $1.623 \pm 2\%$ Wm⁻¹K⁻¹ for the VLQ Probe and $1.652 \pm 2\%$ Wm⁻¹K⁻¹ for the mini HLQ probe. The TK04 calculates a criteria called the 'LET' (logarithm of extreme time) if the measured heating curve corresponds well with the theoretical heating curve. The TK04 manufacturer recommends that thermal conductivities with LET >4 are accepted.

Discrete P-wave velocity and anisotropy measurements

P-wave data can be used to evaluate small-strain moduli, to correlate log and core data, and to evaluate lithology, pore structure, and cementation.

The discrete P-wave measurement system (PWV-D, Geotek LTD London, UK) measures the total travel time of a compressional wave between transducers and sample length. This sample preparation enables measurement of P-wave anisotropies in three orthogonal directions. All cubes were cut with faces orthogonal to the x-, y-, and z-axes of the core.

Orientation of the axes is defined as the z-axis pointing down the core axis, the x-axis pointing into the working half, and the y-axis pointing along the core face. The PWL-D is equipped with two 230 kHz transducers, one used as a transmitter and one as a receiver. Sample length (L) is measured with a laser distance sensor. P -wave total traveltime (t) for the first arrival is picked and logged from the digitally displayed oscilloscope signal. The velocity in any direction (V_p) is calculated from the sample length (D), total traveltime (TT), and system-calibrated delay time (T_{delay}):

$$V_p = D / (TT - T_{delay})$$

The travel time and laser distance sensor correction is calibrated daily. Routine QC measurements are made by measuring velocity on glass and acrylic standards with known lengths and velocities. In order to confirm that P -wave velocity measurements are not affected by the moisture content of the sample, all samples are measured directly after sampling and then again after being soaked for 24 h in artificial seawater. No difference is found between measurements made before and after this period of soaking; therefore, all reported data are from measurements made prior to soaking.

Unconfined compressive strength

The penetrometer provides a measure of unconfined compressive strength in units of kilograms per centimeter squared (kg/cm^2). The Geotester pocket penetrometer is a spring-operated device used to measure compressive strength by pushing a 0.25 inch (6.4 mm) diameter probe 0.25 inches (6.4 mm) deep (to the marker) below the split-core surface (Blum, 1997). Unconfined compressive strength values reported here are calculated from the average of three penetration trials conducted at adjacent points on the core, unless the sample was significantly fractured during penetration. During trials, typical spatial separation is on the order of 1 cm. According to these trials, the maximum unconfined compressive strength that can be measured with the penetrometer is 600 kPa.

Dose equivalent rate and spectra measurement

A spectroscopic Personal Radiation Detector (PM1704M, Polimaster Inc.) is used to measure the ambient dose equivalent rate $H^*(10)$ (herein DER) of gamma radiation from core samples and to identify the radionuclide isotope composition by calculating gamma radiation scintillation spectra. A scintillation detector CsI (TI) with a photodiode is used as a gamma radiation detection block in PM1704M. A detection block with a Geiger-Muller counter is also used to widen the DER measurement range of gamma radiation. The detector can measure DER ranges from 0.1 $\mu\text{Sv}/\text{h}$ to 10 Sv/h and radiation pulse

count rates from 1 to 1000 cps. After every 0.25 s of counting, the quantity of pulses for the last (new) interval is added to the current sum, and the quantity of pulses from the first (oldest) interval is subtracted from the total of pulses. Thus the pulse total recorded by every channel and stored in the processor memory is renewed every 0.25 s. The detector is put on the split surface of working half cores so that the gamma ray channel in the upper area of the instrument touches the split surface (**Fig. 5-3-1-1**). The upper surface of the instrument is covered by a wrap to protect it from dirt. To identify the radionuclide isotope composition, the spectrum is accumulated for 10 to 30 minutes at the same position. DER is measured for 1 to 3 positions per core near the MAD sampling location.

pXRF measurements

The portable XRF spectrometer (pXRF) provides real-time characterization of the core to assess broad chemical variations and how they relate to petrological observables. In this expedition, the pXRF system, the MESA-630 (Horiba Ltd.), is used to assess elemental variations in archive half samples and powdered samples used in XRD analysis (see chapter 5.1).

The MESA-630 (Horiba Ltd.) is a self-contained energy-dispersive XRF survey instrument that includes data correction packages tailored to a variety of applications (alloys, plastics, soils and minerals). Its data correction methods are based on the “fundamental parameters (FP)” method, which solves a series of nonlinear equations for each analyzed element. The parameters used in these equations comprise metrics for the X-ray source, fluorescence intensities, absorption coefficients, and absorption edge effects for each wavelength analyzed. In our use of the instrument, we utilized the “Mining_LE_FP” correction protocol, which presumes a perpendicular sample geometry. The “Mining_LE_FP” protocol analyzes light to heavy elements (Mg, Al, Si, P, S, K, Ca, K, Ti, V, Cr, Mn, Fe, Co, Ni, Cu, Zn, As, Se, Rb, Sr, Y, Zr, Nb, Mo, Ag, Cd, Sn, Sb, Ba, Ta, W, Pt, Au, Hg, Tl, Pb, Bi, and U).

In archive halves, pXRF measurements were performed at the same depth intervals at which MAD measurements were conducted (**Fig. 5-3-1-2**). Polyethylene wrap film (Nipponpaper-pak. Inc.) is used to cover the sample during the measurements. Samples are measured automatically for 30 s. For comparison with XRD measurements, several powdered samples that are prepared for XRD analysis are selected and also analysed by pXRF. For these pXRF measurements, enough of the sample powder is placed on a glass plate to form a layer of 10 mm diameter and <1 mm depth. We selected 6 major elements

(Si, Al, Fe, Ca, K, and S) for this report from all the measured elements, because they are consistently detected at concentrations of > 1 wt%. Measurement data are not corrected in this report, but we provide correlation data for some elements using reference powdered materials (see **Table 5-3-1-2**). The pXRF system measures the concentration of a single element for all elements, therefore to compare concentrations of Al, Si, K, Ca, Ti, Mn, and Fe, the concentrations of single elements are converted to concentrations of their element oxides (Al₂O₃, SiO₂, K₂O, CaO, TiO₂, MnO, and Fe₂O₃). Correlation curves for Al, Si, K, Ca, Ti, Mn, Fe, Zn, Rb, Sr, and Zr (plots of pXRF abundances versus reported consensus values for reference materials) (**Fig. 5-3-1-3**) are of high quality and correlation coefficient, ranging from $R^2 = 0.871$ to 0.999. Slopes vary from 0.53 –2.59.

Electrical Resistivity

Formation resistivity is controlled by many factors: the presence of fluids with high salinity, ore minerals and clays, and high porosity and temperature. Therefore, the formation resistivity is a powerful tool that has the potential to describe the spatial distribution of the above factors.

In general, resistivity is represented as a complex function, and is given as follows:

$$\rho = G * Z \quad (1)$$

where: ρ is the resistivity, Z is the complex impedance of a sample, and G is a function of the geometrical factor of the sample or the cell constant of a probe. G is easily calculated from the geometry of the sample (e.g. area and length) or the probe (e.g., distance between electrodes), so Z is the parameter to be measured.

The present cruise measures the complex impedance of drillcore samples using a third-party tool “VersaSTAT 4-200” manufactured by Princeton Applied Research, which is specialized for electro-chemistry analysis and enables the precise measurement of impedance and phase with a wide range of frequency. Alternating Current (AC) controlled by the tool generates electrical potential on the sample. The measured electrical current and potential are readily converted to the complex impedance (Z), which has real (Re_Z) and imaginary (Im_Z) components. Phase (ϕ) is calculated from the above two components. In the present cruise, a four-electrode method is adopted for the measurement. The impedance of unconsolidated samples is measured by directly inserting two copper wires for current electrode and two non-polarizable Ag-AgCl electrodes for potential measurement into the sample (system A), while hard-rock samples are shaped into cubic or half-round geometry (so-called “discrete samples”) and put between four non-polarizable Cu-CuSO₄ electrodes (system B).

The resistivity calculated from (1) was corrected to that at 25 °C, using the

equation of Revil et al. (1998) as below.

$$\frac{1}{\rho(T)} = \frac{1}{\rho(T_0)} [1 + \theta_f(T - T_0)] \quad (2)$$

where: $\rho(T)$ is the resistivity at the temperature (T) during a measurement, T_0 is the reference temperature (in the present case, $T_0 = 25$ °C), and θ_f is a coefficient ($\theta_f \sim 0.023$ °C⁻¹), noting that the equation assumes that electrical conduction is dominated by ionic conduction within the interstitial water of a sample.

A quality control (QC) is done at every drillhole by measuring the impedance of IAPSO standard sea water of known resistivity (0.21 Ωm at 20 °C) for system A, and by measuring the impedance of a standard sample (Berea sandstone saturated with 0.5 mol/l NaCl solution) for system B. Note that their impedances and phases during the QC measurements have no significant change throughout the cruise.

5.3.2 Site C9017

At Site C9017, physical properties measurements were made to help characterize the lithostratigraphic units. **Fig. 5-3-2-1** plots magnetic susceptibility, natural gamma ray radiation, gamma ray attenuation density, GRA porosity from the MSCL-W measurements, bulk density, porosity, and grain density from MAD measurements, and DER from the spectroscopic detector. **Fig. 5-3-2-2** plots thermal conductivity, resistivity, P-wave velocity, and unconfined compressive strength. **Fig. 5-3-2-3** plots concentrations of major elements from pXRF measurement. **Tables 5-3-2-1** and **-2** show the MSCL-W and MAD data sets, respectively. **Table 5-3-2-3** shows the DER measurements. **Table 5-3-2-4** shows the thermal conductivity data. **Table 5-3-2-5** show the resistivity data. **Table 5-3-2-6** shows the P-wave velocity data. **Table 5-3-2-7** shows unconfined compressive strength measurements. **Table 5-3-2-8** shows the data set of the pXRF measurements.

Coring in C9017C was handled by using aluminum liner from Core 4H to 16X, but the core sections from the core catcher used plastic liner. Therefore, magnetic susceptibility was measured only for core samples in the core catchers. Several core sections do not have core catcher units, therefore there are no magnetic susceptibility data for several core units.

MSCL-W and MAD

Magnetic susceptibility

Magnetic susceptibility near the seafloor shows very high values of $>150 \times 10^{-5}$ SI, and

the values decrease with depth. The susceptibility from 19 to 23 mbsf (Core 3X) is $\sim 0 \times 10^{-5}$ SI. Below 50 mbsf, magnetic susceptibility is variable from 0 to 74×10^{-5} SI.

Natural gamma radiation

NGR values increase with depth from 0 to 25 mbsf (upper resistive zone in Logging Unit 1), and a very high NGR value of 155 cps is observed at around 22 mbsf. NGR values are low at depths between 25 and 70 mbsf before becoming very high at around 70 mbsf, and then decreasing with depth towards low values once more by ~ 100 mbsf. The highest count of 155 cps is observed at 22 mbsf where a sand layer dominates. The average minimum level of dose rate (DER) is around 0.2 to 0.3 $\mu\text{Sv/h}$. Overall, the depth variation of DER is similar to that of NGR counting; however, the maximum DER is observed at around 60 mbsf, whereas NGR counts do not show such an anomaly at the same depth.

Density and porosity

GRA density values show significant scatter with depth, ranging from <1.5 to 2.4 g/cm^3 . Maximum GRA densities within each core interval and wet bulk density values determined from discrete samples generally agree well, although at several depths the bulk density values are much higher than the GRA density values. Bulk density decreases with depth from 0 to 25 mbsf, below which point it increases slightly with depth from 1.9 to 2.0 g/cm^3 . A high density anomaly is observed at around 70 mbsf, and below 70 mbsf the bulk density shows greater scatter.

Overall, porosity from MAD measurements is roughly consistent with porosity estimated from GRA density values at the same core sections. Porosity is low ($\sim 30\%$) near the subsurface. Porosity for MAD measurements at depths below 20 mbsf shows considerable scatter, ranging from 30 to 65%. The highest porosity of $\sim 65\%$ is observed at 72 mbsf.

Grain density increases with depth from 0 to 25 mbsf (the upper resistive zone in Logging Unit 1). Grain density between 25 and 50 mbsf (upper conductive zone in Logging Unit 1) shows a slight reduction with depth, decreasing from 3.0 to 2.8 g/cm^3 . Grain density increases with depth from 50 to 60 mbsf (around the transitional resistive zone in Logging Unit 1), then decreases to 2.6 g/cm^3 at 65 mbsf. A high grain density of 3.7 g/cm^3 is observed at 70 mbsf, but decreases to 2.9 g/cm^3 at 80 mbsf. Below 80 mbsf, grain density ranges from 2.9 to 3.2 g/cm^3 .

Thermal Conductivity

Thermal conductivity measurements were conducted on sediment in whole-round cores

using the needle-probe method and on working half cores using the half-space method (see “Methods” chapter). A total of 24 thermal conductivity values were obtained. Values range from 0.6 W/(m·K) to 1.95 W/(m·K). The data between 0 to 20 mbsf were not obtained because core lengths were not long enough to measure thermal conductivity. From 20 to ~50 mbsf (C9017C 3X-7H), the thermal conductivity ranges from 0.85 to 1.75 W/(m·K) where the core sample consists of mud sediment. Thermal conductivity values correlate with porosity values. From ~50 to ~60 mbsf (C9017C 7H-8H), the data are scattered from 1 to 1.8 W/(m·K) where the core is composed of clay sediment. Below a depth of ~60 mbsf (C9017C 9H- 14X), the lowest value of 0.6 W/(m·K) was obtained at 70 mbsf, which is where the most porous structure was found.

Discrete P-wave velocity and anisotropy measurements

P-wave velocity and relative anisotropy were measured only on samples that are hard enough to cut into polyhedral samples, although hard rock samples were rarely obtained in this hole. All the samples for P-wave velocity measurements were also used for resistivity measurements, and the samples were measured before and after soaking with NaCl solution for 24 h. P-wave velocities determined from six discrete samples in Hole C9017C range from 1862 to 4692 m/s. **Fig. 5-3-2-4** shows correlation between before and after soaking, and shows little variation between pre- and post-soaking measurements.

Unconfined compressive strength

From 10 to 30 mbsf, sediment strength gradually increases with depth from 39 to 79 kPa, and then reaches a maximum recorded value of ~470 kPa at 37 mbsf. Strength values show significant scatter from 40 to 80 mbsf, with clay-rich sediment observed in Core 9H-3 exhibiting lower strength than that of surrounding sediment cores, while high sediment strengths of > 400 kPa are observed at several depths between 60 and 80 mbsf. From 80 to 120 mbsf there is less scatter in the data, with strength measurements ranging from 100 to 150 kPa.

Portable X-ray fluorescence

Many measured points contain relatively high Si (0-29.9 wt %), Al (0-12.1 wt %), Fe (4.7-55.6 wt %) and S (0.4-20.4 wt %) contents, whereas K (0-6.2 wt %) contents are relatively low (**Fig. 5-3-2-3**).

From 31.1 to 32.5 mbsf (bottom of core 4H), Fe and S contents increase sharply, while Si and Al contents decrease. This corresponds to increasing amounts of sulfide and decreasing amounts of siliceous minerals in the core.

A similar trend to that seen in core 4H is observed three times at this site and is particularly pronounced from 69.7 to 72.5 mbsf (core 10H), where increasing Fe and S contents correspond to the appearance of millimeter-sized pyrrhotite. The data from 83.2 to 112.3 mbsf (cores 13X to 16X) show significant heterogeneity, which may be because contamination by foreign rock or mud at the top of the core has a disproportionately larger influence on the overall composition at these depths due to the relatively short length of each core.

Resistivity

Overall, most of the measured resistivity values plot around 1 Ohm·m. Several discrete samples have relatively high resistivities of > 10 Ohm·m, which correspond to consolidated rocks. The smallest resistivity values (0.2-0.3 Ohm·m) are found around 70 mbsf, which appears to correspond to the presence of pyrite.

5.3.3 Site C9019

At Site C9019, measurements of physical properties were made to help characterize the lithostratigraphic units. **Fig. 5-3-3-1** plots magnetic susceptibility, natural gamma ray radiation, gamma ray attenuation density, GRA porosity from the MSCL-W, and bulk density, porosity, and grain density from MAD measurements. DER data from the spectroscopic personal radiation detector is plotted in the same figure as the natural gamma ray radiation data. **Fig. 5-3-3-2** plots thermal conductivity, resistivity, and unconfined compressive strength. **Fig. 5-3-3-3** plots element concentrations measured by pXRF. **Tables 5-3-3-1, -2 and -3** show all of the MSCL-W, MAD, and DER data sets. Note that only one core section is cored in both Hole B and Hole C at site C9019. **Table 5-3-3-4** shows the thermal conductivity data. **Table 5-3-3-5** shows the resistivity data. **Table 5-3-3-6** shows the unconfined compressive strength data. **Table 5-3-3-7** shows the data set of the pXRF measurements.

MSCL-W and MAD

Magnetic susceptibility

Magnetic susceptibility gradually decreases with depth from 40×10^{-5} at the seafloor to nearly 0×10^{-5} SI by 4.4 mbsf. Sharp positive anomalies are observed at several depths, and the highest magnetic susceptibility of 121×10^{-5} SI is observed at 0.9 mbsf.

Natural gamma radiation

The maximum NGR value is observed at 0.3 mbsf, and below 0.8 mbsf NGR values remain between 50 and 10 cps. DER ranges between 0.02 and 0.03 $\mu\text{Sv/h}$ from 0 to 4 mbsf. A maximum DER value of 0.05 $\mu\text{Sv/h}$ is observed at 4.4 mbsf in Hole B.

Density and porosity

The GRA density gradually decreases with depth from 1.7 g/cm^3 at the seafloor to 1.5 g/cm^3 at 3.4 mbsf. Very low density ($\sim 1 \text{ g/cm}^3$) is observed at around 3.5 mbsf, where soupy sediment is observed. The highest density of $\sim 1.8 \text{ g/cm}^3$ is observed at depths of 0.4 and 4.4 mbsf. The bulk densities estimated from discrete core samples are consistent with GRA densities. Porosity from MAD measurement ranges from 60 to 80 %. Grain density is highly variable and ranges from 2.4 to 3.8 g/cm^3 , with the highest density of 3.8 g/cm^3 observed at 0.2 mbsf in Hole C.

Thermal Conductivity

Thermal conductivity measurements were conducted on sediment in whole-round cores using the needle-probe method and in working half cores using the half-space method (see “Methods” chapter). A total of four thermal conductivity values were obtained between 0 and 5 mbsf in C9019B and C9019C. The majority of the core consists of mud. Thermal conductivity values are scattered between 0.59 and 0.92 $\text{W}/(\text{m}\cdot\text{K})$, and thermal conductivity increases with decreasing porosity.

Unconfined compressive strength

The majority of unconfined compressive strength values range from 10 to 20 kPa except for a value of 70.31 kPa at 1.9 mbsf, where higher grain density is observed.

Portable X-ray fluorescence

Many measurements have dominant Fe (4.5-31.0 wt %), Si (6.8-23.2 wt %) and S (6.2-45.4 wt %) contents, while Al (0-4.0 wt %), Ca (0.2-1.1 wt %) and K (1.5-5.5 wt %) contents have relatively low values in Hole B. High Fe and S contents in this site are caused by the presence of iron sulfide (**Fig. 5-3-3-3**). Sulfosalts such as gypsum and anhydrite are also reflected in high S contents. On the other hand, high Si contents are caused by clay or siliceous minerals. Particularly for depths between 0 and 1.4 mbsf and at 1.9 mbsf in section 2 of core 1H, the measured element contents are consistent with the existence of clay-like minerals (shown as **Table 5-3-3-7**).

There are three pXRF measurements for Hole C. Two of these are from section CC and

were taken from the same position on the working half of the core; however, they are analyzing different minerals. This hole is characterized by high Fe (24.8-44.3 wt %) contents, which is probably due to the presence of iron oxide that is observed as brown to reddish fragments in the core.

Resistivity

Measured resistivity values all fall around 0.2 Ohm·m, except at a depth of ~ 4.5 mbsf where resistivity increases to 0.6 Ohm·m.

5.3.4 Site C9021

At Site C9021, measurements of physical properties were made in order to help characterize the lithostratigraphic units. **Fig. 5-3-4-1** plots magnetic susceptibility, natural gamma ray radiation, gamma ray attenuation density, GRA porosity from the MSCL-W, bulk density, porosity, and grain density from MAD measurements, and DER from the spectroscopic detector. **Fig. 5-3-4-2** plots thermal conductivity, resistivity, P-wave velocity, and unconfined compressive strength. **Fig. 5-3-4-3** plots element concentrations from pXRF measurements. **Tables 5-3-4-1, -2 and -3** show all of the MSCL-W, MAD, and DER data sets. Core sections from 9X to 11X have very short lengths and so NGR measurements by MSCL-W were performed at 8 cm intervals in these sections. **Table 5-3-4-4** shows the thermal conductivity data. **Table 5-3-4-5** shows resistivity data. **Table 5-3-4-6** shows P-wave velocity data. **Table 5-3-4-7** shows unconfined compressive strength data. **Table 5-3-4-8** shows the p-XRF data.

MSCL-W and MAD

Magnetic susceptibility

From Core 1H to 7H, magnetic susceptibility at the top of each section (Core XX-H -1) is relatively higher than the deeper part of the section. This high magnetic susceptibility is probably caused by drilling disturbance because sediment debris and rock fragments assemble at the top of core section. Magnetic susceptibility is nearly 0×10^{-5} SI at depths of 0 to 70 mbsf when the susceptibility of the top of each section is disregarded. Magnetic susceptibility is very high (up to 300×10^{-5} SI) at around 70 to 75 mbsf (Core 8X). Below 80 mbsf, magnetic susceptibility drops again and varies from 0 to 100×10^{-5} SI.

Natural gamma radiation

The average background NGR value between 0 and 70 mbsf is ~20 cps. Anomalies where NGR values exceed this background value are observed at depths of ~23, ~43, and ~60 mbsf. On average, the NGR value at depths below 70 mbsf is higher than that at depths less than 70 mbsf. Higher DER values, though the increase is small, are observed at similar depths to those observed in NGR.

Density and porosity

GRA density decreases slightly with depth from 0 to 10 mbsf, and then increases gradually with depth from 20 to 70 mbsf. On the whole, bulk density measurements from discrete samples, ranging from 1.3 to 1.5 g/cm³, are consistent with GRA density measurements for depths of 0 to 70 mbsf. Bulk density at depths below 70 mbsf (logging Unit 2), ranging from 1.9 to 2.3 g/cm³, is much higher than those at shallower depth. Because of the very low recovery rate of core samples, GRA densities exhibit considerable scatter below 70 mbsf, although the maximum GRA density value of each core section is quite consistent with the bulk density from discrete samples.

Porosity ranges from 70 to 90 % for depths of 0 to 70 mbsf, then drops markedly down to 20 to 40 % for depths greater than 70 mbsf. Porosities measured by discrete samples are lower than those from MSCL-W at depths of 0 to 40 mbsf, and greater than 70 mbsf. Grain density decreases with depth from 2.5 to 2.2 g/cm³ from near the seafloor to 8 mbsf. From 10 to 70 mbsf, grain density gradually increases to around 2.5 g/cm³ before remaining relatively constant at 2.5 g/cm³ below 70 mbsf. Sharp positive anomalies superimposed on the gradual increasing trend are observed at ~25 (Core 3H) and ~35 (Core 5H) mbsf, where high NGR values are observed at the same depth intervals.

Thermal Conductivity

Thermal conductivity measurements were conducted on sediment in whole-round cores using the needle-probe method and on working half cores using the half-space method (see “Methods” chapter). A total of 27 thermal conductivity values were obtained. At depths of less than 75 mbsf, the mean value of thermal conductivity is 0.66 W/(m·K). Below 75 mbsf the core has a very porous structure consisting of pumice breccia, and thermal conductivity values are 0.9 and 1.2 W/(m·K).

Discrete P-wave velocity and anisotropy measurements

P-wave velocity and relative anisotropy were measured only when samples were sufficiently indurated to cut sample polyhedrons, which was rare. At Hole C9021B, P-wave velocity was determined from only 1 discrete sample, and the mean value of the x ,

y and z-axes is 3592 m/s.

Unconfined compressive strength

Unconfined compressive strengths of pumiceous gravels exhibit considerable scatter and range from 80 to 260 kPa. Strengths for sandy layers and clay matrix, developed in units 3H (~25 mbsf) and 5H (~ 40 mbsf), are lower than for surrounding pumiceous sand and gravel layers. Volcanic rocks found at depths below 70 mbsf are too hard to measure the strength using the penetrometer.

Portable X-ray fluorescence

At site C9021, most of the major elements show homogeneous values from 0.6 mbsf (core 1H) to 55.3 mbsf (core 6H) except in specific cases such as the measurement of mineral fragments (shown as **Fig. 5-3-4-4**). Si content generally shows high values (24.1-33.8 wt %), while Al (0-5.4 wt %), Ca (0.3-3.7 wt %) and S (0.6-3.5 wt %) contents have low values due to the presence of a thick pumice layer. Ca content often shows a sharp increase, reflecting a Ca-rich mineral being included in the measurement position. Fe contents are high between cores 7H and 8H, corresponding to the distribution of a clay-like greenish mineral.

Resistivity

For depths of 0 to 70 mbsf, bulk resistivity values fall around 0.5 Ohm·m, before increasing below 70 mbsf.

5.3.5 Site C9023

At Site C9023, measurements of physical properties were made in order to help characterize the lithostratigraphic units. **Fig. 5-3-5-1** plots magnetic susceptibility, natural gamma ray radiation, gamma ray attenuation density, GRA porosity from the MSCL-W, bulk density, porosity, and grain density from MAD measurements, and DER from the spectroscopic detector. **Fig. 5-3-5-2** plots thermal conductivity, resistivity, P-wave velocity, and unconfined compressive strength. **Fig. 5-3-5-3** plots element concentrations from pXRF measurements. **Tables 5-3-5-1, -2 and -3** show all of the MSCL-W, MAD, and DER data sets. **Table 5-3-5-4** shows the thermal conductivity data. **Table 5-3-5-5** shows resistivity data. **Table 5-3-5-6** shows P-wave velocity data. **Table 5-3-5-7** shows unconfined compressive strength data. **Table 5-3-5-8** shows the pXRF data.

Coring in C9023D was generally handled using aluminum liner, but core sections from the core catcher were placed in plastic liner. Magnetic susceptibility was therefore measured only for core samples in the core catcher. Magnetic susceptibility and GRA density were highly variable among each core unit. Shallower portions are composed of several-cm size conglomerates without matrix, and deeper portions are composed of rock fragments filled with fine grained matrix. Therefore, the variations in physical properties are probably caused by the filling rate of sediments in the liner and lithological variation.

MSCL-W and MAD

Magnetic susceptibility

Magnetic susceptibility values are highly variable within core units. On the whole, magnetic susceptibility values are lower in the shallower part than in the deeper part within the same core catcher section. This trend is probably explained by the variation in filling rate of core samples in the section. The overall variation of magnetic susceptibility with depth is not clear, ranging from approximately 0 to 100×10^{-5} SI in the majority of sections, but with a very high susceptibility value of $\sim 190 \times 10^{-5}$ SI observed at ~ 119 mbsf (Hole B Core 16X-CC).

Natural gamma radiation

NGR values for sediment near the seafloor range between 13 and 38 cps in Hole B, and are >150 cps in Hole D. The highest counts, around 430 cps, are observed within Core 2H-2 in Hole D. NGR counts decrease with depth from 10 to 125 mbsf and increase again from 135 to 144 mbsf. Below 172 mbsf, the value is relatively low, ranging from 16 to 40 cps. The depth distribution of the dose rate measured by the spectroscopic radiation detector is similar to the NGR distribution measured by MSCL-W, and the highest rate, $0.08 \mu\text{Sv/h}$, is observed within Core 2H-2 in Hole D at 13 mbsf.

Density and porosity

GRA densities determined from whole-round GRA measurements are highly variable within core units, ranging from 1 to 2.8 g/cm^3 . However, the maximum GRA densities within each core interval and the wet bulk density values determined from discrete samples agree well.

Grain density is highly variable at shallow depths above 33 mbsf (Core 5H in Hole D). The grain densities of black ore, yellow ore, and siliceous hydrothermal clay near the seafloor in Hole B (Core 1X-CC) are 4.7 , 3.7 and 3.3 g/cm^3 , respectively. Relatively high grain density around 3.4 to 3.8 g/cm^3 is observed at depths of 10 to 32 mbsf, although

low grain density below 3.0 g/cm^3 was also observed at the same depth (Hole D, Core 2X to 5X). Grain density decreases slightly with depth from 50 to 120 mbsf, and is more variable below 120 mbsf. The lowest grain density of 2.56 g/cm^3 is observed at 190 mbsf. From the seafloor to 23 mbsf, porosity shows scattered values, and porosity of black (22 %) and yellow (12 %) ores is smaller than that of siliceous clay (50 %) near the seafloor in Hole B. Porosity shows little variation with depth from 42 to 50 mbsf, and then decreases from 50 to 12 % with depth. Below 119 mbsf, porosity increases with depth, and a siltstone at 144 mbsf shows high porosity (around 60 %). Porosity values scatter below 150 mbsf, and the lowest porosity, 6 %, in site C2023 is observed at 190 mbsf.

Thermal Conductivity

Thermal conductivity measurements were conducted on sediment on whole-round cores using the needle-probe method and on working half cores using the half-space method (see “Methods” chapter). A total of 30 thermal conductivity values were obtained at Site C9023. Thermal conductivity values, on the whole, increase with depth from 0.309 at the seafloor to $4.491 \text{ Wm}^{-1}\text{K}^{-1}$ by 125 mbsf at the boundary of Hole D and Hole E where greenish colored core appeared. Below a depth of 135 mbsf in Hole E, thermal conductivity values are less than the values of Hole D. The mean value of thermal conductivity between depths of 135 and 200 mbsf is $1.45 \text{ Wm}^{-1}\text{K}^{-1}$. Thermal conductivity shows an inverse correlation with porosity.

Resistivity

Overall, most of the measured resistivity values plot in a range between 1 and 10 $\text{Ohm}\cdot\text{m}$. The bulk resistivity steadily increases with depth from 0.3 $\text{Ohm}\cdot\text{m}$ to $\sim 10 \text{ Ohm}\cdot\text{m}$ between 0 and 130 mbsf, while there is a significant drop in resistivity to 1 $\text{Ohm}\cdot\text{m}$ around 130 mbsf. Below 130 mbsf, the resistivity tends to increase once more.

Discrete P-wave velocity and anisotropy measurements

P-wave velocity and relative anisotropy were measured only on discrete samples that were consolidated enough to cut sample polyhedrons, which were rarely obtained. At Site C9023, 15 P-wave velocity data were obtained, and all the samples used for P-wave velocity measurements were shared with resistivity measurements. The lowest value (1,656 m/s) of this site was obtained at 153 mbsf, while the highest value (5,138 m/s) was measured at 190 mbsf. The depth variation of P-wave velocity at this site shows similar variations to the depth variations seen in the thermal conductivity and porosity data.

Unconfined compressive strength

Unconfined compressive strength data exhibit considerable scatter, ranging from 50 to 150 kPa, for depths of 0 to 70 mbsf. Below 70 mbsf, rock blocks were too hard to measure their strength using the penetrometer.

Portable X-ray fluorescence

At Hole B of site C9023, there are three measurement points from core CC. Two of them (0 and 0.1 mbsf, respectively) show high S content and low Ca and Fe content. Here, the core is influenced not by iron sulfide and sulfosalt, but by non-ferrous sulfides such as sphalerite and galena. The other data (0.2 mbsf) were obtained from an area containing altered clay minerals and show relatively high Al, Ca and Fe contents.

At Hole D, major elements indicate three clear trends from the top to the bottom of the core (shown as **Table 5-3-5-8**). Firstly, Si content (1.0-36.9 wt %) increases from top to bottom, whereas Fe (0.8-21.1 wt %), Ca (0.1-20.7 wt %), and S (0.5-47.7 wt %) contents decrease from top to bottom. Meanwhile, Al (0-8.6 wt %) and K (0-11.1 wt %) contents mainly show high values between core 9X and 10X. These trends are mainly influenced by the variation in rock facies.

Many major elements show high contents between core 2X and 6X, Hole E. Fe (1.2-23.8 wt %), Ca (0.1-13.8 wt %), K (0-22.1 wt %), and S (0.4-36.6 wt %) contents are influenced in particular by the inclusion of sulfide, sulfosalt and the greenish clay mineral. Si content shows generally high values (5.8-33.3 wt %) except in sulfide dominant zones, and is associated with the presence of altered volcanic rock segments.

Reference:

- Blum, P., 1997. Physical properties handbook: a guide to the shipboard measurement of physical properties of deep-sea cores. ODP Tech. Note, 26. doi:10.2973/odp.tn.26.1997
- Revil, A., Cathles III, L.M., Losh, S., 1998. Electrical conductivity in shaly sands with geophysical applications. *J. Geophys. Res.* 103 (B10), 23925–23936. <http://dx.doi.org/10.1029/98JB02125>.
- Von Herzen, R.P., and Maxwell, A.E., 1959. The measurement of thermal conductivity of deep-sea sediments by a needle-probe method. *J. Geophys. Res.*, 64(10):1557–1563. doi:10.1029/JZ064i010p01557.
- Vacquier, V., 1985. The measurement of thermal conductivity of solids with a transient linear heat source on the plane surface of a poorly conducting body. *Earth Planet. Sci. Lett.*, 74(2–3):275–279. doi:10.1016/0012-821X(85)90027-5
- Waples, D., and J. Waples (2004), A Review and Evaluation of Specific Heat Capacities of Rocks, Minerals, and Subsurface Fluids. Part 1: Minerals and Nonporous Rocks, *Nat. Resour. Res.*, 13(2), 97–122, doi:10.1023/B:NARR.0000032647.41046.e7.

Captions:

Table 5-3-1-1 Sampling intervals of physical property measurements. Analyses are conducted on whole round core sample, working half of split core, or archive half of split core according to the property type and condition of the sample.

Table 5-3-1-2 Preferred values for the rock standards used to compare with the value from pXRF analyses.

Table 5-3-2-1 Magnetic susceptibility, natural gamma radiation (NGR), gamma ray attenuation (GRA) density, and porosity calculated from GRA density from the MSCL-W for Hole B and C at Site 9017.

Table 5-3-2-2 Data from moisture and density (MAD) measurements on discrete samples for Hole B and C at Site 9017.

Table 5-3-2-3 Data from DER measurements for Hole B and C at Site 9017.

Table 5-3-2-4 Data from thermal conductivity measurements on whole-round core/working half samples of Hole B and C at Site 9017.

Table 5-3-2-5 Data from resistivity measurements on working half samples/discrete samples for Hole B and C at Site 9017.

Table 5-3-2-6 Data from P-wave velocity measurements on discrete samples for Hole B and C at Site 9017.

Table 5-3-2-7 Data from unconfined compressive strength measurements on working half samples for Hole B and C at Site 9017.

Table 5-3-2-8 Data from pXRF measurements for Hole B and C at Site 9017.

Table 5-3-3-1 Magnetic susceptibility, natural gamma radiation (NGR), gamma ray attenuation (GRA) density, and porosity calculated from GRA density from the MSCL-W for Hole B and C at Site C9019.

Table 5-3-3-2 Data from moisture and density (MAD) measurements on discrete samples

for Hole B and C at Site C9019.

Table 5-3-3-3 Data from DER measurements for Hole B and C at Site C9019.

Table 5-3-3-4 Data from thermal conductivity measurements on whole-round core for Hole B and C at Site C9019.

Table 5-3-3-5 Data from resistivity measurements on working half of core/discrete samples for Hole B and C at Site C9019.

Table 5-3-3-6 Data from unconfined compressive strength measurements on working half of core for Hole B and C at Site C9019.

Table 5-3-3-7 Data from pXRF measurements at Hole B and C at Site C9019.

Table 5-3-4-1 Magnetic susceptibility, natural gamma radiation (NGR), gamma ray attenuation (GRA) density, and porosity calculated from GRA density from the MSCL-W for Hole B at Site C9021.

Table 5-3-4-2 Data from moisture and density (MAD) measurements on discrete samples for Hole B at Site C9021.

Table 5-3-4-3 Data from DER measurements for Hole B at Site C9021.

Table 5-3-4-4 Data from thermal conductivity on whole-round core/working half of core for Hole B at Site C9021.

Table 5-3-4-5 Data from resistivity measurements on working half of core/discrete samples for Hole B at Site C9021.

Table 5-3-4-6 Data from P-wave velocity measurements on discrete samples for Hole B at Site C9021.

Table 5-3-4-7 Data from unconfined compressive strength measurements on working half samples for Hole B at Site C9021.

Table 5-3-4-8 Data from pXRF on archive half of core for Hole B at Site C9021.

Table 5-3-5-1 Magnetic susceptibility, natural gamma radiation (NGR), gamma ray attenuation (GRA) density, and porosity calculated from GRA density from the MSCL-W for Hole B, D and E at Site 9023.

Table 5-3-5-2 Data from moisture and density (MAD) measurements on discrete samples for Hole B, D and E at Site 9023.

Table 5-3-5-3 Data from DER measurements for Hole B, D and E at Site 9023.

Table 5-3-5-4 Data from thermal conductivity on whole-round core/working half of core for Hole B, D and E at Site 9023.

Table 5-3-5-5 Data from resistivity measurements on working half of core/discrete samples for Hole B, D and E at Site 9023.

Table 5-3-5-6 Data from P-wave velocity measurements on discrete samples for Hole B, D and E at Site 9023.

Table 5-3-5-7 Data from unconfined compressive strength measurements on working half samples for Hole B, D and E at Site 9023.

Table 5-3-5-8 Data from pXRF on archive half of core for Hole B, D and E at Site 9023.

Fig. 5-3-1-1 Photo image of DER and spectra measurements undertaken using the personal spectrometer on the working-half of split core samples. Measurements are conducted for 30 min at the same position to measure the scintillation spectra.

Fig. 5-3-1-2 Photo image of pXRF measurement being performed on archive halves. Insulation sheets are laid on the table for archive halves to protect people from exposure to radioactivity.

Fig. 5-3-1-3 pXRF data for element concentrations of reference materials, plotted against their known concentrations or concentrations measured using XRF for comparison.

Fig. 5-3-2-1 Magnetic susceptibility, natural gamma ray radiation, gamma ray attenuation (GRA) density, GRA porosity from the MSCL-W, bulk density, porosity, and grain density measured on discrete samples using moisture and density (MAD) measurements, and DER measured on working half of split core using the spectroscopic detector for Hole C at Site C9017.

Fig. 5-3-2-2 Thermal conductivity, resistivity, P-wave velocity, and unconfined compressive strength measurements on whole-round core/working half of split core for Hole C at Site C9017.

Fig. 5-3-2-3 Concentration of major elements from pXRF measurements on archive half of split core for Hole C at Site C9017.

Fig. 5-3-2-4 Correlation between the samples before and after soaking for 24 h at each site.

Fig. 5-3-3-1 Magnetic susceptibility, natural gamma ray radiation, gamma ray attenuation (GRA) density, GRA porosity from the MSCL-W, bulk density, porosity, and grain density measured on discrete samples using moisture and density (MAD) measurements, and DER measured on the working half of split cores using the spectroscopic detector for Hole B and Hole C at Site C9019.

Fig. 5-3-3-2 Thermal conductivity, resistivity, and unconfined compressive strength measurements on whole-round core/working half of split core for Hole C at Site C9019.

Fig. 5-3-3-3 pXRF measurements on the archive half of split core for Hole C at Site C9019.

Fig. 5-3-4-1 Magnetic susceptibility, natural gamma ray radiation, gamma ray attenuation (GRA) density, GRA porosity from the MSCL-W, bulk density, porosity, and grain density measured on discrete samples using moisture and density (MAD) measurements, and DER measured on the working half of split cores using the spectroscopic detector for Hole B and C at Site C9021.

Fig. 5-3-4-2 Thermal conductivity, resistivity, P-wave velocity, and unconfined

compressive strength measurements on whole-round core/working half of split core for Hole B and C at Site C9021.

Fig. 5-3-4-3 pXRF measurements on the archive half of split cores for Hole B and C at Site C9021.

Fig. 5-3-4-4 Mineral fragment in pumice from section 8 of core 3H of Hole B at Site C9021.

Fig. 5-3-5-1 Magnetic susceptibility, natural gamma ray radiation, gamma ray attenuation (GRA) density, GRA porosity from the MSCL-W, bulk density, porosity, and grain density measured on discrete samples using moisture and density (MAD) measurements, and DER measured on the working half of split cores using the spectroscopic detector for Hole B, D, and E at Site C9023.

Fig. 5-3-5-2 Thermal conductivity, resistivity, P-wave velocity, and unconfined compressive strength measurements on whole-round core/working half of split core for Hole B, D and E at Site C9023.

Fig. 5-3-5-3 pXRF measurements on the archive half of split cores for Hole B, D and E at Site C9023.

Table 5-3-1-1

Physical property		Whole round	Working half	Archive half	Remark
MSCL-W	GRA and MS	4 cm interval			MS measurement is skipped when aluminum liner is used
	NGR	16 cm interval			Interval changes to 8 or 4 cm when core recovery is low
Thermal conductivity		1 - 2/core	1 - 2/core		
Moisture and Density			2 - 3/core		
Impedance analysis			2 - 3/core		3rd party tool
P-wave analysis			2 - 3/core		Samples were used for impedance analysis before measurement
Penetration strength			2 - 3/core		
Dosimetry			1 - 2/core		3rd party tool
Portable XRF				2 - 3/core	3rd party tool, near MAD sampling and location requested by VCD's team

Table 5-3-1-2

	JGb-1	JH-1	JSy-1	JF-1	JG-2	JR-3	JF-2	JA-1	JB-1b
Major element oxide (wt%)									
SiO ₂	43.66	48.18	60.02	66.69	76.83	72.76	65.3	63.97	51.11
TiO ₂	1.6	0.67	0.0015	0.005	0.044	0.21	0.005	0.85	1.26
Al ₂ O ₃	17.49	5.66	23.17	18.08	12.47	11.9	18.52	15.22	14.38
MnO	0.189	0.19	0.0024	0.001	0.016	0.083	0.001	0.157	0.147
MgO	7.85	16.73	0.016	0.006	0.037	0.05	0.004	1.57	8.14
CaO	11.9	15.02	0.25	0.93	0.7	0.093	0.09	5.7	9.6
Na ₂ O	1.2	0.71	10.74	3.37	3.54	4.69	2.39	3.84	2.63
K ₂ O	0.24	0.53	4.82	9.99	4.71	4.29	12.94	0.77	1.32
P ₂ O ₅	0.056	0.099	0.014	0.01	0.002	0.017	0.003	0.165	0.256
T-Fe ₂ O ₃	15.06	10.27	0.084	0.08	0.97	4.72	0.06	7.07	9.02
Trace element (ppm)									
Zn	109	61.8	3.2	4.41	13.6	209	1.4	90.9	0
Rb	6.87	14.4	66.3	266	301	453	218	12.3	39.1
Sr	0	153	19.3	172	17.9	10.4	200	263	0
Zr	0	48.3	70.2	38.6	97.6	1494	6.73	88.3	0

Table 5-3-2-1

Location	Subbottom Depth	GRA ¹⁾	MS ²⁾	NGR ³⁾	GRA Porosity
	[mbsf]	[g/cm ³]	[x10 ⁻⁵ SI]	[cps]	
C9017C-1X-1, 8.0 cm	0.08	1.0039	11.3546	6.199	1.012
C9017C-1X-CC, 1.7 cm	0.122	0.4195	11.3256		1.372
C9017C-1X-CC, 5.7 cm	0.162	0.5449	19.9065	13.199	1.295
C9017C-1X-CC, 9.7 cm	0.202	0.9928	29.2236		1.019
C9017C-1X-CC, 13.7 cm	0.242	1.4858	75.5842	14.1	0.716
C9017C-1X-CC, 17.7 cm	0.282	1.3543	134.452		0.797
C9017C-1X-CC, 21.7 cm	0.322	1.3263	116.8296	13.199	0.814
C9017C-1X-CC, 25.7 cm	0.362	1.5585	124.338		0.671
C9017C-1X-CC, 29.7 cm	0.402	2.0495	149.4094	18	0.369
C9017C-1X-CC, 33.7 cm	0.442	2.0038	152.1341		0.397
C9017C-1X-CC, 37.7 cm	0.482	2.1188	69.3281	14.865	0.326
C9017C-2X-1, 8.0 cm	9.58	1.2993	11.8142		0.830
C9017C-2X-1, 12.0 cm	9.62	1.5762	17.5323		0.660
C9017C-2X-1, 16.0 cm	9.66	1.0456	26.3418	23.766	0.987
C9017C-2X-1, 20.0 cm	9.7	1.7739	46.4443		0.538
C9017C-2X-1, 24.0 cm	9.74	1.4321	37.4152		0.749
C9017C-2X-1, 28.0 cm	9.78	1.7902	38.9977		0.528
C9017C-2X-1, 32.0 cm	9.82	1.1399	24.8573	9.766	0.929
C9017C-2X-1, 36.0 cm	9.86	1.0613	16.1403		0.977
C9017C-2X-CC, 1.8 cm	9.898	1.9205	8.9125		0.448
C9017C-2X-CC, 5.8 cm	9.938	1.7784	13.8037		0.535
C9017C-2X-CC, 9.8 cm	9.978	1.8215	22.8032	27.299	0.509
C9017C-2X-CC, 13.8 cm	10.018	0.8354	10.786		1.116
C9017C-2X-CC, 17.8 cm	10.058	1.8307	8.2686		0.503
C9017C-2X-CC, 21.8 cm	10.098	1.8504	17.152		0.491
C9017C-2X-CC, 25.8 cm	10.138	1.5054	29.3086	21.232	0.704
C9017C-2X-CC, 29.8 cm	10.178	1.8323	19.865		0.502
C9017C-2X-CC, 33.8 cm	10.218	1.9175	42.317		0.450
C9017C-2X-CC, 37.8 cm	10.258	2.0257	58.2753		0.383
C9017C-3X-1, 8.0 cm	19.08	1.9167	35.0296		0.450
C9017C-3X-1, 12.0 cm	19.12	1.5874	22.516		0.653
C9017C-3X-1, 16.0 cm	19.16	1.8688	4.1149	75.533	0.480
C9017C-3X-1, 20.0 cm	19.2	1.6751	2.0601		0.599
C9017C-3X-1, 24.0 cm	19.24	1.847	1.3664		0.493
C9017C-3X-1, 28.0 cm	19.28	1.7574	1.3582		0.548
C9017C-3X-1, 32.0 cm	19.32	1.9051	2.0382	62.867	0.457
C9017C-3X-1, 36.0 cm	19.36	1.7008	0.6734		0.583
C9017C-3X-1, 40.0 cm	19.4	1.8187	0.6754		0.511
C9017C-3X-1, 44.0 cm	19.44	1.8838	1.3594		0.471
C9017C-3X-1, 48.0 cm	19.48	1.8378	1.3456	53.9	0.499
C9017C-3X-1, 52.0 cm	19.52	1.7849	0.6734		0.531
C9017C-3X-1, 56.0 cm	19.56	1.7622	1.3427		0.545
C9017C-3X-1, 60.0 cm	19.6	1.6995	0.6876		0.584
C9017C-3X-1, 64.0 cm	19.64	1.739	0.682	57.999	0.560
C9017C-3X-1, 68.0 cm	19.68	1.8299	1.3646		0.504
C9017C-3X-1, 72.0 cm	19.72	1.699	0.678		0.584
C9017C-3X-1, 76.0 cm	19.76	1.8079	0.6716		0.517
C9017C-3X-1, 80.0 cm	19.8	1.7347	0.6666	57.334	0.562
C9017C-3X-1, 84.0 cm	19.84	1.7851	0.6714		0.531
C9017C-3X-1, 88.0 cm	19.88	1.814	0		0.514
C9017C-3X-1, 92.0 cm	19.92	1.7317	0.6797		0.564
C9017C-3X-1, 96.0 cm	19.96	1.6745	0.6621	42.6	0.599

Table 5-3-2-1

Location	Subbottom Depth	GRA ¹⁾	MS ²⁾	NGR ³⁾	GRA Porosity
	[mbsf]	[g/cm ³]	[x10 ⁻⁵ SI]	[cps]	
C9017C-3X-1, 100.0 cm	20	0.65	0.6321		1.230
C9017C-3X-2, 3.2 cm	20.037	1.7711	0		0.540
C9017C-3X-2, 7.2 cm	20.077	1.7901	0.6716		0.528
C9017C-3X-2, 11.2 cm	20.117	1.8191	0.6734	48.166	0.510
C9017C-3X-2, 15.2 cm	20.157	1.7528	1.3704		0.551
C9017C-3X-2, 19.2 cm	20.197	1.8314	1.3734		0.503
C9017C-3X-2, 23.2 cm	20.237	1.8127	1.3669		0.514
C9017C-3X-2, 27.2 cm	20.277	1.6426	2.0425	49	0.619
C9017C-3X-2, 31.2 cm	20.317	1.7499	2.0663		0.553
C9017C-3X-2, 35.2 cm	20.357	1.7527	1.3734		0.551
C9017C-3X-2, 39.2 cm	20.397	1.8624	0.6794		0.484
C9017C-3X-2, 43.2 cm	20.437	1.7937	0.6829	49.5	0.526
C9017C-3X-2, 47.2 cm	20.477	1.7	0		0.584
C9017C-3X-2, 51.2 cm	20.517	1.5899	0.6791		0.652
C9017C-3X-2, 55.2 cm	20.557	1.8278	0.6841		0.505
C9017C-3X-2, 59.2 cm	20.597	1.8148	0.6947	49.066	0.513
C9017C-3X-2, 63.2 cm	20.637	1.6216	0		0.632
C9017C-3X-2, 67.2 cm	20.677	1.7375	0.678		0.561
C9017C-3X-2, 71.2 cm	20.717	1.8187	0.6716		0.511
C9017C-3X-2, 75.2 cm	20.757	1.8338	0.6817	60.066	0.501
C9017C-3X-2, 79.2 cm	20.797	1.8748	0.6893		0.476
C9017C-3X-2, 83.2 cm	20.837	1.8741	1.3605		0.477
C9017C-3X-2, 87.2 cm	20.877	1.8962	1.3444		0.463
C9017C-3X-2, 91.2 cm	20.917	1.9252	2.0081	71.534	0.445
C9017C-3X-2, 95.2 cm	20.957	1.8844	2.0487		0.470
C9017C-3X-2, 99.2 cm	20.997	1.5675	-0.6411		0.665
C9017C-3X-3, 2.0 cm	21.035	0.5824	1.2658		1.272
C9017C-3X-3, 6.0 cm	21.075	2.0393	3.3229	78.7	0.375
C9017C-3X-3, 10.0 cm	21.115	2.0006	5.4029		0.399
C9017C-3X-3, 14.0 cm	21.155	1.9281	5.3983		0.443
C9017C-3X-3, 18.0 cm	21.195	1.9443	5.4375		0.433
C9017C-3X-3, 22.0 cm	21.235	1.9059	4.7782	94.534	0.457
C9017C-3X-3, 26.0 cm	21.275	1.9159	2.7339		0.451
C9017C-3X-3, 30.0 cm	21.315	1.9011	2.0081		0.460
C9017C-3X-3, 34.0 cm	21.355	1.9376	2.6934		0.437
C9017C-3X-3, 38.0 cm	21.395	1.8843	2.0373	55.267	0.470
C9017C-3X-3, 42.0 cm	21.435	-0.0579	0.6841		1.666
C9017C-3X-3, 46.0 cm	21.475	0.6564	3.3797		1.226
C9017C-3X-3, 50.0 cm	21.515	1.856	2.713		0.488
C9017C-3X-3, 54.0 cm	21.555	1.8054	2.713	84.866	0.519
C9017C-3X-3, 58.0 cm	21.595	1.8337	2.0601		0.501
C9017C-3X-3, 62.0 cm	21.635	1.8638	2.0769		0.483
C9017C-3X-3, 66.0 cm	21.675	1.7831	1.3799		0.533
C9017C-3X-3, 70.0 cm	21.715	1.8057	2.0627	61.266	0.519
C9017C-3X-3, 74.0 cm	21.755	1.8446	2.0434		0.495
C9017C-3X-3, 78.0 cm	21.795	2.0133	2.7084		0.391
C9017C-3X-3, 82.0 cm	21.835	1.9865	2.7292		0.407
C9017C-3X-3, 86.0 cm	21.875	2.0443	3.4101	61.633	0.372
C9017C-3X-3, 90.0 cm	21.915	1.9936	2.7444		0.403
C9017C-3X-3, 94.0 cm	21.955	2.0292	2.6946		0.381
C9017C-3X-3, 98.0 cm	21.995	0.3108	1.257		1.439
C9017C-3X-4, 1.1 cm	22.031	2.055	3.7786	47.1	0.365

Table 5-3-2-1

Location	Subbottom Depth	GRA ¹⁾	MS ²⁾	NGR ³⁾	GRA Porosity
	[mbsf]	[g/cm ³]	[x10 ⁻⁵ SI]	[cps]	
C9017C-3X-4, 5.1 cm	22.071	2.0801	4.6189		0.350
C9017C-3X-4, 9.1 cm	22.111	2.081	6.0423		0.349
C9017C-3X-4, 13.1 cm	22.151	2.3553	7.4227		0.180
C9017C-3X-4, 17.1 cm	22.191	2.3354	8.0769	62.434	0.192
C9017C-3X-4, 21.1 cm	22.231	2.1161	6.7998		0.328
C9017C-3X-4, 25.1 cm	22.271	1.868	2.7107		0.480
C9017C-3X-4, 29.1 cm	22.311	1.8414	2.0399		0.497
C9017C-3X-4, 33.1 cm	22.351	1.6151	2.0149	154.867	0.636
C9017C-3X-4, 37.1 cm	22.391	1.7415	2.0382		0.558
C9017C-3X-4, 41.1 cm	22.431	1.8084	1.3553		0.517
C9017C-3X-4, 45.1 cm	22.471	1.8328	2.698		0.502
C9017C-3X-4, 49.1 cm	22.511	2.0638	2.7061	150.9	0.360
C9017C-3X-4, 53.1 cm	22.551	1.8793	2.7468		0.473
C9017C-3X-4, 57.1 cm	22.591	1.8858	2.0417		0.469
C9017C-3X-4, 61.1 cm	22.631	1.7434	0.6782		0.557
C9017C-3X-4, 65.1 cm	22.671	1.8043	0.6896	108.633	0.520
C9017C-3X-4, 69.1 cm	22.711	1.753	0.6896		0.551
C9017C-3X-4, 73.1 cm	22.751	1.5272	0		0.690
C9017C-3X-4, 77.1 cm	22.791	1.5028	0		0.705
C9017C-3X-4, 81.1 cm	22.831	1.5756	0	49.467	0.660
C9017C-3X-4, 85.1 cm	22.871	1.5842	0		0.655
C9017C-3X-4, 89.1 cm	22.911	1.5709	0.6759		0.663
C9017C-3X-4, 93.1 cm	22.951	1.812	0.668		0.515
C9017C-3X-4, 97.1 cm	22.991	1.752	1.3399	39.667	0.552
C9017C-3X-4, 101.1 cm	23.031	0.5933	1.958		1.265
C9017C-4H-1, 8.0 cm	24.08	-0.0666			1.672
C9017C-4H-1, 12.0 cm	24.12	-0.0447			1.658
C9017C-4H-1, 16.0 cm	24.16	-0.0568		-0.734	1.666
C9017C-4H-1, 20.0 cm	24.2	-0.0542			1.664
C9017C-4H-1, 24.0 cm	24.24	-0.059			1.667
C9017C-4H-1, 28.0 cm	24.28	-0.0174			1.641
C9017C-4H-1, 32.0 cm	24.32	0.2713		-0.334	1.463
C9017C-4H-1, 36.0 cm	24.36	-0.059			1.667
C9017C-4H-1, 40.0 cm	24.4	0.3798			1.397
C9017C-4H-1, 44.0 cm	24.44	0.2757			1.461
C9017C-4H-1, 48.0 cm	24.48	0.0042		0.801	1.628
C9017C-4H-1, 52.0 cm	24.52	-0.0647			1.670
C9017C-4H-1, 56.0 cm	24.56	-0.0617			1.669
C9017C-4H-1, 60.0 cm	24.6	-0.0569			1.666
C9017C-4H-1, 64.0 cm	24.64	-0.0564		-5.767	1.665
C9017C-4H-1, 68.0 cm	24.68	-0.0538			1.664
C9017C-4H-1, 72.0 cm	24.72	-0.0579			1.666
C9017C-4H-1, 76.0 cm	24.76	-0.0613			1.668
C9017C-4H-1, 80.0 cm	24.8	0.0943		-2.267	1.572
C9017C-4H-1, 84.0 cm	24.84	0.0742			1.585
C9017C-4H-1, 88.0 cm	24.88	0.4011			1.384
C9017C-4H-1, 92.0 cm	24.92	0.0098			1.625
C9017C-4H-1, 96.0 cm	24.96	0.0197		-0.9	1.618
C9017C-4H-1, 100.0 cm	25	-0.0065			1.635
C9017C-4H-2, 2.7 cm	25.037	-0.0312			1.650
C9017C-4H-2, 6.7 cm	25.077	-0.0623			1.669
C9017C-4H-2, 10.7 cm	25.117	-0.0493		0.167	1.661

Table 5-3-2-1

Location	Subbottom Depth	GRA ¹⁾	MS ²⁾	NGR ³⁾	GRA Porosity
	[mbsf]	[g/cm ³]	[x10 ⁻⁵ SI]	[cps]	
C9017C-4H-2, 14.7 cm	25.157	0.0772			1.583
C9017C-4H-2, 18.7 cm	25.197	0.1804			1.519
C9017C-4H-2, 22.7 cm	25.237	0.3815			1.396
C9017C-4H-2, 26.7 cm	25.277	0.9545		7.366	1.043
C9017C-4H-2, 30.7 cm	25.317	0.6324			1.241
C9017C-4H-2, 34.7 cm	25.357	1.4092			0.763
C9017C-4H-2, 38.7 cm	25.397	1.3157			0.820
C9017C-4H-2, 42.7 cm	25.437	1.1468		9.199	0.924
C9017C-4H-2, 46.7 cm	25.477	1.0524			0.983
C9017C-4H-2, 50.7 cm	25.517	1.155			0.919
C9017C-4H-2, 54.7 cm	25.557	0.9979			1.016
C9017C-4H-2, 58.7 cm	25.597	0.9709		9.599	1.033
C9017C-4H-2, 62.7 cm	25.637	0.7505			1.168
C9017C-4H-2, 66.7 cm	25.677	1.074			0.969
C9017C-4H-2, 70.7 cm	25.717	0.5619			1.285
C9017C-4H-2, 74.7 cm	25.757	0.6574		3.332	1.226
C9017C-4H-2, 78.7 cm	25.797	0.532			1.303
C9017C-4H-2, 82.7 cm	25.837	0.6838			1.209
C9017C-4H-2, 86.7 cm	25.877	0.6131			1.253
C9017C-4H-2, 90.7 cm	25.917	0.4352		-3.6	1.363
C9017C-4H-2, 94.7 cm	25.957	0.4417			1.359
C9017C-4H-2, 98.7 cm	25.997	0.6777			1.213
C9017C-4H-3, 1.6 cm	26.031	1.0426			0.989
C9017C-4H-3, 5.6 cm	26.071	0.9912		0.466	1.020
C9017C-4H-3, 9.6 cm	26.111	0.9154			1.067
C9017C-4H-3, 13.6 cm	26.151	0.5444			1.295
C9017C-4H-3, 17.6 cm	26.191	0.9434			1.050
C9017C-4H-3, 21.6 cm	26.231	0.3333		-0.867	1.425
C9017C-4H-3, 25.6 cm	26.271	0.4736			1.339
C9017C-4H-3, 29.6 cm	26.311	0.3007			1.445
C9017C-4H-3, 33.6 cm	26.351	0.245			1.480
C9017C-4H-3, 37.6 cm	26.391	0.8542		2.233	1.105
C9017C-4H-3, 41.6 cm	26.431	0.3868			1.392
C9017C-4H-3, 45.6 cm	26.471	1.7428			0.557
C9017C-4H-3, 49.6 cm	26.511	1.1936			0.896
C9017C-4H-3, 53.6 cm	26.551	0.5878		2.666	1.269
C9017C-4H-3, 57.6 cm	26.591	0.4987			1.323
C9017C-4H-3, 61.6 cm	26.631	-0.0249			1.646
C9017C-4H-3, 65.6 cm	26.671	-0.0563			1.665
C9017C-4H-3, 69.6 cm	26.711	-0.0557		-7.333	1.665
C9017C-4H-3, 73.6 cm	26.751	-0.0496			1.661
C9017C-4H-3, 77.6 cm	26.791	-0.0502			1.661
C9017C-4H-3, 81.6 cm	26.831	-0.06			1.667
C9017C-4H-3, 85.6 cm	26.871	-0.058		-9.166	1.666
C9017C-4H-3, 89.6 cm	26.911	-0.0486			1.660
C9017C-4H-3, 93.6 cm	26.951	-0.0523			1.663
C9017C-4H-3, 97.6 cm	26.991	0.0126			1.623
C9017C-4H-4, 0.7 cm	27.027	0.2135		-3.9	1.499
C9017C-4H-4, 4.7 cm	27.067	0.0196			1.618
C9017C-4H-4, 8.7 cm	27.107	0.0206			1.618
C9017C-4H-4, 12.7 cm	27.147	-0.0353			1.652
C9017C-4H-4, 16.7 cm	27.187	0.2278		-4.267	1.490

Table 5-3-2-1

Location	Subbottom Depth	GRA ¹⁾	MS ²⁾	NGR ³⁾	GRA Porosity
	[mbsf]	[g/cm ³]	[x10 ⁻⁵ SI]	[cps]	
C9017C-4H-4, 20.7 cm	27.227	1.2643			0.852
C9017C-4H-4, 24.7 cm	27.267	0.5973			1.263
C9017C-4H-4, 28.7 cm	27.307	0.8097			1.132
C9017C-4H-4, 32.7 cm	27.347	1.1706		-4.433	0.910
C9017C-4H-4, 36.7 cm	27.387	0.9815			1.026
C9017C-4H-4, 40.7 cm	27.427	0.6632			1.222
C9017C-4H-4, 44.7 cm	27.467	0.6733			1.216
C9017C-4H-4, 48.7 cm	27.507	-0.0438		-11.534	1.658
C9017C-4H-4, 52.7 cm	27.547	0.0689			1.588
C9017C-4H-4, 56.7 cm	27.587	1.0138			1.006
C9017C-4H-4, 60.7 cm	27.627	0.9436			1.050
C9017C-4H-4, 64.7 cm	27.667	1.0424		-8.3	0.989
C9017C-4H-4, 68.7 cm	27.707	1.4052			0.765
C9017C-4H-4, 72.7 cm	27.747	1.7568			0.549
C9017C-4H-4, 76.7 cm	27.787	1.7161			0.574
C9017C-4H-4, 80.7 cm	27.827	1.4685		-3.633	0.726
C9017C-4H-4, 84.7 cm	27.867	1.4565			0.734
C9017C-4H-4, 88.7 cm	27.907	1.4558			0.734
C9017C-4H-4, 92.7 cm	27.947	1.5436			0.680
C9017C-4H-4, 96.7 cm	27.987	1.8601		-1.167	0.485
C9017C-4H-4, 100.7 cm	28.027	0.6326			1.241
C9017C-4H-5, 3.7 cm	28.062	1.9			0.461
C9017C-4H-5, 7.7 cm	28.102	1.7462			0.555
C9017C-4H-5, 11.7 cm	28.142	1.9644		1.667	0.421
C9017C-4H-5, 15.7 cm	28.182	1.9935			0.403
C9017C-4H-5, 19.7 cm	28.222	1.9969			0.401
C9017C-4H-5, 23.7 cm	28.262	1.9723			0.416
C9017C-4H-5, 27.7 cm	28.302	1.9689		1.866	0.418
C9017C-4H-5, 31.7 cm	28.342	1.8642			0.483
C9017C-4H-5, 35.7 cm	28.382	1.8422			0.496
C9017C-4H-5, 39.7 cm	28.422	1.904			0.458
C9017C-4H-5, 43.7 cm	28.462	1.9031		0.766	0.459
C9017C-4H-5, 47.7 cm	28.502	1.623			0.631
C9017C-4H-5, 51.7 cm	28.542	1.4468			0.740
C9017C-4H-5, 55.7 cm	28.582	1.1787			0.905
C9017C-4H-5, 59.7 cm	28.622	0.7064		-2.433	1.196
C9017C-4H-5, 63.7 cm	28.662	0.5861			1.270
C9017C-4H-5, 67.7 cm	28.702	0.7973			1.140
C9017C-4H-5, 71.7 cm	28.742	0.9827			1.025
C9017C-4H-5, 75.7 cm	28.782	0.5745		-7.099	1.277
C9017C-4H-5, 79.7 cm	28.822	0.6491			1.231
C9017C-4H-5, 83.7 cm	28.862	0.9271			1.060
C9017C-4H-5, 87.7 cm	28.902	-0.0221			1.644
C9017C-4H-5, 91.7 cm	28.942	0.7904		-6.834	1.144
C9017C-4H-5, 95.7 cm	28.982	1.0876			0.961
C9017C-4H-5, 99.7 cm	29.022	0.9088			1.071
C9017C-4H-6, 2.6 cm	29.056	0.7124			1.192
C9017C-4H-6, 6.6 cm	29.096	1.0101		-6.667	1.009
C9017C-4H-6, 10.6 cm	29.136	0.8031			1.136
C9017C-4H-6, 14.6 cm	29.176	1.1871			0.900
C9017C-4H-6, 18.6 cm	29.216	0.6989			1.200
C9017C-4H-6, 22.6 cm	29.256	1.4654		-5.499	0.728

Table 5-3-2-1

Location	Subbottom Depth	GRA ¹⁾	MS ²⁾	NGR ³⁾	GRA Porosity
	[mbsf]	[g/cm ³]	[x10 ⁻⁵ SI]	[cps]	
C9017C-4H-6, 26.6 cm	29.296	1.4416			0.743
C9017C-4H-6, 30.6 cm	29.336	1.249			0.861
C9017C-4H-6, 34.6 cm	29.376	1.4469			0.740
C9017C-4H-6, 38.6 cm	29.416	1.497		-4.8	0.709
C9017C-4H-6, 42.6 cm	29.456	1.319			0.818
C9017C-4H-6, 46.6 cm	29.496	0.801			1.137
C9017C-4H-6, 50.6 cm	29.536	1.7073			0.579
C9017C-4H-6, 54.6 cm	29.576	1.6862		-3.433	0.592
C9017C-4H-6, 58.6 cm	29.616	1.7562			0.549
C9017C-4H-6, 62.6 cm	29.656	1.7529			0.551
C9017C-4H-6, 66.6 cm	29.696	1.7065			0.580
C9017C-4H-6, 70.6 cm	29.736	1.7401		0.133	0.559
C9017C-4H-6, 74.6 cm	29.776	1.7558			0.549
C9017C-4H-6, 78.6 cm	29.816	1.7612			0.546
C9017C-4H-6, 82.6 cm	29.856	1.7018			0.583
C9017C-4H-6, 86.6 cm	29.896	1.7531		0.5	0.551
C9017C-4H-6, 90.6 cm	29.936	1.7477			0.554
C9017C-4H-6, 94.6 cm	29.976	1.4357			0.746
C9017C-4H-6, 98.6 cm	30.016	1.5638			0.668
C9017C-4H-7, 1.8 cm	30.053	1.6201		-1.667	0.633
C9017C-4H-7, 5.8 cm	30.093	1.4607			0.731
C9017C-4H-7, 9.8 cm	30.133	1.6075			0.641
C9017C-4H-7, 13.8 cm	30.173	1.5962			0.648
C9017C-4H-7, 17.8 cm	30.213	1.5706		-2.801	0.663
C9017C-4H-7, 21.8 cm	30.253	1.5945			0.649
C9017C-4H-7, 25.8 cm	30.293	1.2519			0.860
C9017C-4H-7, 29.8 cm	30.333	1.3569			0.795
C9017C-4H-7, 33.8 cm	30.373	1.6964		6.999	0.586
C9017C-4H-7, 37.8 cm	30.413	1.9081			0.456
C9017C-4H-7, 41.8 cm	30.453	1.7295			0.566
C9017C-4H-7, 45.8 cm	30.493	1.0141			1.006
C9017C-4H-7, 49.8 cm	30.533	0.954		-2.567	1.043
C9017C-4H-7, 53.8 cm	30.573	0.9229			1.062
C9017C-4H-7, 57.8 cm	30.613	1.0297			0.996
C9017C-4H-7, 61.8 cm	30.653	1.1114			0.946
C9017C-4H-7, 65.8 cm	30.693	0.9701		-0.833	1.033
C9017C-4H-7, 69.8 cm	30.733	1.1125			0.946
C9017C-4H-7, 73.8 cm	30.773	1.6977			0.585
C9017C-4H-7, 77.8 cm	30.813	1.7801			0.534
C9017C-4H-7, 81.8 cm	30.853	1.7457		-1.634	0.556
C9017C-4H-7, 85.8 cm	30.893	1.7422			0.558
C9017C-4H-7, 89.8 cm	30.933	1.7387			0.560
C9017C-4H-7, 93.8 cm	30.973	1.7383			0.560
C9017C-4H-7, 97.8 cm	31.013	1.791		1.866	0.528
C9017C-4H-8, 1.2 cm	31.057	1.7961			0.525
C9017C-4H-8, 5.2 cm	31.097	1.7109			0.577
C9017C-4H-8, 9.2 cm	31.137	1.8402			0.497
C9017C-4H-8, 13.2 cm	31.177	1.7922		1.733	0.527
C9017C-4H-8, 17.2 cm	31.217	1.7283			0.566
C9017C-4H-8, 21.2 cm	31.257	1.5696			0.664
C9017C-4H-8, 25.2 cm	31.297	1.0708			0.971
C9017C-4H-8, 29.2 cm	31.337	0.9437		-2.301	1.049

Table 5-3-2-1

Location	Subbottom Depth	GRA ¹⁾	MS ²⁾	NGR ³⁾	GRA Porosity
	[mbsf]	[g/cm ³]	[x10 ⁻⁵ SI]	[cps]	
C9017C-4H-8, 33.2 cm	31.377	0.9482			1.047
C9017C-4H-8, 37.2 cm	31.417	0.7752			1.153
C9017C-4H-8, 41.2 cm	31.457	0.8588			1.102
C9017C-4H-8, 45.2 cm	31.497	0.3122		-4	1.438
C9017C-4H-8, 49.2 cm	31.537	0.4372			1.361
C9017C-4H-8, 53.2 cm	31.577	0.094			1.573
C9017C-4H-8, 57.2 cm	31.617	0.0799			1.581
C9017C-4H-8, 61.2 cm	31.657	0.7759		-4.934	1.153
C9017C-4H-8, 65.2 cm	31.697	0.3359			1.424
C9017C-4H-8, 69.2 cm	31.737	0.6574			1.226
C9017C-4H-8, 73.2 cm	31.777	0.7566			1.165
C9017C-4H-8, 77.2 cm	31.817	0.8341		-2.034	1.117
C9017C-4H-8, 81.2 cm	31.857	1.0961			0.956
C9017C-4H-8, 85.2 cm	31.897	0.9492			1.046
C9017C-4H-8, 89.2 cm	31.937	0.731			1.180
C9017C-4H-8, 93.2 cm	31.977	0.8493		8.1	1.108
C9017C-4H-8, 97.2 cm	32.017	1.0052			1.012
C9017C-5H-1, 8.0 cm	32.08	1.8211			0.509
C9017C-5H-1, 12.0 cm	32.12	1.8873			0.468
C9017C-5H-1, 16.0 cm	32.16	2.0031		22.234	0.397
C9017C-5H-1, 20.0 cm	32.2	1.7444			0.556
C9017C-5H-1, 24.0 cm	32.24	1.8441			0.495
C9017C-5H-1, 28.0 cm	32.28	1.9437			0.434
C9017C-5H-1, 32.0 cm	32.32	2.0602		15.568	0.362
C9017C-5H-1, 36.0 cm	32.36	1.8004			0.522
C9017C-5H-1, 40.0 cm	32.4	1.9947			0.402
C9017C-5H-1, 44.0 cm	32.44	2.088			0.345
C9017C-5H-1, 48.0 cm	32.48	2.0369		17.7	0.376
C9017C-5H-1, 52.0 cm	32.52	0.3708			1.402
C9017C-5H-1, 80.0 cm	32.8	1.831		-2.532	0.503
C9017C-5H-1, 84.0 cm	32.84	1.6733			0.600
C9017C-5H-2, 3.3 cm	32.878	1.7788			0.535
C9017C-5H-2, 7.3 cm	32.918	1.8417			0.496
C9017C-5H-2, 11.3 cm	32.958	1.7408		-0.199	0.559
C9017C-5H-2, 15.3 cm	32.998	1.8353			0.500
C9017C-5H-2, 19.3 cm	33.038	1.8447			0.495
C9017C-5H-2, 23.3 cm	33.078	1.8142			0.513
C9017C-5H-2, 27.3 cm	33.118	1.8051		-0.433	0.519
C9017C-5H-2, 31.3 cm	33.158	1.8476			0.493
C9017C-5H-2, 35.3 cm	33.198	1.7349			0.562
C9017C-5H-2, 39.3 cm	33.238	1.8009			0.522
C9017C-5H-2, 43.3 cm	33.278	1.785		-3.032	0.531
C9017C-5H-2, 47.3 cm	33.318	1.811			0.515
C9017C-5H-2, 51.3 cm	33.358	1.7814			0.534
C9017C-5H-2, 55.3 cm	33.398	1.7909			0.528
C9017C-5H-2, 59.3 cm	33.438	1.8039		-1.4	0.520
C9017C-5H-2, 63.3 cm	33.478	1.8097			0.516
C9017C-5H-2, 67.3 cm	33.518	1.7176			0.573
C9017C-5H-2, 71.3 cm	33.558	1.4338			0.748
C9017C-5H-2, 75.3 cm	33.598	1.6341		-5.266	0.624
C9017C-5H-2, 79.3 cm	33.638	1.7534			0.551
C9017C-5H-2, 83.3 cm	33.678	1.8006			0.522

Table 5-3-2-1

Location	Subbottom Depth	GRA ¹⁾	MS ²⁾	NGR ³⁾	GRA Porosity
	[mbsf]	[g/cm ³]	[x10 ⁻⁵ SI]	[cps]	
C9017C-5H-2, 87.3 cm	33.718	1.7588			0.548
C9017C-5H-2, 91.3 cm	33.758	1.7591		-2.599	0.547
C9017C-5H-2, 95.3 cm	33.798	1.739			0.560
C9017C-5H-2, 99.3 cm	33.838	1.7687			0.541
C9017C-5H-3, 1.9 cm	33.874	1.7639			0.544
C9017C-5H-3, 5.9 cm	33.914	1.7893		-2.332	0.529
C9017C-5H-3, 9.9 cm	33.954	1.6606			0.608
C9017C-5H-3, 13.9 cm	33.994	1.6684			0.603
C9017C-5H-3, 17.9 cm	34.034	1.8308			0.503
C9017C-5H-3, 21.9 cm	34.074	1.7069		-2.233	0.579
C9017C-5H-3, 25.9 cm	34.114	0.3435			1.419
C9017C-5H-3, 29.9 cm	34.154	1.7389			0.560
C9017C-5H-3, 33.9 cm	34.194	1.7662			0.543
C9017C-5H-3, 37.9 cm	34.234	1.6863		-0.965	0.592
C9017C-5H-3, 41.9 cm	34.274	1.7548			0.550
C9017C-5H-3, 45.9 cm	34.314	1.6956			0.586
C9017C-5H-3, 49.9 cm	34.354	1.656			0.611
C9017C-5H-3, 53.9 cm	34.394	1.7109		0.635	0.577
C9017C-5H-3, 57.9 cm	34.434	1.6623			0.607
C9017C-5H-3, 61.9 cm	34.474	1.6898			0.590
C9017C-5H-3, 65.9 cm	34.514	1.6748			0.599
C9017C-5H-3, 69.9 cm	34.554	1.6372		-1.332	0.622
C9017C-5H-3, 73.9 cm	34.594	1.584			0.655
C9017C-5H-3, 77.9 cm	34.634	1.5912			0.651
C9017C-5H-3, 81.9 cm	34.674	1.5354			0.685
C9017C-5H-3, 85.9 cm	34.714	1.5489		-2.532	0.677
C9017C-5H-3, 89.9 cm	34.754	1.7707			0.540
C9017C-5H-3, 93.9 cm	34.794	1.8158			0.512
C9017C-5H-3, 97.9 cm	34.834	1.734			0.563
C9017C-5H-4, 0.6 cm	34.871	1.1137		2.235	0.945
C9017C-5H-4, 4.6 cm	34.911	1.76			0.547
C9017C-5H-4, 8.6 cm	34.951	1.7259			0.568
C9017C-5H-4, 12.6 cm	34.991	0.7862			1.146
C9017C-5H-4, 28.6 cm	35.151	0.2763			1.460
C9017C-5H-4, 32.6 cm	35.191	0.7915		-3.398	1.143
C9017C-5H-4, 36.6 cm	35.231	0.4117			1.377
C9017C-5H-4, 40.6 cm	35.271	0.2165			1.497
C9017C-5H-4, 44.6 cm	35.311	0.194			1.511
C9017C-5H-4, 48.6 cm	35.351	1.7657		-1.267	0.543
C9017C-5H-4, 52.6 cm	35.391	0.2978			1.447
C9017C-5H-4, 72.6 cm	35.591	0.0169			1.620
C9017C-5H-4, 76.6 cm	35.631	1.322			0.817
C9017C-5H-4, 80.6 cm	35.671	0.8911		-6.399	1.082
C9017C-5H-4, 84.6 cm	35.711	0.5681			1.281
C9017C-5H-4, 88.6 cm	35.751	0.5498			1.292
C9017C-5H-4, 92.6 cm	35.791	1.442			0.743
C9017C-5H-4, 96.6 cm	35.831	1.5107		-4.399	0.700
C9017C-5H-4, 100.6 cm	35.871	0.4159			1.374
C9017C-5H-5, 3.9 cm	35.909	1.6299			0.627
C9017C-5H-5, 7.9 cm	35.949	1.5709			0.663
C9017C-5H-5, 11.9 cm	35.989	1.755		-4.699	0.550
C9017C-5H-5, 15.9 cm	36.029	1.6839			0.594

Table 5-3-2-1

Location	Subbottom Depth	GRA ¹⁾	MS ²⁾	NGR ³⁾	GRA Porosity
	[mbsf]	[g/cm ³]	[x10 ⁻⁵ SI]	[cps]	
C9017C-5H-5, 19.9 cm	36.069	1.7269			0.567
C9017C-5H-5, 23.9 cm	36.109	1.7408			0.559
C9017C-5H-5, 27.9 cm	36.149	1.7458		-3.699	0.556
C9017C-5H-5, 31.9 cm	36.189	1.7081			0.579
C9017C-5H-5, 35.9 cm	36.229	1.7001			0.584
C9017C-5H-5, 39.9 cm	36.269	1.7887			0.529
C9017C-5H-5, 43.9 cm	36.309	1.8125		-5.132	0.514
C9017C-5H-5, 47.9 cm	36.349	1.7793			0.535
C9017C-5H-5, 51.9 cm	36.389	1.8898			0.467
C9017C-5H-5, 55.9 cm	36.429	1.7988			0.523
C9017C-5H-5, 59.9 cm	36.469	1.8277		-2.133	0.505
C9017C-5H-5, 63.9 cm	36.509	1.8772			0.475
C9017C-5H-5, 67.9 cm	36.549	1.8479			0.493
C9017C-5H-5, 71.9 cm	36.589	1.8791			0.473
C9017C-5H-5, 75.9 cm	36.629	1.9077		-4.332	0.456
C9017C-5H-5, 79.9 cm	36.669	1.9211			0.448
C9017C-5H-5, 83.9 cm	36.709	1.9615			0.423
C9017C-5H-5, 87.9 cm	36.749	1.9555			0.426
C9017C-5H-5, 91.9 cm	36.789	1.9545		-1.633	0.427
C9017C-5H-5, 95.9 cm	36.829	1.9639			0.421
C9017C-5H-5, 99.9 cm	36.869	1.4085			0.763
C9017C-5H-6, 3.2 cm	36.907	1.833			0.502
C9017C-5H-6, 7.2 cm	36.947	1.8353		-2.833	0.500
C9017C-5H-6, 11.2 cm	36.987	1.9357			0.439
C9017C-5H-6, 15.2 cm	37.027	1.8133			0.514
C9017C-5H-6, 19.2 cm	37.067	1.8667			0.481
C9017C-5H-6, 23.2 cm	37.107	1.858		-3.466	0.486
C9017C-5H-6, 27.2 cm	37.147	1.8484			0.492
C9017C-5H-6, 31.2 cm	37.187	2.0224			0.385
C9017C-5H-6, 35.2 cm	37.227	1.8888			0.467
C9017C-5H-6, 39.2 cm	37.267	1.8892		-0.466	0.467
C9017C-5H-6, 43.2 cm	37.307	1.8021			0.521
C9017C-5H-6, 47.2 cm	37.347	1.8557			0.488
C9017C-5H-6, 51.2 cm	37.387	1.9363			0.438
C9017C-5H-6, 55.2 cm	37.427	1.7308		0.067	0.565
C9017C-5H-6, 59.2 cm	37.467	1.6842			0.593
C9017C-5H-6, 63.2 cm	37.507	1.7326			0.564
C9017C-5H-6, 67.2 cm	37.547	0.9894			1.021
C9017C-5H-6, 71.2 cm	37.587	0.3867		-6.231	1.392
C9017C-5H-6, 75.2 cm	37.627	0.3919			1.389
C9017C-5H-6, 79.2 cm	37.667	0.372			1.401
C9017C-5H-6, 83.2 cm	37.707	0.9818			1.026
C9017C-5H-6, 87.2 cm	37.747	0.2589		-2.999	1.471
C9017C-5H-6, 91.2 cm	37.787	1.3146			0.821
C9017C-5H-6, 95.2 cm	37.827	1.4721			0.724
C9017C-5H-6, 99.2 cm	37.867	1.6788			0.597
C9017C-5H-7, 2.1 cm	37.901	1.426		-2.699	0.752
C9017C-5H-7, 6.1 cm	37.941	0.538			1.299
C9017C-5H-7, 10.1 cm	37.981	0.8295			1.120
C9017C-5H-7, 14.1 cm	38.021	0.7906			1.144
C9017C-5H-7, 18.1 cm	38.061	1.0607		-3.966	0.977
C9017C-5H-7, 22.1 cm	38.101	1.2871			0.838

Table 5-3-2-1

Location	Subbottom Depth	GRA ¹⁾	MS ²⁾	NGR ³⁾	GRA Porosity
	[mbsf]	[g/cm ³]	[x10 ⁻⁵ SI]	[cps]	
C9017C-5H-7, 26.1 cm	38.141	1.8054			0.519
C9017C-5H-7, 30.1 cm	38.181	1.8773			0.475
C9017C-5H-7, 34.1 cm	38.221	0.9286		-0.632	1.059
C9017C-5H-7, 38.1 cm	38.261	0.9471			1.047
C9017C-5H-7, 42.1 cm	38.301	1.1686			0.911
C9017C-5H-7, 46.1 cm	38.341	0.441			1.359
C9017C-5H-7, 50.1 cm	38.381	0.5317		-4.698	1.303
C9017C-5H-7, 54.1 cm	38.421	0.8368			1.115
C9017C-5H-7, 58.1 cm	38.461	0.5538			1.290
C9017C-5H-7, 62.1 cm	38.501	0.8424			1.112
C9017C-5H-7, 66.1 cm	38.541	1.6403		-1.766	0.621
C9017C-5H-7, 70.1 cm	38.581	1.4973			0.709
C9017C-5H-7, 74.1 cm	38.621	1.0589			0.979
C9017C-5H-7, 78.1 cm	38.661	0.4912			1.328
C9017C-5H-7, 82.1 cm	38.701	0.0027		-6.8	1.629
C9017C-5H-7, 86.1 cm	38.741	0.109			1.563
C9017C-5H-7, 90.1 cm	38.781	0.4208			1.371
C9017C-5H-7, 94.1 cm	38.821	1.5063			0.703
C9017C-5H-7, 98.1 cm	38.861	1.6786		-2.966	0.597
C9017C-5H-8, 1.1 cm	38.901	1.5638			0.668
C9017C-5H-8, 5.1 cm	38.941	1.5616			0.669
C9017C-5H-8, 9.1 cm	38.981	1.6469			0.616
C9017C-5H-8, 13.1 cm	39.021	1.2867		-2.899	0.838
C9017C-5H-8, 17.1 cm	39.061	1.2054			0.888
C9017C-5H-8, 21.1 cm	39.101	1.5896			0.652
C9017C-5H-8, 25.1 cm	39.141	0.9912			1.020
C9017C-5H-8, 29.1 cm	39.181	1.3647		-1.6	0.790
C9017C-5H-8, 33.1 cm	39.221	0.9878			1.022
C9017C-5H-8, 37.1 cm	39.261	1.1059			0.950
C9017C-5H-8, 41.1 cm	39.301	0.9547			1.043
C9017C-5H-8, 45.1 cm	39.341	1.1419		-2.999	0.927
C9017C-5H-8, 49.1 cm	39.381	1.3038			0.828
C9017C-5H-8, 53.1 cm	39.421	1.8778			0.474
C9017C-5H-8, 57.1 cm	39.461	1.7073			0.579
C9017C-5H-8, 61.1 cm	39.501	1.7281		-1.166	0.566
C9017C-5H-8, 73.1 cm	39.621	1.6293			0.627
C9017C-5H-8, 77.1 cm	39.661	1.1681		-2.032	0.911
C9017C-5H-8, 81.1 cm	39.701	1.3009			0.829
C9017C-5H-8, 85.1 cm	39.741	1.8571			0.487
C9017C-5H-8, 89.1 cm	39.781	1.9016			0.460
C9017C-5H-8, 93.1 cm	39.821	1.7405		12.235	0.559
C9017C-5H-8, 97.1 cm	39.861	1.6601			0.608
C9017C-5H-8, 101.1 cm	39.901	0.1501			1.538
C9017C-6H-CC, 8.0 cm	40.08	0.1898	35.3678	1.733	1.514
C9017C-7H-1, 8.0 cm	48.58	1.4689	41.9997		0.726
C9017C-7H-1, 12.0 cm	48.62	1.5552	8.5491		0.673
C9017C-7H-1, 16.0 cm	48.66	1.4168	3.9707	-0.199	0.758
C9017C-7H-1, 20.0 cm	48.7	1.672	3.9959		0.601
C9017C-7H-1, 24.0 cm	48.74	1.0061	2.0022		1.011
C9017C-7H-1, 28.0 cm	48.78	0.5179	2.6741		1.312
C9017C-7H-1, 32.0 cm	48.82	1.7867	0	1.667	0.530
C9017C-7H-1, 36.0 cm	48.86	1.7644	0.6358		0.544

Table 5-3-2-1

Location	Subbottom Depth	GRA ¹⁾	MS ²⁾	NGR ³⁾	GRA Porosity
	[mbsf]	[g/cm ³]	[x10 ⁻⁵ SI]	[cps]	
C9017C-7H-1, 40.0 cm	48.9	1.7732	0.6241		0.539
C9017C-7H-1, 44.0 cm	48.94	1.1675	0.6475		0.912
C9017C-7H-1, 48.0 cm	48.98	1.817	0	5.134	0.512
C9017C-7H-2, 1.4 cm	49.019	0.6271			1.244
C9017C-7H-2, 5.4 cm	49.059	1.4416			0.743
C9017C-7H-2, 9.4 cm	49.099	0.8254			1.122
C9017C-7H-3, 1.2 cm	49.142	1.7718		0.333	0.540
C9017C-7H-3, 5.2 cm	49.182	1.7993			0.523
C9017C-7H-3, 9.2 cm	49.222	1.7991			0.523
C9017C-7H-3, 13.2 cm	49.262	1.8102			0.516
C9017C-7H-3, 17.2 cm	49.302	1.8111		1.4	0.515
C9017C-7H-3, 21.2 cm	49.342	1.8512			0.491
C9017C-7H-3, 25.2 cm	49.382	1.8597			0.485
C9017C-7H-3, 57.2 cm	49.702	1.5036			0.705
C9017C-7H-3, 61.2 cm	49.742	1.4667			0.727
C9017C-7H-3, 65.2 cm	49.782	1.7794		0.133	0.535
C9017C-7H-4, 2.1 cm	49.821	1.5746			0.661
C9017C-7H-4, 10.1 cm	49.901	1.7674			0.542
C9017C-7H-4, 14.1 cm	49.941	1.8924		-1.367	0.465
C9017C-7H-4, 18.1 cm	49.981	1.8918			0.466
C9017C-7H-4, 22.1 cm	50.021	1.9169			0.450
C9017C-7H-4, 26.1 cm	50.061	1.9081			0.456
C9017C-7H-4, 30.1 cm	50.101	1.9344		0.966	0.439
C9017C-7H-4, 34.1 cm	50.141	1.9488			0.431
C9017C-7H-4, 38.1 cm	50.181	1.9133			0.452
C9017C-7H-5, 0.9 cm	50.219	1.8817			0.472
C9017C-7H-5, 4.9 cm	50.259	1.8488		1.834	0.492
C9017C-7H-5, 8.9 cm	50.299	1.8541			0.489
C9017C-7H-5, 12.9 cm	50.339	1.9367			0.438
C9017C-7H-5, 16.9 cm	50.379	1.9421			0.435
C9017C-7H-5, 20.9 cm	50.419	1.9624		1.4	0.422
C9017C-7H-5, 24.9 cm	50.459	1.89			0.467
C9017C-7H-5, 28.9 cm	50.499	1.8961			0.463
C9017C-7H-5, 32.9 cm	50.539	1.9041			0.458
C9017C-7H-5, 36.9 cm	50.579	1.9484		-1.767	0.431
C9017C-7H-5, 40.9 cm	50.619	1.8778			0.474
C9017C-7H-5, 44.9 cm	50.659	0.2518			1.475
C9017C-7H-5, 48.9 cm	50.699	1.8805			0.473
C9017C-7H-5, 52.9 cm	50.739	1.8217		-1.5	0.509
C9017C-7H-5, 56.9 cm	50.779	1.8683			0.480
C9017C-7H-5, 60.9 cm	50.819	1.8991			0.461
C9017C-7H-5, 64.9 cm	50.859	1.9267			0.444
C9017C-7H-5, 68.9 cm	50.899	1.8305		-1.666	0.503
C9017C-7H-5, 72.9 cm	50.939	1.8819			0.472
C9017C-7H-5, 76.9 cm	50.979	1.7822			0.533
C9017C-7H-5, 92.9 cm	51.139	1.7509			0.552
C9017C-7H-5, 96.9 cm	51.179	1.9015			0.460
C9017C-7H-6, 0.1 cm	51.216	0.3656		0.701	1.405
C9017C-7H-6, 4.1 cm	51.256	1.8165			0.512
C9017C-7H-6, 8.1 cm	51.296	1.4792			0.720
C9017C-7H-6, 36.1 cm	51.576	1.3724			0.785
C9017C-7H-6, 52.1 cm	51.736	1.8913			0.466

Table 5-3-2-1

Location	Subbottom Depth	GRA ¹⁾	MS ²⁾	NGR ³⁾	GRA Porosity
	[mbsf]	[g/cm ³]	[x10 ⁻⁵ SI]	[cps]	
C9017C-7H-6, 56.1 cm	51.776	0.5376			1.300
C9017C-7H-6, 80.1 cm	52.016	1.5217		-3.567	0.694
C9017C-7H-7, 0.3 cm	52.053	0.6145			1.252
C9017C-7H-7, 4.3 cm	52.093	1.8295			0.504
C9017C-7H-7, 8.3 cm	52.133	1.4813			0.718
C9017C-7H-7, 40.3 cm	52.453	1.8078			0.517
C9017C-7H-7, 44.3 cm	52.493	1.0721		-4.566	0.970
C9017C-7H-8, 2.7 cm	52.532	1.816			0.512
C9017C-7H-8, 6.7 cm	52.572	1.8639			0.483
C9017C-8H-1, 8.0 cm	52.58	1.6646			0.606
C9017C-7H-8, 10.7 cm	52.612	1.661			0.608
C9017C-8H-1, 12.0 cm	52.62	1.7962			0.525
C9017C-7H-8, 14.7 cm	52.652	1.6716		-4.567	0.601
C9017C-8H-1, 16.0 cm	52.66	1.4868		3.367	0.715
C9017C-7H-8, 18.7 cm	52.692	1.8918			0.466
C9017C-8H-1, 20.0 cm	52.7	1.3758			0.783
C9017C-7H-8, 22.7 cm	52.732	1.8823			0.471
C9017C-8H-1, 24.0 cm	52.74	1.4835			0.717
C9017C-7H-8, 26.7 cm	52.772	1.1249			0.938
C9017C-8H-1, 28.0 cm	52.78	1.585			0.655
C9017C-8H-1, 32.0 cm	52.82	1.6275		8.933	0.628
C9017C-8H-1, 36.0 cm	52.86	1.4911			0.712
C9017C-7H-8, 38.7 cm	52.892	1.7961			0.525
C9017C-8H-2, 3.0 cm	52.9	1.8863			0.469
C9017C-7H-8, 42.7 cm	52.932	1.846			0.494
C9017C-8H-2, 7.0 cm	52.94	1.5458			0.679
C9017C-7H-8, 46.7 cm	52.972	1.7631		1.3	0.545
C9017C-8H-2, 11.0 cm	52.98	1.8382		10.033	0.499
C9017C-7H-8, 50.7 cm	53.012	1.6118			0.638
C9017C-8H-2, 15.0 cm	53.02	1.6334			0.625
C9017C-7H-8, 54.7 cm	53.052	1.6857			0.593
C9017C-8H-2, 19.0 cm	53.06	1.6884			0.591
C9017C-8H-2, 27.0 cm	53.14	1.512		9.533	0.700
C9017C-8H-2, 31.0 cm	53.18	1.9552			0.427
C9017C-7H-8, 78.7 cm	53.292	1.7899		-4.101	0.528
C9017C-7H-8, 82.7 cm	53.332	1.6143			0.637
C9017C-7H-8, 86.7 cm	53.372	1.5281			0.690
C9017C-7H-8, 90.7 cm	53.412	1.5252			0.691
C9017C-7H-8, 94.7 cm	53.452	1.4722		-4.666	0.724
C9017C-7H-8, 98.7 cm	53.492	1.4747			0.722
C9017C-7H-9, 1.4 cm	53.529	1.53			0.688
C9017C-7H-9, 5.4 cm	53.569	1.3957			0.771
C9017C-7H-9, 9.4 cm	53.609	1.2662		-0.233	0.851
C9017C-7H-9, 13.4 cm	53.649	1.4831			0.717
C9017C-7H-9, 17.4 cm	53.689	1.6832			0.594
C9017C-7H-9, 21.4 cm	53.729	1.5603			0.670
C9017C-7H-9, 25.4 cm	53.769	1.6036		1.567	0.643
C9017C-7H-9, 29.4 cm	53.809	0.3447			1.418
C9017C-8H-3, 2.4 cm	53.894	1.3466			0.801
C9017C-7H-9, 41.4 cm	53.929	1.6771		-4.1	0.598
C9017C-8H-3, 6.4 cm	53.934	1.8378		2.867	0.499
C9017C-7H-9, 45.4 cm	53.969	1.3515			0.798

Table 5-3-2-1

Location	Subbottom Depth	GRA ¹⁾	MS ²⁾	NGR ³⁾	GRA Porosity
	[mbsf]	[g/cm ³]	[x10 ⁻⁵ SI]	[cps]	
C9017C-8H-3, 10.4 cm	53.974	1.8521			0.490
C9017C-7H-9, 49.4 cm	54.009	1.6738			0.600
C9017C-8H-3, 14.4 cm	54.014	1.8398			0.498
C9017C-7H-9, 53.4 cm	54.049	1.6676			0.604
C9017C-8H-3, 18.4 cm	54.054	1.8523			0.490
C9017C-7H-9, 57.4 cm	54.089	1.4033		-3.5	0.766
C9017C-8H-3, 22.4 cm	54.094	1.9041		4.233	0.458
C9017C-7H-9, 61.4 cm	54.129	1.6571			0.610
C9017C-8H-3, 26.4 cm	54.134	1.8915			0.466
C9017C-7H-9, 65.4 cm	54.169	1.4115			0.761
C9017C-8H-3, 30.4 cm	54.174	1.8774			0.475
C9017C-7H-9, 69.4 cm	54.209	1.5078			0.702
C9017C-8H-3, 34.4 cm	54.214	1.8647			0.482
C9017C-7H-9, 73.4 cm	54.249	1.5723		2.766	0.662
C9017C-8H-3, 38.4 cm	54.254	1.9319		4.067	0.441
C9017C-7H-9, 77.4 cm	54.289	1.5922			0.650
C9017C-7H-9, 81.4 cm	54.329	1.525			0.692
C9017C-8H-3, 70.4 cm	54.574	-0.055		4.766	1.664
C9017C-8H-3, 74.4 cm	54.614	1.8631			0.483
C9017C-8H-4, 0.4 cm	54.649	0.8068			1.134
C9017C-8H-4, 4.4 cm	54.689	1.8663			0.481
C9017C-8H-4, 8.4 cm	54.729	1.801		3.599	0.522
C9017C-8H-4, 12.4 cm	54.769	1.8602			0.485
C9017C-8H-4, 28.4 cm	54.929	1.7984			0.523
C9017C-8H-4, 32.4 cm	54.969	1.918			0.450
C9017C-8H-4, 36.4 cm	55.009	1.889			0.467
C9017C-8H-4, 40.4 cm	55.049	1.8103		9.065	0.516
C9017C-8H-4, 44.4 cm	55.089	1.7507			0.553
C9017C-8H-4, 48.4 cm	55.129	0.425			1.369
C9017C-8H-4, 52.4 cm	55.169	1.7424			0.558
C9017C-8H-4, 92.4 cm	55.569	1.8199			0.510
C9017C-8H-4, 96.4 cm	55.609	1.7782			0.536
C9017C-8H-4, 100.4 cm	55.649	1.568			0.665
C9017C-8H-5, 3.1 cm	55.686	1.8206		1.965	0.509
C9017C-8H-5, 7.1 cm	55.726	0.5394			1.298
C9017C-8H-5, 11.1 cm	55.766	1.8863			0.469
C9017C-8H-5, 15.1 cm	55.806	1.8703			0.479
C9017C-8H-5, 27.1 cm	55.926	1.8646			0.482
C9017C-8H-5, 31.1 cm	55.966	1.809			0.517
C9017C-8H-5, 35.1 cm	56.006	1.8757		1.933	0.476
C9017C-8H-5, 39.1 cm	56.046	1.8284			0.505
C9017C-8H-5, 43.1 cm	56.086	1.8813			0.472
C9017C-8H-5, 47.1 cm	56.126	1.8352			0.500
C9017C-8H-5, 51.1 cm	56.166	1.8416		1.167	0.497
C9017C-8H-5, 55.1 cm	56.206	1.8149			0.513
C9017C-8H-5, 59.1 cm	56.246	1.835			0.501
C9017C-8H-5, 63.1 cm	56.286	1.8263			0.506
C9017C-8H-5, 67.1 cm	56.326	1.8017		0.101	0.521
C9017C-8H-5, 71.1 cm	56.366	1.7919			0.527
C9017C-8H-5, 75.1 cm	56.406	1.7988			0.523
C9017C-8H-5, 79.1 cm	56.446	1.7995			0.522
C9017C-8H-5, 83.1 cm	56.486	1.7795		4	0.535

Table 5-3-2-1

Location	Subbottom Depth	GRA ¹⁾	MS ²⁾	NGR ³⁾	GRA Porosity
	[mbsf]	[g/cm ³]	[x10 ⁻⁵ SI]	[cps]	
C9017C-8H-5, 87.1 cm	56.526	1.8205			0.510
C9017C-8H-5, 91.1 cm	56.566	1.7987			0.523
C9017C-8H-5, 95.1 cm	56.606	1.8195			0.510
C9017C-8H-5, 99.1 cm	56.646	1.8105		3.033	0.516
C9017C-8H-6, 2.7 cm	56.682	1.7749			0.538
C9017C-8H-6, 6.7 cm	56.722	1.7656			0.543
C9017C-8H-6, 10.7 cm	56.762	1.776			0.537
C9017C-8H-6, 14.7 cm	56.802	1.8297		1.733	0.504
C9017C-8H-6, 18.7 cm	56.842	1.737			0.561
C9017C-8H-6, 22.7 cm	56.882	1.8546			0.489
C9017C-8H-6, 26.7 cm	56.922	1.8782			0.474
C9017C-8H-6, 30.7 cm	56.962	1.9385		1.3	0.437
C9017C-8H-6, 34.7 cm	57.002	1.8553			0.488
C9017C-8H-6, 38.7 cm	57.042	1.8094			0.516
C9017C-8H-6, 42.7 cm	57.082	1.792			0.527
C9017C-8H-6, 46.7 cm	57.122	1.845		-0.201	0.494
C9017C-8H-6, 50.7 cm	57.162	1.8197			0.510
C9017C-8H-6, 54.7 cm	57.202	1.8528			0.490
C9017C-8H-6, 58.7 cm	57.242	1.8281			0.505
C9017C-8H-6, 62.7 cm	57.282	1.8435		0.266	0.495
C9017C-8H-6, 66.7 cm	57.322	1.7842			0.532
C9017C-8H-6, 70.7 cm	57.362	1.8073			0.518
C9017C-8H-6, 74.7 cm	57.402	1.7177			0.573
C9017C-8H-6, 78.7 cm	57.442	1.7128		4.733	0.576
C9017C-8H-6, 82.7 cm	57.482	1.7091			0.578
C9017C-8H-6, 86.7 cm	57.522	1.6784			0.597
C9017C-8H-6, 90.7 cm	57.562	1.7118			0.576
C9017C-8H-6, 94.7 cm	57.602	1.6236		5.899	0.631
C9017C-8H-6, 98.7 cm	57.642	1.6851			0.593
C9017C-8H-7, 1.3 cm	57.678	1.6195			0.633
C9017C-8H-7, 5.3 cm	57.718	1.5068			0.703
C9017C-8H-7, 9.3 cm	57.758	1.6984		5.833	0.585
C9017C-8H-7, 13.3 cm	57.798	1.6276			0.628
C9017C-8H-7, 17.3 cm	57.838	1.5298			0.689
C9017C-8H-7, 21.3 cm	57.878	1.7091			0.578
C9017C-8H-7, 25.3 cm	57.918	1.6193		4.799	0.633
C9017C-8H-7, 29.3 cm	57.958	1.6882			0.591
C9017C-8H-7, 33.3 cm	57.998	1.6856			0.593
C9017C-8H-7, 37.3 cm	58.038	1.6603			0.608
C9017C-8H-7, 41.3 cm	58.078	1.7361		6.2	0.562
C9017C-8H-7, 45.3 cm	58.118	1.669			0.603
C9017C-8H-7, 49.3 cm	58.158	1.6089			0.640
C9017C-8H-7, 53.3 cm	58.198	1.6625			0.607
C9017C-8H-7, 57.3 cm	58.238	1.7222		2.4	0.570
C9017C-8H-7, 61.3 cm	58.278	1.7548			0.550
C9017C-8H-7, 65.3 cm	58.318	1.7871			0.530
C9017C-8H-7, 69.3 cm	58.358	1.8398			0.498
C9017C-8H-7, 73.3 cm	58.398	1.859		2.266	0.486
C9017C-8H-7, 77.3 cm	58.438	1.7961			0.525
C9017C-8H-7, 81.3 cm	58.478	1.7135			0.575
C9017C-8H-7, 85.3 cm	58.518	1.7127			0.576
C9017C-8H-7, 89.3 cm	58.558	1.7895		6.067	0.529

Table 5-3-2-1

Location	Subbottom Depth	GRA ¹⁾	MS ²⁾	NGR ³⁾	GRA Porosity
	[mbsf]	[g/cm ³]	[x10 ⁻⁵ SI]	[cps]	
C9017C-8H-7, 93.3 cm	58.598	1.7991			0.523
C9017C-8H-7, 97.3 cm	58.638	1.859			0.486
C9017C-8H-7, 101.3 cm	58.678	0.746			1.171
C9017C-8H-8, 3.9 cm	58.714	1.7365		5.965	0.561
C9017C-8H-8, 7.9 cm	58.754	1.794			0.526
C9017C-8H-8, 11.9 cm	58.794	1.7742			0.538
C9017C-8H-8, 15.9 cm	58.834	1.5905			0.651
C9017C-8H-8, 19.9 cm	58.874	1.2168		0.7	0.881
C9017C-8H-8, 23.9 cm	58.914	1.8077			0.517
C9017C-8H-8, 27.9 cm	58.954	0.0559			1.596
C9017C-8H-8, 31.9 cm	58.994	1.9264			0.444
C9017C-8H-8, 35.9 cm	59.034	1.9291		13.299	0.443
C9017C-8H-8, 39.9 cm	59.074	1.955			0.427
C9017C-8H-8, 51.9 cm	59.194	1.8933		6.766	0.465
C9017C-8H-8, 55.9 cm	59.234	0.6549			1.227
C9017C-8H-8, 59.9 cm	59.274	1.8792			0.473
C9017C-8H-8, 71.9 cm	59.394	1.8755			0.476
C9017C-8H-8, 75.9 cm	59.434	1.6352			0.624
C9017C-8H-8, 79.9 cm	59.474	1.9652			0.420
C9017C-8H-8, 83.9 cm	59.514	-0.0213		17.632	1.644
C9017C-8H-8, 87.9 cm	59.554	0.6956			1.202
C9017C-8H-8, 91.9 cm	59.594	1.9787			0.412
C9017C-8H-8, 95.9 cm	59.634	1.9173			0.450
C9017C-8H-8, 99.9 cm	59.674	0.0528		5.699	1.598
C9017C-9H-1, 8.0 cm	60.58	2.1142			0.329
C9017C-9H-1, 12.0 cm	60.62	1.9051			0.457
C9017C-9H-2, 1.9 cm	60.659	1.8681		11.367	0.480
C9017C-9H-2, 5.9 cm	60.699	1.9281			0.443
C9017C-9H-2, 9.9 cm	60.739	1.8985			0.462
C9017C-9H-2, 13.9 cm	60.779	2.0187			0.388
C9017C-9H-2, 17.9 cm	60.819	1.9886		18.2	0.406
C9017C-9H-2, 21.9 cm	60.859	1.9971			0.401
C9017C-9H-2, 25.9 cm	60.899	2.0185			0.388
C9017C-9H-2, 29.9 cm	60.939	2.0235			0.385
C9017C-9H-2, 33.9 cm	60.979	2.1217		17.734	0.324
C9017C-9H-2, 37.9 cm	61.019	2.1536			0.304
C9017C-9H-2, 41.9 cm	61.059	2.1246			0.322
C9017C-9H-2, 45.9 cm	61.099	1.9939			0.403
C9017C-9H-2, 49.9 cm	61.139	1.9593		23.101	0.424
C9017C-9H-2, 53.9 cm	61.179	1.8949			0.464
C9017C-9H-2, 57.9 cm	61.219	1.8749			0.476
C9017C-9H-2, 61.9 cm	61.259	0.0245			1.615
C9017C-9H-2, 65.9 cm	61.299	1.8699		5.7	0.479
C9017C-9H-2, 69.9 cm	61.339	1.9063			0.457
C9017C-9H-2, 73.9 cm	61.379	0.7489			1.169
C9017C-9H-3, 0.5 cm	61.415	0.979			1.028
C9017C-9H-3, 4.5 cm	61.455	1.7739		9.634	0.538
C9017C-9H-3, 8.5 cm	61.495	1.797			0.524
C9017C-9H-3, 12.5 cm	61.535	1.769			0.541
C9017C-9H-3, 16.5 cm	61.575	1.4584			0.733
C9017C-9H-3, 32.5 cm	61.735	0.6185			1.250
C9017C-9H-3, 36.5 cm	61.775	1.711		1.766	0.577

Table 5-3-2-1

Location	Subbottom Depth	GRA ¹⁾	MS ²⁾	NGR ³⁾	GRA Porosity
	[mbsf]	[g/cm ³]	[x10 ⁻⁵ SI]	[cps]	
C9017C-9H-3, 40.5 cm	61.815	0.8662			1.097
C9017C-9H-3, 44.5 cm	61.855	1.9084			0.455
C9017C-9H-3, 48.5 cm	61.895	1.866			0.482
C9017C-9H-3, 52.5 cm	61.935	1.7857		8.235	0.531
C9017C-9H-3, 56.5 cm	61.975	1.8003			0.522
C9017C-9H-3, 60.5 cm	62.015	1.7564			0.549
C9017C-9H-3, 64.5 cm	62.055	1.8155			0.513
C9017C-9H-3, 68.5 cm	62.095	1.7973		3.234	0.524
C9017C-9H-3, 76.5 cm	62.175	0.7622			1.161
C9017C-9H-3, 80.5 cm	62.215	1.6156			0.636
C9017C-9H-3, 84.5 cm	62.255	1.473		3.167	0.724
C9017C-9H-3, 88.5 cm	62.295	1.732			0.564
C9017C-9H-3, 92.5 cm	62.335	1.5756			0.660
C9017C-9H-3, 96.5 cm	62.375	1.705			0.581
C9017C-9H-3, 100.5 cm	62.415	1.5952		4.9	0.648
C9017C-9H-4, 3.3 cm	62.453	1.7095			0.578
C9017C-9H-4, 7.3 cm	62.493	1.665			0.605
C9017C-9H-4, 11.3 cm	62.533	1.6149			0.636
C9017C-9H-4, 15.3 cm	62.573	1.6793		4.568	0.596
C9017C-9H-4, 19.3 cm	62.613	1.6715			0.601
C9017C-9H-4, 23.3 cm	62.653	1.6157			0.636
C9017C-9H-4, 27.3 cm	62.693	1.6633			0.606
C9017C-9H-4, 31.3 cm	62.733	1.715		5	0.575
C9017C-9H-4, 35.3 cm	62.773	1.7663			0.543
C9017C-9H-4, 39.3 cm	62.813	1.7851			0.531
C9017C-9H-4, 43.3 cm	62.853	1.6501			0.614
C9017C-9H-4, 47.3 cm	62.893	1.771		3.567	0.540
C9017C-9H-4, 51.3 cm	62.933	1.7724			0.539
C9017C-9H-4, 55.3 cm	62.973	1.6688			0.603
C9017C-9H-4, 59.3 cm	63.013	1.5226			0.693
C9017C-9H-4, 63.3 cm	63.053	1.6685		6.2	0.603
C9017C-9H-4, 67.3 cm	63.093	1.5863			0.654
C9017C-9H-4, 71.3 cm	63.133	1.7433			0.557
C9017C-9H-4, 75.3 cm	63.173	1.8336			0.501
C9017C-9H-4, 79.3 cm	63.213	1.7627		6.834	0.545
C9017C-9H-4, 83.3 cm	63.253	1.8615			0.484
C9017C-9H-4, 87.3 cm	63.293	1.8754			0.476
C9017C-9H-4, 91.3 cm	63.333	1.906			0.457
C9017C-9H-4, 95.3 cm	63.373	1.8853		5.334	0.470
C9017C-9H-4, 99.3 cm	63.413	1.7561			0.549
C9017C-9H-5, 2.7 cm	63.452	2.0193			0.387
C9017C-9H-5, 6.7 cm	63.492	1.8697			0.479
C9017C-9H-5, 10.7 cm	63.532	1.9827		2.134	0.410
C9017C-9H-5, 14.7 cm	63.572	1.9245			0.446
C9017C-9H-5, 18.7 cm	63.612	1.8009			0.522
C9017C-9H-5, 22.7 cm	63.652	1.7752			0.537
C9017C-9H-5, 26.7 cm	63.692	1.6947		0.7	0.587
C9017C-9H-5, 30.7 cm	63.732	1.7512			0.552
C9017C-9H-5, 34.7 cm	63.772	1.808			0.517
C9017C-9H-5, 38.7 cm	63.812	1.8667			0.481
C9017C-9H-5, 42.7 cm	63.852	1.8805		1.201	0.473
C9017C-9H-5, 46.7 cm	63.892	1.6453			0.617

Table 5-3-2-1

Location	Subbottom Depth	GRA ¹⁾	MS ²⁾	NGR ³⁾	GRA Porosity
	[mbsf]	[g/cm ³]	[x10 ⁻⁵ SI]	[cps]	
C9017C-9H-5, 50.7 cm	63.932	1.4424			0.742
C9017C-9H-5, 54.7 cm	63.972	1.2162			0.882
C9017C-9H-5, 58.7 cm	64.012	1.2612		2.034	0.854
C9017C-9H-5, 62.7 cm	64.052	1.333			0.810
C9017C-9H-5, 66.7 cm	64.092	1.3989			0.769
C9017C-9H-5, 70.7 cm	64.132	1.4877			0.714
C9017C-9H-5, 74.7 cm	64.172	1.6054		2.333	0.642
C9017C-9H-5, 78.7 cm	64.212	1.7761			0.537
C9017C-9H-5, 82.7 cm	64.252	1.2421			0.866
C9017C-9H-5, 86.7 cm	64.292	1.2439			0.865
C9017C-9H-5, 90.7 cm	64.332	0.9526		1.034	1.044
C9017C-9H-5, 94.7 cm	64.372	1.7563			0.549
C9017C-9H-5, 98.7 cm	64.412	1.8694			0.479
C9017C-9H-6, 2.2 cm	64.447	0.9838			1.025
C9017C-9H-6, 6.2 cm	64.487	1.8345		2.9	0.501
C9017C-9H-6, 10.2 cm	64.527	1.9277			0.444
C9017C-9H-6, 14.2 cm	64.567	1.9782			0.412
C9017C-9H-6, 18.2 cm	64.607	1.9399			0.436
C9017C-9H-6, 22.2 cm	64.647	1.1499		4.9	0.922
C9017C-9H-6, 26.2 cm	64.687	1.9846			0.408
C9017C-9H-6, 30.2 cm	64.727	1.9203			0.448
C9017C-9H-6, 34.2 cm	64.767	1.911			0.454
C9017C-9H-6, 38.2 cm	64.807	1.8951		2.701	0.464
C9017C-9H-6, 42.2 cm	64.847	2.0237			0.384
C9017C-9H-6, 46.2 cm	64.887	1.9702			0.417
C9017C-9H-6, 50.2 cm	64.927	2.0297			0.381
C9017C-9H-6, 54.2 cm	64.967	2.0816		5.4	0.349
C9017C-9H-6, 58.2 cm	65.007	2.1186			0.326
C9017C-9H-6, 62.2 cm	65.047	1.4234			0.754
C9017C-9H-6, 66.2 cm	65.087	1.955			0.427
C9017C-9H-6, 70.2 cm	65.127	0.8528		3.667	1.105
C9017C-9H-6, 74.2 cm	65.167	1.9458			0.432
C9017C-9H-6, 78.2 cm	65.207	1.7876			0.530
C9017C-9H-6, 82.2 cm	65.247	1.7833			0.532
C9017C-9H-6, 86.2 cm	65.287	1.9468		5.1	0.432
C9017C-9H-6, 90.2 cm	65.327	1.9312			0.441
C9017C-9H-6, 94.2 cm	65.367	1.8324			0.502
C9017C-9H-6, 98.2 cm	65.407	1.8816			0.472
C9017C-9H-6, 102.2 cm	65.447	1.8179		2.001	0.511
C9017C-9H-7, 0.8 cm	65.488	1.4313			0.749
C9017C-9H-7, 4.8 cm	65.528	1.8399			0.498
C9017C-9H-7, 8.8 cm	65.568	1.818			0.511
C9017C-9H-7, 12.8 cm	65.608	1.7984		2.401	0.523
C9017C-9H-7, 16.8 cm	65.648	0.6617			1.223
C9017C-9H-7, 24.8 cm	65.728	1.8732			0.477
C9017C-9H-7, 28.8 cm	65.768	1.7719		1.533	0.539
C9017C-9H-7, 32.8 cm	65.808	1.2684			0.850
C9017C-9H-7, 36.8 cm	65.848	1.897			0.462
C9017C-9H-7, 40.8 cm	65.888	1.7933			0.526
C9017C-9H-7, 44.8 cm	65.928	1.7682		2.966	0.542
C9017C-9H-7, 48.8 cm	65.968	1.7868			0.530
C9017C-9H-7, 52.8 cm	66.008	0.6732			1.216

Table 5-3-2-1

Location	Subbottom Depth	GRA ¹⁾	MS ²⁾	NGR ³⁾	GRA Porosity
	[mbsf]	[g/cm ³]	[x10 ⁻⁵ SI]	[cps]	
C9017C-9H-7, 68.8 cm	66.168	1.5955			0.648
C9017C-9H-7, 72.8 cm	66.208	1.88			0.473
C9017C-9H-7, 76.8 cm	66.248	1.5722		5.833	0.662
C9017C-9H-7, 80.8 cm	66.288	1.7705			0.540
C9017C-9H-7, 84.8 cm	66.328	1.5556			0.673
C9017C-9H-7, 88.8 cm	66.368	1.4919			0.712
C9017C-9H-8, 36.3 cm	66.848	1.0693			0.972
C9017C-9H-8, 40.3 cm	66.888	0.8748		1.634	1.092
C9017C-9H-8, 44.3 cm	66.928	1.1123			0.946
C9017C-9H-8, 48.3 cm	66.968	0.8136			1.130
C9017C-9H-8, 52.3 cm	67.008	0.8895			1.083
C9017C-9H-8, 56.3 cm	67.048	0.9181		4.5	1.065
C9017C-9H-8, 60.3 cm	67.088	1.3683			0.788
C9017C-9H-8, 64.3 cm	67.128	0.6901			1.206
C9017C-9H-9, 3.8 cm	67.528	-0.0299		-4.666	1.649
C9017C-9H-9, 7.8 cm	67.568	-0.0633			1.670
C9017C-9H-9, 11.8 cm	67.608	-0.0489			1.661
C9017C-9H-9, 15.8 cm	67.648	1.1248			0.938
C9017C-9H-9, 19.8 cm	67.688	1.0943		4.001	0.957
C9017C-9H-9, 23.8 cm	67.728	0.6908			1.205
C9017C-9H-9, 27.8 cm	67.768	0.0831			1.579
C9017C-9H-9, 31.8 cm	67.808	0.6675			1.220
C9017C-9H-9, 35.8 cm	67.848	0.1252		0.234	1.553
C9017C-9H-9, 39.8 cm	67.888	0.2207			1.495
C9017C-9H-9, 43.8 cm	67.928	0.1622			1.531
C9017C-9H-9, 47.8 cm	67.968	0.2237			1.493
C9017C-9H-9, 51.8 cm	68.008	-0.0232		-0.401	1.645
C9017C-9H-9, 55.8 cm	68.048	-0.0194			1.642
C9017C-9H-9, 59.8 cm	68.088	-0.0207			1.643
C9017C-9H-9, 63.8 cm	68.128	-0.0055			1.634
C9017C-9H-9, 67.8 cm	68.168	-0.03		2.267	1.649
C9017C-9H-9, 71.8 cm	68.208	-0.02			1.643
C9017C-10H-1, 8.0 cm	69.58	1.4599			0.732
C9017C-10H-1, 12.0 cm	69.62	1.7187			0.572
C9017C-10H-1, 16.0 cm	69.66	1.3681		22.7	0.788
C9017C-10H-1, 20.0 cm	69.7	1.73			0.565
C9017C-10H-1, 24.0 cm	69.74	1.9269			0.444
C9017C-10H-1, 28.0 cm	69.78	1.8976			0.462
C9017C-10H-1, 32.0 cm	69.82	1.7587		14.033	0.548
C9017C-10H-1, 36.0 cm	69.86	1.7368			0.561
C9017C-10H-1, 40.0 cm	69.9	2.1215			0.324
C9017C-10H-1, 44.0 cm	69.94	2.1108			0.331
C9017C-10H-1, 48.0 cm	69.98	2.0262		3.067	0.383
C9017C-10H-1, 52.0 cm	70.02	2.1223			0.324
C9017C-10H-1, 56.0 cm	70.06	2.0894			0.344
C9017C-10H-1, 60.0 cm	70.1	0.3031			1.444
C9017C-10H-2, 2.3 cm	70.143	1.822		2.399	0.509
C9017C-10H-2, 6.3 cm	70.183	1.9904			0.405
C9017C-10H-2, 10.3 cm	70.223	1.7876			0.530
C9017C-10H-2, 14.3 cm	70.263	0.1305			1.550
C9017C-10H-2, 18.3 cm	70.303	-0.0286		-2.701	1.648
C9017C-10H-2, 22.3 cm	70.343	-0.0404			1.655

Table 5-3-2-1

Location	Subbottom Depth	GRA ¹⁾	MS ²⁾	NGR ³⁾	GRA Porosity
	[mbsf]	[g/cm ³]	[x10 ⁻⁵ SI]	[cps]	
C9017C-10H-2, 26.3 cm	70.383	-0.0308			1.650
C9017C-10H-2, 30.3 cm	70.423	1.6106			0.639
C9017C-10H-2, 34.3 cm	70.463	1.8067		4.533	0.518
C9017C-10H-2, 38.3 cm	70.503	0.7441			1.172
C9017C-10H-2, 42.3 cm	70.543	0.6792			1.212
C9017C-10H-2, 46.3 cm	70.583	0.6588			1.225
C9017C-10H-2, 50.3 cm	70.623	0.9548		6.732	1.043
C9017C-10H-2, 54.3 cm	70.663	1.6144			0.636
C9017C-10H-2, 58.3 cm	70.703	1.5598			0.670
C9017C-10H-2, 62.3 cm	70.743	1.6076			0.641
C9017C-10H-2, 66.3 cm	70.783	1.6268		31.766	0.629
C9017C-10H-2, 70.3 cm	70.823	1.5594			0.670
C9017C-10H-2, 74.3 cm	70.863	1.4971			0.709
C9017C-10H-2, 78.3 cm	70.903	1.5975			0.647
C9017C-10H-2, 82.3 cm	70.943	1.5726		41.2	0.662
C9017C-10H-2, 86.3 cm	70.983	1.697			0.586
C9017C-10H-2, 90.3 cm	71.023	1.5037			0.705
C9017C-10H-2, 94.3 cm	71.063	1.8503			0.491
C9017C-11H-1, 8.0 cm	71.08	0.5809			1.273
C9017C-10H-2, 98.3 cm	71.103	1.7087		33.5	0.578
C9017C-11H-1, 12.0 cm	71.12	0.99			1.021
C9017C-11H-1, 16.0 cm	71.16	1.1704		18.468	0.910
C9017C-11H-1, 20.0 cm	71.2	1.5065			0.703
C9017C-11H-1, 24.0 cm	71.24	1.5515			0.675
C9017C-11H-1, 28.0 cm	71.28	1.8294			0.504
C9017C-11H-1, 32.0 cm	71.32	1.9747		15.367	0.415
C9017C-11H-1, 36.0 cm	71.36	1.8762			0.475
C9017C-11H-1, 40.0 cm	71.4	1.9629			0.422
C9017C-11H-1, 44.0 cm	71.44	1.8964			0.463
C9017C-11H-1, 48.0 cm	71.48	1.6657		31.568	0.605
C9017C-11H-1, 52.0 cm	71.52	1.7149			0.575
C9017C-11H-1, 56.0 cm	71.56	1.8851			0.470
C9017C-11H-1, 60.0 cm	71.6	1.6277			0.628
C9017C-11H-1, 64.0 cm	71.64	1.6878		34.201	0.591
C9017C-11H-1, 68.0 cm	71.68	1.6985			0.585
C9017C-11H-1, 72.0 cm	71.72	1.4342			0.747
C9017C-11H-1, 76.0 cm	71.76	1.643			0.619
C9017C-11H-1, 80.0 cm	71.8	1.757		40.334	0.549
C9017C-11H-1, 84.0 cm	71.84	1.6629			0.607
C9017C-11H-1, 88.0 cm	71.88	1.6088			0.640
C9017C-11H-1, 92.0 cm	71.92	1.721			0.571
C9017C-11H-1, 96.0 cm	71.96	1.5439		17.934	0.680
C9017C-11H-1, 100.0 cm	72	1.4456			0.740
C9017C-11H-2, 3.3 cm	72.038	1.5091			0.701
C9017C-11H-2, 7.3 cm	72.078	1.6231			0.631
C9017C-11H-2, 11.3 cm	72.118	1.691		43.801	0.589
C9017C-11H-2, 15.3 cm	72.158	1.6565			0.611
C9017C-11H-2, 19.3 cm	72.198	1.6372			0.622
C9017C-11H-2, 23.3 cm	72.238	1.6139			0.637
C9017C-11H-2, 27.3 cm	72.278	1.5681		46.302	0.665
C9017C-11H-2, 31.3 cm	72.318	1.5452			0.679
C9017C-11H-2, 35.3 cm	72.358	1.5445			0.679

Table 5-3-2-1

Location	Subbottom Depth [mbsf]	GRA ¹⁾ [g/cm ³]	MS ²⁾ [x10 ⁻⁵ SI]	NGR ³⁾ [cps]	GRA Porosity
C9017C-11H-2, 39.3 cm	72.398	1.5053			0.704
C9017C-11H-2, 43.3 cm	72.438	1.0704		23.268	0.971
C9017C-11H-2, 47.3 cm	72.478	1.496			0.709
C9017C-11H-2, 51.3 cm	72.518	1.3825			0.779
C9017C-11H-2, 55.3 cm	72.558	1.3347			0.809
C9017C-11H-2, 59.3 cm	72.598	1.301		36.467	0.829
C9017C-11H-2, 63.3 cm	72.638	1.2763			0.845
C9017C-11H-2, 67.3 cm	72.678	1.2762			0.845
C9017C-11H-2, 71.3 cm	72.718	1.2251			0.876
C9017C-11H-2, 75.3 cm	72.758	1.2161		33.933	0.882
C9017C-11H-2, 79.3 cm	72.798	1.1868			0.900
C9017C-11H-2, 83.3 cm	72.838	1.1323			0.933
C9017C-11H-2, 87.3 cm	72.878	1.0875			0.961
C9017C-11H-2, 91.3 cm	72.918	1.144		25.401	0.926
C9017C-11H-2, 95.3 cm	72.958	1.1643			0.914
C9017C-11H-2, 99.3 cm	72.998	1.0317			0.995
C9017C-12X-CC, 8.0 cm	73.58	1.205	22.5387	83.468	0.889
C9017C-12X-CC, 12.0 cm	73.62	2.0467	26.5609		0.370
C9017C-12X-CC, 16.0 cm	73.66	1.9411	39.2104	108.733	0.435
C9017C-12X-CC, 20.0 cm	73.7	1.467	39.2435		0.727
C9017C-12X-CC, 24.0 cm	73.74	0.8308	42.9981	99.834	1.119
C9017C-12X-CC, 28.0 cm	73.78	1.9309	74.0266		0.442
C9017C-12X-CC, 32.0 cm	73.82	2.0553	54.1497	92.833	0.365
C9017C-12X-CC, 36.0 cm	73.86	1.8288	17.8251		0.504
C9017C-13X-CC, 8.0 cm	83.08	0.8214	7.9247	22.7	1.125
C9017C-13X-CC, 12.0 cm	83.12	1.31	12.5634		0.824
C9017C-13X-CC, 16.0 cm	83.16	1.9616	19.544	24.666	0.423
C9017C-13X-CC, 20.0 cm	83.2	1.9014	21.7408		0.460
C9017C-13X-CC, 24.0 cm	83.24	1.3349	17.0503	26.967	0.809
C9017C-13X-CC, 28.0 cm	83.28	1.4409	21.0703		0.743
C9017C-13X-CC, 32.0 cm	83.32	1.7026	58.5823	42.233	0.582
C9017C-13X-CC, 36.0 cm	83.36	1.9503	37.5963		0.430
C9017C-13X-CC, 40.0 cm	83.4	1.7809	16.3581	28.633	0.534
C9017C-14X-1, 8.0 cm	92.58	1.7088			0.578
C9017C-14X-1, 12.0 cm	92.62	1.797			0.524
C9017C-14X-1, 16.0 cm	92.66	1.7931		41.466	0.526
C9017C-14X-1, 20.0 cm	92.7	1.9097			0.455
C9017C-14X-1, 24.0 cm	92.74	1.9577			0.425
C9017C-14X-1, 28.0 cm	92.78	1.9341			0.440
C9017C-14X-1, 32.0 cm	92.82	1.9258		42.701	0.445
C9017C-14X-1, 36.0 cm	92.86	1.8434			0.495

Table 5-3-2-1

Location	Subbottom Depth	GRA ¹⁾	MS ²⁾	NGR ³⁾	GRA Porosity
	[mbsf]	[g/cm ³]	[x10 ⁻⁵ SI]	[cps]	
C9017C-14X-1, 40.0 cm	92.9	1.7666			0.543
C9017C-14X-1, 44.0 cm	92.94	1.831			0.503
C9017C-14X-1, 48.0 cm	92.98	1.8456		47	0.494
C9017C-14X-1, 52.0 cm	93.02	1.7922			0.527
C9017C-14X-1, 56.0 cm	93.06	1.8694			0.479
C9017C-14X-1, 60.0 cm	93.1	1.8353			0.500
C9017C-14X-1, 64.0 cm	93.14	1.8454		51.767	0.494
C9017C-14X-1, 68.0 cm	93.18	1.8276			0.505
C9017C-14X-1, 72.0 cm	93.22	1.8606			0.485
C9017C-14X-1, 76.0 cm	93.26	1.8409			0.497
C9017C-14X-1, 80.0 cm	93.3	1.825		49.399	0.507
C9017C-14X-1, 84.0 cm	93.34	1.8172			0.512
C9017C-14X-1, 88.0 cm	93.38	1.8535			0.489
C9017C-14X-1, 92.0 cm	93.42	1.8842			0.470
C9017C-14X-1, 96.0 cm	93.46	1.8725		76.466	0.478
C9017C-14X-1, 100.0 cm	93.5	1.2944			0.833
C9017C-15X-1, 8.0 cm	102.08	0.7874			1.146
C9017C-15X-1, 12.0 cm	102.12	0.663			1.222
C9017C-15X-1, 16.0 cm	102.16	0.9226		3.166	1.062
C9017C-15X-1, 20.0 cm	102.2	1.3627			0.791
C9017C-15X-1, 24.0 cm	102.24	1.7133			0.576
C9017C-15X-1, 28.0 cm	102.28	1.6909			0.589
C9017C-15X-1, 32.0 cm	102.32	1.7419		11.433	0.558
C9017C-15X-1, 36.0 cm	102.36	1.7851			0.531
C9017C-15X-1, 40.0 cm	102.4	1.823			0.508
C9017C-15X-1, 44.0 cm	102.44	1.8691			0.480
C9017C-15X-1, 48.0 cm	102.48	1.759		12.034	0.547
C9017C-16X-1, 8.0 cm	111.58	1.0085			1.010
C9017C-16X-1, 12.0 cm	111.62	0.5207			1.310
C9017C-16X-1, 16.0 cm	111.66	1.6791		4.6	0.597
C9017C-16X-1, 20.0 cm	111.7	1.0463			0.986
C9017C-16X-1, 24.0 cm	111.74	1.8609			0.485
C9017C-16X-1, 28.0 cm	111.78	1.5348			0.685
C9017C-16X-1, 32.0 cm	111.82	1.3431		11.4	0.804
C9017C-16X-1, 36.0 cm	111.86	1.869			0.480
C9017C-16X-1, 40.0 cm	111.9	2.0909			0.343
C9017C-16X-1, 44.0 cm	111.94	2.0566			0.364
C9017C-16X-CC, 4.1 cm	112.061	1.8934	42.6837		0.465
C9017C-16X-CC, 8.1 cm	112.101	1.4944	45.3469		0.710
C9017C-16X-CC, 12.1 cm	112.141	2.099	45.5876	12.535	0.338
C9017C-16X-CC, 16.1 cm	112.181	2.0429	42.988		0.373
C9017C-16X-CC, 20.1 cm	112.221	1.3826	40.1628		0.779
C9017C-16X-CC, 24.1 cm	112.261	2.1699	40.8276		0.294
C9017C-16X-CC, 28.1 cm	112.301	2.0551	32.9821	12.333	0.365
C9017C-16X-CC, 32.1 cm	112.341	2.1112	34.8931		0.331
C9017C-16X-CC, 36.1 cm	112.381	2.1481	30.2563		0.308
C9017C-16X-CC, 40.1 cm	112.421	0.8421	15.8274		1.112

¹⁾Gamma ray attenuation density (g/cm³)²⁾Magnetic susceptibility (x0.00001 SI)³⁾Natural gamma ray radiation (cps)

Table 5-3-2-2

Top Location of Sample Interval	Subbottom Depth [mbsf]	Bulk Density [g/cm ³]	Grain Density [g/cm ³]	Porosity	Porosity: Syringe
C9017C-1X-1, 6.0 cm	0.060	2.253	2.822	0.316	
C9017C-1X-CC, 24.0 cm	0.345	2.252	2.856	0.330	
C9017C-2X-1, 16.0 cm	9.660	2.052	2.944	0.465	
C9017C-2X-CC, 32.0 cm	10.200	2.264	2.962	0.360	
C9017C-3X-1, 33.0 cm	19.330	1.870	3.072	0.587	0.698
C9017C-3X-2, 32.0 cm	20.325	1.913	2.894	0.525	
C9017C-3X-3, 90.0 cm	21.915	2.128	2.956	0.429	
C9017C-3X-4, 44.0 cm	22.460	1.879	3.023	0.572	
C9017C-4H-4, 94.0 cm	27.960	1.913	2.918	0.531	
C9017C-4H-6, 83.0 cm	29.860	1.847	2.916	0.565	0.636
C9017C-4H-8, 8.0 cm	31.125	1.927	2.924	0.525	
C9017C-5H-1, 45.5 cm	32.455	2.249	2.816	0.316	
C9017C-5H-2, 46.0 cm	33.305	1.879	2.888	0.541	0.586
C9017C-5H-6, 4.0 cm	36.915	1.982	2.877	0.483	0.530
C9017C-5H-8, 83.0 cm	39.720	2.075	2.865	0.429	0.528
C9017C-6H-CC, 0.0 cm	40.000	1.873	2.887	0.545	
C9017C-7H-3, 6.0 cm	49.190	1.909	2.863	0.519	
C9017C-7H-7, 3.0 cm	52.080	1.989	2.781	0.451	0.727
C9017C-7H-9, 80.0 cm	54.315	1.791	2.894	0.590	
C9017C-8H-3, 72.0 cm	54.590	1.912	2.893	0.525	
C9017C-8H-6, 3.0 cm	56.685	2.015	2.974	0.492	
C9017C-8H-8, 3.0 cm	58.705	2.009	3.048	0.513	
C9017C-9H-2, 3.0 cm	60.670	1.979	3.097	0.539	
C9017C-9H-3, 3.0 cm	61.440	1.973	2.674	0.425	
C9017C-9H-6, 67.0 cm	65.095	1.991	2.798	0.455	
C9017C-9H-7, 49.0 cm	65.970	1.990	2.667	0.412	
C9017C-10H-1, 50.0 cm	70.000	2.444	3.675	0.464	
C9017C-10H-2, 5.0 cm	70.170	2.007	3.247	0.558	0.580
C9017C-11H-1, 93.0 cm	71.930	1.947	3.072	0.550	
C9017C-11H-2, 10.0 cm	72.105	1.787	3.231	0.654	0.701
C9017C-12X-CC, 0.0 cm	73.500	2.092	2.944	0.444	
C9017C-13X-CC, 20.0 cm	83.200	1.961	2.939	0.511	0.733
C9017C-13X-CC, 36.5 cm	83.365	2.386	2.989	0.307	0.625
C9017C-14X-1, 68.0 cm	93.180	1.925	2.961	0.535	
C9017C-14X-CC, 10.0 cm	93.600	2.024	2.910	0.470	
C9017C-15X-1, 24.0 cm	102.240	1.789	3.058	0.624	
C9017C-15X-CC, 29.0 cm	102.795	2.223	2.916	0.366	
C9017C-16X-1, 38.5 cm	111.885	2.117	3.224	0.503	

Table 5-3-2-3

Location	Subbottom depth [mbsf]	Average gamma ray pulse count rate [cps]	DER [μSv/h]
C9017C-1X-1, 2.0 cm	0.02	2	0.02
C9017C-1X-CC, 32.0 cm	0.425	2	0.05
C9017C-2X-1, 10.0 cm	9.6	2	0.03
C9017C-2X-CC, 11.0 cm	9.99	2	0.02
C9017C-2X-CC, 23.0 cm	10.11	1	0.03
C9017C-3X-1, 46.0 cm	19.46	3	0.03
C9017C-3X-2, 40.0 cm	20.405	3	0.03
C9017C-3X-3, 86.5 cm	21.88	3	0.04
C9017C-3X-4, 43.0 cm	22.45	7	0.05
C9017C-4H-4, 94.0 cm	27.96	2	0.04
C9017C-4H-7, 10.0 cm	30.135	2	0.02
C9017C-4H-8, 34.0 cm	31.385	2	0.03
C9017C-5H-1, 39.0 cm	32.39	2	0.02
C9017C-5H-3, 45.0 cm	34.305	2	0.03
C9017C-5H-5, 94.0 cm	36.81	1	0
C9017C-5H-8, 90.0 cm	39.79	2	0.02
C9017C-7H-3, 21.0 cm	49.34	2	0.03
C9017C-7H-7, 5.0 cm	52.1	2	0.04
C9017C-7H-7, 6.0 cm	52.11	2	0.02
C9017C-7H-9, 70.0 cm	54.215	2	0.05
C9017C-8H-3, 73.0 cm	54.6	2	0.03
C9017C-8H-6, 7.0 cm	56.725	2	0.05
C9017C-8H-7, 66.0 cm	58.325	2	0.02
C9017C-8H-8, 79.0 cm	59.465	2	0.03
C9017C-8H-8, 93.0 cm	59.605	2	0.06
C9017C-9H-2, 14.0 cm	60.78	2	0.02
C9017C-9H-3, 12.0 cm	61.53	2	0.02
C9017C-9H-5, 82.0 cm	64.245	2	0.03
C9017C-10H-1, 53.0 cm	70.03	2	0.02
C9017C-10H-2, 7.0 cm	70.19	2	0.03
C9017C-11H-1, 85.0 cm	71.85	2	0.04
C9017C-12X-CC, 5.0 cm	73.55	3	0.04
C9017C-13X-CC, 39.0 cm	83.39	2	0.04
C9017C-14X-1, 30.0 cm	92.8	3	0.03
C9017C-15X-1, 31.0 cm	102.31	2	0.02
C9017C-16X-1, 15.0 cm	111.65	2	0.03

Table 5-3-2-4

Location	Subbottom Depth (mbsf)	WR/HS	Thermal conductivity [W/(m·K)]	LET	Probe	Remark
C9017C-3X-2, 88.0 cm	20.885	WR	1.12	Qualified: >10	VLQ60	mud
C9017C-3X-4, 14.0 cm	22.16	WR	1.751	Qualified: >10	VLQ60	mud
C9017C-4H-4, 94.0 cm	27.96	W	0.85	Qualified: >10	HLQ50	core solid
C9017C-4H-6, 60.0 cm	29.63	W	1.219	Qualified: >10	HLQ50	breccia, pumice
C9017C-4H-8, 8.0 cm	31.125	W	1.258	Qualified: >10	HLQ50	mud
C9017C-5H-2, 60.0 cm	33.445	W	1.294	Qualified: >10	HLQ50	
C9017C-5H-6, 15.0 cm	37.025	W	1.359	Qualified: >10	HLQ50	
C9017C-7H-3, 10.0 cm	49.23	W	1.282	Qualified: >10	HLQ50	mud, clay
C9017C-7H-7, 5.0 cm	52.1	W	1.128	Qualified: >10	HLQ50	oil compound, clay, gravel
C9017C-7H-9, 62.5 cm	54.14	W	1	Qualified: >10	HLQ50	oil compound, clay, gravel
C9017C-8H-3, 75.0 cm	54.62	W	1.839	Qualified: >10	HLQ50	oil compound, clay, mud
C9017C-8H-6, 6.0 cm	56.715	W	1.452	Qualified: >10	HLQ50	oil compound, clay, mud
C9017C-8H-8, 10.0 cm	58.775	W	1.226	Qualified: >10	HLQ50	oil compound, clay, mud, anhydrite, no weight measurement
C9017C-8H-8, 10.0 cm	58.775	W	1.633	Qualified: >10	HLQ50	oil compound, clay, mud, anhydrite, 2nd
C9017C-9H-2, 20.0 cm	60.84	W	1.329	Qualified: >10	HLQ50	oil compound, mudstone
C9017C-9H-6, 50.0 cm	64.925	W	1.946	Qualified: >10	HLQ50	oil compound, pebble and mud
C9017C-9H-7, 27.0 cm	65.75	W	1.001	Qualified: >10	HLQ50	oil compound, mudstone with white fragment
C9017C-10H-2, 7.0 cm	70.19	W	0.593	Qualified: >10	HLQ50	oil compound, 2nd run, siltstone, bubble
C9017C-13X-CC, 16.0 cm	83.16	W	1.569	Qualified: >10	HLQ50	oil compound, gravel and sand
C9017C-14X-1, 93.0 cm	93.43	W	1.31	Qualified: >10	HLQ50	oil compound, siltstone with mud
C9017C-14X-1, 93.0 cm	93.43	W	1.327	Qualified: >10	HLQ50	siltstone with mud
C9017C-14X-CC, 29.0 cm	93.79	W	1.689	Qualified: >10	HLQ50	
C9017C-14X-CC, 29.0 cm	93.79	W	1.647	Qualified: >10	HLQ50	2nd
C9017C-14X-CC, 29.0 cm	93.79	W	1.382	Qualified: >10	HLQ50	oil compound, 3rd

Table 5-3-2-5

Location	Subbottom Depth [mbsf]	Bulk resistivity at 1 kHz [Ω m]	Remarks
C9017C-1X-CC, 31.0 cm	0.415	12.28393115	discrete, shared with PWVD
C9017C-2X-1, 25.0 cm	9.75	23.73909847	discrete, shared with PWVD
C9017C-2X-CC, 17.0 cm	10.05	2.341001304	section
C9017C-3X-1, 34.0 cm	19.34	0.64880106	section
C9017C-3X-2, 28.0 cm	20.285	1.842095435	discrete, shared with PWVD
C9017C-3X-4, 21.5 cm	22.235	1.092726595	section
C9017C-3X-CC, 2.5 cm	23.085	1.071906266	section
C9017C-4H-4, 96.0 cm	27.98	2.023923518	section
C9017C-4H-6, 85.5 cm	29.885	1.809722527	section
C9017C-4H-8, 2.0 cm	31.065	1.542016258	section
C9017C-5H-1, 47.5 cm	32.475	15.72912679	discrete, shared with PWVD
C9017C-5H-2, 42.0 cm	33.265	1.791345571	section
C9017C-5H-6, 2.0 cm	36.895	1.629654146	section
C9017C-7H-3, 3.0 cm	49.16	2.168068163	section
C9017C-7H-7, 2.5 cm	52.075	1.614024298	section
C9017C-8H-3, 75.0 cm	54.62	1.4593382	discrete
C9017C-8H-6, 0.0 cm	56.655	2.087171716	discrete
C9017C-8H-8, 0.0 cm	58.675	2.271364827	discrete
C9017C-9H-2, 0.0 cm	60.64	1.427043199	discrete
C9017C-9H-3, 2.5 cm	61.435	3.928515709	section
C9017C-9H-7, 50.0 cm	65.98	4.968175968	section
C9017C-10H-1, 56.0 cm	70.06	0.227724596	section
C9017C-10H-2, 3.0 cm	70.15	0.198691322	section
C9017C-11H-1, 97.0 cm	71.97	1.647838317	section
C9017C-11H-2, 12.5 cm	72.13	0.433811662	section
C9017C-12X-CC, 10.5 cm	73.605	13.32703214	discrete, shared with PWVD
C9017C-13X-CC, 18.0 cm	83.18	0.976247738	section
C9017C-14X-1, 70.0 cm	93.2	0.60777633	section
C9017C-14X-CC, 12.5 cm	93.625	0.745916767	section
C9017C-15X-CC, 32.0 cm	102.825	0.885778812	discrete
C9017C-16X-1, 35.0 cm	111.85	1.271052104	discrete, shared with PWVD

Table 5-3-2-6

Location	Subbottom Depth [mbsf]	P-wave velocity [m/s]				P-wave velocity [m/s] : saturated for 24 hours				Remarks
		X	Y	Z	Average	X	Y	Z	Average	
C9017C-1X-CC, 31.0 cm	0.415	4726	4137	4441	4434.67	4569	4570	4733	4624.00	shared with IMP
C9017C-2X-1, 25.0 cm	9.75	4297	4611	4692	4533.33	4426	4623	4386	4478.33	shared with IMP
C9017C-3X-2, 28.0 cm	20.285	1982	1876	1862	1906.67	3761	4013	3707	3827.00	shared with IMP
C9017C-5H-1, 47.5 cm	32.475	3999	4045	4020	4021.33		2039	1862	1950.50	failed to measure X axis
C9017C-12X-CC, 10.5 cm	73.605	3761	4013	3707	3827.00	3869	4121	4060	4016.67	shared with IMP
C9017C-16X-1, 35.0 cm	111.85		2039	1862	1950.50	-	-	-	-	

Table 5-3-2-7

Location	Subbottom Depth [mbsf]	Unconfined compressive strength [kPa]	Remarks
C9017C-2X-1, 10.0 cm	9.6	39.24	mud and fragment
C9017C-3X-1, 14.0 cm	19.14	76.19	mud, breccia
C9017C-3X-1, 62.0 cm	19.62	82.4	mud, breccia
C9017C-3X-2, 17.0 cm	20.175	43.16	mud
C9017C-3X-3, 80.0 cm	21.815	48.07	mud
C9017C-3X-4, 40.0 cm	22.42	56.24	mud
C9017C-4H-2, 10.0 cm	25.11	55.92	mud, breccia
C9017C-4H-4, 90.0 cm	27.92	79.46	mud, breccia
C9017C-4H-7, 38.0 cm	30.415	274.68	fractured, uncertain value
C9017C-4H-7, 43.0 cm	30.465	68.67	mud, breccia
C9017C-4H-8, 16.0 cm	31.205	170.37	fractured
C9017C-5H-1, 81.0 cm	32.81	165.14	mud, breccia
C9017C-5H-2, 50.0 cm	33.345	282.86	breccia
C9017C-5H-6, 7.0 cm	36.945	470.88	mudstone
C9017C-5H-8, 88.0 cm	39.77	168.41	breccia
C9017C-7H-3, 6.0 cm	49.19	323.73	clay, mud
C9017C-7H-7, 2.0 cm	52.07	131.45	clay, mud
C9017C-7H-9, 76.0 cm	54.275	26.16	clay, mud
C9017C-9H-2, 7.0 cm	60.71	398.94	mudstone
C9017C-9H-3, 13.0 cm	61.54	102.02	mud (soft)
C9017C-9H-6, 72.0 cm	65.145	438.18	uncertain value (3rd), pebbles with mud
C9017C-9H-7, 68.0 cm	66.16	532.19	uncertain value, mudstone
C9017C-10H-1, 50.0 cm	70	362.97	sand, silt
C9017C-10H-2, 33.0 cm	70.45	176.58	sand, fractured
C9017C-11H-2, 70.0 cm	72.705	67.04	sand
C9017C-13X-CC, 18.0 cm	83.18	117.72	silt
C9017C-14X-1, 25.0 cm	92.75	91.56	silt, hydrothermally altered
C9017C-16X-1, 42.0 cm	111.92	125.24	silt, hydrothermally altered

Table 5-3-2-8

Location	Subbottom	Major element (wt%)					
	Depth [mbsf]	Si	Al	Fe	Ca	K	S
C9017C-2X-1, 11	9.6	12.6	3.3	26.0	3.3	0.0	18.4
C9017C-2X-cc, 23	10.1	18.0	6.1	12.9	5.9	0.7	6.3
C9017C-3X-1, 47	19.5	0.0	0.0	47.5	2.5	0.7	3.2
C9017C-3X-2, 31	20.3	5.2	0.0	36.6	5.5	0.7	7.6
C9017C-3X-4, 22	21.6	16.6	6.8	14.9	3.5	0.0	15.8
C9017C-3X-3, 60	22.2	6.3	0.0	36.1	5.1	0.0	6.1
C9017C-4H-4, 95	28.0	17.6	5.5	17.2	2.5	0.0	12.8
C9017C-4H-5, 40	28.4	21.1	7.7	13.6	0.7	0.0	9.9
C9017C-4H-6, 85	29.9	18.6	6.6	16.5	1.1	0.0	11.7
C9017C-4H-7, 41	30.4	16.9	7.9	15.1	1.6	0.0	14.3
C9017C-4H-8, 8	31.1	10.3	0.0	33.3	2.6	0.7	11.8
C9017C-5H-1, 48	32.5	12.1	2.5	26.2	6.7	0.9	5.6
C9017C-5H-2, 46	33.3	21.3	9.3	11.2	0.4	0.0	11.0
C9017C-5H-6, 5	36.9	18.3	8.6	10.7	6.0	0.0	11.3
C9017C-5H-8, 84	39.7	17.6	7.8	10.8	8.4	0.0	10.7
C9017C-7H-3, 7	49.2	17.7	10.8	12.3	1.2	0.6	11.9
C9017C-7H-5, 25	50.5	2.2	0.0	9.7	0.8	0.0	2.9
C9017C-7H-7, 8	52.1	17.7	8.1	12.4	4.4	0.0	12.9
C9017C-7H-7, 79	52.8	5.4	0.0	39.7	2.7	1.0	7.6
C9017C-8H-3, 75	54.6	19.9	10.3	10.5	2.3	0.0	10.8
C9017C-8H-6, 4	56.7	18.3	10.8	11.8	1.4	0.5	11.6
C9017C-8H-6, 19	56.8	21.2	10.8	9.0	2.1	0.0	9.7
C9017C-8H-8, 4	58.7	16.8	10.0	13.1	0.9	1.7	13.6
C9017C-9H-2, 3	60.7	13.5	8.3	12.8	3.3	2.5	20.0
C9017C-9H-2, 11	60.7	15.1	9.4	11.2	3.0	2.7	16.8
C9017C-9H-3, 4	61.4	22.2	9.8	8.2	4.9	0.8	5.9
C9017C-9H-6, 67	65.1	21.5	9.1	9.4	5.5	0.0	6.6
C9017C-9H-7, 27	65.7	14.6	12.1	12.6	7.7	0.0	2.5
C9017C-9H-7, 50	66.0	15.2	10.1	22.8	2.2	0.0	4.4
C9017C-10H-1, 20	69.7	4.4	2.9	46.0	1.4	1.8	13.2
C9017C-10H-1, 51	70.0	2.7	0.0	52.4	2.9	1.1	7.4
C9017C-10H-1, 56	70.1	3.4	0.0	53.9	2.3	0.6	11.6
C9017C-10H-2, 6	70.2	6.1	2.6	40.2	4.9	0.8	7.3
C9017C-11H-1, 11	71.1	7.5	0.0	41.7	3.0	4.7	4.5
C9017C-11H-1, 94	71.9	4.9	2.0	50.2	1.0	0.8	10.9
C9017C-11H-2, 11	72.1	7.7	2.6	38.1	2.0	3.5	5.0
C9017C-11H-2, 49	72.5	4.8	0.0	55.6	1.1	0.8	0.4
C9017C-12X-cc, 12	73.6	25.0	4.2	11.8	0.8	4.9	3.7
C9017C-13X-cc, 21	83.2	10.3	4.1	35.3	1.9	2.2	11.7
C9017C-13X-cc, 37	83.4	29.9	5.3	4.7	3.3	0.8	3.8
C9017C-14X-1, 66	93.2	16.2	7.5	17.6	0.6	6.2	7.3
C9017C-14X-cc, 11	93.6	16.7	6.8	15.7	3.3	4.0	4.3
C9017C-15X-1, 25	102.2	5.7	0.0	53.2	0.6	1.3	1.6
C9017C-15X-cc, 30	102.8	22.8	8.3	12.0	2.4	1.0	3.1
C9017C-15X-cc, 37	102.9	22.3	8.3	11.2	3.9	0.0	6.6
C9017C-16X-cc, 28.5	112.3	7.8	4.9	35.2	1.1	0.0	20.4

Table 5-3-3-1
Hole B

Location	Subbottom Depth	GRA ¹⁾	MS ²⁾	NGR ³⁾	GRA Porosity
	[mbsf]	[g/cm ³]	[x10 ⁻⁵ SI]	[cps]	
C9019B-1H-1, 8.0 cm	0.08	-0.056	35.26		1.665
C9019B-1H-1, 12.0 cm	0.12	-0.047	37.31		1.660
C9019B-1H-1, 16.0 cm	0.16	0.180	37.31	33.967	1.520
C9019B-1H-1, 20.0 cm	0.2	0.497	35.63		1.325
C9019B-1H-1, 24.0 cm	0.24	0.800	40.42		1.138
C9019B-1H-1, 28.0 cm	0.28	1.363	55.07		0.791
C9019B-1H-1, 32.0 cm	0.32	1.573	77.63	154.333	0.662
C9019B-1H-1, 36.0 cm	0.36	1.629	83.35		0.627
C9019B-1H-1, 40.0 cm	0.4	1.721	78.26		0.571
C9019B-1H-1, 44.0 cm	0.44	1.908	53.32		0.456
C9019B-1H-1, 48.0 cm	0.48	1.605	46.17	125.134	0.642
C9019B-1H-1, 52.0 cm	0.52	1.579	32.81		0.658
C9019B-1H-1, 56.0 cm	0.56	1.543	26.79		0.681
C9019B-1H-1, 60.0 cm	0.6	1.765	34.23		0.544
C9019B-1H-1, 64.0 cm	0.64	1.736	36.80	50.134	0.562
C9019B-1H-1, 68.0 cm	0.68	1.617	38.04		0.635
C9019B-1H-1, 72.0 cm	0.72	1.639	38.74		0.621
C9019B-1H-1, 76.0 cm	0.76	1.352	33.13		0.798
C9019B-1H-1, 80.0 cm	0.8	1.452	55.90	21.033	0.736
C9019B-1H-1, 84.0 cm	0.84	1.514	87.54		0.698
C9019B-1H-1, 88.0 cm	0.88	1.961	120.65		0.423
C9019B-1H-1, 92.0 cm	0.92	1.410	46.44		0.763
C9019B-1H-1, 96.0 cm	0.96	1.480	33.06	17.299	0.719
C9019B-1H-1, 100.0 cm	1	1.190	57.04		0.898
C9019B-1H-2, 3.7 cm	1.037	1.684	50.76		0.593
C9019B-1H-2, 7.7 cm	1.077	1.564	27.73		0.668
C9019B-1H-2, 11.7 cm	1.117	1.547	23.95	20.133	0.678
C9019B-1H-2, 15.7 cm	1.157	1.485	20.17		0.716
C9019B-1H-2, 19.7 cm	1.197	1.410	20.90		0.762
C9019B-1H-2, 23.7 cm	1.237	1.444	23.72		0.741
C9019B-1H-2, 27.7 cm	1.277	1.399	29.23	22.367	0.769
C9019B-1H-2, 31.7 cm	1.317	1.507	33.33		0.703
C9019B-1H-2, 35.7 cm	1.357	1.494	27.96		0.710
C9019B-1H-2, 39.7 cm	1.397	1.484	21.21		0.717
C9019B-1H-2, 43.7 cm	1.437	1.457	23.86	21.666	0.733
C9019B-1H-2, 47.7 cm	1.477	1.430	26.65		0.750
C9019B-1H-2, 51.7 cm	1.517	1.542	21.37		0.681
C9019B-1H-2, 55.7 cm	1.557	1.534	24.73		0.686
C9019B-1H-2, 59.7 cm	1.597	1.512	22.67	23.333	0.700
C9019B-1H-2, 63.7 cm	1.637	1.494	20.64		0.711
C9019B-1H-2, 67.7 cm	1.677	1.577	31.28		0.660
C9019B-1H-2, 71.7 cm	1.717	1.587	22.61		0.653
C9019B-1H-2, 75.7 cm	1.757	1.635	15.68	21.300	0.624
C9019B-1H-2, 79.7 cm	1.797	1.675	11.67		0.599
C9019B-1H-2, 83.7 cm	1.837	1.541	11.40		0.682
C9019B-1H-2, 87.7 cm	1.877	1.609	17.01		0.640
C9019B-1H-2, 91.7 cm	1.917	1.574	15.40	20.033	0.661
C9019B-1H-2, 95.7 cm	1.957	1.540	16.56		0.682
C9019B-1H-2, 99.7 cm	1.997	1.515	17.70		0.698

Location	Subbottom Depth	GRA ¹⁾	MS ²⁾	NGR ³⁾	GRA Porosity
	[mbsf]	[g/cm ³]	[x10 ⁻⁵ SI]	[cps]	
C9019B-1H-3, 2.6 cm	2.036	1.522	19.31		0.693
C9019B-1H-3, 6.6 cm	2.076	1.524	31.28	28.566	0.692
C9019B-1H-3, 10.6 cm	2.116	1.617	45.99		0.635
C9019B-1H-3, 14.6 cm	2.156	1.687	58.24		0.592
C9019B-1H-3, 18.6 cm	2.196	1.501	68.71		0.706
C9019B-1H-3, 22.6 cm	2.236	1.473	77.93	46.167	0.723
C9019B-1H-3, 26.6 cm	2.276	1.614	51.53		0.636
C9019B-1H-3, 30.6 cm	2.316	1.581	29.86		0.657
C9019B-1H-3, 34.6 cm	2.356	1.581	23.40		0.657
C9019B-1H-3, 38.6 cm	2.396	1.575	20.01	36.534	0.661
C9019B-1H-3, 42.6 cm	2.436	1.580	21.41		0.658
C9019B-1H-3, 46.6 cm	2.476	1.615	22.11		0.636
C9019B-1H-3, 50.6 cm	2.516	1.580	21.47		0.658
C9019B-1H-3, 54.6 cm	2.556	1.500	21.49	36.466	0.707
C9019B-1H-3, 58.6 cm	2.596	1.501	21.54		0.706
C9019B-1H-3, 62.6 cm	2.636	1.480	31.79		0.719
C9019B-1H-3, 66.6 cm	2.676	1.488	19.06		0.714
C9019B-1H-3, 70.6 cm	2.716	1.444	18.37	27.233	0.742
C9019B-1H-3, 74.6 cm	2.756	1.447	18.99		0.739
C9019B-1H-3, 78.6 cm	2.796	1.430	18.95		0.750
C9019B-1H-3, 82.6 cm	2.836	1.426	19.42		0.753
C9019B-1H-3, 86.6 cm	2.876	1.460	22.61	24.834	0.732
C9019B-1H-3, 90.6 cm	2.916	1.527	22.18		0.690
C9019B-1H-3, 94.6 cm	2.956	1.467	21.80		0.728
C9019B-1H-3, 98.6 cm	2.996	1.386	18.88		0.777
C9019B-1H-4, 1.5 cm	3.035	1.428	15.22	24.799	0.752
C9019B-1H-4, 5.5 cm	3.075	1.484	17.93		0.717
C9019B-1H-4, 9.5 cm	3.115	1.459	12.89		0.732
C9019B-1H-4, 13.5 cm	3.155	1.409	12.36		0.763
C9019B-1H-4, 17.5 cm	3.195	1.404	12.37	25.032	0.766
C9019B-1H-4, 21.5 cm	3.235	1.460	11.21		0.732
C9019B-1H-4, 25.5 cm	3.275	1.420	9.25		0.756
C9019B-1H-4, 29.5 cm	3.315	1.481	20.52		0.718
C9019B-1H-4, 33.5 cm	3.355	1.535	39.76	31.434	0.685
C9019B-1H-4, 37.5 cm	3.395	1.443	17.89		0.742
C9019B-1H-4, 41.5 cm	3.435	1.339	4.64		0.806
C9019B-1H-4, 45.5 cm	3.475	1.254	1.97		0.858
C9019B-1H-4, 49.5 cm	3.515	1.055	0.00	6.967	0.981
C9019B-1H-4, 53.5 cm	3.555	1.057	-0.66		0.980
C9019B-1H-4, 57.5 cm	3.595	1.096	0.00		0.956
C9019B-1H-4, 61.5 cm	3.635	1.100	-0.67		0.953
C9019B-1H-4, 65.5 cm	3.675	1.120	0.67	6.332	0.941
C9019B-1H-4, 69.5 cm	3.715	1.253	4.02		0.859
C9019B-1H-4, 73.5 cm	3.755	1.361	5.25		0.792
C9019B-1H-4, 77.5 cm	3.795	1.388	5.20		0.776
C9019B-1H-4, 81.5 cm	3.835	1.402	5.93	16.366	0.767
C9019B-1H-4, 85.5 cm	3.875	1.417	7.25		0.758
C9019B-1H-4, 89.5 cm	3.915	1.387	5.90		0.776
C9019B-1H-4, 93.5 cm	3.955	1.381	4.57		0.780
C9019B-1H-4, 97.5 cm	3.995	1.352	3.05	20.533	0.798
C9019B-1H-5, 0.4 cm	4.034	0.727	2.41		1.183

Location	Subbottom Depth [mbsf]	GRA ¹⁾ [g/cm ³]	MS ²⁾ [x10 ⁻⁵ SI]	NGR ³⁾ [cps]	GRA Porosity
C9019B-1H-5, 4.4 cm	4.074	1.401	2.44		0.768
C9019B-1H-5, 8.4 cm	4.114	1.385	2.59		0.778
C9019B-1H-5, 12.4 cm	4.154	1.370	2.53	19.566	0.787
C9019B-1H-5, 16.4 cm	4.194	1.447	4.58		0.740
C9019B-1H-5, 20.4 cm	4.234	1.383	4.79		0.779
C9019B-1H-6, 2.0 cm	4.28	1.568	15.43		0.665
C9019B-1H-6, 6.0 cm	4.32	1.397	22.75	17.334	0.771
C9019B-1H-6, 10.0 cm	4.36	1.782	68.83		0.533
C9019B-1H-6, 14.0 cm	4.4	1.758	84.60		0.548
C9019B-1H-6, 18.0 cm	4.44	1.822	21.56		0.509
C9019B-1H-6, 22.0 cm	4.48	1.552	14.65	12.433	0.675

¹⁾Gamma ray attenuation density (g/cm³)

²⁾Magnetic susceptibility (x0.00001 SI)

³⁾Natural gamma ray radiation (cps)

Hole C

Location	Subbottom Depth [mbsf]	GRA ¹⁾ [g/cm ³]	MS ²⁾ [x10 ⁻⁵ SI]	NGR ³⁾ [cps]	GRA Porosity
C9019C-1X-1, 8.0 cm	0.08	1.390	102.686		0.775
C9019C-1X-1, 12.0 cm	0.12	1.480	128.794		0.719
C9019C-1X-1, 16.0 cm	0.16	1.557	158.023	67.533	0.672
C9019C-1X-1, 20.0 cm	0.2	1.472	162.070		0.724
C9019C-1X-1, 24.0 cm	0.24	1.636	238.862		0.623
C9019C-1X-1, 28.0 cm	0.28	1.704	314.150		0.581
C9019C-1X-1, 32.0 cm	0.32	1.597	309.882	71.167	0.647

¹⁾Gamma ray attenuation density (g/cm³)

²⁾Magnetic susceptibility (x0.00001 SI)

³⁾Natural gamma ray radiation (cps)

Table 5-3-3-2**Hole B**

Top Location of Sample Interval	Subbotto m Depth [mbsf]	Bulk Density [g/cm ³]	Grain Density [g/cm ³]	Porosity
C9019B-1H-1, 77.0 cm	0.77	1.4028	3.0237	0.8106
C9019B-1H-2, 32.0 cm	1.32	1.4546	2.4231	0.6922
C9019B-1H-2, 85.0 cm	1.85	1.5797	2.4113	0.5994
C9019B-1H-3, 77.0 cm	2.78	1.4447	2.7516	0.7565
C9019B-1H-4, 94.0 cm	3.96	1.355	2.8429	0.818
C9019B-1H-6, 16.0 cm	4.42	1.853	2.9054	0.5594

Hole C

Top Location of Sample Interval	Subbotto m Depth [mbsf]	Bulk Density [g/cm ³]	Grain Density [g/cm ³]	Porosity
C9019C-1X-1, 20.0 cm	0.2		3.8344	

Table 5-3-3-3

Location	Subbottom Depth [mbsf]	Average gamma ray pulse count rate [cps]	DER [μSv/h]
Hole B			
C9019B-1H-1, 85.0 cm	0.85	2	0.02
C9019B-1H-2, 32.0 cm	1.32	3	0.03
C9019B-1H-3, 86.0 cm	2.87	2	0.01
C9019B-1H-4, 91.0 cm	3.93	2	0.03
C9019B-1H-6, 9.0 cm	4.35	2	0.05
Hole C			
C9019C-1X-1, 10.0 cm	0.1	2	0.03
C9019C-1X-CC, 22.0 cm	0.575	2	0.03

Table 5-3-3-4**Hole B**

Location	Subbottom Depth (mbsf)	WR/HS	Thermal conductivity [W/(m·K)]	LET	Probe	Remark
C9019B-1H-3, 60.0 cm	2.61	WR	0.918	Qualified: >10	V11005	mud
C9019B-1H-4, 86.0 cm	3.88	WR	0.652	Unqualified: <4	V11036	mud
C9019B-1H-4, 95.0 cm	3.97	WR	0.717	Unqualified: <4	V11036	mud

Hole C

Location	Subbottom Depth (mbsf)	WR/HS	Thermal conductivity [W/(m·K)]	LET	Probe	Remark
C9019C-1X-1, 10.0 cm	0.1	WR	0.59	Unqualified: <4	V11005	mud

Table 5-3-3-5**Hole B**

Location	Subbottom Depth [mbsf]	Bulk resistivity at 1 kHz [Ω m]	Remarks
C9019B-1H-1, 77.0 cm	0.77	0.266885572	section
C9019B-1H-2, 31.0 cm	1.31	0.27426425	section
C9019B-1H-3, 72.0 cm	2.73	0.286484016	section
C9019B-1H-4, 92.0 cm	3.94	0.258996104	section
C9019B-1H-6, 19.0 cm	4.45	0.60596309	section

Hole C

Location	Subbottom Depth [mbsf]	Bulk resistivity at 1 kHz [Ω m]	Remarks
C9019C-1X-1, 19.0 cm	0.19	0.253005868	section

Table 5-3-3-6**Hole B**

Location	Subbottom Depth [mbsf]	Unconfined compressive strength [kPa]	Remarks
C9019B-1H-1, 85.0 cm	0.85	12.1	high water content, mud
C9019B-1H-2, 32.0 cm	1.32	19.62	high water content, mud
C9019B-1H-2, 87.0 cm	1.87	70.31	hydrothermal alteration, mud
C9019B-1H-3, 83.0 cm	2.84	15.7	mud
C9019B-1H-4, 99.0 cm	4.01	10.46	mud
C9019B-1H-6, 20.0 cm	4.46	17	mud with sand

Hole C

Location	Subbottom Depth [mbsf]	Unconfined compressive strength [kPa]	Remarks
C9019C-1X-1, 18.0 cm	0.18	12.43	soft mud sediment

Table 5-3-3-7

Location	Subbottom Depth [mbsf]	Major element (wt%)					
		Si	Al	Fe	Ca	K	S
Hole B							
C9019B-1H-1, 36	0.4	7.7	1.4	27.3	0.2	1.5	12.3
C9019B-1H-1, 90	0.9	11.4	1.4	27.0	0.5	2.6	9.4
C9019B-1H-2, 40	1.4	23.2	3.0	5.6	1.1	4.1	22.7
C9019B-1H-2, 86	1.9	14.9	1.7	4.5	1.1	3.6	45.4
C9019B-1H-3, 11	2.1	6.8	0.0	31.0	0.3	1.9	9.5
C9019B-1H-3, 85	2.8	18.1	2.8	16.1	1.1	4.4	6.2
C9019B-1H-4, 35	3.3	14.5	2.1	24.7	0.6	1.9	14.0
C9019B-1H-4, 92	3.9	16.7	2.3	16.2	0.5	5.5	6.3
C9019B-1H-6, 10	5.1	15.5	4.0	24.5	1.1	2.0	15.0
Hole C							
C9019C-1X-1, 13	0.1	3.2	0.0	44.3	0.3	0.0	11.1
C9019C-1X-cc, 21	1.2	16.9	3.2	24.8	6.4	1.4	0.9
C9019C-1X-cc, 21	1.2	15.3	3.8	26.4	6.8	0.9	0.8

Table 5-3-4-1

Location	Subbottom Depth	GRA ¹⁾	MS ²⁾	NGR ³⁾	GRA Porosity
	[mbsf]	[g/cm ³]	[x10 ⁻⁵ SI]	[cps]	
C9021B-1H-1, 8.0 cm	0.08	1.4415	36.8777		0.743
C9021B-1H-1, 12.0 cm	0.12	1.4071	27.1278		0.764
C9021B-1H-1, 16.0 cm	0.16	1.392	20.0982	13.034	0.773
C9021B-1H-1, 20.0 cm	0.2	1.3323	13.8217		0.810
C9021B-1H-1, 24.0 cm	0.24	1.3387	10.6065		0.806
C9021B-1H-1, 28.0 cm	0.28	1.3168	9.2261		0.820
C9021B-1H-1, 32.0 cm	0.32	1.2673	8.5707	8.935	0.850
C9021B-1H-1, 36.0 cm	0.36	1.3132	9.9478		0.822
C9021B-1H-1, 40.0 cm	0.4	1.2856	10.6333		0.839
C9021B-1H-1, 44.0 cm	0.44	1.273	9.2728		0.847
C9021B-1H-1, 48.0 cm	0.48	1.3163	7.8948	16.301	0.820
C9021B-1H-1, 52.0 cm	0.52	1.3494	9.2222		0.800
C9021B-1H-1, 56.0 cm	0.56	1.336	9.9814		0.808
C9021B-1H-1, 60.0 cm	0.6	1.3599	10.0449		0.793
C9021B-1H-1, 64.0 cm	0.64	1.3584	8.5779	14.233	0.794
C9021B-1H-1, 68.0 cm	0.68	1.3482	9.1952		0.800
C9021B-1H-1, 72.0 cm	0.72	1.3004	7.1945		0.830
C9021B-1H-1, 76.0 cm	0.76	1.3184	6.535		0.819
C9021B-1H-1, 80.0 cm	0.8	1.3086	5.2127	13.267	0.825
C9021B-1H-1, 84.0 cm	0.84	1.2685	3.8867		0.849
C9021B-1H-1, 88.0 cm	0.88	1.3072	6.4455		0.826
C9021B-1H-1, 92.0 cm	0.92	1.3193	5.2018		0.818
C9021B-1H-1, 96.0 cm	0.96	1.3438	5.1521	18.134	0.803
C9021B-1H-1, 100.0 cm	1	1.2202	5.4323		0.879
C9021B-1H-2, 3.2 cm	1.037	1.3315	5.4765		0.811
C9021B-1H-2, 7.2 cm	1.077	1.3681	5.7458		0.788
C9021B-1H-2, 11.2 cm	1.117	1.3674	5.7817	26.6	0.789
C9021B-1H-2, 15.2 cm	1.157	1.3837	4.6247		0.779
C9021B-1H-2, 19.2 cm	1.197	1.3734	3.959		0.785
C9021B-1H-2, 23.2 cm	1.237	1.3992	4.6111		0.769
C9021B-1H-2, 27.2 cm	1.277	1.3626	4.6072	24.101	0.792
C9021B-1H-2, 31.2 cm	1.317	1.3305	3.964		0.811
C9021B-1H-2, 35.2 cm	1.357	1.3186	2.6349		0.819
C9021B-1H-2, 39.2 cm	1.397	1.3414	2.6261		0.805
C9021B-1H-2, 43.2 cm	1.437	1.3463	3.2661	26.668	0.802
C9021B-1H-2, 47.2 cm	1.477	1.4781	3.273		0.720
C9021B-1H-2, 51.2 cm	1.517	1.3883	2.6206		0.776
C9021B-1H-2, 55.2 cm	1.557	1.3042	2.636		0.827
C9021B-1H-2, 59.2 cm	1.597	1.3127	1.9804	29.501	0.822
C9021B-1H-2, 63.2 cm	1.637	1.292	2.6383		0.835
C9021B-1H-2, 67.2 cm	1.677	1.3069	2.6031		0.826
C9021B-1H-2, 71.2 cm	1.717	1.348	2.602		0.800
C9021B-1H-2, 75.2 cm	1.757	1.2954	1.9646	21.767	0.833
C9021B-1H-2, 79.2 cm	1.797	1.2808	2.6505		0.842
C9021B-1H-2, 83.2 cm	1.837	1.3133	2.5858		0.822
C9021B-1H-2, 87.2 cm	1.877	1.3168	2.5675		0.820
C9021B-1H-2, 91.2 cm	1.917	1.3127	2.6042	29.167	0.822
C9021B-1H-2, 95.2 cm	1.957	1.3031	2.6505		0.828
C9021B-1H-2, 99.2 cm	1.997	1.2785	1.794		0.843
C9021B-1H-3, 1.4 cm	2.034	1.2848	1.7368		0.839

Table 5-3-4-1

Location	Subbottom Depth	GRA ¹⁾	MS ²⁾	NGR ³⁾	GRA Porosity
	[mbsf]	[g/cm ³]	[x10 ⁻⁵ SI]	[cps]	
C9021B-1H-3, 5.4 cm	2.074	1.2949	1.2642	24.001	0.833
C9021B-1H-3, 9.4 cm	2.114	1.3296	1.3097		0.812
C9021B-1H-3, 13.4 cm	2.154	1.3406	1.9663		0.805
C9021B-1H-3, 17.4 cm	2.194	1.3263	1.9679		0.814
C9021B-1H-3, 21.4 cm	2.234	1.3308	1.9712	25.368	0.811
C9021B-1H-3, 25.4 cm	2.274	1.2998	1.3119		0.830
C9021B-1H-3, 29.4 cm	2.314	1.2902	1.3081		0.836
C9021B-1H-3, 33.4 cm	2.354	1.2846	1.3158		0.840
C9021B-1H-3, 37.4 cm	2.394	1.2972	2.6338	24.134	0.832
C9021B-1H-3, 41.4 cm	2.434	1.3544	2.6305		0.797
C9021B-1H-3, 45.4 cm	2.474	1.3028	1.9679		0.828
C9021B-1H-3, 49.4 cm	2.514	1.352	2.625		0.798
C9021B-1H-3, 53.4 cm	2.554	1.2363	1.9762	24.268	0.869
C9021B-1H-3, 57.4 cm	2.594	1.3222	1.9737		0.816
C9021B-1H-3, 61.4 cm	2.634	1.3439	2.6449		0.803
C9021B-1H-3, 65.4 cm	2.674	1.2982	3.2923		0.831
C9021B-1H-3, 69.4 cm	2.714	1.2694	1.3153	24	0.849
C9021B-1H-3, 73.4 cm	2.754	1.3137	1.3354		0.822
C9021B-1H-3, 77.4 cm	2.794	1.2203	1.3197		0.879
C9021B-1H-3, 81.4 cm	2.834	1.3291	1.9531		0.812
C9021B-1H-3, 85.4 cm	2.874	1.2656	1.2923	24.201	0.851
C9021B-1H-3, 89.4 cm	2.914	1.2918	1.9929		0.835
C9021B-1H-3, 93.4 cm	2.954	1.326	1.3359		0.814
C9021B-1H-3, 97.4 cm	2.994	1.2544	1.2784		0.858
C9021B-1H-3, 101.4 cm	3.034	0.5145	0.5999	20.8	1.314
C9021B-1H-4, 4.0 cm	3.07	1.251	1.2674		0.860
C9021B-1H-4, 8.0 cm	3.11	1.2773	1.3037		0.844
C9021B-1H-4, 12.0 cm	3.15	1.2981	1.963		0.831
C9021B-1H-4, 16.0 cm	3.19	1.3093	1.9704	27.934	0.824
C9021B-1H-4, 20.0 cm	3.23	1.3363	1.9862		0.808
C9021B-1H-4, 24.0 cm	3.27	1.2939	1.9896		0.834
C9021B-1H-4, 28.0 cm	3.31	1.2588	1.3269		0.855
C9021B-1H-4, 32.0 cm	3.35	1.278	2.0141	19.802	0.844
C9021B-1H-4, 36.0 cm	3.39	1.3068	2.0373		0.826
C9021B-1H-4, 40.0 cm	3.43	1.1792	1.3548		0.904
C9021B-1H-4, 44.0 cm	3.47	1.2591	1.3496		0.855
C9021B-1H-4, 48.0 cm	3.51	1.2818	1.3399	16.134	0.841
C9021B-1H-4, 52.0 cm	3.55	1.3548	2.0391		0.796
C9021B-1H-4, 56.0 cm	3.59	1.2887	1.353		0.837
C9021B-1H-4, 60.0 cm	3.63	1.3364	1.3623		0.808
C9021B-1H-4, 64.0 cm	3.67	1.3298	1.3479	20.267	0.812
C9021B-1H-4, 68.0 cm	3.71	1.2091	1.3456		0.886
C9021B-1H-4, 72.0 cm	3.75	1.1859	1.3456		0.900
C9021B-1H-4, 76.0 cm	3.79	1.3158	1.9921		0.820
C9021B-1H-4, 80.0 cm	3.83	1.2958	1.9787	19.668	0.833
C9021B-1H-4, 84.0 cm	3.87	1.2234	1.3252		0.877
C9021B-1H-4, 88.0 cm	3.91	1.2574	1.3169		0.856
C9021B-1H-4, 92.0 cm	3.95	1.2182	1.3309		0.880
C9021B-1H-4, 96.0 cm	3.99	1.0755	0.651	12.634	0.968
C9021B-1H-4, 100.0 cm	4.03	0.8506	0.607		1.107

Table 5-3-4-1

Location	Subbottom Depth	GRA ¹⁾	MS ²⁾	NGR ³⁾	GRA Porosity
	[mbsf]	[g/cm ³]	[x10 ⁻⁵ SI]	[cps]	
C9021B-1H-5, 2.9 cm	4.069	0.9043	0.6117		1.074
C9021B-1H-5, 6.9 cm	4.109	0.4505	0.6456		1.353
C9021B-1H-5, 10.9 cm	4.149	0.797	0.6568	12.601	1.140
C9021B-1H-5, 14.9 cm	4.189	1.031	0.6688		0.996
C9021B-1H-5, 18.9 cm	4.229	0.8516	1.3275		1.106
C9021B-1H-5, 22.9 cm	4.269	0.942	1.3275		1.050
C9021B-1H-5, 26.9 cm	4.309	1.1079	1.3331	21.301	0.948
C9021B-1H-5, 30.9 cm	4.349	1.0125	1.364		1.007
C9021B-1H-5, 34.9 cm	4.389	1.1071	2.0452		0.949
C9021B-1H-5, 38.9 cm	4.429	0.8876	2.0244		1.084
C9021B-1H-5, 42.9 cm	4.469	1.1879	2.69	25.101	0.899
C9021B-1H-5, 46.9 cm	4.509	0.9801	2.713		1.027
C9021B-1H-5, 50.9 cm	4.549	1.0688	2.7141		0.972
C9021B-1H-5, 54.9 cm	4.589	1.3387	4.066		0.806
C9021B-1H-5, 58.9 cm	4.629	1.3135	2.69	25.867	0.822
C9021B-1H-5, 62.9 cm	4.669	1.3424	2.009		0.804
C9021B-1H-5, 66.9 cm	4.709	1.2938	1.332		0.834
C9021B-1H-5, 70.9 cm	4.749	1.313	1.9971		0.822
C9021B-1H-5, 74.9 cm	4.789	1.2935	1.998	23.8	0.834
C9021B-1H-5, 78.9 cm	4.829	1.3041	1.998		0.828
C9021B-1H-5, 82.9 cm	4.869	1.293	1.9729		0.834
C9021B-1H-5, 86.9 cm	4.909	1.232	1.3153		0.872
C9021B-1H-5, 90.9 cm	4.949	1.3073	1.9971	21.901	0.826
C9021B-1H-5, 94.9 cm	4.989	1.3055	2.0081		0.827
C9021B-1H-5, 98.9 cm	5.029	1.176	1.238		0.906
C9021B-1H-6, 1.4 cm	5.059	1.258	1.2028		0.856
C9021B-1H-6, 5.4 cm	5.099	1.2607	1.2918	20.201	0.854
C9021B-1H-6, 9.4 cm	5.139	1.3125	1.9997		0.822
C9021B-1H-6, 13.4 cm	5.179	1.2846	1.3225		0.840
C9021B-1H-6, 17.4 cm	5.219	1.2533	1.9737		0.859
C9021B-1H-6, 21.4 cm	5.259	1.2028	2.625	12.2	0.890
C9021B-1H-6, 25.4 cm	5.299	1.2191	1.9929		0.880
C9021B-1H-6, 29.4 cm	5.339	1.2238	3.9674		0.877
C9021B-1H-6, 33.4 cm	5.379	1.2261	1.3303		0.876
C9021B-1H-6, 37.4 cm	5.419	1.2169	0.6651	16.835	0.881
C9021B-1H-6, 41.4 cm	5.459	1.2494	0.6697		0.861
C9021B-1H-6, 45.4 cm	5.499	1.2586	0.6702		0.856
C9021B-1H-6, 49.4 cm	5.539	1.2593	1.345		0.855
C9021B-1H-6, 53.4 cm	5.579	1.2249	1.3461	20.901	0.876
C9021B-1H-6, 57.4 cm	5.619	1.2796	2.0124		0.843
C9021B-1H-6, 61.4 cm	5.659	1.2583	1.3393		0.856
C9021B-1H-6, 65.4 cm	5.699	1.3223	2.009		0.816
C9021B-1H-6, 69.4 cm	5.739	1.3153	2.0056	21.234	0.821
C9021B-1H-6, 73.4 cm	5.779	1.3026	1.3405		0.828
C9021B-1H-6, 77.4 cm	5.819	1.2154	1.313		0.882
C9021B-1H-6, 81.4 cm	5.859	1.2343	1.3141		0.871
C9021B-1H-6, 85.4 cm	5.899	1.2727	1.3141	18.101	0.847
C9021B-1H-6, 89.4 cm	5.939	1.2789	1.3236		0.843
C9021B-1H-6, 93.4 cm	5.979	1.1907	1.3153		0.897
C9021B-1H-6, 97.4 cm	6.019	1.2638	1.2559		0.852

Table 5-3-4-1

Location	Subbottom Depth	GRA ¹⁾	MS ²⁾	NGR ³⁾	GRA Porosity
	[mbsf]	[g/cm ³]	[x10 ⁻⁵ SI]	[cps]	
C9021B-1H-7, 0.1 cm	6.051	0.7634	1.1893	11.968	1.160
C9021B-1H-7, 4.1 cm	6.091	1.2221	1.2716		0.878
C9021B-1H-7, 8.1 cm	6.131	1.2532	0.6565		0.859
C9021B-1H-7, 12.1 cm	6.171	1.186	1.3086		0.900
C9021B-1H-7, 16.1 cm	6.211	1.2433		16.067	0.865
C9021B-1H-7, 20.1 cm	6.251	1.2296	2.6427		0.873
C9021B-1H-7, 24.1 cm	6.291	1.2544	0.6626		0.858
C9021B-1H-7, 28.1 cm	6.331	1.2381	1.3258		0.868
C9021B-1H-7, 32.1 cm	6.371	1.2451	0.6643	13.733	0.864
C9021B-1H-7, 36.1 cm	6.411	1.1045	0		0.950
C9021B-1H-7, 40.1 cm	6.451	0.8309	0		1.119
C9021B-1H-7, 44.1 cm	6.491	1.0345	0		0.994
C9021B-1H-7, 48.1 cm	6.531	1.3011	1.332	14.668	0.829
C9021B-1H-7, 52.1 cm	6.571	1.3026	1.3376		0.828
C9021B-1H-7, 56.1 cm	6.611	1.2218	0.6657		0.878
C9021B-1H-7, 60.1 cm	6.651	1.3101	2.0167		0.824
C9021B-1H-7, 64.1 cm	6.691	1.2916	1.3433	20.5	0.835
C9021B-1H-7, 68.1 cm	6.731	1.2339	0		0.871
C9021B-1H-7, 72.1 cm	6.771	1.2063	0.6587		0.888
C9021B-1H-7, 76.1 cm	6.811	1.2318	1.3015		0.872
C9021B-1H-7, 80.1 cm	6.851	1.2314	1.9499	17.6	0.872
C9021B-1H-7, 84.1 cm	6.891	1.1979	1.3258		0.893
C9021B-1H-7, 88.1 cm	6.931	1.2106	0.6521		0.885
C9021B-1H-7, 92.1 cm	6.971	1.1944	0.6505		0.895
C9021B-1H-7, 96.1 cm	7.011	1.1826	1.2695	16.934	0.902
C9021B-1H-7, 100.1 cm	7.051	0.7678	1.217		1.158
C9021B-1H-8, 3.2 cm	7.087	0.9739	0.618		1.031
C9021B-1H-8, 7.2 cm	7.127	1.1717	0.6691		0.909
C9021B-1H-8, 11.2 cm	7.167	0.8297	0.6685	13.301	1.120
C9021B-1H-8, 15.2 cm	7.207	0.6396	0.6739		1.237
C9021B-1H-8, 19.2 cm	7.247	0.9674	0.6765		1.035
C9021B-1H-8, 23.2 cm	7.287	0.822	0.6771		1.124
C9021B-1H-8, 27.2 cm	7.327	1.2062	1.9787	19.801	0.888
C9021B-1H-8, 31.2 cm	7.367	1.0842	1.323		0.963
C9021B-1H-8, 35.2 cm	7.407	0.9422	0.6557		1.050
C9021B-1H-8, 39.2 cm	7.447	1.1944	1.3075		0.895
C9021B-1H-8, 43.2 cm	7.487	0.9811	1.9531	13.034	1.026
C9021B-1H-8, 47.2 cm	7.527	0.0511	3.6436		1.599
C9021B-2H-1, 8.0 cm	9.58	1.3079	19.8286		0.825
C9021B-2H-1, 12.0 cm	9.62	1.2719	15.9433		0.847
C9021B-2H-1, 16.0 cm	9.66	1.1298	16.7699	18.434	0.935
C9021B-2H-1, 20.0 cm	9.7	1.2342	24.1793		0.871
C9021B-2H-1, 24.0 cm	9.74	1.194	17.4925		0.895
C9021B-2H-1, 28.0 cm	9.78	1.1499	17.8457		0.922
C9021B-2H-1, 32.0 cm	9.82	1.1561	12.5952	14.067	0.919
C9021B-2H-1, 36.0 cm	9.86	1.1512	11.4229		0.922
C9021B-2H-1, 40.0 cm	9.9	1.0947	10.7555		0.956
C9021B-2H-1, 44.0 cm	9.94	1.0966	10.0406		0.955
C9021B-2H-1, 48.0 cm	9.98	1.253	10.6874	16.167	0.859
C9021B-2H-1, 52.0 cm	10.02	1.1382	10.0321		0.930

Table 5-3-4-1

Location	Subbottom Depth	GRA ¹⁾	MS ²⁾	NGR ³⁾	GRA Porosity
	[mbsf]	[g/cm ³]	[x10 ⁻⁵ SI]	[cps]	
C9021B-2H-1, 56.0 cm	10.06	1.1648	10.7601		0.913
C9021B-2H-1, 60.0 cm	10.1	1.16	10.7966		0.916
C9021B-2H-1, 64.0 cm	10.14	1.1457	12.1514	17.401	0.925
C9021B-2H-1, 68.0 cm	10.18	1.1811	10.1305		0.903
C9021B-2H-1, 72.0 cm	10.22	1.1807	10.8058		0.904
C9021B-2H-1, 76.0 cm	10.26	1.1173	12.1102		0.943
C9021B-2H-1, 80.0 cm	10.3	1.1991	14.1405	15.267	0.892
C9021B-2H-1, 84.0 cm	10.34	1.1246	8.7685		0.938
C9021B-2H-1, 88.0 cm	10.38	1.0468	8.0291		0.986
C9021B-2H-1, 92.0 cm	10.42	0.862	8.6069		1.100
C9021B-2H-1, 96.0 cm	10.46	0.659	5.8864	12.733	1.225
C9021B-2H-1, 100.0 cm	10.5	0.7309	5.6238		1.180
C9021B-2H-2, 2.9 cm	10.539	1.2635	4.9887		0.853
C9021B-2H-2, 6.9 cm	10.579	1.2945	5.3167		0.833
C9021B-2H-2, 10.9 cm	10.619	1.2651	6.0244	18.667	0.852
C9021B-2H-2, 14.9 cm	10.659	1.3026	5.301		0.828
C9021B-2H-2, 18.9 cm	10.699	1.2879	7.2613		0.838
C9021B-2H-2, 22.9 cm	10.739	1.2654	5.9737		0.851
C9021B-2H-2, 26.9 cm	10.779	1.2962	4.6916	17.166	0.832
C9021B-2H-2, 30.9 cm	10.819	1.223	4.1113		0.877
C9021B-2H-2, 34.9 cm	10.859	1.2706	3.4115		0.848
C9021B-2H-2, 38.9 cm	10.899	1.2831	4.0712		0.840
C9021B-2H-2, 42.9 cm	10.939	1.2626	4.0574	16.366	0.853
C9021B-2H-2, 46.9 cm	10.979	1.3161	2.6855		0.820
C9021B-2H-2, 50.9 cm	11.019	1.2975	2.6855		0.832
C9021B-2H-2, 54.9 cm	11.059	1.3802	2.698		0.781
C9021B-2H-2, 58.9 cm	11.099	1.3118	3.3999	16.367	0.823
C9021B-2H-2, 62.9 cm	11.139	1.2809	4.0973		0.842
C9021B-2H-2, 66.9 cm	11.179	1.3458			0.802
C9021B-2H-2, 70.9 cm	11.219	1.3354	4.7578		0.808
C9021B-2H-2, 74.9 cm	11.259	1.3756	3.3711	14.767	0.783
C9021B-2H-2, 78.9 cm	11.299	1.292	2.6505		0.835
C9021B-2H-2, 82.9 cm	11.339	1.2499	1.9812		0.861
C9021B-2H-2, 86.9 cm	11.379	1.2291	1.9837		0.874
C9021B-2H-2, 90.9 cm	11.419	1.2475	1.3331	13.467	0.862
C9021B-2H-2, 94.9 cm	11.459	1.2776	2.0175		0.844
C9021B-2H-2, 98.9 cm	11.499	1.2428	1.8909		0.865
C9021B-2H-3, 0.7 cm	11.532	0.5379	1.235		1.299
C9021B-2H-3, 4.7 cm	11.572	1.0722	1.9654	14.2	0.970
C9021B-2H-3, 8.7 cm	11.612	1.2325	3.3611		0.872
C9021B-2H-3, 12.7 cm	11.652	1.135	2.0073		0.932
C9021B-2H-3, 16.7 cm	11.692	1.1186	2.0073		0.942
C9021B-2H-3, 20.7 cm	11.732	1.1785	1.3433	16.167	0.905
C9021B-2H-3, 24.7 cm	11.772	1.2765	1.3496		0.845
C9021B-2H-3, 28.7 cm	11.812	1.2512	2.0244		0.860
C9021B-2H-3, 32.7 cm	11.852	1.2372	2.0252		0.869
C9021B-2H-3, 36.7 cm	11.892	1.1235	2.0227	18.367	0.939
C9021B-2H-3, 40.7 cm	11.932	1.2603	2.0124		0.854
C9021B-2H-3, 44.7 cm	11.972	1.2477	1.9929		0.862
C9021B-2H-3, 48.7 cm	12.012	1.2731	1.9954		0.847

Table 5-3-4-1

Location	Subbottom Depth	GRA ¹⁾	MS ²⁾	NGR ³⁾	GRA Porosity
	[mbsf]	[g/cm ³]	[x10 ⁻⁵ SI]	[cps]	
C9021B-2H-3, 52.7 cm	12.052	1.1869	2.0167	16.567	0.900
C9021B-2H-3, 56.7 cm	12.092	1.2531	1.3582		0.859
C9021B-2H-3, 60.7 cm	12.132	1.2736	2.0365		0.846
C9021B-2H-3, 64.7 cm	12.172	1.2377	2.0252		0.868
C9021B-2H-3, 68.7 cm	12.212	1.2172	2.0192	16.867	0.881
C9021B-2H-3, 72.7 cm	12.252	1.0459	1.3502		0.987
C9021B-2H-3, 76.7 cm	12.292	1.2845	2.0175		0.840
C9021B-2H-3, 80.7 cm	12.332	1.1674	1.328		0.912
C9021B-2H-3, 84.7 cm	12.372	0.9984	1.3125	13.866	1.016
C9021B-2H-3, 88.7 cm	12.412	1.1295	2.0098		0.935
C9021B-2H-3, 92.7 cm	12.452	0.9	1.3422		1.076
C9021B-2H-3, 96.7 cm	12.492	0.7538	1.3081		1.166
C9021B-2H-3, 100.7 cm	12.532	0.4494	1.2289	15.201	1.354
C9021B-2H-4, 3.1 cm	12.566	0.7248	1.2747		1.184
C9021B-2H-4, 7.1 cm	12.606	1.2981	1.3119		0.831
C9021B-2H-4, 11.1 cm	12.646	1.1932	1.3097		0.896
C9021B-2H-4, 15.1 cm	12.686	1.0953	1.3147	19.733	0.956
C9021B-2H-4, 19.1 cm	12.726	1.0513	1.3337		0.983
C9021B-2H-4, 23.1 cm	12.766	1.0444	1.3269		0.987
C9021B-2H-4, 27.1 cm	12.806	1.1223	1.3252		0.939
C9021B-2H-4, 31.1 cm	12.846	1.02	1.3342	13.6	1.002
C9021B-2H-4, 35.1 cm	12.886	0.8419	1.3496		1.112
C9021B-2H-4, 39.1 cm	12.926	0.7649	-1.3571		1.160
C9021B-2H-4, 43.1 cm	12.966	0.9583	1.3496		1.040
C9021B-2H-4, 47.1 cm	13.006	0.9245	1.3399	13.834	1.061
C9021B-2H-4, 51.1 cm	13.046	0.9725	2.0321		1.032
C9021B-2H-4, 55.1 cm	13.086	0.6703	2.7049		1.218
C9021B-2H-4, 59.1 cm	13.126	0.8327	1.3241		1.118
C9021B-2H-4, 63.1 cm	13.166	0.6192	1.3236	10.2	1.249
C9021B-2H-4, 67.1 cm	13.206	0.6993	1.3331		1.200
C9021B-2H-4, 71.1 cm	13.246	0.5872	1.3186		1.269
C9021B-2H-4, 75.1 cm	13.286	0.7173	1.8555		1.189
C9021B-2H-5, 1.8 cm	13.323	1.279	4.3669	21.967	0.843
C9021B-2H-5, 5.8 cm	13.363	1.3266	2.6764		0.814
C9021B-2H-5, 9.8 cm	13.403	1.2658	1.332		0.851
C9021B-2H-5, 13.8 cm	13.443	1.2482	2.0047		0.862
C9021B-2H-5, 17.8 cm	13.483	1.2703	2.0124	21.734	0.848
C9021B-2H-5, 21.8 cm	13.523	1.3622	2.033		0.792
C9021B-2H-5, 25.8 cm	13.563	1.2789	2.0227		0.843
C9021B-2H-5, 29.8 cm	13.603	1.2111	2.0013		0.885
C9021B-2H-5, 33.8 cm	13.643	1.2274	1.3388	18.6	0.875
C9021B-2H-5, 37.8 cm	13.683	1.2268	1.3525		0.875
C9021B-2H-5, 41.8 cm	13.723	1.2126	2.0278		0.884
C9021B-2H-5, 45.8 cm	13.763	1.2606	1.3405		0.854
C9021B-2H-5, 49.8 cm	13.803	1.2236	2.0073	16.234	0.877
C9021B-2H-5, 53.8 cm	13.843	1.2977	1.3553		0.831
C9021B-2H-5, 57.8 cm	13.883	1.2363	2.6855		0.869
C9021B-2H-5, 61.8 cm	13.923	1.2425	2.0339		0.865
C9021B-2H-5, 65.8 cm	13.963	1.2928	-0.6705	15.2	0.834
C9021B-2H-5, 69.8 cm	14.003	1.2521	2.009		0.860

Table 5-3-4-1

Location	Subbottom Depth	GRA ¹⁾	MS ²⁾	NGR ³⁾	GRA Porosity
	[mbsf]	[g/cm ³]	[x10 ⁻⁵ SI]	[cps]	
C9021B-2H-5, 73.8 cm	14.043	1.2656	2.0022		0.851
C9021B-2H-5, 77.8 cm	14.083	1.2644	-0.6635		0.852
C9021B-2H-5, 81.8 cm	14.123	1.2365	1.9804	15.201	0.869
C9021B-2H-5, 85.8 cm	14.163	1.2717	1.9988		0.847
C9021B-2H-5, 89.8 cm	14.203	1.2589	1.9663		0.855
C9021B-2H-5, 93.8 cm	14.243	1.3129	1.9997		0.822
C9021B-2H-5, 97.8 cm	14.283	1.3074	1.9321	16	0.825
C9021B-2H-6, 0.2 cm	14.317	0.6888	1.2668		1.206
C9021B-2H-6, 4.2 cm	14.357	1.3187	1.2988		0.819
C9021B-2H-6, 8.2 cm	14.397	1.3118	1.9988		0.823
C9021B-2H-6, 12.2 cm	14.437	1.3283	2.0047	18.934	0.813
C9021B-2H-6, 16.2 cm	14.477	1.3794	2.7003		0.781
C9021B-2H-6, 20.2 cm	14.517	1.2919	2.6877		0.835
C9021B-2H-6, 24.2 cm	14.557	1.2679	1.345		0.850
C9021B-2H-6, 28.2 cm	14.597	1.2668	2.0158	17.767	0.850
C9021B-2H-6, 32.2 cm	14.637	1.2576	2.0184		0.856
C9021B-2H-6, 36.2 cm	14.677	1.2731	2.0149		0.847
C9021B-2H-6, 40.2 cm	14.717	1.2636	2.0132		0.852
C9021B-2H-6, 44.2 cm	14.757	1.2835	1.3342	14.2	0.840
C9021B-2H-6, 48.2 cm	14.797	1.2551	1.9854		0.858
C9021B-2H-6, 52.2 cm	14.837	1.264	1.9988		0.852
C9021B-2H-6, 56.2 cm	14.877	1.2265	1.3461		0.875
C9021B-2H-6, 60.2 cm	14.917	1.2221	1.3611	16.234	0.878
C9021B-2H-6, 64.2 cm	14.957	1.2528	2.0184		0.859
C9021B-2H-6, 68.2 cm	14.997	1.3332	1.3382		0.810
C9021B-2H-6, 72.2 cm	15.037	1.2697	1.3376		0.849
C9021B-2H-6, 76.2 cm	15.077	1.2309	1.9845	15.733	0.873
C9021B-2H-6, 80.2 cm	15.117	1.2739	1.9954		0.846
C9021B-2H-6, 84.2 cm	15.157	1.3359	1.9754		0.808
C9021B-2H-6, 88.2 cm	15.197	1.3098	1.9745		0.824
C9021B-2H-6, 92.2 cm	15.237	1.2978	1.3309	19.6	0.831
C9021B-2H-6, 96.2 cm	15.277	1.3713	1.3405		0.786
C9021B-2H-6, 100.2 cm	15.317	1.2816	1.8909		0.841
C9021B-2H-7, 2.1 cm	15.351	1.035	1.2314		0.993
C9021B-2H-7, 6.1 cm	15.391	1.2979	1.9663	20.667	0.831
C9021B-2H-7, 10.1 cm	15.431	1.2288	0		0.874
C9021B-2H-7, 14.1 cm	15.471	1.2834	2.0081		0.840
C9021B-2H-7, 18.1 cm	15.511	1.2737	2.6662		0.846
C9021B-2H-7, 22.1 cm	15.551	1.2042	2.0073	15.234	0.889
C9021B-2H-7, 26.1 cm	15.591	1.2244	2.6752		0.877
C9021B-2H-7, 30.1 cm	15.631	1.2063	2.6662		0.888
C9021B-2H-7, 34.1 cm	15.671	1.2758	2.6651		0.845
C9021B-2H-7, 38.1 cm	15.711	1.1971	3.3356	15.367	0.893
C9021B-2H-7, 42.1 cm	15.751	1.1704	2.6832		0.910
C9021B-2H-7, 46.1 cm	15.791	1.2555	2.6775		0.857
C9021B-2H-7, 50.1 cm	15.831	1.1591	2.673		0.917
C9021B-2H-7, 54.1 cm	15.871	1.3657	3.3398	18.801	0.790
C9021B-2H-7, 58.1 cm	15.911	1.2602	2.6855		0.855
C9021B-2H-7, 62.1 cm	15.951	1.2618	2.6809		0.854
C9021B-2H-7, 66.1 cm	15.991	1.3337	3.3173		0.809

Table 5-3-4-1

Location	Subbottom Depth	GRA ¹⁾	MS ²⁾	NGR ³⁾	GRA Porosity
	[mbsf]	[g/cm ³]	[x10 ⁻⁵ SI]	[cps]	
C9021B-2H-7, 70.1 cm	16.031	1.2296	2.6438	17.467	0.873
C9021B-2H-7, 74.1 cm	16.071	1.2031	2.0022		0.890
C9021B-2H-7, 78.1 cm	16.111	1.1821	1.9854		0.903
C9021B-2H-7, 82.1 cm	16.151	1.2036	1.9754		0.889
C9021B-2H-7, 86.1 cm	16.191	1.1502	1.958	15.067	0.922
C9021B-2H-7, 90.1 cm	16.231	1.0035	1.3275		1.013
C9021B-2H-7, 94.1 cm	16.271	0.8892	1.3303		1.083
C9021B-2H-7, 98.1 cm	16.311	0.1976	1.9034		1.509
C9021B-2H-8, 0.2 cm	16.347	0.4233	1.8494	8.734	1.370
C9021B-2H-8, 4.2 cm	16.387	0.7965	1.3037		1.140
C9021B-2H-8, 8.2 cm	16.427	0.6784	1.328		1.213
C9021B-2H-8, 12.2 cm	16.467	0.7302	1.9887		1.181
C9021B-2H-8, 16.2 cm	16.507	1.0743	1.9845	13.934	0.969
C9021B-2H-8, 20.2 cm	16.547	1.1008	2.673		0.953
C9021B-2H-8, 24.2 cm	16.587	1.1305	3.302		0.934
C9021B-2H-8, 28.2 cm	16.627	1.2258	3.302		0.876
C9021B-2H-8, 32.2 cm	16.667	1.1957	2.6527	17.266	0.894
C9021B-2H-8, 36.2 cm	16.707	1.2397	2.0261		0.867
C9021B-2H-8, 40.2 cm	16.747	1.1197	2.0252		0.941
C9021B-2H-8, 44.2 cm	16.787	1.1053	2.0218		0.950
C9021B-2H-8, 48.2 cm	16.827	1.136	2.0201	16.433	0.931
C9021B-2H-8, 52.2 cm	16.867	1.0609	1.3576		0.977
C9021B-2H-8, 56.2 cm	16.907	1.0891	2.0487		0.960
C9021B-2H-8, 60.2 cm	16.947	0.9263	2.0478		1.060
C9021B-2H-8, 64.2 cm	16.987	1.3061	3.3783	21.834	0.826
C9021B-2H-8, 68.2 cm	17.027	1.331	2.7084		0.811
C9021B-2H-8, 72.2 cm	17.067	1.2539	2.6673		0.858
C9021B-2H-8, 76.2 cm	17.107	1.3188	3.9741		0.818
C9021B-2H-8, 80.2 cm	17.147	1.208	4.6364	25.2	0.887
C9021B-2H-8, 84.2 cm	17.187	0.9816	2.0167		1.026
C9021B-2H-8, 88.2 cm	17.227	0.8591	1.9954		1.102
C9021B-2H-8, 92.2 cm	17.267	0.6107	1.9474		1.254
C9021B-3H-1, 8.0 cm	19.08	1.2593	18.214		0.855
C9021B-3H-1, 12.0 cm	19.12	1.269	17.7633		0.849
C9021B-3H-1, 16.0 cm	19.16	1.2497	19.8369	13.2	0.861
C9021B-3H-1, 20.0 cm	19.2	1.2891	20.7682		0.837
C9021B-3H-1, 24.0 cm	19.24	1.2564	19.4448		0.857
C9021B-3H-1, 28.0 cm	19.28	1.3125	19.4613		0.822
C9021B-3H-1, 32.0 cm	19.32	1.3213	20.9007	15.433	0.817
C9021B-3H-1, 36.0 cm	19.36	1.2244	22.8167		0.877
C9021B-3H-1, 40.0 cm	19.4	1.2678	22.0988		0.850
C9021B-3H-1, 44.0 cm	19.44	1.2648	23.4182		0.852
C9021B-3H-1, 48.0 cm	19.48	1.23	25.2969	12.468	0.873
C9021B-3H-1, 52.0 cm	19.52	1.2461	23.2702		0.863
C9021B-3H-1, 56.0 cm	19.56	1.191	27.1447		0.897
C9021B-3H-1, 60.0 cm	19.6	1.2159	22.7395		0.882
C9021B-3H-1, 64.0 cm	19.64	1.3008	23.9756	16.966	0.830
C9021B-3H-1, 68.0 cm	19.68	1.2501	21.1861		0.861
C9021B-3H-1, 72.0 cm	19.72	1.241	18.9913		0.866
C9021B-3H-1, 76.0 cm	19.76	1.2539	18.7937		0.858

Table 5-3-4-1

Location	Subbottom Depth	GRA ¹⁾	MS ²⁾	NGR ³⁾	GRA Porosity
	[mbsf]	[g/cm ³]	[x10 ⁻⁵ SI]	[cps]	
C9021B-3H-1, 80.0 cm	19.8	1.2337	18.1987	15.634	0.871
C9021B-3H-1, 84.0 cm	19.84	1.2467	18.3441		0.863
C9021B-3H-1, 88.0 cm	19.88	1.2412	17.6297		0.866
C9021B-3H-1, 92.0 cm	19.92	1.3189	15.7235		0.818
C9021B-3H-1, 96.0 cm	19.96	1.1038	11.0585	10.501	0.951
C9021B-3H-1, 100.0 cm	20	0.9367	9.327		1.054
C9021B-3H-2, 2.4 cm	20.029	1.2411	10.847		0.866
C9021B-3H-2, 6.4 cm	20.069	1.2505	10.2786		0.861
C9021B-3H-2, 10.4 cm	20.109	1.3064	10.1852	14.367	0.826
C9021B-3H-2, 14.4 cm	20.149	1.2993	11.0216		0.830
C9021B-3H-2, 18.4 cm	20.189	1.2285	11.0539		0.874
C9021B-3H-2, 22.4 cm	20.229	1.2827	10.5397		0.841
C9021B-3H-2, 26.4 cm	20.269	1.2976	9.8893	17.633	0.832
C9021B-3H-2, 30.4 cm	20.309	1.2855	10.6513		0.839
C9021B-3H-2, 34.4 cm	20.349	1.2663	10.6244		0.851
C9021B-3H-2, 38.4 cm	20.389	1.3291	9.2767		0.812
C9021B-3H-2, 42.4 cm	20.429	1.3253	7.975	16.433	0.814
C9021B-3H-2, 46.4 cm	20.469	1.2985	7.3787		0.831
C9021B-3H-2, 50.4 cm	20.509	1.2608	7.3787		0.854
C9021B-3H-2, 54.4 cm	20.549	1.2356	6.6346		0.870
C9021B-3H-2, 58.4 cm	20.589	1.2575	5.9636	13.134	0.856
C9021B-3H-2, 62.4 cm	20.629	1.2926	5.3664		0.835
C9021B-3H-2, 66.4 cm	20.669	1.2893	6.0346		0.837
C9021B-3H-2, 70.4 cm	20.709	1.2389	6.0116		0.868
C9021B-3H-2, 74.4 cm	20.749	1.2563	5.3122	17.067	0.857
C9021B-3H-2, 78.4 cm	20.789	1.2347	4.6364		0.870
C9021B-3H-2, 82.4 cm	20.829	1.2429	4.5688		0.865
C9021B-3H-2, 86.4 cm	20.869	1.2741	4.5611		0.846
C9021B-3H-2, 90.4 cm	20.909	1.2666	3.9607	13.1	0.851
C9021B-3H-2, 94.4 cm	20.949	1.279	3.9691		0.843
C9021B-3H-2, 98.4 cm	20.989	1.2862	3.1619		0.839
C9021B-3H-3, 0.6 cm	21.021	1.1003	2.4163		0.953
C9021B-3H-3, 4.6 cm	21.061	1.1921	2.5421	10.767	0.896
C9021B-3H-3, 8.6 cm	21.101	1.2926	3.3117		0.835
C9021B-3H-3, 12.6 cm	21.141	1.301	3.9391		0.829
C9021B-3H-3, 16.6 cm	21.181	1.2579	4.5957		0.856
C9021B-3H-3, 20.6 cm	21.221	1.238	3.9458	19.866	0.868
C9021B-3H-3, 24.6 cm	21.261	1.3043	3.9976		0.827
C9021B-3H-3, 28.6 cm	21.301	1.3187	4.0248		0.819
C9021B-3H-3, 32.6 cm	21.341	1.3308	3.3597		0.811
C9021B-3H-3, 36.6 cm	21.381	1.3303	3.3768	23.167	0.811
C9021B-3H-3, 40.6 cm	21.421	1.2603	3.397		0.854
C9021B-3H-3, 44.6 cm	21.461	1.3246	2.69		0.815
C9021B-3H-3, 48.6 cm	21.501	1.3199	4.035		0.818
C9021B-3H-3, 52.6 cm	21.541	1.2973	4.047	19.235	0.832
C9021B-3H-3, 56.6 cm	21.581	1.2753	3.3984		0.845
C9021B-3H-3, 60.6 cm	21.621	1.2889	3.4144		0.837
C9021B-3H-3, 64.6 cm	21.661	1.3162	4.0539		0.820
C9021B-3H-3, 68.6 cm	21.701	1.3604	4.0453	18.667	0.793
C9021B-3H-3, 72.6 cm	21.741	1.3269	4.0419		0.813

Table 5-3-4-1

Location	Subbottom Depth	GRA ¹⁾	MS ²⁾	NGR ³⁾	GRA Porosity
	[mbsf]	[g/cm ³]	[x10 ⁻⁵ SI]	[cps]	
C9021B-3H-3, 76.6 cm	21.781	1.3179	3.9875		0.819
C9021B-3H-3, 80.6 cm	21.821	1.3365	3.9309		0.808
C9021B-3H-3, 84.6 cm	21.861	1.2804	4.5081	24.6	0.842
C9021B-3H-3, 88.6 cm	21.901	1.3506	3.3145		0.799
C9021B-3H-3, 92.6 cm	21.941	1.3455	2.6527		0.802
C9021B-3H-3, 96.6 cm	21.981	1.3427	1.9605		0.804
C9021B-3H-3, 100.6 cm	22.021	1.2099	1.8196	13.367	0.886
C9021B-3H-4, 2.9 cm	22.054	1.245	1.2411		0.864
C9021B-3H-4, 6.9 cm	22.094	1.2619	1.301		0.854
C9021B-3H-4, 10.9 cm	22.134	1.2356	1.9679		0.870
C9021B-3H-4, 14.9 cm	22.174	1.2194	1.3208	21.301	0.880
C9021B-3H-4, 18.9 cm	22.214	1.2706	2.0167		0.848
C9021B-3H-4, 22.9 cm	22.254	1.2256	1.3439		0.876
C9021B-3H-4, 26.9 cm	22.294	1.266	2.0115		0.851
C9021B-3H-4, 30.9 cm	22.334	1.2945	2.6775	24.3	0.833
C9021B-3H-4, 34.9 cm	22.374	1.3107	2.6923		0.823
C9021B-3H-4, 38.9 cm	22.414	1.2741	2.0184		0.846
C9021B-3H-4, 42.9 cm	22.454	1.2966	2.6764		0.832
C9021B-3H-4, 46.9 cm	22.494	1.287	3.3356	24.166	0.838
C9021B-3H-4, 50.9 cm	22.534	1.291	3.3229		0.836
C9021B-3H-4, 54.9 cm	22.574	1.2898	2.6505		0.836
C9021B-3H-4, 58.9 cm	22.614	1.303	1.9929		0.828
C9021B-3H-4, 62.9 cm	22.654	1.2306	1.9954	18.234	0.873
C9021B-3H-4, 66.9 cm	22.694	1.2496	1.3325		0.861
C9021B-3H-4, 70.9 cm	22.734	1.2373	1.3103		0.869
C9021B-3H-4, 74.9 cm	22.774	1.2714	1.9564		0.848
C9021B-3H-4, 78.9 cm	22.814	1.2547	1.3108	21.634	0.858
C9021B-3H-4, 82.9 cm	22.854	1.1994	1.3286		0.892
C9021B-3H-4, 86.9 cm	22.894	1.2284	1.3158		0.874
C9021B-3H-4, 90.9 cm	22.934	1.0655	1.313		0.974
C9021B-3H-4, 94.9 cm	22.974	1.0831	0.6557	14.967	0.964
C9021B-3H-4, 98.9 cm	23.014	1.0204	0.6353		1.002
C9021B-3H-5, 1.0 cm	23.055	0.7223	0.6102		1.186
C9021B-3H-5, 5.0 cm	23.095	1.028	0.6411		0.998
C9021B-3H-5, 9.0 cm	23.135	0.961	0.6462	6.701	1.039
C9021B-3H-5, 13.0 cm	23.175	0.959	0.6535		1.040
C9021B-3H-5, 17.0 cm	23.215	1.0686	0.6543		0.973
C9021B-3H-5, 21.0 cm	23.255	1.0506	1.9845		0.984
C9021B-3H-5, 25.0 cm	23.295	1.1581	1.9879	15.467	0.917
C9021B-3H-5, 29.0 cm	23.335	1.1847	1.3405		0.901
C9021B-3H-5, 33.0 cm	23.375	1.2185	2.0064		0.880
C9021B-3H-5, 37.0 cm	23.415	1.1697	2.0158		0.910
C9021B-3H-5, 41.0 cm	23.455	1.1962	2.0391	25.168	0.894
C9021B-3H-5, 45.0 cm	23.495	1.2796	2.7468		0.843
C9021B-3H-5, 49.0 cm	23.535	1.3012	2.0583		0.829
C9021B-3H-5, 53.0 cm	23.575	1.2704	2.735		0.848
C9021B-3H-5, 57.0 cm	23.615	1.2236	4.0868	41.501	0.877
C9021B-3H-5, 61.0 cm	23.655	1.2519	4.7822		0.860
C9021B-3H-5, 65.0 cm	23.695	1.2236	2.728		0.877
C9021B-3H-5, 69.0 cm	23.735	1.2276	1.3646		0.875

Table 5-3-4-1

Location	Subbottom Depth	GRA ¹⁾	MS ²⁾	NGR ³⁾	GRA Porosity
	[mbsf]	[g/cm ³]	[x10 ⁻⁵ SI]	[cps]	
C9021B-3H-5, 73.0 cm	23.775	1.2442	1.3646	27.234	0.864
C9021B-3H-5, 77.0 cm	23.815	1.2175	1.3502		0.881
C9021B-3H-5, 81.0 cm	23.855	1.2092	1.3297		0.886
C9021B-3H-5, 85.0 cm	23.895	1.2689	1.977		0.849
C9021B-3H-5, 89.0 cm	23.935	1.2492		49.8	0.861
C9021B-3H-5, 93.0 cm	23.975	1.3428	2.6405		0.804
C9021B-3H-5, 97.0 cm	24.015	1.3137	1.8956		0.822
C9021B-3H-6, 0.4 cm	24.059	1.2369	1.2116		0.869
C9021B-3H-6, 4.4 cm	24.099	1.2518	0.6313	44.9	0.860
C9021B-3H-6, 8.4 cm	24.139	1.3259	1.9704		0.814
C9021B-3H-6, 12.4 cm	24.179	1.3596	1.972		0.793
C9021B-3H-6, 16.4 cm	24.219	1.3669	1.3103		0.789
C9021B-3H-6, 20.4 cm	24.259	1.2689	1.3169	23.833	0.849
C9021B-3H-6, 24.4 cm	24.299	1.2582	0.6739		0.856
C9021B-3H-6, 28.4 cm	24.339	1.2606	1.3473		0.854
C9021B-3H-6, 32.4 cm	24.379	1.321	2.0209		0.817
C9021B-3H-6, 36.4 cm	24.419	1.2719	1.3439	20.534	0.847
C9021B-3H-6, 40.4 cm	24.459	1.2382	1.3681		0.868
C9021B-3H-6, 44.4 cm	24.499	1.4023	1.3681		0.767
C9021B-3H-6, 48.4 cm	24.539	1.3337	1.3687		0.809
C9021B-3H-6, 52.4 cm	24.579	1.3197	2.7084	31.167	0.818
C9021B-3H-6, 56.4 cm	24.619	1.3721	3.384		0.786
C9021B-3H-6, 60.4 cm	24.659	1.2392	2.0487		0.867
C9021B-3H-6, 64.4 cm	24.699	1.2836	1.3669		0.840
C9021B-3H-6, 68.4 cm	24.739	1.2926	1.3675	30.534	0.835
C9021B-3H-6, 72.4 cm	24.779	1.3456	1.364		0.802
C9021B-3H-6, 76.4 cm	24.819	1.2941	2.0347		0.834
C9021B-3H-6, 80.4 cm	24.859	1.3237	2.682		0.815
C9021B-3H-6, 84.4 cm	24.899	1.3172	3.243	40.934	0.819
C9021B-3H-6, 88.4 cm	24.939	1.3482	2.6516		0.800
C9021B-3H-6, 92.4 cm	24.979	1.329	2.6283		0.812
C9021B-3H-6, 96.4 cm	25.019	1.3641	2.5718		0.791
C9021B-3H-6, 100.4 cm	25.059	1.2987	1.219	34.601	0.831
C9021B-3H-7, 3.3 cm	25.098	1.0476	1.8816		0.985
C9021B-3H-7, 7.3 cm	25.138	1.2592	1.9548		0.855
C9021B-3H-7, 11.3 cm	25.178	1.2949	3.2579		0.833
C9021B-3H-7, 15.3 cm	25.218	1.333	2.6173	39.834	0.810
C9021B-3H-7, 19.3 cm	25.258	1.2779	2.0158		0.844
C9021B-3H-7, 23.3 cm	25.298	1.4102	2.0218		0.762
C9021B-3H-7, 27.3 cm	25.338	1.3021	2.0218		0.829
C9021B-3H-7, 31.3 cm	25.378	1.1815		30.533	0.903
C9021B-3H-7, 35.3 cm	25.418	1.3144	1.3811		0.821
C9021B-3H-7, 39.3 cm	25.458	1.1785	2.0356		0.905
C9021B-3H-7, 43.3 cm	25.498	1.1481	1.3658		0.924
C9021B-3H-7, 47.3 cm	25.538	1.1051	2.0469	25.2	0.950
C9021B-3H-7, 51.3 cm	25.578	1.059	2.0478		0.978
C9021B-3H-7, 55.3 cm	25.618	1.2894	0.6811		0.837
C9021B-3H-7, 59.3 cm	25.658	1.3413	2.0469		0.805
C9021B-3H-7, 63.3 cm	25.698	1.2479	1.3669	29.434	0.862
C9021B-3H-7, 67.3 cm	25.738	1.279	2.7084		0.843

Table 5-3-4-1

Location	Subbottom Depth	GRA ¹⁾	MS ²⁾	NGR ³⁾	GRA Porosity
	[mbsf]	[g/cm ³]	[x10 ⁻⁵ SI]	[cps]	
C9021B-3H-7, 71.3 cm	25.778	0.8772	1.9988		1.090
C9021B-3H-7, 75.3 cm	25.818	1.099	1.323		0.954
C9021B-3H-7, 79.3 cm	25.858	1.0459	0.6607	20.033	0.987
C9021B-3H-7, 83.3 cm	25.898	1.0175	0.6739		1.004
C9021B-3H-7, 87.3 cm	25.938	1.0146	0.6612		1.006
C9021B-3H-7, 91.3 cm	25.978	0.9831	0.6629		1.025
C9021B-3H-7, 95.3 cm	26.018	1.1541	1.3054	23	0.920
C9021B-3H-7, 99.3 cm	26.058	1.0839	1.8464		0.963
C9021B-3H-8, 1.8 cm	26.093	0.9953	1.2365		1.018
C9021B-3H-8, 5.8 cm	26.133	1.1132	1.9646		0.945
C9021B-3H-8, 9.8 cm	26.173	1.137	1.3037	24.2	0.930
C9021B-3H-8, 13.8 cm	26.213	1.0491	1.3153		0.985
C9021B-3H-8, 17.8 cm	26.253	0.806	1.323		1.134
C9021B-3H-8, 21.8 cm	26.293	0.7172	0.6646		1.189
C9021B-3H-8, 25.8 cm	26.333	1.0549	0.668	28.4	0.981
C9021B-3H-8, 29.8 cm	26.373	1.2735	2.7141		0.846
C9021B-3H-8, 33.8 cm	26.413	1.2211	2.0192		0.879
C9021B-3H-8, 37.8 cm	26.453	1.1612	1.3444		0.916
C9021B-3H-8, 41.8 cm	26.493	1.1776	1.3348	28.633	0.905
C9021B-3H-8, 45.8 cm	26.533	1.3255	1.3342		0.814
C9021B-3H-8, 49.8 cm	26.573	1.2553	1.9971		0.858
C9021B-3H-8, 53.8 cm	26.613	1.0158	1.323		1.005
C9021B-3H-8, 57.8 cm	26.653	0.7879	1.3108	32.6	1.145
C9021B-3H-8, 61.8 cm	26.693	1.202	2.6427		0.890
C9021B-3H-8, 65.8 cm	26.733	0.8756	1.9539		1.091
C9021B-3H-8, 69.8 cm	26.773	0.0569	4.2578		1.596
C9021B-4H-1, 8.0 cm	28.58	1.336	13.3367		0.808
C9021B-4H-1, 12.0 cm	28.62	1.3042	11.3314		0.827
C9021B-4H-1, 16.0 cm	28.66	1.18	10.0152	17.001	0.904
C9021B-4H-1, 20.0 cm	28.7	1.2056	8.75		0.888
C9021B-4H-1, 24.0 cm	28.74	1.1593	8.836		0.917
C9021B-4H-1, 28.0 cm	28.78	1.1947	9.6178		0.895
C9021B-4H-1, 32.0 cm	28.82	1.1924	15.1396	16.4	0.896
C9021B-4H-1, 36.0 cm	28.86	1.2894	20.6892		0.837
C9021B-4H-1, 40.0 cm	28.9	1.369	19.1535		0.788
C9021B-4H-1, 44.0 cm	28.94	1.2694	11.5547		0.849
C9021B-4H-1, 48.0 cm	28.98	1.1961	10.9122	17.8	0.894
C9021B-4H-1, 52.0 cm	29.02	1.1831	7.5407		0.902
C9021B-4H-1, 56.0 cm	29.06	1.1691	7.5536		0.911
C9021B-4H-1, 60.0 cm	29.1	1.1904	6.9142		0.898
C9021B-4H-1, 64.0 cm	29.14	1.1204	8.8737	18.467	0.941
C9021B-4H-1, 68.0 cm	29.18	1.0643	13.6402		0.975
C9021B-4H-1, 72.0 cm	29.22	1.1796	10.8565		0.904
C9021B-4H-1, 76.0 cm	29.26	1.3587	17.5297		0.794
C9021B-4H-1, 80.0 cm	29.3	1.2465	10.6738	22.733	0.863
C9021B-4H-1, 84.0 cm	29.34	1.1569	7.2644		0.918
C9021B-4H-1, 88.0 cm	29.38	1.1383	4.5879		0.930
C9021B-4H-1, 92.0 cm	29.42	1.1285	3.9657		0.936
C9021B-4H-1, 96.0 cm	29.46	0.892	2.664	13.167	1.081
C9021B-4H-1, 100.0 cm	29.5	0.7614	1.8987		1.162

Table 5-3-4-1

Location	Subbottom Depth	GRA ¹⁾	MS ²⁾	NGR ³⁾	GRA Porosity
	[mbsf]	[g/cm ³]	[x10 ⁻⁵ SI]	[cps]	
C9021B-4H-2, 3.0 cm	29.535	1.2137	1.2559		0.883
C9021B-4H-2, 7.0 cm	29.575	1.2442	1.9837		0.864
C9021B-4H-2, 11.0 cm	29.615	1.2734	1.3292	14.101	0.846
C9021B-4H-2, 15.0 cm	29.655	1.2949	1.3467		0.833
C9021B-4H-2, 19.0 cm	29.695	1.2435	1.3513		0.865
C9021B-4H-2, 23.0 cm	29.735	1.2725	0.6811		0.847
C9021B-4H-2, 27.0 cm	29.775	1.2735	0.6829	16.167	0.846
C9021B-4H-2, 31.0 cm	29.815	1.2913	2.0522		0.835
C9021B-4H-2, 35.0 cm	29.855	1.3297	2.0522		0.812
C9021B-4H-2, 39.0 cm	29.895	1.3633	2.0513		0.791
C9021B-4H-2, 43.0 cm	29.935	1.3366	2.0495	23.867	0.808
C9021B-4H-2, 47.0 cm	29.975	1.3444	2.0495		0.803
C9021B-4H-2, 51.0 cm	30.015	1.2135	2.0373		0.883
C9021B-4H-2, 55.0 cm	30.055	1.2771	1.3588		0.844
C9021B-4H-2, 59.0 cm	30.095	1.2615	1.3611	20.867	0.854
C9021B-4H-2, 63.0 cm	30.135	1.2653	1.3675		0.851
C9021B-4H-2, 67.0 cm	30.175	1.2809	0.6728		0.842
C9021B-4H-2, 71.0 cm	30.215	1.2974	2.0158		0.832
C9021B-4H-2, 75.0 cm	30.255	1.3373	1.3433	22.868	0.807
C9021B-4H-2, 79.0 cm	30.295	1.3278	2.0399		0.813
C9021B-4H-2, 83.0 cm	30.335	1.2994	0.6714		0.830
C9021B-4H-2, 87.0 cm	30.375	1.2509	0.6582		0.860
C9021B-4H-2, 91.0 cm	30.415	1.2865	0.6593	23.833	0.838
C9021B-4H-2, 95.0 cm	30.455	1.2802	0.6722		0.842
C9021B-4H-2, 99.0 cm	30.495	1.1875	1.2637		0.899
C9021B-4H-3, 1.6 cm	30.531	1.3202	0.621		0.818
C9021B-4H-3, 5.6 cm	30.571	1.3398	0.6562	24.134	0.806
C9021B-4H-3, 9.6 cm	30.611	1.3256	0.6632		0.814
C9021B-4H-3, 13.6 cm	30.651	1.3513	1.3269		0.798
C9021B-4H-3, 17.6 cm	30.691	1.294	1.3331		0.834
C9021B-4H-3, 21.6 cm	30.731	1.3009	0.6714	20.334	0.829
C9021B-4H-3, 25.6 cm	30.771	1.2886	0.6771		0.837
C9021B-4H-3, 29.6 cm	30.811	1.3055	1.364		0.827
C9021B-4H-3, 33.6 cm	30.851	1.3072	0.6861		0.826
C9021B-4H-3, 37.6 cm	30.891	1.3605	0.6888	20.499	0.793
C9021B-4H-3, 41.6 cm	30.931	1.3074	0.6908		0.825
C9021B-4H-3, 45.6 cm	30.971	1.3106	1.3816		0.824
C9021B-4H-3, 49.6 cm	31.011	1.3331	1.3728		0.810
C9021B-4H-3, 53.6 cm	31.051	1.2953	0.6826	16.667	0.833
C9021B-4H-3, 57.6 cm	31.091	1.32	1.3757		0.818
C9021B-4H-3, 61.6 cm	31.131	1.2863	0.6838		0.838
C9021B-4H-3, 65.6 cm	31.171	1.2483	0.6829		0.862
C9021B-4H-3, 69.6 cm	31.211	1.258	0.6867	15.734	0.856
C9021B-4H-3, 73.6 cm	31.251	1.3012	0.6926		0.829
C9021B-4H-3, 77.6 cm	31.291	1.2903	0.6873		0.836
C9021B-4H-3, 81.6 cm	31.331	1.2801	1.3467		0.842
C9021B-4H-3, 85.6 cm	31.371	1.2258	0.6682	18.9	0.876
C9021B-4H-3, 89.6 cm	31.411	1.2254	0.6754		0.876
C9021B-4H-3, 93.6 cm	31.451	1.2876	0.6722		0.838
C9021B-4H-3, 97.6 cm	31.491	1.2941	0.6408		0.834

Table 5-3-4-1

Location	Subbottom Depth	GRA ¹⁾	MS ²⁾	NGR ³⁾	GRA Porosity
	[mbsf]	[g/cm ³]	[x10 ⁻⁵ SI]	[cps]	
C9021B-4H-4, 0.4 cm	31.529	0.9286	0.6135	17.968	1.059
C9021B-4H-4, 4.4 cm	31.569	1.3347	0.6416		0.809
C9021B-4H-4, 8.4 cm	31.609	1.2963	0.6643		0.832
C9021B-4H-4, 12.4 cm	31.649	1.3499	1.3286		0.799
C9021B-4H-4, 16.4 cm	31.689	1.3208	0.6637	16.4	0.817
C9021B-4H-4, 20.4 cm	31.729	1.321	0		0.817
C9021B-4H-4, 24.4 cm	31.769	1.2555	0.6719		0.857
C9021B-4H-4, 28.4 cm	31.809	1.2688	0.6757		0.849
C9021B-4H-4, 32.4 cm	31.849	1.2521	0.6788	14.9	0.860
C9021B-4H-4, 36.4 cm	31.889	1.2528	0.6905		0.859
C9021B-4H-4, 40.4 cm	31.929	1.2733	0.6917		0.846
C9021B-4H-4, 44.4 cm	31.969	1.2893	0		0.837
C9021B-4H-4, 48.4 cm	32.009	1.2709	0	12.668	0.848
C9021B-4H-4, 52.4 cm	32.049	1.2412	0.6835		0.866
C9021B-4H-4, 56.4 cm	32.089	1.2687	0.6811		0.849
C9021B-4H-4, 60.4 cm	32.129	1.2759	0.6858		0.845
C9021B-4H-4, 64.4 cm	32.169	1.3614	0.6855	17.967	0.792
C9021B-4H-4, 68.4 cm	32.209	1.354	0.6846		0.797
C9021B-4H-4, 72.4 cm	32.249	1.3349	1.3444		0.809
C9021B-4H-4, 76.4 cm	32.289	1.2609	1.3337		0.854
C9021B-4H-4, 80.4 cm	32.329	1.2631	0.6601	18.167	0.853
C9021B-4H-4, 84.4 cm	32.369	1.2817	0.6708		0.841
C9021B-4H-4, 88.4 cm	32.409	1.1869	0		0.900
C9021B-4H-4, 92.4 cm	32.449	1.1539	0.6702		0.920
C9021B-4H-4, 96.4 cm	32.489	1.1846	0.6483	16.067	0.901
C9021B-4H-4, 100.4 cm	32.529	0.9814	0		1.026
C9021B-4H-5, 3.1 cm	32.566	1.1094	0.6238		0.947
C9021B-4H-5, 7.1 cm	32.606	1.1884	0.6618		0.899
C9021B-4H-5, 11.1 cm	32.646	1.2498	0.6663	13.467	0.861
C9021B-4H-5, 15.1 cm	32.686	1.3358	0.6719		0.808
C9021B-4H-5, 19.1 cm	32.726	1.2816	0.6694		0.841
C9021B-4H-5, 23.1 cm	32.766	1.3072	1.3456		0.826
C9021B-4H-5, 27.1 cm	32.806	1.373	1.3439	16.633	0.785
C9021B-4H-5, 31.1 cm	32.846	1.2612	1.3722		0.854
C9021B-4H-5, 35.1 cm	32.886	1.2803	0.6855		0.842
C9021B-4H-5, 39.1 cm	32.926	1.2146	0.6888		0.883
C9021B-4H-5, 43.1 cm	32.966	1.3069	1.3757	19.301	0.826
C9021B-4H-5, 47.1 cm	33.006	1.3064	1.3763		0.826
C9021B-4H-5, 51.1 cm	33.046	1.3405	1.3787		0.805
C9021B-4H-5, 55.1 cm	33.086	1.3004	1.3799		0.830
C9021B-4H-5, 59.1 cm	33.126	1.2657	0.6902	18.634	0.851
C9021B-4H-5, 63.1 cm	33.166	1.2742	1.3775		0.846
C9021B-4H-5, 67.1 cm	33.206	1.2171	0.6882		0.881
C9021B-4H-5, 71.1 cm	33.246	1.2552	1.3763		0.858
C9021B-4H-5, 75.1 cm	33.286	1.1986	0.6791	21.034	0.892
C9021B-4H-5, 79.1 cm	33.326	1.1481	0.6777		0.924
C9021B-4H-5, 83.1 cm	33.366	1.2074	1.3337		0.887
C9021B-4H-5, 87.1 cm	33.406	1.1083	0.6585		0.948
C9021B-4H-5, 91.1 cm	33.446	1.0843	0	17.334	0.963
C9021B-4H-5, 95.1 cm	33.486	1.1568	1.349		0.918

Table 5-3-4-1

Location	Subbottom Depth	GRA ¹⁾	MS ²⁾	NGR ³⁾	GRA Porosity
	[mbsf]	[g/cm ³]	[x10 ⁻⁵ SI]	[cps]	
C9021B-4H-5, 99.1 cm	33.526	0.8056	0.6382		1.134
C9021B-4H-6, 1.0 cm	33.56	1.3133	0.6213		0.822
C9021B-4H-6, 5.0 cm	33.6	1.3433	0.6629	20.567	0.803
C9021B-4H-6, 9.0 cm	33.64	1.32	0.6685		0.818
C9021B-4H-6, 13.0 cm	33.68	1.367	1.3371		0.789
C9021B-4H-6, 17.0 cm	33.72	1.3066	1.328		0.826
C9021B-4H-6, 21.0 cm	33.76	1.3406	0.6716	22.4	0.805
C9021B-4H-6, 25.0 cm	33.8	1.3013	0.6841		0.829
C9021B-4H-6, 29.0 cm	33.84	1.3523	0.6893		0.798
C9021B-4H-6, 33.0 cm	33.88	1.3231	1.3852		0.816
C9021B-4H-6, 37.0 cm	33.92	1.3235	0.6938	18.666	0.816
C9021B-4H-6, 41.0 cm	33.96	1.3103	0.695		0.824
C9021B-4H-6, 45.0 cm	34	1.3403	1.3816		0.805
C9021B-4H-6, 49.0 cm	34.04	1.4174	1.3846		0.758
C9021B-4H-6, 53.0 cm	34.08	1.3245	1.3864	20.833	0.815
C9021B-4H-6, 57.0 cm	34.12	1.3181	1.3704		0.819
C9021B-4H-6, 61.0 cm	34.16	1.3264	0.6908		0.814
C9021B-4H-6, 65.0 cm	34.2	1.3793	0.6791		0.781
C9021B-4H-6, 69.0 cm	34.24	1.3141	1.3536	18.467	0.821
C9021B-4H-6, 73.0 cm	34.28	1.3315	0.6771		0.811
C9021B-4H-6, 77.0 cm	34.32	1.3932	0.6685		0.773
C9021B-4H-6, 81.0 cm	34.36	1.4079	1.3286		0.764
C9021B-4H-6, 85.0 cm	34.4	1.368	1.3005	23.101	0.788
C9021B-4H-6, 89.0 cm	34.44	1.3221	1.3393		0.816
C9021B-4H-6, 93.0 cm	34.48	1.293	0.6722		0.834
C9021B-4H-6, 97.0 cm	34.52	1.307	0.6682		0.826
C9021B-4H-6, 101.0 cm	34.56	0.696	0	13.9	1.202
C9021B-4H-7, 3.5 cm	34.59	1.3018	0.6368		0.829
C9021B-4H-7, 7.5 cm	34.63	1.3579	1.3264		0.794
C9021B-4H-7, 11.5 cm	34.67	1.3541	1.3342		0.797
C9021B-4H-7, 15.5 cm	34.71	1.3848	0.6719	22.134	0.778
C9021B-4H-7, 19.5 cm	34.75	1.3089	0.6808		0.825
C9021B-4H-7, 23.5 cm	34.79	1.2209	0.6814		0.879
C9021B-4H-7, 27.5 cm	34.83	1.3298	1.3664		0.812
C9021B-4H-7, 31.5 cm	34.87	1.3361	0.6864	17.567	0.808
C9021B-4H-7, 35.5 cm	34.91	1.2879	0		0.838
C9021B-4H-7, 39.5 cm	34.95	1.2856	0.6902		0.839
C9021B-4H-7, 43.5 cm	34.99	1.2971	0.6885		0.832
C9021B-4H-7, 47.5 cm	35.03	1.3195	0.6797	17.567	0.818
C9021B-4H-7, 51.5 cm	35.07	1.2912	0.6826		0.835
C9021B-4H-7, 55.5 cm	35.11	1.3654	1.3675		0.790
C9021B-4H-7, 59.5 cm	35.15	1.3522	1.371		0.798
C9021B-4H-7, 63.5 cm	35.19	1.2597	0.6888	17.866	0.855
C9021B-4H-7, 67.5 cm	35.23	1.3175	0.6923		0.819
C9021B-4H-7, 71.5 cm	35.27	1.3251	0.6893		0.815
C9021B-4H-7, 75.5 cm	35.31	1.3229	0.6742		0.816
C9021B-4H-7, 79.5 cm	35.35	1.2515	0.6702	15.1	0.860
C9021B-4H-7, 83.5 cm	35.39	1.2379	0.6736		0.868
C9021B-4H-7, 87.5 cm	35.43	1.2573	0.6685		0.856
C9021B-4H-7, 91.5 cm	35.47	1.3214	0.6725		0.817

Table 5-3-4-1

Location	Subbottom Depth	GRA ¹⁾	MS ²⁾	NGR ³⁾	GRA Porosity
	[mbsf]	[g/cm ³]	[x10 ⁻⁵ SI]	[cps]	
C9021B-4H-7, 95.5 cm	35.51	1.2875	0.6626	17.434	0.838
C9021B-4H-7, 99.5 cm	35.55	1.2552	0		0.858
C9021B-4H-8, 1.1 cm	35.581	1.2095	0		0.886
C9021B-4H-8, 5.1 cm	35.621	1.2444	0.6618		0.864
C9021B-4H-8, 9.1 cm	35.661	1.2919	0.6702	8.634	0.835
C9021B-4H-8, 13.1 cm	35.701	1.2604	0		0.854
C9021B-4H-8, 17.1 cm	35.741	1.2736	0.6757		0.846
C9021B-4H-8, 21.1 cm	35.781	1.2429	0		0.865
C9021B-4H-8, 25.1 cm	35.821	1.2802	0.6808	11.467	0.842
C9021B-4H-8, 29.1 cm	35.861	1.2897	0.6858		0.836
C9021B-4H-8, 33.1 cm	35.901	1.3115	1.3576		0.823
C9021B-4H-8, 37.1 cm	35.941	1.3171	1.3553		0.820
C9021B-4H-8, 41.1 cm	35.981	1.2722	0.6841	12.467	0.847
C9021B-4H-8, 45.1 cm	36.021	1.2994	0.6917		0.830
C9021B-4H-8, 49.1 cm	36.061	1.2621	0.6882		0.853
C9021B-4H-8, 53.1 cm	36.101	1.2457	0.687		0.863
C9021B-4H-8, 57.1 cm	36.141	1.2398	0.682	11.1	0.867
C9021B-4H-8, 61.1 cm	36.181	1.2972	0.7013		0.832
C9021B-4H-8, 65.1 cm	36.221	1.2788	0.6974		0.843
C9021B-4H-8, 69.1 cm	36.261	1.2515	0.6968		0.860
C9021B-4H-8, 73.1 cm	36.301	1.2429	0.6867	10.134	0.865
C9021B-4H-8, 77.1 cm	36.341	1.2422	0.6759		0.866
C9021B-4H-8, 81.1 cm	36.381	1.2057	0.6629		0.888
C9021B-4H-8, 85.1 cm	36.421	1.2715	0.6601		0.848
C9021B-4H-8, 89.1 cm	36.461	1.277	0.6629	15	0.844
C9021B-4H-8, 93.1 cm	36.501	1.2575	0.6754		0.856
C9021B-4H-8, 97.1 cm	36.541	1.3034	0.6621		0.828
C9021B-4H-8, 101.1 cm	36.581	1.0135	0.6157		1.006
C9021B-4H-9, 3.8 cm	36.618	1.3373	1.2653	28.567	0.807
C9021B-4H-9, 7.8 cm	36.658	1.3453	2.0141		0.802
C9021B-4H-9, 11.8 cm	36.698	1.489	4.7015		0.714
C9021B-4H-9, 15.8 cm	36.738	1.6334	8.6725		0.625
C9021B-4H-9, 19.8 cm	36.778	1.5367	8.0121	48.934	0.684
C9021B-4H-9, 23.8 cm	36.818	1.545	8.7019		0.679
C9021B-4H-9, 27.8 cm	36.858	1.438	9.2885		0.745
C9021B-4H-9, 31.8 cm	36.898	1.1353	8.2073		0.931
C9021B-5H-1, 8.0 cm	38.08	1.4548	53.1052		0.735
C9021B-5H-1, 12.0 cm	38.12	1.4806	45.0577		0.719
C9021B-5H-1, 16.0 cm	38.16	1.4153	37.9493	21.799	0.759
C9021B-5H-1, 20.0 cm	38.2	1.3833	21.713		0.779
C9021B-5H-1, 24.0 cm	38.24	1.3898	17.6945		0.775
C9021B-5H-1, 28.0 cm	38.28	1.3649	19.5523		0.790
C9021B-5H-1, 32.0 cm	38.32	1.366	22.8942	13.3	0.789
C9021B-5H-1, 36.0 cm	38.36	1.3736			0.785
C9021B-5H-1, 40.0 cm	38.4	1.4266	22.9429		0.752
C9021B-5H-1, 44.0 cm	38.44	1.3583	30.4172		0.794
C9021B-5H-1, 48.0 cm	38.48	1.3502	15.54	15.499	0.799
C9021B-5H-1, 52.0 cm	38.52	1.3555	16.8985		0.796
C9021B-5H-1, 56.0 cm	38.56	1.3693	11.4568		0.787
C9021B-5H-1, 60.0 cm	38.6	1.4565	13.6286		0.734

Table 5-3-4-1

Location	Subbottom Depth	GRA ¹⁾	MS ²⁾	NGR ³⁾	GRA Porosity
	[mbsf]	[g/cm ³]	[x10 ⁻⁵ SI]	[cps]	
C9021B-5H-1, 64.0 cm	38.64	1.4466	15.6662	25.432	0.740
C9021B-5H-1, 68.0 cm	38.68	1.4218	17.6644		0.755
C9021B-5H-1, 72.0 cm	38.72	1.3198	13.5591		0.818
C9021B-5H-1, 76.0 cm	38.76	1.3312	10.0705		0.811
C9021B-5H-1, 80.0 cm	38.8	1.3332	10.0025	17.666	0.810
C9021B-5H-1, 84.0 cm	38.84	1.3429	9.3396		0.804
C9021B-5H-1, 88.0 cm	38.88	1.3352	8.7019		0.808
C9021B-5H-1, 92.0 cm	38.92	1.3073	6.7079		0.826
C9021B-5H-1, 96.0 cm	38.96	1.3245	5.9787	21.7	0.815
C9021B-5H-1, 100.0 cm	39	1.3542	4.3687		0.797
C9021B-5H-2, 3.0 cm	39.04	1.2856	3.1295		0.839
C9021B-5H-2, 7.0 cm	39.08	1.2999	4.0197		0.830
C9021B-5H-2, 11.0 cm	39.12	1.3394	4.7255	18.666	0.806
C9021B-5H-2, 15.0 cm	39.16	1.3723	4.0625		0.786
C9021B-5H-2, 19.0 cm	39.2	1.338	4.7437		0.807
C9021B-5H-2, 23.0 cm	39.24	1.3725	4.7619		0.785
C9021B-5H-2, 27.0 cm	39.28	1.3769	4.7477	22.733	0.783
C9021B-5H-2, 31.0 cm	39.32	1.3913	5.4306		0.774
C9021B-5H-2, 35.0 cm	39.36	1.3115	3.4013		0.823
C9021B-5H-2, 39.0 cm	39.4	1.298	3.4028		0.831
C9021B-5H-2, 43.0 cm	39.44	1.3866	4.0886	27.434	0.777
C9021B-5H-2, 47.0 cm	39.48	1.4184	6.1538		0.757
C9021B-5H-2, 51.0 cm	39.52	1.3539	4.0799		0.797
C9021B-5H-2, 55.0 cm	39.56	1.3416	3.397		0.804
C9021B-5H-2, 59.0 cm	39.6	1.2876	4.0816	19.433	0.838
C9021B-5H-2, 63.0 cm	39.64	1.3099	3.429		0.824
C9021B-5H-2, 67.0 cm	39.68	1.2439	3.3854		0.865
C9021B-5H-2, 71.0 cm	39.72	1.3154	3.3711		0.821
C9021B-5H-2, 75.0 cm	39.76	1.2711	3.3328	26.333	0.848
C9021B-5H-2, 79.0 cm	39.8	1.2754	3.3869		0.845
C9021B-5H-2, 83.0 cm	39.84	1.3289	4.0299		0.812
C9021B-5H-2, 87.0 cm	39.88	1.3546	3.3398		0.796
C9021B-5H-2, 91.0 cm	39.92	1.3107	4.0248	17.932	0.823
C9021B-5H-2, 95.0 cm	39.96	1.3264	3.3697		0.814
C9021B-5H-2, 99.0 cm	40	1.3795	3.7786		0.781
C9021B-5H-3, 1.2 cm	40.032	1.2919	1.8093		0.835
C9021B-5H-3, 5.2 cm	40.072	1.2901	1.9605	13.332	0.836
C9021B-5H-3, 9.2 cm	40.112	1.33	2.6969		0.812
C9021B-5H-3, 13.2 cm	40.152	1.296	3.3869		0.833
C9021B-5H-3, 17.2 cm	40.192	1.2773	2.7141		0.844
C9021B-5H-3, 21.2 cm	40.232	1.3117	2.7164	14.399	0.823
C9021B-5H-3, 25.2 cm	40.272	1.3115	2.7292		0.823
C9021B-5H-3, 29.2 cm	40.312	1.3425	3.3754		0.804
C9021B-5H-3, 33.2 cm	40.352	1.3199	3.3725		0.818
C9021B-5H-3, 37.2 cm	40.392	1.3191	2.6992	11.066	0.818
C9021B-5H-3, 41.2 cm	40.432	1.3011	2.7199		0.829
C9021B-5H-3, 45.2 cm	40.472	1.2785	2.0356		0.843
C9021B-5H-3, 49.2 cm	40.512	1.2749	2.0098		0.846
C9021B-5H-3, 53.2 cm	40.552	1.2972	2.0005	12.2	0.832
C9021B-5H-3, 57.2 cm	40.592	1.3048	2.7234		0.827

Table 5-3-4-1

Location	Subbottom Depth	GRA ¹⁾	MS ²⁾	NGR ³⁾	GRA Porosity
	[mbsf]	[g/cm ³]	[x10 ⁻⁵ SI]	[cps]	
C9021B-5H-3, 61.2 cm	40.632	1.2963	2.728		0.832
C9021B-5H-3, 65.2 cm	40.672	1.2989	2.7246		0.831
C9021B-5H-3, 69.2 cm	40.712	1.3118	2.7188	9.634	0.823
C9021B-5H-3, 73.2 cm	40.752	1.3238	3.397		0.815
C9021B-5H-3, 77.2 cm	40.792	1.285	2.7107		0.839
C9021B-5H-3, 81.2 cm	40.832	1.3328	4.0146		0.810
C9021B-5H-3, 85.2 cm	40.872	1.4205	4.0078	18.767	0.756
C9021B-5H-3, 89.2 cm	40.912	1.3949	3.3783		0.772
C9021B-5H-3, 93.2 cm	40.952	1.3727	3.3611		0.785
C9021B-5H-3, 97.2 cm	40.992	1.2912	1.9729		0.835
C9021B-5H-3, 101.2 cm	41.032	0.7008	1.8769	12.534	1.199
C9021B-5H-4, 3.8 cm	41.068	1.2867	2.6118		0.838
C9021B-5H-4, 7.8 cm	41.108	1.2985	2.6707		0.831
C9021B-5H-4, 11.8 cm	41.148	1.3727	3.3257		0.785
C9021B-5H-4, 15.8 cm	41.188	1.2624	2.6752	9.6	0.853
C9021B-5H-4, 19.8 cm	41.228	1.2781	2.033		0.844
C9021B-5H-4, 23.8 cm	41.268	1.2468	2.0417		0.863
C9021B-5H-4, 27.8 cm	41.308	1.2525	2.7222		0.859
C9021B-5H-4, 31.8 cm	41.348	1.2821	2.7199	8.1	0.841
C9021B-5H-4, 35.8 cm	41.388	1.2619	1.3588		0.854
C9021B-5H-4, 39.8 cm	41.428	1.214	1.3582		0.883
C9021B-5H-4, 43.8 cm	41.468	1.2651	2.0382		0.852
C9021B-5H-4, 47.8 cm	41.508	1.237	2.0399	10.399	0.869
C9021B-5H-4, 51.8 cm	41.548	1.2532	2.0417		0.859
C9021B-5H-4, 55.8 cm	41.588	1.2671	2.7199		0.850
C9021B-5H-4, 59.8 cm	41.628	1.2735	2.0707		0.846
C9021B-5H-4, 63.8 cm	41.668	1.273	2.7491	20.299	0.847
C9021B-5H-4, 67.8 cm	41.708	1.3281	3.432		0.813
C9021B-5H-4, 71.8 cm	41.748	1.2921	4.6956		0.835
C9021B-5H-4, 75.8 cm	41.788	1.4373	4.6817		0.746
C9021B-5H-4, 79.8 cm	41.828	1.3234	3.3469	44.666	0.816
C9021B-5H-4, 83.8 cm	41.868	1.33	4.0903		0.812
C9021B-5H-4, 87.8 cm	41.908	1.5282	5.3641		0.690
C9021B-5H-4, 91.8 cm	41.948	1.1744	4.6738		0.907
C9021B-5H-4, 95.8 cm	41.988	0.7574	2.614	24.966	1.164
C9021B-5H-4, 99.8 cm	42.028	0.7097	2.4831		1.194
C9021B-5H-5, 2.7 cm	42.062	1.3836	2.5452		0.779
C9021B-5H-5, 6.7 cm	42.102	1.3711	2.6866		0.786
C9021B-5H-5, 10.7 cm	42.142	1.3633	2.6786	22.899	0.791
C9021B-5H-5, 14.7 cm	42.182	1.3686	2.0201		0.788
C9021B-5H-5, 18.7 cm	42.222	1.2908	2.0227		0.836
C9021B-5H-5, 22.7 cm	42.262	1.293	2.0382		0.834
C9021B-5H-5, 26.7 cm	42.302	1.3591	2.0417	20.633	0.794
C9021B-5H-5, 30.7 cm	42.342	1.3461	3.3912		0.802
C9021B-5H-5, 34.7 cm	42.382	1.3286	3.3826		0.812
C9021B-5H-5, 38.7 cm	42.422	1.3498	3.3898		0.799
C9021B-5H-5, 42.7 cm	42.462	1.4491	4.0851	46.3	0.738
C9021B-5H-5, 46.7 cm	42.502	1.4482	4.7904		0.739
C9021B-5H-5, 50.7 cm	42.542	1.4203	4.7517		0.756
C9021B-5H-5, 54.7 cm	42.582	1.4425	4.0695		0.742

Table 5-3-4-1

Location	Subbottom Depth	GRA ¹⁾	MS ²⁾	NGR ³⁾	GRA Porosity
	[mbsf]	[g/cm ³]	[x10 ⁻⁵ SI]	[cps]	
C9021B-5H-5, 58.7 cm	42.622	1.477	4.0712	33.433	0.721
C9021B-5H-5, 62.7 cm	42.662	1.4006	4.1735		0.768
C9021B-5H-5, 66.7 cm	42.702	1.3778	3.4349		0.782
C9021B-5H-5, 70.7 cm	42.742	1.3496	2.7397		0.800
C9021B-5H-5, 74.7 cm	42.782	1.3801	2.7049	30.198	0.781
C9021B-5H-5, 78.7 cm	42.822	1.3674	3.4101		0.789
C9021B-5H-5, 82.7 cm	42.862	1.3496	3.3984		0.800
C9021B-5H-5, 86.7 cm	42.902	1.305	2.69		0.827
C9021B-5H-5, 90.7 cm	42.942	1.4925	4.0027	28.466	0.712
C9021B-5H-5, 94.7 cm	42.982	1.4709	4.6817		0.725
C9021B-5H-5, 98.7 cm	43.022	1.4246	3.1632		0.753
C9021B-5H-6, 1.3 cm	43.053	1.2375	1.8777		0.869
C9021B-5H-6, 5.3 cm	43.093	1.3605	3.2937	23.666	0.793
C9021B-5H-6, 9.3 cm	43.133	1.3083	3.3711		0.825
C9021B-5H-6, 13.3 cm	43.173	1.3373	4.0539		0.807
C9021B-5H-6, 17.3 cm	43.213	1.3691	3.3941		0.788
C9021B-5H-6, 21.3 cm	43.253	1.3746	4.7659	18.6	0.784
C9021B-5H-6, 25.3 cm	43.293	1.3439	4.0903		0.803
C9021B-5H-6, 29.3 cm	43.333	1.2131	3.3625		0.884
C9021B-5H-6, 33.3 cm	43.373	1.195	3.3611		0.895
C9021B-5H-6, 37.3 cm	43.413	1.3557	3.3654	21.733	0.796
C9021B-5H-6, 41.3 cm	43.453	1.3974	4.7396		0.770
C9021B-5H-6, 45.3 cm	43.493	1.2899	4.0591		0.836
C9021B-5H-6, 49.3 cm	43.533	1.2721	3.3497		0.847
C9021B-5H-6, 53.3 cm	43.573	1.134	3.3384	24.466	0.932
C9021B-5H-6, 57.3 cm	43.613	1.2642	3.4013		0.852
C9021B-5H-6, 61.3 cm	43.653	1.1921	2.7211		0.896
C9021B-5H-6, 65.3 cm	43.693	1.2886	2.7199		0.837
C9021B-5H-6, 69.3 cm	43.733	1.2069	2.0304	24.832	0.887
C9021B-5H-6, 73.3 cm	43.773	1.2056	2.0347		0.888
C9021B-5H-6, 77.3 cm	43.813	1.2758	2.7107		0.845
C9021B-5H-6, 81.3 cm	43.853	1.2603	3.3697		0.854
C9021B-5H-6, 85.3 cm	43.893	1.2754	2.6934	41.566	0.845
C9021B-5H-6, 89.3 cm	43.933	1.2794	2.682		0.843
C9021B-5H-6, 93.3 cm	43.973	1.2728	2.6809		0.847
C9021B-5H-6, 97.3 cm	44.013	0.6697	1.9361		1.218
C9021B-5H-7, 0.5 cm	44.05	1.2277	1.8654	25.833	0.875
C9021B-5H-7, 4.5 cm	44.09	1.3855	3.3469		0.777
C9021B-5H-7, 8.5 cm	44.13	1.3716	4.0044		0.786
C9021B-5H-7, 12.5 cm	44.17	1.3499	3.337		0.799
C9021B-5H-7, 16.5 cm	44.21	1.3225	3.3611	25.6	0.816
C9021B-5H-7, 20.5 cm	44.25	1.398	4.0574		0.770
C9021B-5H-7, 24.5 cm	44.29	1.2853	3.3768		0.839
C9021B-5H-7, 28.5 cm	44.33	1.4811	4.0402		0.719
C9021B-5H-7, 32.5 cm	44.37	1.4699	4.7115	32.399	0.725
C9021B-5H-7, 36.5 cm	44.41	1.4681	4.7863		0.727
C9021B-5H-7, 40.5 cm	44.45	1.3727	4.0729		0.785
C9021B-5H-7, 44.5 cm	44.49	1.3466	2.7095		0.801
C9021B-5H-7, 48.5 cm	44.53	1.3552	3.374	24.533	0.796
C9021B-5H-7, 52.5 cm	44.57	1.2197	3.3912		0.879

Table 5-3-4-1

Location	Subbottom Depth	GRA ¹⁾	MS ²⁾	NGR ³⁾	GRA Porosity
	[mbsf]	[g/cm ³]	[x10 ⁻⁵ SI]	[cps]	
C9021B-5H-7, 56.5 cm	44.61	1.3043	2.7153		0.827
C9021B-5H-7, 60.5 cm	44.65	1.3387	2.7538		0.806
C9021B-5H-7, 64.5 cm	44.69	1.3321	3.4203	29.4	0.810
C9021B-5H-7, 68.5 cm	44.73	1.2853	2.7153		0.839
C9021B-5H-7, 72.5 cm	44.77	1.301	2.6572		0.829
C9021B-5H-7, 76.5 cm	44.81	1.2461	2.673		0.863
C9021B-5H-7, 80.5 cm	44.85	1.3174	2.0365	24.6	0.819
C9021B-5H-7, 84.5 cm	44.89	1.2001	2.0408		0.892
C9021B-5H-7, 88.5 cm	44.93	1.2992	3.3568		0.831
C9021B-5H-7, 92.5 cm	44.97	1.277	2.6843		0.844
C9021B-5H-7, 96.5 cm	45.01	1.3231	2.6673	28.766	0.816
C9021B-5H-7, 100.5 cm	45.05	1.1752	1.9018		0.907
C9021B-5H-8, 3.4 cm	45.089	1.3045	3.1763		0.827
C9021B-5H-8, 7.4 cm	45.129	1.252	3.3006		0.860
C9021B-5H-8, 11.4 cm	45.169	1.328	3.3089	39.866	0.813
C9021B-5H-8, 15.4 cm	45.209	1.3061	3.3625		0.826
C9021B-5H-8, 19.4 cm	45.249	1.0626	2.6923		0.976
C9021B-5H-8, 23.4 cm	45.289	1.3248	2.69		0.815
C9021B-5H-8, 27.4 cm	45.329	1.219	2.0013	43.633	0.880
C9021B-5H-8, 31.4 cm	45.369	1.2842	2.0124		0.840
C9021B-5H-8, 35.4 cm	45.409	1.338	3.3568		0.807
C9021B-5H-8, 39.4 cm	45.449	1.2306	3.3568		0.873
C9021B-5H-8, 43.4 cm	45.489	1.2123	3.3682	39.866	0.884
C9021B-5H-8, 47.4 cm	45.529	1.0938	2.7084		0.957
C9021B-5H-8, 51.4 cm	45.569	1.3048	3.354		0.827
C9021B-5H-8, 55.4 cm	45.609	1.3606	3.3469		0.793
C9021B-5H-8, 59.4 cm	45.649	1.3518	3.354	26.833	0.798
C9021B-5H-8, 63.4 cm	45.689	1.2172	3.4261		0.881
C9021B-5H-8, 67.4 cm	45.729	1.3217	4.0677		0.817
C9021B-5H-8, 71.4 cm	45.769	1.3386	3.3854		0.806
C9021B-5H-8, 75.4 cm	45.809	1.3526	4.0453	32.799	0.798
C9021B-5H-8, 79.4 cm	45.849	1.4489	4.0781		0.738
C9021B-5H-8, 83.4 cm	45.889	1.4253	4.0903		0.753
C9021B-5H-8, 87.4 cm	45.929	1.2917	4.0973		0.835
C9021B-5H-8, 91.4 cm	45.969	1.2726	3.4115	26.4	0.847
C9021B-5H-8, 95.4 cm	46.009	1.2435	2.713		0.865
C9021B-5H-8, 99.4 cm	46.049	0.318	1.3399		1.435
C9021B-5H-8, 103.4 cm	46.089	0.3465	1.2731		1.417
C9021B-6H-1, 8.0 cm	47.08	1.3485	13.1857		0.800
C9021B-6H-1, 12.0 cm	47.12	1.3784	15.7896		0.782
C9021B-6H-1, 16.0 cm	47.16	1.3985	22.3969	19.768	0.769
C9021B-6H-1, 20.0 cm	47.2	1.3576	17.1198		0.795
C9021B-6H-1, 24.0 cm	47.24	1.3427	15.8963		0.804
C9021B-6H-1, 28.0 cm	47.28	1.325	13.3029		0.815
C9021B-6H-1, 32.0 cm	47.32	1.2978	10.6513	18.534	0.831
C9021B-6H-1, 36.0 cm	47.36	1.3551	11.3314		0.796
C9021B-6H-1, 40.0 cm	47.4	1.27	12.5793		0.849
C9021B-6H-1, 44.0 cm	47.44	1.2926	16.0514		0.835
C9021B-6H-1, 48.0 cm	47.48	1.3289	15.4087	17.267	0.812
C9021B-6H-1, 52.0 cm	47.52	1.2969	11.3987		0.832

Table 5-3-4-1

Location	Subbottom Depth	GRA ¹⁾	MS ²⁾	NGR ³⁾	GRA Porosity
	[mbsf]	[g/cm ³]	[x10 ⁻⁵ SI]	[cps]	
C9021B-6H-1, 56.0 cm	47.56	1.2819	9.3633		0.841
C9021B-6H-1, 60.0 cm	47.6	1.2609	12.1566		0.854
C9021B-6H-1, 64.0 cm	47.64	1.2716	10.7875	17.568	0.848
C9021B-6H-1, 68.0 cm	47.68	1.2907	12.0284		0.836
C9021B-6H-1, 72.0 cm	47.72	1.2661	11.2315		0.851
C9021B-6H-1, 76.0 cm	47.76	1.3283	10.4911		0.813
C9021B-6H-1, 80.0 cm	47.8	1.3102	14.2335	19.067	0.824
C9021B-6H-1, 84.0 cm	47.84	1.3522	11.0354		0.798
C9021B-6H-1, 88.0 cm	47.88	1.3682	9.126		0.788
C9021B-6H-1, 92.0 cm	47.92	1.3534	13.7178		0.797
C9021B-6H-1, 96.0 cm	47.96	1.3871	9.6322	19.901	0.776
C9021B-6H-1, 100.0 cm	48	1.2994	7.8784		0.830
C9021B-6H-2, 3.0 cm	48.035	1.275	10.6271		0.845
C9021B-6H-2, 7.0 cm	48.075	1.3084			0.825
C9021B-6H-2, 11.0 cm	48.115	1.3315	9.931	16.568	0.811
C9021B-6H-2, 15.0 cm	48.155	1.3028	7.9314		0.828
C9021B-6H-2, 19.0 cm	48.195	1.3125	7.8783		0.822
C9021B-6H-2, 23.0 cm	48.235	1.2981	4.615		0.831
C9021B-6H-2, 27.0 cm	48.275	1.31	6.643	16.501	0.824
C9021B-6H-2, 31.0 cm	48.315	1.3084	6.6571		0.825
C9021B-6H-2, 35.0 cm	48.355	1.3255	6.6655		0.814
C9021B-6H-2, 39.0 cm	48.395	1.2918			0.835
C9021B-6H-2, 43.0 cm	48.435	1.3105	5.9964	15.934	0.824
C9021B-6H-2, 47.0 cm	48.475	1.3041	4.0214		0.828
C9021B-6H-2, 51.0 cm	48.515	1.2916	4.6916		0.835
C9021B-6H-2, 55.0 cm	48.555	1.3252	4.6896		0.815
C9021B-6H-2, 59.0 cm	48.595	1.3601	5.9914	21.668	0.793
C9021B-6H-2, 63.0 cm	48.635	1.3112	4.6896		0.823
C9021B-6H-2, 67.0 cm	48.675	1.3528	4.6916		0.798
C9021B-6H-2, 71.0 cm	48.715	1.3543	4.6364		0.797
C9021B-6H-2, 75.0 cm	48.755	1.3777	3.9741	21.501	0.782
C9021B-6H-2, 79.0 cm	48.795	1.3969	4.6462		0.770
C9021B-6H-2, 83.0 cm	48.835	1.2907	3.9358		0.836
C9021B-6H-2, 87.0 cm	48.875	1.3717	3.9063		0.786
C9021B-6H-2, 91.0 cm	48.915	1.3051	3.2416	18.735	0.827
C9021B-6H-2, 95.0 cm	48.955	1.296	3.3048		0.833
C9021B-6H-2, 99.0 cm	48.995	1.4436	5.0092		0.742
C9021B-6H-3, 1.0 cm	49.025	1.312	2.437		0.823
C9021B-6H-3, 5.0 cm	49.065	1.3766	3.2322	19.334	0.783
C9021B-6H-3, 9.0 cm	49.105	1.2828	2.6272		0.841
C9021B-6H-3, 13.0 cm	49.145	1.2975	2.6272		0.832
C9021B-6H-3, 17.0 cm	49.185	1.3644	3.2867		0.790
C9021B-6H-3, 21.0 cm	49.225	1.4798	4.6169	23.201	0.719
C9021B-6H-3, 25.0 cm	49.265	1.3566	4.6836		0.795
C9021B-6H-3, 29.0 cm	49.305	1.3656	4.6599		0.790
C9021B-6H-3, 33.0 cm	49.345	1.3911	4.6698		0.774
C9021B-6H-3, 37.0 cm	49.385	1.3763	4.0231	23.6	0.783
C9021B-6H-3, 41.0 cm	49.425	1.3635	4.0695		0.791
C9021B-6H-3, 45.0 cm	49.465	1.3963	4.0522		0.771
C9021B-6H-3, 49.0 cm	49.505	1.3102	3.3426		0.824

Table 5-3-4-1

Location	Subbottom Depth	GRA ¹⁾	MS ²⁾	NGR ³⁾	GRA Porosity
	[mbsf]	[g/cm ³]	[x10 ⁻⁵ SI]	[cps]	
C9021B-6H-3, 53.0 cm	49.545	1.272	2.6718	19.267	0.847
C9021B-6H-3, 57.0 cm	49.585	1.291	2.7049		0.836
C9021B-6H-3, 61.0 cm	49.625	1.3747	3.3711		0.784
C9021B-6H-3, 65.0 cm	49.665	1.4087	4.0061		0.763
C9021B-6H-3, 69.0 cm	49.705	1.4003	3.9707	26.201	0.768
C9021B-6H-3, 73.0 cm	49.745	1.3608	3.9959		0.793
C9021B-6H-3, 77.0 cm	49.785	1.2733	3.3006		0.846
C9021B-6H-3, 81.0 cm	49.825	1.2862	3.2854		0.839
C9021B-6H-3, 85.0 cm	49.865	1.3176	3.2771	21.468	0.819
C9021B-6H-3, 89.0 cm	49.905	1.4354	4.5957		0.747
C9021B-6H-3, 93.0 cm	49.945	1.4434	4.6072		0.742
C9021B-6H-3, 97.0 cm	49.985	1.3742	3.273		0.784
C9021B-6H-3, 101.0 cm	50.025	0.9406	2.4659	19.167	1.051
C9021B-6H-4, 3.4 cm	50.059	1.4625	3.7849		0.730
C9021B-6H-4, 7.4 cm	50.099	1.4032	3.9292		0.767
C9021B-6H-4, 11.4 cm	50.139	1.3619	3.9276		0.792
C9021B-6H-4, 15.4 cm	50.179	1.3694	3.9358	22.301	0.787
C9021B-6H-4, 19.4 cm	50.219	1.4166	3.959		0.758
C9021B-6H-4, 23.4 cm	50.259	1.3661	3.9342		0.789
C9021B-6H-4, 27.4 cm	50.299	1.3554	3.2812		0.796
C9021B-6H-4, 31.4 cm	50.339	1.3771	3.9524	22.167	0.783
C9021B-6H-4, 35.4 cm	50.379	1.3537	4.0163		0.797
C9021B-6H-4, 39.4 cm	50.419	1.4133	3.3328		0.760
C9021B-6H-4, 43.4 cm	50.459	1.3099	3.3089		0.824
C9021B-6H-4, 47.4 cm	50.499	1.3845	3.3089	24.334	0.778
C9021B-6H-4, 51.4 cm	50.539	1.3568	3.354		0.795
C9021B-6H-4, 55.4 cm	50.579	1.2934	3.3511		0.8341133
C9021B-6H-4, 59.4 cm	50.619	1.3602	3.3455		0.792980296
C9021B-6H-4, 63.4 cm	50.659	1.384	3.3215	20.334	0.778325123
C9021B-6H-4, 67.4 cm	50.699	1.3541	3.3117		0.796736453
C9021B-6H-4, 71.4 cm	50.739	1.3791	3.9657		0.781342365
C9021B-6H-4, 75.4 cm	50.779	1.4034	3.9707		0.76637931
C9021B-6H-4, 79.4 cm	50.819	1.3885	3.3075	20.567	0.775554187
C9021B-6H-4, 83.4 cm	50.859	1.349	3.9491		0.799876847
C9021B-6H-4, 87.4 cm	50.899	1.3564	3.273		0.795320197
C9021B-6H-4, 91.4 cm	50.939	1.3702	3.2661		0.78682266
C9021B-6H-4, 95.4 cm	50.979	1.3021	2.6283	21.001	0.828756158
C9021B-6H-4, 99.4 cm	51.019	1.3485	3.2675		0.800184729
C9021B-6H-4, 103.4 cm	51.059	1.3494	3.1103		0.799630542
C9021B-6H-5, 0.7 cm	51.092	1.284	2.43		0.839901478
C9021B-6H-5, 4.7 cm	51.132	1.3946	3.2484	17.034	0.77179803
C9021B-6H-5, 8.7 cm	51.172	1.3451	3.3173		0.802278325
C9021B-6H-5, 12.7 cm	51.212	1.3023	3.3034		0.828633005
C9021B-6H-5, 16.7 cm	51.252	1.2564	2.6338		0.856896552
C9021B-6H-5, 20.7 cm	51.292	1.3179	3.2923	17.8	0.819027094
C9021B-6H-5, 24.7 cm	51.332	1.3865	3.3243		0.776785714
C9021B-6H-5, 28.7 cm	51.372	1.3613	3.3215		0.792302956
C9021B-6H-5, 32.7 cm	51.412	1.32	3.3187		0.81773399
C9021B-6H-5, 36.7 cm	51.452	1.3176	3.3048	18.334	0.819211823
C9021B-6H-5, 40.7 cm	51.492	1.3893	3.2992		0.775061576

Table 5-3-4-1

Location	Subbottom Depth	GRA ¹⁾	MS ²⁾	NGR ³⁾	GRA Porosity
	[mbsf]	[g/cm ³]	[x10 ⁻⁵ SI]	[cps]	
C9021B-6H-5, 44.7 cm	51.532	1.3649	3.9574		0.790086207
C9021B-6H-5, 48.7 cm	51.572	1.3979	3.2978		0.76976601
C9021B-6H-5, 52.7 cm	51.612	1.3094	3.2937	19.233	0.824261084
C9021B-6H-5, 56.7 cm	51.652	1.4264	3.9358		0.752216749
C9021B-6H-5, 60.7 cm	51.692	1.3139	3.9259		0.821490148
C9021B-6H-5, 64.7 cm	51.732	1.3971	4.0078		0.770258621
C9021B-6H-5, 68.7 cm	51.772	1.3642	3.3048	21.567	0.790517241
C9021B-6H-5, 72.7 cm	51.812	1.3641	3.3075		0.790578818
C9021B-6H-5, 76.7 cm	51.852	1.3217	3.2771		0.816687192
C9021B-6H-5, 80.7 cm	51.892	1.314	3.2579		0.821428571
C9021B-6H-5, 84.7 cm	51.932	1.3886	4.5497	19.734	0.775492611
C9021B-6H-5, 88.7 cm	51.972	1.4146	3.9194		0.759482759
C9021B-6H-5, 92.7 cm	52.012	1.288	3.2607		0.837438424
C9021B-6H-5, 96.7 cm	52.052	1.2598	2.5933		0.854802956
C9021B-6H-5, 100.7 cm	52.092	1.3615	3.2228	17.835	0.792179803
C9021B-6H-5, 104.7 cm	52.132	1.317	2.4892		0.819581281
C9021B-6H-6, 2.0 cm	52.165	1.3717	2.4153		0.785899015
C9021B-6H-6, 6.0 cm	52.205	1.3223	3.2268		0.816317734
C9021B-6H-6, 10.0 cm	52.245	1.3461	2.5911	16.267	0.801662562
C9021B-6H-6, 14.0 cm	52.285	1.3203	3.2744		0.817549261
C9021B-6H-6, 18.0 cm	52.325	1.3217	2.6206		0.816687192
C9021B-6H-6, 22.0 cm	52.365	1.3716	3.9358		0.785960591
C9021B-6H-6, 26.0 cm	52.405	1.4403	3.2826	25.1	0.743657635
C9021B-6H-6, 30.0 cm	52.445	1.3165	3.2964		0.819889163
C9021B-6H-6, 34.0 cm	52.485	1.3565	3.9557		0.795258621
C9021B-6H-6, 38.0 cm	52.525	1.4332	3.9875		0.748029557
C9021B-6H-6, 42.0 cm	52.565	1.4246	3.9892	26.367	0.753325123
C9021B-6H-6, 46.0 cm	52.605	1.4714	3.9959		0.724507389
C9021B-6H-6, 50.0 cm	52.645	1.4314	3.9875		0.749137931
C9021B-6H-6, 54.0 cm	52.685	1.3884	3.9808		0.775615764
C9021B-6H-6, 58.0 cm	52.725	1.3853	3.9892	23.433	0.777524631
C9021B-6H-6, 62.0 cm	52.765	1.4051	3.3483		0.765332512
C9021B-6H-6, 66.0 cm	52.805	1.3948	4.0574		0.771674877
C9021B-6H-6, 70.0 cm	52.845	1.3841	3.959		0.778263547
C9021B-6H-6, 74.0 cm	52.885	1.3508	3.2964	24.734	0.798768473
C9021B-6H-6, 78.0 cm	52.925	1.3658	3.3455		0.78953202
C9021B-6H-6, 82.0 cm	52.965	1.382	3.3243		0.77955665
C9021B-6H-6, 86.0 cm	53.005	1.3447	3.3173		0.802524631
C9021B-6H-6, 90.0 cm	53.045	1.2889	3.2744	20.635	0.836884236
C9021B-6H-6, 94.0 cm	53.085	1.2484	2.6217		0.86182266
C9021B-6H-6, 98.0 cm	53.125	1.2968	2.6173		0.832019704
C9021B-6H-6, 102.0 cm	53.165	1.2581	2.5201		0.855849754
C9021B-6H-6, 106.0 cm	53.205	1.2116	1.75	21.934	0.884482759
C9021B-6H-7, 3.2 cm	53.237	1.3141	2.4599		0.821366995
C9021B-6H-7, 7.2 cm	53.277	1.4123	3.2443		0.760899015
C9021B-6H-7, 11.2 cm	53.317	1.3229	3.2757		0.815948276
C9021B-6H-7, 15.2 cm	53.357	1.4078	3.9391	23.666	0.763669951
C9021B-6H-7, 19.2 cm	53.397	1.3778	3.9557		0.782142857
C9021B-6H-7, 23.2 cm	53.437	1.375	3.9408		0.783866995
C9021B-6H-7, 27.2 cm	53.477	1.3531	3.2744		0.797352217

Table 5-3-4-1

Location	Subbottom Depth	GRA ¹⁾	MS ²⁾	NGR ³⁾	GRA Porosity
	[mbsf]	[g/cm ³]	[x10 ⁻⁵ SI]	[cps]	
C9021B-6H-7, 31.2 cm	53.517	1.3127	3.2757	26.1	0.822229064
C9021B-6H-7, 35.2 cm	53.557	1.3043	3.3075		0.827401478
C9021B-6H-7, 39.2 cm	53.597	1.376	3.2978		0.783251232
C9021B-6H-7, 43.2 cm	53.637	1.3089	3.2881		0.824568966
C9021B-6H-7, 47.2 cm	53.677	1.2797	3.2757	28.102	0.842549261
C9021B-6H-7, 51.2 cm	53.717	1.3728	3.2923		0.785221675
C9021B-6H-7, 55.2 cm	53.757	1.3898	3.9424		0.774753695
C9021B-6H-7, 59.2 cm	53.797	1.3391	3.9358		0.805972906
C9021B-6H-7, 63.2 cm	53.837	1.432	4.5822	26.333	0.748768473
C9021B-6H-7, 67.2 cm	53.877	1.4392	4.6267		0.744334975
C9021B-6H-7, 71.2 cm	53.917	1.3521	3.284		0.79796798
C9021B-6H-7, 75.2 cm	53.957	1.2789	3.2867		0.843041872
C9021B-6H-7, 79.2 cm	53.997	1.3965	3.9391	26.6	0.770628079
C9021B-6H-7, 83.2 cm	54.037	1.3683	3.9063		0.787992611
C9021B-6H-7, 87.2 cm	54.077	1.345	3.2255		0.802339901
C9021B-6H-7, 91.2 cm	54.117	1.3713	3.8867		0.78614532
C9021B-6H-7, 95.2 cm	54.157	1.4118	3.9177	25.6	0.761206897
C9021B-6H-7, 99.2 cm	54.197	1.3859	3.921		0.777155172
C9021B-6H-7, 103.2 cm	54.237	1.4123	4.4395		0.760899015
C9021B-6H-7, 107.2 cm	54.277	1.3608	2.3978		0.792610837
C9021B-6H-8, 2.9 cm	54.314	1.2889	2.4579	21.934	0.836884236
C9021B-6H-8, 6.9 cm	54.354	1.2249	3.2867		0.876293103
C9021B-6H-8, 10.9 cm	54.394	1.3047	3.2854		0.827155172
C9021B-6H-8, 14.9 cm	54.434	1.2664	2.6261		0.850738916
C9021B-6H-8, 18.9 cm	54.474	1.2616	2.6228	21.701	0.853694581
C9021B-6H-8, 22.9 cm	54.514	1.2349	2.6283		0.870135468
C9021B-6H-8, 26.9 cm	54.554	1.3241	3.284		0.81520936
C9021B-6H-8, 30.9 cm	54.594	1.3042	3.9524		0.827463054
C9021B-6H-8, 34.9 cm	54.634	1.3056	3.2895	23.734	0.826600985
C9021B-6H-8, 38.9 cm	54.674	1.3068	3.2552		0.825862069
C9021B-6H-8, 42.9 cm	54.714	1.2255	3.243		0.875923645
C9021B-6H-8, 46.9 cm	54.754	1.2383	3.2593		0.868041872
C9021B-6H-8, 50.9 cm	54.794	1.3331	3.9375	26.101	0.809667488
C9021B-6H-8, 54.9 cm	54.834	1.3549	4.6111		0.796243842
C9021B-6H-8, 58.9 cm	54.874	1.3129	4.5688		0.822105911
C9021B-6H-8, 62.9 cm	54.914	1.2949	4.5611		0.833189655
C9021B-6H-8, 66.9 cm	54.954	1.3445	4.6131	32.567	0.802647783
C9021B-6H-8, 70.9 cm	54.994	1.2443	3.9424		0.864347291
C9021B-6H-8, 74.9 cm	55.034	1.4023	4.5899		0.76705665
C9021B-6H-8, 78.9 cm	55.074	1.3814	4.5535		0.779926108
C9021B-6H-8, 82.9 cm	55.114	1.3017	4.5288	37.367	0.829002463
C9021B-6H-8, 86.9 cm	55.154	1.305	4.5995		0.826970443
C9021B-6H-8, 90.9 cm	55.194	1.3898	5.2324		0.774753695
C9021B-6H-8, 94.9 cm	55.234	1.3654	3.9161		0.789778325
C9021B-6H-8, 98.9 cm	55.274	1.2801	3.2094	39.733	0.842302956
C9021B-6H-8, 102.9 cm	55.314	1.3845	3.8609		0.778017241
C9021B-6H-8, 106.9 cm	55.354	1.3276	4.8739		0.813054187
C9021B-7H-1, 8.0 cm	56.58	1.3811	12.9937		0.780110837
C9021B-7H-1, 12.0 cm	56.62	1.4842	26.8272		0.716625616
C9021B-7H-1, 16.0 cm	56.66	1.5655	41.2396	38.301	0.666564039

Table 5-3-4-1

Location	Subbottom Depth	GRA ¹⁾	MS ²⁾	NGR ³⁾	GRA Porosity
	[mbsf]	[g/cm ³]	[x10 ⁻⁵ SI]	[cps]	
C9021B-7H-1, 20.0 cm	56.7	1.4463	24.2302		0.739963054
C9021B-7H-1, 24.0 cm	56.74	1.4335	8.5205		0.747844828
C9021B-7H-1, 28.0 cm	56.78	1.3672	17.6889		0.788669951
C9021B-7H-1, 32.0 cm	56.82	1.3442	13.1249	33.2	0.802832512
C9021B-7H-1, 36.0 cm	56.86	1.4332	13.7985		0.748029557
C9021B-7H-1, 40.0 cm	56.9	1.3512	10.4385		0.798522167
C9021B-7H-1, 44.0 cm	56.94	1.3469	11.5731		0.801169951
C9021B-7H-1, 48.0 cm	56.98	1.2607	24.5442	22.267	0.854248768
C9021B-7H-1, 52.0 cm	57.02	1.2924	30.0484		0.834729064
C9021B-7H-1, 56.0 cm	57.06	1.3789	22.4251		0.781465517
C9021B-7H-1, 60.0 cm	57.1	1.4082	18.6634		0.763423645
C9021B-7H-1, 64.0 cm	57.14	1.3797	16.4406	30.366	0.780972906
C9021B-7H-1, 68.0 cm	57.18	1.4574	15.0557		0.733128079
C9021B-7H-1, 72.0 cm	57.22	1.4345	13.7293		0.747229064
C9021B-7H-1, 76.0 cm	57.26	1.4314	10.5043		0.749137931
C9021B-7H-1, 80.0 cm	57.3	1.3967	9.1605	39.001	0.770504926
C9021B-7H-1, 84.0 cm	57.34	1.2953	7.1079		0.83294335
C9021B-7H-1, 88.0 cm	57.38	1.3494	5.8058		0.799630542
C9021B-7H-1, 92.0 cm	57.42	1.3465	5.8889		0.801416256
C9021B-7H-1, 96.0 cm	57.46	1.388	6.3842	31.9	0.775862069
C9021B-7H-1, 100.0 cm	57.5	1.2795	5.4257		0.842672414
C9021B-7H-2, 3.2 cm	57.532	1.3681	6.1023		0.788115764
C9021B-7H-2, 7.2 cm	57.572	1.4123	7.011		0.760899015
C9021B-7H-2, 11.2 cm	57.612	1.375	6.4563	56.466	0.783866995
C9021B-7H-2, 15.2 cm	57.652	1.3916	6.5515		0.77364532
C9021B-7H-2, 19.2 cm	57.692	1.3819	5.9286		0.779618227
C9021B-7H-2, 23.2 cm	57.732	1.4625	5.9762		0.729987685
C9021B-7H-2, 27.2 cm	57.772	1.3995	6.6374	28.934	0.768780788
C9021B-7H-2, 31.2 cm	57.812	1.4219	6.5956		0.754987685
C9021B-7H-2, 35.2 cm	57.852	1.4197	6.5597		0.756342365
C9021B-7H-2, 39.2 cm	57.892	1.399	5.9411		0.76908867
C9021B-7H-2, 43.2 cm	57.932	1.4321	5.9486	25.167	0.748706897
C9021B-7H-2, 47.2 cm	57.972	1.45	5.3055		0.737684729
C9021B-7H-2, 51.2 cm	58.012	1.3844	5.2876		0.778078818
C9021B-7H-2, 55.2 cm	58.052	1.4008	5.2832		0.767980296
C9021B-7H-2, 59.2 cm	58.092	1.4377	5.3732	25.1	0.745258621
C9021B-7H-2, 63.2 cm	58.132	1.3875	4.7035		0.776169951
C9021B-7H-2, 67.2 cm	58.172	1.3952	4.7055		0.771428571
C9021B-7H-2, 71.2 cm	58.212	1.3319	4.0129		0.810406404
C9021B-7H-2, 75.2 cm	58.252	1.2616	3.3328	22.201	0.853694581
C9021B-7H-2, 79.2 cm	58.292	1.289	3.9774		0.83682266
C9021B-7H-2, 83.2 cm	58.332	1.3506	4.5803		0.798891626
C9021B-7H-2, 87.2 cm	58.372	1.3679	5.2193		0.788238916
C9021B-7H-2, 91.2 cm	58.412	1.4053	6.5405	27.633	0.76520936
C9021B-7H-2, 95.2 cm	58.452	1.3085	4.5764		0.824815271
C9021B-7H-2, 99.2 cm	58.492	1.2318	2.4241		0.872044335
C9021B-7H-3, 2.7 cm	58.527	1.2442	3.0624		0.864408867
C9021B-7H-3, 6.7 cm	58.567	1.252	2.6228	15.201	0.859605911
C9021B-7H-3, 10.7 cm	58.607	1.2583	3.3257		0.855726601
C9021B-7H-3, 14.7 cm	58.647	1.2468	3.3201		0.862807882

Table 5-3-4-1

Location	Subbottom Depth	GRA ¹⁾	MS ²⁾	NGR ³⁾	GRA Porosity
	[mbsf]	[g/cm ³]	[x10 ⁻⁵ SI]	[cps]	
C9021B-7H-3, 18.7 cm	58.687	1.313	4.6423		0.822044335
C9021B-7H-3, 22.7 cm	58.727	1.4692	5.3032	23.933	0.725862069
C9021B-7H-3, 26.7 cm	58.767	1.455	5.9964		0.734605911
C9021B-7H-3, 30.7 cm	58.807	1.3998	7.3414		0.768596059
C9021B-7H-3, 34.7 cm	58.847	1.3598	6.6994		0.793226601
C9021B-7H-3, 38.7 cm	58.887	1.3573	5.3983	24.367	0.79476601
C9021B-7H-3, 42.7 cm	58.927	1.3506	4.7437		0.798891626
C9021B-7H-3, 46.7 cm	58.967	1.37	6.0912		0.786945813
C9021B-7H-3, 50.7 cm	59.007	1.4414	6.0783		0.742980296
C9021B-7H-3, 54.7 cm	59.047	1.342	5.3641	26.866	0.804187192
C9021B-7H-3, 58.7 cm	59.087	1.347	5.419		0.801108374
C9021B-7H-3, 62.7 cm	59.127	1.4095	6.1094		0.762623153
C9021B-7H-3, 66.7 cm	59.167	1.3362	5.4029		0.807758621
C9021B-7H-3, 70.7 cm	59.207	1.4079	6.0602	25.067	0.763608374
C9021B-7H-3, 74.7 cm	59.247	1.3232	5.3892		0.815763547
C9021B-7H-3, 78.7 cm	59.287	1.3681	4.7035		0.788115764
C9021B-7H-3, 82.7 cm	59.327	1.3974	5.9511		0.770073892
C9021B-7H-3, 86.7 cm	59.367	1.3745	5.2478	25.134	0.784174877
C9021B-7H-3, 90.7 cm	59.407	1.4039	5.2854		0.766071429
C9021B-7H-3, 94.7 cm	59.447	1.3923	5.9536		0.773214286
C9021B-7H-3, 98.7 cm	59.487	1.4268	5.059		0.751970443
C9021B-7H-4, 1.4 cm	59.524	1.3253	4.2751	66.4	0.814470443
C9021B-7H-4, 5.4 cm	59.564	1.3708	5.2149		0.786453202
C9021B-7H-4, 9.4 cm	59.604	1.3984	5.2522		0.769458128
C9021B-7H-4, 13.4 cm	59.644	1.3946	5.9336		0.77179803
C9021B-7H-4, 17.4 cm	59.684	1.4126	5.2809	23.867	0.760714286
C9021B-7H-4, 21.4 cm	59.724	1.3969	5.9787		0.770381773
C9021B-7H-4, 25.4 cm	59.764	1.4774	7.3012		0.720812808
C9021B-7H-4, 29.4 cm	59.804	1.3844	7.2981		0.778078818
C9021B-7H-4, 33.4 cm	59.844	1.3862	7.3043	21.467	0.776970443
C9021B-7H-4, 37.4 cm	59.884	1.3461	6.6966		0.801662562
C9021B-7H-4, 41.4 cm	59.924	1.3903	8.0291		0.774445813
C9021B-7H-4, 45.4 cm	59.964	1.4007	7.2827		0.768041872
C9021B-7H-4, 49.4 cm	60.004	1.4268	6.6179	19.4	0.751970443
C9021B-7H-4, 53.4 cm	60.044	1.3605	6.6853		0.792795567
C9021B-7H-4, 57.4 cm	60.084	1.3419	5.3279		0.804248768
C9021B-7H-4, 61.4 cm	60.124	1.3762	5.4259		0.783128079
C9021B-7H-4, 65.4 cm	60.164	1.3638	5.9863	54.967	0.790763547
C9021B-7H-4, 69.4 cm	60.204	1.3994	5.9687		0.768842365
C9021B-7H-4, 73.4 cm	60.244	1.4271	6.5845		0.751785714
C9021B-7H-4, 77.4 cm	60.284	1.5689	7.24		0.664470443
C9021B-7H-4, 81.4 cm	60.324	1.5206	5.9411	25.5	0.694211823
C9021B-7H-4, 85.4 cm	60.364	1.4418	4.6521		0.74273399
C9021B-7H-4, 89.4 cm	60.404	1.5369	4.5957		0.684174877
C9021B-7H-4, 93.4 cm	60.444	1.5271	3.9342		0.69020936
C9021B-7H-4, 97.4 cm	60.484	1.4125	3.7911	16.133	0.760775862
C9021B-7H-5, 0.5 cm	60.515	1.2533	2.477		0.858805419
C9021B-7H-5, 4.5 cm	60.555	1.3632	3.1359		0.791133005
C9021B-7H-5, 8.5 cm	60.595	1.4177	3.9375		0.757573892
C9021B-7H-5, 12.5 cm	60.635	1.3999	4.6131	17.967	0.768534483

Table 5-3-4-1

Location	Subbottom Depth	GRA ¹⁾	MS ²⁾	NGR ³⁾	GRA Porosity
	[mbsf]	[g/cm ³]	[x10 ⁻⁵ SI]	[cps]	
C9021B-7H-5, 16.5 cm	60.675	1.44	4.6836		0.743842365
C9021B-7H-5, 20.5 cm	60.715	1.3478	4.0163		0.800615764
C9021B-7H-5, 24.5 cm	60.755	1.3453	4.6916		0.802155172
C9021B-7H-5, 28.5 cm	60.795	1.4093	5.3573	13.933	0.762746305
C9021B-7H-5, 32.5 cm	60.835	1.3867	5.355		0.776662562
C9021B-7H-5, 36.5 cm	60.875	1.3967	5.3505		0.770504926
C9021B-7H-5, 40.5 cm	60.915	1.4035	5.3527		0.766317734
C9021B-7H-5, 44.5 cm	60.955	1.3254	5.3641	16.833	0.814408867
C9021B-7H-5, 48.5 cm	60.995	1.2621	4.6956		0.8533867
C9021B-7H-5, 52.5 cm	61.035	1.3301	5.3369		0.811514778
C9021B-7H-5, 56.5 cm	61.075	1.2793	4.6738		0.842795567
C9021B-7H-5, 60.5 cm	61.115	1.2801	4.1096	10.566	0.842302956
C9021B-7H-5, 64.5 cm	61.155	1.2854	4.0487		0.839039409
C9021B-7H-5, 68.5 cm	61.195	1.2986	4.6718		0.83091133
C9021B-7H-5, 72.5 cm	61.235	1.2885	4.658		0.837130542
C9021B-7H-5, 76.5 cm	61.275	1.3043	3.9875	19.1	0.827401478
C9021B-7H-5, 80.5 cm	61.315	1.295	5.3459		0.833128079
C9021B-7H-5, 84.5 cm	61.355	1.574	7.9281		0.661330049
C9021B-7H-5, 88.5 cm	61.395	1.33	5.8496		0.811576355
C9021B-7H-5, 92.5 cm	61.435	1.3051	5.1823	21.1	0.826908867
C9021B-7H-5, 96.5 cm	61.475	1.2532	2.5633		0.858866995
C9021B-7H-5, 100.5 cm	61.515	0.9159	1.216		1.066564039
C9021B-7H-6, 3.7 cm	61.552	1.2405	2.5056		0.866687192
C9021B-7H-6, 7.7 cm	61.592	1.2822	3.262	18.867	0.841009852
C9021B-7H-6, 11.7 cm	61.632	1.3429	4.6053		0.803633005
C9021B-7H-6, 15.7 cm	61.672	1.6281	7.8948		0.628017241
C9021B-7H-6, 19.7 cm	61.712	1.3877	5.9586		0.776046798
C9021B-7H-6, 23.7 cm	61.752	1.3982	5.3257	26.667	0.769581281
C9021B-7H-6, 27.7 cm	61.792	1.3926	4.6659		0.773029557
C9021B-7H-6, 31.7 cm	61.832	1.3313	3.9959		0.810775862
C9021B-7H-6, 35.7 cm	61.872	1.3623	3.9926		0.791687192
C9021B-7H-6, 39.7 cm	61.912	1.2431	4.0095	16.066	0.865086207
C9021B-7H-6, 43.7 cm	61.952	1.2158	3.3697		0.881896552
C9021B-7H-6, 47.7 cm	61.992	1.2948	3.3682		0.833251232
C9021B-7H-6, 51.7 cm	62.032	1.3602	3.3469		0.792980296
C9021B-7H-6, 55.7 cm	62.072	1.2375	3.3257	11.367	0.868534483
C9021B-7H-6, 59.7 cm	62.112	1.2649	3.3811		0.851662562
C9021B-7H-6, 63.7 cm	62.152	1.3762	4.7863		0.783128079
C9021B-7H-6, 67.7 cm	62.192	1.3201	5.4075		0.817672414
C9021B-7H-6, 71.7 cm	62.232	1.2937	4.7215	14.799	0.833928571
C9021B-7H-6, 75.7 cm	62.272	1.2819	4.0129		0.841194581
C9021B-7H-6, 79.7 cm	62.312	1.301	4.6442		0.829433498
C9021B-7H-6, 83.7 cm	62.352	1.4861	8.625		0.715455665
C9021B-7H-6, 87.7 cm	62.392	1.6405	11.1328	46.634	0.620381773
C9021B-7H-6, 91.7 cm	62.432	1.4478	7.9148		0.739039409
C9021B-7H-6, 95.7 cm	62.472	1.3803	6.4429		0.780603448
C9021B-7H-6, 99.7 cm	62.512	1.4271	6.0505		0.751785714
C9021B-7H-7, 1.7 cm	62.547	1.0364	4.8958	27.666	0.992364532
C9021B-7H-7, 5.7 cm	62.587	1.4128	6.5929		0.760591133
C9021B-7H-7, 9.7 cm	62.627	1.6598	7.8289		0.608497537

Table 5-3-4-1

Location	Subbottom Depth	GRA ¹⁾	MS ²⁾	NGR ³⁾	GRA Porosity
	[mbsf]	[g/cm ³]	[x10 ⁻⁵ SI]	[cps]	
C9021B-7H-7, 13.7 cm	62.667	1.8034	10.3603		0.520073892
C9021B-7H-7, 17.7 cm	62.707	0.7542	7.1197	37.099	1.166133005
C9021B-7H-7, 33.7 cm	62.867	1.3419	4.6619	18.267	0.804248768
C9021B-7H-7, 37.7 cm	62.907	1.4104	6.0783		0.762068966
C9021B-7H-7, 41.7 cm	62.947	1.3209	6.768		0.817179803
C9021B-7H-7, 45.7 cm	62.987	1.3037	7.3321		0.827770936
C9021B-7H-7, 49.7 cm	63.027	1.3372	7.3104	20.566	0.807142857
C9021B-7H-7, 53.7 cm	63.067	1.4003	7.3445		0.768288177
C9021B-7H-7, 57.7 cm	63.107	1.3198	6.674		0.817857143
C9021B-7H-7, 61.7 cm	63.147	1.3826	6.7969		0.779187192
C9021B-7H-7, 65.7 cm	63.187	1.3143	7.467	19.534	0.821243842
C9021B-7H-7, 69.7 cm	63.227	1.4412	8.1458		0.743103448
C9021B-7H-7, 73.7 cm	63.267	1.3567	7.3694		0.795135468
C9021B-7H-7, 77.7 cm	63.307	1.3232	6.629		0.815763547
C9021B-7H-7, 81.7 cm	63.347	1.2981	4.6462	14.933	0.831219212
C9021B-7H-7, 85.7 cm	63.387	1.3492	4.658		0.799753695
C9021B-7H-7, 89.7 cm	63.427	1.309	5.2522		0.824507389
C9021B-7H-7, 93.7 cm	63.467	1.3132	5.2171		0.821921182
C9021B-7H-7, 97.7 cm	63.507	1.368	3.74	18.2	0.78817734
C9021B-7H-8, 0.6 cm	63.541	0.5363	3.1077		1.300307882
C9021B-7H-8, 4.6 cm	63.581	1.4108	5.7745		0.76182266
C9021B-7H-8, 8.6 cm	63.621	1.3249	5.8864		0.814716749
C9021B-7H-8, 12.6 cm	63.661	1.359	5.8938	28.7	0.793719212
C9021B-7H-8, 16.6 cm	63.701	1.3166	4.6247		0.819827586
C9021B-7H-8, 20.6 cm	63.741	1.3528	4.6403		0.797536946
C9021B-7H-8, 24.6 cm	63.781	1.3955	5.3414		0.771243842
C9021B-7H-8, 28.6 cm	63.821	1.2557	4.0078	12.799	0.857327586
C9021B-7H-8, 32.6 cm	63.861	1.1955	3.3455		0.894396552
C9021B-7H-8, 36.6 cm	63.901	1.3743	4.6757		0.78429803
C9021B-7H-8, 40.6 cm	63.941	1.312	4.6876		0.822660099
C9021B-7H-8, 44.6 cm	63.981	1.2847	2.682	13.1	0.839470443
C9021B-7H-8, 48.6 cm	64.021	1.3351	3.3639		0.808435961
C9021B-7H-8, 52.6 cm	64.061	1.2702	4.0265		0.848399015
C9021B-7H-8, 56.6 cm	64.101	1.3394	4.0248		0.805788177
C9021B-7H-8, 60.6 cm	64.141	1.2708	4.1043	10.834	0.848029557
C9021B-7H-8, 64.6 cm	64.181	1.2781	4.066		0.843534483
C9021B-7H-8, 68.6 cm	64.221	1.3025	4.0384		0.828509852
C9021B-7H-8, 72.6 cm	64.261	1.2706	3.3497		0.848152709
C9021B-7H-8, 76.6 cm	64.301	1.3145	3.9892	15.134	0.82112069
C9021B-7H-8, 80.6 cm	64.341	1.3031	4.6698		0.828140394
C9021B-7H-8, 84.6 cm	64.381	1.2787	4.6208		0.843165025
C9021B-7H-8, 88.6 cm	64.421	1.2552	3.9194		0.857635468
C9021B-7H-8, 92.6 cm	64.461	1.2458	3.9128	11.566	0.863423645
C9021B-7H-8, 96.6 cm	64.501	1.2946	5.2083		0.833374384
C9021B-7H-8, 100.6 cm	64.541	0.5843	3.6688		1.270751232
C9021B-7H-9, 3.6 cm	64.576	1.2525	4.9541		0.85929803
C9021B-7H-9, 7.6 cm	64.616	1.3839	5.884	13.466	0.7783867
C9021B-7H-9, 11.6 cm	64.656	1.3822	4.6286		0.779433498
C9021B-7H-9, 15.6 cm	64.696	1.004	4.6228		1.012315271
C9021B-7H-9, 19.6 cm	64.736	1.3288	5.3077		0.812315271

Table 5-3-4-1

Location	Subbottom Depth	GRA ¹⁾	MS ²⁾	NGR ³⁾	GRA Porosity
	[mbsf]	[g/cm ³]	[x10 ⁻⁵ SI]	[cps]	
C9021B-7H-9, 23.6 cm	64.776	1.2914	5.3077	18.466	0.835344828
C9021B-7H-9, 27.6 cm	64.816	1.2692	3.302		0.849014778
C9021B-7H-9, 31.6 cm	64.856	0.9514	2.5761		1.044704433
C9021B-7H-9, 35.6 cm	64.896	0.5246	3.6054		1.307512315
C9021B-8H-1, 8.0 cm	66.08	1.5076	261.5881		0.702216749
C9021B-8H-1, 12.0 cm	66.12	1.476	199.2323		0.721674877
C9021B-8H-1, 16.0 cm	66.16	1.4991	174.4741	21.932	0.707450739
C9021B-8H-1, 20.0 cm	66.2	1.4412	136.7262		0.743103448
C9021B-8H-1, 24.0 cm	66.24	1.3956	87.9859		0.771182266
C9021B-8H-1, 28.0 cm	66.28	1.4847	75.5419		0.716317734
C9021B-8H-1, 32.0 cm	66.32	1.5036	47.6391	24.299	0.704679803
C9021B-8H-1, 36.0 cm	66.36	1.5165	52.336		0.696736453
C9021B-8H-1, 40.0 cm	66.4	1.3775	36.5784		0.782327586
C9021B-8H-1, 44.0 cm	66.44	1.3425	21.6669		0.80387931
C9021B-8H-1, 48.0 cm	66.48	1.4174	13.5822	12.133	0.757758621
C9021B-8H-1, 52.0 cm	66.52	1.4017	9.5116		0.767426108
C9021B-8H-1, 56.0 cm	66.56	1.3576	8.1493		0.794581281
C9021B-8H-1, 60.0 cm	66.6	1.3309	7.4734		0.811022167
C9021B-8H-1, 64.0 cm	66.64	1.3824	7.4734	10.365	0.779310345
C9021B-8H-1, 68.0 cm	66.68	1.3323	7.3228		0.810160099
C9021B-8H-1, 72.0 cm	66.72	1.407	7.3228		0.764162562
C9021B-8H-1, 76.0 cm	66.76	1.4148	6.6486		0.759359606
C9021B-8H-1, 80.0 cm	66.8	1.348	5.9737	14.332	0.800492611
C9021B-8H-1, 84.0 cm	66.84	1.4136	5.9486		0.760098522
C9021B-8H-1, 88.0 cm	66.88	1.3774	6.6402		0.782389163
C9021B-8H-1, 92.0 cm	66.92	1.3844	6.6909		0.778078818
C9021B-8H-1, 96.0 cm	66.96	1.4106	7.2308	17.566	0.761945813
C9021B-8H-1, 100.0 cm	67	1.372	8.0933		0.785714286
C9021B-8H-2, 3.0 cm	67.04	1.364	8.1133		0.790640394
C9021B-8H-2, 7.0 cm	67.08	1.4089	7.9683		0.762992611
C9021B-8H-2, 11.0 cm	67.12	1.4167	8.2016	21.399	0.758189655
C9021B-8H-2, 15.0 cm	67.16	1.4841	8.9003		0.716687192
C9021B-8H-2, 19.0 cm	67.2	1.488	12.9527		0.714285714
C9021B-8H-2, 23.0 cm	67.24	1.4477	12.9416		0.739100985
C9021B-8H-2, 27.0 cm	67.28	1.4414	21.0973	27.133	0.742980296
C9021B-8H-2, 31.0 cm	67.32	1.4228	28.4983		0.754433498
C9021B-8H-2, 35.0 cm	67.36	1.4203	54.5421		0.755972906
C9021B-8H-2, 39.0 cm	67.4	1.6305	120.4802		0.626539409
C9021B-8H-2, 43.0 cm	67.44	1.9115	185.417	53.699	0.453509852
C9021B-8H-2, 47.0 cm	67.48	2.0538	307.3129		0.3658867
C9021B-8H-2, 51.0 cm	67.52	1.4533	78.9093		0.735652709
C9021B-9X-CC, 8.0 cm	75.08	1.3755	94.1656	48.5	0.783559113
C9021B-9X-CC, 12.0 cm	75.12	1.8723	64.8097		0.477647783
C9021B-9X-CC, 16.0 cm	75.16	1.2952	52.2525	51.532	0.833004926
C9021B-9X-CC, 20.0 cm	75.2	1.7152	55.5085		0.574384236
C9021B-10X-CC, 8.0 cm	84.58	1.6056	29.3654	31.6	0.641871921
C9021B-10X-CC, 12.0 cm	84.62	1.6957	33.9678		0.586391626
C9021B-10X-CC, 16.0 cm	84.66	0.5369	27.424	19.1	1.299938424
C9021B-11X-CC, 8.0 cm	90.78	1.2644	28.2423	48.368	0.851970443
C9021B-11X-CC, 12.0 cm	90.82	1.1768	27.6319		0.90591133

Table 5-3-4-1

Location	Subbottom Depth [mbsf]	GRA ¹⁾ [g/cm ³]	MS ²⁾ [x10 ⁻⁵ SI]	NGR ³⁾ [cps]	GRA Porosity
C9021B-11X-CC, 16.0 cm	90.86	1.7307	52.6542	50.933	0.564839901
C9021B-11X-CC, 20.0 cm	90.9	1.9207	86.916		0.447844828
C9021B-11X-CC, 24.0 cm	90.94	1.5721	60.9983	32.3	0.6625
C9021B-12X-CC, 8.0 cm	98.08	1.2003	12.1856		0.891440887
C9021B-12X-CC, 12.0 cm	98.12	0.8544	33.9772		1.104433498
C9021B-12X-CC, 16.0 cm	98.16	1.0642	32.8723	47.2	0.975246305
C9021B-12X-CC, 20.0 cm	98.2	1.448	41.6493		0.738916256
C9021B-12X-CC, 24.0 cm	98.24	1.6943	58.5694		0.587253695
C9021B-12X-CC, 28.0 cm	98.28	1.7325	53.9914		0.563731527
C9021B-12X-CC, 32.0 cm	98.32	1.8541	26.637	61.399	0.48885468
C9021B-12X-CC, 36.0 cm	98.36	1.7595	42.8612		0.547105911
C9021B-12X-CC, 40.0 cm	98.4	1.3855	38.3691		0.777401478
C9021B-12X-CC, 44.0 cm	98.44	1.5225	37.5741		0.693041872

Table 5-3-4-2

Top Location of Sample Interval	Subbotto m Depth [mbsf]	Bulk Density [g/cm ³]	Grain Density [g/cm ³]	Porosity	Porosity: Syringe
C9021B-1H-1, 60.0 cm	0.6	1.332	2.490	0.790	0.848
C9021B-1H-4, 41.0 cm	3.44	1.311	2.319	0.779	
C9021B-1H-7, 93.0 cm	6.98	1.269	2.184	0.789	
C9021B-2H-2, 24.0 cm	10.75	1.346	2.300	0.748	
C9021B-2H-8, 62.0 cm	16.965	1.335	2.141	0.722	
C9021B-3H-1, 88.0 cm	19.88	1.356	2.164	0.709	
C9021B-3H-5, 90.0 cm	23.945	1.278	2.434	0.820	
C9021B-3H-7, 50.0 cm	25.565	1.356	2.336	0.747	0.783
C9021B-4H-3, 47.0 cm	30.985	1.360	2.273	0.731	0.782
C9021B-4H-6, 70.0 cm	34.25	1.315	2.252	0.763	0.835
C9021B-4H-7, 32.0 cm	34.875	1.260	2.128	0.786	0.824
C9021B-4H-9, 19.0 cm	36.77	1.577	2.547	0.637	0.628
C9021B-5H-2, 41.0 cm	39.42	1.307	2.644	0.825	0.838
C9021B-5H-4, 34.0 cm	41.37	1.201	2.445	0.875	
C9021B-5H-5, 50.0 cm	42.535	1.415	2.416	0.720	0.769
C9021B-5H-7, 56.0 cm	44.605	1.268	2.292	0.808	
C9021B-6H-1, 50.0 cm	47.5	1.323	2.447	0.790	
C9021B-6H-3, 12.0 cm	49.135	1.295	2.462	0.812	0.845
C9021B-6H-3, 23.0 cm	49.245	1.554	2.483	0.637	0.795
C9021B-6H-3, 34.0 cm	49.355	1.373	2.430	0.752	0.855
C9021B-6H-4, 42.0 cm	50.445	1.282	2.376	0.809	
C9021B-6H-4, 56.5 cm	50.59	1.349	2.457	0.773	
C9021B-7H-4, 52.0 cm	60.03	1.301	2.457	0.807	
C9021B-7H-4, 52.0 cm	60.03		2.272		
C9021B-7H-7, 85.0 cm	63.38		2.614		
C9021B-7H-8, 91.0 cm	64.445	1.239	2.560	0.860	
C9021B-8H-1, 64.0 cm	66.64	1.281	2.422	0.816	
C9021B-8H-2, 3.0 cm	67.04	1.285	2.573	0.832	
C9021B-9X-CC, 12.0 cm	75.12	1.996	2.494	0.339	
C9021B-10X-CC, 4.0 cm	84.54	2.053	2.520	0.312	
C9021B-11X-CC, 8.5 cm	90.785	2.240	2.544	0.200	
C9021B-11X-CC, 17.0 cm	90.87	2.040	2.467	0.296	
C9021B-12X-CC, 12.0 cm	98.12	2.211	2.509	0.201	
C9021B-12X-CC, 29.0 cm	98.29	1.933	2.546	0.403	

Table 5-3-4-3

Location	Subbottom	Average	DER
	depth	gamma ray	
	[mbsf]	pulse count	[μ Sv/h]
		rate	
		[cps]	
C9021B-1H-1, 69.0 cm	0.69	2	0.03
C9021B-1H-2, 60.0 cm	1.605	2	0.04
C9021B-1H-4, 83.0 cm	3.86	3	0.03
C9021B-2H-2, 26.0 cm	10.77	2	0.03
C9021B-2H-5, 69.0 cm	13.995	2	0.03
C9021B-3H-3, 50.0 cm	21.515	2	0.04
C9021B-4H-5, 50.0 cm	33.035	2	0.03
C9021B-4H-7, 47.0 cm	35.025	2	0.03
C9021B-5H-1, 85.0 cm	38.85	2	0.02
C9021B-5H-4, 87.0 cm	41.9	2	0.04
C9021B-5H-8, 77.0 cm	45.825	2	0.04
C9021B-6H-2, 82.0 cm	48.825	2	0.03
C9021B-6H-5, 79.0 cm	51.875	2	0.03
C9021B-7H-3, 87.0 cm	59.37	2	0.04
C9021B-8H-1, 36.0 cm	66.36	2	0.04
C9021B-8H-2, 46.0 cm	67.47	2	0.02
C9021B-9X-CC, 20.0 cm	75.2	2	0.03
C9021B-12X-CC, 40.0 cm	98.4	2	0.02

Table 5-3-4-4

Location	Subbotto m Depth [mbsf]	WR/HS	Thermal conductivity [W/(m•K)]	LET	Probe	Remark
C9021B-1H-4, 80.0 cm	3.83	W	0.233	Qualified: >10	HLQ50	pumice
C9021B-1H-5, 54.0 cm	4.58	W	0.757	Qualified: >10	HLQ50	pumice
C9021B-1H-5, 54.0 cm	4.58	W	0.663	Qualified: >10	HLQ50	pumice
C9021B-1H-7, 88.0 cm	6.93	W	0.668	Qualified: >10	HLQ50	pumice
C9021B-2H-2, 27.0 cm	10.78	W	0.705	Qualified: >10	HLQ50	oil compound, pumice
C9021B-2H-8, 65.0 cm	16.995	W	0.605	Qualified: >10	HLQ50	oil compound, pumice, 2nd
C9021B-3H-1, 89.0 cm	19.89	W	0.56	Qualified: >10	HLQ50	oil compound, pumice
C9021B-3H-1, 89.0 cm	19.89	W	0.557	Qualified: >10	HLQ50	oil compound, pumice, 2nd
C9021B-3H-5, 91.0 cm	23.955	W	0.781	Qualified: >10	HLQ50	pumice
C9021B-4H-3, 58.0 cm	31.095	W	0.723	Qualified: >10	HLQ50	oil compound, 2nd run
C9021B-4H-6, 65.0 cm	34.2	W	0.489	Qualified: >10	HLQ50	oil compound
C9021B-4H-9, 23.0 cm	36.81	W	0.79	Qualified: >10	HLQ50	oil compound
C9021B-5H-2, 44.0 cm	39.45	W	0.686	Qualified: >10	HLQ50	oil compound
C9021B-5H-5, 25.0 cm	42.285	WR	0.596	Unqualified: <4	VLQ60	pumice
C9021B-5H-5, 52.0 cm	42.555	W	0.556	Qualified: >10	HLQ50	oil compound
C9021B-6H-1, 33.0 cm	47.33	W	0.648	Qualified: >10	HLQ50	oil compound, clay, breccia
C9021B-6H-1, 55.0 cm	47.55	W	0.503	Qualified: >10	HLQ50	oil compound, clay, breccia
C9021B-6H-4, 30.0 cm	50.325	W	0.701	Qualified: >10	HLQ50	oil compound, clay, breccia
C9021B-6H-8, 55.0 cm	54.835	W	0.746	Qualified: >10	HLQ50	oil compound, clay, breccia
C9021B-7H-1, 85.0 cm	57.35	W	0.755	Qualified: >10	HLQ50	oil compound, clay, breccia
C9021B-7H-4, 55.0 cm	60.06	W	0.656	Qualified: >10	HLQ50	oil compound, clay, breccia
C9021B-7H-8, 91.0 cm	64.445	W	0.657	Qualified: >10	HLQ50	oil compound, clay, breccia
C9021B-8H-1, 60.0 cm	66.6	WR	0.611	Qualified: >10	VLQ60	
C9021B-8H-1, 64.0 cm	66.64	WR	0.695	Qualified: >10	VLQ60	
C9021B-8H-1, 71.0 cm	66.71	W	0.626	Qualified: >10	HLQ50	oil compound, clay, breccia
C9021B-9X-CC, 12.0 cm	75.12	W	1.248	Qualified: >10	HLQ50	oil compound, breccia
C9021B-12X-CC, 32.0 cm	98.32	W	0.931	Qualified: >10	HLQ50	oil compound

Table 5-3-4-5

Location	Subbottom Depth [mbsf]	Bulk resistivity at 1 kHz [Ω m]	Remarks
C9021B-1H-1, 65.5 cm	0.655	0.551256822	section
C9021B-1H-3, 0.0 cm	2.02	5.185695084	discrete
C9021B-2H-2, 24.0 cm	10.75	1.118760611	section
C9021B-2H-8, 63.0 cm	16.975	0.695620073	section
C9021B-3H-1, 87.5 cm	19.875	0.85757039	section
C9021B-3H-5, 92.0 cm	23.965	0.321677642	section
C9021B-3H-7, 45.0 cm	25.515	0.850184634	section
C9021B-4H-3, 50.0 cm	31.015	0.988687939	section
C9021B-4H-6, 67.0 cm	34.22	0.836763205	section
C9021B-4H-9, 16.0 cm	36.74	0.434250457	section
C9021B-5H-2, 44.0 cm	39.45	0.322784316	section
C9021B-5H-5, 52.5 cm	42.56	0.474954135	section
C9021B-6H-1, 57.0 cm	47.57	0.837576188	section
C9021B-6H-4, 40.5 cm	50.43	0.436911645	section
C9021B-6H-8, 63.5 cm	54.92	0.663543659	section
C9021B-7H-1, 86.5 cm	57.365	0.316469895	section
C9021B-7H-4, 51.0 cm	60.02	0.66487288	section
C9021B-7H-8, 87.0 cm	64.405	0.602171149	section
C9021B-8H-1, 63.0 cm	66.63	0.346988597	section
C9021B-8H-2, 5.0 cm	67.06	0.418658197	section
C9021B-8H-CC, 2.5 cm	67.55	1.610884269	section
C9021B-9X-CC, 21.0 cm	75.21	1.352947379	section
C9021B-11X-CC, 8.5 cm	90.785	6.984774491	discrete, shared with PWVD
C9021B-11X-CC, 17.5 cm	90.875	2.190975443	section
C9021B-12X-CC, 29.5 cm	98.295	2.930571316	section

Table 5-3-4-6

Location	Subbottom Depth [mbsf]	P-wave velocity [m/s]				P-wave velocity [m/s] : saturated for 24 hours				Remarks
		X	Y	Z	Average	X	Y	Z	Average	
C9021B-11X-CC, 8.5 cm	90.785	3617	3681	3478	3592.00	3596.00	3902.00	3639.00	3712.33	shared with IMP

Table 5-3-4-7

Location	Subbottom Depth [mbsf]	Unconfined compressive strength [kPa]	Remarks
C9021B-1H-1, 66.0 cm	0.66	37.28	sand, pumice
C9021B-1H-4, 18.0 cm	3.21	231.84	sand, pumice
C9021B-1H-7, 79.0 cm	6.84	268.14	sand, pumice
C9021B-2H-2, 39.0 cm	10.9	169.71	sand, pumice
C9021B-2H-5, 25.0 cm	13.555	146.5	sand, pumice
C9021B-3H-3, 83.0 cm	21.845	85.02	pumice, breccia
C9021B-3H-6, 96.0 cm	25.015	195.22	pumice, breccia
C9021B-3H-8, 35.0 cm	26.425	176.58	pumice, breccia
C9021B-4H-3, 40.0 cm	30.915	142.25	pumice, breccia
C9021B-4H-5, 53.0 cm	33.065	140.61	pumice, breccia
C9021B-4H-7, 25.0 cm	34.805	245.25	pumice, breccia
C9021B-4H-9, 26.0 cm	36.84	120.99	silt
C9021B-5H-2, 48.0 cm	39.49	53.96	mud, blueish
C9021B-5H-4, 87.0 cm	41.9	49.05	mud
C9021B-5H-5, 60.0 cm	42.635	39.24	sand
C9021B-6H-2, 79.0 cm	48.795	91.23	pumice, gravel, fractured
C9021B-6H-4, 33.0 cm	50.355	255.06	pumice, gravel, fractured
C9021B-7H-2, 83.0 cm	58.33	147.15	green pumice
C9021B-7H-6, 80.0 cm	62.315	124.91	green pumice

Table 5-3-4-8

Location	Subbottom Depth [mbsf]	Major element (wt%)					
		Si	Al	Fe	Ca	K	S
C9021B-1H-1, 61	0.6	10.9	0.0	27.3	3.7	3.7	1.6
C9021B-1H-4, 41	3.4	16.7	0.0	10.4	1.1	1.1	1.6
C9021B-1H-5, 16	4.2	5.7	0.0	15.8	1.4	1.4	2.2
C9021B-1H-5, 44	4.5	3.1	0.0	16.8	1.3	1.3	2.5
C9021B-1H-7, 93	7.0	10.6	0.0	14.1	1.1	1.1	1.3
C9021B-2H-2, 25	10.8	19.3	0.0	11.6	0.8	0.8	0.9
C9021B-2H-8, 63	17.0	21.3	0.0	9.9	0.9	0.9	1.0
C9021B-3H-1, 88	19.9	19.4	0.0	10.1	0.9	0.9	1.2
C9021B-3H-5, 91	23.9	11.4	0.0	11.8	1.0	1.0	2.0
C9021B-3H-7, 56	25.6	17.7	0.0	8.1	0.8	0.8	1.9
C9021B-3H-8, 49	26.6	27.4	0.0	4.0	0.5	0.5	1.0
C9021B-4H-1, 41	28.9	10.5	0.0	14.2	2.5	2.5	1.7
C9021B-4H-3, 48	31.0	12.0	0.0	12.3	1.1	1.1	2.0
C9021B-4H-6, 71	34.3	15.9	0.0	13.5	0.9	0.9	1.6
C9021B-4H-7, 33	34.9	19.2	0.0	10.1	0.9	0.9	1.2
C9021B-4H-9, 20	36.8	21.2	2.5	12.9	0.8	0.8	0.9
C9021B-5H-2, 42	39.4	10.1	0.0	26.4	0.7	0.7	1.7
C9021B-5H-4, 35	41.4	19.2	0.0	15.6	0.5	0.5	1.2
C9021B-5H-5, 51	42.5	22.4	2.0	12.7	0.5	0.5	0.7
C9021B-5H-7, 53	44.6	17.3	0.0	17.6	0.5	0.5	1.1
C9021B-6H-1, 51	47.5	19.0	0.0	22.4	0.5	0.5	0.6
C9021B-6H-3, 24	49.2	21.9	0.0	15.7	0.4	0.4	0.6
C9021B-6H-4, 43	50.4	17.9	0.0	17.3	0.5	0.5	0.9
C9021B-6H-8, 103	55.3	4.9	0.0	30.0	0.8	0.8	2.4
C9021B-7H-1, 86	57.4	2.9	0.0	47.6	0.3	0.3	2.3
C9021B-7H-4, 53	60.0	9.1	0.0	35.4	0.5	0.5	1.8
C9021B-7H-7, 14	62.7	12.8	0.0	17.0	0.6	0.6	2.3
C9021B-7H-8, 92	64.4	24.3	5.4	10.1	0.3	0.3	2.8
C9021B-8H-1, 65	66.6	4.4	0.0	39.5	0.5	0.5	2.0
C9021B-8H-1, 92	66.9	5.3	0.0	40.8	0.4	0.4	2.9
C9021B-8H-2, 4	67.0	6.9	0.0	30.5	0.7	0.7	2.5
C9021B-8H-2, 31	67.3	10.5	0.0	33.1	0.4	0.4	3.4
C9021B-8H-2, 49	67.5	16.3	0.0	12.9	1.3	1.3	2.6
C9021B-9X-cc, 15	75.1	11.9	0.0	14.4	1.4	1.4	3.5
C9021B-10X-cc, 5	84.5	31.7	4.4	3.4	0.5	0.5	1.2
C9021B-10X-cc, 9	84.6	24.1	2.7	6.4	0.9	0.9	2.4
C9021B-11X-cc, 11	90.8	30.2	4.3	3.3	0.6	0.6	2.0
C9021B-11X-cc, 18	90.9	25.1	4.1	7.2	0.7	0.7	2.4
C9021B-12X-cc, 3	98.0	25.6	2.9	6.9	0.8	0.8	2.7
C9021B-12X-cc, 10	98.1	33.8	5.4	1.4	0.3	0.3	0.8
C9021B-12X-cc, 14	98.1	26.6	3.4	5.7	0.8	0.8	2.5
C9021B-12X-cc, 30	98.3	26.6	2.6	5.8	0.7	0.7	2.4

Table 5-3-5-1**Hole B**

Location	Subbottom Depth	GRA ¹⁾	MS ²⁾	NGR ³⁾	GRA Porosity
	[mbsf]	[g/cm ³]	[x10 ⁻⁵ SI]	[cps]	
C9023B-1X-CC, 8.0 cm	0.08	1.2011	26.0963	12.566	0.891
C9023B-1X-CC, 12.0 cm	0.12	2.3017	103.5999		0.213
C9023B-1X-CC, 16.0 cm	0.16	2.2854	90.7659	33.265	0.223
C9023B-1X-CC, 20.0 cm	0.2	1.7344	40.8665		0.563
C9023B-1X-CC, 24.0 cm	0.24	1.7496	13.1746	38.2	0.553
C9023B-1X-CC, 28.0 cm	0.28	1.0899	18.904		0.959
C9023B-1X-CC, 32.0 cm	0.32	2.445	8.777	18.699	0.125

Hole D

Location	Subbottom Depth	GRA ¹⁾	MS ²⁾	NGR ³⁾	GRA Porosity
	[mbsf]	[g/cm ³]	[x10 ⁻⁵ SI]	[cps]	
C9023D-1X-1, 8.0 cm	0.08	1.4631		151.234	0.730
C9023D-1X-2, 1.8 cm	0.118	2.3095			0.208
C9023D-1X-2, 5.8 cm	0.158	2.637		129.4	0.007
C9023D-1X-2, 9.8 cm	0.198	2.8952			-0.152
C9023D-2H-1, 8.0 cm	9.58	1.503			0.705
C9023D-2H-1, 12.0 cm	9.62	1.6301			0.627
C9023D-2H-1, 16.0 cm	9.66	1.7391		78.367	0.560
C9023D-2H-1, 20.0 cm	9.7	1.749			0.554
C9023D-2H-2, 0.4 cm	9.739	1.6838			0.594
C9023D-2H-2, 4.4 cm	9.779	2.0477			0.370
C9023D-2H-2, 8.4 cm	9.819	2.2483		182.733	0.246
C9023D-2H-2, 12.4 cm	9.859	2.3763			0.167
C9023D-2H-2, 16.4 cm	9.899	2.4451			0.125
C9023D-2H-2, 20.4 cm	9.939	2.4474			0.124
C9023D-2H-2, 24.4 cm	9.979	2.3133		235.067	0.206
C9023D-2H-2, 28.4 cm	10.019	2.4368			0.130
C9023D-2H-2, 32.4 cm	10.059	2.3678			0.173
C9023D-2H-2, 36.4 cm	10.099	2.2677			0.234
C9023D-2H-2, 40.4 cm	10.139	2.2606		213.8	0.239
C9023D-2H-2, 44.4 cm	10.179	2.3354			0.192
C9023D-2H-2, 48.4 cm	10.219	2.3116			0.207
C9023D-2H-2, 52.4 cm	10.259	2.2622			0.238
C9023D-2H-2, 56.4 cm	10.299	2.3019		429.834	0.213
C9023D-2H-2, 60.4 cm	10.339	2.3708			0.171
C9023D-2H-2, 64.4 cm	10.379	2.7476			-0.061
C9023D-2H-2, 68.4 cm	10.419	2.2318			0.256
C9023D-2H-2, 72.4 cm	10.459	2.3905		304.601	0.159
C9023D-2H-2, 76.4 cm	10.499	2.3807			0.165
C9023D-2H-2, 80.4 cm	10.539	2.1072			0.333
C9023D-2H-2, 84.4 cm	10.579	2.27			0.233
C9023D-2H-2, 88.4 cm	10.619	2.186		69.5	0.284
C9023D-2H-2, 92.4 cm	10.659	1.8363			0.500
C9023D-2H-2, 96.4 cm	10.699	1.9983			0.400
C9023D-2H-3, 0.6 cm	10.741	1.9039			0.458
C9023D-2H-3, 4.6 cm	10.781	1.6864		51.966	0.592
C9023D-2H-3, 8.6 cm	10.821	1.6113			0.638
C9023D-2H-3, 12.6 cm	10.861	1.9877			0.407

Location	Subbottom Depth [mbsf]	GRA ¹⁾ [g/cm ³]	MS ²⁾ [x10 ⁻⁵ SI]	NGR ³⁾ [cps]	GRA Porosity
C9023D-2H-3, 16.6 cm	10.901	2.0754			0.353
C9023D-2H-3, 20.6 cm	10.941	2.2893		47.934	0.221
C9023D-2H-3, 24.6 cm	10.981	1.4622			0.730
C9023D-2H-3, 28.6 cm	11.021	1.4721			0.724
C9023D-2H-3, 32.6 cm	11.061	1.4415			0.743
C9023D-2H-3, 36.6 cm	11.101	1.4673		56.467	0.727
C9023D-2H-3, 40.6 cm	11.141	1.4792			0.720
C9023D-2H-3, 44.6 cm	11.181	1.4562			0.734
C9023D-2H-3, 48.6 cm	11.221	1.4392			0.744
C9023D-2H-3, 52.6 cm	11.261	1.4657		55.9	0.728
C9023D-2H-3, 56.6 cm	11.301	1.4931			0.711
C9023D-2H-3, 60.6 cm	11.341	1.5327			0.687
C9023D-2H-3, 64.6 cm	11.381	1.6029			0.644
C9023D-2H-3, 68.6 cm	11.421	1.6374		50.467	0.622
C9023D-2H-3, 72.6 cm	11.461	1.852			0.490
C9023D-2H-3, 76.6 cm	11.501	2.2521			0.244
C9023D-2H-3, 80.6 cm	11.541	2.57			0.048
C9023D-2H-3, 84.6 cm	11.581	2.1707		29.668	0.294
C9023D-2H-3, 88.6 cm	11.621	2.0892			0.344
C9023D-2H-3, 92.6 cm	11.661	1.8965			0.463
C9023D-2H-3, 96.6 cm	11.701	1.8572			0.487
C9023D-2H-3, 100.6 cm	11.741	1.1435		38	0.926
C9023D-2H-4, 3.8 cm	11.783	1.7109			0.577
C9023D-2H-4, 7.8 cm	11.823	1.9395			0.436
C9023D-2H-4, 11.8 cm	11.863	2.0522			0.367
C9023D-2H-4, 15.8 cm	11.903	1.8546		31.266	0.489
C9023D-2H-4, 19.8 cm	11.943	2.0185			0.388
C9023D-2H-4, 23.8 cm	11.983	1.8751			0.476
C9023D-2H-4, 27.8 cm	12.023	1.9229			0.446
C9023D-2H-4, 31.8 cm	12.063	1.9517		39.933	0.429
C9023D-2H-4, 35.8 cm	12.103	2.1805			0.288
C9023D-2H-4, 39.8 cm	12.143	1.434			0.748
C9023D-2H-4, 43.8 cm	12.183	1.6745			0.599
C9023D-2H-4, 47.8 cm	12.223	1.7258		36.766	0.568
C9023D-2H-4, 51.8 cm	12.263	2.3192			0.202
C9023D-2H-4, 55.8 cm	12.303	1.4626			0.730
C9023D-2H-4, 59.8 cm	12.343	1.6479			0.616
C9023D-2H-4, 63.8 cm	12.383	2.2147		44.801	0.267
C9023D-2H-4, 67.8 cm	12.423	1.5113			0.700
C9023D-2H-4, 71.8 cm	12.463	1.8763			0.475
C9023D-2H-4, 75.8 cm	12.503	2.1016			0.336
C9023D-2H-4, 79.8 cm	12.543	1.6883		36.834	0.591
C9023D-2H-4, 83.8 cm	12.583	1.7481			0.554
C9023D-2H-4, 87.8 cm	12.623	1.8535			0.489
C9023D-2H-4, 91.8 cm	12.663	1.7461			0.555
C9023D-2H-4, 95.8 cm	12.703	1.5304		26.934	0.688
C9023D-2H-4, 99.8 cm	12.743	1.5364			0.684
C9023D-3X-CC, 8.0 cm	13.08	1.8609	7.3445	19.666	0.485
C9023D-3X-CC, 12.0 cm	13.12	2.0606	4.7195		0.362
C9023D-3X-CC, 16.0 cm	13.16	2.1368	8.0803	26.966	0.315
C9023D-3X-CC, 20.0 cm	13.2	2.0385	15.4873		0.375

Location	Subbottom Depth [mbsf]	GRA ¹⁾ [g/cm ³]	MS ²⁾ [x10 ⁻⁵ SI]	NGR ³⁾ [cps]	GRA Porosity
C9023D-3X-CC, 24.0 cm	13.24	2.2128	78.176	32.434	0.268
C9023D-3X-CC, 28.0 cm	13.28	2.2458	59.9446		0.248
C9023D-3X-CC, 32.0 cm	13.32	1.9869	27.114	23.2	0.407
C9023D-4H-1, 8.0 cm	22.58	2.5003			0.091
C9023D-4H-1, 12.0 cm	22.62	2.5603			0.054
C9023D-4H-1, 16.0 cm	22.66	2.6124		243.235	0.022
C9023D-4H-1, 20.0 cm	22.7	2.7002			-0.032
C9023D-4H-1, 24.0 cm	22.74	2.6848			-0.023
C9023D-4H-1, 28.0 cm	22.78	2.8455			-0.122
C9023D-4H-1, 32.0 cm	22.82	2.6247		206.835	0.014
C9023D-4H-1, 36.0 cm	22.86	2.5173			0.080
C9023D-4H-1, 40.0 cm	22.9	2.1392			0.313
C9023D-4H-1, 44.0 cm	22.94	1.9383			0.437
C9023D-4H-1, 48.0 cm	22.98	2.2705		76.167	0.232
C9023D-4H-1, 52.0 cm	23.02	2.0586			0.363
C9023D-5H-1, 8.0 cm	31.08	2.448			0.123
C9023D-5H-1, 12.0 cm	31.12	2.5015			0.090
C9023D-5H-1, 16.0 cm	31.16	2.5735		85	0.046
C9023D-5H-1, 20.0 cm	31.2	2.6198			0.017
C9023D-5H-1, 24.0 cm	31.24	2.6922			-0.027
C9023D-5H-1, 28.0 cm	31.28	2.6752			-0.017
C9023D-5H-1, 32.0 cm	31.32	2.5556		142.8	0.057
C9023D-5H-1, 36.0 cm	31.36	2.5125			0.083
C9023D-5H-1, 40.0 cm	31.4	2.495			0.094
C9023D-5H-1, 44.0 cm	31.44	2.4187			0.141
C9023D-5H-1, 48.0 cm	31.48	2.2659		166.567	0.235
C9023D-5H-1, 52.0 cm	31.52	2.2914			0.220
C9023D-5H-1, 56.0 cm	31.56	2.2929			0.219
C9023D-5H-1, 60.0 cm	31.6	2.3447			0.187
C9023D-5H-1, 64.0 cm	31.64	2.3658		157.533	0.174
C9023D-5H-1, 68.0 cm	31.68	2.4201			0.140
C9023D-5H-1, 72.0 cm	31.72	2.3935			0.157
C9023D-5H-1, 76.0 cm	31.76	2.4168			0.142
C9023D-5H-1, 80.0 cm	31.8	2.4224		156.667	0.139
C9023D-5H-1, 84.0 cm	31.84	2.4792			0.104
C9023D-5H-1, 88.0 cm	31.88	2.5187			0.080
C9023D-5H-1, 92.0 cm	31.92	2.4981			0.092
C9023D-5H-1, 96.0 cm	31.96	2.5422		144.401	0.065
C9023D-5H-1, 100.0 cm	32	2.4184			0.141
C9023D-5H-2, 2.5 cm	32.035	2.412			0.145
C9023D-5H-2, 6.5 cm	32.075	2.4324			0.133
C9023D-5H-2, 10.5 cm	32.115	2.4563		139.934	0.118
C9023D-5H-2, 14.5 cm	32.155	2.5101			0.085
C9023D-5H-2, 18.5 cm	32.195	2.4871			0.099
C9023D-5H-2, 22.5 cm	32.235	2.5232			0.077
C9023D-5H-2, 26.5 cm	32.275	2.4838		150.734	0.101
C9023D-5H-2, 30.5 cm	32.315	2.4665			0.112
C9023D-5H-2, 34.5 cm	32.355	2.4705			0.109
C9023D-5H-2, 38.5 cm	32.395	2.5458			0.063
C9023D-5H-2, 42.5 cm	32.435	2.5616		155.233	0.053
C9023D-5H-2, 46.5 cm	32.475	2.5004			0.091

Location	Subbottom Depth [mbsf]	GRA ¹⁾ [g/cm ³]	MS ²⁾ [x10 ⁻⁵ SI]	NGR ³⁾ [cps]	GRA Porosity
C9023D-5H-2, 50.5 cm	32.515	2.2967			0.216
C9023D-5H-2, 54.5 cm	32.555	2.499			0.092
C9023D-5H-2, 58.5 cm	32.595	2.5015		182.1	0.090
C9023D-5H-2, 62.5 cm	32.635	2.5214			0.078
C9023D-5H-2, 66.5 cm	32.675	2.4914			0.096
C9023D-5H-2, 70.5 cm	32.715	1.727			0.567
C9023D-5H-2, 74.5 cm	32.755	2.4337		123.199	0.132
C9023D-5H-2, 78.5 cm	32.795	2.4703			0.109
C9023D-5H-2, 82.5 cm	32.835	2.2829			0.225
C9023D-5H-2, 86.5 cm	32.875	2.2743			0.230
C9023D-5H-2, 90.5 cm	32.915	2.1873		124.632	0.284
C9023D-5H-2, 94.5 cm	32.955	2.2687			0.234
C9023D-5H-2, 98.5 cm	32.995	2.1095			0.332
C9023D-6X-CC, 4.0 cm	33.54	1.4681	2.5212	10.367	0.727
C9023D-7X-CC, 8.0 cm	43.08	1.1593	3.9358		0.917
C9023D-7X-CC, 12.0 cm	43.12	1.7791	4.6053		0.535
C9023D-7X-CC, 16.0 cm	43.16	2.1232	6.6095	111.333	0.323
C9023D-7X-CC, 20.0 cm	43.2	1.6663	7.3259		0.604
C9023D-7X-CC, 24.0 cm	43.24	1.5033	7.9986		0.705
C9023D-7X-CC, 28.0 cm	43.28	1.3144	14.5532		0.821
C9023D-7X-CC, 32.0 cm	43.32	2.2041	34.4274	200.9	0.273
C9023D-7X-CC, 36.0 cm	43.36	2.1598	41.4652		0.301
C9023D-7X-CC, 40.0 cm	43.4	0.5857	11.524		1.270
C9023D-8X-CC, 8.0 cm	52.58	1.0346	16.3581		0.993
C9023D-8X-CC, 12.0 cm	52.62	1.6495	21.2846		0.615
C9023D-8X-CC, 16.0 cm	52.66	1.7265	12.7721	65.401	0.567
C9023D-8X-CC, 20.0 cm	52.7	1.7749	7.467		0.538
C9023D-8X-CC, 24.0 cm	52.74	1.7364	9.5482		0.561
C9023D-8X-CC, 28.0 cm	52.78	1.6186	9.5645		0.634
C9023D-8X-CC, 32.0 cm	52.82	1.3704	25.1592	49.467	0.787
C9023D-8X-CC, 36.0 cm	52.86	0.4256	15.9366		1.368
C9023D-8X-CC, 40.0 cm	52.9	2.182	22.4251		0.287
C9023D-8X-CC, 44.0 cm	52.94	2.2151	58.7505		0.267
C9023D-8X-CC, 48.0 cm	52.98	2.1142	97.1439	30.7	0.329
C9023D-9X-1, 8.0 cm	60.58	1.6125		80.466	0.638
C9023D-9X-1, 12.0 cm	60.62	1.619			0.634
C9023D-9X-1, 16.0 cm	60.66	1.023		43.033	1.001
C9023D-9X-CC, 7.8 cm	60.743	2.0345	7.2369		0.378
C9023D-9X-CC, 11.8 cm	60.783	1.5134	8.75		0.699
C9023D-9X-CC, 15.8 cm	60.823	1.9094	11.6538	124.734	0.455
C9023D-9X-CC, 19.8 cm	60.863	1.9064	12.4508		0.457
C9023D-9X-CC, 23.8 cm	60.903	1.7996	9.7131		0.522
C9023D-9X-CC, 27.8 cm	60.943	1.9285	15.2832		0.443
C9023D-9X-CC, 31.8 cm	60.983	2.0181	17.4573	115.467	0.388
C9023D-9X-CC, 35.8 cm	61.023	0.6773	25.0952		1.213
C9023D-9X-CC, 39.8 cm	61.063	0.8916	13.8998		1.082
C9023D-9X-CC, 43.8 cm	61.103	1.667	18.1087		0.604
C9023D-9X-CC, 47.8 cm	61.143	1.6965	24.3038	66.034	0.586
C9023D-9X-CC, 51.8 cm	61.183	1.9443	22.2568		0.433
C9023D-10X-1, 8.0 cm	70.08	1.5344			0.686
C9023D-10X-1, 12.0 cm	70.12	1.6577			0.610

Location	Subbottom Depth [mbsf]	GRA ¹⁾ [g/cm ³]	MS ²⁾ [x10 ⁻⁵ SI]	NGR ³⁾ [cps]	GRA Porosity
C9023D-10X-1, 16.0 cm	70.16	1.7838		55.601	0.532
C9023D-10X-1, 20.0 cm	70.2	1.869			0.480
C9023D-10X-1, 24.0 cm	70.24	1.7553			0.550
C9023D-10X-1, 28.0 cm	70.28	1.7191			0.572
C9023D-10X-1, 32.0 cm	70.32	1.7901		50.568	0.528
C9023D-10X-1, 36.0 cm	70.36	1.8924			0.465
C9023D-10X-1, 40.0 cm	70.4	1.4963			0.709
C9023D-10X-1, 44.0 cm	70.44	0.3362			1.424
C9023D-10X-CC, 6.8 cm	70.518	2.004	7.1765		0.397
C9023D-10X-CC, 10.8 cm	70.558	1.9089	7.9048		0.455
C9023D-10X-CC, 14.8 cm	70.598	1.9282	8.5851		0.443
C9023D-10X-CC, 18.8 cm	70.638	1.8191	9.2611	73.701	0.510
C9023D-10X-CC, 22.8 cm	70.678	2.1003	8.6032		0.337
C9023D-10X-CC, 26.8 cm	70.718	1.7502	23.231		0.553
C9023D-10X-CC, 30.8 cm	70.758	1.8003	16.5936		0.522
C9023D-10X-CC, 34.8 cm	70.798	1.7982	14.5962	65.834	0.523
C9023D-10X-CC, 38.8 cm	70.838	0.8389	31.8194		1.114
C9023D-10X-CC, 42.8 cm	70.878	1.4635	17.4757		0.729
C9023D-10X-CC, 46.8 cm	70.918	1.9278	72.1601		0.443
C9023D-10X-CC, 50.8 cm	70.958	1.8342	31.4129	53.399	0.501
C9023D-10X-CC, 54.8 cm	70.998	0.7396	23.7101		1.175
C9023D-10X-CC, 58.8 cm	71.038	2.099	45.5545		0.338
C9023D-10X-CC, 62.8 cm	71.078	2.0666	22.7632		0.358
C9023D-11X-CC, 8.0 cm	79.58	2.0764	6.0525	57.966	0.352
C9023D-11X-CC, 12.0 cm	79.62	1.5653	6.7307		0.667
C9023D-11X-CC, 16.0 cm	79.66	1.6012	9.3871	58.667	0.645
C9023D-11X-CC, 20.0 cm	79.7	0.9775	34.8665		1.029
C9023D-11X-CC, 24.0 cm	79.74	1.2307	24.8194	49.466	0.873
C9023D-11X-CC, 28.0 cm	79.78	2.1249	18.5759		0.322
C9023D-12X-CC, 8.0 cm	86.58	1.5265	4.0214	24.133	0.691
C9023D-12X-CC, 12.0 cm	86.62	1.2053	6.0346		0.888
C9023D-12X-CC, 16.0 cm	86.66	2.1477	12.6271	33.266	0.308
C9023D-12X-CC, 20.0 cm	86.7	1.5075	38.0738		0.702
C9023D-12X-CC, 24.0 cm	86.74	1.8207	76.9782	43.866	0.509
C9023D-12X-CC, 28.0 cm	86.78	2.1312	43.2034		0.318
C9023D-12X-CC, 32.0 cm	86.82	1.326	11.1148	21.065	0.814
C9023D-13X-CC, 8.0 cm	93.08	1.6102	3.3754	19.7	0.639
C9023D-13X-CC, 12.0 cm	93.12	1.2654	6.1198		0.851
C9023D-13X-CC, 16.0 cm	93.16	1.3086	13.6577	26.832	0.825
C9023D-13X-CC, 20.0 cm	93.2	2.0735	47.1191		0.354
C9023D-13X-CC, 24.0 cm	93.24	1.4079	53.3561	34	0.764
C9023D-13X-CC, 28.0 cm	93.28	1.0658	36.9073		0.974
C9023D-13X-CC, 32.0 cm	93.32	1.7359	24.2709	31.433	0.562
C9023D-14X-CC, 8.0 cm	102.08	0.561	5.7482		1.285
C9023D-14X-CC, 12.0 cm	102.12	0.5858	5.2699		1.270
C9023D-14X-CC, 16.0 cm	102.16	0.4978	5.9636	49.833	1.324
C9023D-14X-CC, 20.0 cm	102.2	1.7684	10.6154		0.542
C9023D-14X-CC, 24.0 cm	102.24	2.1882	20.5587		0.283
C9023D-14X-CC, 28.0 cm	102.28	2.4558	22.2433		0.118
C9023D-14X-CC, 32.0 cm	102.32	1.9283	18.1154	34.034	0.443
C9023D-14X-CC, 36.0 cm	102.36	2.1691	38.8162		0.295

Location	Subbottom Depth [mbsf]	GRA ¹⁾ [g/cm ³]	MS ²⁾ [x10 ⁻⁵ SI]	NGR ³⁾ [cps]	GRA Porosity
C9023D-14X-CC, 40.0 cm	102.4	2.2482	44.438		0.246
C9023D-14X-CC, 44.0 cm	102.44	0.904	23.3398		1.074
C9023D-14X-CC, 48.0 cm	102.48	2.1462	29.3092	33.333	0.309
C9023D-14X-CC, 52.0 cm	102.52	2.1942	20.9978		0.279
C9023D-15X-CC, 8.0 cm	109.08	1.1787	5.654		0.905
C9023D-15X-CC, 12.0 cm	109.12	1.531	6.8877		0.688
C9023D-15X-CC, 16.0 cm	109.16	1.4356	9.4116	23.801	0.747
C9023D-15X-CC, 20.0 cm	109.2	1.6806	15.888		0.596
C9023D-15X-CC, 24.0 cm	109.24	2.3576	48.2996		0.179
C9023D-15X-CC, 28.0 cm	109.28	2.0868	29.8448		0.346
C9023D-15X-CC, 32.0 cm	109.32	1.963	22.7374	24.601	0.422
C9023D-15X-CC, 36.0 cm	109.36	0.1317	22.0602		1.549
C9023D-16X-CC, 8.0 cm	118.58	1.4559	10.3623		0.734
C9023D-16X-CC, 12.0 cm	118.62	1.0897	11.2793		0.960
C9023D-16X-CC, 16.0 cm	118.66	2.2359	12.5855	13.401	0.254
C9023D-16X-CC, 20.0 cm	118.7	1.25	36.2798		0.861
C9023D-16X-CC, 24.0 cm	118.74	1.8127	104.7632		0.514
C9023D-16X-CC, 28.0 cm	118.78	1.2238	97.239		0.877
C9023D-16X-CC, 32.0 cm	118.82	1.753	51.6786	14.767	0.551
C9023D-16X-CC, 36.0 cm	118.86	1.9835	74.7213		0.409
C9023D-16X-CC, 40.0 cm	118.9	1.2271	147.323		0.875
C9023D-16X-CC, 44.0 cm	118.94	1.5177	189.1216		0.696
C9023D-16X-CC, 48.0 cm	118.98	2.2033	126.189	28.401	0.274
C9023D-16X-CC, 52.0 cm	119.02	1.3432	66.5368		0.803

Hole E

Location	Subbottom Depth [mbsf]	GRA ¹⁾ [g/cm ³]	MS ²⁾ [x10 ⁻⁵ SI]	NGR ³⁾ [cps]	GRA Porosity
C9023E-1X-CC, 8.0 cm	125.08	0.1451	1.2309	25.933	1.541
C9023E-1X-CC, 12.0 cm	125.12	1.3386	1.1798	18.899	0.806
C9023E-2X-CC, 8.0 cm	135.08	1.6614	3.4335	57.034	0.608
C9023E-2X-CC, 12.0 cm	135.12	1.0871	4.1026		0.961
C9023E-2X-CC, 16.0 cm	135.16	1.1818	13.6519	98.568	0.903
C9023E-2X-CC, 20.0 cm	135.2	1.3847	29.3515		0.778
C9023E-2X-CC, 24.0 cm	135.24	2.0347	21.8523	143.633	0.378
C9023E-2X-CC, 28.0 cm	135.28	1.8726	19.4613		0.477
C9023E-2X-CC, 32.0 cm	135.32	2.0668	13.6404	80.967	0.358
C9023E-3X-CC, 8.0 cm	144.08	1.5012	4.7055	265.7	0.706
C9023E-3X-CC, 12.0 cm	144.12	1.7123	8.1493		0.576
C9023E-3X-CC, 16.0 cm	144.16	1.9913	11.5892	278.533	0.404
C9023E-3X-CC, 20.0 cm	144.2	1.3973	10.2345		0.770
C9023E-3X-CC, 24.0 cm	144.24	2.0254	15.6395	280.533	0.383
C9023E-3X-CC, 28.0 cm	144.28	2.1668	16.3056		0.296
C9023E-3X-CC, 32.0 cm	144.32	1.9707	16.2986	276.699	0.417
C9023E-3X-CC, 36.0 cm	144.36	2.2249	12.0794		0.261
C9023E-3X-CC, 40.0 cm	144.4	1.3615	6.7262	92.166	0.792
C9023E-4X-CC, 8.0 cm	153.58	1.6151	3.9491	72.165	0.636
C9023E-4X-CC, 12.0 cm	153.62	1.5268	5.3392		0.690
C9023E-4X-CC, 16.0 cm	153.66	1.0616	5.3279	77.799	0.977
C9023E-4X-CC, 20.0 cm	153.7	1.7264	7.9381		0.567
C9023E-4X-CC, 24.0 cm	153.74	1.3751	14.59	88.533	0.784

Location	Subbottom Depth [mbsf]	GRA ¹⁾ [g/cm ³]	MS ²⁾ [x10 ⁻⁵ SI]	NGR ³⁾ [cps]	GRA Porosity
C9023E-4X-CC, 28.0 cm	153.78	1.2502	15.2468		0.861
C9023E-4X-CC, 32.0 cm	153.82	0.9247	13.2525	91.332	1.061
C9023E-4X-CC, 36.0 cm	153.86	2.0176	17.0767		0.388
C9023E-4X-CC, 40.0 cm	153.9	2.0682	16.9201	80.433	0.357
C9023E-5X-1, 8.0 cm	163.08	1.6157	9.1682	41.334	0.636
C9023E-5X-1, 12.0 cm	163.12	1.5215	8.5169		0.694
C9023E-5X-1, 16.0 cm	163.16	0.9394	9.0942	56	1.052
C9023E-5X-CC, 3.8 cm	163.203	2.0109	20.1113		0.392
C9023E-5X-CC, 7.8 cm	163.243	2.137	21.4291	91.267	0.315
C9023E-5X-CC, 11.8 cm	163.283	1.902	26.9229		0.459
C9023E-5X-CC, 15.8 cm	163.323	2.1025	31.2923	86.734	0.336
C9023E-5X-CC, 19.8 cm	163.363	2.0295	33.7826		0.381
C9023E-5X-CC, 23.8 cm	163.403	1.0531	21.5201	93.668	0.982
C9023E-5X-CC, 27.8 cm	163.443	2.0433	14.7575		0.372
C9023E-5X-CC, 31.8 cm	163.483	2.0096	15.279	40.766	0.393
C9023E-5X-CC, 35.8 cm	163.523	2.1455	18.3069		0.309
C9023E-6X-CC, 8.0 cm	172.58	1.4645	5.5824		0.729
C9023E-6X-CC, 12.0 cm	172.62	1.3918	6.7016		0.774
C9023E-6X-CC, 16.0 cm	172.66	1.4785	73.7364	15.699	0.720
C9023E-6X-CC, 20.0 cm	172.7	1.2018	36.0916		0.891
C9023E-6X-CC, 24.0 cm	172.74	1.6575	14.0296		0.610
C9023E-6X-CC, 28.0 cm	172.78	1.9991	32.9391		0.400
C9023E-6X-CC, 32.0 cm	172.82	2.1416	12.8462	23.267	0.312
C9023E-8X-CC, 8.0 cm	189.58	1.7063	1.2175	24.7	0.580
C9023E-9X-1, 8.0 cm	199.08	0.9743			1.031
C9023E-9X-1, 12.0 cm	199.12	0.9893			1.021
C9023E-9X-1, 16.0 cm	199.16	2.0192		30.933	0.387
C9023E-9X-1, 20.0 cm	199.2	2.1236			0.323
C9023E-9X-1, 24.0 cm	199.24	1.918			0.450
C9023E-9X-1, 28.0 cm	199.28	1.9833			0.409
C9023E-9X-1, 32.0 cm	199.32	1.8082		32.733	0.517
C9023E-9X-1, 36.0 cm	199.36	1.987			0.407
C9023E-9X-1, 40.0 cm	199.4	1.8466			0.493
C9023E-9X-1, 44.0 cm	199.44	1.7131			0.576
C9023E-9X-1, 48.0 cm	199.48	2.1429		38.065	0.311
C9023E-9X-1, 52.0 cm	199.52	1.9318			0.441
C9023E-9X-1, 56.0 cm	199.56	2.005			0.396
C9023E-9X-1, 60.0 cm	199.6	1.8387			0.498
C9023E-9X-1, 64.0 cm	199.64	1.8744		38.6	0.476
C9023E-9X-1, 68.0 cm	199.68	1.9652			0.420
C9023E-9X-1, 72.0 cm	199.72	2.053			0.366
C9023E-9X-1, 76.0 cm	199.76	1.9775			0.413
C9023E-9X-1, 80.0 cm	199.8	1.9553		42.399	0.427
C9023E-9X-1, 84.0 cm	199.84	1.8948			0.464
C9023E-9X-1, 88.0 cm	199.88	1.27			0.849
C9023E-9X-1, 92.0 cm	199.92	1.7079			0.579
C9023E-9X-CC, 5.9 cm	199.999	1.9163	40.5908		0.451
C9023E-9X-CC, 9.9 cm	200.039	1.2209	32.7645		0.879
C9023E-9X-CC, 13.9 cm	200.079	1.5611	28.0701		0.669
C9023E-9X-CC, 17.9 cm	200.119	2.1663	20.6272	38.533	0.297
C9023E-9X-CC, 21.9 cm	200.159	2.1155	13.588		0.328

Location	Subbottom Depth [mbsf]	GRA ¹⁾ [g/cm ³]	MS ²⁾ [x10 ⁻⁵ SI]	NGR ³⁾ [cps]	GRA Porosity
C9023E-9X-CC, 25.9 cm	200.199	1.9855	10.5841		0.408
C9023E-9X-CC, 29.9 cm	200.239	0.8329	4.333		1.118

Table 5-3-5-2**HoleB**

Top Location of Sample Interval	Subbotto m Depth [mbsf]	Bulk Density [g/cm ³]	Grain Density [g/cm ³]	Porosity
C9023B-1X-CC, 3.0 cm	0.03	3.8609	4.6555	0.2188
C9023B-1X-CC, 13.0 cm	0.13	3.3892	3.706	0.1181
C9023B-1X-CC, 22.0 cm	0.22	2.1725	3.3178	0.4993

HoleD

Top Location of Sample Interval	Subbotto m Depth [mbsf]	Bulk Density [g/cm ³]	Grain Density [g/cm ³]	Porosity	Porosity:Syringe
C9023D-1X-1, 4.0 cm	0.04	2.3904	3.4091	0.4271	
C9023D-1X-2, 8.5 cm	0.185	2.9708	3.7266	0.2797	
C9023D-2H-2, 52.0 cm	10.255	2.7324	3.456	0.2975	0.463477778
C9023D-2H-3, 30.0 cm	11.035	1.5247	2.7811	0.715	
C9023D-2H-3, 80.0 cm	11.535	2.3012	3.4189	0.4667	0.439777778
C9023D-2H-4, 78.0 cm	12.525	2.0637	3.1289	0.5061	0.646788889
C9023D-3X-CC, 23.0 cm	13.23	2.3318	2.9142	0.3081	0.4738
C9023D-4H-1, 29.0 cm	22.79	3.1836	3.7273	0.2011	
C9023D-4H-1, 45.0 cm	22.95	1.8034	2.8282	0.568	0.62975
C9023D-4H-CC, 6.0 cm	23.095	1.806	2.8932	0.5816	0.547557143
C9023D-5H-1, 68.0 cm	31.68	2.5349	3.6432	0.4231	0.54429
C9023D-5H-2, 83.0 cm	32.84	2.86	3.8424	0.3486	0.5022
C9023D-7X-CC, 0.0 cm	43	1.9901	2.7863	0.4518	
C9023D-7X-CC, 30.0 cm	43.3	1.9558	2.9572	0.518	
C9023D-8X-CC, 15.0 cm	52.65	1.9509	2.9496	0.5187	
C9023D-8X-CC, 38.0 cm	52.88	2.6239	2.7903	0.0942	
C9023D-9X-1, 14.0 cm	60.64	1.8497	2.8895	0.5574	
C9023D-9X-CC, 9.0 cm	60.755	1.9123	2.9931	0.5489	
C9023D-9X-CC, 22.0 cm	60.885	1.8775	2.8185	0.5244	
C9023D-10X-1, 18.0 cm	70.18	1.7838	2.9123	0.5976	
C9023D-10X-CC, 13.0 crr	70.58	1.9145	2.7736	0.491	
C9023D-10X-CC, 41.0 crr	70.86	2.0213	2.7543	0.4236	
C9023D-11X-CC, 19.0 crr	79.69	2.2296	2.8305	0.3327	
C9023D-12X-CC, 23.0 crr	86.73	2.3701	2.7484	0.2194	
C9023D-13X-CC, 0.0 cm	93	2.4885	2.7636	0.1582	
C9023D-13X-CC, 10.0 crr	93.1	2.4048	2.7116	0.1818	
C9023D-14X-CC, 30.0 crr	102.3	2.3506	2.7092	0.2128	
C9023D-14X-CC, 42.0 crr	102.42	2.3995	2.77	0.2122	
C9023D-15X-CC, 12.0 crr	109.12	2.5214	2.7254	0.1199	
C9023D-16X-CC, 24.0 crr	118.74	2.5011	2.7218	0.13	

Hole E

Top Location of Sample Interval	Subbotto m Depth [mbsf]	Bulk Density [g/cm ³]	Grain Density [g/cm ³]	Porosity
C9023E-1X-CC, 4.0 cm	125.04	2.3182	2.6908	0.2235
C9023E-2X-CC, 9.0 cm	135.09	2.2958	2.7554	0.2654
C9023E-2X-CC, 16.0 cm	135.16	2.1251	2.7182	0.35
C9023E-3X-CC, 1.0 cm	144.01	1.7546	2.9548	0.6216

Top Location of Sample Interval	Subbottom Depth [mbsf]	Bulk Density [g/cm^3]	Grain Density [g/cm^3]	Porosity
C9023E-3X-CC, 17.0 cm	144.17	2.208	2.7326	0.307
C9023E-4X-CC, 10.0 cm	153.6	2.1689	2.7207	0.3252
C9023E-4X-CC, 33.0 cm	153.83	2.1937	2.7764	0.3325
C9023E-5X-1, 3.0 cm	163.03	2.4682	2.9366	0.2449
C9023E-5X-CC, 22.0 cm	163.385	2.0721	2.8952	0.4399
C9023E-6X-CC, 13.0 cm	172.63	2.3051	2.744	0.2552
C9023E-8X-CC, 5.0 cm	189.55	2.4722	2.563	0.059
C9023E-8X-CC, 7.0 cm	189.57	2.5175	2.6337	0.0722
C9023E-9X-1, 8.0 cm	199.08	2.0926	2.7089	0.3658
C9023E-9X-1, 50.0 cm	199.5	2.1106	2.7279	0.3623
C9023E-9X-CC, 8.0 cm	200.02	2.1079	2.6944	0.3511

Table 5-3-5-3

Location	Subbotto m depth [mbsf]	Average gamma ray pulse count rate [cps]	DER [μSv/h]
Hole B			
C9023B-1X-CC, 25.0 cm	0.25	2	0.03
Hole D			
C9023D-1X-2, 7.0 cm	0.17	3	0.04
C9023D-1X-CC, 3.0 cm	0.265	2	0.03
C9023D-2H-1, 7.0 cm	9.57	2	0.03
C9023D-2H-3, 29.0 cm	11.025	2	0.05
C9023D-2H-3, 61.0 cm	11.345	7	0.07
C9023D-2H-4, 45.0 cm	12.195	3	0.04
C9023D-3X-CC, 27.0 cm	13.27	2	0.08
C9023D-4H-1, 23.0 cm	22.73	4	0.05
C9023D-4H-1, 23.0 cm	22.73	4	0.05
C9023D-4H-CC, 14.0 cm	23.175	4	0.02
C9023D-5H-1, 8.0 cm	31.08	2	0.02
C9023D-5H-1, 50.0 cm	31.5	6	0.02
C9023D-5H-2, 60.0 cm	32.61	4	0.06
C9023D-5H-CC, 15.0 cm	33.165	3	0.04
C9023D-6X-CC, 2.0 cm	33.52	2	0.03
C9023D-7X-CC, 11.0 cm	43.11	3	0.03
C9023D-7X-CC, 25.0 cm	43.25	4	0.05
C9023D-8X-CC, 48.0 cm	52.98	2	0.04
C9023D-9X-CC, 17.0 cm	60.835	3	0.04
C9023D-10X-1, 30.0 cm	70.3	3	0.03
C9023D-10X-CC, 34.0 cm	70.79	3	0.04
C9023D-11X-CC, 29.0 cm	79.79	2	0.02
C9023D-12X-CC, 30.0 cm	86.8	2	0.03
C9023D-13X-CC, 19.0 cm	93.19	3	0.04
C9023D-13X-CC, 34.0 cm	93.34	2	0.03
C9023D-14X-CC, 29.0 cm	102.29	2	0.02
C9023D-15X-CC, 25.0 cm	109.25	2	0.03
C9023D-16X-CC, 44.0 cm	118.94	2	0.03
Hole E			
C9023E-1X-CC, 5.0 cm	125.05	2	0.03
C9023E-2X-CC, 24.0 cm	135.24	3	0.04
C9023E-3X-CC, 16.0 cm	144.16	6	0.05
C9023E-4X-CC, 9.0 cm	153.59	2	0.03
C9023E-5X-CC, 16.0 cm	163.325	2	0.03
C9023E-5X-CC, 28.0 cm	163.445	2	0.07
C9023E-6X-CC, 20.0 cm	172.7	2	0.03
C9023E-8X-CC, 5.0 cm	189.55	2	0.03
C9023E-8X-CC, 5.0 cm	189.55	2	0.01
C9023E-9X-1, 89.0 cm	199.89	3	0
C9023E-9X-CC, 17.0 cm	200.11	2	0.03

Table 5-3-5-4**Hole B**

Location	Subbotto m Depth [mbsf]	WR/HS	Thermal conductivity [W/(mK)]	LET	Probe	Remark
C9023B-1X-CC, 22.0 cm	0.22	W	1.564	Qualified: >10	HLQ50	hydrothermally altered sand

Hole D

Location	Subbotto m Depth [mbsf]	W/WR	Thermal conductivity [W/(mK)]	LET	Probe	Remark
C9023D-1X-2, 7.0 cm	0.17	W	0.543	Qualified: >10	HLQ50	Kuroko? Oil compound
C9023D-1X-CC, 3.0 cm	0.265	W	1.148	Qualified: >10	HLQ50	Kuroko? Oil compound, hydrothermally altered
C9023D-2H-1, 9.0 cm	9.59	W	1.206	Qualified: >10	HLQ50	oil compound, sand, hydrothermally altered
C9023D-2H-3, 19.0 cm	10.925	W	1.206	Qualified: >10	HLQ50	oil compound
C9023D-2H-3, 62.0 cm	11.355	W	1.511	Qualified: >10	HLQ50	oil compound, sand
C9023D-3X-CC, 16.0 cm	13.16	W	0.309	Qualified: >10	HLQ50	oil compound, sand
C9023D-4H-1, 49.0 cm	22.99	W	1.793	Qualified: >10	HLQ50	oil compound, sand
C9023D-5H-1, 64.0 cm	31.64	W	2.149	Qualified: >10	HLQ50	oil compound, sand
C9023D-5H-2, 35.0 cm	32.36	W	0.695	Qualified: >10	HLQ50	oil compound, sand
C9023D-8X-CC, 13.0 cm	52.63	WR	1.405	Qualified: >10	VLQ60	sand
C9023D-9X-CC, 22.0 cm	60.885	WR	1.911	Qualified: >10	VLQ60	clay
C9023D-10X-1, 20.0 cm	70.2	WR	1.104	Qualified: >10	VLQ60	clay
C9023D-10X-CC, 20.0 cm	70.65	WR	1.643	Qualified: >10	VLQ60	clay
C9023D-11X-CC, 28.0 cm	79.78	W	0.648	Qualified: >10	HLQ50	oil compound, clay
C9023D-12X-CC, 28.0 cm	86.78	W	3.257	Qualified: >10	HLQ50	oil compound, anhydrite? clay
C9023D-13X-CC, 19.0 cm	93.19	W	1.414	Qualified: >10	HLQ50	oil compound, siltstone
C9023D-14X-CC, 27.0 cm	102.27	W	3.956	Qualified: >10	HLQ50	oil compound, siltstone
C9023D-15X-CC, 24.0 cm	109.24	W	4.491	Qualified: >10	HLQ50	oil compound, mudstone
C9023D-16X-CC, 14.0 cm	118.64	W	4.168	Qualified: >10	HLQ50	oil compound, mudstone

Hole E

Location	Subbotto m Depth [mbsf]	W/WR	Thermal conductivity [W/(mK)]	LET	Probe	Remark
C9023E-1X-CC, 3.0 cm	125.03	W	6.392	Qualified: >10	HLQ50	oil compound, volcanic rock, green
C9023E-1X-CC, 3.0 cm	125.03	W	4.133	Qualified: >10	HLQ50	oil compound, volcanic rock, green
C9023E-2X-CC, 3.0 cm	135.03	W	1.256	Qualified: >10	HLQ50	oil compound, hydrothermally altered hard rock
C9023E-2X-CC, 28.0 cm	135.28	W	1.831	Qualified: >10	HLQ50	oil compound, clay
C9023E-3X-CC, 7.0 cm	144.07	W	1.163	Qualified: >10	HLQ50	oil compound, silt, clay
C9023E-4X-CC, 40.0 cm	153.9	W	1.202	Qualified: >10	HLQ50	oil compound, 2nd
C9023E-5X-1, 10.0 cm	163.1	W	3.207	Qualified: >10	HLQ50	oil compound, block
C9023E-5X-CC, 16.0 cm	163.325	W	1.629	Qualified: >10	HLQ50	oil compound, mud breccia
C9023E-9X-1, 47.0 cm	199.47	W	0.383	Qualified: >10	HLQ50	oil compound, silt, 2nd
C9023E-9X-CC, 16.0 cm	200.1	W	0.98	Qualified: >10	HLQ50	oil compound, silt

Table 5-3-5-5**Hole B**

Location	Subbottom Depth [mbsf]	Bulk resistivity at 1 kHz [Ω m]	Remarks
C9023B-1X-CC, 5.0 cm	0.05	0.496134517	discrete, shared with PWVD
C9023B-1X-CC, 23.0 cm	0.23	2.519926094	section

Hole D

Location	Subbottom Depth [mbsf]	Bulk resistivity at 1 kHz [Ω m]	Remarks
C9023D-1X-2, 8.5 cm	0.185	2.249631505	discrete, shared with PWVD
C9023D-1X-CC, 1.5 cm	0.25	2.810936092	section
C9023D-2H-2, 17.0 cm	9.905	2.979837817	section
C9023D-2H-2, 40.0 cm	10.135	3.068542355	section
C9023D-2H-3, 55.0 cm	11.285	0.538811184	section
C9023D-2H-4, 2.0 cm	11.765	3.108279618	section
C9023D-3X-CC, 16.0 cm	13.16	1.734185173	section
C9023D-4H-1, 52.0 cm	23.02	1.374689312	section
C9023D-4H-CC, 16.0 cm	23.195	1.343038656	section
C9023D-5H-1, 74.0 cm	31.74	2.226612844	section
C9023D-5H-2, 97.0 cm	32.98	4.576881825	section
C9023D-7X-CC, 12.0 cm	43.12	3.090869763	discrete, shared with PWVD
C9023D-7X-CC, 34.0 cm	43.34	0.968287682	section
C9023D-8X-CC, 15.5 cm	52.655	0.951118704	section
C9023D-8X-CC, 39.0 cm	52.89	24.32316326	discrete
C9023D-8X-CC, 46.0 cm	52.96	8.009901569	section
C9023D-9X-1, 13.5 cm	60.635	0.719359938	section
C9023D-9X-CC, 32.0 cm	60.985	3.6682656	section
C9023D-10X-1, 23.0 cm	70.23	0.704348028	section
C9023D-10X-CC, 14.0 cm	70.59	0.870365402	section
C9023D-11X-CC, 26.5 cm	79.765	6.541730525	section
C9023D-12X-CC, 2.0 cm	86.52	10.07730198	discrete, shared with PWVD
C9023D-12X-CC, 29.0 cm	86.79	2.753077691	section
C9023D-13X-CC, 17.0 cm	93.17	7.20175812	discrete, shared with PWVD
C9023D-14X-CC, 16.0 cm	102.16	13.826089	discrete, shared with PWVD
C9023D-14X-CC, 49.0 cm	102.49	8.575407617	section
C9023D-15X-CC, 7.5 cm	109.075	15.29394907	discrete, shared with PWVD
C9023D-16X-CC, 24.0 cm	118.74	16.60850465	discrete, shared with PWVD

Hole E

Location	Subbottom Depth [mbsf]	Bulk resistivity at 1 kHz [Ω m]	Remarks
C9023E-1X-CC, 7.0 cm	125.07	15.44220526	discrete, shared with PWVD
C9023E-2X-CC, 5.5 cm	135.055	1.257995339	discrete, shared with PWVD
C9023E-2X-CC, 28.5 cm	135.285	1.617794551	section
C9023E-3X-CC, 33.0 cm	144.33	1.139574463	section
C9023E-4X-CC, 7.0 cm	153.57	1.8903348	discrete, shared with PWVD
C9023E-4X-CC, 28.0 cm	153.78	2.6290262	section
C9023E-5X-CC, 1.0 cm	163.175	4.767628232	discrete, shared with PWVD
C9023E-5X-CC, 28.0 cm	163.445	2.248988729	section
C9023E-6X-CC, 5.0 cm	172.55	10.06431741	discrete, shared with PWVD
C9023E-9X-1, 8.0 cm	199.08	23.32588931	discrete, shared with PWVD
C9023E-9X-1, 16.0 cm	199.16	1.897651602	section
C9023E-9X-1, 56.0 cm	199.56	1.162930762	section
C9023E-9X-CC, 5.5 cm	199.995	1.936824783	section

Table 5-3-5-6**Hole B**

Location	Subbottom Depth [mbsf]	P-wave velocity [m/s]				Remarks
		X	Y	Z	Average	
C9023B-1X-CC, 5.0 cm	0.05	3510	3469	3211	3396.67	shared with IMP

Hole D

Location	Subbottom Depth [mbsf]	P-wave velocity [m/s]				Remarks
		X	Y	Z	Average	
C9023D-1X-1, 3.5 cm	0.035	2373	2529	2922	2608.00	shared with IMP
C9023D-1X-2, 8.5 cm	0.185	2764	2737	3398	2966.33	shared with IMP
C9023D-7X-CC, 12.0 cm	43.12	2560	2508	2492	2520.00	shared with IMP
C9023D-12X-CC, 2.0 cm	86.52	3391	3500	3491	3460.67	shared with IMP
C9023D-13X-CC, 17.0 cm	93.17					shared with IMP
C9023D-14X-CC, 16.0 cm	102.16	3731	3469	3820	3673.33	shared with IMP
C9023D-15X-CC, 7.5 cm	109.075	4024	4284	4175	4161.00	shared with IMP
C9023D-16X-CC, 24.0 cm	118.74	4083	4034	3986	4034.33	shared with IMP

Hole E

Location	Subbottom Depth [mbsf]	P-wave velocity [m/s]				Remarks
		X	Y	Z	Average	
C9023E-1X-CC, 7.0 cm	125.07	3600	3369	3757	3575.33	shared with IMP
C9023E-2X-CC, 5.5 cm	135.055	3823	4126	4024	3991.00	shared with IMP
C9023E-4X-CC, 7.0 cm	153.57	2190	1656	2092	1979.33	shared with IMP
C9023E-5X-CC, 1.0 cm	163.175	2730	2252	2540	2507.33	shared with IMP
C9023E-6X-CC, 5.0 cm	172.55	3958	3849	3755	3854.00	shared with IMP
C9023E-8X-CC, 7.0 cm	189.57	4611	5138	4458	4735.67	shared with IMP
C9023E-9X-1, 8.0 cm	199.08	2640	2860	2773	2757.67	shared with IMP

Table 5-3-5-7**Hole B**

Location	Subbottom Depth [mbsf]	Unconfined compressive strength [kPa]	Remarks
C9023B-1X-CC, 25.0 cm	0.25	73.58	silicon ore, white

HoleD

Location	Subbottom Depth [mbsf]	Unconfined compressive strength [kPa]	Remarks
C9023D-2H-1, 20.0 cm	9.7	19.62	fine sand
C9023D-2H-3, 93.0 cm	11.665	86.66	medium grained sand
C9023D-2H-4, 93.0 cm	12.675	75.21	coarse sand
C9023D-3X-CC, 6.0 cm	13.06	588.6	white block , >6
C9023D-3X-CC, 25.0 cm	13.25	323.24	2nd run fractured clay
C9023D-4H-1, 40.0 cm	22.9	132.44	clay
C9023D-4H-CC, 11.0 cm	23.145	39.24	soft mud
C9023D-5H-1, 65.0 cm	31.65	39.24	sand
C9023D-5H-2, 87.0 cm	32.88	32.7	sand
C9023D-7X-CC, 24.0 cm	43.24	98.1	clay
C9023D-8X-CC, 27.0 cm	52.77	149.6	clay 3rd fractured
C9023D-9X-1, 14.0 cm	60.64	32.05	clay
C9023D-10X-1, 15.0 cm	70.15	49.05	clay
C9023D-10X-CC, 6.0 cm	70.51	58.86	clay 3rd fractured
C9023D-13X-CC, 9.0 cm	93.09	588.6	>6

Hole E

Location	Subbottom Depth [mbsf]	Unconfined compressive strength [kPa]	Remarks
C9023E-4X-CC, 38.0 cm	153.88	412.02	soft silt

Table 5-3-5-8

Location	Subbottom Depth [mbsf]	Major element (wt%)					
		Si	Al	Fe	Ca	K	S
Hole B							
C9023B-1X-cc, 1	0	0.3	0.0	6.8	0.0	0.0	31.6
C9023B-1X-cc, 14	0.1	12.4	2.0	10.2	0.1	1.4	20.4
C9023B-1X-cc, 23	0.2	11.6	4.5	24.3	4.5	0.0	20.1
Hole D							
C9023D-1X-1, 5	0.0	2.2	0.0	7.1	3.6	3.6	23.5
C9023D-1X-2, 9.5	0.2	2.0	0.0	3.2	1.0	1.0	26.8
C9023D-2H-2, 53	10.3	2.9	0.0	4.8	10.7	10.7	34.1
C9023D-2H-3, 31	11.0	18.6	3.6	14.0	1.8	1.8	7.3
C9023D-2H-3, 81	11.5	8.9	0.0	21.1	3.5	3.5	21.6
C9023D-2H-4, 79	12.5	7.3	2.6	10.9	9.4	9.4	32.2
C9023D-3X-cc, 24	13.2	7.1	0.0	1.6	20.7	20.7	47.7
C9023D-4H-1, 31	22.8	2.7	0.0	6.3	13.0	13.0	38.6
C9023D-4H-1, 47	23.0	14.2	7.9	11.5	4.5	4.5	19.5
C9023D-4H-cc, 8	23.1	9.9	4.4	13.7	8.3	8.3	24.5
C9023D-5H-1, 69	31.7	1.0	1.4	20.6	5.0	5.0	33.0
C9023D-5H-2, 84	32.8	3.0	0.0	16.5	3.7	3.7	29.7
C9023D-7X-cc, 1	43.0	24.3	2.8	9.4	0.4	0.4	1.2
C9023D-7X-cc, 30	43.3	2.8	1.6	11.7	18.1	18.1	40.6
C9023D-8X-cc, 16	52.7	15.8	7.2	14.7	2.0	2.0	10.1
C9023D-8X-cc, 29	52.8	17.6	8.6	15.2	0.3	0.3	4.5
C9023D-8X-cc, 39	52.9	21.6	1.0	3.1	8.4	8.4	29.7
C9023D-9X-1, 15	60.6	16.1	8.3	13.3	0.3	0.3	4.4
C9023D-9X-cc, 10	60.8	13.4	7.6	14.8	3.4	3.4	14.7
C9023D-9X-cc, 31	61.0	9.7	3.8	10.4	11.5	11.5	30.1
C9023D-9X-cc, 47	61.1	23.1	7.9	6.0	0.2	0.2	3.7
C9023D-10X-1, 19	70.2	12.2	4.2	15.2	0.7	0.7	3.2
C9023D-10X-cc, 14	70.6	21.3	7.7	7.0	0.8	0.8	6.3
C9023D-11X-cc, 17	79.7	26.7	7.0	4.5	0.1	0.1	4.4
C9023D-12X-cc, 5	86.5	28.1	3.3	3.8	0.3	0.3	1.3
C9023D-12X-cc, 30	86.8	36.9	4.0	0.8	0.1	0.1	0.5
C9023D-13X-cc, 19	93.2	22.9	1.9	9.4	0.7	0.7	3.5
C9023D-14X-cc, 27	102.3	7.7	0.0	5.2	18.2	18.2	41.7
C9023D-14X-cc, 41	102.4	34.0	3.8	2.8	0.2	0.2	1.5
C9023D-15X-cc, 25	109.2	31.5	3.3	3.9	0.3	0.3	2.3
C9023D-15X-cc, 34	109.3	32.2	4.7	4.5	0.1	0.1	2.7
C9023D-16X-cc, 14	118.6	35.5	3.6	3.5	0.1	0.1	1.8
C9023D-16X-cc, 47	119.0	32.1	3.9	4.7	0.1	0.1	2.2
Hole E							
C9023E-1x-cc, 10	125.1	32.0	4.7	1.2	0.9	6.9	5.6
C9023E-2x-cc, 7	135.1	22.1	1.8	3.3	0.4	20.0	1.1
C9023E-2x-cc, 32	135.3	15.2	7.7	22.7	0.2	0.0	4.0
C9023E-3x-cc, 10	144.1	12.0	4.6	17.3	0.4	13.4	2.7
C9023E-3x-cc, 26	144.3	12.3	6.6	8.1	8.3	6.0	22.3
C9023E-4x-cc, 11	153.6	8.6	0.0	15.7	0.8	22.1	2.1
C9023E-4x-cc, 34	153.8	25.9	5.1	8.3	0.3	5.8	3.7
C9023E-5x-1, 10	163.1	5.8	2.6	11.2	13.8	1.3	36.6
C9023E-5x-cc, 19	163.3	10.9	5.2	23.8	5.2	0.0	19.6
C9023E-5x-cc, 28	163.4	13.8	7.7	23.2	0.3	0.0	8.8
C9023E-6x-cc, 12	172.6	14.2	0.0	17.2	0.7	5.4	1.9

Table 5-3-5-8

Location	Subbottom Depth [mbsf]	Major element (wt%)					
		Si	Al	Fe	Ca	K	S
C9023E-8x-cc, 5	189.5	33.3	4.4	1.7	0.1	7.2	1.8
C9023E-9x-1, 9	199.1	24.0	2.4	5.6	0.5	9.1	1.4
C9023E-9x-1, 47	199.5	26.7	5.0	3.4	3.9	3.0	13.3
C9023E-9x-cc, 6	200.0	31.1	7.2	2.5	0.1	4.8	0.4

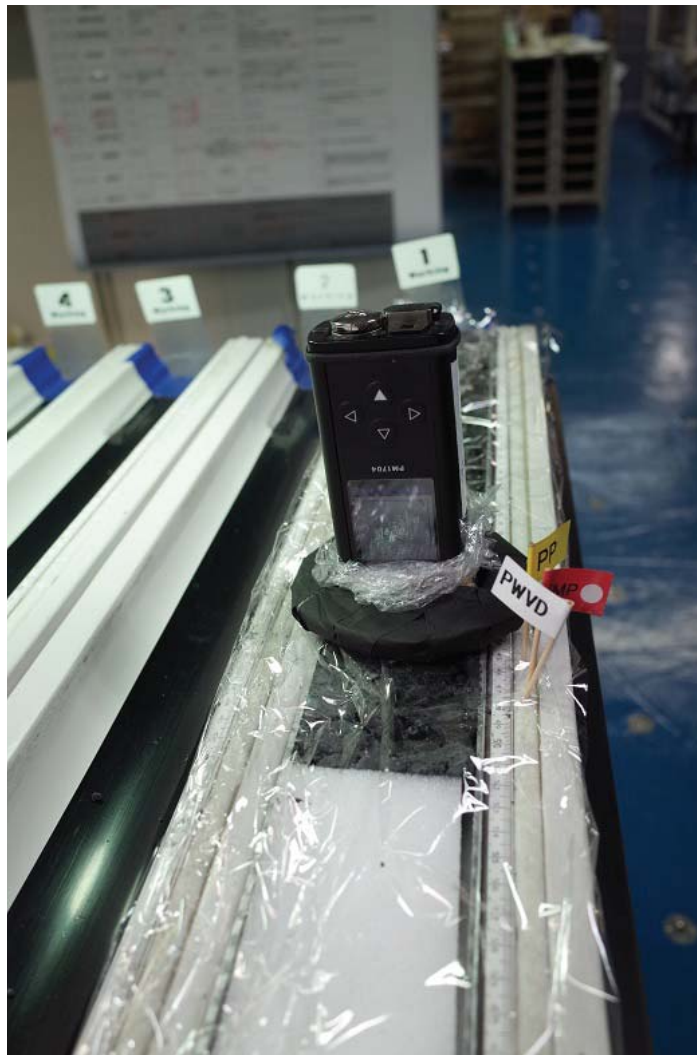
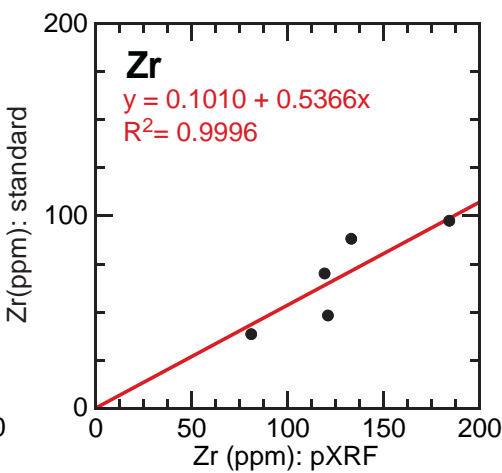
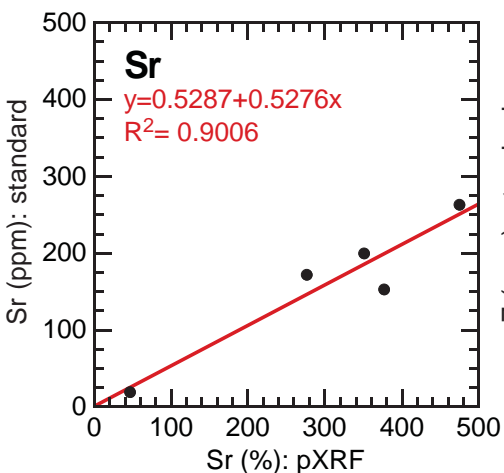
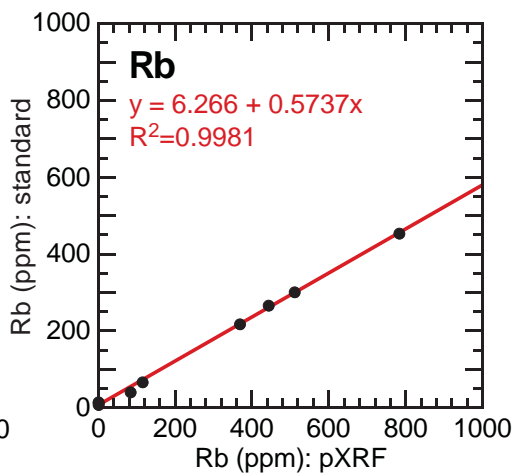
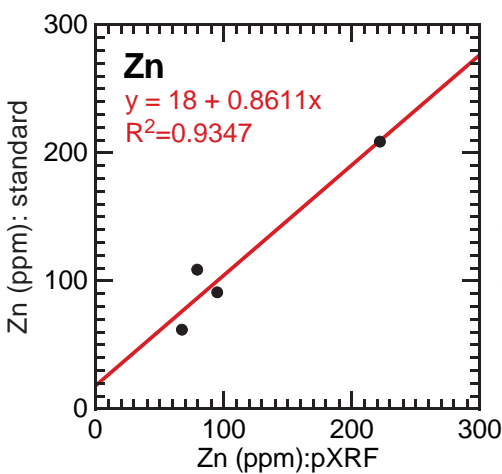
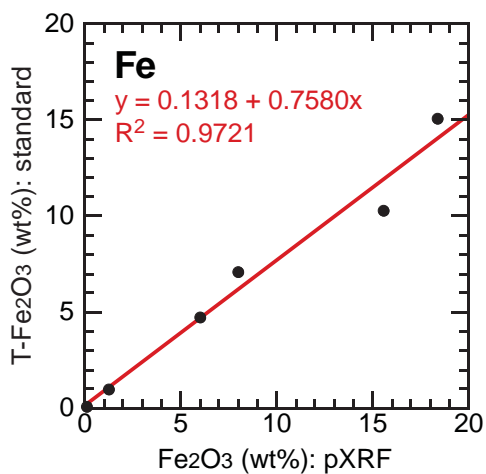
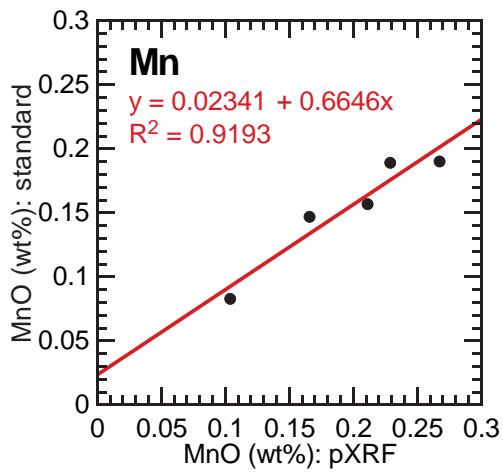
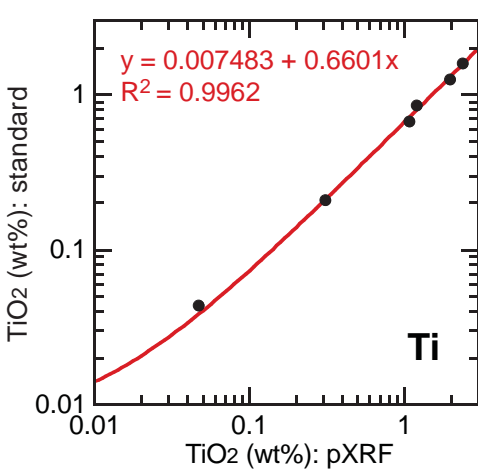
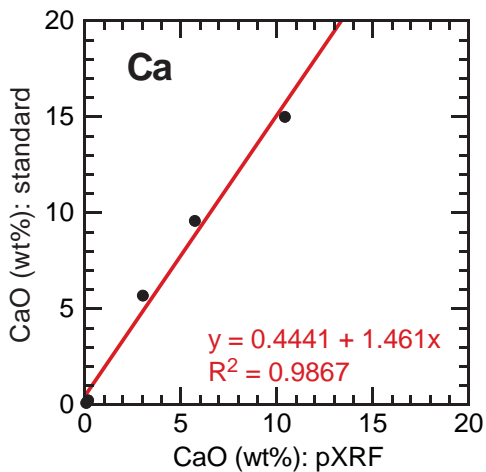
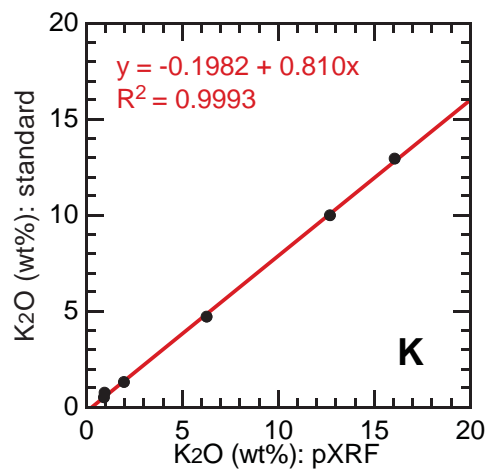
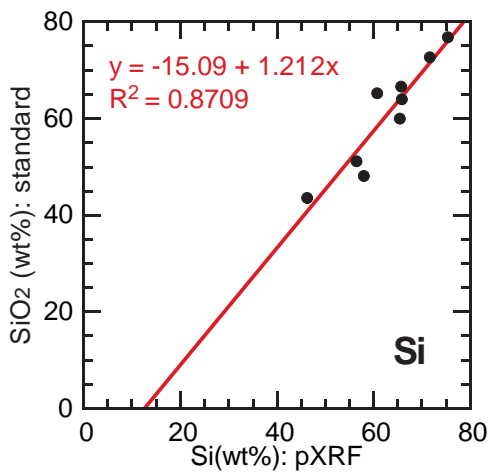
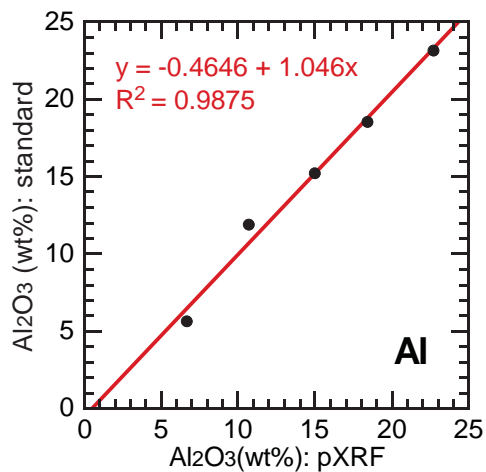


Figure 5-3-1-1



Figure 5-3-1-2



C9017

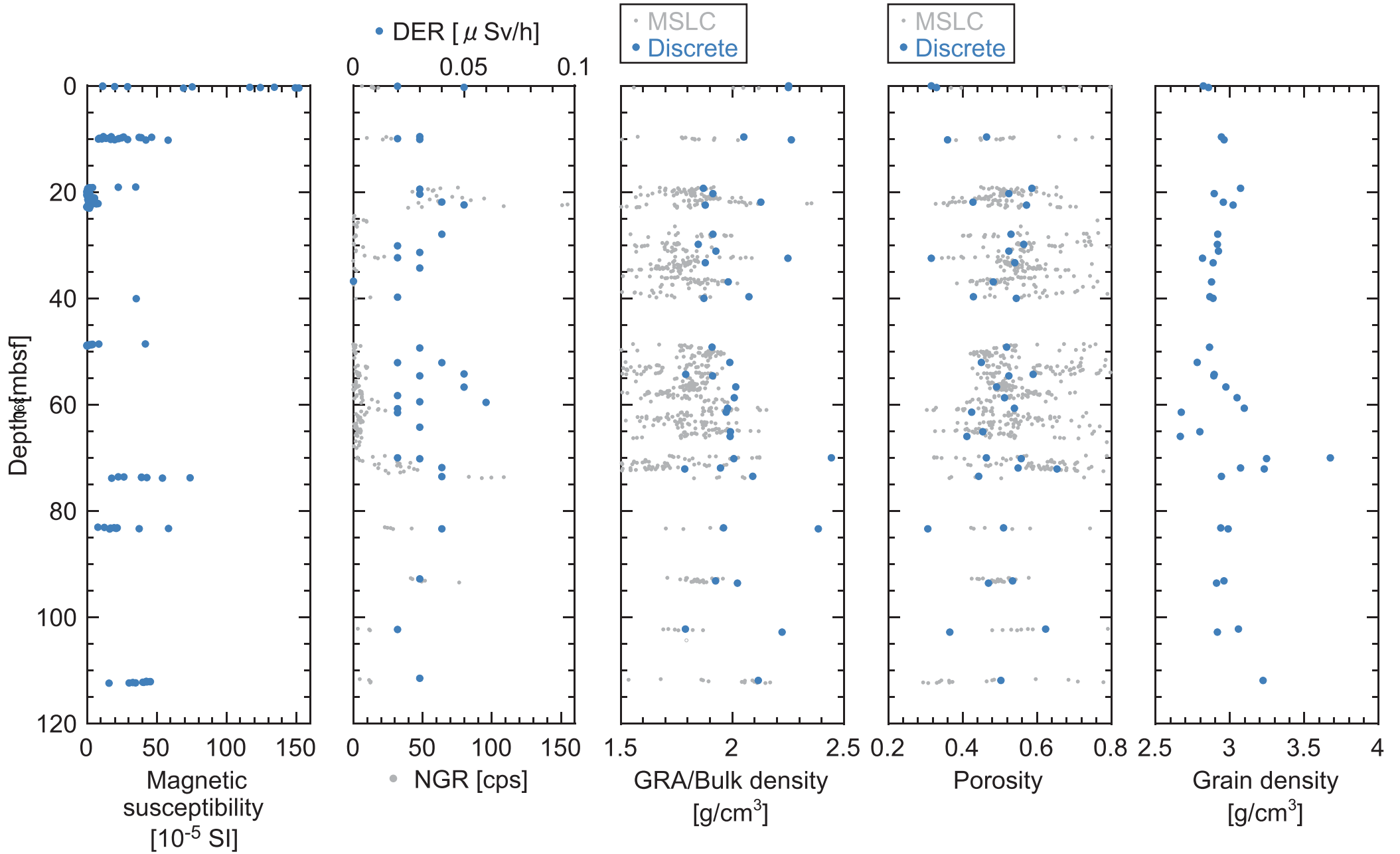


Figure 5-3-2-1

C9017

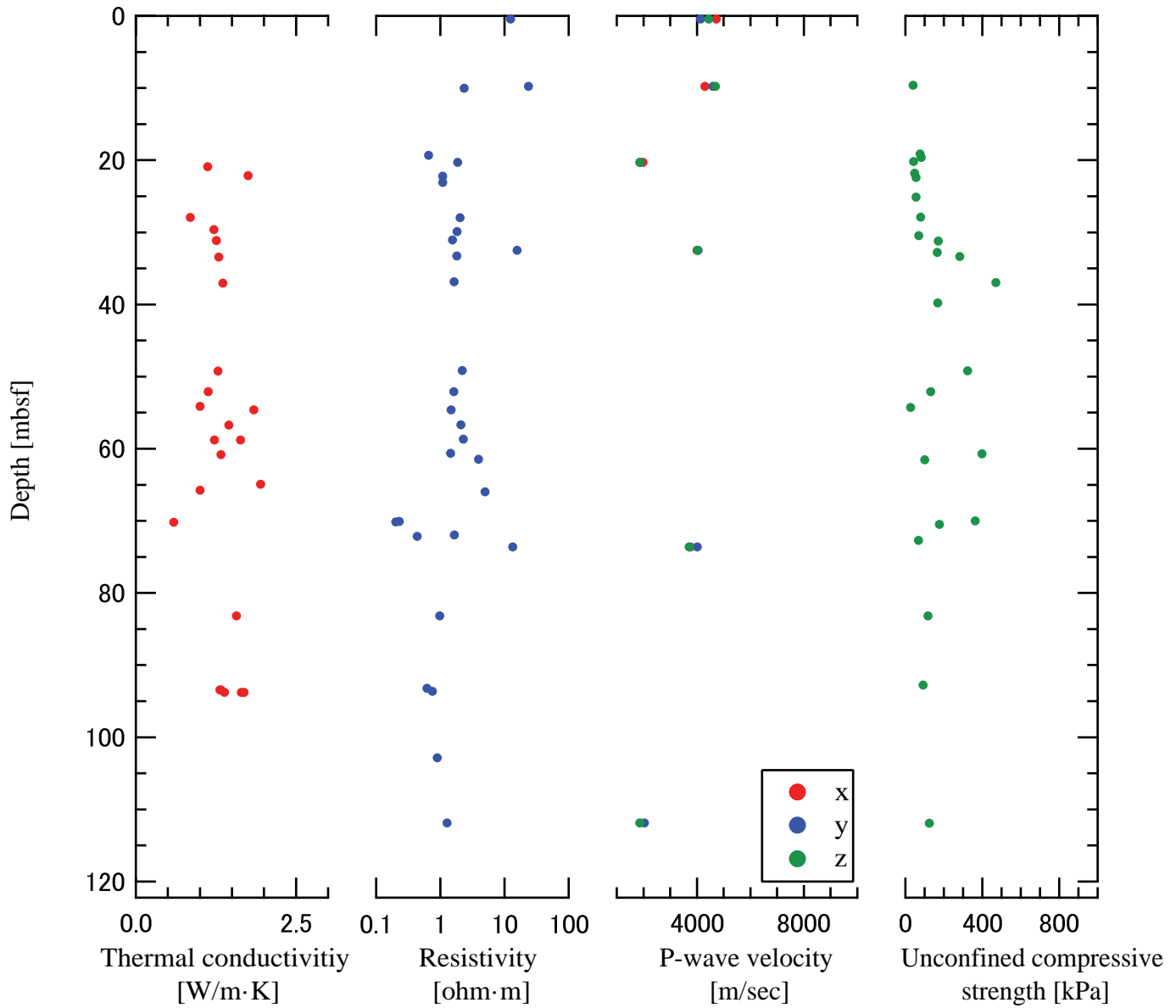


Figure 5-3-2-2

C9017

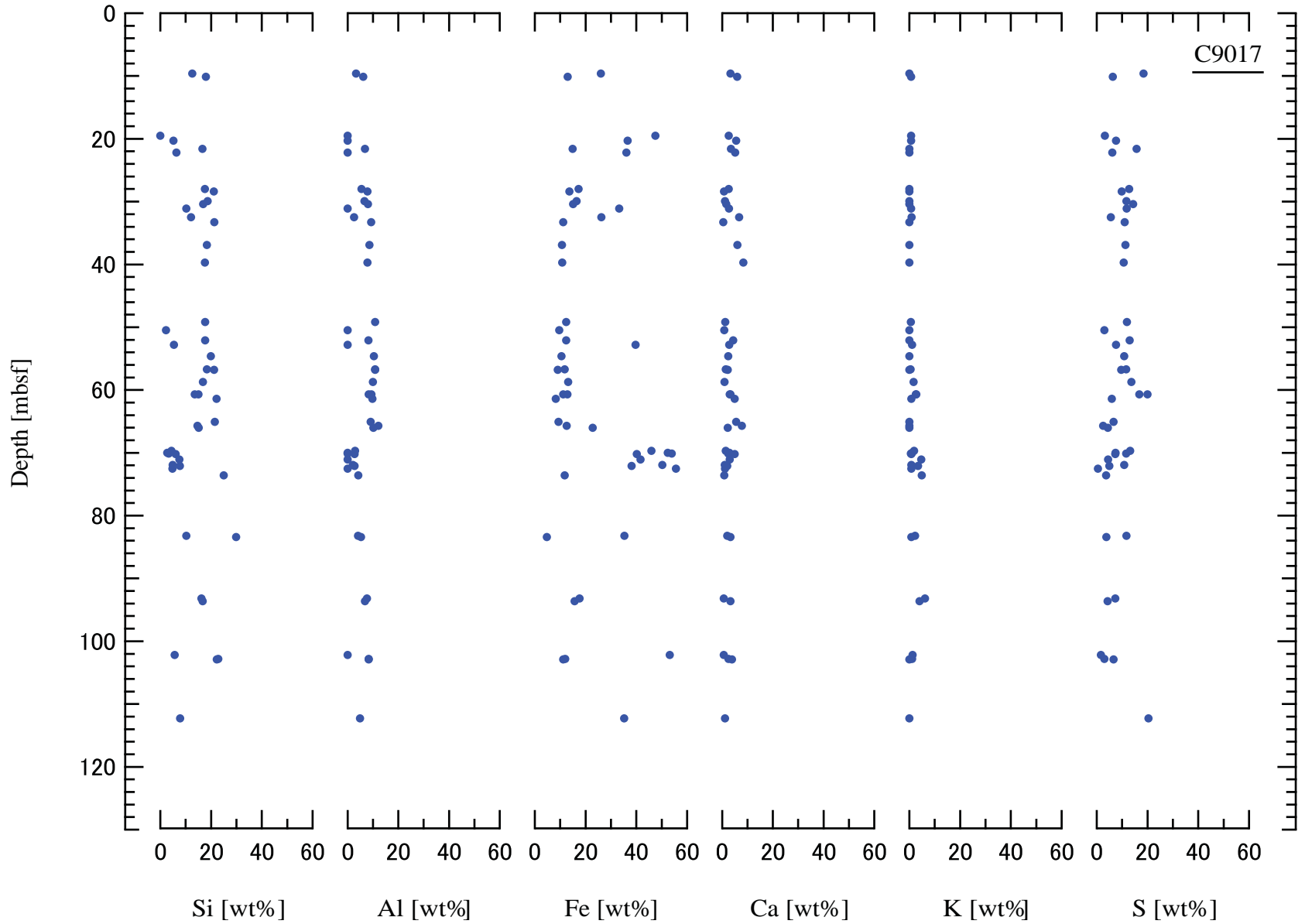


Figure 5-3-2-3

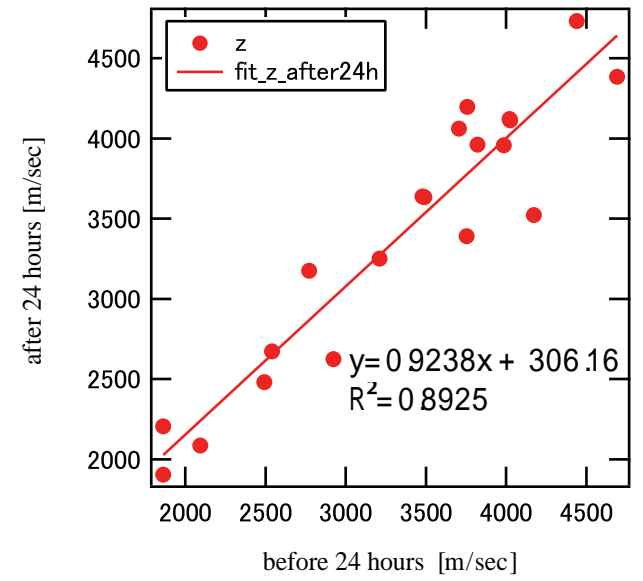
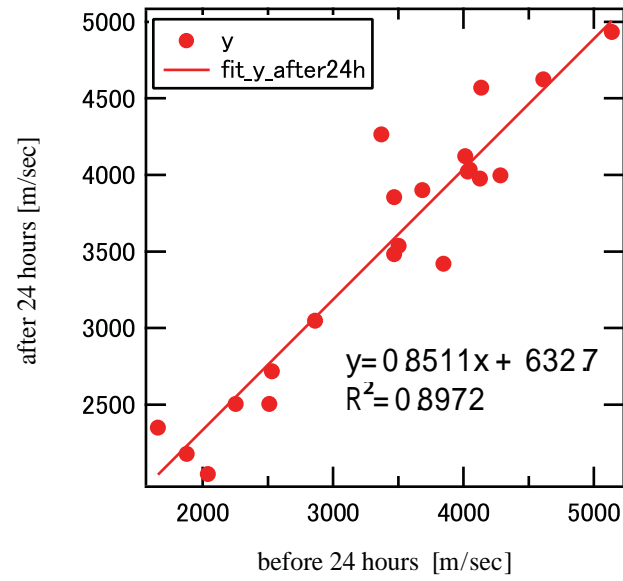
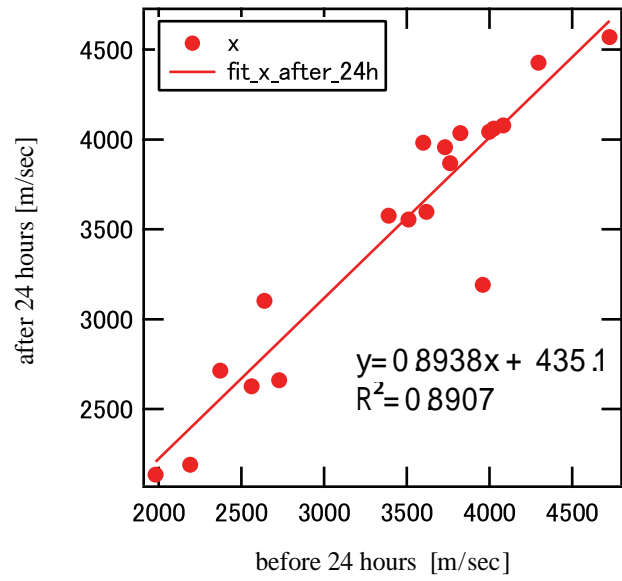


Figure 5-3-2-4

C9019

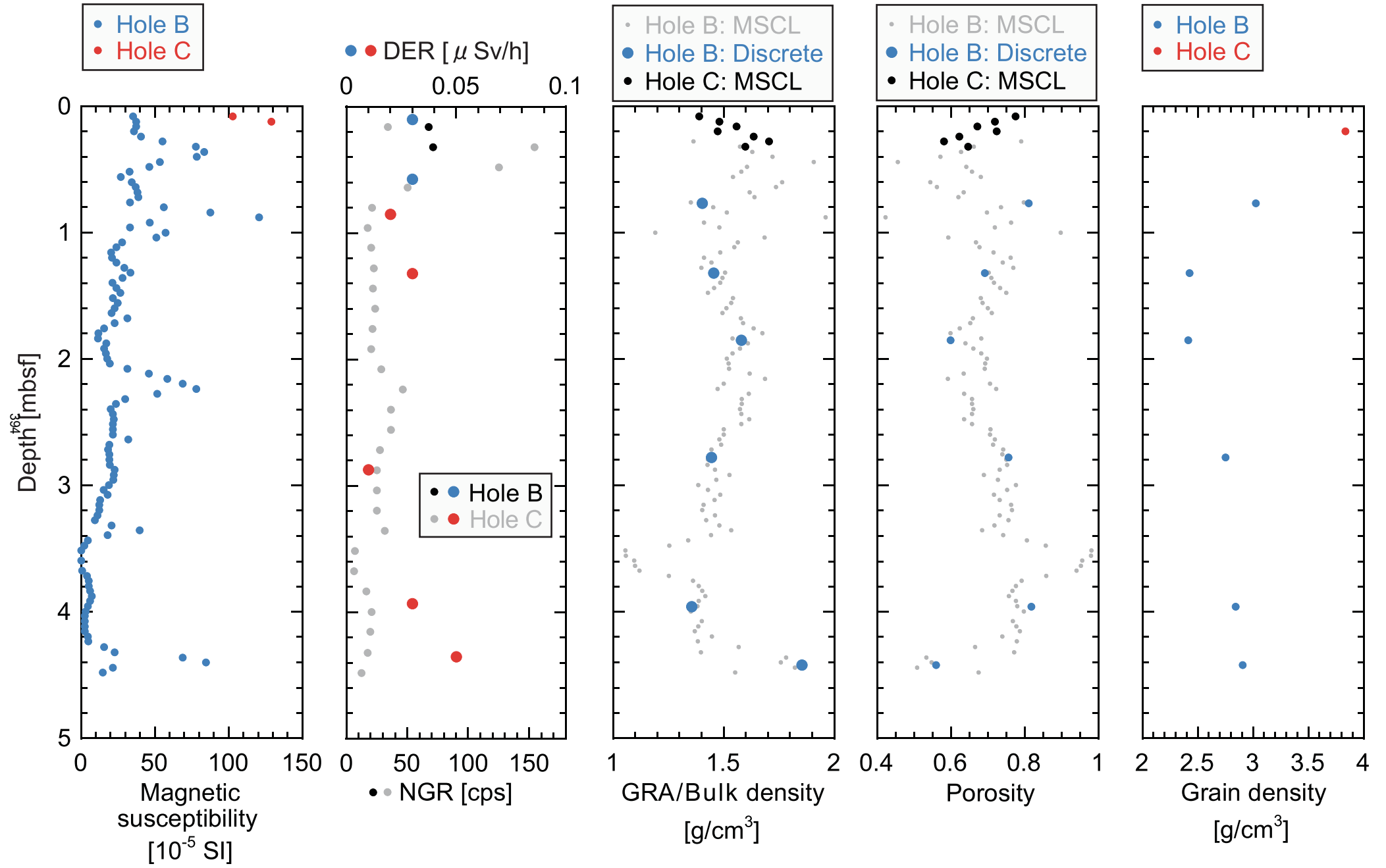


Figure 5-3-3-1

C9019

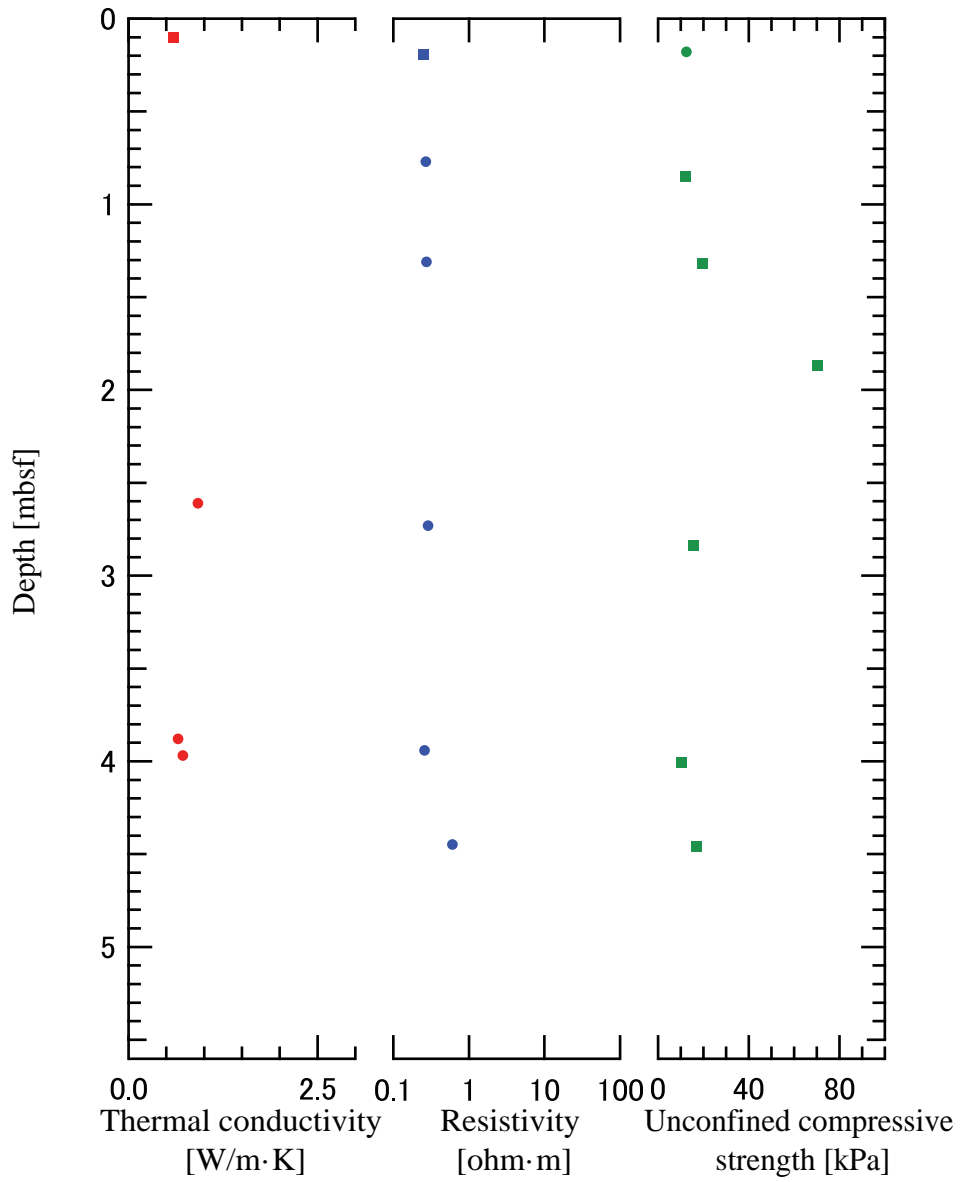


Figure 5-3-3-2

C9019

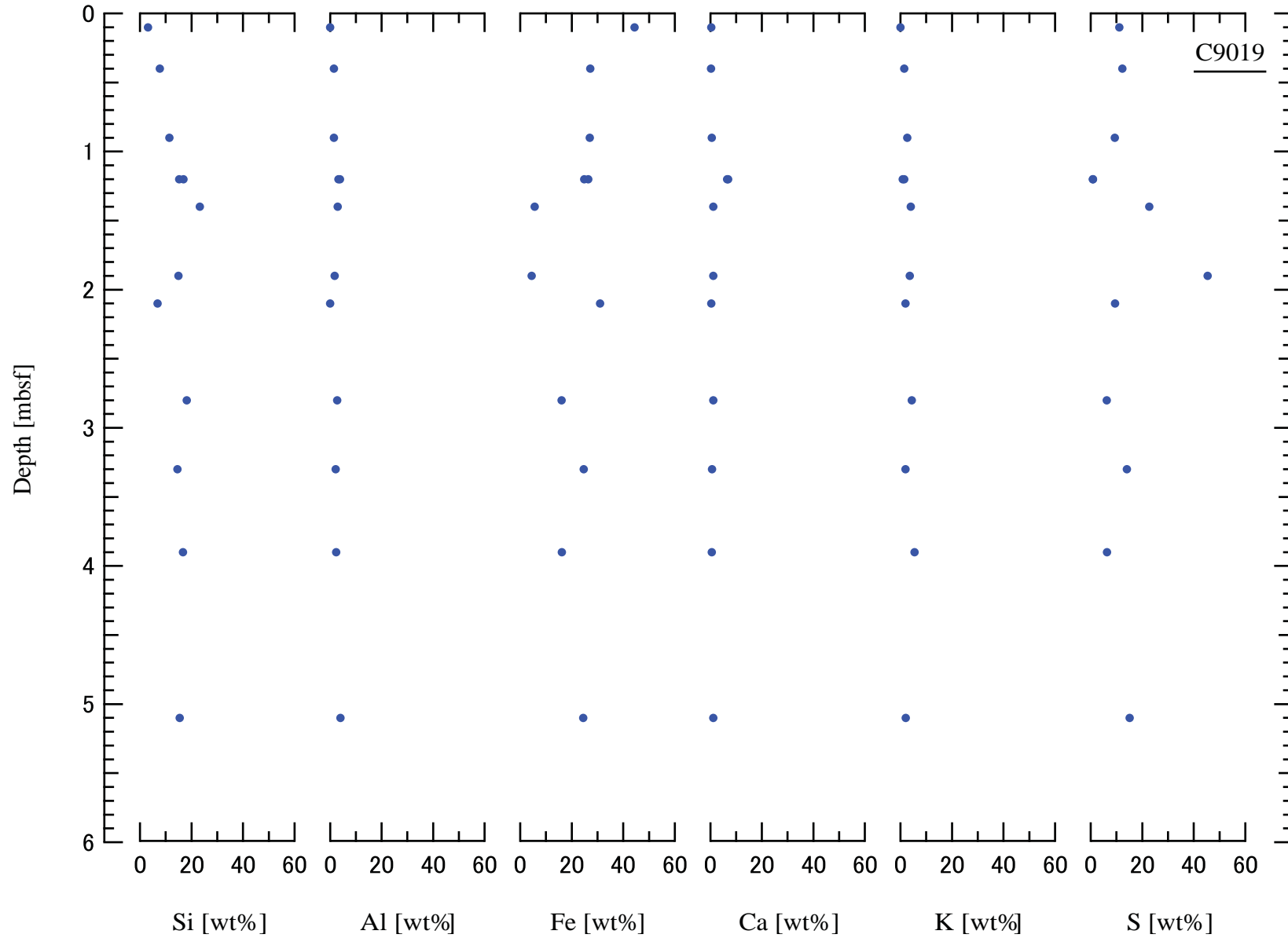


Figure 5-3-3-3

C9021

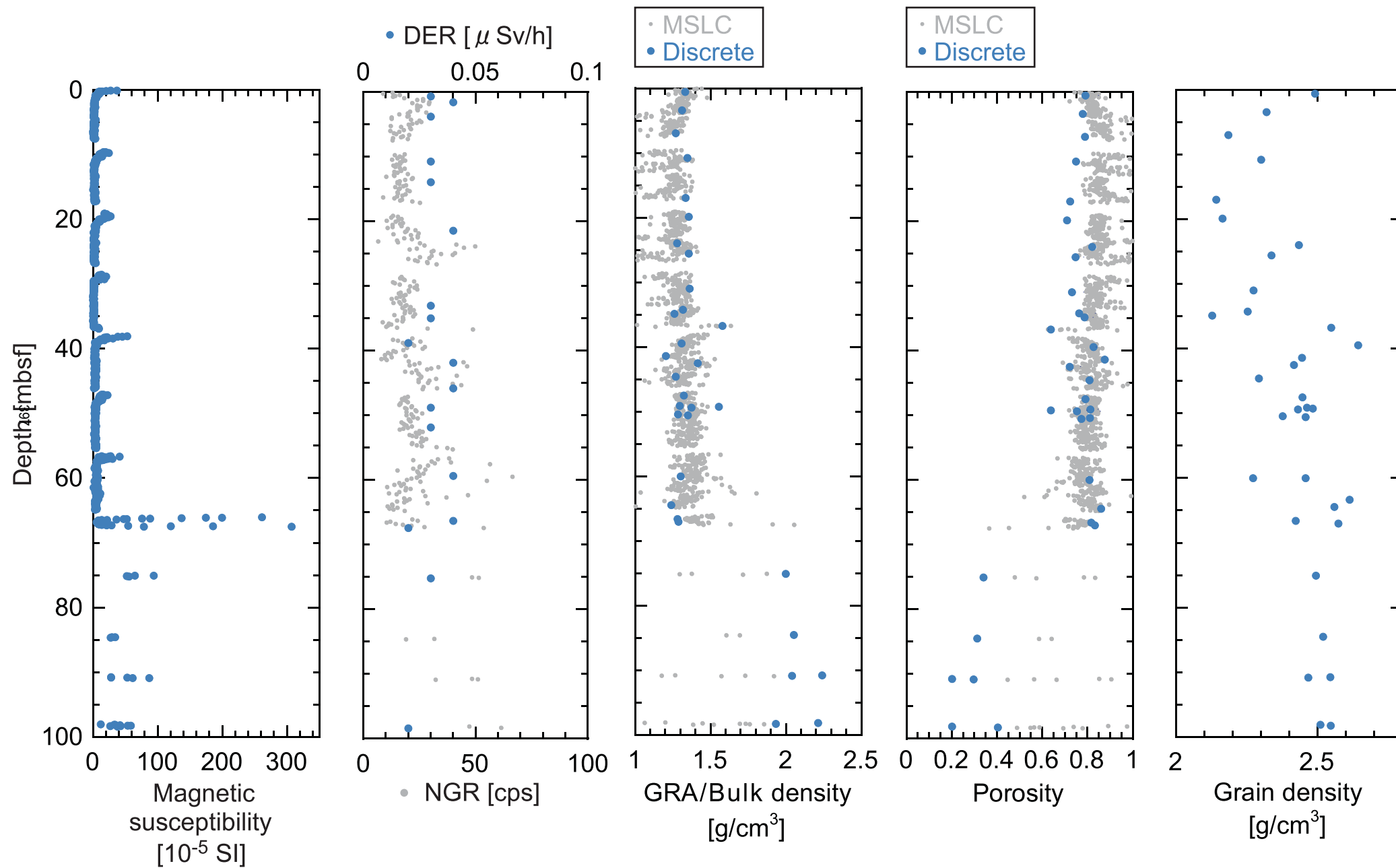


Figure 5-3-4-1

C9021

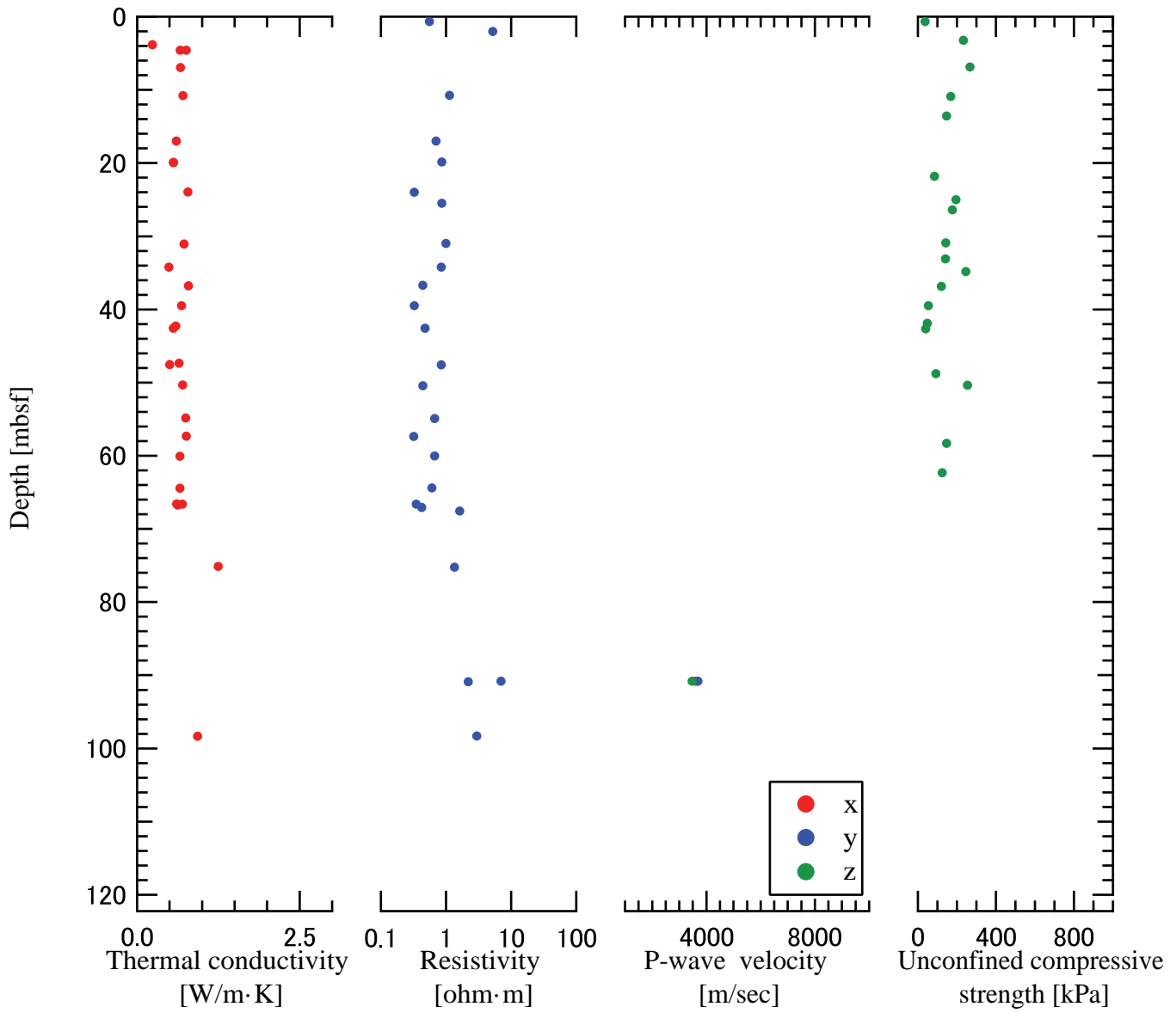
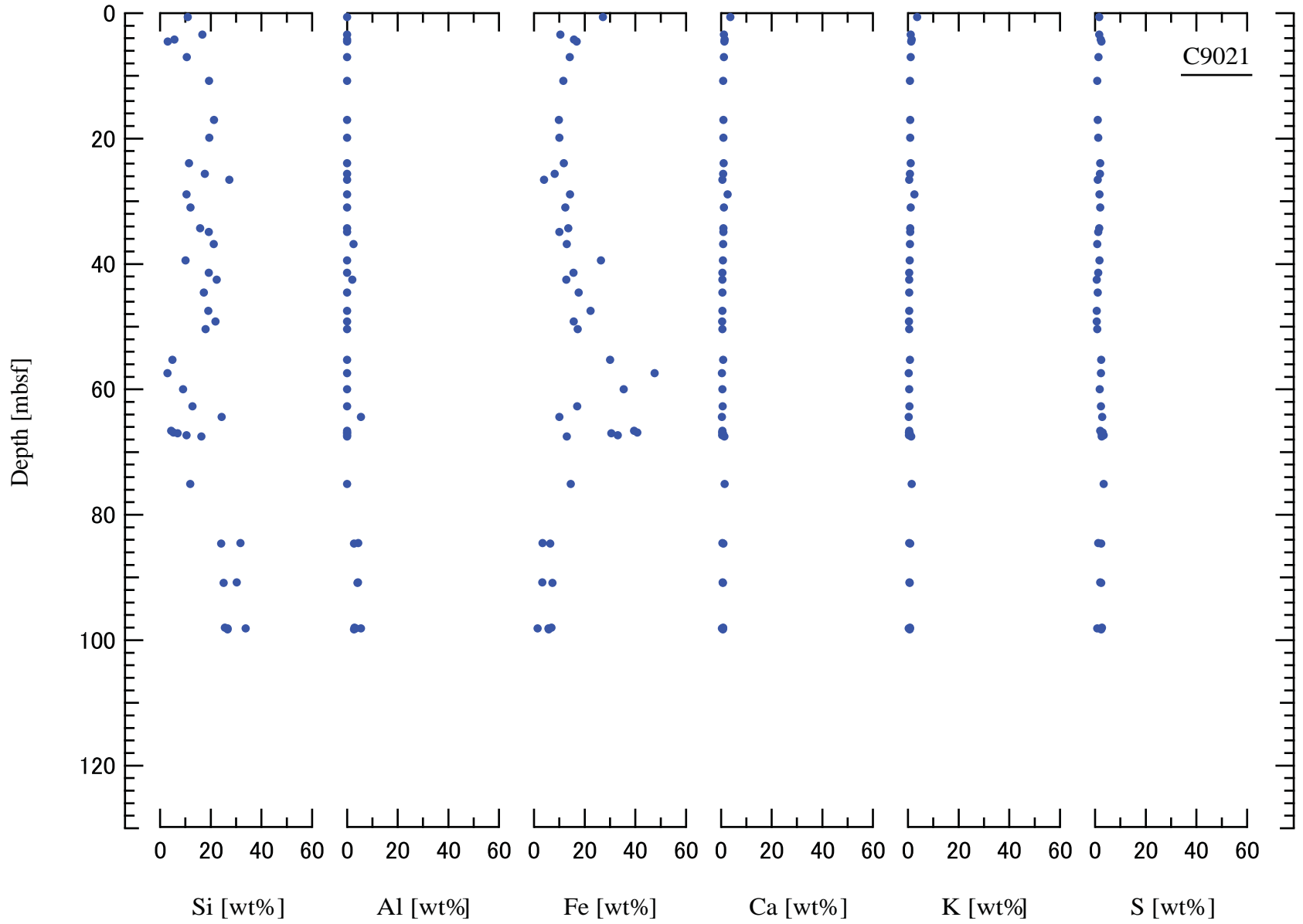


Figure 5-3-4-2

C9021



398

Figure 5-3-4-3

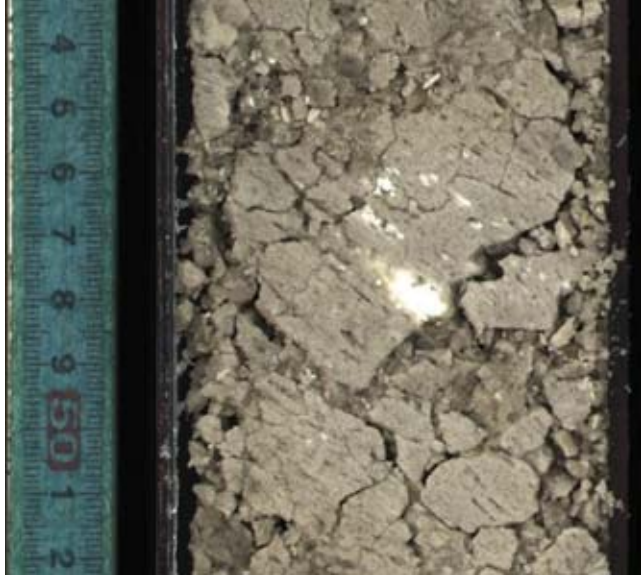


Figure 5-3-4-4

C9023

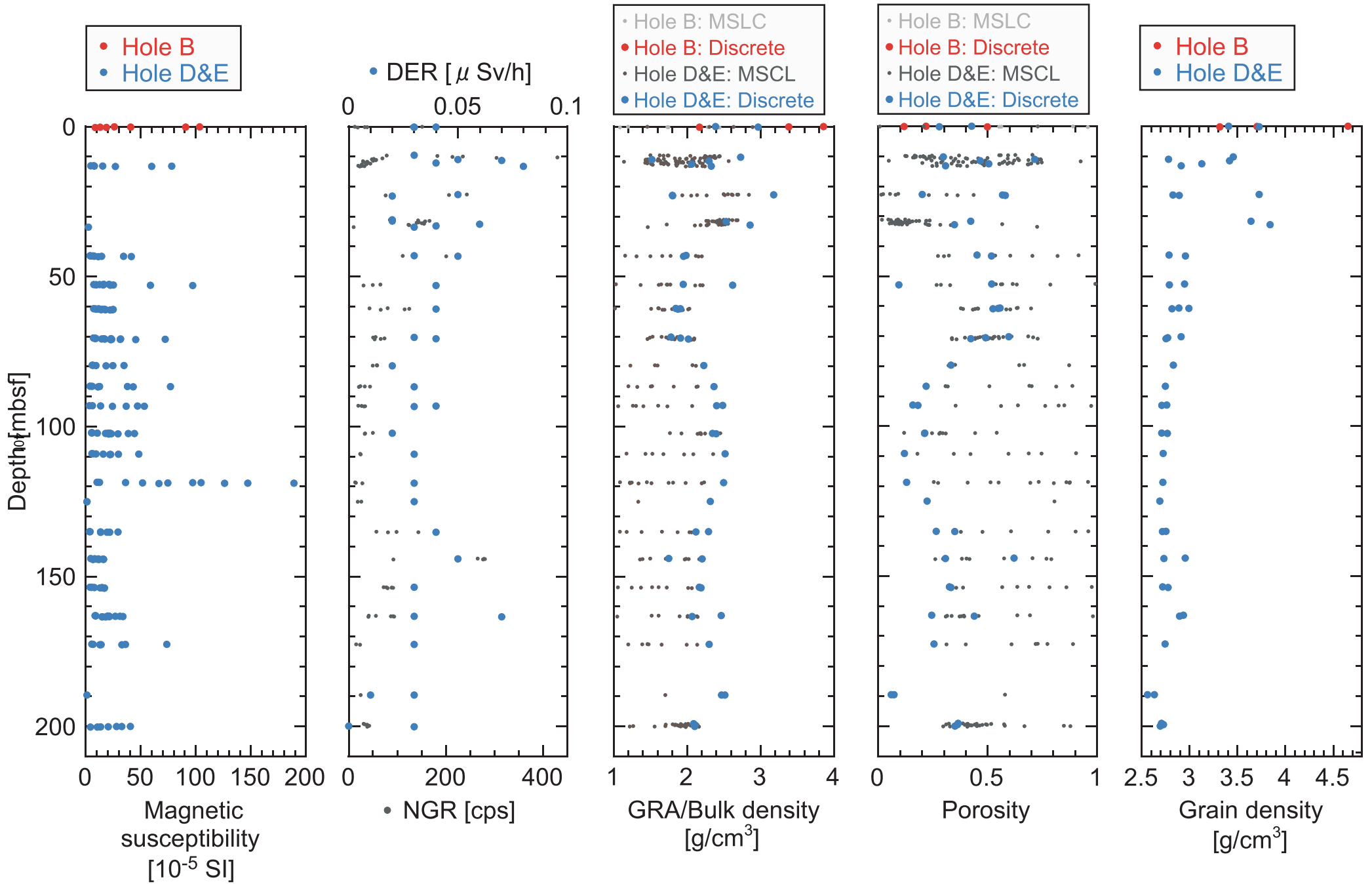


Figure 5-3-5-1

C9023

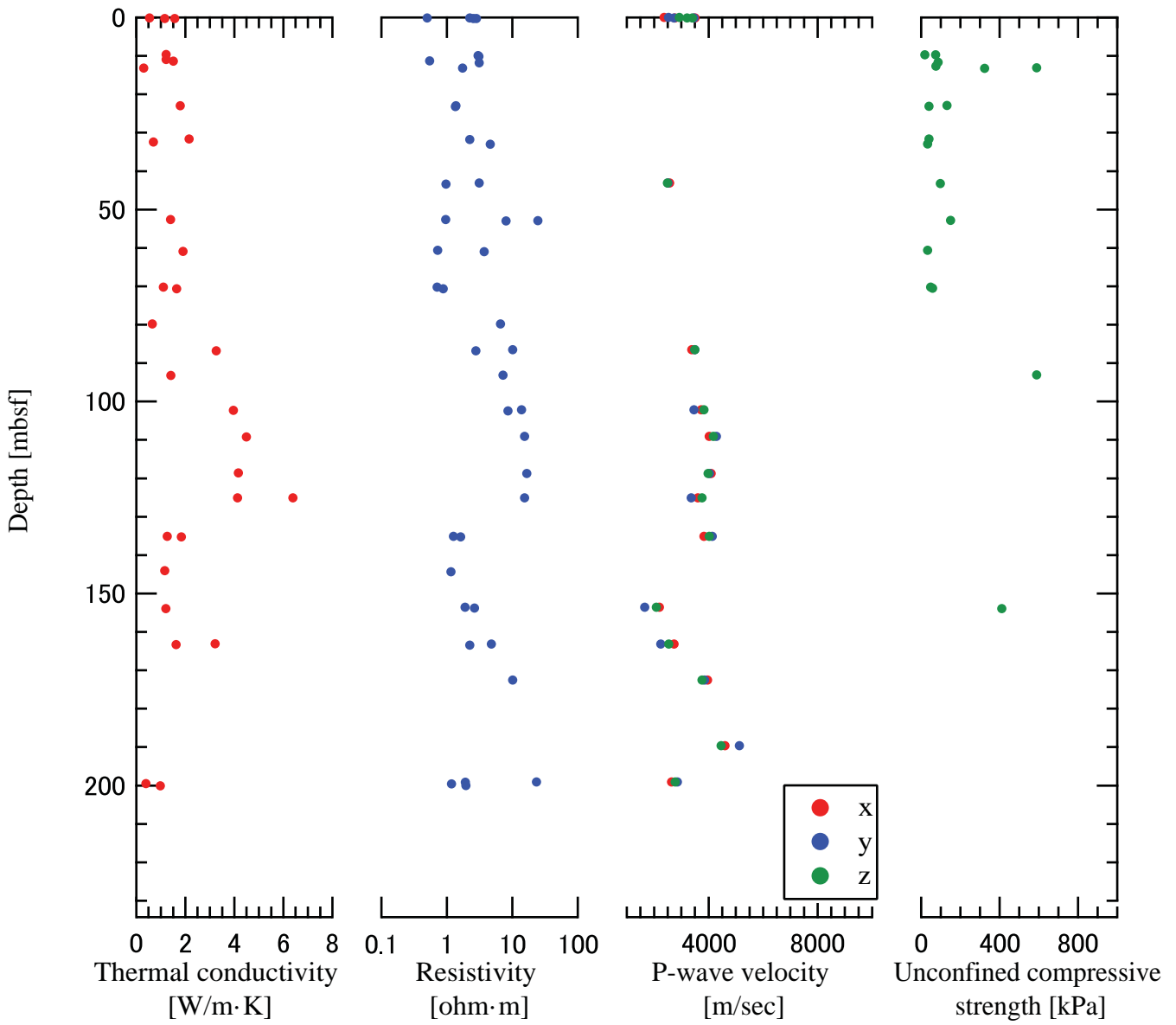
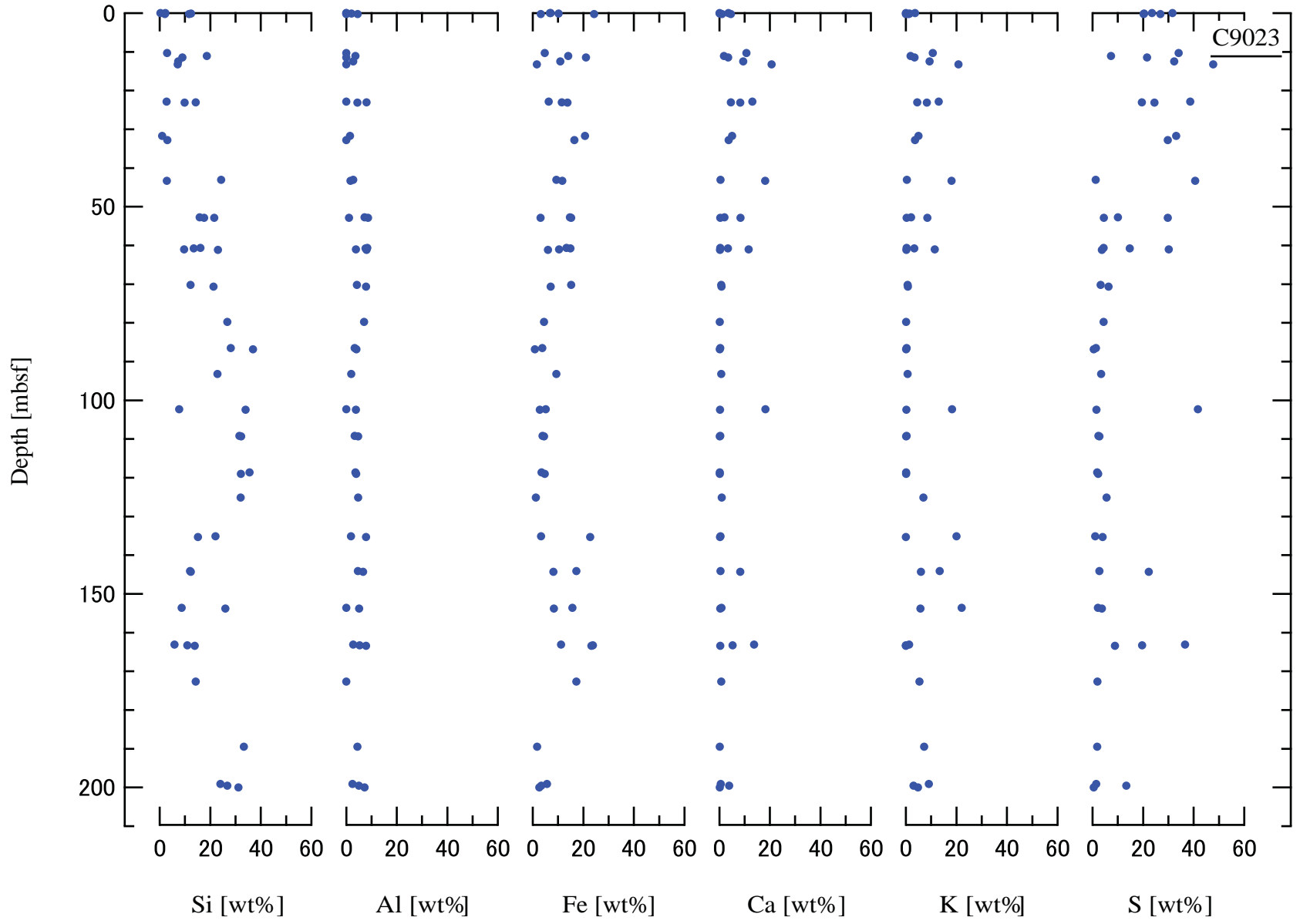


Figure 5-3-5-2

C9023



403

Figure 5-3-5-3

5. 4 Interstitial water

T. Toki and IW Team

5.4.1 Interstitial water extraction

After core recovery, a core liner up to 9.5 meters was cut off at 1 m long on the Lab. Roof Deck. When a plastic liner was used, holes at the side of the core liner were drilled at intervals of 30 cm. H₂ sensor was inserted into the holes to measure dissolved H₂ concentrations in interstitial waters in the cored sediments (see Chapter 6 in a detail). When we drilled seafloor close to hydrothermal vents, we used an aluminium (Al) liner for a heat tolerance. We drilled holes at the side of the Al liner for the H₂ sensor in advance in using the ESCS coring system, but we quit the H₂ sensor analysis in using the HPCS system. The sectioned cores were then moved to the Core Processing Deck, and scanned by using X-ray computed tomography (CT). Subsequently, a density, magnetic susceptibility, and natural gamma ray (NGR) of all sectioned cores were measured by using Multi-Sensor Core Logger (MSCL). The whole-round core (WRC) samples for interstitial water (IW) analysis were selected from the core sections based on the CT-scan images and direct observations with the representatives of the visual core description (VCD) and microbiology groups. The WRC samples must be a homogeneous and dense 10–25 cm long part of the sediments just above or below those for microbial and gas analyses. Generally, two samples were selected for IW analysis in each core sample. The selected sample for IW analysis was cut off from the core section, together with its liner, by using a cutter. After cutting, the top and bottom of the cut liner were immediately sealed by plastic caps, and then the sample was moved to the Lab. Street Deck. In the Lab. Street Deck, the outer surface of the sample were scraped off in a N₂-filled anaerobic glove bag to avoid contamination of injected fluids for drilling. The scraped sample was squeezed in a titanium cylinder (Manheim, 1966) by using manual- and automatic-type oil pressure pumps under ca. 100–170 atm at room temperature. The interstitial water (< 90 cc) in the sediment sample was filtered through two titanium meshes and a filter paper in the cylinder, poured out from a hole in the bottom part of the cylinder, and collected in a syringe. The IW sample was then filtered through a disposable filter (a pore size: 0.45 μm), and distributed into several plastic bottles for geochemical analyses. An aliquot of the sample water was acidified with HCl to be 1 vol% of 6N HCl to stably dissolve cations and minor and trace metal ions. Another aliquot of the sample was stored in a requested temperature without further treatment for the analyses of major anions and water isotopic compositions. A part of the sample was used for measurements of salinity, pH, alkalinity, nutrients, and hydrogen sulfide (H₂S) on board according to the method in next section.

5.4.2 Analytical method

5.4.2.1 Salinity

Salinity of interstitial water was determined with a refractometer (Atago RX-5000i, Tokyo, Japan) using three drops of water sample (~100 μL). Before measurement of salinity, the refractometer was calibrated with International Association for the Physical Sciences of the Oceans (IAPSO) standard seawater; the refraction index was ranged between 1.33943 and 1.33947.

5.4.2.2 pH and alkalinity

For pH and alkalinity analyses, a 3 mL aliquot of unacidified water sample was analyzed with an automatic titrator (794 Basic Titrino, Metrohm-Sibata, Herisau, Switzerland) and pH and alkalinity were determined by the Gran plot method (Gieskes et al., 1991). Before analysis, pH meter was calibrated using Tris (8.200) and Bis (8.934) buffered solutions, which were prepared using artificial seawater. The accuracy of the alkalinity was checked by comparison with results of analyses of sodium carbonate solution (alkalinity 100 mM) and sodium bicarbonate solution (alkalinity 50 mM); precisions were 0.01% and 3% for the sodium carbonate and sodium bicarbonate solutions, respectively.

5.4.2.3 Chlorinity

Chlorinity was measured on a 100 μL aliquot by potentiometric titration using a Metrohm autotitrator and silver nitrate (AgNO_3) as a titrant in 30 mL of 0.2 M sodium nitrate (NaNO_3) solution. Relative standard deviation (RSD) for chlorinity was better than $\pm 0.2\%$, based on repeated analyses of International Association for the Physical Sciences of the Oceans (IAPSO) standard seawater, which were conducted between the measurements of every 5 samples.

5.4.2.4 Nutrients

Concentrations of silica (Si), ammonium (NH_4^+), nitrite (NO_2^-), and nitrate ions (NO_3^-) were measured by colorimetry using AQ2 Discrete Analyzer (SEAL Analytical, Inc.). For the Si analysis, the molybdate blue method was used (Presley, 1971). For the NH_4^+ analysis, the phenol blue method (Gieskes et al., 1991). The NO_2^- was colored by Griess reagents, and the NO_3^- was reduced to NO_2^- to measure the concentration as NO_2^- (García-Robledo et al., 2014). The aliquot for each analysis was 300, 200, 200, and 180 μL for Si, NH_4^+ , NO_2^- , and NO_3^- analysis, respectively. The colored solution was flowed through a cuvette, and measured the absorbance at 880 nm for Si, 620 nm for NH_4^+ , 546 nm for NO_2^- , and 520 nm for NO_3^- . The precisions were within 12% (Si), 12% (NH_4^+), 10% (NO_2^-), and 4% (NO_3^-).

5.4.2.5 H_2S

H_2S concentration was analyzed by the mixed diamine method (Cline, 1969) using spectrophotometer (HACH DR2800). Interstitial water samples of 2 mL were mixed with the diamine coloring reagent (dissolved N,N-dimethyle-p-phenylenediamine

sulfate and ferric chloride in HCl matrix) of 200 μ L. After 2 minutes, the absorbance was measured at 670 nm in a cuvette. A standard solution was 10 mM Na₂S solution, which had been calibrated in advance at on-land laboratory. The analytical precision was within 4%.

5.4.3 Analytical results

Noho Site

In the Noho Site, we collected interstitial water samples from C9019B and C9017C, and the analytical results are shown in Table 5-4-3-1. The vertical profiles of these chemical compositions are shown in Fig. 5-4-3-1. From C9019B, we took only two samples, and the chemical compositions are mostly same as that of seawater. From C9017C, we collected samples from the intervals between 19.8 mbsf and 102.4 mbsf. Salinity showed extremely low value at 62.5 mbsf and slightly high values below 72.3 mbsf relative to that of seawater. The pH values are relatively constant between 20 and 70 mbsf, but the values below 70 mbsf are slightly lower than those above 70 mbsf. The alkalinity was very high between 20 and 62.5 mbsf, but they are relatively low values below 65.4 mbsf. The chlorinity is lower than that of seawater from 20 to 56.1 mbsf, showed the lowest value at 62.5 mbsf, and they are higher than that of seawater below 65.4 mbsf. The Si concentrations are higher than that of seawater below 20 mbsf, and, especially, they showed two remarkable peaks at 62.5 mbsf and 72.3 mbsf. The NH₄⁺ concentrations gradually increased with depth. The H₂S concentrations are relatively high between 30 and 60 mbsf, and, especially, showed the extremely high value at 62.5 mbsf. The NO₂⁻ and NO₃⁻ concentrations were relatively high between 20 and 70 mbsf.

Iheya North Knoll

Site C9021B

This Site was aimed to check the connection of the Natsu and Aki Sites in the Iheya North Knoll. Based on the LWD results during the former of this expedition, a layer of pumice would be distributed above ~60 mbsf, and high-temperature fluids would be distributed below the boundary of ~60 mbsf. Additionally, based on the seismic data, fluids would be distributed below ~100 mbsf (Tsuji et al., 2012). The analytical results are shown in Table 5-4-3-1 and Fig. 5-4-3-2. As a lithology, pumice was distributed above ~40 mbsf, greenish clay was distributed from ~40 to ~65 mbsf, and altered volcanic rock was distributed below ~65 mbsf. As an interstitial water chemistry, the salinity and chlorinity decreased, and the Si and NO₃⁻ concentrations and pH value increased around 30 mbsf. Between 40 and 60 mbsf, the alkalinity and the Si and H₂S concentrations increased. The NO₃⁻ concentration decreased with depth from 0 to 10 mbsf.

Site C9023D & E

These Sites were aimed to confirm LWD data by the lithological observation, and find hydrothermal paths and their structural constraints. First, we drilled at Site

C9023D, close to Site C9023A for LWD operation. When the drill bit reached to a depth of 127 mbsf at Site C9023D, however, a bit accident occurred and we had to abandon the hole. To get drill core samples from deeper than 127 mbsf in the same area, we chose the alternative Site C9023E. At Site C9023E, the total depth of the drilling was 208.5 mbsf and the drill bit possibly reached to a hydrothermal fluid reservoir. The analytical results of IWs at Site C9023D and E are shown in Table 5-4-3-1 and Fig. 5-4-3-3. From the seafloor to ca. 40 mbsf, the salinity and Cl^- concentration gradually increase with depth. Around 40 mbsf, the NH_4^+ concentration increases up to 3 mM. Between 40 and 200 mbsf, the salinity, Cl^- concentration, and pH value are rather constant. Between 60 and 80 mbsf, the NO_3^- concentration increases up to 100 μM .

REFERENCES:

- Cline, J. D. (1969) Spectrophotometric determination of hydrogen sulfide in natural waters. *Limnology and Oceanography*. **14**, 454-458.
- García-Robledo, E., Corzo, A. and Papaspyrou, S. (2014) A fast and direct spectrophotometric method for the sequential determination of nitrate and nitrite at low concentrations in small volumes. *Marine Chemistry*. **162**, 30-36.
- Gieskes, J. M., Gamo, T. and Brumsack, H. (1991) Chemical methods for interstitial water analysis aboard JOIDES Resolution. Ocean Drilling Program Texas A&M University Technical Note. **15**, 1-60.
- Manheim, F. T. (1966) A hydraulic squeezer for obtaining interstitial water from consolidated and unconsolidated sediments. Geological Survey Professional Paper (United States). **550**, 256-261.
- Presley, B. J. (1971) Techniques for analyzing interstitial water samples. Appendix Part 1: Determination of selected minor and major inorganic constituents. Initial Reports, DSDP (Winterer, E. L., et al. ed.), 1749-1755, U.S. Govt. Printing Office.
- Tsuji, T., Takai, K., Oiwane, H., Nakamura, Y., Masaki, Y., Kumagai, H., Kinoshita, M., Yamamoto, F., Okano, T. and Kuramoto, S. i. (2012) Hydrothermal fluid flow system around the Iheya North Knoll in the mid-Okinawa trough based on seismic reflection data. *Journal of Volcanology and Geothermal Research*. **213–214**, 41-50.

Captions:

Table 5-4-3-1: Analytical results for interstitial water from the Noho site and Iheya North Knoll during Exp. 908. mbsf = meters below seafloor.

Fig. 5-4-3-1: Depth profiles of (a) salinity, (b) pH, (c) alkalinity, (d) chlorinity, (e) Si concentration, (f) NH_4^+ concentration, (g) H_2S concentration, (h) NO_2^- concentration, and (i) NO_3^- concentration in interstitial water from the Noho site. The dashed lines indicate the value of seawater.

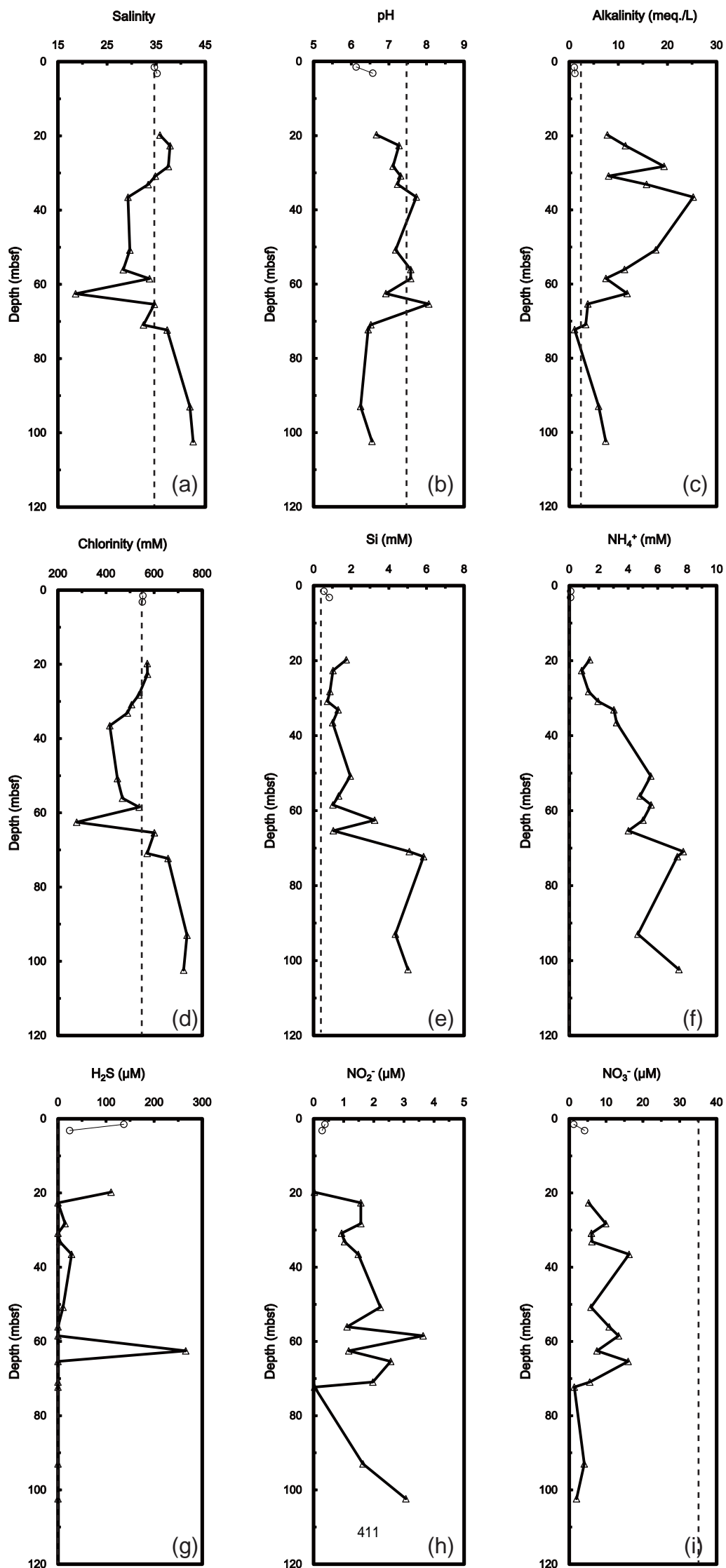
Fig. 5-4-3-2: Depth profiles of (a) salinity, (b) pH, (c) alkalinity, (d) chlorinity, (e) Si concentration, (f) NH_4^+ concentration, (g) H_2S concentration, (h) NO_2^- concentration, and (i) NO_3^- concentration in interstitial water from Site C9021B in the Iheya North Knoll. The dashed lines indicate the value of seawater.

Fig. 5-4-3-3: Depth profiles of (a) salinity, (b) pH, (c) alkalinity, (d) chlorinity, (e) Si concentration, (f) NH_4^+ concentration, (g) H_2S concentration, (h) NO_2^- concentration, and (i) NO_3^- concentration in interstitial water from Site C9023D and C9023E in the Iheya North Knoll. The dashed lines indicate the value of seawater.

Table 5-4-3-1 Analytical results for interstitial water from the Noho site and Iheya North Knoll during Exp. 908. mbsf = meters below seafloor.

Exp-Hole- Core-section, interval (cm)	Depth (mbsf)	Salinity (refractive index)*	pH	Alkalinity (meq./L)	Chlorinity (mM)	Si (mM)	NH ₄ ⁺ (mM)	H ₂ S (?M)	NO ₃ ⁻ (?M)	NO ₂ ⁻ (?M)
908-C9019B-										
1H-2, 44-54	1.5	34.6	6.13	1.0	553	0.55	0.10	137	1.2	0.4
1H-4, 10-20	3.2	35.2	6.57	1.2	551	0.83	0.09	24	4.2	0.3
908-C9017C-										
3X-1, 66-89	19.8	35.8	6.67	7.8	571	1.74	1.39	111	8.7	N.D.
3X-4, 60-67	22.7	37.8	7.27	11.4	573	1.03	0.85	N.D.	5.3	1.6
4H-5, 15-27	28.2	37.5	7.11	19.3	537	0.87	1.32	15	9.9	1.6
4H-7, 75-87	30.8	34.8	7.31	8.0	506	0.74	1.96	N.D.	6.1	0.9
5H-2, 30-33	33.1	33.4	7.23	15.8	489	1.30	3.03	4	6.2	1.0
5H-5, 60-73	36.5	29.3	7.73	25.3	416	1.01	3.22	28	16.2	1.5
7H-5, 45-68	50.8	29.6	7.18	17.6	448	1.95	5.53	11	5.9	2.2
8H-5, 30-53	56.1	28.3	7.58	11.3	468	1.33	4.80	N.D.	10.9	1.1
8H-7, 71-94	58.5	33.6	7.58	7.5	538	1.02	5.55	N.D.	13.4	3.6
9H-4, 0-23	62.5	18.6	6.92	11.8	278	3.24	5.00	266	7.5	1.2
9H-6, 82.5-105.5	65.4	34.6	8.06	3.8	601	1.05	4.02	N.D.	16.0	2.6
10H-2, 70.5-93.5	70.9	32.4	6.52	3.4	571	5.09	7.74	N.D.	5.6	2.0
11H-2, 21-35	72.3	37.2	6.45	1.1	658	5.85	7.34	N.D.	1.4	N.D.
14X-1, 35-60	93.0	41.9	6.25	6.0	737	4.35	4.66	N.D.	4.1	1.6
15X-1, 32-44	102.4	42.5	6.55	7.4	723	5.02	7.44	N.D.	2.0	3.1
908-C9021B-										
1H-2, 0-10	1.1	34.6	7.36	1.5	549	0.20	0.03	N.D.	30.2	0.3
1H-7, 0-10	6.1	34.6	7.27	1.3	551	0.27	0.05	N.D.	10.9	0.7
2H-2, 0-10	10.6	34.6	7.20	1.5	553	0.23	0.04	N.D.	2.8	0.4
2H-7, 0-10	15.4	34.5	7.20	1.4	551	0.22	0.03	N.D.	6.0	0.3
3H-2, 0-10	20.1	34.6	7.25	2.1	553	0.21	0.04	N.D.	4.2	2.0
3H-7, 0-10	25.1	34.6	6.97	1.9	548	0.24	0.03	N.D.	2.6	0.4
4H-1, 73-83	29.3	33.7	7.98	2.1	536	0.31	0.03	N.D.	23.1	0.4
4H-7, 0-10	34.6	34.6	7.49	1.9	552	0.15	0.03	N.D.	16.9	0.7
5H-2, 0-10	39.1	34.6	7.30	1.6	552	0.15	0.04	N.D.	7.1	1.9
5H-4, 0-10	41.1	34.6	7.27	1.5	552	0.20	0.04	N.D.	0.7	0.1
5H-5, 0-10	42.1	34.6	6.98	4.6	553	0.60	0.03	9	0.7	0.3
5H-7, 0-10	44.1	34.7	7.09	9.0	553	0.88	0.04	42	0.5	0.3
6H-2, 0-10	48.1	34.7	7.04	10.5	551	0.74	0.05	28	0.7	0.2
6H-5, 0-10	51.1	34.6	7.28	8.6	551	0.63	0.03	15	N.C.	1.5
6H-8, 0-10	54.3	34.6	7.23	11.2	551	0.59	0.04	26	1.6	N.D.
7H-2, 0-10	57.6	34.5	6.88	2.2	550	0.54	0.03	N.D.	4.8	0.6
7H-8, 20-30	63.8	34.6	7.25	2.3	551	0.41	0.04	N.D.	7.7	N.D.
8H-1, 40-50	66.5	34.2	7.25	2.7	543	0.43	0.02	N.D.	12.0	N.D.
908-C9023D-										
2H-2, 20-30	10.0	34.8	7.10	9.7	479	1.80	0.82	N.D.	0.9	1.8
2H-3, 35-45	11.1	34.1	7.16	14.9	466	2.92	0.91	2	4.3	1.6
4H-1, 5-15	22.6	39.6	7.47	—	—	—	—	—	—	—
5H-1, 14-29	31.2	38.7	6.59	9.0	541	1.05	0.14	N.D.	0.3	1.5
5H-1, 76-96	31.9	39.0	7.33	3.1	553	0.20	0.12	N.D.	15.4	1.4
7X-CC, 35-40	43.4	43.2	7.21	14.9	648	1.67	2.84	N.D.	8.0	4.0
8X-CC, 21-26.5	52.7	39.7	6.97	11.1	629	2.75	1.18	N.D.	6.5	2.0
9X-CC, 36.5-44	61.1	40.7	7.35	6.0	656	2.04	1.46	N.D.	24.0	5.8
10X-CC, 55-65	71.1	43.7	7.77	—	686	—	—	—	—	—
11X-CC, 8-16	79.6	40.6	7.32	5.5	614	0.80	1.47	N.D.	102.2	2.5
12X-CC, 11-21	86.7	41.0	7.74	—	—	—	—	—	—	—
13X-CC, 28-31	93.3	—	—	—	—	—	—	—	—	—
908-C9023E-										
4X-CC, 13-21	153.7	39.9	7.53	—	581	1.04	0.38	N.D.	109.1	3.5
5X-CC, 30-35	163.5	—	—	—	—	—	—	—	—	—
6X-CC, 31-36	172.8	40.6	7.65	—	657	—	—	—	—	—
9X-1, 59-79	199.7	36.8	6.97	8.3	612	3.13	1.18	1	66.8	1.9

N.D. : Not detected
N.C. : Not calculated
— : No data



○ : C9019B
 △ : C9017C

Figure 5-4-3-1

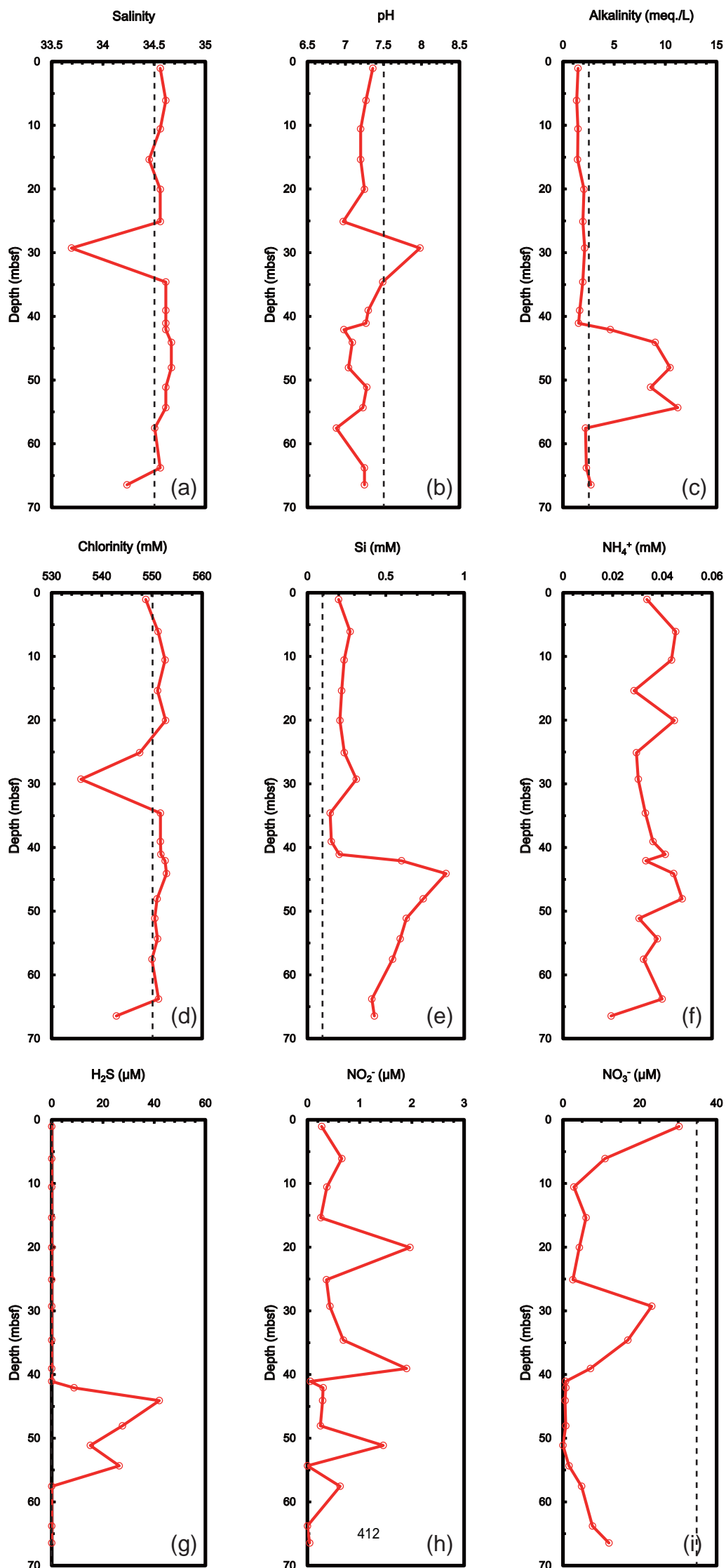


Figure 5-4-3-2

○ : C9021B

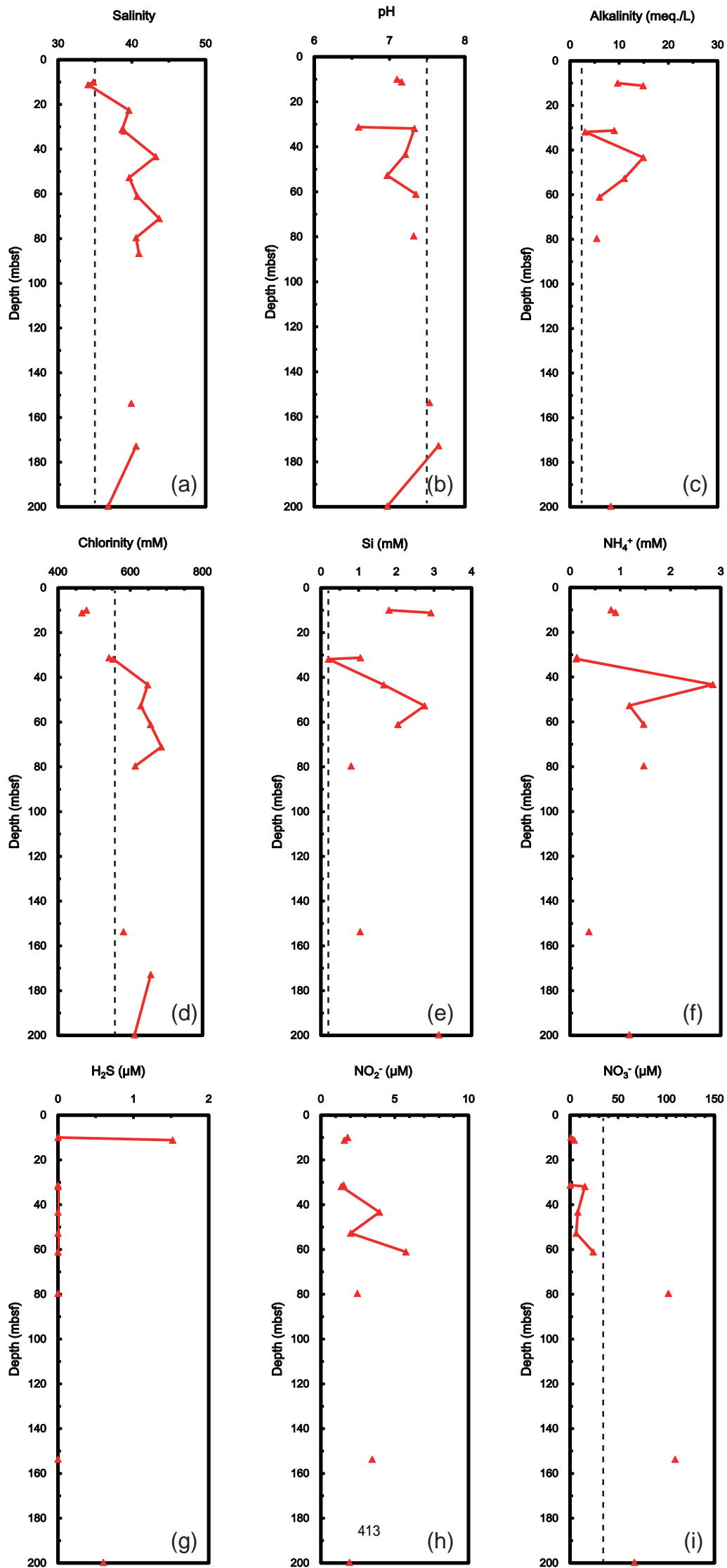


Figure 5-4-3-3

\blacktriangle : C9023D/E

5.5 Gas Geochemistry and Microbiology

M. Abe, M. Hirai, S. Kato, S. Nakagawa, T. Nunoura and E. Tasumi

Objectives

Gas geochemistry combined with microbiological interpretation is essential to understand the subseafloor fluid circulation under hydrothermal vent systems. Concentration and/or stable isotopic signatures of gas components such as H₂, CH₄ and CO₂ can be signatures of subseafloor hydrothermal fluid circulation in comparison with interstitial water geochemistry. On the other hand, microbial production and consumption affect on concentration and stable isotopic signatures of these gases. Accordingly, microbial analyses to estimate the microbial effects on subseafloor geochemical cycles are necessary for interpretation gas geochemistry. In addition, G+C content of rRNA genes also could be a biological temperature probe in subseafloor environments (Kimura et al. 2013). In order to understand the subseafloor geochemical cycles and hydrothermal circulation in the Iheya North and Noho hydrothermal fields, we will conduct analyses for gas geochemistry and environmental microbiology as listed below.

1. Measurement of concentrations of gas species such as methane, ethane, hydrogen and carbon dioxide in subseafloor sediments and soft rocks.
2. Stable isotopic analyses of methane.
3. Estimation of microbial abundance by direct cell counting and quantitative PCR.
4. Microbial activity measurements such as methanogenesis, methanotrophy and heterotrophy using radio isotope.
5. Microbial diversity analyses targeting SSU rRNA gene and functional genes such as *mcrA* and *amoA*.
6. Shotgun metagenomics to know the potential metabolic function of microbial communities if necessary.

Methods

Whole Round Core Sampling

Whole round core (WRC) sediment cores for gas geochemistry and microbiology were taken from sectioned sediment core. In all the cases, WRC for gas geochemistry and microbiology were taken from a position juxtaposed to that of

interstitial water geochemistry.

Gas Geochemistry

Hydrogen concentration of the sediment core was monitored using a Unisense Microsensor Monometer ver. 1.0 (Unisense, Denmark) on the core cutting area of D/V Chikyu. Sediment samples (approximately 2.5 ml) for headspace gas measurements of H₂ and CH₄ were collected from the bottom of sectioned sediment cores in every 1-3 meters (if possible), and were immediately extruded into 20-mL-capacity headspace vials. In addition, sediments for headspace gas measurements were subsampled from all the WRCs for gas chemistry and microbiology. Mercury chloride solution was added to the sediment samples in glass vials to stop microbial activity associated with the sediments. H₂ concentration was measured onboard, and concentration and stable isotopic signatures of CH₄ will be measured in an onshore laboratory in JAMSTEC.

H₂ concentration was measured with an Agilent Technologies model 7890B gas chromatograph (GC) equipped with an Agilent 7697A headspace sampler and a pulsed discharge helium ionization detector (PDHID) (Agilent Technologies, Santa Clara, CA). The measurement conditions used on the GC were as follows: Column, Shincarbon-ST stainless steel column (2 m long, 1 mm i.d.) (Shinwa Industrial Co.); carrier gas, helium (30 mL min⁻¹); injector temperature, 100 °C; oven temperature, 40 °C for 3min followed by ramping at 10 °C min⁻¹ to final temperature of 150 °C; detector temperature, 200 °C. Headspace vials containing sediment samples were heated at 70 °C for 30 min to release H₂ gas from the sediment. An aliquot (1 mL) of headspace gas was automatically injected GC through a 1-mL injection loop heated at 100 °C.

Concentration and stable isotope ratios of CH₄ were analyzed in JAMSTEC Yokosuka HQ. CH₄ concentration was measured with a GL Science model GC4000 gas chromatograph (GC) equipped with a flame ionization detector (FID). Stable carbon and hydrogen isotope ratios of CH₄ were measured with an isotope ratio mass spectrometer (IRMS) connected with hand-made pre-concentrations line [Okumura et al. 2016].

Microbiology

Subsamples for microbiology were taken from interior parts of all the WRCs corrected from a potential biosphere (<125°C). From selected WRCs corrected from abiotic seafloor environments, samples for microbiology were also obtained as

negative control of the microbiology experiments. Subsamples for cell counting, molecular analyses and cultivation and activity measurements were taken from WRC. Samples for cell counting and molecular analyses were stored at -80°C and those of cultivation and activity measurements were stored at 5°C .

The abundance of microbial cells in the sediment will be examined using SYBR Green I under fluorescence microscopy (Weibauer et al. 1998) and the procedure of sample preparation in our lab was described previously (Nomaki et al. 2016). Microbial diversity will be assessed by tag-sequencing of SSU rRNA gene using MiSeq sequencer. The primer sequences and PCR amplification condition for the tag-sequencing and DNA extraction were described previously (Nunoura et al. 2012). Microbial abundance will also be assessed by SSU rRNA gene quantitative PCR described previously (Takai and Horikoshi 2000) with modifications (Nunoura et al. in submission).

Contamination Test

The contamination of drilling mud fluids for microbiology and interstitial water geochemistry was assessed using perfluorocarbon tracer (PFT) as a chemical indicator. The PFT method in *D/V Chikyu* was described previously (Yanagawa et al. 2013). Perfluoromethylcyclohexane (C_7F_{14}) was added in the drilling mud fluids (approximately 1 ppm in the original mud fluids), and the interior and exterior of WRCs (approximately 2 ml) were sampled onboard. The PFT concentrations were measured with an Agilent Technologies model 7890B gas chromatograph (GC) equipped with an Agilent G1888 headspace sampler and a micro electron capture detector (μECD) (Agilent Technologies, Santa Clara, CA). The measurement conditions of the GC were somewhat different from those previously used by Smith et al. (2000): Column, GS-GasPro column (30 m long, 0.32 mm i.d.) (Agilent); carrier gas, Helium (3.4 mL min^{-1}); make-up gas, 30 mL min^{-1} ; injector temperature, 180°C ; oven temperature, 120°C followed by ramping upward at $20^{\circ}\text{C min}^{-1}$ to a final temperature of 180°C for 3.5 min; detector temperature, 250°C . Headspace vials containing sediment samples were heated at 80°C for 30 min to release C_7F_{14} from sediment. Subsequently, an aliquot (1 mL) of headspace gas was automatically injected through a 1-mL injection loop heated at 100°C . In addition, drilling mud fluids were also taken from mud tank to assess molecular biological signatures of potential contaminants in every 12 to 24 hours and stored at -20°C .

Onboard Results

H₂ concentration

Sensor measurements at Hole C9021B were likely successfully achieved. The profile of H₂ concentration was consistent with the profiles of interstitial water geochemistry that suggested the occurrence of the hydrothermal fluids in certain layers (data not shown). In contrast, the headspace gas measurement of H₂ at this hole was not so successfully. Due to the very low H₂ concentration, sampling processing might affect the results of each measurement.

PFT test

The result suggests that the whole round cores (WRCs) used for microbiology and geochemistry (gas and interstitial water) were generally taken non- or less-contaminated sections (Table 5-5-1). However, in most of the cases that PFT was detected in the interior of WRC, the contamination of drilling fluids in interior of the WRC was identical to those in exterior of the WRC.

Note: PFT test is one of the indicators of drilling fluids contamination. The absence of PFT in interior of WRC does not guarantee that the WRC is not completely contaminated by drilling fluids.

References :

- Kimura H, Mori K, Yamanaka T, Ishibashi J-I (2013) Growth temperatures of archaeal communities can be estimated from the guanine-plus-cytosine contents of 16S rRNA gene fragments. *Environ Microbiol Rep* 5: 468-474.
- Nomaki H, Mochizuki T, Kitahashi T, Nunoura T, Arai K, Toyofuku T, Tanaka G, Shigeno S, Tasumi E, Fujikura K (2016) Effects of mass sedimentation event after the 2011 off the Pacific coast of Tohoku earthquake on benthic prokaryotes and meiofauna inhabiting the upper bathyal sediments. *J Oceanogr.* 72: 113-128.
- Nunoura T, Takaki Y, Kazama H, Hirai M, Ashi J, Imachi H, Takai K (2012) Microbial diversity in deep-sea methane seep sediments presented by SSU rRNA gene tag sequencing. *Microbes & Environments.* 27, 382-390.
- Smith, D.C., Spivack, A.J., Fisk, M.R., Haveman, S.A., and Staudigel, H. (2000). Tracer-based estimates of drilling-induced microbial contamination of deep sea crust. *Geomicrobiol. J.* 17, 207–219.
- Takai, K., and Horikoshi, K. (2000) Rapid detection and quantification of members of the archaeal community by quantitative PCR using fluorogenic probes. *Appl Environ Microbiol* 66: 5066–5072.
- Weinbauer, M.G., Beckmann, C., and Höfle, M.G., 1998. Utility of green fluorescent nucleic acid dyes and aluminium oxide membrane filters for rapid epifluorescence enumeration of soil and sediment bacteria. *Appl. Environ. Microbiol.*, 64:5000–5003.
- Yanagawa K, Nunoura T, McAllister S, Hirai M, Breuker A, Brandt L, House C, Moyer CL, Birrien J-L, Aoike K, Sunamura M, Urabe T, Mottl M, Takai K (2013) The first microbiological contamination assessment by deep-sea drilling and coring by the D/V Chikyu at the Iheya North hydrothermal field in the Mid-Okinawa Trough (IODP Expedition 331). *Front Microbiol* 4: 327.

Caption:

Table 5-5-1 : Summary of PFT test for the whole round cores taken for geochemistry (gas and interstitial water) and microbiology during CK16-01 cruise.

Table 5-5-1

Summary of PFT test for the whole round cores taken for geochemistry (gas and interstitial water) and microbiology during CK16-01 cruise

Hole-Core-Section	Interval in each section	PFC nmol/kg sediment		Contamination level
		Interior	Exterior	
C9019B-1H-2	54.0-56.0 cm	N.D.	N.D.	
C9019B-1H-4	20.0-22.0 cm	0.59	0.27	218%
C9017C-3X-1	89.0-91.0 cm	N.D.	1.16	
C9017C-3X-4	67.0-69.0 cm	N.D.	N.D.	
C9017C-4H-5	27.0-29.0 cm	N.D.	N.D.	
C9017C-4H-7	87.0-89.0 cm	N.D.	N.D.	
C9017C-5H-2	33.0-35.0 cm	1	127.04	1%
C9017C-5H-5	73.0-75.0 cm	N.D.	N.D.	
C9017C-7H-5	68.0-70.0 cm	N.D.	0.85	
C9017C-8H-5	53.0-55.0 cm	N.D.	N.D.	
C9017C-8H-7	94.0-96.0 cm	N.D.	N.D.	
C9017C-9H-4	23.0-25.0 cm	N.D.	N.D.	
C9017C-9H-7	0.0-2.0 cm	N.D.	N.D.	
C9017C-10H-2	93.5-95.5 cm	N.D.	N.D.	
C9017C-11H-2	19.0-21.0 cm	0.44	0.34	129%
C9017C-14X-1	60.0-62.0 cm	N.D.	0.76	
C9017C-15X-1	44.0-46.0 cm	N.D.	0.54	
C9021B-1H-2	10.0-12.0 cm	N.D.	N.D.	
C9021B-1H-7	10.0-12.0 cm	N.D.	N.D.	
C9021B-2H-2	10.0-12.0 cm	N.D.	N.D.	
C9021B-2H-7	10.0-12.0 cm	N.D.	N.D.	
C9021B-3H-2	10.0-12.0 cm	N.D.	N.D.	
C9021B-3H-7	10.0-12.0 cm	N.D.	N.D.	
C9021B-4H-1	83.0-85.0 cm	32.33	78.47	41%
C9021B-4H-7	10.0-12.0 cm	0.41	0.7	59%
C9021B-5H-2	10.0-12.0 cm	4.42	2.82	157%
C9021B-5H-4	10.0-12.0 cm	N.D.	1.49	
C9021B-5H-5	10.0-12.0 cm	N.D.	0.86	
C9021B-5H-7	10.0-12.0 cm	N.D.	N.D.	
C9021B-6H-2	10.0-12.0 cm	0.36	0.65	56%
C9021B-6H-5	10.0-12.0 cm	N.D.	N.D.	
C9021B-6H-8	10.0-12.0 cm	N.D.	N.D.	
C9021B-7H-2	10.0-12.0 cm	0.64	7.5	9%
C9021B-7H-8	30.0-32.0 cm	N.D.	N.D.	
C9021B-8H-1	50.0-52.0 cm	N.D.	13.45	
C9023D-2H-2	30.0-32.0 cm	0.27	0.37	74%
C9023D-2H-3	45.0-47.0 cm	0.7	0.73	95%
C9023D-4H-1	3.0-5.0 cm	2.19	2.77	70%
C9023D-5H-1	29.0-31.0 cm	63.04	71.1	89%
C9023D-5H-1	96.0-98.0 cm	28.99	8.93	325%
C9023D-8X-CC	21.0-23.0 cm	N.D.	N.D.	
C9023D-9X-CC	36.5-38.5 cm	N.D.	N.D.	
C9023D-10X-CC	55.0-57.0 cm	N.D.	N.D.	
C9023D-11X-CC	8.0-10.0 cm	N.D.	N.D.	
C9023D-12X-CC	11.0-13.0 cm	0.3	0.17	173%

Table 5-5-1

Summary of PFT test for the whole round cores taken for geochemistry
(gas and interstitial water) and microbiology during CK16-01 cruise

C9023D-13X-CC	28.0-31.0 cm	N.D.	0.26	
C9023E-4X-CC	13.0-15.0 cm	3.96	6.39	62%
C9023E-5X-CC	30.0-32.0 cm	3.01	0.31	966%
C9023E-6X-CC	31.0-33.0 cm	0.65	0.34	192%
C9023E-9X-1	79.0-81.0 cm	N.D.	0.25	

Chapter 6: Operation

H. Kumagai, L. Maeda, Y. Kido and K. Aoike

6.1 Summary of operations

The CK16-01 Cruise by D/V Chikyu (Expedition 908) was performed as SIP-HOT II “Explorer” from February 11th to March 17th of Year 2016 under an umbrella of Cross-ministerial Strategic Innovation Promotion Program (SIP) “Next-generation technology for ocean resources exploration”. Logging while drilling (LWD) operation, installation of long-term monitoring apparatuses, coring operation, and borehole logging using a thermometer or a geothermal tool were conducted (Table 6-1-1) at Iheya Minor Ridge (Sites C9017-C9020, Fig. 6-1-1) and Iheya -North Knoll (Sites C9021-C9024, Fig. 6-1-2) in middle Okinawa Trough, in order to investigate the seafloor hydraulic structure and geology aiming to construct the genetic model of seafloor hydrothermal deposits.

During the former half of the cruise (Leg. 1: from February 11th to 29th), logging while drilling (LWD) operation was performed at 7 Sites (C9017-C9023) in order to obtain physical parameters beneath active hydrothermal fields (Table 6-1-2). Moreover, the long-term monitoring apparatuses, "Kuroko-ore cultivation apparatus" that is equipped with sensors to monitor the secular variation of pressure, temperature, flow rate and precipitation weight were installed on the hydrothermal vent artificially made by drilling at Site C9017 and C9024.

During the latter half of the cruise (Leg. 2: from February 29th to March 17th), coring was performed at Sites C9017, C9019, C9021 and C9023 using the HPCS/ESCS assembly (Table 6-1-2). As listed in Table 6.1-3, obtained core length was 51.2 m for Hole C9017C, 4.6 m for Hole C9019B, 0.67 m for Hole C9019C, 59.9 m for Hole C9021B, 9.5 m for Hole C9023B, 12.8 m for Hole C9023D and 125.0 m for Hole C9023E. After the coring operation, temperature measurement by an in-situ thermometer and borehole logging using a geothermal tool PPS71 that is equipped with pressure, temperature, flow rate and gamma-ray sensors.

Abbreviations:

BHA: borehole assembly

CHRT: casing hanger running tool

ESCS: extended shoe coring system. It is designed for collecting moderately hard formations which cannot be penetrated by HPCS. The cutting shoe is extended 8-14

inch below the drill bit in soft formation but drawn in as firmer formation are encountered, while drilling down to collect a core sample. The core type code in the sample database is “X.”

HPCS: hydraulic piston coring system. It is designed for collecting soft formations. The inner core barrel is run to the bottom of the coring BHA with the coring wireline. Hydraulic pressure through the drill strings is applied to sever the shear pins, which strokes the inner core barrel up to 9.5 m into the formation. The inner core barrel, containing a core sample, is then retrieved by wireline. The core type code in the sample database is “H.”

LWD: logging while drilling

mBRT: meter below rotary table. The sum of lengths of all drill string components deployed beneath the rotary table in the drill floor. It is 28.5 m of the elevation from the sea level for D/V Chikyu.

mbsf: meter below seafloor. The length of all drill string components between seafloor and the drill bit. It is found by subtracting water depth (m) and 28.5 m from depth in mBRT.

PHG: pre-hydrated gel. It consists of seawater and bentonite.

ROV: remotely operated underwater vehicle

SPP: standpipe pressure. It is calculated as total loss amount of annulus pressure, drill string pressure, BHA pressure and pressure across the drill bit.

SWG: seawater gel. It consists of seawater, sodium hydroxide, calcium hydroxide, and 12% of PHG.

TD: total depth

WOB: weight on bit

Captions:

Table 6-1-1 Borehole Summary

Table 6-1-2 Borehole Assembly Record

Table 6-1-3 Coring Summary

Fig. 6-1-1 Area map of Sites C9017-C9020 along Iheya Minor Ridge.

Fig. 6-1-2 Area map of Sites C9021-C9024 at Iheya North Knoll. Sites investigated during previous drilling cruises were also shown.

Table 6-1-1 Borehole Summary

Site Proposed	Site	Hole	Operation	Coordinates				Water Depth (mbsl)	Hole Top Depth		Final CSG Detph		Total Depth		Advance (m)	Spud-in	End of hole	Remarks
				Latitude	Longitude	Northing	Easting		(mBRT)	(mbsf)	(mBRT)	(mbsf)	(mBRT)	(mbsf)				
SIP-NH#01	-	-	Observatory	27°30.9909'N	126°58.9892'E	300780.3	3045266.6	-	-	-	-	-	-	-	-	-	-	POODLE and SAHF deploy
	C9017	A	LWD	27°31.0085'N	126°58.8963'E	300644.3	3045301.4	1558.0	1586.5	0.0	-	-	1700.0	113.5	113.5	2016/02/16 14:30	2016/02/17 05:00	Canceled to set observatory
		B	Observatory	27°31.0059'N	126°58.8904'E	300634.5	3045296.7	1557.5	1586.0	0.0	1608.5	22.5	1636.0	50.0	50.0	2016/02/27 08:30	2016/02/28 20:00	13m offset from Hole A
		C	Core/TRDT/PPS71	27°31.0077'N	126°58.8945'E	300641.3	3045299.9	1558.0	1586.5	0.0	-	-	1707.5	121.0	121.0	2016/03/02 06:52	2016/03/04 21:00	
SIP-NH02	C9018	A	LWD	27°31.1597'N	126°58.9860'E	300796.6	3045578.2	1585.0	1613.5	0.0	-	-	1623.0	9.5	9.5	2016/02/17 08:00	2016/02/17 13:00	
SIP-NH03	C9019	A	LWD	27°31.3286'N	126°59.0230'E	300862.5	3045889.1	1602.0	1630.5	0.0	-	-	1645.5	15.0	15.0	2016/02/17 14:30	2016/02/18 01:00	Damage to BHA while drilling
		B	Core	27°31.3292'N	126°59.0251'E	300866.1	3045890.2	1600.0	1628.5	0.0	-	-	1633.1	4.6	4.6	2016/03/01 19:37	2016/03/01 21:30	
		C	Core	27°31.3292'N	126°59.0241'E	300864.4	3045891.3	1600.5	1629.0	0.0	-	-	1638.5	9.5	9.5	2016/03/01 22:07	2016/03/02 02:00	
SIP-NH04	C9020	A	LWD	27°31.4847'N	126°59.0221'E	300865.8	3046177.4	1599.5	1628.0	0.0	-	-	1637.0	9.0	9.0	2016/02/18 13:00	2016/02/18 22:30	Used backup LWD tools
SIP-IN03	C9021	A	LWD	27°46.4119'N	126°54.1304'E	293280.5	3073879.6	1020.5	1049.0	0.0	-	-	1150.5	101.5	101.5	2016/02/19 06:45	2016/02/19 18:00	Used backup LWD tools
		B	Core/TRDT/PPS71	27°46.4134'N	126°54.1310'E	293281.5	3073882.4	1020.5	1049.0	0.0	-	-	1156.5	107.5	107.5	2016/03/05 11:41	2016/03/07 05:15	
SIP-IN02	C9022	A	LWD	27°46.9246'N	126°54.0810'E	293215.4	3074827.9	1088.0	1116.5	0.0	-	-	1354.5	238.0	238.0	2016/02/19 22:30	2016/02/20 19:30	Used backup LWD tools
SIP-IN14	C9023	A	LWD	27°46.0694'N	126°54.1559'E	293311.6	3073246.5	1071.5	1100.0	0.0	-	-	1300.0	200.0	200.0	2016/02/21 00:00	2016/02/22 10:00	Used backup LWD tools
		B	Core	27°46.0688'N	126°54.1574'E	293314.0	3073245.3	1076.0	1104.5	0.0	-	-	1114.0	9.5	9.5	2016/03/07 18:00	2016/03/07 22:00	
		C	Core	27°46.0687'N	126°54.1578'E	293314.7	3073245.1	1073.0	1101.5	0.0	-	-	1103.0	1.5	1.5	2016/03/07 23:10	2016/03/08 09:25	
		D	Core	27°46.0695'N	126°54.1569'E	293313.2	3073246.6	1072.5	1101.0	0.0	-	-	1228.0	127.0	127.0	2016/03/08 22:58	2016/03/10 22:10	
		E	Core/TRDT/PPS71	27°46.0694'N	126°54.1593'E	293317.2	3073246.4	1071.5	1100.0	0.0	-	-	1308.5	208.5	208.5	2016/03/11 02:32	2016/03/16 06:00	Drilled down without coring to 125 mbsf
SIP-IN16	C9024	A	Observatory	27°47.4094'N	126°54.0397'E	293163.0	3075724.5	1058.0	1086.5	0.0	1104.5	18.0	1286.5	200.0	200.0	2016/02/23 05:30	2016/02/25 22:30	

mbsl: meter below mean sea level
mBRT: meter below rotary table (elevation from sea level: 28.5 m)
mbsf: meter below seafloor
CSG 5-1/2 inch casing

Table 6-1-2 Borehole Assembly Record

Hole	Assembly	Components
C9017A	Primary LWD	8-1/2" Bit (X20GSJ-G: Nz 18 x 3) x Bit Sub w/ float valve for high temp x XO x 6-3/4"NMDC x 8-3/8"Stab x 6.75" ARC HT x GVR x 6.75" Telescope HT x 8-3/8" String Stab x 6-3/4"DC(9) x XO x 5-1/2" DP S-150 (15 stds) x XO x 5-1/2" DP S-140
C9018A		
C9019A		
C9020A	Backup LWD	8-1/2" Bit (X20GSJ-G: Nz 18 x 3) x Bit Sub w/ float valve for high temp x XO x 6-3/4" NMDC x 8-3/8" Stab x 6.75" ARC HT x GVR x 6.75" Telescope HT x 8-3/8" String Stab x 6-3/4" DC(9) x XO x 5-1/2" DP S-150 (15 stds) x XO x 5-1/2" DP S-140
C9021A		
C9022A		
C9023A		
C9024A	Jetting	17-1/2"Bit (TMZGC: Nz 20 x 3, 26 x 1) x Motor x 17-1/2" Stab x XO x 5-1/2" DP S140 3 m pup (2) x XO x HART x 8-1/2" Coring DC (3)
	Observatory	10-5/8" HPCS/ESCS PDC Bit (SC513: Nz 13 x 5) x Bit Sub x SBOCB x Landing Sub x Top Sub x Head Sub x 10-5/8" Stab x 8-1/2" Coring DC (5) x XO x 5-1/2" DP S-150 (15 stds) x XO x 5" DP S-140
	Observatory	8-1/2" Coring DC 6 m pup x HART x 8-1/2" Coring DC (6) x XO x 5-1/2" DP S-150 (15 stds) x XO x 5-1/2" DP S-140
C9017A	Observatory	8-1/2" Coring DC 6 m pup x HART x 8-1/2" Coring DC (6) x XO x 5-1/2" DP S-150 (15 stds) x XO x 5-1/2" DP S-140
	Tripod Retrieval	8-1/2" Coring DC 3 m pup x HART w/stabing guide x 8-1/2" Coring DC (3) x XO x 5-1/2" DP S-150 (15 stds) x XO x 5-1/2" DP S-140
C9017B	Observatory	8-1/2" Coring DC 6 m pup x HART x 8-1/2" Coring DC (6) x XO x 5-1/2" DP S-150 (15 stds) x XO x 5-1/2" DP S-140
	Simple Observatory	5-1/2" CSG x CSGHGR x Monitoring Manifold x CHRT x 8-1/2" Coring DC (4) x XO x 5-1/2" DP S-150 (15 stds) x XO x 5-1/2" DP S-140
C9017C	HPCS/ESCS	10-5/8" PDC Bit x BS x SBOCB x Landing Sub x Top Sub x Head Sub x 10-5/8" Stab x 8-1/2" Coring DC(8) x XO x 5-1/2" DP S-150 (15 stds) x XO x 5-1/2" DP S-140
C9019B		
C9019C		
C9021B		
C9023B	HPCS/ESCS	11-7/16" Insert Bit x BS x SBOCB x Landing Sub x Top Sub x Head Sub x 10-5/8" Stab x 8-1/2" Coring DC(8) x XO x 5-1/2"DP S-150 (15 stds) x XO x 5-1/2" DP S-140
C9023C		
C9023D		
C9023E		

Table 6-1-3 Coring Summary

Hole	Core	Type	Coring Start Time (JST) ¹⁾	Coring Termination Time (JST)	Core on Deck Time (JST)	Top of Core (mBRT)	Bottom of Core (mBRT)	Top of Core (mbsf)	Bottom of Core (mbsf)	Advance ²⁾ (m)	Initial Core Length ³⁾ (m)	Initial Recovery ⁴⁾ (%)	Remarks
C9019B	1	H	2016/03/01 19:37	2016/03/01 19:37	2016/03/01 20:32	1628.5	1633.1	0.0	4.6	4.6	4.60	100.0	Shot@16.9 MPa directly from seabed. Partial penetration. Pull up w/ coreline winch. Detected 35 ppm CO while picking up sinker bar. Most part of core (dark gray clay) deviated upward due to gas expansion.
C9019C	1	X	2016/03/01 22:07	2016/03/01 23:37	2016/03/02 00:57	1629.0	1638.5	0.0	9.5	9.5	0.67	7.1	Cut core w/ 20-50 RPM, 40-50SPM, 0-40kN No gas detected. Plugging @shoe
C9017C	1	X	2016/03/02 06:52	2016/03/02 08:09	2016/03/02 09:13	1586.5	1596.0	0.0	9.5	9.5	0.50	5.3	No gas detected from core barrel
C9017C	2	X	2016/03/02 10:39	2016/03/02 12:08	2016/03/02 13:23	1596.0	1605.5	9.5	19.0	9.5	0.68	7.2	No gas detected from core barrel
C9017C	3	X	2016/03/02 14:30	2016/03/02 15:03	2016/03/02 16:10	1605.5	1610.5	19.0	24.0	5.0	4.24	84.8	Stop cut core as hard formation confirmed. Over 100 ppm H2S detected after laydown.
C9017C	4	H	2016/03/03 16:47	2016/03/03 16:47	2016/03/02 17:26	1610.5	1618.5	24.0	32.0	8.0	8.00	100.0	Aluminium liner. Partial penetration. Immediate overpull when picking up w/ draw works, however, advance determined from core length. 100 ppm H2S detected after laydown. Stuck core liner. Delivered to core cutting area 4.5 hours later after core on deck. Formation consisting of water-rich and impermeable solid zones expected.
C9017C	5	H	2016/03/03 01:07	2016/03/03 01:07	2016/03/03 01:51	1618.5	1626.5	32.0	40.0	8.0	8.00	100.0	Aluminium liner. Shoot from 1618.0 mBRT, 16.1 MPa. 0.5 m fill. Partial penetration. Expected penetration = 8.5 m. Over 200 ppm H2S from inner barrel after laydown.
C9017C	6	H	2016/03/03 05:25	2016/03/03 05:25	2016/03/03 05:55	1626.5	1635.0	40.0	48.5	8.5	0.08	0.9	Aluminium liner. Shoot from 1626.5 mBRT, 17.2 MPa. 0.5 m fill. Partial penetration. Expected penetration = 9.0 m. No sample in core liner. Liner collapse at lower part.
C9017C	7	H	2016/03/03 08:23	2016/03/03 08:23	2016/03/03 08:57	1635.0	1639.0	48.5	52.5	4.0	6.24	156.0	Aluminium liner. Shoot at 15.0 MPa. Partial penetration. Over 200 ppm H2S from inner barrel after laydown. Blowout from core bottom.
C9017C	8	H	2016/03/03 11:16	2016/03/03 11:16	2016/03/03 12:09	1639.0	1647.0	52.5	60.5	8.0	7.40	92.5	Aluminium liner. Shoot at 14.7 MPa. Partial penetration. Over 100 ppm H2S from core barrel after laydown
C9017C	9	H	2016/03/03 14:08	2016/03/03 14:08	2016/03/03 14:38	1647.0	1656.0	60.5	69.5	9.0	8.15	90.6	Aluminium liner. Shoot at 18.9MPa. Partial penetration. Over 200 ppm H2S and CO detected after laydown. Strong blowout from core bottom. Materials brown out reached to Core Cutting Area. Liner collapse at 2 places. Formation consisting of water-rich and impermeable solid zones expected.
C9017C	10	H	2016/03/03 17:33	2016/03/03 17:33	2016/03/03 18:05	1656.0	1657.5	69.5	71.0	1.5	1.82	121.3	Aluminum liner. Shoot at 14MPa. Partial penetration. Over 100 ppm H2S from inner barrel after laydown.
C9017C	11	H	2016/03/03 20:22	2016/03/03 20:22	2016/03/03 20:52	1657.5	1660.0	71.0	73.5	2.5	2.12	84.8	Aluminum liner. Shoot at 13.7MPa. Partial penetration. No overpull. 100 ppm H2S from inner barrel after
C9017C	12	X	2016/03/03 22:36	2016/03/03 23:12	2016/03/04 00:23	1660.0	1669.5	73.5	83.0	9.5	0.37	3.9	Aluminium liner (unholed). No gas detected. Plugged shoe.
C9017C	13	X	2016/03/04 02:16	2016/03/04 02:36	2016/03/04 03:33	1669.5	1679.0	83.0	92.5	9.5	0.44	4.6	Aluminium liner (holed). Stable coring w/ 60 rpm, 40 spm, 10-30 kN. No gas detected. Plugged shoe.
C9017C	14	X	2016/03/04 05:19	2016/03/04 05:28	2016/03/04 06:23	1679.0	1688.5	92.5	102.0	9.5	1.40	14.7	Aluminium liner (holed). Stable coring w/ 60 rpm, 50 spm, 15-35 kN. <100 ppm H2S detected in inner tube . Plugged shoe.
C9017C	15	X	2016/03/04 07:33	2016/03/04 07:44	2016/03/04 08:41	1688.5	1698.0	102.0	111.5	9.5	0.88	9.3	Aluminium liner (holed). Stable coring w/ 60spm, 60 rpm, 20-35 kN. No gas detected after laydown. Plugged shoe.
C9017C	16	X	2016/03/04 10:20	2016/03/04 10:49	2016/03/04 11:38	1698.0	1707.5	111.5	121.0	9.5	0.92	9.7	Aluminium liner (holed). 70-80 spm, 40-60 rpm, 5-50 kN. Harder formation at 1699.0-1706.5 mBRT. No strong gas detected. Plugged shoe.
C9021B	1	H	2016/03/05 11:41	2016/03/05 11:41	2016/03/05 12:11	1049.0	1058.5	0.0	9.5	9.5	7.68	80.8	Shoot at 15.0 MPa. Full penetration. Wash down.
C9021B	2	H	2016/03/05 13:20	2016/03/05 13:20	2016/03/05 13:42	1058.5	1068.0	9.5	19.0	9.5	7.85	82.6	Shoot at 15.8 MPa. Full penetration. Wash down.
C9021B	3	H	2016/03/05 15:14	2016/03/05 15:14	2016/03/05 15:33	1068.0	1077.5	19.0	28.5	9.5	7.95	83.7	Shoot at 14.8 MPa. Full penetration. Drill down from this core.
C9021B	4	H	2016/03/05 17:23	2016/03/05 17:23	2016/03/05 17:50	1077.5	1087.0	28.5	38.0	9.5	8.57	90.2	Shoot at 15.8 MPa. Full penetration.
C9021B	5	H	2016/03/05 19:14	2016/03/05 19:14	2016/03/05 19:39	1087.0	1096.0	38.0	47.0	9.0	8.27	91.9	Shoot at 16.5 MP from 1086.7 mBRT, 0.3 m fill. Full penetration. 60 ppm of H2S from inner barrel after laydown.

Table 6-1-3 Coring Summary

Hole	Core	Type	Coring Start Time (JST) ¹⁾	Coring Termination Time (JST)	Core on Deck Time (JST)	Top of Core (mBRT)	Bottom of Core (mBRT)	Top of Core (mbsf)	Bottom of Core (mbsf)	Advance ²⁾ (m)	Initial Core Length ³⁾ (m)	Initial Recovery ⁴⁾ (%)	Remarks
C9021B	6	H	2016/03/05 21:08	2016/03/05 21:08	2016/03/05 21:08	1096.0	1105.5	47.0	56.5	9.5	8.40	88.4	Shoot at 16.5 MPa. Over 200 ppm H2S from inner barrel after laydown.
C9021B	7	H	2016/03/05 23:04	2016/03/05 23:04	2016/03/05 23:28	1105.5	1115.0	56.5	66.0	9.5	8.47	89.2	Shoot at 15.5 MPa. Full penetration. Green mineral aggregate: celadonite.
C9021B	8	H	2016/03/06 01:43	2016/03/06 01:43	2016/03/06 02:05	1115.0	1124.0	66.0	75.0	9.0	1.68	18.7	Shoot at 14.9 MPa from 1114.5 mBRT. Partial penetration, 0.5 m fill. Pick up w/ draw works. No gas detected. Slightly plugged shoe. Hole condition gets worse below 1119-1120 mBRT after drill down. Altered tuff. amorphous silica w/ celadonite
C9021B	9	X	2016/03/06 12:08	2016/03/06 12:30	2016/03/06 13:24	1124.0	1133.5	75.0	84.5	9.5	0.20	2.1	Cut core at 60 rpm, 50 spm, 0-60 kN. Sudden WOB drop @ 1131.7 mBRT (82.7 mbsf). No strong gas detected. Plugged shoe.
C9021B	10	X	2016/03/06 14:14	2016/03/06 14:30	2016/03/06 15:35	1133.5	1139.7	84.5	90.7	6.2	0.20	3.2	Cut core at 60 rpm, 80 spm, 0-60 kN. Stop coring @ 1139.7 mBRT due to over torque and SPP increases. No gas detected. Plugged shoe.
C9021B	11	X	2016/03/06 16:37	2016/03/06 17:18	2016/03/06 18:04	1139.7	1147.0	90.7	98.0	7.3	0.25	3.4	Cut core w/ diamond shoe at 60 - 80 rpm, 50 spm, 0-60 kN. No gas detected. Plugged shoe.
C9021B	12	X	2016/03/06 19:48	2016/03/06 20:36	2016/03/06 21:35	1147.0	1156.5	98.0	107.5	9.5	0.40	4.2	Cut core w/ diamond shoe at 60 - 80 rpm, 60-70 spm, 0-60 kN. No gas detected. Plugged shoe.
C9023B	1	X	2016/03/07 18:06	2016/03/07 19:02	2016/03/07 20:15	1104.5	1114.0	0.0	9.5	9.5	0.45	4.7	Cut core w/ 5-25 rpm, 20-30 spm, 0-20 kN. Plugged shoe.
C9023C	Drill-out		2016/03/07 23:10	2016/03/08 00:12	-	1101.5	1103.0	0.0	1.5	1.5	0.00	0.0	Wash/drill down. Take weight at 1102.6 mBRT while ream down.
C9023C	1	H	2016/03/08 01:03	2016/03/08 01:03	2016/03/08 01:27	1103.0	1103.0	1.5	1.5	0.0	0.00	0.0	Shoot at 13.0 MPa, then SPP rise up to 33 MPa. Lost shoe.
C9023D	1	X	2016/03/08 22:58	2016/03/09 01:24	2016/03/09 02:13	1101.0	1110.5	0.0	9.5	9.5	0.28	2.9	Holed Al liner. W/o core catcher and sleeve to Cut at 40-60 spm, 0-10 kN, 14-20 rpm. Liner collapse at bottom part. Plugged shoe. No gas detected.
C9023D	2	H	2016/03/09 04:05	2016/03/09 04:05	2016/03/08 04:43	1110.5	1114.0	9.5	13.0	3.5	3.42	97.7	Al liner. Shoot at 13 MPa. Partial penetration. Over 200 ppm H2S inside.
C9023D	3	X	2016/03/09 07:15	2016/03/09 07:35	2016/03/09 08:33	1114.0	1123.5	13.0	22.5	9.5	0.32	3.4	Holed Al liner. Holed sleeve w/ 4-pedal catcher. 10-30 spm, 10-20 rpm, 0-15 kN. No gas detected. Plugged shoe.
C9023D	4	H	2016/03/09 10:10	2016/03/09 10:10	2016/03/09 10:34	1123.5	1132.0	22.5	31.0	8.5	0.77	9.1	Al liner. Shoot at from 1122.8 mBRT at 12.4 MPa. 1m fill. Partial penetration. Pick up w/ drawworks. 45 ppm H2S detected when break shoe off.
C9023D	5	H	2016/03/09 12:42	2016/03/09 12:42	2016/03/09 13:02	1132.0	1134.5	31.0	33.5	2.5	2.21	88.4	Al liner. Partial penetration. Pull out w/ coreline winch. Advance determined from initial core length. No H2S detected.
C9023D	6	X	2016/03/09 14:25	2016/03/09 14:39	2016/03/09 15:27	1134.5	1144.0	33.5	43.0	9.5	0.15	1.6	Core catcher; 4-petal. Holed Al liner. 30 spm, 60 rpm, 0-20 kN. No gas detected
C9023D	7	X	2016/03/09 16:12	2016/03/09 16:18	2016/03/09 17:04	1144.0	1153.5	43.0	52.5	9.5	0.40	4.2	Core catcher: slip, short finger. Holed Al liner. 15-20 spm, 60 rpm 0-20kN. No gas detected
C9023D	8	X	2016/03/09 18:04	2016/03/09 18:33	2016/03/09 19:20	1153.5	1161.5	52.5	60.5	8.0	0.60	7.5	Core catcher: slip. Holed Al liner. 20 spm, 50-70rpm, 0-40 kN. No gas detected
C9023D	9	X	2016/03/09 20:11	2016/03/09 20:34	2016/03/09 21:24	1161.5	1171.0	60.5	70.0	9.5	0.85	8.9	Core catcher: slip. Holed Al liner. 30 spm, 50-60rpm, 0-30 kN. No gas detected
C9023D	10	X	2016/03/09 22:04	2016/03/09 22:27	2016/03/09 23:14	1171.0	1180.5	70.0	79.5	9.5	1.13	11.9	Core catcher: slip w/ notch sleeve. Holed Al liner. 30 spm, 60-80 rpm, 0-30 kN. No gas detected from bottom of shoe
C9023D	11	X	2016/03/10 00:51	2016/03/10 01:32	2016/03/10 02:27	1180.5	1187.5	79.5	86.5	7.0	0.31	4.4	Holed Al liner. Slip core catcher. 60 spm, 30-35 rpm, ~55 kN. Take weight from 1179.3 mBRT (1.2 m fill?) at 00:33. Terminate coring earlier due to low ROP. No gas detected. Plugged shoe.
C9023D	12	X	2016/03/09 03:56	2016/03/09 04:32	2016/03/10 06:22	1187.5	1194.0	86.5	93.0	6.5	0.32	4.9	Holed Al liner. W/o catcher (spacer only). 70-60 spm, 30-60 rpm, ~110 kN. High heave. Terminate coring earlier due to low ROP and connection. No gas detected. Plugged shoe.
C9023D	13	X	2013/03/10 07:18	2013/03/10 08:14	2016/03/10 09:03	1194.0	1203.0	93.0	102.0	9.0	0.36	4.0	Holed Al liner. Holed sleeve & slip catcher. Take weight from 1194.9 mBRT. 40-60-70 spm, 40-50-65-50-45 rpm, ~100 kN. No gas detected. Plugged shoe.
C9023D	14	X	2013/03/10 10:43	2013/03/10 12:34	2016/03/10 13:29	1203.0	1210.0	102.0	109.0	7.0	0.60	8.6	Holed Al liner. Holed sleeve & spacer only, w/o catcher. Diamond shoe. Take weight at 0.5 m shallower depth than expected. Not regarded as fill, but formation, then changed TD of 13X. Terminate coring at 7.0 m advance due to low ROP and sudden torque rise at 1210 mBRT. Damage on shoe (cracks). Vain of sulfide ore.

Table 6-1-3 Coring Summary

Hole	Core	Type	Coring Start Time (JST) ¹⁾	Coring Termination Time (JST)	Core on Deck Time (JST)	Top of Core (mBRT)	Bottom of Core (mBRT)	Top of Core (mbsf)	Bottom of Core (mbsf)	Advance ²⁾ (m)	Initial Core Length ³⁾ (m)	Initial Recovery ⁴⁾ (%)	Remarks
C9023D	15	X	2013/03/10 14:18	2013/03/10 16:18	2016/03/10 17:10	1210.0	1219.5	109.0	118.5	9.5	0.55	5.8	Holed Al liner. Spacer only (w/o catcher). 60 spm, 50-70 rpm -60 kN. Damage on shoe (severely abraded, all cutters lost, 3 cutters found inside core). No gas detected. Plugged shoe. Vain of sulfide ore.
C9023D	16	X	2013/03/10 17:58	2013/03/10 20:36	2016/03/10 21:25	1219.5	1228.0	118.5	127.0	8.5	0.50	5.9	Holed Al liner. Slip catcher. Retraction limit spacer. 60 spm, 50-70 rpm, -70 kN. 4 cutters of shoe found inside core. Lost edge part of shoe. Decided to abandon Hole D.
C9023E	Drill-out		2016/03/11 02:25	2016/03/11 15:38	-	1100.0	1225.0	0.0	125.0	125.0			Drill down w/ center bit
C9023E	1	X	2016/03/11 17:26	2016/03/11 17:36	2016/03/11 18:38	1225.0	1226.0	125.0	126.0	1.0	0.14	14.0	Holed Al liner, slip catcher. 40 spm, 40 rpm, 20-50 kN. No gas detected. Jammed at slip catcher.
C9023E	Drill-out		2016/03/11 19:10	2016/03/11 22:10	-	1226.0	1235.0	126.0	135.0	9.0			Drill down w/ center bit
C9023E	2	X	2016/03/11 23:35	2016/03/12 00:09	2016/03/12 00:53	1235.0	1244.0	135.0	144.0	9.0	0.33	3.7	Holed Al liner. Slip catcher. 40 spm, 30 rpm, 20-40 kN. Autodriller throughout. No gas detected. Plugged shoe (jammed at slip catcher). Silver colored sulfide (sphalerite?) veins and chalcopyrite (?) specks.
C9023E	3	X	2016/03/12 02:01	2016/03/12 02:42	2016/03/12 03:33	1244.0	1253.5	144.0	153.5	9.5	0.41	4.3	Holed Al liner. Slip catcher. 50 spm, 20-30 rpm, 20-35 kN, Autodriller throughout except manual at top 1 m and bottom 0.5m. Take weight @1243.8 mBRT. No gas detected. Plugged shoe.
C9023E	4	X	2016/03/12 04:53	2016/03/12 05:43	2016/03/12 06:26	1253.5	1263.0	153.5	163.0	9.5	0.43	4.5	Holed Al liner. Slip catcher. 50 spm, 30 rpm. Autodriller to 1256 mBRT then manual to TD. Fluctuated WOB (0-70kN) while autodriller then stable while manual (15-35 kN). No gas detected. Plugged shoe.
C9023E	5	X	2016/03/12 07:27	2016/03/12 08:21	2016/03/12 09:14	1263.0	1272.5	163.0	172.5	9.5	0.54	5.7	Holed Al liner. Slip catcher. 50 spm, 20-30 rpm. Autodriller to TD throughout (20-30, 50-70 kN) except top 1 m. No gas detected. Strongly plugged shoe.
C9023E	6	X	2016/03/12 10:22	2016/03/12 11:20	2016/03/12 12:16	1272.5	1282.0	172.5	182.0	9.5	0.45	4.7	Holed Al liner. "Oniba" shoe & slip catcher. 50 spm, 20 rpm, 25-35 kN. Autodriller to TD throughout except top 1.5 m and bottom 0.5 m. Large WOB drop @1279 mBRT. Take torque @1281.3 & 1281.5 mBRT. Plugged shoe not so strongly. Water overflowed from drill pipe when drill pipe was disconnected for recovering core barrel.
C9023E	7	X	2016/03/12 13:18	2016/03/12 14:53	2016/03/12 15:41	1282.0	1289.5	182.0	189.5	7.5	0.00	0.0	No recovery. Holed Al liner, "Oniba" shoe & Slip catcher. Coring terminated due to low ROP. 30 spm, 20-60 rpm, 20-40 kN. Autodriller to 1289.5 mBRT Response time of autodriller changed at 1286.7 mBRT
C9023E	8	X	2016/03/12 16:40	2016/03/12 17:15	2016/03/12 18:11	1289.5	1299.0	189.5	199.0	9.5	0.10	1.1	Holed Al liner, normal shoe and short finger catcher. 20-50 spm, 40-60 rpm, 20-30 kN. WOB dropped at 1228.0 mBRT. No plugging @shoe except nozzles (plugged with white sandy clay).
C9023E	9	X	2016/03/12 19:04	2016/03/12 19:51	2016/03/12 20:43	1299.0	1308.5	199.0	208.5	9.5	1.24	13.1	Holed Al liner. "Nazo" shoe (diamond cutting shoe), combo catcher. 50 ppm of H2S detected before laydown. 30-40 spm, 20-40 rpm, 20-50 kN. Plugged shoe. Formation boundary (?) in CC from tuff/volcanic rock to claystone.

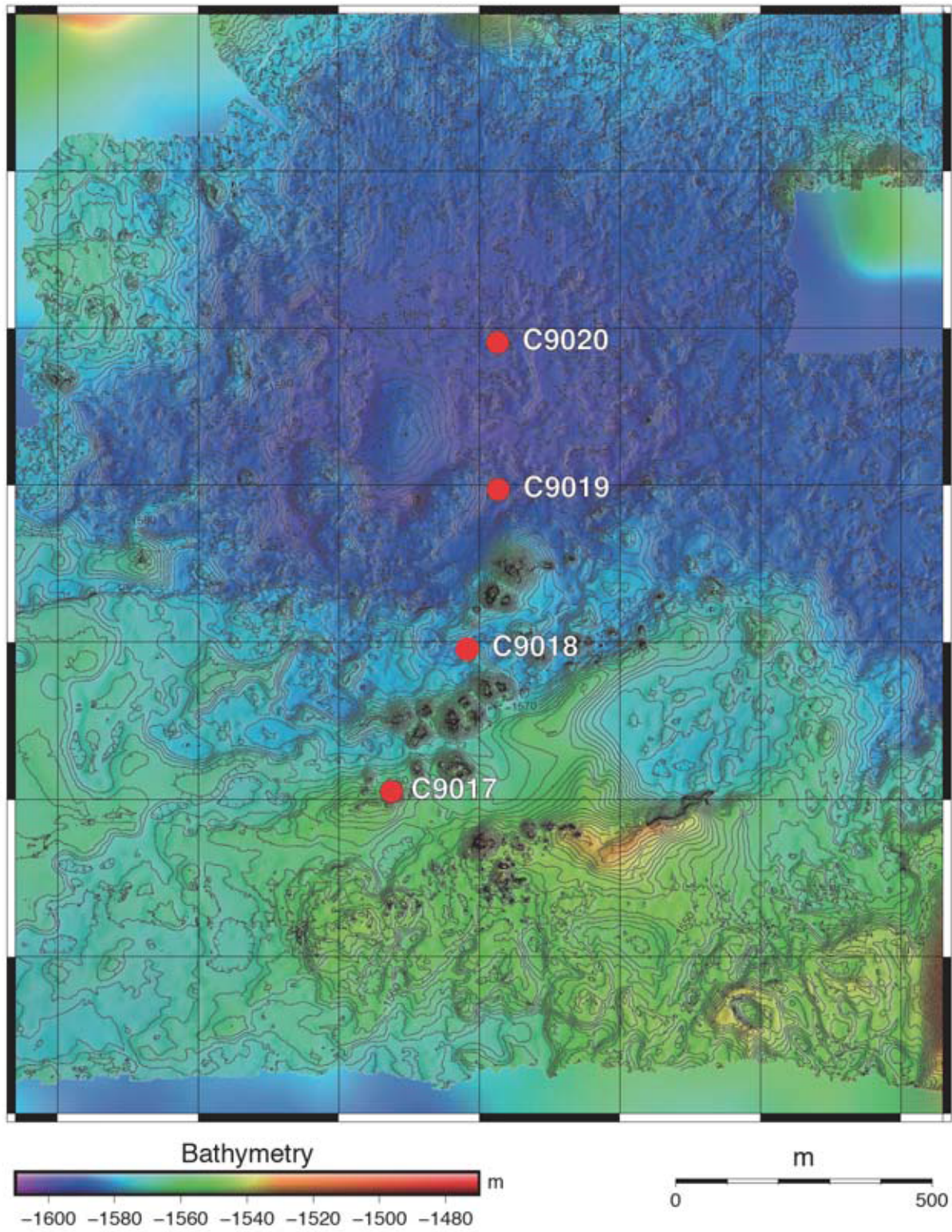


Figure 6-1-1

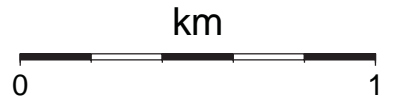
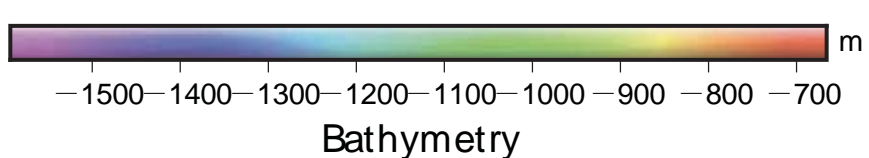
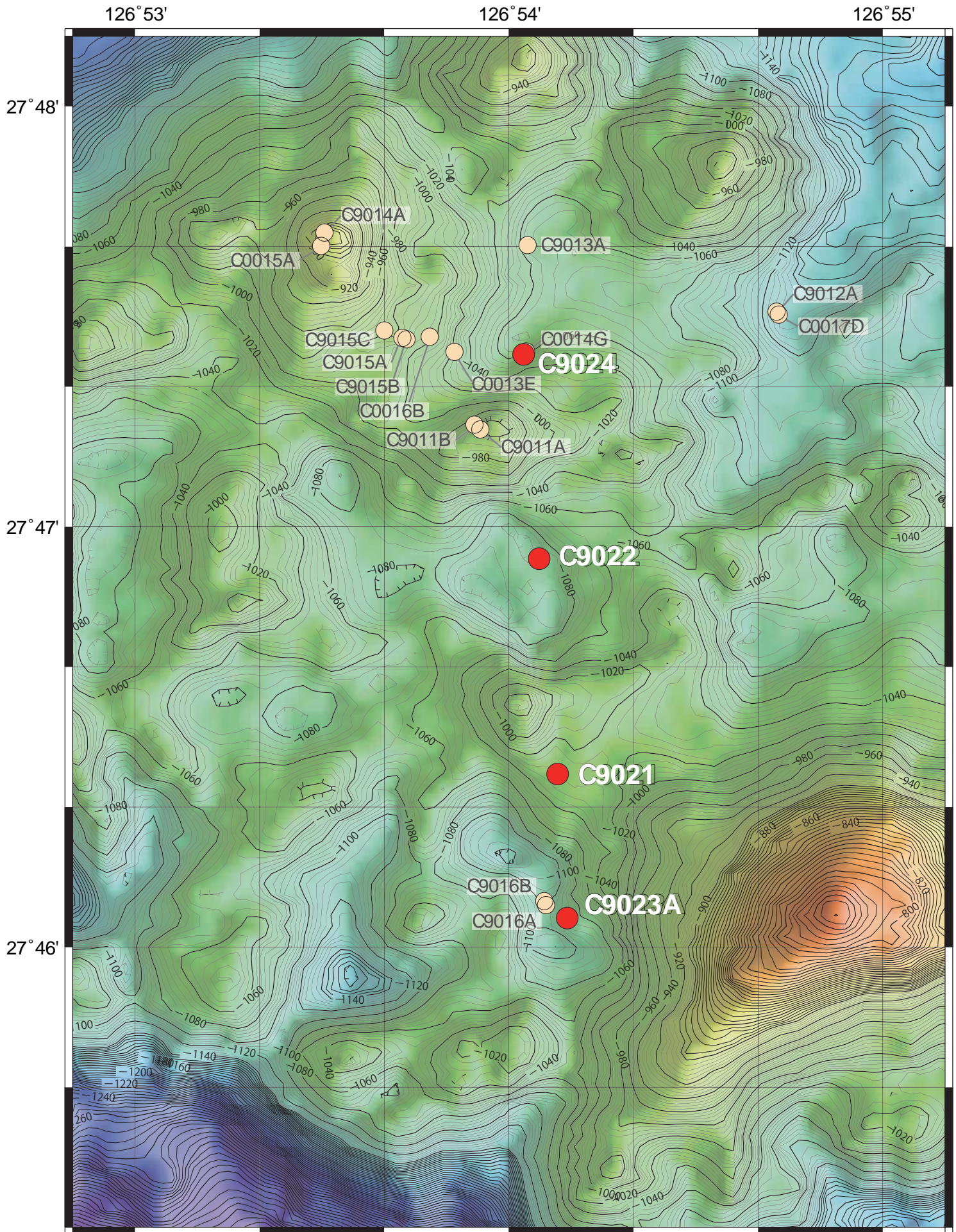


Figure 6-1-2

6.2 Operation log of Leg. 1

6.2.1 Transit to Nago Bay

D/V Chikyu left a quay of Shimizu Port at 09:00 h on 11 February 2016 with 4 shipboard scientists, and started sailing to Nago Bay from 16:30 h after taking a movie by a drone. Test operations for ship's emergency system and a remotely operated underwater vehicle (ROV) were also performed off Shimizu Port. Making up a borehole assembly (BHA) for logging while drilling (LWD) (see Table 6-1-2), setup and maintenance for hydraulic drills, preparation of cultivation monitoring system, POODLE and SAHF, function test on casing hunger running tools (CHRT), safety training for operations in were continued while sailing. The ship reached Nago Bay at 03:00 h on 15 February. Before approaching a rendezvous point of the 1st crew change, a function test in the water for the hydraulic drill with the ROV was performed. The ship arrived at the rendezvous point at 06:00 h, had a crew change including embarkation of 9 scientists while installing a guide rail for the ROV, and departed from Nago Bay at 12:30 h.

6.2.2 Operations in Iheya Small Ridge

Deployment 3rd party tools on Site SIP-NH01, LWD operations at Holes C9017A, C9018A and C9019A were continuously carried out from 16 to 17 February 2016. The memory data of LWDs at Holes C9017A, C9018A and C9019A were successfully retrieved after LWD operation at Hole C9019A. LWD at Hole C9020A was conducted with backup LWD tools on 18 February because primary LWD tools were broken at C9019A. The Hybrid System for Cultivation Monitoring with a temporary flow meter was installed on Hole C9017B on 28 February 2016.

Site SIP-NH01

The first operation of Leg 1 was deployments of SAHF and POODLE (see Chapter 4) by the ROV at a proposal site SIP-NH01. It was 04:00 h on 16 February 2016 of the arrival on-site, then took 2.5 hours to set dynamic positioning mode for the ship control. The ROV dived into the water at 06:45 h with holding SAHF and POODLE, and installed them on the seabed by 08:15 h while preparing shallow hole test for the LWD tools. The ship started moving at 08:30 h to the 1st LWD site after the ROV got back in a cage.

Site C9017

The ship arrived at Site C9017 (proposal site SIP-NH#01) at 08:45 h on 16 February 2016 while conducting the 1st shallow hole test for the LWD tools at water depth of 130.0

mBRT with pumping rates 350 gpm (with stand pipe pressure (SPP) at 2.6 MPa), 500 gpm (SPP at 5.2 MPa), and 600 gpm (SPP at 7.2 MPa), respectively, and running the BHA. The ROV left the cage for seabed survey at 10:15 h. Meanwhile the BHA was lowered, and the 2nd shallow hole test on LWD tools was conducted at 1514.0 mBRT at 13:00 h without any problems. The BHA spudded in Hole C9017A at the water depth of 1586.5 mBRT (1558.0 mbsl) at 14:30 h, and started LWD with weight on bit (WOB) about 0-20 kN, rotation rate of drill strings about 60 rpm, and pump rate 350 gpm (SPP at 3.0 MPa). The planned target depth was 1787 mBRT (200 mbsf) but we terminated LWD at 1700.0 mBRT (113.5 mbsf) at 01:00 h on 17 February, because rate of penetration (ROP) dropped and inclination showed 5.65 and 5.20 degrees at depths of 1614.6 mBRT (1586.1 mbsf) and 1645.3 mBRT (1616.8 mbsf), respectively. The BHA was recovered above the seabed at 03:45 h, and confirmed no obvious visual damages by ROV observation. The ship started drifting to Site C9018 at 04:30 h while the BHA was pulled out to 1289.0 mBRT.

To install the Hybrid System for Cultivation Monitoring, which consisted of 1st and 2nd Generation Cultivation Cells with a temporary flow meter, on Hole C9017A, the ship came back to the site at 02:00 h on 26 February 2016, and the dynamic positioning system was set at 04:00 h. A running assembly to land Tripod on Hole C9017A was made up from 04:00 h to 07:00 h. The ROV observed a very aggressive hydrothermal flow blew from Hole C9017A. The running assembly was run down, and attempted re-entry in Hole C9017A, but failed due to poor visibility by the hydrothermal flow at 12:00 h. The ROV found a pressure gauge of a tilt lock function of a wellhead on Tripod showed 0 psi (lost pressure to hold the wellhead), so operated ball valves on the wellhead to apply 1000 psi. The tilt lock function recovered and held pressure of 1000 psi. The bottom part (8-1/2 drill collar) of the running assembly was successfully got re-entry at 13:15 h. WOB was took at 30 kN to land Tripod. ROV confirmed all legs of Tripod stranded properly, and then open a ball valve to lock the wellhead at 14:00 h. The running assembly was released from Tripod at 15:30 h, and recovered on deck at 20:00 h. A 10-5/8 inch drilling BHA for opening Hole C9017A was made up and lowered from 21:00 h, and then attempted re-entry through the wellhead of Tripod in poor visibility from 02:15 h on 27 February. The ROV found the wellhead inclined around 30 degree at 03:00 h. The ROV unlocked the tilt lock function at 04:14 h. The wellhead position was set at level by using the drill pipe position with support by the ROV at 06:00 h. The 10-5/8 inch drilling BHA entered in at 06:00 h and started opening hole with WOB about 0-15 kN, rotation rates about 10-30 rpm and pump rates around 200-250 gpm (SSP around 0.4-0.9 MPa) from 1587.5 to 1600.0 mBRT (1.0 to 13.5 mbsf). The ROV observed the inclination became larger while

drilling. We decided to abandon Hole C9017A and to drill new hole for deployment the monitoring system without Tripod. The 10-5/8 drilling BHA was pulled out 2 m above the seabed at 08:30 h.

Hole C9017B was spudded at 13 m from Hole C9017A at the water depth of 1586.0 mBRT (1586.0 mbsl) at 08:30 h on 27 February 2016, and drilled out to 1636.0 mBRT (50.0 mbsf) with 10-5/8 inch drilling BHA by 12:30 h. The 10-5/8 inch drilling BHA was pulled out and recovered on deck at 16:00 h while the ship moved to 8 mile upstream of Hole C9017B. Five and a half inch casing was made up from 16:00 h to 19:45 h. The master bushing and outer ring of the rotary table was removed to transport the Hybrid System from the drill floor to the moon pool. Making up the Hybrid System and connecting on the top of the 5-1/2 inch casing assembly was completed at 22:00 h. Lowering the 5-1/2 inch casing assembly was started at 23:00 h. The ship started approaching to Hole C9017B at 01:30 h on 28 February. The ROV started seabed survey to find the hole at 03:15 h, and found the hole blew a hydrothermal flow at 04:15 h. The 5-1/2 inch casing assembly was successfully got re-entry in Hole C9017B at 05:00 h and run down to 1608.5 mBRT (22.5 mbsf) with WOB at less than 10 kN. The Hybrid system was landed directly on Hole C9017B and released from the running tool at 05:30 h. The running tool was pulled out and recovered on deck at 09:00 h.

A running tool for recovering Tripod was made up at 13:15 h on 28 February 2016, and lower to Tripod on C9017A at 13:45 h. The running tool latched on Tripod at 15:00 h, and Tripod was successfully recovered on deck at 18:30 h.

Site C9018

The ship reached Site C9018 (proposal site SIP-NH02) at 05:15 h on 17 February 2016. The BHA was run from 1289 mBRT at 06:00 h. We had a seabed survey with the ROV from 06:30 h while running and a shallow test on the LWD tools. The BHA spudded in Hole C9018A at the water depth of 1613.5 mBRT (1585.0 mbsl) at 08:00 h, and started LWD with WOB about 0-25 kN, rotation rates about 50 rpm, and pump rate 350 gpm (SPP at 3.2 MPa). However, LWD was quitted at 1623.0 mBRT (9.5 mbsf) at 11:15 h due to increase of SPP and quite low ROP. The BHA was pulled out to 1562 mBRT, and confirmed no obvious visual damage by the ROV at 12:30 h. The ship started drifting to Site C9019 while pulling out BHA from 1562 mBRT to 1478 mBRT.

Site C9019

Seabed survey at Site C9019 (proposal site SIP-NH03) was started from 13:30 h on 17 February 2016. The BHA was lowered from 14:00 h and spudded in Hole C9019A at the

water depth of 1630.5 mBRT (1602.0 mbsl) at 14:30 h. LWD was started with washing down to 1634.0 mBRT (3.5 mbsf) and drilling down with WOB about 0-20 kN, rotation rates about 30 rpm, and pump rate about 350 gpm (SPP at 3.1 MPa). However, LWD was stopped at 1645.5 mBRT (15.0 mbsf) because SPP dropped from 3.0 MPa to 2.0 MPa at 19:15 h. The BHA was pulled out of the hole above the seabed, and found severe damage on a connecting part between geoVISION and arcVISION of LWD tools. We decided to abandon the hole and started recovering the BHA to the surface at 20:00 h. While preparing backup LWD tools, we took a seabed survey around Hole C9017A if any hydrothermal flow occurred as a preparation for installation of a cultivation monitoring system.

Site C9020

We arrived at Site C9020 (proposal site SIP-NH04) at 06:00 h on 18 February 2016 while making up and running LWD BHA. Shallow hole tests on the backup LWD tools was conducted without any problem at water depths of 77.5 mBRT and 1508.0 mBRT with pump rates at 350 gpm, 500 gpm and 600 gpm, respectively. The BHA spudded in Hole C9020A at the water depth of 1628.0 mBRT (1599.5 mbsl) at 13:00 h. LWD was conducted while increasing rotation rate to 50 rpm and pump rate at 500 gpm (SPP at 6.7 MPa), but given up at 1637.0 mBRT (9.0 mbsf) at 18:00 h because ROP showed less than 3 m/hour. The ship started sailing to Iheya North Knoll after the BHA was recovered on deck at 22:30 h.

6.2.3 Operations in Iheya North Knoll

LWD operations at Holes C9021A, C9022A and C9023A and deployments the 2nd Generation Cultivation Monitoring System with a temporary flow meter on Hole C9024A (see Table 6-2 for each location) were carried out from 18 February to 25 February 2016. Also, ROV penetrated each corrosion cap of Holes C0014G and C0013E with a hydraulic drill to set a temporary flow meter on 22 February; it was set only on Hole C0014G because no hydrothermal activity was observed at C0013E.

Site C9021

The ship reached Site C9021 (proposal site SIP-IN03) and set the dynamic positioning mode at 01:00 h on 19 February 2016. The ROV dove into the water for seabed survey, and started survey from 02:30 h. Meanwhile, the BHA was make up and started running at 02:00 h. The Shallow hole tests on LWD tools at water depths of 78.5 mBRT and 956 mBRT were carried out and confirmed no problem with pump rates 350 gpm (SPP at 3.0

MPa), 500 gpm (SPP at 6.3 MPa) and 600 gpm (SPP at 9.3 MPa). The BHA spudded in Hole C9021A at the water depth of 1049.0 mBRT (1020.5 mbsl) at 06:45 h, and started LWD with washing down to 1060.5 mBRT (11.5 mbsf) with WOB at 0-5 kN and pump rate at 350 gpm (SPP at 3.0 MPa). LWD was continued with rotating the drill string at 45 rpm at the depth of 1060.5 mBRT (11.5 mbsf) with WOB at 0-5 kN and pump rate at 350 gpm (SPP at 3.2 MPa) at 08:00 h, but paused at the depth of 1064.5 mBRT (15.5 mbsf) due to signal lost from LWD tools at 08:15 h. The signal recovered when the pump rate was set at 380 rpm (SPP at 3.6 MPa). LWD was resumed and continued from 1064.5 to 1150.5 mBRT (15.5 to 101.5 mbsf) with WOB around 0-10 kN, rotation rate around 50-80 rpm, pump rate at 350 gpm (SPP at 3.6 MPa). Several stalls and increases of torque and SPP were observed below 1128 mBRT (79.0 mbsf). Over-pull about 100 kN happened at the depth of 1050.5 mBRT (101.5 mbsf). The drill strings were released at 15:45 h after working pipe with rotation rate at 80 rpm, pump rate at 500 gpm (SPP around 7.0-7.6 MPa), spotting 10 cubic meters of seawater gel (SWG) 3 times. We decided to abandon Hole C9021A, and started pulling out the BHA. The BHA was recovered for rearranging drill stands by 800 mBRT, confirmed no obvious visual damage by the ROV, and then run back to 873 mBRT. The ship started drifting to Site C9022 at 19:30 h.

Site C9022

Seabed survey at Site C9022 (proposal site SIP-IN02) by the ROV was conducted from 21:00 h 19 February 2016 while shallow hole on the LWD tools with pump rates at 350 gpm (SPP at 3.0 MPa), 500 gpm (SPP at 6.3 MPa), and 600 gpm (SPP at 8.7 MPa), respectively. Hole C9022A was spudded in at the water depth at 1116.5 mBRT (1088.0 mbsl) at 22:30 h, and started LWD with WOB around 0-13 kN and pump rate at 350 gpm (SPP at 3.0 MPa). LWD was continued with WOB around 0-20 kN, rotation rate at 60 rpm and pump rate around 350-380 gpm (SPP around 3.2-4.3 MPa), and reached the TD 1354.5 mBRT (238.0 mbsf) at 15:45 h on 20 February. The BHA was pulled out of the hole and confirmed no obvious visual damage by the ROV. Pulling out was continued to 568.0 mBRT at 19:30 h to rearrange drill stands for the next operation while the ROV took a survey on the hole. The ROV was recovered on deck at 20:00 h to equip a hydraulic drill.

Site C9023

The ROV dove into the water at 22:00 h on 20 February 2016, and started seabed survey at 23:00 h while running the BHA and shallow hole test at 1015.0 mBRT on the LWD tools with pump rates at 350 gpm (SPP at 3.0 MPa), 500 gpm (SPP at 6.3 MPa) and

600 gpm (SPP at 8.7 MPa). The BHA spudded in Hole C9023A at the water depth at 1100.0 mBRT (1071.5 mbsl) at 00:00 h on 21 February, and started LWD with WOB around 0-40 kN, rotation rate at 45 rpm, and pump rate at 350 gpm (SPP at 3.0 MPa). LWD was continued to 1278.0 mBRT (178.0 mbsf) while spotting 5 cubic meter of SWG at every 9 m penetration below 1118.0 mBRT (18.0 mbsf). The pump rate was set at 380 gpm (SPP at 3.8 MPa) from 1121.0 to 1152.5 mBRT (21.0 to 52.5 mbsf) to reduce signal noise of LWD tools, and returned to 350 gpm when the signal quality was recovered. The pump rate was escalated from 350 gpm to 400 gpm (SPP at 4.1 MPa), 450 gpm (SPP at 5.3 MPa) and 475 gpm (SPP at 6.0 MPa) at 1278.0 mBRT (178.0 mbsf) because temperature signal from arcVISION showed higher than 48°C. The signal was stayed around 60°C when the pump rate was decreased at 450 gpm. So, LWD was resumed with pump rate at 450 gpm (SPP at 6.0 MPa), and reached the TD 1300.0 mBRT (200.0 mbsf) at 17:45 h. The speed of pulling out was controlled at 35 m/h to take up-logging with pump rate at 400 gpm and rotation rate at 60 rpm from 1300.0 to 1278.0 mBRT (200.0 to 178.0 mbsf), then increased after up-logging. The pump rate was increased to 500 gpm, 600 gpm, 700 gpm and finally 800 gpm with spotting kill mud while pulling out the BHA because the temperature signal jumped above 100 °C. The SPP suddenly increased from 5 MPa to 25.4 MPa at 1122.0 mBRT (22.0 mbsf). The BHA was pulled out above the seabed without pumping. Meanwhile, we observed massive hydrothermal flow from Hole C9023A by ROV, and started sailing to Hole C0014G from 23:30 h. The BHA was recovered on deck at 04:00 h on 22 February.

Hole C0014G

The ROV dove into the water with a hydraulic drill to penetrate the corrosion cap of Hole C0014G at 00:30 h on 22 February 2016. At the first trial was failed due to short stroke. The ROV was recovered on deck to change the hydraulic drill from short to long one, and then dove again at 04:15 h. At the second time, we successfully penetrated through the cap and made an aggressive hydrothermal flow. The ROV was recovered on deck to hold the 1st Generation Temporary Flowmeter at 05:45 h, and dove into the water again at 07:30 h. The ROV successfully installed the 1st Generation Temporary Flowmeter on the corrosion cap of C0014G at 08:45 h. We confirmed an analogue flow meter equipped on the 1st Generation Temporary Flowmeter worked well by reading the gauge by the ROV at 19:45 h.

Hole C0013E

The ROV dove into the water to make a hole on the corrosion cap of Hole C0013E

with hydraulic dill at 14:00 h 22 February 2016 after maintenance and trouble shooting on communication system. The corrosion cap was drilled but no hydrothermal flow was observed. We decided to cancel to set the 1st Generation Temporary Flowmeter on this hole.

Site C9024

A jetting assembly of 20 inch casing with a wellhead was started making up from 10:30 h on 22 February while ROV operation at Holes C0014G and C0013E for reactivation hydrothermal flow and temporary flow meter deployment. Seabed survey was conducted 19:45 h - 20:30 h. The jetting assembly was lowered from 23:15 h and tagged the seabed at the water depth of 1086.5 mBRT (1058.0 mbsl) at 05:30 h on 23 February. The 20 inches casing was successfully jetted down to 1104.0 mBRT (17.5 mbsf) at Hole C9024A at 06:30 h. The ROV activated a releasing function on a running tool of the jetting assembly, and confirmed the casing was released from the running tool at 08:00 h. The running tool was recovered on deck and making a 10-5/8 inch drilling BHA was started at 15:15 h. The drilling BHA was lowered from 17:00 h and got re-entry in the wellhead at 22:00 h. Hole C9024A was washed down from 1104.0 to 1113.0 mBRT (17.5 to 26.5 mbsf), and then drilled down with sweeping 5 cubic meter of SWG at every joint. Drilling down was paused at 1186.5 mBRT (100.0 mbsf) when hydrothermal flow was coming out from the wellhead at 04:00 h on 24 February, and resumed at 04:15 h after confirming the flow was stable. The drilling BHA reached the TD 1286.5 mBRT (200.0 mbsf) at 11:45 h, and pulled out to the surface at 15:15 h. Five and a half inch casing assembly was made up from 15:15 h to 19:30 h. The ship moved to 10 miles up-current from Hole C9024A. The 5-1/2 inch casing assembly was run down from 23:30 h while the ship approaching to Hole C9024A. The master bushing and outer ring of the rotary table was removed to transport the 2nd Generation Cultivation Monitoring System equipped a temporary flow meter from the drill floor to the moon pool. Making up the monitoring system and connecting on the top of the 5-1/2 inch casing assembly was completed at 09:00 h on 25 February. Lowering the 5-1/2 inch casing assembly was resumed at 09:00 h. The 5-1/2 inch casing assembly went through the wellhead of Hole C9024A at 12:00 h and run down to 1268.4 mBRT (181.9 mbsf; 0.5 m above the landing point) with taking weight at 10-15 kN. Pulling out and running in the 5-1/2 inch casing assembly was repeated because inclination of the string was observed. Over-pull around 30-50 kN (maximum 100 kN) was observed while the 5-1/2 inch casing assembly was pulled out to 1250.5 mBRT (164.0 mbsf) to check the condition of the landing seal. The 5-1/2 inch casing assembly was run down again with taking 50 kN to land the monitoring system.

The monitoring system was installed on the wellhead but not completely landed; a 15 cm gap was observed between the wellhead and the monitoring system. The ROV activated the releasing function on the casing running tool to leave the monitoring system 15:30 h, closed valves except a line to the flow meter, and then was recovered on deck at 18:30 h. The running tool was released and recovered on deck at 22:30 h. The ship started sailing to Site C9017 in Noho at 22:30 h.

6.2.4 Transit to Nago Bay

All the operation on site in Leg 1 was completed on 28 February 2016. The ship started sailing from Site C9017 to Nago Bay from 20:00 h and reached the meeting point for crew change in Nago Bay at 04:45 h on 29 February. All Leg 1 shipboard scientists except 3 persons disembarked safely by 13:30 h.

6.3 Operation log of Leg. 2

6.3.1 Exchange of members

Twenty-seven shipboard scientists for Leg 2 embarked Chikyu by 13:30 on 29 February 2016. The ship sailed to Noho site in Iheya Small Ridge while preparing coring tools (hydraulic piston coring system (HPCS) and extended shoe coring system (ESCS)). Also, all crews and scientists attended safety trainings for operation under hydrogen sulfide during transit.

6.3.2 Operation in Iheya Small Ridge

Cores were collected at Sites C9019 and C9017 from 2 to 4 March 2016 (Table 6-1-3). Borehole temperature measurement with TRDT and PPS71 was attempted at Hole C9017C. Also, the ROV recovered the temporary flow meter installed at Hole C9017B during Leg 1 on 5 March.

Site C9019

The ship arrived at Site C9019 at 05:00 h on 1 March 2016. Making up and running a coring BHA (see Table 6-1) were started after Guide Horn was installed under the drill floor. The BHA spudded in Hole C9019B at 19:37 h at water depth of 1628.5 mBRT (1600.0 mbsl), and cut a core with HPCS. Coring tools was changed from HPCS to ESCS because Core C9019B-1H showed partial penetration. Hole C9019C was spudded at 22:07 h at water depth at 1629.0 mBRT (1600.5 mbsl). Coring operation was quitted after cutting the 1st core due to bad hole condition. The coring BHA was pulled out to 1400 mBRT, and the ship started moving to Site C9017 at 03:00 h on 2 March.

Site C9017

The coring BHA was run down and spudded in Hole C9017C at water depth of 1586.5 mBRT (1558.0 mbsl) at 06:52 h on 2 March 2016. Coring at Hole C9017C was started and cut 3 cores with ESCS from 1586.5 to 1618.5 mBRT (0 to 32.0 mbsf) while sweeping with 5 cubic meter of SWG every after core retrieving. Coring system was changed to HPCS and cut 8 cores from 1618.5 to 1660.0 mBRT (32.0 to 73.5 mbsf) while sweeping with 5 cubic meter of SWG every after core retrieving. Coring system was returned to ESCS and cut 5 cores from 1660.0 to 1707.5 mBRT (73.5 to 121.0 mbsf) while sweeping with 5 cubic meters of SWG every after core retrieving. After hole cleaning with 10 cubic meters of SWG, TRDT was deployed through the drill string to attempt logging for borehole temperature at 12:00 h on 4 March. After keeping 10 minutes at the bottom,

TRDT was recovered on deck at 14:30 h and found no data recorded. PPS71 was run down through the drill string to attempt logging for borehole temperature at 15:00 h after sweeping hole with 10 cubic meter of SWG. PPS71 took survey from 1703.9 to 1591.5 mBRT (117.4 to 5.0 mbsf) while pulled out with 0.1 m/sec. An excessive over-pull (20-30 kN) was observed around 1675-1670 mBRT (88.5-83.5 mbsf). A sinker bar was run to reach PPS71 at 18:15 h. PPS71 was recovered on deck at 20:00 h and found no data recorded. The 2nd trial for TRDT was conducted from 20:00 h to 21:00 h but failed again. A decision was made to quit the logging at Hole C9019C. The ROV recovered the temporarily flow meter set on Hole C9017B while the coring BHA was pulled out of the hole. The coring BHA was recovered on deck at 02:30 h on 5 March, and the ship started sailing to Iheya North Knoll.

6.3.3 Operation Iheya North Knoll

Coring operation at Sites C9021 and C9023 were conducted from 5 to 12 March 2016 (Table 6-1-3). ROV operations to recover the temporary flow meter at Holes C9024A and C0014G during Leg 1 were attempted on 13 March.

Site C9021

We arrived at Site C9021 and started seabed survey with the ROV at 09:30 h on 5 March 2016 while making up and running the coring BHA. The coring BHA touched the seabed at Hole C9021B at water depth of 1049.0 mBRT (1020.5 mbsl) at 10:30 h. Coring operation was started with HPCS at 11:41 h. After cutting Core C9021-1H, the BHA tagged on the seabed again and jetted down from 1049 mBRT to 1058.5 mBRT (0 to 9.5 mbsf). Cores C9021B-2H to 8H was cut with HPCS while sweeping with 5 or 10 cubic meters of SWG every after coring. Several mud waters (SWG, pre-hydrated gel (PHG), and kill mud) were spotted and circulated in the borehole for hole cleaning from 04:00 h to 11:30 h on 6 March because a high torque (around 10 kN m) and an excessive drag down (around 10-15 kN) were observed while drilling down from 1119.0 to 1124.0 mBRT (70.0 to 75.0 mbsf). Coring system was changed to ESCS when cutting the 9th core at 1124.0 mBRT (75.0 mbsf). An over-pull (around 220-240 kN) and a stall from 1127.0 to 1128.0 mBRT (78.0 to 79.0 mbsf) were observed while drilling down after collected Core C9021B-10X. The coring BHA reached TD 1156.5 mBRT (107.5 mbsf) when cutting Core C9021B-12X, and pulled out to 1115.0 mBRT (66.0 mbsf) for TRDT and PPS71 operations. TRDT was started to run down to 1115.0 mBRT (66.0 mbsf) by using the core line winch at 22:00 h, took 10 minutes survey, and then recovered on deck at 01:15 h on

7 March. PPS71 was started to run down to 1115.0 mBRT (66.0 mbsf) at 01:15 h, logged borehole temperature from 1115.0 to 1054.0 mBRT (66.0 to 5.0 mbsf) with 0.1 m/sec, and then recovered on deck at 04:45 h. The coring BHA was pulled out to the surface to confirm if there were any damages, and found the coring bit got damaged.

Site C9023

The coring BHA was made up with a new bit from 09:30 h on 7 March 2016 and run down 1025 mBRT. Seabed survey was carried out from 17:30 h to 18:00 h. After cutting the 1st core at C9023B with ESCS, we noticed a large rock near the hole was in danger of falling on the hole. The coring BHA was pulled out of hole to attempt to move the rock away by the coring BHA but failed. Seabed survey was conducted to core at new hole from 22:30 h to 23:15 h. The coring BHA spudded in C9023C at water depth of 1101.5 mBRT at 23:10 h, and then washed/drilled down from 1101.5 to 1103.0 mBRT (0 to 1.5 mbsf). The 1st core at C9023C with HPCS was attempted to cut from 1103.0 mBRT, but we found a coring shoe was broken and lost when retrieving the core on deck at 01:27 h on 8 March. Seabed survey was performed to get re-entry to Hole C9023B. Hole C9023B was washed and reamed for coring but faced continuous high torques (around 6.0-8.9 kN m) and excessive drag down (around 10-30 kN) around 1114.0 mBRT (9.5 mbsf). We abandoned Hole C9023B at 09:30 h on 8 March, because the condition did not become better by sweeping with 10 kL of PHG with continuous pumping with SWG. Seabed survey was resumed 09:30 h and continued till 13:00 h. We found no mud water flowed from the coring bit when spudding new hole. We attempted to recover the flow by increasing flow rate to remove congestion but failed. The coring BHA was pulled out to the surface at 17:00 h, and the bit was cleaned and removed the congestion by 18:15 h. The coring BHA was made up again and run down to 1030.0 mBRT. Seabed survey was executed at 22:00 h, and the coring BHA tagged on the seabed at Hole C9023D at water depth of 1101.0 mBRT. Coring operation was started at 22:58 h and continued with using HPCS or ESCS while sweeping with 5 or 10 cubic meters of SWG, PHG and/or Guar Gum. The coring BHA was pulled out of the hole because we found ESCS cutting shoe was lost in hole when retrieving Core C9023D-16X on deck at 21:25 h on 10 March. The ROV visually confirmed no obvious damages on the coring BHA were found, and took seabed survey for new hole at 02:30 h on 11 March. The coring BHA tagged on the seabed at water depth at 1100.0 mBRT (1071.5 mbsf) at Hole C9023E. Drilling down without coring was started at 02:32 h and continued to 1225.0 mBRT (125.0 mbsf). The 1st core at Hole C9023E was cut with ESCS from 1125.0 to 1226.0 mBRT (125.0 to 126.0 mbsf). Drilling down without coring was resumed at 20:00 h and reached 1235.0 mBRT at 23:00

h. Coring with ESCS was started and continued from 23:00 h on 11 March through 20:30 h on 12 March. Eight cores were cut from 1235.0 to 1308.5 mBRT (135.0 to 208.5 mbsf) while sweeping 5 or 10 cubic meters of SWG every after core retrieving. TRDT was run down to 1288.0 mBRT (188.0 mbsf) and took survey by using the core line winch at 21:30 h after sweeping hole with 10 cubic meters of PHG and SWG. TRDT was recovered on deck at 23:15 h. PPS71 was run down to 1298.0 mBRT (198.0 mbsf), logged borehole temperature from 1298.0 to 1105.0 mBRT (198.0 to 5.0 mbsf) with 0.1 m/sec, and recovered on deck at 04:45 h but failed data downloading. The coring BHA was pulled out to the surface and laid down by 09:00 h. The Guide Horn was also removed under the drill floor.

Site C0014

The ship arrived at Hole C0014G at 05:54 h 13 March 2016. The ROV dived at 07:30 h and successfully recovered the temporary flow meter installed during Leg 1 while the coring BHA was pulled out of Hole C9023E.

Site C9024

The ROV dived into water at 07:30 h on 13 March 2016 to attempt recover the temporary flow meter installed during Leg 1, moved to Hole C9024A after operation at C0014G. However, all attempts failed to pull the flow meter, and finally the pull rope was torn off. A decision was made to quit the operation at 13:30 h. The ROV was recovered on deck at 14:30 h, and the guide rail for ROV was removed by 16:00 h.

6.3.4 Sailing to Shimizu Port

The ship started sailing to Shimizu at 16:00 h on 13 March 2016 and reached Shimizu port at 09:30 h on March 17.